CRANFIELD UNIVERSITY

A. VELLA

THE DEVELOPMENT OF X-RAY BACKSCATTER IMAGING SYSTEMS THROUGH SIMULATION

CRANFIELD DEFENCE AND SECURITY
Cranfield Forensics Institute

PhD
Academic Year: 2015 - 2018

Supervisor: Dr Matthew J. F. Healy
December 2018

CRANFIELD UNIVERSITY

CRANFIELD DEFENCE AND SECURITY
Cranfield Forensics Institute

PhD

Academic Year 2015 - 2018

A. VELLA

THE DEVELOPMENT OF X-RAY BACKSCATTER IMAGING SYSTEMS THROUGH SIMULATION

Supervisor: Dr Matthew J. F. Healy
December 2018

ABSTRACT

X-ray backscatter has applications in defence and security, medical imaging, astrophysics and industry. The development and testing of X-ray backscatter imaging systems can be achieved not only by experiment, but also by using Monte-Carlo modelling.

The PENELOPE simulation package was chosen for its versatility and transparency. However, PENELOPE is a radiation transport package that is not user-friendly, is not inherently compatible with parallel processing, and is not equipped with the facility to process output data in a way that replicates the output from imaging plates or energy dispersive detectors. Tools called PENMAT and PAXI were written in MATLAB to extend the capability of PENELOPE and so enable the efficient exploration of X-ray backscatter imaging which is the focus of this study.

The enhanced PENELOPE suite was used to model a real thermionic source to validate the process by comparison with experiment, and model virtual sources suitable for exploring fundamental principles of backscatter. Virtual sources were conceived and designed to efficiently characterise various imaging system features. These include mono-directional and mono-energetic sources (to isolate energy dependant scattering cross sections), flat spectrum sources (to objectively characterise transmission through mask materials) and thin ‘wire form’ sources (to simultaneously characterise the spatial resolution and field of view of X-ray optics).

A process of using virtual detectors to feed the input of virtual sources was used to shortcut the repeated computationally expensive modelling of a thermionic tube. With this efficient process and parallel computing, various combinations of pinhole and Coded Aperture optics could be efficiently tested and compared. To enable systematic comparisons the image quality metrics of signal, noise, contrast, resolution, field of view etc. are identified and procedures developed to extract them from images.

For the experimental energy range of likely practical use, it was found that pure tungsten masks were superior to other alloys studied and that a 2mm pinhole gave the most generally suitable resolution/signal compromise. The results were consistent with physical experiment. A range of Coded Apertures were also modelled and compared favourably to experiment. The pinhole work on field of view informs the envelope within which coded apertures could avoid partial coding.

The HEXITEC energy dispersive image plate was used to collect experimental images from a multi material quadrant. The image was simulated accurately using PAXI. Further, modelling with PAXI allowed the distinct interaction processes giving rise to image characteristics to be isolated.

This concept was extended with a unique and innovative 2π hemispherical detector, which efficiently captured backscatter X-rays from carbon, copper, manganese dioxide, and lead when shielded and unshielded. This process allowed the brightness of materials to be studied, as governed by the complex combination of attenuation and cross section with angle. Further, the relative contributions from Compton, elastic and fluorescent processes to image brightness and spectral features could be isolated and compared with angle. This was conducted with/without shielding. This cannot be achieved by experiment, and pilots how modelling can inform the best beam energies and detector angles where the backscatter X-rays contain the right information to characterise materials and structures.

This work includes significant use of simulation and also a strong supporting element of physical experimentation. The development of modelling techniques and their exploitation can give information that physical experiment cannot, whilst experimentation has been shown to validate the use of simulation and identify some limitations.

Keywords:

PENELOPE, Monte Carlo simulation, radiation transport, image quality metrics, contrast, signal-to-noise ratio, spatial resolution, MATLAB, X-ray optics, X-ray sources, X-ray tube, Compton scattering, pinhole mask, coded apertures masks, HEXITEC, xraylib, NIST, Klein-Nishina differential cross section, image brightness, relative yield, energy-probability spectrum, phase-space file, point-spread function.

ACKNOWLEDGEMENTS

First and foremost, I would like to express my sincere gratitude to my supervisor Dr Matthew J. F. Healy for his continuous support of my PhD study. I am extremely grateful for his patience, motivation, and immense knowledge; his guidance helped me in all my research and writing. I could not imagine having a better supervisor and mentor.

I would also like to thank the others on my thesis committee: Prof. David W. Lane and Prof. Shaun Forth, for their insightful comments and encouragement, and feedback which helped me to widen my research from various perspectives.

Special thanks are due to Dr David Lockley, Dr Ian Jupp, and the Defence Science and Technology Laboratory (Dstl) for supporting my research, and for their input and feedback over several years.

My sincere gratitude also goes to Dr Annie Maddison-Warren, Dr Laura Lacey and Dr Mandy Smith, who provided me with useful feedback and support, as well as Beatrice Kingdon and the DocCom for the remarkable work they do for all of the PhD students.

I would like to thank my fellow doctoral students for their feedback, cooperation and (of course) friendship. Working together and sharing the troubles of the PhD path was outstanding.

Finally, I would like to thank my family and friends. Words are not enough to express my gratitude towards my parents Angela and Marcello. Although they hardly understood what I was researching, they were willing to support any decision I made. I consider myself very fortunate to have such a lovely and caring family, standing beside me with their love and unconditional support.

A special thank you goes to my brother Ciro, and my good friend Stefania for always being there whenever I needed someone to talk, and for a genuine laugh.

I owe thanks to an extraordinary person, Giuseppe, for his continued and unfailing love, support and understanding during my pursuit of a PhD degree that made the completion of this thesis possible. He was always there during any times I

thought that it impossible to continue and helped me keep things in perspective. I much value his contribution and sincerely appreciate his belief in me.

Last but not least, I would like to express my eternal gratitude to my dearest uncle Sandro, who, in his short but meaningful life, taught me always to be true to myself and encouraged me to pursue the study of science.

To them I owe everything I am today, and the person I will be tomorrow, and to them I would like to dedicate this thesis.

TABLE OF CONTENTS

ABSTRACT i
ACKNOWLEDGEMENTS v
LIST OF FIGURES xvi
LIST OF TABLES xxxi
LIST OF ABBREVIATIONS xxxiii
1 INTRODUCTION 1
1.1 Chapter Outline 1
1.2 Background 1
1.3 Aims and objectives 3
1.4 Thesis Outline 4
2 X-RAY INTERACTIONS WITH MATTER 7
2.1 Chapter Outline 7
2.2 Definition of X-rays 7
2.3 Definition of interaction cross section 8
2.4 Definition of X-ray general attenuation 10
2.5 Specific interactions leading to beam attenuation 12
2.6 Compton Scatter 13
2.7 Klein-Nishina differential cross section for Compton scatter 15
2.7.1 Calculation of Klein-Nishina Cross Section 17
2.7.2 Correcting Compton scatter cross section with incoherent scattering function 18
2.8 Elastic Scatter 19
2.9 Photoelectric Effect 21
2.10 X-ray Production 21
2.11 Fluorescence X-rays and Auger Electrons 25
2.12 Pair Production 27
2.13 Elemental and molecular available databases 29
2.14 NIST database 29
2.15 Xraylib: X-ray library for X-ray interactions with the matter 30
2.15.1 Data output: xraylib Klein – Nishina differential cross section 30
2.16 Chapter Summary and Critical analysis 31
3 X-RAY IMAGING PRINCIPLES 33
3.1 Chapter Outline 33
3.2 X-ray imaging techniques 33
3.3 X-ray Compton Backscatter Imaging 36
3.4 X-ray backscatter imaging with pinhole 39
3.5 X-ray backscatter imaging with Coded Apertures 42
3.6 Chapter Summary and critical analysis 44
4 REVIEW OF CURRENT MONTE CARLO PARTICLE/PHOTON TRANSPORT SOFTWARE 47

4.1 Chapter Outline 47
4.2 General principles of simulation and modelling 47
4.3 Principles of analytical method 50
4.3.1 SpekCalc deterministic simulation for X-ray tubes 50
4.4 Principles of Monte Carlo modelling 52
4.5 Monte Carlo Simulation or analytical methods? 53
4.6 Monte Carlo simulation of radiation transport 54
4.6.1 Random Number generation in Monte Carlo simulation of radiation transport 55
4.6.1 Mean-free path and interaction cross section defined in Monte Carlo radiation transport 57
4.6.2 Particle tracking and state variables 61
4.6.3 Statistical averages and uncertainties 62
4.6.4 Variance reduction techniques in Monte Carlo codes 63
4.7 Current Monte Carlo codes 65
4.7.1 GEANT 4 68
4.7.2 FLUKA 69
4.7.3 MCNP 70
4.7.4 ESGnrc 70
4.7.5 PENELOPE 71
4.8 Guidelines for choosing the Monte Carlo code 72
4.9 Chapter Summary and critical analysis 73
5 PENELOPE MONTE CARLO SIMULATION CODE FOR BACKSCATTER IMAGING 77
5.1 Chapter Outline 77
5.2 The Monte Carlo simulation code PENELOPE 77
5.3 The radiation transport simulation in PENELOPE 78
5.4 PENELOPE Photon interactions 79
5.4.1 Photoelectric effect 80
5.4.2 Photoelectric absorption and characteristic X-ray emission 81
5.4.3 Compton scattering 81
5.4.4 Elastic scattering 83
5.5 PENELOPE Fortran code structure 84
5.5.1 Penelope.f 85
5.5.2 Rita.f 86
5.5.3 Source.f 87
5.5.4 Timer.f 87
5.5.5 Penvared.f 87
5.5.6 Other features 89
5.6 PENELOPE preliminary input parameters: material.f, PENGEOM and the input file 90
5.7 Material.f for material input information 90

5.7.1 List of materials and tables.f 90
5.8 PENGEOM for modelling the geometries 91
5.8.1 PENGEOM java application 92
5.8.2 PENGEOM parameters 93
5.9 PENMAIN simulation program 97
5.10 How to run a simulation with PENMAIN 99
5.11 The Input file 100
5.11.1 Source description in the input file 101
5.11.2 Materials for running the simulations 102
5.11.3 Geometry definition 103
5.11.4 Variance reduction techniques 103
5.11.5 Emerging particles and angular distributions 103
5.11.6 Impact detector, energy spectra and phase-space file 104
5.11.7 Energy-deposition detectors 105
5.11.8 Absorbed dose distribution 106
5.11.9 Job properties 106
5.12 PENELOPE on High Performance Computer and parallel coding 107
5.13 Phase-Space file as data output for image processing 109
5.14 Integrated energy and PAXI algorithm for PENELOPE image processing 111
5.15 PENMAT: PENELOPE GUI on MATLAB 113
5.16 Chapter summary and critical analysis 114
6 MODELLING X-RAY SOURCES 117
6.1 Chapter Outline 117
6.2 Modelling virtual X-ray Sources 117
6.3 Modelling an X-ray tube in PENELOPE 119
6.3.1 Simulation parameters in the input file 120
6.3.2 Simulation with SpekCalc 122
6.3.3 Measuring the VJ Technologies X-ray source spectra 124
6.3.4 Identifying artefacts in experimental X-ray spectra 127
6.3.5 Modelling Amptek X-123 CdTe in the laboratory environment 129
6.3.1 Peak area comparisons between simulations and experiment 132
6.4 Extended sources and custom energy-distributions 137
6.4.1 Wire source for testing backscatter X-ray detector 137
6.4.1 The thin wire 0-200keV flat X-ray emitter for appraisal of leakage through the masks, image brightness and image quality metrics 139
6.5 Chapter summary and critical analysis 140
7 MODELLING BACKSCATTER IMAGING SYSTEM 144
7.1 Chapter Outline 144
7.2 Modelling the X-ray imaging system 145
7.3 X-ray camera model: first setup 145
7.4 Thin wire 0-200 keV flat X-ray emitter for testing the camera 146

7.5 Energy spectra of the incident beam through the mask materials 148
7.6 Preliminary study on mask materials transmission 150
7.7 Modelling pinhole masks 158
7.8 Adapting the phase-space file to replicate an imaging plate. 158
7.9 Determining the ROI 162
7.10 Imaging quality metrics 163
7.10.1 Spatial resolution 163
7.10.2 Spatial resolution as function of aperture diameter and thickness 163
7.10.3 Estimating the Field of View and Collimation effects 167
7.10.4 Contrast 171
7.10.5 Signal-to-noise ratio 174
7.11 Finding the optimum thickness and aperture diameter of pinhole masks 176
7.12 X-ray camera model: updated model for pinhole and CA imaging 183
7.12.1 Modelling Coded Aperture MURA and mosaicked MURA masks. 185
7.13 Preliminary testing the CA imaging system with a thin wire X-ray emitter 191
7.13.1 Energy-Spectra at the detector 192
7.13.2 200 keV flat wire source image correlation with MATLAB Encoding 193
7.13.3 Exposures from simulating the wire emitter 194
7.13.4 Line-spread-function calculation 194
7.13.5 Signal-to-noise, Contrast-to-noise ratios and Full-Width at half maximum 195
7.14 Measuring point spread functions of simulated pinhole and CA masks 199
7.15 Modelling Am-241 point source 200
7.16 Signal-to-noise, Contrast-to-noise ratios and Full-Width at half maximum 211
7.17 Pilot backscatter simulation of a quadrant test object 215
7.18 Chapter summary and critical analysis 218
8 MODELLING AND TESTING HEXITEC DETECTOR 222
8.1 Chapter Outline 222
8.2 HEXITEC for backscatter imaging 222
8.3 HEXITEC as energy-dispersive detector 223
8.3.1 Characteristics of the HEXITEC detector 223
8.3.2 How the HEXITEC can be used for material characterisation 225
8.3.3 Detector and target layout, shielding and collimation 225
8.3.4 Detector energy calibration, noise and dead pixels. 228
8.4 Pilot use and optimisation of the HEXITEC detector 232
8.4.1 Pilot backscatter images for system optimisation. 233
8.4.2 Noise mitigation by tailoring the low energy threshold 236

8.4.3 Imaging and material characterisation with the HEXITEC detector 239
8.5 Unpacking HEXITEC energy data using MATLAB scripts 240
8.5.1 Spatial windowing / Region of Interest 242
8.6 Monte Carlo modelling HEXITEC image and spectra with different materials and structures. 245
8.6.1 Construction of the geometry file for the HEXITEC detector and test objects 245
8.6.2 Optimising PENELOPE for high backscatter simulation 247
8.6.3 Practical aspects of running on the High-Performance Computer .. 248
8.6.4 Running on HPC 248
8.7 Simulating backscatter from the quadrant as detected by the HEXITEC 249
8.7.1 Simulating backscatter from the single objects of the quadrant as detected by the HEXITEC 252
8.8 Energy windowing to discriminate materials from a whole quadrant simulated image 255
8.9 Determining the origin of image features through particle tracking 257
8.10 Chapter summary and critical analysis 260
9 EXPLORING THE FUNDAMENTAL PHYSICS OF X-RAY BACKSCATTER IMAGING BY SIMULATION WITH A HEMISPHERICAL DETECTOR 264
9.1 Chapter Outline 264
9.2 Exploring the fundamental physics of X-ray backscatter imaging by simulation with a hemispherical detector 264
9.3 Rationale and modelling of a hemispherical detector 265
9.4 Target materials studied with the hemispherical detector 267
9.5 The X-ray source 267
9.6 Hemispherical detector for backscatter X-ray imaging of concealed materials 268
9.7 Image ‘brightness’ as a function of angle 269
9.8 Relative yield as a function of angle 272
9.9 Cross-section as a function of angle 273
9.10 Xraylib for calculating the theoretical cross section 274
9.11 Benchmarking PENELOPE differential cross section against xraylib database with PAXI 274
9.12 Comparison of PENELOPE Compton differential cross section against NIST data 278
9.13 Energy-probability as a function of angle 289
9.14 Interpretation of brightness data 292
9.14.1 Interpretation of brightness data for thin materials 292
9.14.2 Interpretation of brightness data for rotated materials 300
9.14.3 Interpretation of brightness data for thick materials 308

9.14.4 Interpretation of brightness data for thick materials through barriers 315
9.15 Interpretation of relative yield data for thick materials 329
9.15.1 Fluorescence 330
9.15.2 Compton scattering 332
9.16 Interpretation of relative yield data for thick materials through barrier 335
9.17 Interpretation of energy-probability data 344
9.17.1 Interpretation of energy-probability data for thin materials 344
9.18 Interpretation of energy-probability data for thin rotated materials 351
9.18.1 Fluorescence 356
9.18.2 Interpretation of energy-probability data for thick materials 358
9.19 Interpretation of energy-probability data for thick materials with barrier 364
9.20 Chapter summary and critical analysis 377
10 DISCUSSION, CONCLUSIONS AND FUTURE WORK 380
10.1 Chapter Outline 380
10.2 Adapting PENELOPE as a computational instrument for exploring backscatter imaging 381
10.2.1 Discussion 381
10.2.1 Conclusions regarding the use of PENELOPE 382
10.2.1 Future work regarding the use of PENELOPE 383
10.3 Development of PAXI: converting the phase-space file into an image 383
10.3.1 Discussion 383
10.3.1 Conclusions regarding PAXI 384
10.3.1 Future work regarding PAXI 385
10.4 X-ray/gamma-ray sources 385
10.4.1 Discussion 385
10.4.1 Conclusions regarding X-ray/gamma-ray sources 386
10.4.1 Future work regarding X-ray/gamma-ray sources 387
10.5 Pinhole imaging 387
10.5.1 Discussion 387
10.5.2 Conclusions regarding pinhole imaging 388
10.5.3 Future work regarding pinhole imaging 388
10.6 Image quality metrics of pinhole masks 389
10.6.1 Discussion 389
10.6.2 Conclusions regarding image quality metrics of pinhole masks 389
10.6.3 Future work regarding image quality metrics of pinhole masks 390
10.7 Coded aperture imaging 390
10.7.1 Discussion 390
10.7.2 Conclusions regarding coded aperture imaging 391
10.7.1 Future work regarding coded aperture imaging 392
10.8 Image quality metrics of CAs vs pinholes 392

10.8.1 Discussion 392
10.8.1 Conclusions regarding image quality metrics of CAs vs pinholes. 392
10.8.1 Future work regarding image quality metrics of CAs vs pinholes . 393
10.9 Modelling detectors in PENGEOM 393
10.9.1 Discussion 393
10.9.1 Conclusions regarding modelling detectors 393
10.9.1 Future work regarding modelling detectors 393
10.10 Energy-dispersive backscatter X-ray Imaging with the HEXITEC detector 394
10.10.1 Discussion 394
10.10.1 Conclusions regarding the HEXITEC detector 395
10.10.1 Future work regarding the HEXITEC detector 396
10.11 Fundamentals of backscatter imaging with the hemispherical detector 396
10.11.1 Discussion regarding the hemispherical detector 396
10.11.1 Conclusions regarding the hemispherical detector 397
10.11.2 Future work regarding the hemispherical detector 398
10.12 Overall conclusions 399
REFERENCES 402
APPENDICES 417
Appendix A PUBLISHED PAPERS 417
Appendix B NIST Element and Mixtures Cross Sections 420
Appendix C Xraylib Klein-Nishina DCS 431
Appendix D Image brightness – materials kind of interactions 437

LIST OF FIGURES

Figure 2.1 The electromagnetic spectrum. The X-rays are in the range of ionising radiation, with a frequency between 10^{16} and 10^{20} Hz [10]. 8

Figure 2.2 Definition of scattering cross section..... 10

Figure 2.3 X-ray interactions with the matter. When X-rays are emitted from a source and interact with a sample material of thickness dt, they can either be absorbed, transmitted or scattered forwards or backwards. The X-ray beam has initial intensity $I0E$, then the thickness dt absorbs intensity dIE, thus the final intensity is the difference between the beam initial and absorbed intensities..... 11

Figure 2.4 X-rays interaction with matter – cadmium telluride cross section. The photoelectric is the dominant effect for energies up to 50 keV, between 50keV and 5 MeV Compton effect arises and prevails. For energies greater than 1.02 MeV, pair production takes place. 13

Figure 2.5 Compton scattering. The incident photon of energy $h\nu$ interacts with a valence-shell electron that results in ejection of the Compton electron (E_e) and simultaneously emission of a Compton scattered photon $h\nu'$ [15]. 14

Figure 2.6 Compton scattering energy dependence on energy of primary radiation at 45˚, 90˚ and 180˚ scatter angles. 15

Figure 2.7 Klein-Nishina differential cross section as function of the scattering angle for 10 keV (outermost curve), 100 keV (intermediate curve), 1000 keV (innermost curve). Cross-section is represented by the unit radius $re2$ [18]. 17

Figure 2.8 Comparison of incoherent scattering cross section and Klein-Nishina cross section against atomic number Z at 1 keV, 10 keV, 100 keV. 19

Figure 2.9 Elastic scattering process. The incident photon of wavelength λ_1 interacts with an atom, and the scattered photon λ_2 is emitted with the same wavelength and energy. Elastically scattered photons are usually emitted in the forward direction, close to the trajectory of the incident photon. 20

Figure 2.10 X-ray production by bremsstrahlung radiation. Energetic electrons interact with an atomic nucleus of the target material. In a close approach, the positive nucleus attracts the negative electron, causing deceleration and redirection, resulting in a loss of kinetic energy that is converted to an X-ray. The X-ray energy depends on the interaction distance between the electron and the nucleus; it decreases as the distance increases [15]. 22

Figure 2.11 Schematic of X-ray tube. The X-rays are produced by the bremsstrahlung process of energetic electrons. 24

Figure 2.12 X-ray tube spectrum from tungsten target at 60 kV and 100 kV anode voltages. The X-ray continuous spectrum is produced by bremsstrahlung

process, and the characteristic radiation is produced by fluorescence of the tungsten anode target..... 24

Figure 2.13 Generation of a characteristic X-ray in a target atom for an X-ray tube. The incident electron interacts with the K-shell electron (1). If the energy of the incident electron is greater than the K-shell binding energy, the K-shell electron is removed. This leaves a vacancy (2). An electron from the adjacent L-shell fills the vacancy (3). A K_α characteristic X-ray photon is emitted with energy equal to the difference between the binding energy of the two shells. For the tungsten atom (W), a 59.3 keV atom is emitted (4)..... 27

Figure 2.14 Pair production process: a high-energy incident photon, under the influence of the atomic nucleus, is converted into an electron-positron pair. Both electron and positron lose their kinetic energy by excitation and ionisation in the matter they traverse. However, when the positron comes to rest, it combines with an electron producing the two 511-keV annihilation radiation photons. K, L, and M are electron shells. 28

Figure 3.1 X-ray transmission geometry (a) and transmission X-ray image of a suitcase (b). 35

Figure 3.2 X-ray Compton backscatter geometry (a) and X-ray Compton backscatter image of a suitcase (b)..... 37

Figure 3.3 COMScan imaging system..... 37

Figure 3.4 Principle of pinhole imaging projection. The object (letter A), which is assumed to be irradiated, is located at a distance a from the pinhole mask, while the distance pinhole-detector is b. The magnification factor is the ratio $(a + b)a$ of the sum of the distances divided by the object-pinhole distance. The object is reflected or emitted through the pinhole aperture, inverted on the central optical axis and then projected onto the detector. 40

Figure 3.5 Pinhole imaging (a) and multihole imaging (b)..... 43

Figure 3.6 Coded aperture imaging principle. The recorded image of the object through the multihole mask needs to be decoded for the final image reconstruction. 43

Figure 3.7 CA mask patterns: (a) 19x19 MURA, (b) 37x37 NTHT MURA (c) 17x21 Singer Set. 44

Figure 4.1 Computational physics against theoretical and experimental physics 49

Figure 4.2 SpekCalc GUI. This is an example of a 160 keV energy spectrum from a W target. 52

Figure 4.3 Beam attenuation through a thin material of thickness dt. 59

Figure 4.4 Angular deflections in single-scattering event. 62

Figure 4.5 Schematic of a Monte Carlo simulation of an electron producing one (a) and five (b) X-ray photons (when particle splitting is enabled)..... 64

Figure 5.1 Atomic photoelectric cross sections for carbon, iron, and uranium as function of photon energy E [1]..... 81

Figure 5.2 Structure of the PENELOPE package. The fsource folder includes the libraries Penelope.f, rita.f, penvared.f, material.f, pengeom.f, timer.f. 85

Figure 5.3 PENGEOM.jar Java text editor. In this example, an accelerator head is designed. 92

Figure 5.4 Example of 2D (a) and 3D (b) view in PENGEOM of an accelerator head and a water phantom. The different colours represent a different kind of materials in the geometry file..... 93

Figure 5.5 Reduced quadrics and their indexes. 95

Figure 5.6 Rotation of axes with Euler angles. 95

Figure 5.7 Bodies and modules inclusion hierarchy (a) and PENGEOM space sphere definition (b). 97

Figure 5.8 Steps for running a simulation in PENELOPE code system. 100

Figure 6.1 The model of the VJT X-ray tube in PENELOPE. The model has been designed with PENGEOM and consists of a tungsten target anode (Mat 1), and four layers of window material in vacuum (beryllium, glass, transformer oil, Ultem 1000, Mat 2-5). A pencil beam of electrons hits the tungsten and then the photons irradiate the layers before being collected by a virtual CdTe detector placed just outside the exit window. 122

Figure 6.2 X-ray spectra at 80 kV (a), 90 kV (b), 100 kV (c), 120 kV (d), 140 kV (e) and 160 kV (f) simulated in SpekCalc (red) and PENELOPE -A (blue). 125

Figure 6.3 Experimental setup for detecting the X-rays emitted by the X-ray tube with the Amptek X123 CdTe detector. The unshielded detector was placed 1.50 m from the source, then it was shielded with lead to minimize scatter from walls. 127

Figure 6.4 Experimental spectra without shielding (in black), with the shielding (in green), both without RTD, and simulated in PENELOPE-A (in red) and SpekCalc (in blue). The scatter artefact is present in the experiment within the region 70-120 keV, more evident without the shielding (red circle). Hole tailing affects the tungsten peak areas without RTD enabled (orange circle). 128

Figure 6.5 PENGEOM three-dimensional model of the laboratory environment (a). The concrete wall is in red, the lead table top in blue, the lead shielding is in orange, and the lead pinhole is in purple. Inside, the model of Amptek X-123 CdTe (b) with aluminum box (in dark blue) and tungsten collimator in green. (c) is the section of the inside of the Al box (in dark blue), the CdTe

crystal is in purple and the thin beryllium window (in orange) between the CdTe crystal and the tungsten collimator (in green). 130

Figure 6.6 X-ray spectra at 80 kV (a), 90 kV (b), 100 kV (c), 120 kV (d), 140 kV (e) and 160 kV (f) simulated in PENELOPE-B (orange) and experiment (green). 134

Figure 6.7 Spatial distribution of scatter photons over the pixel area 100x100. The pixel area is generated as virtual pixel grid over the 3 mm x 3 mm surface of the detector. In figures, the brightness at 160 kV for Compton scatter (a), and elastic scatter (b). 136

Figure 6.8 Energy-probability spectrum of PENELOPE-B between 70-160 keV. Scatter contribution from simulation is ~10^{-4} less than the total spectrum. 136

Figure 6.9 Wire 0-200 keV flat X-ray emitter (in blue, on the right) in front of the X-ray pinhole camera (on the left). 137

Figure 6.10 Wire 0-200 keV flat X-ray emission. 139

Figure 7.1 (a) shows the X-Ray camera in the experimental setup, (b) shows the PENGEOM model in 3D. (c) is a cross section showing the position of the detector inside the shielding. The following components can be seen in 1b and 1c with the PENGEOM colour code: pinhole mask (W, W Ep. Or Bi All.), in purple, rotation disk, placed in front in front (Al), in red, rotation stage (brass), in light blue, extension (Al), in red, external cylindrical envelopment (Pb), in green, CCD detector (Si), in orange, wire test object (metal) in dark blue. 148

Figure 7.2 The photon energy-probability spectrum for 0.5 mm thickness masks for W, W Epoxy composite and Bi alloy masks without a pinhole [79]. Spectra were tallied at the detector (in orange in figure 1c), behind the pinhole mask (in purple in figure 1b-c) and shielded by a lead-aluminium cylinder (in green in figure 1b-c). 150

Figure 7.3 Transmission of X-rays through masks of material-thickness (1-6 mm) of (a) solid tungsten, (b) lead, (c) tungsten epoxy resin, (d) tungsten epoxy on a 1 mm layer of PLA, (e) bismuth low-melting alloy, (f) bismuth low-melting alloy on a layer of 1 mm ABS, (g) PLA and (h) ABS. 153

Figure 7.4 Transmission of X-rays through masks of material-thickness combinations suitable for use with small pinholes. 155

Figure 7.5 (a) is a scatter plot of the energy of each photon incident on the detector for a 4 mm thickness W mask with a 2 mm diameter aperture (colour scale energy in keV). Fig (b) shows the same integrated energy per pixel presented in 2D to reflect the brightness of an image. 159

Figure 7.6 Image of 0-200 keV photons through pure tungsten for a 1 mm aperture diameter and (a) 1 mm thickness, (b) 2 mm thickness, (c) 4 mm

thickness and (d) 10 mm thickness. At 10 mm thickness, only the central area of the ROI is detected, and the detected wire appears cropped. 160

Figure 7.7 (a) Image of 0-200 keV photons through pure tungsten for a 2 mm thickness and (a) 1 mm aperture diameter, (b) 2 mm aperture diameter, (c) 3 mm aperture diameter. Note large apertures (c) admit more photons than small ones (a, b). 161

Figure 7.8 Image of 0-200 keV photons through a) pure tungsten for thickness 2 mm, b) W Epoxy for thickness 4 mm, and c) Bi alloy for thickness 4 mm. 161

Figure 7.9 Image obtained from test wire using a 2 mm aperture in 2 mm W epoxy. (a) represents the whole image, (b) just the area closely surrounding where the test object signal should geometrically lie, (c) the background region only. 162

Figure 7.10 Image of the test object for a 2 mm thick 2 mm aperture tungsten pinhole mask (a) and the summed y-column pixels across the thin x-axis (maximum uncertainty $\pm 0.87 \cdot 103$) (b). A Gaussian fit has been plotted on the histogram to calculate the FWHM (red line). 164

Figure 7.11 The image spatial resolution available for pinhole masks of different apertures and materials and 2 mm thickness pure tungsten and 4 mm thickness tungsten-epoxy resin and bismuth alloy. 165

Figure 7.12 Image spatial resolution available for pinhole masks of 1 mm, 2 mm and 3 mm apertures, 0.5 – 10 mm thicknesses for W, W epoxy, Bi alloy. 166

Figure 7.13 Image of 200 keV photons through pure W for thickness (a) 2 mm and (b) 10 mm. (b) shows how the effect of the collimation occurs when the mask is thick. The wire is not fully resolved, and edges appear cropped. 167

Figure 7.14 The Field of view in terms of the apparent length (left axis) of a 46 mm test object as a function of pinhole mask thickness at 1 mm (a), 2 mm (b) and 3 mm (c) aperture diameters. 169

Figure 7.15 The Field of View in terms of angle as a function of pinhole mask aperture diameter for 2 mm (a), 4 mm (b) and 7 mm (c) thicknesses. 171

Figure 7.16 Contrast for a 1 mm (A), 2 mm (B) and 3 mm (C) diameter aperture. 173

Figure 7.17 SNR for a 1 mm (A), 2 mm (B) and 3 mm (C) diameter aperture. 175

Figure 7.18 Contrast-object detail 3D surface plot of W (a), W Ep. (b), and Bi all. (c) at 0.5-10 mm thicknesses and 1-2-3 mm aperture diameters. 178

Figure 7.19 Contrast-object detail 2D plot as object size of W, W Ep., and Bi all. at 0.5-10 mm thicknesses and 1-2-3 mm aperture diameters. 178

Figure 7.20 Contrast-angle of view 3D surface plot of W (a), W Ep. (b), and Bi all. (c) at 0.5-10 mm thicknesses and 1-2-3 mm aperture diameters. 180

Figure 7.21 Contrast-object detail as angle of view 2D plot of W, W Ep., and Bi all. at 0.5-10 mm thicknesses and 1-2-3 mm aperture diameters. 180

Figure 7.22 SNR-FWHM 3D surface plot of W (a), W Ep. (b), and Bi all. (c) at 0.5-10 mm thicknesses and 1-2-3 mm aperture diameters. 182

Figure 7.23 FWHM SNR 2D plot of W, W Ep., and Bi all. at 0.5-10 mm thicknesses and 1-2-3 mm aperture diameters. 182

Figure 7.24 The upgraded (a) X-ray camera system setup. (b) Measurements of the X-ray camera. 184

Figure 7.25 Three-dimensional representation of the X-ray camera with air filled 2mm thick pure tungsten pinhole mask (a) (top left) and 4mm thick tungsten-epoxy PLA filled aperture (b) (top right). Two-dimensional camera sections for pure tungsten (c) (bottom left) and tungsten-epoxy (d) (bottom right) mask. The CCD camera is in orange, enclosed in lead-lined shielding in blue while pinhole masks in purple. The X-ray detector is coloured orange and placed in a space filled with air (green). 185

Figure 7.26 X-ray camera with 19x19 mosaicked MURA 2 mm aperture diameter (b) (in front in 3D..... 187

Figure 7.27 CA masks modelled in PENGEOM (on the left) and theoretical (on the right). 188

Figure 7.28 CA 19x19 MURA mosaicked mask modelled in PENGEOM. The mask appears having a symmetric unit pattern, which was reproduced in PENGEOM by using the CLONE function. 189

Figure 7.29 Model of the X-ray detector with a thin wire test object that emits X-rays up to 200 keV..... 191

Figure 7.30 X-ray spectra as energy-probability distribution for W and W Ep. Pinhole masks, 19 MURA and mosaicked MURA masks. All the spectra show characteristic lines from tungsten. MURA and mosaicked MURA present higher intensity as more photons are coming through, and the spectrum appears as a combination of PLA and tungsten spectra. 192

Figure 7.31 MURA pattern (a) is correlated with the image generated at the detector (b) from a 200 keV flat X-ray wire source emitting 10^6 photons to give the correlated (decoded) image (c). 193

Figure 7.32 Exposures generated from a 200 keV flat X-ray wire source emitting 10^6 photons detected and recorded at the detector on the psf-file: (a) pinhole mask, (b) W epoxy pinhole, (c) 19 MURA and (d) mosaicked MURA. Pinhole exposures show a well-defined wire, while MURA and mosaicked MURA exposures appear more blurred and mosaicked MURA presents tails on both sides of the wire (artefact). 195

Figure 7.33 Line-spread functions generated from a 200 keV flat X-ray wire source emitting 106 photons detected and recorded at the detector on the

psf-file: (a) pinhole mask, (b) W epoxy pinhole, (c) 19 MURA and (d) mosaicked MURA. 196

Figure 7.34 Gaussian profile from the exposure (a) of a 200 keV X-ray flat X-ray wire source for calculating the FWHM (b). 197

Figure 7.35 CA 19x19 MURA image correlation for generating the point spread function. (a) is the theoretical 19 MURA mask, (b) is from the phase-space file, (c) is the psf exposure. 200

Figure 7.36 Am-241 source scheme. 201

Figure 7.37 Description of the Am-241 point source in PENELOPE input file. 202

Figure 7.38 Am-241 model in PENGEOM. 203

Figure 7.39 Pinhole and CA masks exposures (on the left) and point spread functions (on the right) of Am-241 point source. (a) (b) are 2 mm thick 2 mm aperture diameter W pinhole, (c) (d) are 4 mm thick 2 mm aperture diam. (filled with PLA) W Epoxy pinhole, (e) (f) are 19 mosaicked MURA, (g) (h) are NTHT 19 mosaicked MURA, (i)(j) are Singer Set and (k)(l) are NTHT Singer Set masks. 206

Figure 7.40 Pinhole and CA masks exposures (on the left) and point spread functions (on the right) of physical Am-241. (a) (b) are 2 mm thick 2 mm aperture diameter W pinhole, (c) (d) are 4 mm thick 2 mm aperture diam. (filled with PLA) W Epoxy pinhole, (e) (f) are 19 mosaicked MURA, (g) (h) are NTHT 19 mosaicked MURA, (i)(j) are Singer Set and (k)(l) are NTHT Singer Set masks. 208

Figure 7.41 Pinhole and CA masks experimental exposures (on the left) and point spread functions (on the right) of physical Am-241. (a) (b) are 2 mm thick 2 mm aperture diameter W pinhole, (c) (d) are 19 mosaicked MURA, (e) (f) are NTHT 19 mosaicked MURA, (g)(h) are Singer Set and (i)(j) are NTHT Singer Set masks. 210

Figure 7.42 Example of profile along y-axis of the central bright area for calculating the FWHM. 211

Figure 7.43 CNR (a), SNR (b), and FWHM (c) of the different pinhole and CA masks. 213

Figure 7.44 Geometrical model of the quadrant exposure setup in front of a 1 m x 1 m x 0.5 m wall and a 0.2 thick lead panel. The detector is placed at 1.30 m and has a 2 mm thickness 2 mm aperture tungsten pinhole mask or a 19 MURA mosaicked mask in front. 216

Figure 7.45 Pinhole simulated (a) and physical (b) exposures, and 19 MURA mosaicked simulated (c) and physical (d) exposures. 217

Figure 8.1 HEXITEC detector experimental setup. The detector was shielded with lead bricks and a tungsten pinhole mask placed in front. 226

Figure 8.2 HEXITEC detector mounted on the X-Y stage. It is possible to move the HEXITEC up/down and/or left/right by driving the two motors using the Autostep application. 227

Figure 8.3 Tungsten pinhole mask 20 x 20 x 2 mm with 1 mm aperture (on the left), and 2 mm aperture (on the right). 227

Figure 8.4 Sample alignment to the X-ray source. 228

Figure 8.5 HEXITEC software processing panel. It is possible to browse the calibration files from the options 'Gradients file' and 'Intercepts file'. 230

Figure 8.6 (a) Backscatter images of the quadrant with the false dead pixels (red circles) and the adjusted calibration (b). The edges of the detector are in white as they are overcounting (blue circle). 232

Figure 8.7 Quadrant test object on an aluminium support and lead sheet on the back. On the top left the copper cube, on the top right the PLA cylinder, on the bottom left the wax cube and, on the bottom, right tin sheet on the aluminium cube. 234

Figure 8.8 Quadrant plus tin 100 s, 1 mm aperture exposure at 70 kV, 100 kV and 160 kV tube anode voltages. Wax appears top left, tin on Al top right, copper bottom left and PLA circle bottom right. 235

Figure 8.9 Quadrant plus tin 100 s, 1 mm aperture energy spectra at 70 kV, 100 kV and 160 kV tube anode voltage. 236

Figure 8.10 Quadrant plus tin 100 seconds exposure, 1 mm aperture, 70 kV (a), 100 kV (b) and 160 kV (c) tube anode voltage with the tailored threshold applied. 238

Figure 8.11 Quadrant plus tin, 100 seconds exposure, 1 mm aperture, 70 kV (green), 100 kV (blue) and 160 kV (red) tube anode voltages, with the tailored threshold applied. 238

Figure 8.12 Fan on aluminium support 100 sec at 1 mm (a) and 2 mm (b) aperture exposure at 160 kV and tailored threshold applied. 239

Figure 8.13 Fan on aluminium support 100 second exposure, 1 mm (blue) 2 mm (red) aperture, 160 kV and tailored threshold applied. 240

Figure 8.14 Quadrant plus tin 100 seconds exposure at 160 kV and 1 mm pinhole aperture in MATLAB. 241

Figure 8.15 MATLAB images of four distinct regions of interest from figure 8.14. MATLAB auto-scales the brightness so each quadrant does not appear exactly the same as in figure 8.14. 243

Figure 8.16 MATLAB energy spectra for the four regions of interest identified in figure 40 with different vertical axis scales. Tin's strong fluorescence at 25.27 keV is not enough for it to exceed the summed energy of Compton scattered

photons off wax, and so it does not appear brighter in a conventional image. Energy windowing at 24 keV would reveal tin clearly. 244

Figure 8.17 The MATLAB spectra from fig 8.16 are summed to create the spectrum visibly identical to the whole spectrum from the whole quadrant shown in figure 8.11, 160 kV, red line. This demonstrates successful deconstruction and synthesis of component spectra. 245

Figure 8.18 The HEXITEC detector modelled in PENELOPE through PENGEOM. 246

Figure 8.19 Geometry of the quadrant sample. The different colours correspond to the different simulated materials, red for the tin cube, blue for wax, green for copper and blue-teal for the PLA. 251

Figure 8.20 Simulated quadrant plus tin integrated energy for number of simulated showers equal to 2.5E10 (a). (b) is the quadrant from HEXITEC pinhole mask exposure. 251

Figure 8.21 Simulated quadrant plus tin spectrum at 180˚ backscatter. The characteristic peaks are: copper at 8.05 keV (K_α), tin at 25.27 keV (K_α) and 28.49 keV (K_β), tungsten at 48.81 keV (Compton), 59.32 (K_α), lead at 74.97 keV (K_α). 252

Figure 8.22 MATLAB energy spectra for the four regions of interest identified in figure 40 with different vertical axis scales. Tin's strong fluorescence at 25.27 keV is not enough for it to exceed the summed energy of Compton scattered photons off wax, and so it does not appear brighter in a conventional image. Energy windowing at 24 keV would reveal tin clearly. 253

Figure 8.23 MATLAB energy spectra for the four regions of interest identified in figure 40 with different vertical axis scales. Tin's strong fluorescence at 25.27 keV is not enough for it to exceed the summed energy of Compton scattered photons off wax, and so it does not appear brighter in a conventional image. Energy windowing at 24 keV would reveal tin clearly. 254

Figure 8.24 Simulated image emphasising the copper in the quadrant. 256

Figure 8.25 Simulated image emphasising the tin in the quadrant. 256

Figure 8.26 Simulated image emphasising materials with large Compton scatter cross sections. 257

Figure 8.27 PENELOPE simulation revealing only photons generated by fluorescence. 258

Figure 8.28 PENELOPE simulation revealing only photons undergoing Compton scatter. 259

Figure 8.29 PENELOPE simulation revealing photons that have been generated by fluorescence and have also been scattered in the test object. 259

Figure 9.1 Hemispherical detector model in purple and the target material in orange are shown in two dimensions and three dimensions in (a) and (b). Target materials were carbon, copper, manganese dioxide, aluminium, iron and lead simulated with different configurations..... 266

Figure 9.2 Hemispherical detector annulus from the azimuthal angle recorded on the phase-space file. Annuli were calculated from 0 to 90 degrees. Each annulus is 2.5 degrees thick. 269

Figure 9.3 Detected inelastic scatter relative brightness in terms of I(E) at all angles in XY (a) and I(E) YZ (c) projections for MnO_2 at 25keV. From the psf-file it is possible to select the annulus from the azimuthal angle (b) (d). .. 270

Figure 9.4 Detector detected fluorescence relative brightness in terms of I(E) at all angles in XY (a) and YZ (b) projections for MnO2 at 25keV. From the psf-file it is possible to select the annulus from the azimuthal angle (c) (d). .. 271

Figure 9.5 Differential cross section of thin carbon, copper and manganese dioxide at different monoenergetic and monodirectional beam (25, 150 and 500 keV) at 10˚ (a), 45˚ (b) and 75˚ (c). The dashed lines are the theoretical DCS from NIST database [104], while the bars are the DCS from PENELOPE simulations..... 278

Figure 9.6 Differential cross section derived from 1 mm thick carbon at 25 keV (a), 150 keV (b) and 500 keV (c). The differential cross section calculated in PENELOPE is plotted in red with error bars, while the Compton scatter differential cross section extracted from NIST database with xraylib tool is plotted in blue. 281

Figure 9.7 Differential cross section derived from 0.1 mm thick aluminium at 25 keV (a), and 1 mm thick aluminium at 150 keV (b) and 500 keV (c). The differential cross section calculated in PENELOPE is plotted in red with error bars, while the Compton scatter differential cross section extracted from NIST database with xraylib tool is plotted in blue. 282

Figure 9.8 Differential cross section derived from 0.01 mm thick iron at 25 keV (a), 0.1 mm thick iron at 150 keV (b) and 1 mm thick iron 500 keV (c). The differential cross section calculated in PENELOPE is plotted in red with error bars, while the Compton scatter differential cross section extracted from NIST database with xraylib tool is plotted in blue. 284

Figure 9.9 Differential cross section derived from 0.01 mm thick copper at 25 keV (a), 0.01 mm thick copper at 150 keV (b) and 1 mm thick copper 500 keV (c). The differential cross section calculated in PENELOPE is plotted in red with error bars, while the Compton scatter differential cross section extracted from NIST database with xraylib tool is plotted in blue. 285

Figure 9.10 Differential cross section derived from 0.1 mm thick manganese dioxide at 25 keV (a), 0.1 mm thick manganese dioxide at 150 keV (b) and 1 mm thick manganese dioxide 500 keV (c). The differential cross section calculated in PENELOPE is plotted in red with error bars, while the Compton

scatter differential cross section extracted from NIST database with xraylib tool is plotted in blue. 287

Figure 9.11 Differential cross section derived from 0.001 mm thick lead at 25 keV (a), 0.01 mm thick lead at 150 keV (b) and 0.1 mm thick lead 500 keV (c). The differential cross section calculated in PENELOPE is plotted in red with error bars, while the Compton scatter differential cross section extracted from NIST database with xraylib tool is plotted in blue. 288

Figure 9.12 Example of image brightness separated by kind of interactions and relative spectra. They include Compton scatter (a)(b), fluorescence (c)(d) and elastic scatter (e)(f) of 20˚ thick annulus manganese dioxide. 291

Figure 9.13 Compton scatter brightness angular distribution at 25 keV (a), 150 keV (b) and 500 keV (c) for carbon, copper, manganese dioxide, lead, aluminium and iron thin films. In (a) the graph I(E) y-scale was zoomed (top right) to a smaller scale. 295

Figure 9.14 Elastic scatter brightness angular distribution at 25 keV (a), 150 keV (b) and 500 keV (c) for carbon, copper, manganese dioxide, lead, aluminium and iron thin films. In (a) the graph I(E) y-scale was zoomed (top right) to a smaller scale. 297

Figure 9.15 Fluorescence brightness angular distribution at 25 keV (a), 150 keV (b) and 500 keV (c) for carbon, copper, manganese dioxide, lead, aluminium and iron thin films. 300

Figure 9.16 Compton scatter brightness angular distribution at 25 keV (a), 150 keV (b) and 500 keV (c) for carbon, copper, manganese dioxide, lead thin rotated 45˚ film. In (a) the graph I(E) y-scale was zoomed (top right) to a smaller scale. 303

Figure 9.17 Elastic scatter brightness angular distribution at 25 keV (a), 150 keV (b) and 500 keV (c) for carbon, copper, manganese dioxide, lead thin rotated 45˚ film. In (a) the graph I(E) y-scale was zoomed (top right) to a smaller scale. 305

Figure 9.18 Fluorescence brightness angular distribution at 25 keV (a), 150 keV (b) and 500 keV (c) for carbon, copper, manganese dioxide, lead thin rotated 45˚ film. 307

Figure 9.19 Compton scatter brightness angular distribution at 25 keV (a), 150 keV (b) and 500 keV (c) for carbon, copper, manganese dioxide, lead thick films. In (a) the graph I(E) y-scale was zoomed (top right) to a smaller scale. 310

Figure 9.20 Elastic scatter brightness angular distribution at 25 keV (a), 150 keV (b) and 500 keV (c) for carbon, copper, manganese dioxide, lead thick films. In (a) the graph I(E) y-scale was zoomed (top right) to a smaller scale. .. 312

Figure 9.21 Fluorescence brightness angular distribution at 25 keV (a), 150 keV (b) and 500 keV (c) for carbon, copper, manganese dioxide, lead thick films. 315

Figure 9.22 Compton scatter brightness angular distribution at 25 keV (a), 150 keV (b) and 500 keV (c) for carbon, copper, manganese dioxide thick films with aluminium barrier. 318

Figure 9.23 Compton scatter brightness angular distribution at 25 keV (a), 150 keV (b) and 500 keV (c) for carbon, copper, manganese dioxide thick films with iron barrier. 321

Figure 9.24 Elastic scatter brightness angular distribution at 25 keV (a), 150 keV (b) and 500 keV (c) for carbon, copper, manganese dioxide thick films with aluminium barrier. 323

Figure 9.25 Compton scatter brightness angular distribution at 25 keV (a), 150 keV (b) and 500 keV (c) for carbon, copper, manganese dioxide thick films with iron barrier. 325

Figure 9.26 Fluorescence brightness angular distribution at 25 keV (a), 150 keV (b) and 500 keV (c) for carbon, copper, manganese dioxide thick films with aluminium barrier. 327

Figure 9.27 Fluorescence brightness angular distribution at 25 keV (a), 150 keV (b) and 500 keV (c) for carbon, copper, manganese dioxide with iron barrier. 329

Figure 9.28 Fluorescence relative yield angular distribution at 25 keV (a), 150 keV (b) and 500 keV (c) for 5 cm thick carbon, copper, manganese dioxide and lead. 332

Figure 9.29 Compton scatter relative yield angular distribution at 25 keV (a), 150 keV (b) and 500 keV (c) for 50 mm thick carbon, copper, manganese dioxide, lead. 335

Figure 9.30 Fluorescence yield angular distribution at 25 keV (a), 150 keV (b) and 500 keV (c) for 5 cm thick carbon, copper, manganese dioxide, lead and 2 mm aluminium barrier on top. 337

Figure 9.31 Compton scatter yield angular distribution at 25 keV (a), 150 keV (b) and 500 keV (c) for 5 cm thick carbon, copper, manganese dioxide, lead and 2 mm aluminium barrier on top. 339

Figure 9.32 Fluorescence relative yield angular distribution at 25 keV (a), 150 keV (b) and 500 keV (c) for 50 mm thick carbon, copper, manganese dioxide, lead and 2 mm iron barrier on top. 341

Figure 9.33 Compton scatter relative yield angular distribution at 25 keV (a), 150 keV (b) and 500 keV (c) for 50 mm thick carbon, copper, manganese dioxide, lead and 2 mm iron barrier on top. 343

Figure 9.34 Compton scatter energy-probability angular distribution at 25 keV (a), 150 keV (b) and 500 keV (c) for 1 mm thick carbon, copper, manganese dioxide, lead, aluminium and iron thin films. 347

Figure 9.35 Elastic scatter energy-probability angular distribution at 25 keV (a), 150 keV (b) and 500 keV (c) for 1 mm thick carbon, copper, manganese dioxide, lead, aluminium and iron thin films. 349

Figure 9.36 Fluorescence energy-probability angular distribution at 25 keV (a), 150 keV (b) and 500 keV (c) for 1 mm thick carbon, copper, manganese dioxide, lead, aluminium and iron thin films. 351

Figure 9.37 Compton scatter energy-probability angular distribution at 25 keV (a), 150 keV (b) and 500 keV (c) of 1 mm thick rotated carbon, copper, manganese dioxide, lead, aluminium and iron thin rotated 45˚ films..... 353

Figure 9.38 Elastic scatter energy-probability angular distribution at 25 keV (a), 150 keV (b) and 500 keV (c) of 1 mm thick rotated carbon, copper, manganese dioxide, lead, aluminium and iron thin rotated 45˚ films..... 355

Figure 9.39 Fluorescence energy-probability angular distribution at 25 keV (a), 150 keV (b) and 500 keV (c) of 1 mm thick rotated carbon, copper, manganese dioxide, lead, aluminium and iron thin rotated 45˚ films..... 357

Figure 9.40 Compton scatter energy-probability angular distribution at 25 keV (a), 150 keV (b) and 500 keV (c) of 50 mm thick carbon, copper, manganese dioxide and lead thick films..... 360

Figure 9.41 Elastic scatter energy-probability angular distribution at 25 keV (a), 150 keV (b) and 500 keV (c) of 50 mm thick carbon, copper, manganese dioxide, and lead thick films..... 362

Figure 9.42 Fluorescence energy-probability angular distribution at 25 keV (a), 150 keV (b) and 500 keV (c) of 50 mm thick carbon, copper, manganese dioxide, and lead thick films..... 364

Figure 9.43 Compton scatter energy-probability angular distribution at 25 keV (a), 150 keV (b) and 500 keV (c) of 50 mm thick carbon, copper, manganese dioxide and 2 mm barrier of aluminium on top. 366

Figure 9.44 Compton scatter energy-probability angular distribution at 25 keV (a), 150 keV (b) and 500 keV (c) of 5 cm thick carbon, copper, manganese dioxide and 2 mm barrier of iron on top. 368

Figure 9.45 Elastic scatter energy-probability angular distribution at 25 keV (a), 150 keV (b) and 500 keV (c) of 50 mm thick carbon, copper, manganese dioxide and 2 mm barrier of aluminium on top. 370

Figure 9.46 Elastic scatter energy-probability angular distribution at 25 keV (a), 150 keV (b) and 500 keV (c) of 50 mm thick carbon, copper, manganese dioxide and 2 mm barrier of, iron on top. 372

Figure 9.47 Fluorescence energy-probability angular distribution at 25 keV (a), 150 keV (b) and 500 keV (c) of 50 mm thick carbon, copper, manganese dioxide and 2 mm barrier of aluminium on top. 374

Figure 9.48 Fluorescence energy-probability angular distribution at 25 keV (a), 150 keV (b) and 500 keV (c) of 50 mm thick carbon, copper, manganese dioxide and 2 mm barrier of, iron on top. 376

LIST OF TABLES

Table 4.1 Main advantages and disadvantages of analytical and Monte-Carlo simulation models (adapted from (Safety and Reliability Society, 2018)). . 54

Table 4.2 Comparison of Monte Carlo codes PENELOPE, GEANT4, FLUKA, MCNP/MCNPX and ESGnrc. 66

Table 5.1 Predefined reduced quadric surfaces in PenGeom.jar..... 94

Table 5.2 ILB parameters. They identify the details of the beam interaction with the matter. 111

Table 6.1 Window materials and thicknesses used for the simulations. This information was provided by VJ Technologies (VJ Technologies, 2018) manufacturer. 120

Table 6.2 Tungsten characteristic peak areas at the different anode voltages of SpekCalc (SK) simulation and experiment against PENELOPE-A (PEN-A) and PENELOPE-B (PEN-B), and SpekCalc against the experiment (EXP). The peak areas' comparisons are presented as percentage. 132

Table 7.1 Chemical composition in %wt and density of range of materials suitable 156

Table 7.2 Transmission of X-rays detected at 170 keV for practical mask thicknesses. The materials and thicknesses identified as suitable for manufacturing are those with * in the table. 157

Table 7.3 CAs modelled in PENGEOM, material and thicknesses. 186

Table 7.4 Fraction of photons at the detector, SNR, CNR and FWHM from the exposure of a 200 keV flat X-ray wire source. 198

Table 7.5 Am-241 physical source gamma emission lines and geometrical parameters. 200

Table 7.6 Pinhole and CA masks simulated and measured CNR, SNR, and FWHM. 212

Table 7.7 Pinhole and 19 MURA mask backscatter simulation data..... 216

Table 8.1 Energy threshold values calculated from the average of the calibration files and the ADU channels. 231

LIST OF ABBREVIATIONS

ABS	Acrylonitrile butadiene styrene
AOV	Angle Of View
CA	Coded Apertures
CBI	Compton Backscatter Imaging
CDS	Cranfield Defence and Security
CdTe	Cadmium Telluride
CFI	Cranfield Forensics Institute
CNR	Contrast-to-Noise Ratio
CT	Computed Tomography
DCS	Differential Cross Section
EGSnrc	Electron Gamma Shower for National Research Council
FLUKA	FLUktuierende KAskade
FOV	Field Of View
FWHM	Full-Width at Half Maximum
GEANT4	GEometry ANd Tracking
GUI	Graphic User Interface
HPC	High-Performances Computer
HPC	High energy X-ray imaging technology
IE	Integrated Energy
ILB	Interaction LaBel
IT	Information Technology
KN	Klein-Nishina
MCNP	Monte Carlo N-Particle transport code
MURA	Modified Uniformly Redundant Array
NEA	Nuclear Energy Agency
NIST	National Institute of Standards and Technology
NSHI	Number of Simulated Showers
NTHT	No-Two-Holes-Touching

OS	Operative System
PAXI	Phase-space file Algorithm for X-ray Imaging
PENELOPE	PENetration and Energy LOss of Positrons and Electrons
PENGEOM	PENelope GEOMetry editor
PENMAIN	PENelope MAIN program
PENMAT	PENelope MATLAB application
PLA	Polylactic Acid
ROI	Region of Interest
RTD	Rise Time Discriminator
SKPAR	Source Kind of PARticle
SNR	Signal-to-Noise Ratio
VRT	Variance Reduction Techniques
XRAYLIB	X-ray library

1 INTRODUCTION

1.1 Chapter Outline

In this thesis an X-ray backscatter imaging system will be developed, explored, and characterised by simulations. We do this using a novel computational approach developed with the use of the PENELOPE Monte Carlo simulation tool [1].

In this chapter a brief introduction of the research work will be given. The aim and objective of this work will be identified, and the structure of the rest of this thesis will be outlined.

1.2 Background

X-ray backscatter imaging is a non-destructive technique with a single-sided access. X-ray backscatter imaging is based on Compton scattering and it permits inspection and screening of concealed objects in sea containers, a wide variety of vehicles, luggage, and even people. The single-sided imaging technique consists in placing the source, normally an X-ray tube with voltages up to 200 keV, and the target object, such as a sea container or luggage, on the same side. This imaging technique is particularly advantageous when access on both sides of the target object in transmission geometry is not feasible, and it is only possible to inspect objects from the same side, for example large containers (see chapter 3).

The information provided by the backscatter imaging is X-ray backscatter imaging systems can be achieved physically, but such systems can be also simulated computationally by using Monte-Carlo modelling of radiation transport. Simulations have the advantage to design the X-ray backscatter imaging system and to help towards planning the experiment without the need to run experiments. With simulations, it is possible to explore different combinations of detector/source/target material and can guide the experiment. In addition, simulations can be used for designing and testing new systems before the application, saving time and costs.

Simulations represent the easiest and most cost-effectively instrument for developing and testing an imaging system. Simulation involves modelling and testing physical experiments, all the user needs is a powerful computational environment. Simulations make it easier to plan an experiment without wasting time and resources. But this is not limited to experiment: with simulations it is also possible to explore theoretical conditions presently experimentally impossible to achieve, but which might be achieved in the future.

In this research, the PENELOPE-2014 [1] Monte Carlo simulation package was used to design, develop and test backscatter X-ray imaging systems.

PENELOPE Monte Carlo simulation was used to: investigate the fundamental physics of backscatter imaging; determine image quality metrics; characterise pinhole and coded aperture mask thicknesses and aperture diameters. It was also employed to design and explore virtual sources such as those which are mono-energetic, mono-directional (i.e. pencil beam), and monochromatic. An extended wire object capable of emitting 0-200 keV flat X-rays was also designed with the aim of being non-specific to any known sources. The characteristic X-ray tube emission used in the backscatter experiments was also simulated. The investigation includes the design of the imaging systems in the near-field, using a wide conical beam as the source of X-ray emission for backscatter imaging.

PENELOPE is written in Fortran and distributed as an ensemble of source libraries. It does not include an internal data output viewer/analysis program. Thus, a MATLAB [2] tool for image processing and data analysis was developed. Our tool is fully capable of reading all the data from the simulations, including energy-spectra, particle fluence, and all in all the phase-space file. It can fully replicate the pixel area of a detector by translating the raw data of the phase-space file, i.e. the state variables recorded at the detector, into an image. In addition, the algorithm can discriminate between the kind of particle recorded, the kind of interaction occurring, and does so as a function of the energy integrated over the pixel area of the detector. In backscatter imaging, tracking the contribution of each kind of interaction is a fundamental parameter for discrimination of specific material signatures, especially in defence and security.

The models designed for this research are not only applicable in defence and security, but also in medical imaging, astrophysics and industry.

Although the approach of this work is mostly theoretical, simulations and experiments were compared against each other, and experiment was used for validating part of this thesis work. However, experimental investigations under some conditions were not possible. Hence, such investigations were validated by using well-known theoretical databases, such as NIST [3], and LLNL [4].

1.3 Aims and objectives

The aim of this work was to extend our knowledge of backscatter X-ray physical interactions by numerical simulation.

Our specific objectives for backscatter X-ray imaging systems were developed, characterised and optimised through simulations by:

- Model physical sources such as the X-ray tube used in the backscatter experiments at different anode voltages;
- Explore pinhole mask imaging camera with different materials, thicknesses and aperture diameters for coded apertures applications;
- Test the pinhole masks with a virtual, and currently physically unrealised 0-200 keV flat virtual thin wire X-ray emitter;
- Determine image brightness by image processing with novel MATLAB scripts;
- Calculate image quality metrics, such as signal-to-noise ratio (SNR), contrast-to-noise ratio (CNR), spatial resolution;
- Optimise pinhole aperture diameter and thickness to mitigate collimation;
- Model real detectors, such as the Gemstar camera and HEXITEC;
- Model Coded Aperture masks and calculate point-spread functions to extract image quality metrics of the modelled imaging system to be compared with experiment;
- Simulate backscatter images of the physical test objects, for comparison with experiment;

- Explore the fundamental physics of backscatter imaging with an all-in-one hemispherical detector, by testing different virtual X-ray mono-chromatic sources and simultaneously determining angular distributions;
- Describe the exact photon tracking history with the parameters PENELOPE records in the data output and discriminate against the different kind of interactions occurring within the different materials as seen by the detector.

Additionally, the PENMAT application was developed with the aim of improving PENELOPE user experience, and optimising simulation time. With the regards to simulation time, PENELOPE also run on the High-Performances Computer (HPC) at Cranfield University, which is a dedicated scientific computing facility the user can access remotely for running batch jobs. Image processing was implemented by the Phase-space file Algorithm for X-ray Imaging (PAXI) [5] algorithm, which is capable of processing the image within a few minutes for a large data file using parallel cores.

1.4 Thesis Outline

This thesis was divided into three main sections to cover all the possible aspects of simulating an X-ray backscatter imaging system.

Chapter 1 gives an introduction to this research work. Chapters 2 to 5 explore the background knowledge required for the thesis project. X-ray interaction with the matter is discussed in chapter 2, with particular focus on Compton scatter and Klein-Nishina differential cross sections. Chapter 2 includes also NIST database and Xraylib database link scripts. In chapter 3, X-ray imaging techniques will be covered, and X-ray backscatter will be compared with X-ray transmission. In chapter 4, a review of the current Monte Carlo simulation codes will be given, and the Monte Carlo principles will be described and compared with the analytical methods. In particular, SpekCalc, which was used for this research, will be described and compared with PENELOPE. Chapter 5 is entirely focused on PENELOPE. PENELOPE Monte Carlo simulation of the radiation transport was chosen for designing, modelling and testing X-ray backscatter imaging system, and all the features of the code will be discussed, together with all the libraries

and sub-tools. Material, geometry, input file, and impact detector settings will be examined. Data output, including energy-probability spectra, phase-space file and others will be reviewed. In this chapter, also PAXI algorithm for image processing, PENMAT application development, and PENELOPE simulations on HPC will be illustrated.

The second section of the thesis work (chapters 6-9) will be dedicated the results. Chapter 6 will explore how to model X-ray sources. The models explored will include physical sources, such as the VJ Technologies [6] X-ray tube, and virtual X-ray sources, such as the novel 0-200 keV flat X-ray wire emitter source. The model of the VJ-Technologies X-ray tube will also be validated with experiment and compared with spectra generated with SpekCalc analytical software. In chapter 7, the backscatter imaging system will be described, together with pinhole imaging simulation principles, image quality metrics explored by using the 0-200 keV flat thin wire X-ray emitter, and coded aperture imaging. In Chapter 8, HEXITEC detector will be modelled and tested, and compared with experiment. Finally, chapter 9 will discuss the fundamental physics of the backscatter X-ray imaging with a hemispherical detector and data will be extracted as angular distributions for the different kind of interactions recorded at the detector. PENELOPE data will be benchmarked against xraylib and the NIST databases.

The final part of this research work involves the discussion of all the results, conclusions, and future work (chapter 10).

2 X-RAY INTERACTIONS WITH MATTER

2.1 Chapter Outline

In this chapter, the key principles of X-ray interactions with matter will be introduced.

A general definition of X-rays and their energy range within the electromagnetic spectrum will be given in 2.2, while the fundamental definitions of interaction cross section, general attenuation and specific interactions leading to beam attenuation are described in section 2.3, 2.4 and 2.5, respectively.

The chapter will also include a detailed descriptions of Compton scatter, Klein-Nishina (KN) Differential Cross-Section (DCS), and the scattering function as these are involved in the basic physical process of X-ray backscatter imaging (section 2.6, 2.7).

Then, elastic scatter will be briefly described in 2.8, while photoelectric effect, X-ray production and fluorescence X-rays will be in 2.9, 2.10 and 2.11, respectively.

Pair production will be briefly discussed (section 2.12).

This chapter includes also the description of the NIST XCOM [7], and xraylib [8] [9] databases. Both databases contain theoretical cross sections of the X-ray interaction with matter and will be used as reference for the research work for validation of the hemispherical detector model in chapter 9.

2.2 Definition of X-rays

X-rays are ionising radiation in the electromagnetic spectrum, with energy range in the keV region, that is frequencies between 10^{16} and 10^{20} Hz, and hence lie between the visible spectrum and gamma rays (fig. 2.1) [10]. X-rays were discovered by the German physicist Röntgen in 1895.

When X-rays enter the matter, they can be either scattered or attenuated. The two fundamental definitions of scatter cross section and X-ray attenuation will be discussed in sections 2.3 and 2.4, respectively.

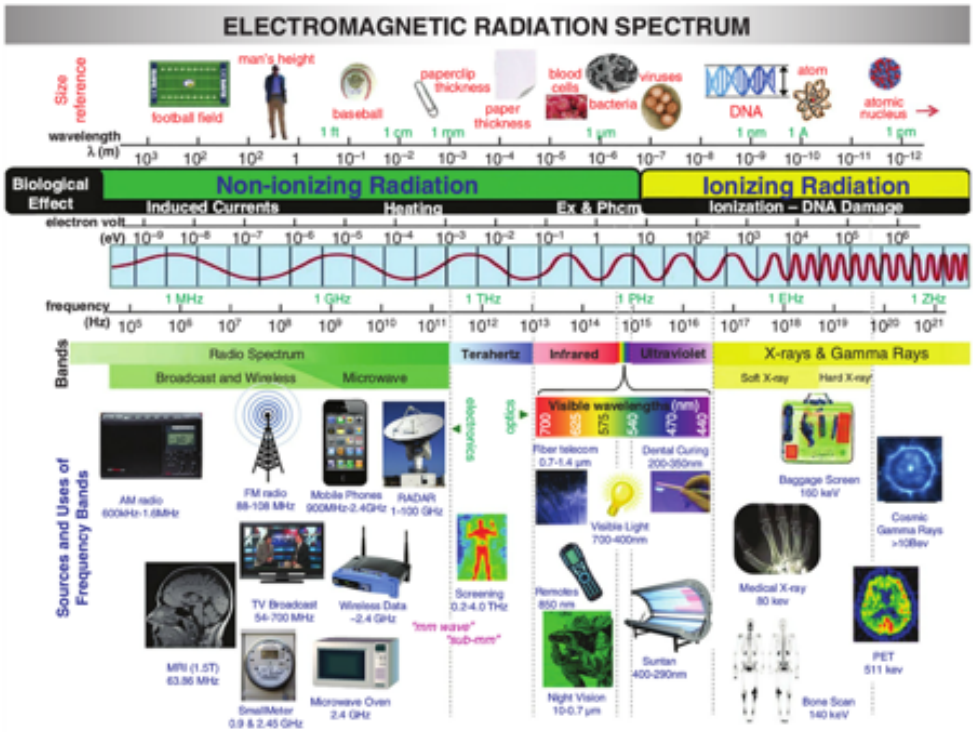

Figure 2.1 The electromagnetic spectrum. The X-rays are in the range of ionising radiation, with a frequency between 10^{16} and 10^{20} Hz [10].

2.3 Definition of interaction cross section

The interaction of X-rays with matter can be described by a fundamental quantity which gives a measure of the probability of such interaction. This quantity is called the *X-ray interaction cross section*, often just referred to as the *cross section*.

Formally, the cross section is defined as follows. Let us consider a beam of particles/photons incident upon a target material as shown in

Figure **2.2**. The target material is assumed to be homogeneous and thin.

Let us assume the beam hits the target with an initial beam flux N_0, which is the total incident particles per unit time, and the particles in the beam are uniformly distributed. When the flux N_0 of particles enters the matter, on average, dN of them will be scattered into a solid angle $d\Omega$ per unit time.

We define the differential cross section (DCS) as the ratio:

$$\frac{d\sigma}{d\Omega}(E,\Omega) = \frac{1}{N_0}\frac{dN}{d\Omega} \qquad 2.1$$

That is $\frac{d\sigma}{d\Omega}$ is the average fraction of the particles scattered into solid angle $d\Omega$ per unit time per unit flux N_0 [11]. The differential cross section can be interpreted as the geometric cross sectional area of the target intercepting the beam and has dimensions of area.

Now, let us assume the beam interacts with a homogenous thin target object of thickness δt. The beam is assumed to hit the target normally to the thickness δt. The density per unit area is $n\delta t$, where n is the density number and δt is the thickness of the material. Then, if the beam interacts with an area A of the target, the number of incident particles is $N_0 A$. The average number scattered into the solid angle $d\Omega$ per unit time is

$$N(\Omega) = N_0 A\, n\, \delta t \frac{d\sigma}{d\Omega}(E,\Omega) \qquad 2.2$$

By integrating eq. 2.2 in terms of the solid angle,

$$N_{TOT} = N_0 A\, n\, \delta t\, \sigma \qquad 2.3$$

where

$$\sigma = \int d\Omega \frac{d\sigma}{d\Omega}(E,\Omega) \qquad 2.4$$

is the cross section. We can determine the probability of interaction within the thickness δt thus is

$$P(\delta t) = n\ \sigma\delta t \qquad 2.5$$

For a material of given thickness, the probability of interaction can be calculated by integrating 2.5.

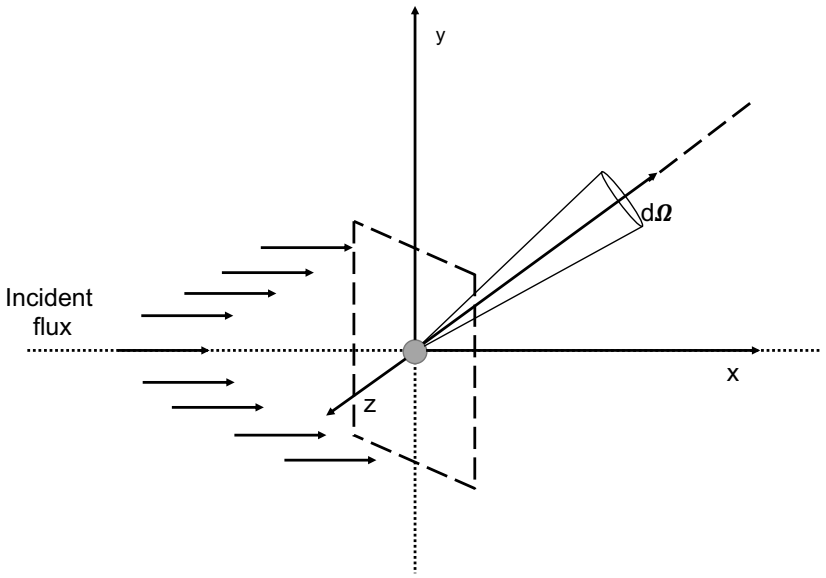

Figure 2.2 Definition of scattering cross section

2.4 Definition of X-ray general attenuation

X-ray general attenuation is defined as follows. Let us consider a material of density ρ and infinitesimal thickness $\delta t \approx dt\ (t \to 0)$. The X-ray beam with an initial flux N_0 has intensity $I_0(E)$, and it strikes perpendicularly the surface of the material. The intensity is defined as the number of photons hitting the target of thickness dt. Attenuation is the reduction of the intensity of the X-ray beam as it traverses the matter. The reduction may be caused by either absorption or by scatter of photons from the beam, and can be affected by different factors, such as beam energy and atomic number of the material thickness. If each photon of the incident beam has energy E, then the number of photons interacting with the atoms within the volume of the material is $dI(E)$. Thus, the rate of photons transmitted through the sample without interaction with the material is $I_0(E) - dI(E)$. This number is less than the photons of the incident beam, as part of the incident beam has been attenuated.

The number of photons per second interacting in the infinitesimal volume is then proportional to both the incident photon rate $I_0(E)$, and the number of electrons encountered within the infinitesimal thickness dt:

$$dI(E) = \mu(E)\, I\ \ (E)\, dt \qquad 2.6$$

with $I(E) = I_0(E)$ for $t = 0$. The constant of proportionality $\mu(E)$ is called the *mass attenuation coefficient*. This constant is characteristic of the material and energy of the incident X-ray photons and has units cm^2/g (density is g/cm^3, thickness is in cm). A schematic supporting the definition of the mass attenuation coefficient is shown in figure 2.3.

For a piece of material of density ρ and finite thickness t, integration of Eq. 2.6 shows the transmitted intensity of photons passing through the material without interacting, satisfies the Beer-Lambert law:

$$I(E) = I_0(E)\, e^{-\mu(E)\rho\, t} \qquad 2.7$$

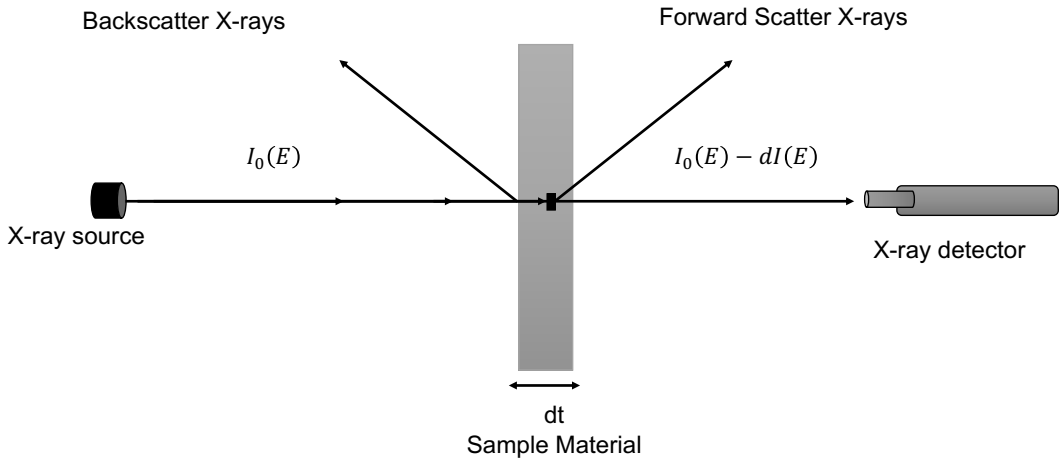

Figure 2.3 X-ray interactions with the matter. When X-rays are emitted from a source and interact with a sample material of thickness dt, they can either be absorbed, transmitted or scattered forwards or backwards. The X-ray beam has initial intensity $I_0(E)$, then the thickness dt absorbs intensity $dI(E)$, thus the final intensity is the difference between the beam initial and absorbed intensities.

2.5 Specific interactions leading to beam attenuation

As already described in the previous section, when a beam of X-ray photons passes through a material of thickness t, some of the photons will interact with the material's atoms. The interactions which could take place are: photoelectric effect, elastic or Rayleigh scatter, inelastic or Compton scatter, and pair production.

The mass attenuation coefficient $\mu(E)$ takes into account the different interactions occurring within the sample volume.

$$\mu(E) = \tau(E) + \sigma_{el}(E) + \sigma_{inel}(E). \qquad 2.8$$

In eq. 2.8, $\tau(E)$ is the photoelectric mass absorption coefficient, which characterises the photoelectric effect. The photoelectric effect is the kind of interaction responsible for the generation of characteristic lines in the X-ray spectrum, which are unique and specific signatures of the kind of material. Elastic scatter is characterised by $\sigma_{el}(E)$, while $\sigma_{inel}(E)$ defines the inelastic or Compton scattering. Both scatter interactions are expressed as cross sections σ. Compton scattering, elastic scattering, photoelectric effect, and pair production will be described in details in sections 2.6, 2.8, 2.9, and 2.12.

The photoelectric effect is dominant for energies between 1 eV and 50 keV, while the Compton scattering energy range is 50 keV to 1 MeV. When the beam energy is higher than 1.02 MeV, pair production takes place. For energies below 1 keV, elastic or Compton scatter may occur, while for energies above 1 MeV, pair production becomes relevant, together with photonuclear absorption. The different kind of interactions are presented in Figure 2.4 [12].

The coefficients $\mu(E), \tau(E), \sigma_{el}(E), \sigma_{inel}(E)$ were computed by Hubbel and Seltzer [13] for all elements of the periodic table plus 48 compounds and mixtures of radiological interest. The calculated coefficients are included in the NIST (National Institute of Standards and Technology) XCOM photon cross sections standard reference database [7], and will be discussed in section 2.14. In this thesis work, the NIST XCOM database is used as the standard source for theoretical comparisons. The computational functions from xraylib [8], which can

perform a look up of NIST [7] tabulated data, are instead reviewed in section 2.15.

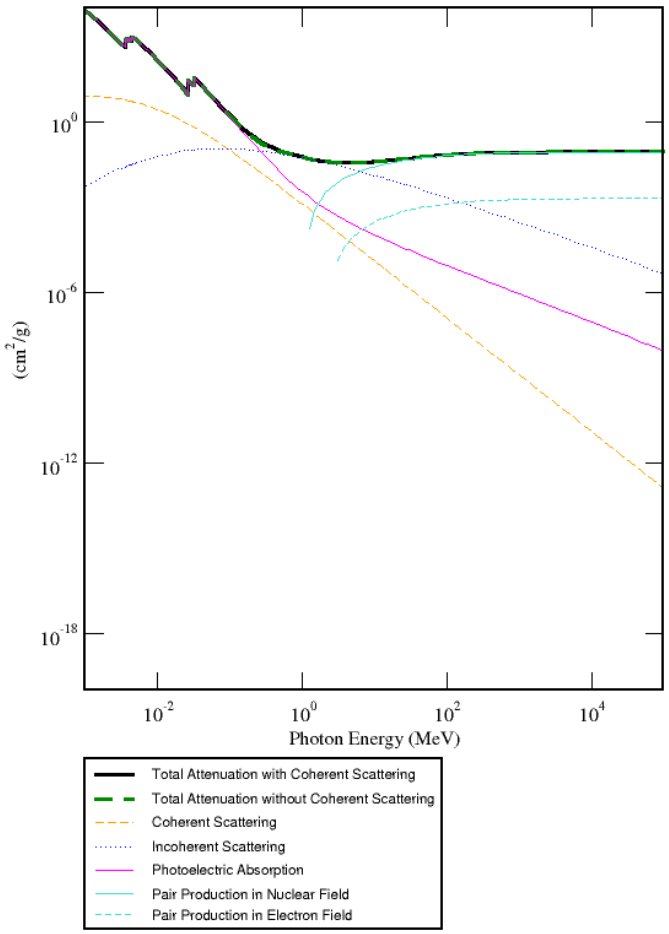

Figure 2.4 X-rays interaction with matter – cadmium telluride cross section. The photoelectric is the dominant effect for energies up to 50 keV, between 50keV and 5 MeV Compton effect arises and prevails. For energies greater than 1.02 MeV, pair production takes place.

2.6 Compton Scatter

The physical process of Compton scatter can be summarised as follows. Let us consider a photon entering matter with energy $h\nu$ (with h Plank's constant, ν photon frequency). Let us consider electrons in the outer quantum shells. These electrons are considered (almost) free electrons, as the electromagnetic field

decreases with the distance between the nucleus and the electrons. That is the binding energy of the outer shells' electrons are weaker compared to the inner shells.

If an incident photon of energy $h\nu$ collides with one of the electrons in the outer shells, the photon energy is significantly greater than the free electron energy. The electron is then dislodged, and a new photon of energy $h\nu'$ is generated. The newly created scattered photon partially loses the initial incident energy, and is deflected by an angle θ (Figure 2.5) [14].

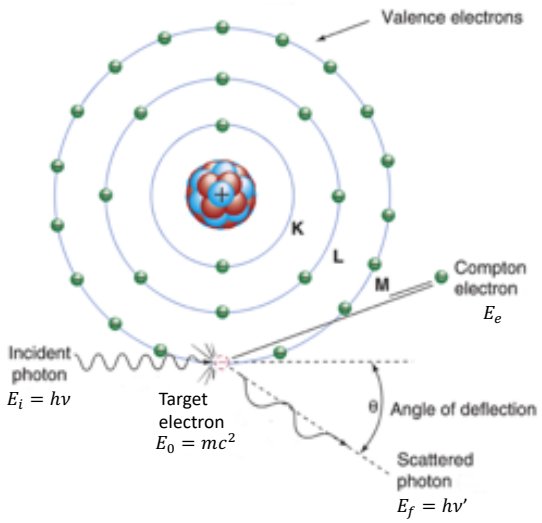

Figure 2.5 Compton scattering. The incident photon of energy $h\nu$ interacts with a valence-shell electron that results in ejection of the Compton electron (E_e) and simultaneously emission of a Compton scattered photon $h\nu'$ [15].

The final energy $E_f = h\nu'$ of the scattered photon will be:

$$E_f = \frac{E_i}{1+\frac{E_i}{511\ keV}(1-\cos\theta)} \qquad 2.9$$

where $E_i = h\nu$ is the incident photon energy, θ is the angle of the scattered photon, h is Plank's constant. The maximum energy occurs at $\theta = 0°$, when

$\cos\theta = 1$, while the minimum energy is at $\theta = 180^{\circ}$ when $\cos\theta = -1$ (see figure 2.6). This is called full-backscatter and will be further discussed in chapters 7, 8 and 9.

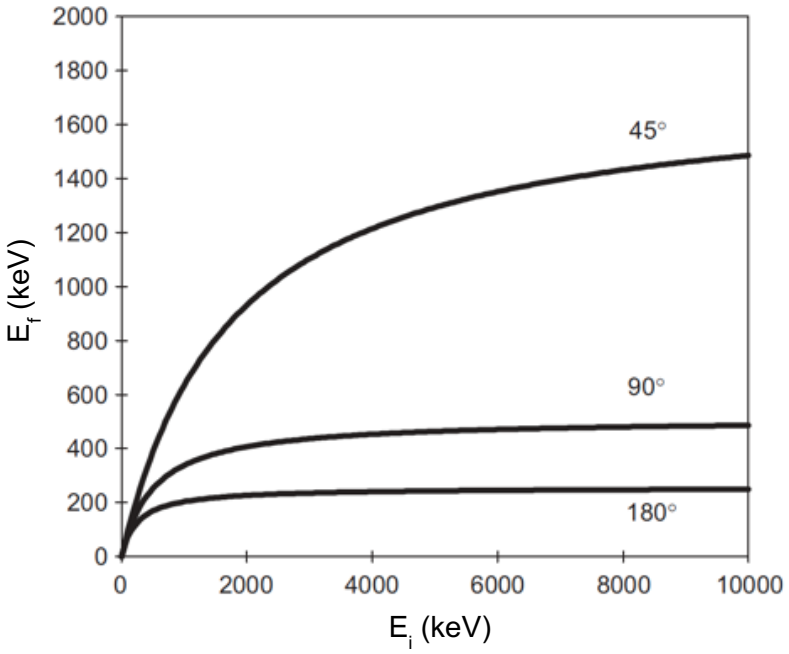

Figure 2.6 Compton scattering energy dependence on energy of primary radiation at 45˚, 90˚ and 180˚ scatter angles.

Compton scattering is also known as inelastic or incoherent scatter for its inelastic nature. Thanks to his discovery, Compton received the Nobel Prize in Physics in 1927.

2.7 Klein-Nishina differential cross section for Compton scatter

After Compton's discovery, Klein and Nishina elaborated the theory which is now the basics of Compton scatter cross section [16]. In Compton scatter, is it assumed a photon collides with an electron which is initially at rest, loses some of its energy and is deflected from its original direction of travel [17]. Klein and Nishina calculated the differential cross section of photons scattered from a single

free electron. They developed a unified theory which included both classical Thomson scattering (elastic) and Compton (inelastic) scattering. At low energies this results in Thomson scattering; at higher energies to Compton scattering.

The Klein-Nishina angular distribution function per steradian of solid angle Ω is

$$\frac{d\sigma_C^{KN}(\theta)}{d\Omega} = \frac{1}{2} r_e^2 [1 + k(1 - \cos\theta)]^{-2} \times$$

$$\left[1 + \cos^2\theta + \frac{k^2(1-\cos\theta)^2}{1+k(1-\cos\theta)}\right] \left[\frac{cm^2/electron}{steradians}\right] \qquad 2.10$$

In which $k = \frac{1}{\lambda} = \frac{E}{mc^2} = \frac{E[MeV]}{0.5110}$ is the reciprocal of the incident photon wavelength.

For $k \gg 1$, equation (2.10) gives the differential Compton scatter cross section from free stationary electrons:

$$\frac{d\sigma_c\ (\theta)}{d\Omega} = \frac{1}{2} r_e^2 k^2 \left(k + \frac{1}{k} - \sin^2\theta\right) \left[\frac{cm^2/electron}{steradians}\right] \qquad 2.11$$

The Klein-Nishina differential cross section depends on energy and the scattering angle. Figure 2.7 shows the differential cross section as an angular distribution in the keV region, where Compton interaction is predominant. The angular distribution is at 10 keV (outermost curve), 100 keV (intermediate curve) and 1 MeV (innermost curve). At the lower energies, Compton differential cross section is spread in all the space within the unit radius r_e^2, but as the energy increases, the differential cross section is increasingly in the forward direction (0˚).

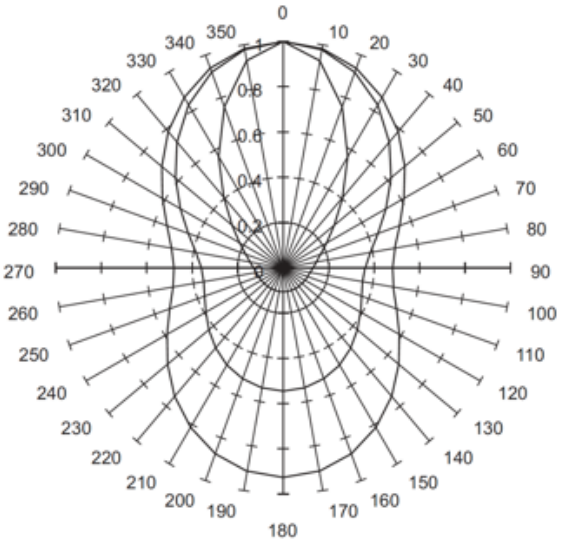

Figure 2.7 Klein-Nishina differential cross section as function of the scattering angle for 10 keV (outermost curve), 100 keV (intermediate curve), 1000 keV (innermost curve). Cross-section is represented by the unit radius r_e^2 [18].

2.7.1 Calculation of Klein-Nishina Cross Section

By integrating eq. 2.10 over 4π, we can obtain the Klein-Nishina total cross section:

$$\sigma_C^{KN} = 2\pi r_e^2 \left\{ \frac{1+k}{k^2} \left[\frac{2(1+k)}{1+2k} - \frac{ln(1+2k)}{k} \right] + \frac{ln(1+2k)}{2k} - \frac{1+3k}{(1+2k)^2} \right\} \left[\frac{cm^2}{electron} \right] \qquad 2.12$$

This formula is not suitable for evaluating σ_C^{KN} at low energies because of near cancellation between the logarithmic term and algebraic terms. Thus σ_C^{KN} was calculated for $k \ll 1$, and eq. 2.12 will then be expanded:

$$\sigma_C^{KN} = \frac{8}{3}\pi r_e^2 \left(\frac{1}{(1+2k)^2} \right) \left(1 + 2k + \frac{6}{5}k^2 - \frac{1}{2}k^3 + \cdots \right) \qquad 2.13$$

By using only terms through to k^2, in the low energy limit $k \to 0$ the expression 2.13 becomes the classical Thomson cross section:

$$\sigma_t = \frac{8}{3}\pi r_e^2 = 0.6652 \cdot 10^{-24} \left[\frac{cm^2}{electron} \right] \qquad 2.14$$

For $k \gg 1$, which is equivalent to $k \to \infty$ instead, eq. 2.12 is approximated as:

$$\sigma_C^{KN} \approx \pi r_e^2 \frac{1+2\ln(2k)}{2k} \left[\frac{cm^2}{electron} \right] \qquad 2.15$$

This equation was fitted by Hastings [19] for photon energies up to 1 MeV and tabulated and later used for NIST database [17].

2.7.2 Correcting Compton scatter cross section with incoherent scattering function

The Klein-Nishina formula can calculate the Compton differential cross section with a good approximation. However, their formula disregards, or treats very approximately, electron binding effects. This can be acceptable for low-Z elements (Z is the atomic number), as their K-shell binding energies are low in comparisons with the photon energies considered. On the other hand, it is not acceptable for high-Z materials, which have higher K-shell binding energies compared to low-Z materials [17].

The scattering of 0.662 MeV photons by K-shell electrons of various heavy atoms was measured by [20], Varma and Eswaran [21]. They observed the ratio between the measured experimental differential cross section and Klein-Nishina differential cross section for tin and gold. They estimated there was a difference between experiment and Klein-Nishina theory, so they calculated the correction factor, and applied to the Klein-Nishina differential cross section. This factor is the incoherent scattering function $S(q,Z)$:

$$\frac{d\sigma_C\,(\theta)}{d\Omega} = S(q,Z)\,\frac{d\sigma_C^{KN}(\theta)}{d\Omega}\left[\frac{cm^2/electron}{steradians}\right] \qquad 2.16$$

The incoherent scattering function $S(q,Z)$ represents the probability that an atom is raised to any excited or ionised state as result of a sudden impulse which imparts a recoil momentum q to an atomic electron [17]. The differential Compton cross section of different materials (carbon, aluminium, iron, tungsten and lead) is plotted from 1keV-1MeV for $\theta = 30^{\circ}$ in appendix C.

By integrating the eq. 2.16 over 4π, it is possible to calculate the total cross Compton section, which is also known as incoherent or inelastic cross section, the incoherent scattering function can be calculated as the ratio of the two cross sections. It was observed that the function increases linearly with Z [22]. The ratio

between the Compton and Klein-Nishina cross section was calculated for different Z and energies by Hubbell et al. [22] and the relationship can be seen in Figure 2.8. In figure 2.8, the energies are 1 keV, 10 keV, 100 keV. In the calculations, three different models were applied: Thomas-Fermi (solid line in the figure) [23], Cromer, Cromer-Mann (circles in the figure) [24], and Brown (triangles in the figure) [25].

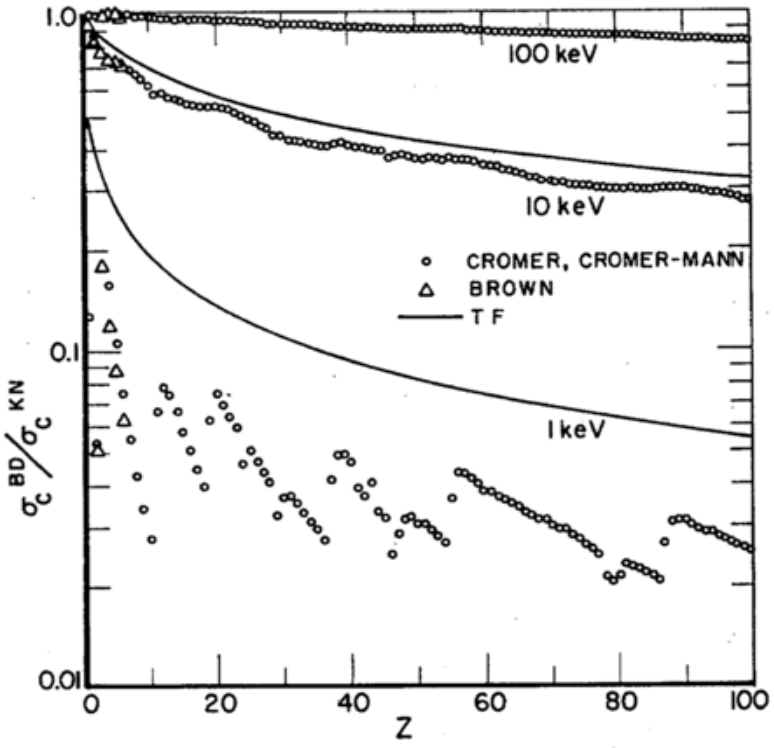

Figure 2.8 Comparison of incoherent scattering cross section and Klein-Nishina cross section against atomic number Z at 1 keV, 10 keV, 100 keV.

2.8 Elastic Scatter

Elastic scatter is the scatter of an incident photon hitting a non-relativistic free charged particle with no loss of energy of the incident primary photon [17]. That is elastically scattered electrons can change direction but do not change their wavelength and momentum is conserved. Elastic scatter occurs if the energy of

the incident photon is considerably less than binding energies of orbiting electrons of an atom ($h\nu \ll mc^2$). Elastic scatter is also called coherent or classic or Thomson or Rayleigh scatter. A schematic of the elastic scattering process is shown in Figure 2.9.

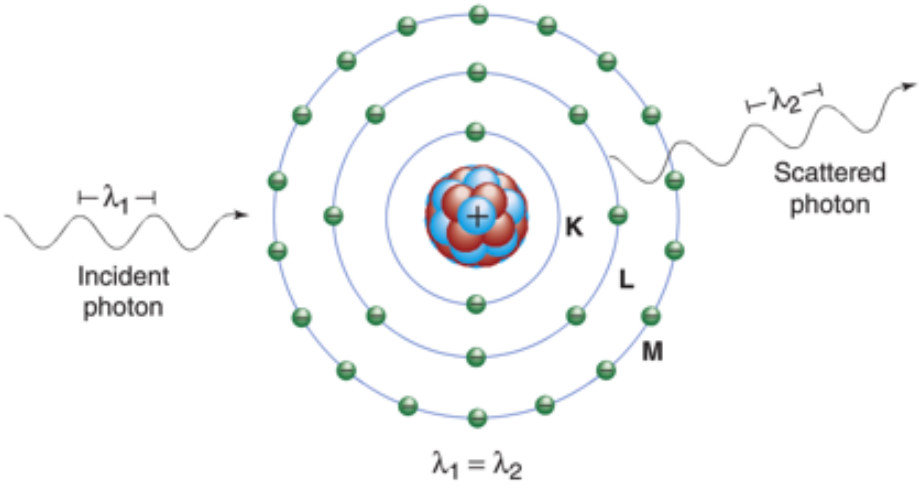

Figure 2.9 Elastic scattering process. The incident photon of wavelength λ_1 interacts with an atom, and the scattered photon λ_2 is emitted with the same wavelength and energy. Elastically scattered photons are usually emitted in the forward direction, close to the trajectory of the incident photon.

As opposed to Compton scatter, elastic scatter is considered the low energy limit of inelastic scatter, as the energy of the incident photon is much less than the binding energy and photons do not lose energy in the interaction with the atomic electrons. Coherent elastic scattering produces the effect of electron diffraction, which is used to analyse crystal structure.

Thomson differential cross section is given by the well-known following formula:

$$\frac{d\sigma_T(\theta)}{d\Omega} = \frac{1}{2} r_e^2 (1 + \cos^2\theta) \left[\frac{cm^2/electron}{steradians}\right] \qquad 2.17$$

the atomic form factor was calculated from the Klein-Nishina differential cross section in the low-energy limits [22].

Rayleigh calculated that the binding corrections, treated in the impulse approximation, must be applied to the Klein-Nishina differential cross section for calculating the elastic differential cross section by relating it to the square of the form factor as follows:

$$\frac{d\sigma_R(\theta)}{d\Omega} = [F(q,Z)]^2 \frac{d\sigma_T(\theta)}{d\Omega} \left[\frac{cm^2/electron}{steradians}\right] \qquad 2.18$$

The atomic form factor is a function able to describe the charge distribution of an atom [17]. The square of the Form Factor $[F(q,Z)]^2$ is the probability that the Z electrons of an atom take up a recoil momentum q without absorbing any energy.

2.9 Photoelectric Effect

The photoelectric effect is one of the several ways in which electrons and photons can be emitted by materials. In the photoelectric effect, a photon transfers its energy to an electron, the electron may then escape from the atom to which it was bound [26].

Photons cannot give up part of their energy, but they have to release all their energy. The energy is equal to

$$E = h\nu = \frac{hc}{\lambda} \qquad 2.19$$

where ν is the frequency of the electromagnetic wave associated with the light, h is Plank's constant ($h = 6.6361 \times 10^{-31} J \cdot s$) and λ is the wavelength.

If in some physical process only part of photon's energy was required, then a new photon would be created to carry away the remaining energy. This representation is valid over the entire electromagnetic spectrum, including X-rays and gamma rays. During emission or absorption of any forms of electromagnetic radiation, photons must be created or absorbed.

2.10 X-ray Production

When electrons of incident energy E_i pass through the matter, the positive nuclei attract the negative electrons, causing deceleration and redirection, resulting in a

loss of kinetic energy that is converted into X-ray photons with varying energies, each equal to $E = h\nu$. The final energy of each X-ray photon will be determined from the conservation of energy, that is:

$$E_f = E_i - h\nu \qquad 2.20$$

The process of energy loss which produces X-rays is called bremsstrahlung radiation (from German, “bremsstrahlung” meaning braking radiation). The process of X-ray production by the photoelectric effect with bremsstrahlung radiation is shown in fig. 2.10 [15].

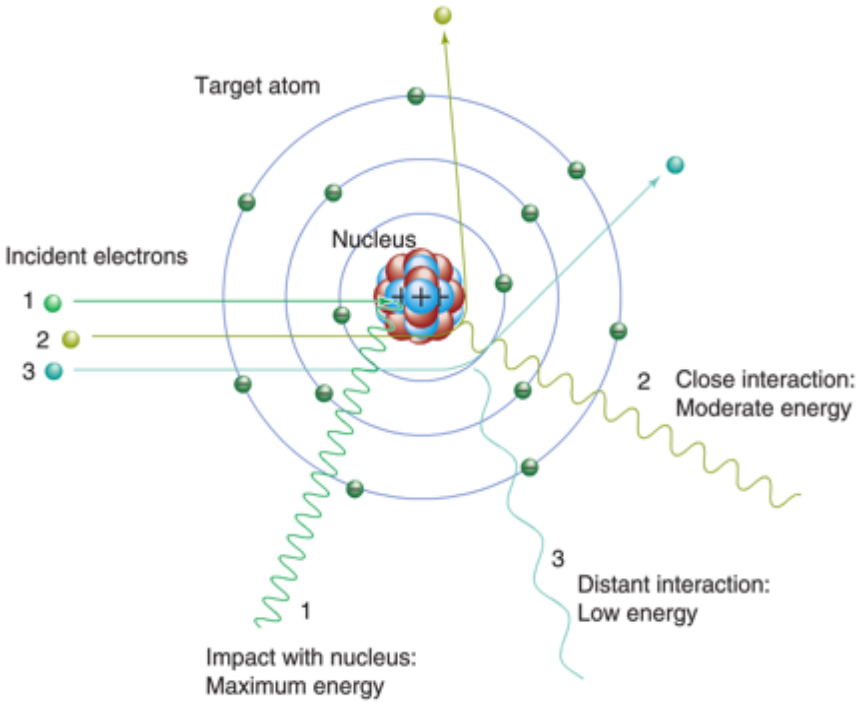

Figure 2.10 X-ray production by bremsstrahlung radiation. Energetic electrons interact with an atomic nucleus of the target material. In a close approach, the positive nucleus attracts the negative electron, causing deceleration and redirection, resulting in a loss of kinetic energy that is converted to an X-ray. The X-ray energy depends on the interaction distance between the electron and the nucleus; it decreases as the distance increases [15].

An example of X-ray production by bremsstrahlung effect is the X-ray tube. Current passing through a filament produces electrons in cascade by thermionic emission. Electrons are accelerated from the cathode by high potential

differences until they hit the metal anode surface, producing X-rays by bremsstrahlung. Just 1% of the cathode electrons are able to produce X-rays; all the others are lost by heating the anode. The X-ray tube filament and anode are in vacuum, so electrons are not scattered. The produced X-rays pass through filtering layers towards the exit window. X-rays from a standard tube are used for medical diagnosis, therapy, research, engineering, and security. An example of an X-ray tube is illustrated in fig. 2.11. Target anode materials are normally heavy elements, because they have stronger nuclear electric field, thus they are more effective in accelerating electrons. Target anode materials include chromium, molybdenum and rhodium, but tungsten is the material more frequently used. Intensity of the X-rays increases with the square of the atomic number of the target, and approximately proportional to the square of the voltage used to accelerate electrons. This is why tungsten anodes are so often used, as it has a high atomic number. Tungsten is also a reliable material, because it has a very high melting temperature; thus, it can be employed with high electron-beam currents [15].

X-ray tubes produce a continuous spectrum, due to bremsstrahlung, upon which are superimposed sharp ‘characteristic’ or ‘fluorescence’ peaks generated by atomic excitations and are characteristic of the target material [15]. An example of X-ray spectrum generated from tungsten target at 60 kV and 100 kV is given in fig. 2.12.

In this work, the physical VJ Technologies [6] X-ray tube layers were simulated in PENELOPE [1] Monte Carlo tool to generate X-ray spectra at different anode voltages. More details on the X-ray tube model can be found in chapter 6.

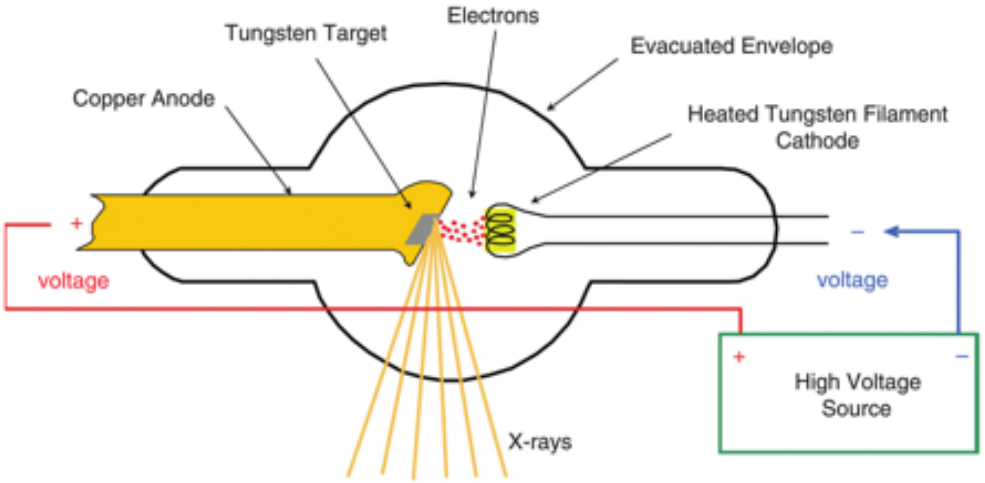

Figure 2.11 Schematic of X-ray tube. The X-rays are produced by the bremsstrahlung process of energetic electrons.

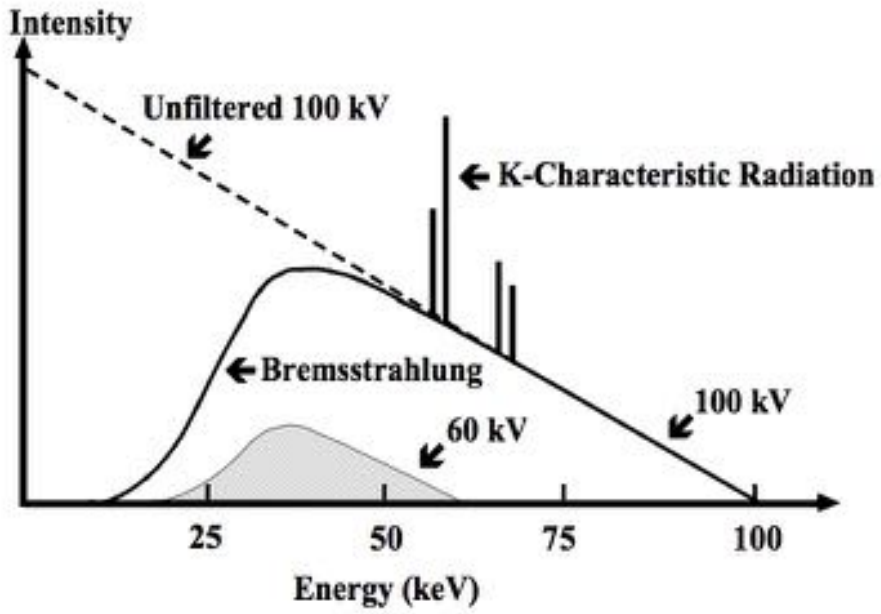

Figure 2.12 X-ray tube spectrum from tungsten target at 60 kV and 100 kV anode voltages. The X-ray continuous spectrum is produced by bremsstrahlung process, and the characteristic radiation is produced by fluorescence of the tungsten anode target.

2.11 Fluorescence X-rays and Auger Electrons

When a high-energy X-ray or electron hits an orbiting electron, the electron is ejected from its orbit by the incident radiation. The atom thus achieves an excited state. Shortly after, the electrons will rearrange themselves to return the atom to the ground state or non-excited state. During this transition, energy is released in the form of an X-ray photon with energy equal to the difference between the ground state and the excited state:

$$E = E_u - E_l \tag{2.21}$$

where E_u is the ground state energy and E_l is the excited state energy of the atomic electron. This X-ray is called a characteristic or fluorescence X-ray, because its energy is characteristic of the atom or element undergoing the transition. For heavy elements, photon emission is more common, while for lighter elements, electron emission dominates. The electrons emitted are called Auger electrons, and the photons emitted are called characteristic radiation.

Characteristic X-ray radiation is typically superimposed on the bremsstrahlung radiation, as shown in fig. 2.12.

The name characteristic comes from the fact that the binding energies for electrons in an atom are unique for a specific element. Therefore, the difference in binding energy is also a unique characteristic of the element. The characteristic radiation produced by electron transitions between shells is named as follows:

- the symbol of the chemical element;

- the symbol representing the shell (K, L, M, etc.) the electron was dislodged from or the shell with a missing electron;

- a lowercase Greek letter, usually with a numerical subscript, which represents the transitions adjacent or non-adjacent transitions.

Characteristic radiation resulting from an outer-shell (e.g., L or M) electron filling a vacant site in the K shell is thus named K-characteristic radiation; L-characteristic radiation occurs when a vacant site in the L shell is filled with an

electron from a shell more distant to the nucleus. The letters K, L, etc., are given a Greek letter subscript (α, β), α referring to an adjacent shell transition (e.g., L to K, M to L) and β referring to a nonadjacent shell transition (e.g., M to K, N to K, N to L). A Kα radiation is therefore less energetic than a Kβ radiation [26].

Even between electrons within the same shell, there are slight energy differences. The resulting different characteristic radiation energies are designated by the subscript 1, 2, 3, etc. Several possibilities therefore exist for K-characteristic radiation, e.g., $K\alpha_1$, $K\alpha_2$, $K\beta_1$, etc.

K-series are the highest energy X-rays and the most penetrating. The highest-energy K-series X-ray is created when the vacancy is filled with a free unbound electron. The K-series X-rays increase in energy with increasing atomic number [27].

In an X-ray tube with a tungsten target atom, for example, the incident electron interacts with the K-shell electron with the Coulumbic repulsive electrical force. The K-shell electron is removed, but only if the energy of the incident electron is greater than the K-shell binding energy, leaving a vacancy in the K-shell. An electron from the adjacent L-shell fills the vacancy [15]. A $K\alpha_1$ characteristic X-ray photon is emitted with energy equal to the difference between the binding energy of the two shells. For the tungsten atom (W), a 59.3 keV atom is emitted. The process is illustrated in Figure 2.13.

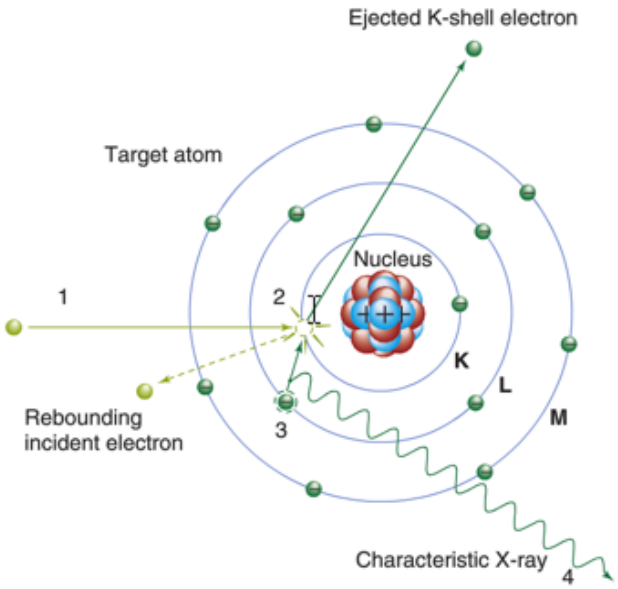

Figure 2.13 Generation of a characteristic X-ray in a target atom for an X-ray tube. The incident electron interacts with the K-shell electron (1). If the energy of the incident electron is greater than the K-shell binding energy, the K-shell electron is removed. This leaves a vacancy (2). An electron from the adjacent L-shell fills the vacancy (3). A K_α characteristic X-ray photon is emitted with energy equal to the difference between the binding energy of the two shells. For the tungsten atom (W), a 59.3 keV atom is emitted (4).

2.12 Pair Production

In the photoelectric effect, bremsstrahlung and Compton scatter, photons and electrons can exchange energy. However, there are other possible mechanisms involving kinetic energy which can be converted into particle mass and vice versa.

In 1933, Anderson observed a positively charged electron e^+ in cosmic radiation [28]. This particle was called the positron, and its existence was previously predicted by Dirac [29]. The positron has the same mass as the electron, but an opposite charge. Positrons are also observed when high-energy gamma rays pass through matter. A photon's energy can be converted entirely into an electron-positron pair. This process is called pair production and the reaction is the following:

$$\gamma \rightarrow e^+ + e^- \qquad 2.22$$

For pair-production to occur, the photon must have energy equal or greater than $2m_e c^2$ for generating the rest masses:

$$h\nu \geq 2m_e c^2 = 1.022\ MeV \qquad 2.23$$

The probability of pair production increases with higher photon incident energy and with higher atomic number Z (higher electromagnetic field of nucleus).

A positron produced by this pair production passing through matter will quickly lose its energy through atomic collisions and is likely to annihilate on collision with an electron producing a photon. The process $e^+ + e^- \rightarrow 2\gamma$ is called pair annihilation. Each γ photon will be emitted in opposite directions at 180˚, each with energy equal to $\mathrm{E} = 0.511\ \mathrm{MeV}$. The pair production process is illustrated in fig. 2.14.

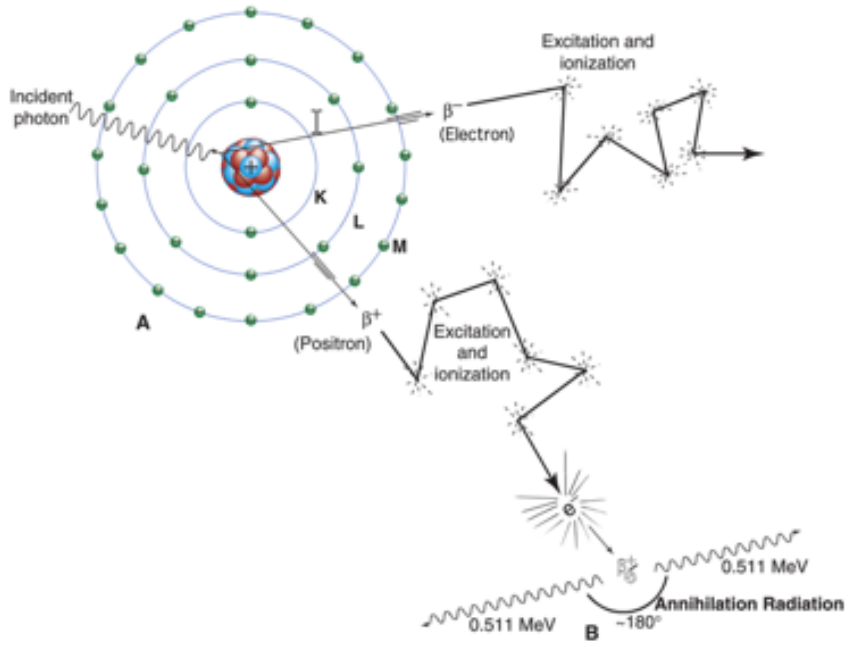

Figure 2.14 Pair production process: a high-energy incident photon, under the influence of the atomic nucleus, is converted into an electron-positron pair. Both electron and positron lose their kinetic energy by excitation and ionisation in the matter they traverse. However, when the positron comes to rest, it combines with an electron producing the two 511-keV annihilation radiation photons. K, L, and M are electron shells.

In this research work, the energy range is kept below 500 keV. For this reason, pair production is unlikely to occur, thus no further discussions will be on pair production.

2.13 Elemental and molecular available databases

Quantitative estimate of elemental composition by spectroscopic and imaging techniques using X-rays requires accurate data for X-ray interactions with matter. Traditionally, the NIST [3] database XCOM [7] is the most popular reference database for photon cross sections of elements, compounds and mixtures as tables within user-defined energy range (1 keV – 100 GeV). However, NIST is not presented in the form of freely available library functions which can be easily included in software applications for X-rays. For this reason, xraylib [8] was included in this thesis work (see chapter 5). Xraylib is a compilation of data sets from different published works distributed as a set of libraries which the user can recall from any programming languages. Cross sections of interactions like photoionization, coherent scattering and Compton scattering, as well as form factors and anomalous scattering and fluorescence functions are available. The following sections (2.14 and 2.15) will describe the two databases.

2.14 NIST database

National Institute of Standard and Technology [3] is one of the nation's oldest physical science laboratories. NIST database contains tables of calculated photon cross sections for scattering, photoelectric absorption and pair production, as well as total attenuation coefficients, for any element, compound or mixture ($Z \leq 100$), at energies from 1 keV to 100 GeV. For this thesis work, the reference database is XCOM [7], which was used for extracting the theoretical cross section for all the materials included in our Monte Carlo simulations.

NIST XCOM contains the theoretical cross section as total cross section, which is the sum of photoelectric absorption, Thomson – elastic scattering, Compton – inelastic scattering, and electron-positron pair production (for higher energies).

In this work, theoretical cross sections were retrieved for up to 500 keV for the materials of interest by inputting the element of the periodic table, such as carbon, copper, iron, tungsten and lead, the energy range and by specifying the units barns/atom. Cross sections were also calculated for some mixtures such as tungsten epoxy resin, bismuth alloy, PLA and ABS for comparisons in transmission properties of these materials (see appendix B). The program will compute values for predefined energies, but the user may also input additional energies. This can be done by inputting the values by hand or by using file-uploading.

For elements, the user may choose to change the cross sections units from cm^2/g, barns/atom, where 1 barn = 10^{-24} cm^2, or calculating partial interaction coefficients in barns/atom and total attenuation coefficients in cm^2/g. For compounds and mixtures, all quantities are in cm^2/g.

2.15 Xraylib: X-ray library for X-ray interactions with the matter

Xraylib [8] provides access to some of the most respected databases of physical data in the field of X-rays. The core of xraylib is a library, written in ANSI C, containing over 40 functions to be used to retrieve data from these databases. This C library can be directly linked with any program written in C, C++ or Objective-C. Furthermore, the xraylib package contains bindings to several popular programming languages: Fortran 2003, Perl, Python, Java, IDL, Lua, Ruby, PHP and .NET, as well as a command-line utility which can be used as a pocket-calculator. Xraylib can also be useable within MATLAB and LabView. In this thesis work, xraylib was fully integrated in the MATLAB code PAXI for data analysis and image processing. PAXI will be further discussed in chapters 5, and will be applied for the results chapters 6-9.

2.15.1 Data output: xraylib Klein – Nishina differential cross section

Xraylib was used to extract tabulated cross section within MATLAB environment. Some examples of the Klein-Nishina differential cross sections extracted from

xraylib is in the Appendix C. The materials include carbon, aluminium, copper, iron, tungsten and lead. For these materials, the Klein-Nishina differential cross section were calculated for energies up to 500 keV and at 5˚, 45˚, 90˚ and 180˚ for investigating the theoretical differential cross section of backscatter imaging as energy and angular distributions and understanding the fundamental physics behind the process. These data are compared against Monte Carlo simulation in future chapters for a possible prediction of angles where the contrast from target could be maximised in backscatter geometry against other materials.

2.16 Chapter Summary and Critical analysis

In this chapter, the key principles of X-rays interaction with the matter were discussed. The fundamental principles of Compton scatter and Klein-Nishina differential cross section calculation were described against competing mechanisms in X-ray interaction with the matter. Compton scatter and Klein-Nishina DCS are fundamental information for X-ray backscatter imaging, as the contribution to the total cross section is relevant, and can only be compared with the signal generated by fluorescence.

Although the contribution of fluorescence can be significant, Compton scatter may generate the predominant information for certain materials and energies, and could represent the future for material identification. Further discussion on this topic will follow in the results section, chapter 9, dedicated to the study of the fundamental physics of backscatter imaging with a hemispherical detector.

NIST XCOM, the database containing the theoretical cross section relative to the interactions of electrons and photons with the matter was introduced and will be used in chapter 9 for validating the Monte Carlo calculations. However, NIST does not provide freely available library functions which can be easily included in other software applications for X-rays. For this reason, xraylib was used in this research work, and examples of data which can be extracted was given. These data include Klein-Nishina DCS with the possibility to generate energy-angular plots for a better understanding of the fundamental physics of backscatter imaging.

3 X-RAY IMAGING PRINCIPLES

3.1 Chapter Outline

In this chapter, current X-ray imaging techniques will be explored. Particular focus will be given to Compton backscatter imaging compared to X-ray transmission. X-ray imaging techniques will be briefly reviewed in section 3.2, X-ray Compton backscatter imaging will be described in section 3.3. Finally, X-ray Compton backscatter imaging can be achieved by using a pinhole mask (section 3.4) or coded apertures (section 3.5)

3.2 X-ray imaging techniques

Since their discovery in 1895 by Wilhelm Roëtgen, X-rays have been used for developing imaging systems, which are nowadays widely used for medicine, industry, security, astrophysics.

An X-ray imaging system comprises of three basic elements: an X-ray beam, an object of investigation, and a detector. In X-ray imaging, if the X-ray beam and the detector are on opposite sides of the target object, then the image exposures are captured by X-ray transmission. On the other hand, if the detector and the X-ray beam are located on the same side of the target object, then the imaging system geometry is X-ray backscatter.

Traditional X-ray by transmission imaging systems consist of an X-ray beam hitting the target and going on to strike the detector behind. The X-ray beam is usually generated by an X-ray tube, which emits photons towards the target material, and is normally collimated by a beam-limiting device (see fig. 3.1(a)).

In X-ray transmission, image brightness depends on the amount of transmission, (compared to scatter or absorption) of X-rays within the target (see chapter 2), which produces a dark area on the photographic film/detector. Conversely scatter and absorption within the target will result in a bright area on the detector. Absorption and scatter are functions of the material density, that is the denser the material, the more X-rays are absorbed, the less the density, the more X-rays are transmitted. The traditional X-ray imaging device is known as radiographer, while

the imaging process itself is called radiography. In the past, the image exposure was impressed in a photographic film; nowadays the radiography is digitally recorded, offering greater sharing flexibility.

The image brightness is displayed in grey-scale and reflects the density of the materials. Spatial variation in brightness across the image therefore represent variations in shape, thickness and composition of the target. The brightest image element is the denser element in the target unless thin, while the darkest has the lowest density unless thick. Thick, high-density, high-Z features produce a greater reduction in photon flux than thin, low density, low atomic number objects.

Traditional radiography is based on the rectilinear propagation of X-rays from the radiation source to the detector where they are counted. Radiography, however, cannot be applied to thick objects, as X-rays would not penetrate the target and be attenuated before reaching the surface of the detector [18].

X-ray radiography may be used in security systems to search for concealed materials by an operator viewing the X-ray image. The X-ray beam is usually from a relatively low-potential (around 150kVp) X-ray tube and is typically used for inspection of carry-on items at airports and public buildings, incoming parcels to businesses and agencies, and elements shipped through the mail or via another carrier [30]. A typical X-ray transmission image is shown in figure 3.2(b). The difference in attenuation causes objects within a luggage to appear in different shades of grey and the difference in contrast gives the shape of the objects in the transmission image (Wells and Bradley, 2012).

X-ray imaging by transmission was further developed into other X-ray imaging techniques, such as X-ray dual-energy imaging and X-ray Computed Tomography (X-CT).

X-ray dual-energy imaging is similar to the conventional X-ray radiography but is realised by varying the voltage of the anode tube, which produces coupled low-high energy spectra hitting the object of investigation. The final image is still generated by transmission, but in this case is the summed image of the two energy-spectra at the two different voltages through the target, This technique

has the advantage of generating the image by exposing low-Z materials and high-Z materials thanks to the two-energy sets.

X-ray Computed Tomography (X-CT) consists in translation and/or rotation of the object relative to the source and detector. Well-known for its use in medical imaging, this technique consists of a detector and X-ray tube, mounted in a rotating gantry. The gantry rapidly spins around the patient and moves up-down in a guided slit. X-ray CT produces three dimensional images by recombination of layer images. However, this technique requires correction and reconstruction algorithms, which are fundamental for generating the final 3D images. On the other hand, backscatter imaging has the potential to deliver 3D data sets and also layer images with no prior need for reconstruction as proved by Neuman and Zahorodny [31].

There are also other techniques to be mentioned, such as X-ray Diffraction (XRD) and X-ray Fluorescence (XRF). These methods are often applied (but not limited to) for detecting features for security applications. Wells and Bradley (2012) reviewed these detection techniques for aviation security. They will not be included as a part of this discussion, as the main focus of this work is X-ray backscatter imaging.

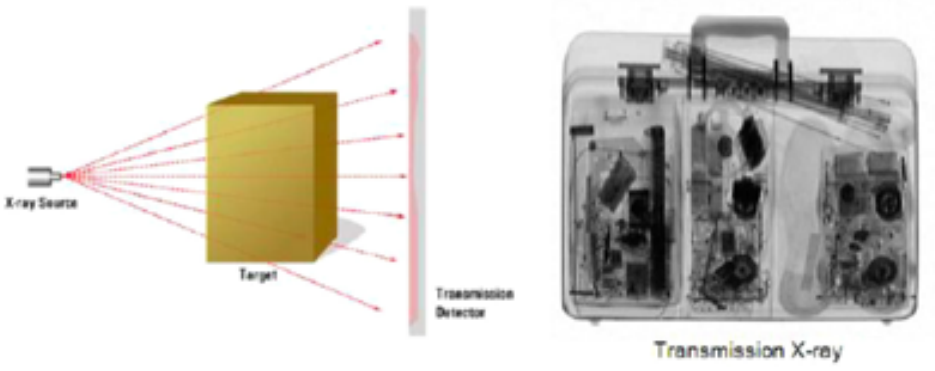

(a) (b)

Figure 3.1 X-ray transmission geometry (a) and transmission X-ray image of a suitcase (b).

3.3 X-ray Compton Backscatter Imaging

Traditional X-ray radiography provides information in a 2D image about the location and orientation of the object; it provides sharp images with relatively high flux. But X-ray imaging by transmission is not able to give information about the depth of a feature. Additionally, if there is a low-Z feature in one plane, this may be hidden by an overlapped high-Z material, as in transmission X-rays would be attenuated within the volume of the material. Finally, there are cases where access is physically restricted for taking exposures in transmission geometry, i.e. from both sides of the target object.

These issues have led to the development of a wide range of X-ray methods of depth determination. Compton backscatter imaging has proven to be the most suitable technique for depth determination with access from one side of the target only [32], [33], [34]. Compton backscatter was one of the first methods with the ability to determine material depth and it was first acknowledged as 'Z-backscatter' (fig. 3.2(b)) for the advantage of greater sensitivity than X-ray transmission to density variations in low-density materials, such as carbon-based materials (plastics, paraffin), liquids, and gases [18]. However, Compton backscatter imaging is limited by the depth X-rays can reach within the thickness of the target object and also requires longer exposure time than X-ray transmission systems. This means such an imaging system still does not work for a thick object, as only the surface would be visible. As we have said before, Compton backscatter imaging has the advantage compared to X-ray transmission of being able to capture images from one-side (figure 3.2(a))

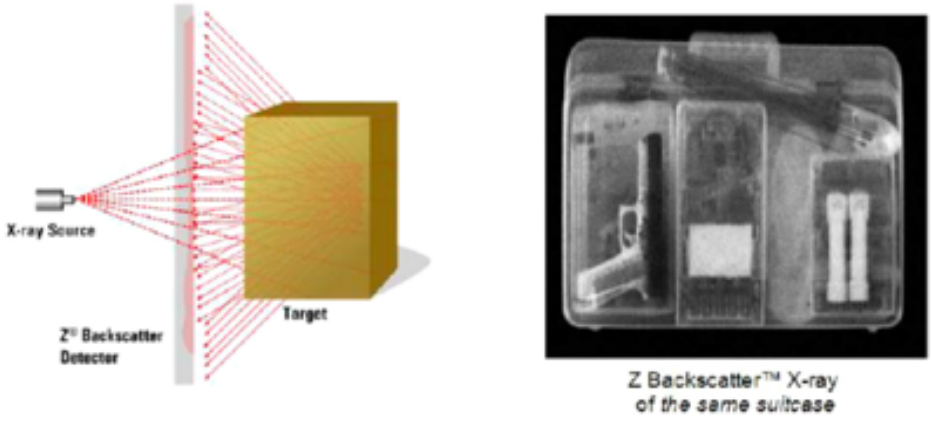

(a) (b)

Figure 3.2 X-ray Compton backscatter geometry (a) and X-ray Compton backscatter image of a suitcase (b)

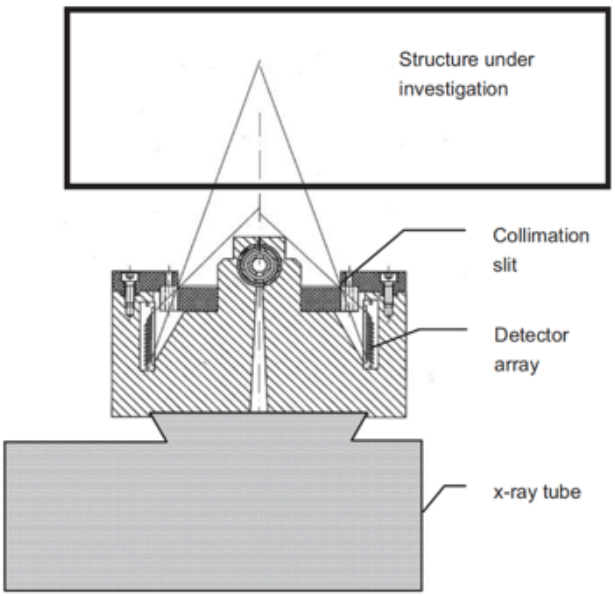

Figure 3.3 COMScan imaging system.

There are few Compton Backscatter Imaging (CBI) systems commercially available; however, ComScan [33] should be mentioned, as this was the first Compton scatter imaging system device. ComScan consists of a linear scanner with a collimated X-ray beam able to collect up to 10 lines per second and a 60 mm length 2mm depth crystal scintillator detector array. ComScan has the ability

to detect up to 50mm depth with maximum 0.5 mm spatial resolution [18]. A cross section of the equipment is shown in figure 3.3.

In Compton backscatter imaging, the scattered photons are observed using a detector, usually a CCD (pixelated) camera.

Compton scatter depends on the beam energy, which generates X-ray emission substantially in all directions, especially at low and intermediate energies. Hence, the detector can potentially be placed in any desired position relative to the radiation source and scattering object. This implies the CBI technique allows us to freely choose the measurement geometry for monitoring the backscattered radiation from voluminous or strongly absorbing material [18]. CBI can also reveal, with its angular distribution, specific structures at different angles. These features could reveal a unique signature allowing the detection of low-Z materials such as polyethylene or Lucite, which are not easy to identify with other X-ray imaging techniques. However, a regular CCD detector is not capable to collect energy-spectra, just exposures. Thus, Compton imaging would benefit from the use of a pixelated detector which should not just be able to collect the images, but also with the properties of an energy-dispersive detector, capable of generating energy-spectra at each pixel. Currently, the only device able to determine energy-spectra together with exposures is the HEXITEC detector [35] [36], which was used in this research work in both simulation and experiment and is illustrated in chapter 8. There are physical limitations with the HEXITEC detector (such as spatial resolution and detector size). The design of an imaging device for Compton scatter can be efficiently optimized by exploring the fundamental physics of backscatter imaging by simulation, the key tool for determining the optimum configuration for CBI at just the cost of computational time. In this thesis, Compton backscatter fundamental physics was investigated by simulation with the PENELOPE [37] Monte Carlo simulation code (chapter 5), and will be further discussed in chapter 9.

Scatter radiation requires the beam to be mechanically collimated to form the image [18], with the collimator, a device that narrows the incident beam, in the form of a pinhole mask or coded apertures masks.

In this work, the backscatter images are produced by using an X-ray tube with a 40˚ cone beam at 60-160 kV anode voltage. The X-ray tube is placed aside a CCD shielded detector, which has a thin collimator in front. The collimator can either consist of a pinhole mask or Coded Apertures (CA) masks of different apertures and thicknesses. Sections 3.4 and 3.5 will describe the principles of pinhole and CA imaging. Detailed descriptions of the simulation and experiment of the physical system are given in the chapters 6 for the X-ray tube, and 7 for the imaging system.

3.4 X-ray backscatter imaging with pinhole

In optics, usually a camera lens is used to focus the image on to a light-sensitive detector. With X-rays, this is not achievable as X-rays are not refracted (refractive index equal to ~1) [10], and X-rays pass through the lenses without focusing.

X-rays can only generate an image by using a pinhole or a multi-hole radiopaque mask, placed between the irradiated object and the detector. For a pinhole, the hole is located in the center, and serves to project the scattered photons from the radiative source towards the detector. The scheme of pinhole imaging is shown in figure 3.4.

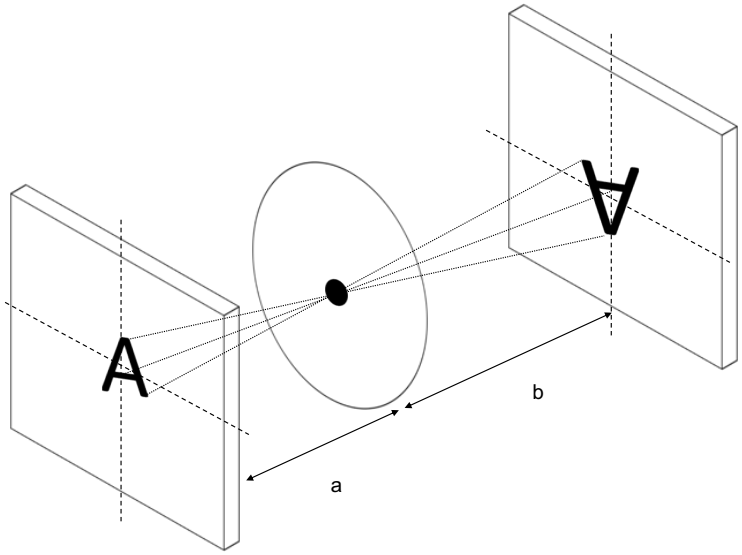

Figure 3.4 Principle of pinhole imaging projection. The object (letter A), which is assumed to be irradiated, is located at a distance a from the pinhole mask, while the distance pinhole-detector is b. The magnification factor is the ratio $(a+b)/a$ of the sum of the distances divided by the object-pinhole distance. The object is reflected or emitted through the pinhole aperture, inverted on the central optical axis and then projected onto the detector.

In principle, the spatial resolution of a pinhole mask is defined by the aperture diameter. In practice, it is also influenced by the masks' material and its thickness which must both be carefully chosen when manufacturing a pinhole collimator.

The first parameter to consider is the material, which is chosen based on the attenuation coefficient. For a lower attenuation coefficient, the mask thickness must be higher to reduce X-ray penetration. Yet, higher thickness would lead to artefacts such as collimation effects, which would limit the field of view. Let us assume the chosen material has a relatively low attenuation coefficient compared to others. It would be natural to increase the thickness of the mask to absorb X-rays. But in the near-field application and for a large field of view, then the image would not be fully resolved, and partial coding would occur.

Consequently, the other option is to use a larger pinhole aperture, and giving the advantage of exposure time decrease. But this would occur at the expense of the

spatial resolution, which would drop, and the detected object would appear blurred and noisy as more X-rays are passing through the hole.

Thus, the design of a pinhole mask is a combination of material, thickness and aperture, and that is highly related to the kind of application. In this work (see chapter 7), the pinhole mask was simulated to explore the combination of all these factors, and to find out the optimum configuration with different materials, thicknesses and apertures and with application to the near-field and for a field of view compatible with backscatter imaging application.

There are other parameters to be considered when estimating spatial resolution, pinhole mask sensitivity and magnification factor. Generally, sensitivity is the fraction of photons emitted from a point source that reach the camera surface.

For a pinhole mask or collimator, the sensitivity is a function of the inverse square of the distance between the source and the pinhole aperture. It also increases as the square of the pinhole diameter, with consequent loss in spatial resolution [38].

The magnification factor is the ratio between the sum of the distances object-pinhole and pinhole-detector divided by the distance pinhole-detector. The object is reflected or emitted through the pinhole aperture, inverted on the central optical axis and then projected onto the detector (fig. 3.6). The magnification factor affects the spatial resolution of a pinhole imaging system inversely. With increased magnification factor, the detector intrinsic resolution decreases, with an effect on the spatial resolution of the total system [39].

The pinhole mask is usually fabricated with high atomic number material sheets, such as lead and tungsten, but other materials will be considered for this work, such as tungsten epoxy resin, and bismuth alloy. These materials, which were carefully chosen for CA applications in the CBI, were simulated in PENELOPE, and results will be found in chapter 7.

3.5 X-ray backscatter imaging with Coded Apertures

Although pinhole imaging process is simple, it only allows a small amount of light to penetrate, producing a very faint image or else requiring a long exposure time. In order to produce a recognizable image, the amount of light detected must be increased. Longer exposure time will improve light intensity, while any movement during this time will tend to blur the image. A larger pinhole will improve light intensity by allowing more light to enter in a given time, but at the cost of image resolution. This means that a larger pinhole will produce a brighter image, with lower resolution.

The only way to increase the light intensity is with multiple pinholes (fig. 3.5), which can be mathematically coded to form a specific pattern. These masks are called Coded Aperture masks (CAs) [40]. Coded aperture masks increase the sensitivity of the imaging camera as more photons pass through the holes.

The CA mask produces a convoluted image, which needs to be encoded by using a complementary decoding aperture, represented digitally in the reconstruction code.

A CA mask comprises a number of discrete elements, either opaque or transparent to the incident photons. In mathematical terms, masks are represented as binary arrays with the ones corresponding to the transparent elements, and the zeros to opaque elements [41]. The raw signal from the detector is the encoded signal from the object and not a directly recognizable image. The recorded signal can then be digitally or optically processed to extract the reconstructed image of the object. An example of the decoding process is given in figure 3.6.

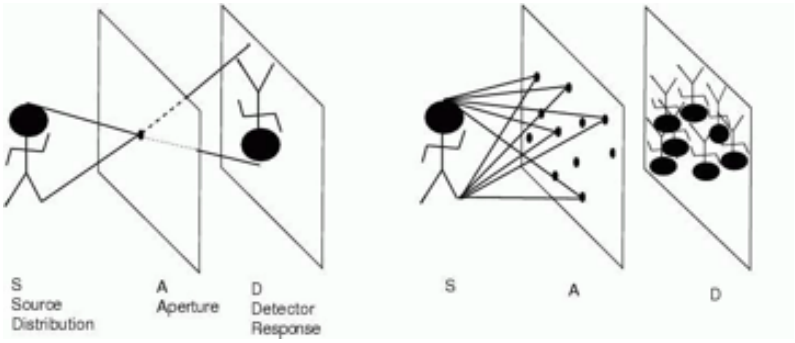

(a) (b)

Figure 3.5 Pinhole imaging (a) and multihole imaging (b)

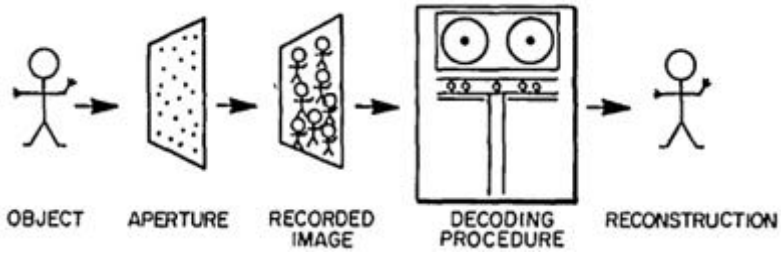

Figure 3.6 Coded aperture imaging principle. The recorded image of the object through the multihole mask needs to be decoded for the final image reconstruction.

The coded aperture approach for radiation detection has its origin in scatter-hole camera applications for X-rays and gamma rays for astronomy.

Introduction of a multi-hole mask improves the SNR while maintaining a good angular resolution of a small diameter, pinhole camera.

Different types of coded aperture X-ray cameras and telescopes were implemented. In this thesis work some CA will be simulated for comparisons with experiment, such as the 19x19 MURA (Modified Uniform Redundant Array), the 37x37 Non-Two-Holes-Touching (NTHT) MURA, and 17x21 Singer Set (fig. 3.7), and the correspondent mosaicked version [42].

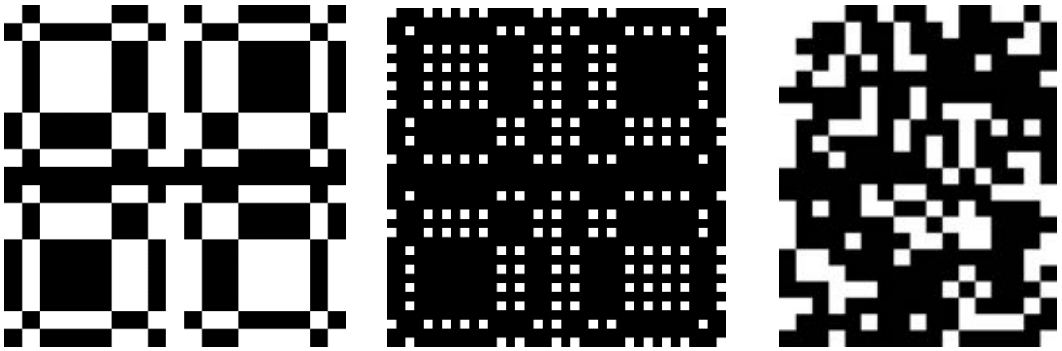

(a) (b) (c)

Figure 3.7 CA mask patterns: (a) 19x19 MURA, (b) 37x37 NTHT MURA (c) 17x21 Singer Set.

3.6 Chapter Summary and critical analysis

Compton Backscatter Imaging principles with both pinhole and Coded Apertures were illustrated in this chapter. CBI is an one-side imaging technique based on Compton scatter cross section, as described by Klein-Nishina [16].

Compton scatter imaging requires three basic elements: an X-ray source, typically a diagnostic X-ray tube, a target sample, and an imaging camera coupled with an X-ray collimator/mask. The image generated by Compton scatter offers unique depth features against transmission [18]. Applying CBI to situations with the target located behind a barrier has a huge advantage over X-ray transmission for which it is impossible to access both sides of the target.

CBI has also the advantage that we may position the device anywhere in space, and it is still capable of delivering 3D information of the scattered object. This represents a plus against Computed Tomography (CT), which works in transmission: the object size is limited by the diameter of the rotating gantry where the imaging system is confined.

Finally, CBI has been historically used in medicine and astrophysics, but finds its one of the applications in security and counter terrorism for its exceptional geometric flexibility and its ability to detect concealed object through barriers.

ComScan is the only commercially available CBI device, but it suffers from a limited field of view and requires long exposure times. For these reasons, it is desirable to develop by simulation and experiment a fan beam device equipped with coded aperture to minimise the exposure time and enhance the field of view. This would result in a fast and reliable X-ray imaging system capable of easily detecting concealed materials.

Exploring backscatter X-ray imaging, both for pinhole and coded apertures, by simulation is advantageous compared to the use of experiment, as modelling requires only computational time. With simulations, it is possible to determine the parameters such as geometry, material choice and mask parameters to optimise performance of any physical detector.

4 REVIEW OF CURRENT MONTE CARLO PARTICLE/PHOTON TRANSPORT SOFTWARE

4.1 Chapter Outline

Monte Carlo simulation is historically one of the most reliable methods for modelling the particles and photons radiation transport. In this chapter, an overview of the principles of modelling and simulations will be given (section 4.2), and the different approaches between Monte Carlo and semi-empirical modelling highlighted. The most prominent Monte Carlo codes will be reviewed and compared against deterministic simulation codes (sections 4.3-4.5).

In this work, Monte Carlo simulation was applied to radiation transport, which will be reviewed in 4.6. The current Monte Carlo codes will be briefly described in section 4.7. The parameters for choosing the suitable Monte Carlo code for the specific application will be explored and benchmarks showed in 4.8. Finally, an overview of the chapter and the reasons for justifying PENELOPE Monte Carlo code for the application in this research work will be examined in 4.9.

4.2 General principles of simulation and modelling

Computer simulation provides an important method of analysis for solving real-world problems safely and efficiently. It gives valuable solutions by giving clear insights into complex systems represented as computational models [43]. Computer simulation is a mathematical model that describes or computationally creates a system process [44].

In a simulation, computational models can be used to study existing or proposed characteristics of a system. Unlike physical modelling, computational modelling is computer based and uses algorithms and equations, that is simulation enables experimentation on the computational model [44].

Simulations are fundamental when conducting experiments on a real system is impossible or impractical, often because of cost or time. Simulations offer the user to investigate the effects of specific design decisions and explore the merits of alternative designs without actually physically building the systems.

Consequently, the overall cost of making the physical model decreases significantly [44].

Usually, a simulation tool is a software program/package, which includes a dynamic environment for design and analysis of computer models, with the possibility of rendering in 2D and/or 3D.

Computer simulations may vary from computer programs that run a few minutes, to network-based groups of computers running for hours, to ongoing simulations that run for days. Depending on the nature of the physical problem, a simulation can be simply performed in a laptop/desktop machine, or High Performances Computer. A simulation can run on a single core, or on multiple cores in parallel, in which case the simulation will be as fast as the number of cores called by the simulation program during the execution. Generally, the higher performance specifications of the computational environment, the faster the simulation is. However, the speed of a simulation depends also on the accuracy the computed model is described. Computational modelling typically involves:

- A mathematical model – typically a set of mathematical equations (might include ODEs or PDEs). The more accurate the model typically the more expensive it is to solve. Modelling errors lead to inaccuracies that cannot be reduced without improving the model.
- A discretisation – the mathematical model is converted to a discrete form that may be solved on the computer. Higher order accuracy discretisations given a greater rate of convergence than lower order ones to the solution of the mathematical model as a discretisation parameter (time step, mesh size) is reduced. Discretisation errors may be reduced at the expense of CPU time, memory or both.
- A computer program – an implementation of the discretisation on a computer. It may be subject to programming errors which are reduced by reducing quality software libraries or good/experienced programmers.
- A simulation run on a computer that is subject to floating point round-off errors that might accumulate for a long-running simulation.

- Results – subject to modelling errors, discretisation errors, programming errors (bugs), round-off errors, and also possibly human errors (inappropriate settings etc.)

The use of simulation has a wide and diverse range of applications, including physics, medicine, industry, engineering, aeronautics, chemistry, bioinformatics, social sciences, defence, Artificial Intelligence (AI), and most other scientific fields. Computer simulations have become a fundamental part of tackling mathematical modelling of many natural systems in science and in the process of engineering new technologies, to gain insight into the operation of those systems, or to observe their behaviour. Nevertheless, computational physics does not replace theory or experiment, but enhances our understanding of physical processes, by combining the mathematical models, and validating or even planning a physical experiment (fig. 4.1). One example is designing and characterising a detector which can be either used for particle physics, medicine and/or engineering.

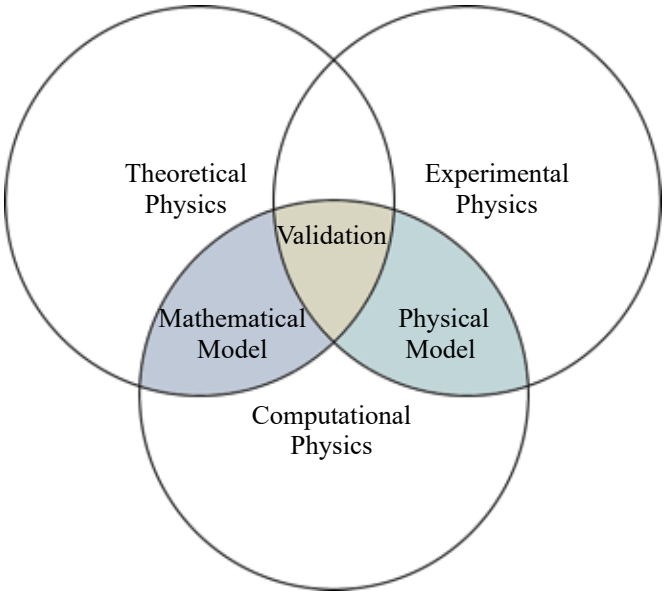

Figure 4.1 Computational physics against theoretical and experimental physics

With current technologies, it is relatively easy to manufacture instruments for experimental work. However, to fully optimise the design to enhance the

characteristics of an instrument, or create and explore a new one, simulation is fundamental. For example, simulating a prototype detector is essential to reduce design manufacturing costs until the final application in an experiment. But simulations are also helpful to gain an insight into the structures, e.g. regarding their operation principles, as well as their advantages and limitations, or even exploring their optimisation before the physical manufacture.

Classically, computer simulations concern predicting performance of a system under given operating conditions. More recently computer simulations have been concerned with predicting performances subject to the uncertainty of input data, model geometry, etc.

Computer simulations applied to particle and photon transport are based on estimating probability distributions, and generally require sophisticated mathematical models. There are two main approaches to modelling for computer simulations, analytical and Monte Carlo. Analytical method is equation based, while Monte Carlo approach is stochastic. The definition of analytical methods will be outlined in 4.3, while Monte Carlo methods will be discussed in detail in 4.4. Monte Carlo approach will then be compared against analytical methods in 4.5.

4.3 Principles of analytical method

In the analytical method, the probability distributions is equation-based or deterministic, that is the probability associated with the output random variables are calculated from the probability distributions associated with the input variables. Generally, analytical simulations are simple, accurate, computationally efficient, and provide the exact relationship between the input variables and final results [45]. Analytical methods are suitable for relatively simple models. Analytical models may be preferred for quick look analysis, because of their speed of execution [46].

4.3.1 SpekCalc deterministic simulation for X-ray tubes

SpekCalc [47] is an example of a program based on analytical methods, with a model based on deterministic equations. SpekCalc is a computer code for

simulating the output of medical X-ray sources. This software creates a simple model including target, anode voltage and filters of different thickness. The theoretical approach underlying SpekCalc combines semi-empirical models of X-ray production. It uses pre-calculated survival probabilities for an electron reaching certain depths within the target, and the electron energy distributions at those depths [48]. SpekCalc allows the user to calculate, display and save, in energy bins of user-defined width, X-ray spectra emitted from tungsten anode tubes. The user selects the electron energy in keV, the X-ray take-off angle, and the amount of filtration by layer thicknesses [49]. Filtration can be selected according to thickness and is limited to ten materials: air, beryllium, aluminium, copper, tin, tungsten, tantalum, water, titanium, graphite (see fig. 4.2). The range of voltages that can be modelled is wide (40–300 kV) making the utility useful in both diagnostic imaging and radiotherapy. Spectra are generated within a few seconds computation time. Although this program is user-friendly, it presents some limitations. These include limited materials, physical interactions, such as bremsstrahlung spectra of tungsten target only, and more importantly it is only possible to model the generation of X-rays rather than model the transport and interactions of X-rays beyond the generator and its filters [50]. SpekCalc will be used in this research work for validating PENELOPE simulations of a VJ Technology X-ray tube (chapter 6).

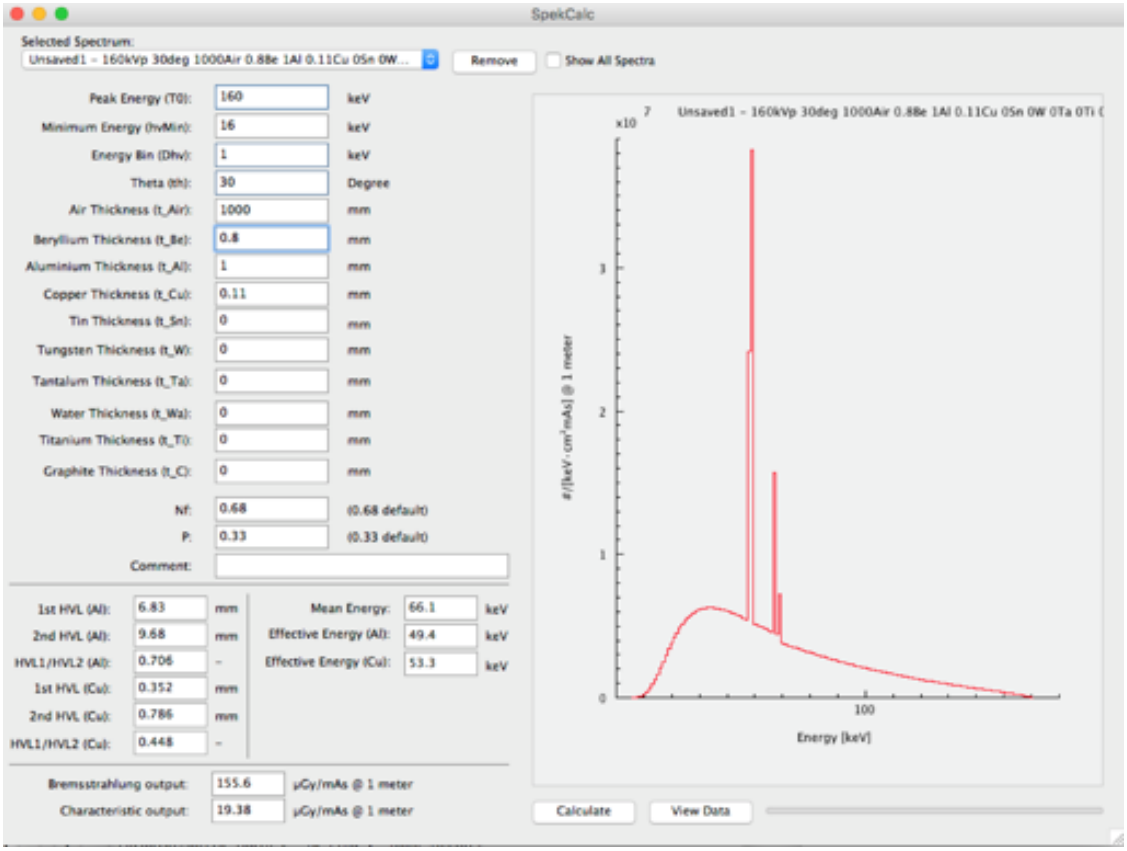

Figure 4.2 SpekCalc GUI. This is an example of a 160 keV energy spectrum from a W target.

4.4 Principles of Monte Carlo modelling

The name “Monte Carlo" stems from scientists in 1940s working on the nuclear weapon project at Los Alamos, who created numerical methods based on random numbers [51]. Nowadays, Monte Carlo methods are widely used. Monte Carlo techniques are particularly applicable to solve complex physical and mathematical problems, particularly those involving multiple independent variables where more conventional analytical methods would not be applicable.

The essential characteristic of Monte Carlo simulation is the use of random numbers and random variables. A random variable is a quantity resulting from a repeatable process, whose actual values cannot be predicted with certainty. By repeating the process a large number of times, the distribution of the output random variable estimates the parameters of interest, e.g. mean, standard

deviations, etc. [51]. Monte Carlo methods can be applied to simulate probabilistic phenomena, e.g. games of chance, or the more complex radiation transport.

4.5 Monte Carlo Simulation or analytical methods?

Knowing the principles of both analytical methods and Monte Carlo simulation, we can now compare and choose the most suitable for the cases of study. Both analytical and Monte Carlo have their advantages and disadvantages, the main ones are listed in table 4.1. Generally, Monte Carlo simulation is preferred for its flexibility in handling complex systems that may be subject to change. For simpler systems, or studies of the trends, analytical methods may suffice.

The decision as to whether or not to use analytical, e.g. deterministic equations, or Monte Carlo simulation methods may be influenced by the following factors. First of all, we should take into account the complexity of the model. Monte Carlo simulation often gives better physical visibility of a complex system analysis than a set of equations, aiding interpretation of the output. Secondly, the aim of the model should be considered. If the model is complex, Monte Carlo simulations achieve more accurate results than analytical models. The third factor to consider is accuracy. Although analytical models are deterministic, they usually involve simplifying assumptions to make the model analytically tractable. Then, we should carefully think about future development of the model. If a model is likely to be further refined ad developed, an initial model that may be initially handled analytically may not be so when further development requirements are placed. A Monte Carlo simulation model may therefore be appropriate from the beginning. Finally, we should consider the model application. For quick look analysis, analytical models may be preferred, because of their speed of execution. The repeated running involved in Monte-Carlo simulation can cause long execution times before estimates of system parameters of interest are obtained. However, the application of Monte Carlo may be preferred if the model is trying to determine solutions to problems which are not achievable with analytical methods. Then, there are techniques which can be applied for reducing computational time.

Table 4.1 Main advantages and disadvantages of analytical and Monte-Carlo simulation models (adapted from [46]).

	Simulation Method	
Advantages	Analytical	Monte-Carlo
	a. Once the model is defined, it gives exact results.	a. Flexibility and no analysis limits, including capability to handle empirical distributions.
	b. Output is rapidly generated.	b. Can be further extended, developed and managed as required.
Disadvantages	a. Requires assumptions to solve the problem.	a. It requires a computer.
	b. Less flexible than Monte-Carlo.	b. Calculations can take much longer than analytical models.

4.6 Monte Carlo simulation of radiation transport

In Monte Carlo simulation of radiation transport, the dynamics of a nuclear/particle physics system are modelled. The transport of particles/photons is tracked as a weighted random sequence of free flights. Particle tracking, also known as particle history, may end with an interaction event where the particle changes its direction of movement, loses energy and, occasionally, produces secondary particles [52].

Monte Carlo simulation of radiation transport consists of a numerical generation of random histories based on initial conditions determined by the kind of source.

To simulate the particle histories, the interaction model is a set of differential cross sections (DCS) describing the relevant interaction mechanisms.

The DCSs determine the Probability Distribution Functions (PDFs) of the random variables which characterise the transport tracking, i.e.:

1) free path between successive interaction events;

2) kind of interaction taking place;

3) energy loss and angular deflection in a particular event;

4) initial state of emitted secondary particles, if any.

Once these PDFs are known, random histories can be generated by using appropriate sampling methods. If the number of generated histories is large enough, quantitative information on the transport process may be obtained by simply averaging over the simulated histories [51].

Monte Carlo simulation programs comprise a number of algorithms with different functions. In the following sections, the fundamental elements of a Monte Carlo code will be defined, including the random number generator (RNG), mean-free path and radiation transport through the matter, interaction cross section, random track generation and state variables, statistical uncertainties. Finally, variance reduction (VR) techniques will be briefly reviewed.

4.6.1 Random Number generation in Monte Carlo simulation of radiation transport

The core of a Monte Carlo program is the random number generator (RNG). A computer is not realistically capable of generating random numbers, because the output of any program is by definition predictable. Therefore, the results of the RNG are pseudo-random numbers. Using pseudo-random numbers is a way to solve complex problems. A pseudo-RNG consists of an algorithm calling a sequence of uncorrelated numbers within a defined period. Numbers in this sequence must be uncorrelated to allow the simulation to be independent of the random sequence. The defined period in the sequence should be large enough to avoid correlation in the Monte Carlo simulation. Otherwise, the RNG will

generate repetitive results if the sequence is reused several times. Typically, a RNG produces random numbers distributed near uniformly within a defined interval (usually $[0,1]$), i.e. the random numbers within the defined interval all have an equal probability of being generated [53].

In radiation transport simulation, the RNG cannot simply use uniformly distributed random numbers. The distribution should be that associated with the physical process being modelled. The RNG is therefore weighted with a specific probability weight distribution function $p(x)$. The probability weight distribution is a function which governs the general probability distribution by weighting the number of events recorded. In radiation transport, this is particularly useful, for example, when simulating secondary particles generated after the primary beam interacts with the matter.

Let us suppose the RNG can only produce uniformly distributed random numbers η within $[0,1]$. But we want to generate a random number ξ within the interval $[a, b]$ with a non-uniform probability weight function $p(x) \geq 0$.

To calculate the random number ξ it is possible to use the cumulative distribution function $P(x)$ by defining

$$\xi = P^{-1}(\eta) \qquad 4.1$$

where $P^{-1}(x)$ is the inverse of the integral

$$P(x) = \int_a^x dx' p(x') \qquad 4.2$$

with $\mathrm{a} \leq \mathrm{x} \leq \mathrm{b}$, and $P(a) = 0$ and $P(b) = 1$.

The non-negativity of $p(x)$ ensures $P(x)$ is monotonically increasing in the interval $[a, b]$. The function 4.2 is defined within the interval $[0,1]$ and is distributed according to the probability weight function $p(x)$. This method was devised by Nelson et al. [54] and is known as the transformation method. The transformation method has the advantage to be monotonically increasing and produces 1-to-1 variables, within [0,1]. However, this method may not always be computable as it may not be defined [55].

Let us suppose it is not possible to simulate a value of directly using inverse transform algorithm. We can use the acceptance-rejection algorithm. The acceptance-rejection method is a basic technique used to generate observations from a distribution. The rejection method is a type of exact simulation method and works for any distribution. It consists of defining a comparison weighting function $g(x)$, with $g(x) > p(x)$ within the defined interval $[a, b]$.

Rejection sampling is based on the observation that to sample a random variable one can perform a uniformly random sampling of the 2D cartesian graph, and keep the samples in the region under the graph of its density function. Note that this property can be extended to N-dimension functions [55].

The function $g(x)$ should not differ too much from $p(x)$. For instance, let us sample a random number ξ_0 from $g(x)$ using the transformation method. A new number η_0 from the interval $[0, g(\xi_0)]$ is now generated. We can only accept ξ_0 as valid random number if $\eta_0 < p(\xi_0)$; otherwise, if $p(\xi_0) \leq \eta_0 \leq g(\xi_0)$, ξ_0 is rejected, and the sampling of a new number starts [53]. For instance, in radiation transport the rejection method is useful when calculating the probability of interaction of the beam with the matter when the matter is a composition of objects. The rejection method, in this case, is applied for stopping the beam, change direction, or stopping the generation of secondary particles.

4.6.1 Mean-free path and interaction cross section defined in Monte Carlo radiation transport

A Monte Carlo code for radiation transport must contain algorithms for describing the trajectory of particles/photons through the matter. Generally, we assume particle/photons travel through a homogeneous random scattering media of uniform density with a certain probability of interaction.

The probability of interaction depends on the mean free path, which is the average path length particles/photons travel free from interactions with the medium. Theoretically speaking, the mean free path is a function of the interaction cross section $\sigma(E)$, with the cross section as already defined in chapter 2, and the unit path length [1].

Let us consider a homogeneous beam of particles/photons hitting normally on a very thin material of thickness dt (see figure 4.3). Let us suppose also the material is made of N particles (atoms or molecules) per unit volume, which we can be approximated as small spheres. The incident beam will see a uniform distribution of spheres per unit surface equal to $\mathrm{N}dt$. If I I s the particle density at thickness of the incident beam, then the density of particles transmitted through the thickness dt without interacting is $I - dI$, where $dI = I\mathrm{N}\sigma dt$ is the number of particles that goes through interactions per unit time and unit surface of the material, N is the number of particles, σ is the interaction cross section and dt the distance travelled by the beam through the target. The interaction probability per unit path length or mean free path λ is:

$$\frac{dI}{dt} = I\mathrm{N}\sigma = \frac{I}{\lambda} \qquad 4.3$$

The solution of this differential equation is the Beer-Lambert law (see chapter 2).

Eq. 4.3 comes from the calculation of the probability of having the following interaction integrated over the travelled length

$$P(t) = \int_t^\infty p(t)dt = \int_t^\infty \frac{I(t)-I(t+dt)}{I(t)} = \lambda^{-1}e^{-t\lambda^{-1}} \qquad 4.4$$

where the travelled length is defined within the interval $(t, t+dt)$. Therefore, it follows that the probability of interaction is

$$p(t) = \mathrm{N}\sigma e^{-N\sigma t} \qquad 4.5$$

The mean free path is then

$$\lambda = \langle t \rangle = \int_t^\infty t\, p(t)dt = \frac{1}{\mathrm{N}\sigma} \qquad 4.6$$

whereas $\lambda^{-1} = \mathrm{N}\sigma$ is the interaction probability per unit path length.

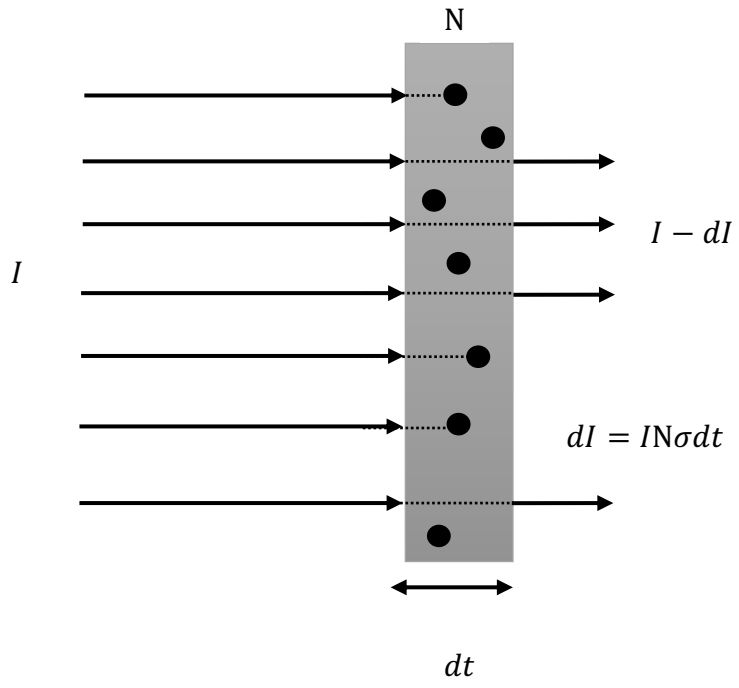

Figure 4.3 Beam attenuation through a thin material of thickness dt**.**

Let us now consider a particle with energy E moving towards a material of thickness t. In each interaction the particle may lose a certain energy W and change its direction. Let us assume that particles can interact with the thickness t through two independent mechanisms, which represent elastic (A) and inelastic (B) scatter. The scattering model is then described by the molecular DCSs:

$$\frac{d^2\sigma_A(E,\theta,W)}{d\Omega\, dW} \text{ and } \frac{d^2\sigma_B(E,\theta,W)}{d\Omega\, dW} \qquad 4.7$$

where $d\Omega$ is the solid angle element in the direction (θ, ϕ), with the azimuthal scattering angle equal to $1/2\pi$, while W is the energy loss with the interaction. Considering that the molecules are randomly orientated, the DCS is then independent of the azimuthal angle ϕ. Thus, the total cross section per molecule for elastic (A) and inelastic (B) scattering, is:

$$\sigma_{A,B}(E) = \int_0^E dW \int_0^\pi 2\pi \sin\theta d\theta \frac{d^2\sigma_{A,B}(E,\theta,W)}{d\Omega\, dW} \qquad 4.8$$

Therefore, the total cross section is:

$$\sigma_T(E) = \sigma_A(E) + \sigma_B(E). \quad 4.9$$

From 4.6, the interaction probability per unit path length is:

$$\lambda_T^{-1} = \mathrm{N}\sigma_T \quad 4.10$$

Consequently

$$\lambda_T^{-1} = \lambda_A^{-1} + \lambda_B^{-1} \quad 4.11$$

When the particle interacts with the material, the kind of interaction that occurs is a discrete random variable. By applying 4.5 to 4.13, the probabilities for A and B scatter is

$$p_A = \frac{\sigma_A}{\sigma_T} \text{ and } p_B = \frac{\sigma_B}{\sigma_T} \quad 4.12$$

The PDFs of the polar scatter angle and the energy and the energy loss in individual scattering events are

$$p_{A,B}(E,\theta,W) = \frac{2\pi \sin\theta}{\sigma_{A,B}(E)} \frac{d^2\sigma_{A,B}(E,\theta,W)}{d\Omega dW} \quad 4.13$$

Note that $p_{A,B}(E,\theta,W)d\theta dW$ gives the probability that, in a scatter event, the particle loses energy in the interval $(W, W + dW)$ and is deflected into directions with polar angle relative to the initial direction in the interval $(\theta, \theta + d\theta)$.

The analysis of interactions in a random-scattering within a material thickness involves the DCSs, which describe the interaction with individual molecules, and the density of molecules N, which characterises the macroscopic state of the material. The DCSs can be affected by the different material densities/composition, thus it is more appropriate to describe each interaction mechanism by means of the so-called differential inverse mean free path. The differential inverse mean free path for the interaction process A is defined as:

$$\frac{d^2\lambda_A^{-1}(E,\theta,W)}{d\Omega dW} = N \frac{d^2\sigma_A(E,\theta,W)}{d\Omega dW} \quad 4.14$$

The differential inverse mean free path has the dimensions of $(length \times solid\ angle \times energy)^{-1}$; the product $\frac{d^2\lambda_A^{-1}(E,\theta,W)}{d\Omega dW} d\Omega dW$ is the probability per unit path length that a particle undergoes a collision of type A with angular deflection within $d\Omega$ and energy loss between W and W + dW. The integral of the differential inverse mean free path gives the inverse mean free path for the process

$$\lambda_A^{-1} = \int dW \int 2\pi \sin\theta d\theta \frac{d^2\lambda_A^{-1}(E,\theta,W)}{d\Omega dW} = N\sigma_A \qquad 4.15$$

where $N\sigma_A$ is the macroscopic cross section.

4.6.2 Particle tracking and state variables

At this point, we have all the elements for particle/photon tracking through the matter. Particle tracking begins at a given position, with its initial direction and energy obtained from the source specifications.

After collision with the material, the state of the particle changes, and is then described by its position coordinates $\boldsymbol{r} = (x, y, z)$, energy E and direction of flight, which is determined by the components of the unit velocity vector $\hat{\boldsymbol{d}} = (u, v, w)$ (seen from the laboratory reference frame).

Each simulation track is characterised by a series of state variables, $\boldsymbol{r}_n$, E_n, $\hat{\boldsymbol{d}}_n$, where $\boldsymbol{r}_n$ is the position of the n-th scattering event, E_n is the energy after the event, and $\hat{\boldsymbol{d}}_n$ describes the direction of motion after collision.

After having simulated the state $\boldsymbol{r}_n$, E_n, $\hat{\boldsymbol{d}}_n$, then the length s of the free path to the next collision, the involved scattering mechanism, the change of direction, and the energy loss in this collision are random variables that are sampled from the corresponding PDFs. Thus, the subsequent interaction takes place at the position

$$r_{n+1} = r_n + s\hat{d}_n \qquad 4.16$$

The polar scattering angle θ and the energy loss W (see figure 4.4) are sampled from the distribution $p_{A,B}(E, \theta, W)$ from eq. 4.13, while the azimuthal scattering angle ϕ is defined within $(0,2\pi)$.

After sampling the values of W, θ, ϕ, the energy of the particle is reduced to $E_{n+1} = E_n - W$, and the direction after the interaction becomes $\widehat{\boldsymbol{d}}_{n+1} = (u', v', w')$ as seen in fig. 4.4, with the direction cosines as follows:

$$u' = \pm \sin\theta \cos\phi,\ v' = \pm \sin\theta \sin\phi,\ w' = \pm \cos\theta \qquad 4.17$$

The simulation of the particle tracking is finished when the particle leaves the material system or when the energy becomes smaller than a given absorption energy. This model is only valid when the diffraction effects resulting from coherent scattering are negligible.

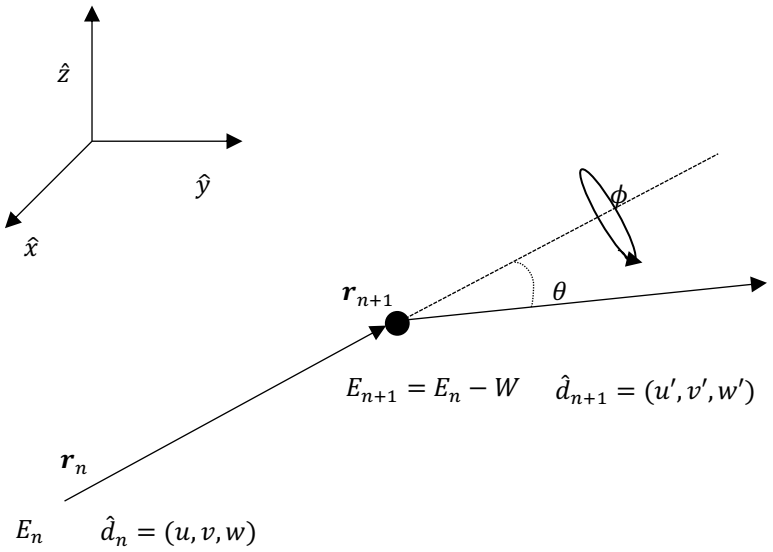

Figure 4.4 Angular deflections in single-scattering event.

4.6.3 Statistical averages and uncertainties

In Monte Carlo simulations any quantity of interest Q is evaluated as the average of a large number N of simulated random showers. The value of Q is normally calculated by integration:

$$Q = \int q(x)p(x)dx \qquad 4.18$$

whereas $p(x)$ is the PDF of the set x of random variables which determine the value $q(x)$.

In simulation of radiation transport, each interaction is described as an individual shower. This generates a set of random values of the variable x and the associated value $q(x)$. In Monte Carlo simulations, the PDF $p(x)$ is described as a cascade of random interaction events, each with its characteristic PDF. Thus, Q is estimated from the mean

$$\bar{Q} = \frac{1}{N}\sum_{i=1}^{N} q_i \qquad 4.19$$

where q_i is the i-th simulated shower.

The statistical uncertainty, i.e. the standard deviation (i.e. the square root of the variance $var(q)$) of the Monte Carlo evaluation is:

$$\sigma_Q = \sqrt{\frac{var(q)}{N}} = \sqrt{\frac{1}{N}\left[\frac{1}{N}\sum_{i=1}^{N} q_i^2 - \bar{Q}^2\right]} \qquad 4.20$$

Note the standard deviation is $\sigma_Q = \sqrt{var(q)}$ if $N \to \infty$.

4.6.4 Variance reduction techniques in Monte Carlo codes

One of the greatest issues of Monte Carlo code is simulation time. As anticipated in the introduction of this chapter, simulation time can be from a few seconds to days. Computational scientists worked on different ways to decrease simulation time. Faster computers and high performances computers (HPC) are the best environment to run complex simulation algorithms. However, in some cases this is not enough, thus computational scientists worked on techniques to improve the efficiency of Monte Carlo codes by introducing variance reduction algorithms.

Variance reduction techniques (VRT) are methods to improve the efficiency of the Monte Carlo results by reducing the simulation time. VRT algorithms aim to decrease simulation time while maintaining an unbiased estimate of the variance, that is the results from the Monte Carlo simulation must not deviate from the corresponding results without VRT.

Among the different VRT, the first to be mentioned is uniform particle splitting [53]. Uniform particle splitting is a VRT which consists in the multiplication of the number of particles in that specific status. This technique can be applied both to

particles and photons. For instance, this technique is commonly used for simulation of X-ray tubes, represented as follows. An electron beam hits a target material (tungsten, molybdenum, etc.), and produces bremsstrahlung photons. This phenomenon is quite inefficient in nature, as most of the electrons are absorbed within the target. For the Monte Carlo code that means high computational time as the probability of generating X-rays is low. The efficiency of the simulated process can be corrected by applying particle splitting, that is for each electron hitting the target, instead of generating one X-ray photon, there will be more independent X-rays. For example, if for each electron hitting the target the particle splitting factor was five, one plus additional four X-rays will be generated by bremsstrahlung instead of just one (fig. 4.5). This technique will reduce the computational time by a number which is equal to the particle splitting factor [1].

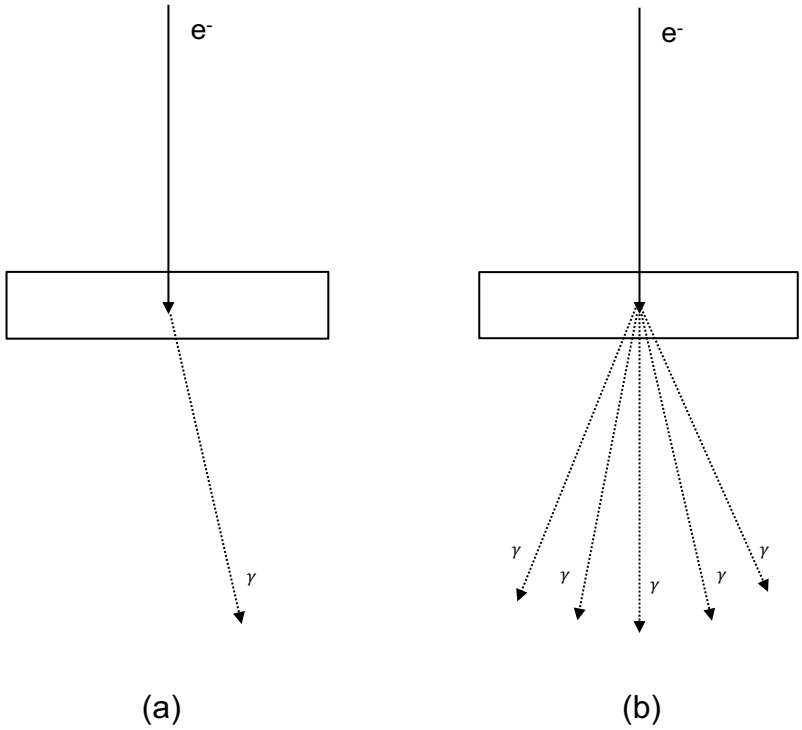

Figure 4.5 Schematic of a Monte Carlo simulation of an electron producing one (a) and five (b) X-ray photons (when particle splitting is enabled).

Russian roulette algorithm provides the particle/photon with a survival probability and is often used in conjunction with particle splitting VRT. For example, while some electrons can generate bremsstrahlung photons, the most part is absorbed

within the target without producing any secondary radiation. In principle, a Monte Carlo code should follow those electrons up, but in that case simulation time will be wasted. Thus, it makes sense to kill those electrons with a probability, which is called probability of killl p_{kill}. The probability of kill is related to probability of survival $p_{survive}$, which is the inverse of the number of split particles N_{split}. The number of killed electrons is $p_{kill} = 1 - p_{survive} = 1 - \frac{1}{N_{split}}$, while the surviving electrons will have a probability increased by a factor of $\frac{1}{p_{survive}} = N_{split}$ [1].

Finally, interaction forcing is a VRT which enhances the interaction cross section within a preferred region. When a particle/photon enters a medium, in the Monte Carlo tracking algorithm the calculation of the trajectory starts. At this point, there are three possibilities: 1) the particle/photon is absorbed 2) the particle/photon exits the material without interacting 3) the particle/photon interacts but is not absorbed. In the second case, however, the Monte Carlo algorithm will still follow the particle/photon but kills the particle/photon as the mean free path of the trajectory falls outside the material. This means wasting simulation time. For this reason, we can enable the interaction forcing VRT, so we can force the particle/photon to interact with that medium.

For photons, for example, interaction forcing is possible if the mean free path lengths are $\lambda = \sum_A^B \mu_i t_i = N \sum_A^B \sigma_i t_i$, where μ_i is the linear attenuation coefficient, N is the number of atoms/molecule per volume, σ_i is the interaction cross section, t_i is the path length, A and B are start and end points of the medium [1]. In principle, it is possible to always enable variance reduction techniques while simulating. However, there are some cases where the information generated with the aid of VRT is distorted, as they can bias the radiation transport by simulating untrue interactions. VRT effects are currently still under investigation.

4.7 Current Monte Carlo codes

Several Monte Carlo particle transport codes are under active development around the world. Among the most widely used are GEANT4 [52], FLUKA [56], MCNP [57] and ESGnrc [58]. Currently dedicated to electron-photon transport

through matter is the PENELOPE [59] Monte Carlo code. PENELOPE is the code applied for this research work, and it will be briefly introduced in this chapter. All the features of the code will be later discussed in chapter 5.

The other Monte Carlo codes will be briefly described in the following paragraphs.

An overview of the codes is captured in table 4.1. Some guidelines of parameters for choosing the Monte Carlo code suitable for the application will be given in 4.8. Finally, the reasons for choosing PENELOPE Monte Carlo code are discussed at the end of this chapter.

Table 4.2 Comparison of Monte Carlo codes PENELOPE, GEANT4, FLUKA, MCNP/MCNPX and ESGnrc.

	PENELOPE	GEANT4	FLUKA	MCNP	EGSnrc
VERSION	2014	10.4 (stable)	2011.2x.3	6.1	
LAB. AFFILIATION	NEA	CERN IN2P3 INFN KEK SLAC TRIUMF ESA	CERN INFN	LANL	National Research Council of Canada University of Wisconsin–Madiso
LANGUAGE	Fortran 77	C++	Fortran 77	Fortran 90/C	Fortran 77-90/C++
COST	Free	Free	Free	RSSIC User licence	Free
RELEASE FORMAT	Source & binary	Source & binary	Source & binary	Source & binary	Source & binary
OPEN SOURCE	Yes	Yes	Yes	No	Yes
WEBSITE	oecd-nea.org/tools/abstract/detail/nea-1525	geant4.web.cern.ch	fluka.org/fluka.php	mcnpx.lanl.gov	nrc-cnrc.gc.ca/eng/solutions/advisory/egsnrc_index.html
INPUT FORMAT	Fixed	C++ main fixed geometry	Fixed or free	Free	C++ main fixed geometry
PARALLEL EXECUTION	Yes (partially)	Yes	Yes	Yes	Yes

GEOMETRY GUI	PENGEOM	Dawn Wired RayTracer OpenGL OpenInventor VRML	FLAIR	VisedX	Grace
ENERGY RANGE	100 eV - 1 GeV	up to 100 TeV	up to 10000 TeV	up to 100 GeV	1 keV to 10 GeV
PRIMARY PARTICLES	Electrons Photons (X-rays, gamma rays) Positrons (Protons)	Electrons Photons Hadrons (protons, neutrons) Leptons (muon, pions, kaons)	Electrons Photons Hadrons (protons, neutrons) Leptons (muon, pions, kaons) Neutrinos and antiparticles	Electrons Photons (X-rays, gamma rays) Positrons Hadrons	Electrons Photons (X-rays, gamma rays) Positrons
Physical model	Photoelectric effect Pair production Incoherent scattering Coherent scattering	Photoelectric effect Pair production Incoherent scattering Coherent scattering Hadronic Decay Optical Photolepton_hadron Parameterization Transportation	Photoelectric effect Pair production Incoherent scattering Coherent scattering Hadronic Hadron-nucleus Evaporation Fission and nuclear break-up	Photoelectric effect Pair production Incoherent scattering Coherent scattering	Photoelectric effect Pair production Incoherent scattering Coherent scattering
Source	Pencil beam Cone/rectangular beam Energy-probability distribution Physical emitter User defined	Pencil beam Cone/rectangular beam Energy-probability distribution Physical emitter	Pencil beam Cone/rectangular beam Energy-probability distribution Physical emitter	Pencil beam Cone/rectangular beam Energy-probability distribution Physical	Pencil beam Cone/rectangular beam Energy-probability distribution Physical emitter User defined

		User defined	User defined	emitter User defined	
Tallies	Flux Energy-probability Energy deposition Dose	Flux Current Charge Kinetic energy Particle density Reaction rates Energy deposition Dose	Flux Current Charge Kinetic energy Particle density Reaction rates Energy deposition Dose	Flux Energy-probability Energy deposition Dose	Flux Energy-probability Energy deposition Dose
EM FIELD	Under development	Yes	Yes	Yes	No
DATA PLOT	GNUPLOT	ROOT	FLAIR	MCPLOT	GNUPLOT
VARIANCE REDUCTION	Yes	Yes	Yes	Yes	Yes

4.7.1 GEANT 4

Geant4 (GEometry ANd Tracking) [52] is a Monte Carlo toolkit for simulating the passage of particles through matter. GEANT4 includes a complete range of functionality including tracking, geometry, physics models and hits. The physics processes offered cover a comprehensive range, including electromagnetic, hadronic and optical processes, a large set of long-lived particles, materials and elements, over a wide energy range from a few eV to the 100 TeV. It has been designed and constructed to expose the physics models utilised, to handle complex geometries, and to enable its easy adaptation for optimal use in different sets of applications. The toolkit is the result of a worldwide collaboration of physicists and software engineers. It has been created exploiting software engineering and object-oriented technology and implemented in the C++

programming language. It has been applied in particle physics, nuclear physics, accelerator design, space engineering and medical physics [60].

In the GEANT4 standard package, physical processes are valid for gamma rays and electrons from 1 keV to 100 TeV. Transport of X and gamma rays takes into account Compton scattering using the free-electron approximation, gamma conversion into electron-positron pair, and photoelectric effect. Bremsstrahlung and ionization are the available processes for electrons and positron [61].

4.7.2 FLUKA

FLUKA (FLUktuierende KAskade) [56] is a general purpose tool for calculation of particle transport and interaction with matter, covering an extended range of applications from proton and electron accelerator shielding to target design, calorimetry, activation, dosimetry, detector design, Accelerator Driven Systems, cosmic rays, neutrino physics, radiotherapy etc.

FLUKA can simulate with high accuracy the interaction and propagation in matter of about 60 different particles, including photons and electrons from 100 eV-1 keV to thousands of TeV, neutrinos, muons of any energy, hadrons of energies up to 20 TeV (up to 10 PeV by linking FLUKA with the DPMJET code) and all the corresponding antiparticles, neutrons down to thermal energies and heavy ions. The program can also transport polarised photons (e.g., synchrotron radiation) and optical photons. Various visualisation and debugging tools are also available.

For most applications, no programming is required from the user. However, a number of user interface routines in Fortran 77 are available for users with special requirements. Another feature of FLUKA, probably not found in any other Monte Carlo program, is its double capability to be used in a biased mode as well as a fully analogue code. That means that while it can be used to predict fluctuations, signal coincidences and other correlated events, a wide choice of statistical techniques are also available to investigate punch through or other rare events in connection with attenuations by many orders of magnitude [62].

4.7.3 MCNP

Monte Carlo N-Particle transport code (MCNP) [57] is a family of Monte Carlo codes for simulating the transport of ionizing radiation (neutrons, photons, electrons, etc.). MCNP was developed at Los Alamos National Laboratory (LANL). The code was written in Fortran at first, then it was integrated with ANSI C. The latest release of the code is currently MCNP6.2, which is the convolution of the latest version of MCNPX and MCNP5. MCNP code-specific areas of application include, but are not limited to, radiation protection and dosimetry, radiation shielding, radiography, medical physics, nuclear criticality safety, detector design and analysis, nuclear oil well logging, accelerator target design, fission and fusion reactor design, decontamination and decommissioning. The code treats an arbitrary three-dimensional configuration of materials in geometric cells bounded by first- and second-degree surfaces and fourth-degree elliptical tori [57].

For photons, the code accounts for incoherent and coherent scattering, the possibility of fluorescent emission after photoelectric absorption, absorption in pair production with local emission of annihilation radiation, and bremsstrahlung. A continuous-slowing-down model is used for electron transport that includes positrons, K X-rays, and bremsstrahlung, but does not include external or self-induced fields.

4.7.4 ESGnrc

EGSnrc [58] is a toolkit for Monte Carlo simulations of coupled electron-photon transport, for particle energies ranging from 1 keV to 10 GeV. It is widely used internationally in a variety of radiation-related fields.

EGSnrc is an extended and improved version of the EGS4 code system developed jointly by NRC and the Stanford Linear Accelerator Center in the 1980s [54].

EGSnrc includes BEAMnrc component which scores the dose using DOSXYZnrc to estimate radiation dose in a voxel geometry. It also includes data processing tools to analyse the beam characteristic in detail and generate radiation dose profiles. EGSnrc provides accuracy and precision of the charged particle transport mechanics and the atomic scattering cross-section data. The charged particle multiple scattering algorithm allows for large step sizes without sacrificing accuracy - a key feature of the toolkit that leads to fast simulation speeds. EGSnrc also includes a C++ class library called egs++ that can be used to model elaborate geometries and particle sources.

EGSnrc is open source and distributed on GitHub. EGSnrc has a wide range of applications that utilise the radiation transport physics to calculate absorbed dose, kerma (kinetic energy released per unit mass), particle fluence, and much more, with complex geometrical conditions. One of the most well-known EGSnrc applications is BEAMnrc, which was developed as part of the OMEGA project. This was a collaboration between the National Research Council of Canada and a research group at the University of Wisconsin–Madison. All types of medical linear accelerators can be modelled using the BEAMnrc's component module system.

4.7.5 PENELOPE

The PENELOPE Monte Carlo simulation code is distributed by NEA databank as a Fortran libraries package. PENELOPE was written by Baró, et al. in 1995 [59].

The computer code system PENELOPE (version 2014) (PENetration and Energy LOss of Positrons and Electrons - photon simulation was introduced later) performs Monte Carlo simulation of coupled electron-photon transport in arbitrary materials and complex quadric geometries for a wide energy range, from a few hundred eV to about 1 GeV. Photon transport is simulated by means of the standard, detailed simulation scheme. Electron and positron histories are generated on the basis of a mixed procedure, which combines detailed simulation of hard events with condensed simulation of soft interactions. A geometry

package called PENGEOM permits the generation of random electron-photon showers in material systems consisting of homogeneous bodies limited by quadric surfaces, i.e., planes, spheres, cylinders, etc.

A mixed procedure is used for the simulation of electron and positron interactions (elastic scattering, inelastic scattering and bremsstrahlung emission), in which 'hard' events (i.e. those with deflection angle and/or energy loss larger than pre-selected cut-offs) are simulated in a detailed way, while 'soft' interactions are calculated from multiple scattering approaches. Photon interactions (Rayleigh scattering, Compton scattering, photoelectric effect and electron-positron pair production) and positron annihilation are simulated in a detailed way [37].

4.8 Guidelines for choosing the Monte Carlo code

The most widely used Monte Carlo codes PENELOPE, GEANT4, FLUKA, MCNP, ESGnrc were described. Using one of these codes against the others depends on several factors, which will be summarised in this section.

The first characteristics a user should appreciate is the primary particles (e.g. electron, photons, protons, etc.) for the kind of interaction to simulate, and output data to tally (e.g. energy-deposition detectors, particle fluence, dose distribution, etc.), and the reliability of the physical model of interest the Monte Carlo code can simulate. For instance, all of the codes shown in table 4.2 are capable of simulating electron/photon radiation transport. For example, the PENELOPE model of electron/photon transport is quite accurate, and in excellent agreement with the NIST data. In particular, Prof. Salvat, one of the main code developers, contributed himself to compile the electron scatter cross section database in NIST [63]. The PENELOPE model of multiple scattering is also included in GEANT4 electron/photon radiation transport in the 2008 version [64]. Competitors such as EGSnrc, FLUKA and MCNP have a fair agreement with the well-known cross section databases, but the PENELOPE model appears more accurate [65] [66]; however, FLUKA and GEANT4 both have wider application, as they can simulate any kind of particle interaction with the matter [52] [56].

Another factor to consider when running a simulation is how fast it can be. Nowadays, most of the available codes works with parallel computing, and a simulation running in parallel on HPC is generally quite fast (depending on the number of the simulated particles and the simulated physical model), as the number of simulated showers is distributed among the available cores, improving the algorithm efficiency. All the codes in table 4.2 are parallel or can be built as parallel. This capability depends on the kind of licence; for instance, all the codes illustrated in the previous section are open source, except MCNP, which is not free [57]. This can represent a limitation for the more expert user: the potential to customise the application and blend code inputs/outputs with other software is fundamental for cross-developing data analysis algorithm. Moreover, the expert user will need a transparent, flexible and transportable code which can work on any computational environment.

On the other hand, users who are not familiar with coding may find easier to just install the application and run simulations with a simple click on a Graphic User Interface (GUI), whereas they can design the physical system, and see the data output. But that means there are some constraints, for example in the parameter the user can input.

Another factor to consider is the availability of a 3D renderer for geometric modelling of the experimental configuration. This is a common factor for all the codes, and some of them have their own dedicated application. For example, PENELOPE's own geometry viewer is PENGEOM [67], available with the PENELOPE distribution package on NEA databank website. This is a user-friendly and well-built application the user can utilise to quickly and easily design the virtual laboratory environment.

4.9 Chapter Summary and critical analysis

In this chapter, an overview of the principles of modelling and simulations were given. Analytical modelling was compared with Monte Carlo simulation approach, and advantages of one model against the other were given. An example of

analytical (deterministic) code was given with SpekCalc, used for this thesis work for validation of the data output from PENELOPE. SpekCalc gives fast results, but its features are limited compared to a Monte Carlo code. However, SpekCalc could be used for having an idea of X-ray spectra from tungsten target with some layers across the beam. For this research, the Monte Carlo approach was applied, as Monte Carlo simulation gives more flexibility when building and developing the model, especially for radiation transport through the matter. Monte Carlo methods for simulating particle/photon transport was reviewed and the concept of particle random generation was introduced. Monte Carlo simulation may be computationally expensive; for this reason, variance reduction techniques were introduced for improving the efficiency of the tracking algorithm, together with some characteristics of the most efficient computational environment. Finally, a shortlist of the most commonly used Monte Carlo simulation codes was given.

Nowadays, there is such a large number of codes available for radiation transport and preferring one over the other codes may be challenging. PENELOPE Monte Carlo code was chosen for this thesis work. Various factors balanced this decision-making. First of all, the scattering model reliability was the key factor for putting PENELOPE on the top of the list.

The basis of this work is to simulate the electron-photon transport through the matter for exploring backscatter X-ray imaging system, and, in this sense, PENELOPE has the best overall performances. PENELOPE is a dedicated tool for electron-photon transport; it is flexible and versatile. The user can change input parameters by following a given format (but this can be changed too, depending on the user coding knowledge).

PENELOPE can be run in any computational environment and is provided with the user-friendly geometry application PENGEOM. The PENELOPE scatter model is widely known and included within the NIST database, and it also used for modelling electron-photon transport in other codes such as GEANT4. This is an example of the capability of PENELOPE to be incorporated in any other simulation and/or data analysis codes. A practical example will be discussed in

the next chapter with the algorithm PAXI [5], which processes the state variables recorded in the phase-space file for recreating an image, as physical detectors do.

5 PENELOPE MONTE CARLO SIMULATION CODE FOR BACKSCATTER IMAGING

5.1 Chapter Outline

PENELOPE is a Monte Carlo code able to simulate electron-photon transport through the matter.

In this thesis work, PENELOPE was used for investigating the fundamental physics of backscatter imaging, for comparing experimental performances and for exploring imaging quality metrics and imaging optimisation parameters.

In this chapter, PENELOPE Monte Carlo simulation code will be described. Firstly, the nature of the code itself will be discussed, including the physics PENELOPE is capable to simulate. Radiation transport in PENELOPE will be described in 5.3, PENELOPE photon interactions in 5.4, including Compton scatter model 5.4.3. Secondly the structure of the code, which contains the Fortran libraries describing the radiation transport, the source, material tables, geometries, and simulation parameters, will be illustrated (sections 5.5 to 5.11). The phase-space file was identified as the output data for image processing and image quality metrics calculation. PENELOPE simulations run on High Performances Computer at Cranfield University (5.12). Finally, PAXI algorithm and PENMAT application will be described in 5.14 and 5.15 respectively.

5.2 The Monte Carlo simulation code PENELOPE

PENELOPE, acronym for PENetration and ENErgy Loss of Positrons and Electrons[1], is a Monte Carlo code that simulates the coupled transport of electrons, positrons and photons showers in material systems consisting of homogeneous bodies with arbitrary chemical compositions within the energy range from 50 eV to 1 GeV [68].

[1] The first release of PENELOPE did not include photon transport, but only electrons and positrons.

PENELOPE was first released in 1995 [59], and was recently upgraded to PENELOPE-2014 [1] [51]. The code is distributed by NEA Data Bank [69].
Since its first release, PENELOPE has evolved into both a flexible and reliable tool through a remarkable amount of improvements in the physics interaction models, the sampling algorithms, the description of the geometry, and the available variance-reduction techniques.
PENELOPE can be applied to a wide variety of problems in dosimetry and micro-dosimetry, radiotherapy, radiation protection, nuclear spectroscopy, electron microscopy, electron probe microanalysis.
In this work, PENELOPE code has been applied in defence and security for the design and test of an experimental coded apertures backscatter imaging system under development. In the following sections, PENELOPE code features will be detailed.

5.3 The radiation transport simulation in PENELOPE

In this section, the Monte Carlo simulation of the radiation transport in PENELOPE will be illustrated. PENELOPE can perform Monte Carlo simulations of coupled electron-photon transport in materials for a wide energy range, from a few hundred eV to about 1 GeV. The simulated materials are homogeneous modules defined by quadric surfaces [51]. Photon transport is simulated by means of the standard, detailed simulation scheme [37]. The detailed simulation scheme consists of calculating the probability of interaction collision-by-collision. Typically, photons are simulated with detailed simulation in terms of a step-by-step mean free path. Electron and positron histories are generated on the basis of a mixed procedure, which combines detailed simulation of hard events with condensed simulation of soft interactions [1]. Hard events are those with energy loss greater than cut-off energy, while soft interactions have energy loss less than the corresponding cut-offs. Hard events follow the detailed simulation scheme. Soft events are described by means of multiple-scattering approaches, that is the elastic-inelastic events are grouped together for optimising the tracking.

PENELOPE simulation of the radiation transport is based on tracking a particle which is viewed as a random sequence of free flights. The random sequence will

end when an interaction event occurs, i.e. when a particle changes its direction, loses energy, and/or produces secondary particles. To simulate the particle history, it is necessary to use an interaction model, which is identified with a set of differential cross sections (DCS) for the relevant interaction mechanisms. The DCSs determine the probability distribution functions (PDF) of the random variables that characterise the track. These variables include the free path between successive interaction events, kind of interaction occurring, and energy loss and/or angular deflection together with the initial state of the eventually emitted secondary particles. Once the PDFs are known, it is possible to generate the random histories by using sampling methods. [1]

PENELOPE implements interaction models combining results from first-principles calculations, semi-empirical formulas and evaluated databases (i.e. NIST [3], LLNL [4]). Each interaction mechanism is described by a differential cross section (DCS), which is either defined numerically or given by an analytical formula with parameters fitted to available theoretical or experimental information. Most of the considered DCSs refer to models based on free atoms or single element materials; the DCSs for compounds and mixtures are obtained by means of Bragg's additivity rule: the molecular DCS is set equal to the sum of DCSs of all the atoms in a molecule. Inelastic collisions of electrons and positrons are modelled in terms of the mass density and the mean excitation energy of the material. Therefore, the DCSs for these interactions within the simulated materials are calculated with approximation.

For the application of this work, the energy range which will be considered is between 0-500 keV, for both electrons and X-ray photons. Within this energy range, the competing mechanisms are photoelectric absorption, Rayleigh (coherent) scattering, and Compton (incoherent) scattering. Pair-production will not be included as it occurs at energies greater than 1 MeV.

5.4 PENELOPE Photon interactions

In this section, the models of photon interactions with the matter in PENELOPE are described.

Monte Carlo codes extensively use databases such us NIST and LLNL for calculating DCSs. Numerical information from these databases are accessed in PENELOPE with a combination of analytical DCSs and numerical tables. The correspondent total cross sections are calculated by numerical quadrature by using an external function SUMGA [1]. The analytical expressions for DCSs are normalised to reproduce the total cross sections the are read from the input material data files (see section 5.7).

5.4.1 Photoelectric effect

In the photoelectric effect, a photon of energy E is absorbed by the target atom, which makes a transition to an excited state (see section 2.9).

In PENELOPE, the photoelectric effect is described by interpolating DCSs from LLNL database [70]. Partial cross section are calculated using the program PHOTOABS [1]. PHOTOABS is able to compute the partial cross section of a given shell up to 1 MeV energies. For higher energies, the partial cross section is calculated using Pratt analytical formula in 1960. PENELOPE database consists of photoelectric absorption tables of total atomic cross section, and the partial cross sections for the K shell and L, M, and N subshells of neutral atoms for Z= 1-99 and from 50 eV to 1 GeV. These tables are within a few percent accurate for photon energies above 1 keV, while at lower energies between 0.5 keV and 1 keV the uncertainty order is 10-20%. Atomic wave functions are represented as single Slater determinants built with one-electron orbitals that are solutions of the Dirac equation for the Dirac-Hartree-Fock-Slater self-consistent potential [68]. All cross sections are obtained from free-atom theoretical calculation, therefore near-edge absorption structures produced by molecular or crystalline ordering are ignored.

An example of atomic photoelectric cross sections for carbon, iron and uranium is given in figure 5.1. For compounds, the photoelectric cross section is calculated as the sum of the atomic cross sections of the molecular elements.

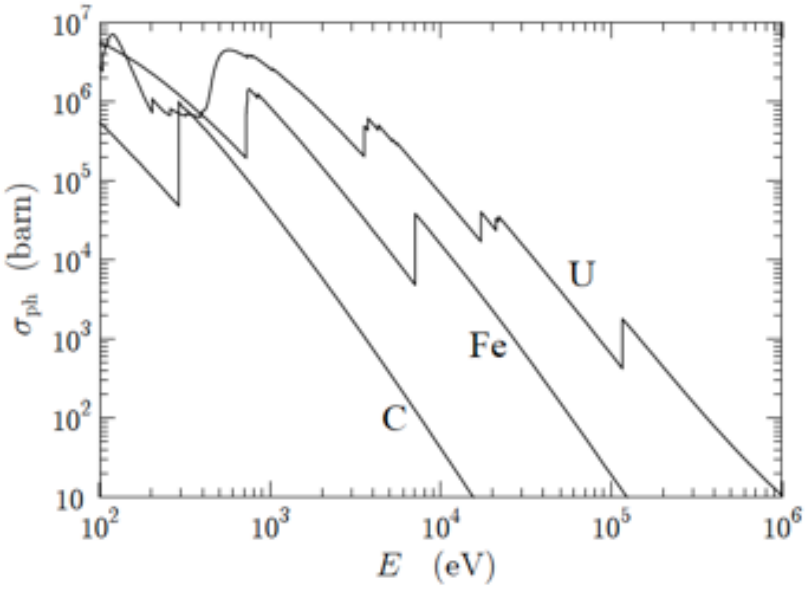

Figure 5.1 Atomic photoelectric cross sections for carbon, iron, and uranium as function of photon energy E [1].

5.4.2 Photoelectric absorption and characteristic X-ray emission

PENELOPE simulates the emission of characteristic X-rays and Auger electrons with energies larger than E_{abs} that result from the vacancies produced in inner shells of atoms by photoelectric absorption and Compton scattering of photons and by electron or positron impact. The relaxation of excited ions is followed-up until all vacancies have migrated to subshells with binding energies less than E_{abs}.

5.4.3 Compton scattering

In Compton scattering, a photon of energy E interacts with an atomic electron, which absorbs it and re-emits a secondary photon of energy E' in the direction $\Omega = (\theta, \phi)$ relative to the direction of the original photon (see section 2.6).

The sampling algorithm used in PENELOPE is due to Brusa et al. [71]. The sampling of Compton scattering consists of simulations of unpolarised photons whereas DCSs are calculated from the relativistic impulse approximation with

analytical one-electron Compton profiles. This approximation consistently accounts for the effect of binding and Doppler broadening [68].

The PDF of the polar deflection $\cos\theta$ and the energy E' of the scattered photon is given by:

$$P_{Co}(\cos\theta) = \left(\frac{E_c}{E}\right)^2 \left(\frac{E_c}{E} + \frac{E}{E_c} - \sin^2\theta\right) S(E,\theta) \qquad 5.1$$

where $E_c = \frac{E}{1+\frac{E}{mc^2}(1-\cos\theta)}$ is the energy of the scattered photon, $S(E,\theta)$ is the incoherent scattering function. In order to compute Compton scattering function, Baró et al. wrote an algorithm for PENELOPE to generate the random values of $\cos\theta$ by considering the following formula:

$$\tau = \frac{E_c}{E} = \frac{1}{1+\frac{E}{mc^2}(1-\cos\theta)} = \frac{1}{1+\kappa(1-\cos\theta)} \qquad 5.2$$

where $\frac{1}{1+2\kappa} \leq \tau \leq 1$. The minimum and maximum values of τ correspond to the backward ($\theta = \pi$) or forward ($\theta = 0$) scattering, respectively.

The sampling algorithm calculates the PDF of τ and applying Nelson et al. approximation [72]:

$$P_\tau(\tau) = P_\theta(\cos\theta)\frac{d(\cos\theta)}{d\tau} = \left(\frac{1}{\tau^2} + \frac{\kappa^2-2\kappa-2}{\tau} - (2\kappa+1) + \kappa^2\tau\right) S(E,\theta) \qquad 5.3$$

The rejection methods was applied to the following function:

$$T(\cos\theta) = \left\{1 - \frac{(1-\tau)[(2\kappa+1)\tau-1]}{\kappa^2\tau(1+\tau^2)}\right\}\frac{S(E,\theta)}{S(E,\theta=\pi)} \qquad 5.4$$

which is positive and is equal to 1 when $\tau = 1$, < 1 otherwise. In addition, the incoherent scattering function is also < 1 if $\theta < \pi$. For these reasons, the function $T(\cos\theta)$ is the ideal candidate for applying the rejection method for the generation of the random values of τ.

The algorithm generates:

1. Two-point probability functions

$$\tau(1) = \tau_{min}^{\xi} \text{ and } \tau(2) = \sqrt{[\tau_{min}^2 + \xi(1 - \tau_{min}^2)]} \qquad 5.5$$

where $0 \leq \xi \leq 1$ is a random number used for rejecting/accepting the value of $T(\cos\theta)$;

2. Secondly, $\cos\theta$ is determined from 5.2 as

$$\cos\theta = 1 - \frac{1-\tau}{\kappa\tau} \qquad 5.6$$

3. Then, the scattering function is calculated.
4. Finally, the random number ξ is generated and the rejection method applied. $\cos\theta$ is delivered if $\xi \leq T(\cos\theta)$.

This algorithm is independent from Z and increases monotonically with photon energy (35% for E = 1 keV, 80% for E =1 MeV, 95% for E =10 MeV).

Once the direction is determined, the energy of the emerging photon is calculated.

The azimuthal angle in simulating Compton scattering is sampled uniformly between $(0, 2\pi)$.

5.4.4 Elastic scattering

Elastic scattering is the process by which photons are scattered by the atomic electrons without losing energy. This means there is no excitation of the target atoms and the initial and final values of energy remain the same (see section 2.8).

In PENELOPE elastic scattering is described by means of the Born DCS [68] with atomic form factors and angle-independent effective anomalous scattering factors taken from the LLNL Evaluated Photon Data Library [4]. Elastic scatter algorithm sampling method only variable is the scattering angle, which is sampled as $\cos\theta$. The scattering angle is a calculated as a function of the random variable and the form factor and delivered following the rejection method [73]. The calculated scattering angle is compared with a random variable and it is accepted

only if the value is positive and equal or less than unity as seen for Compton scatter.

5.5 PENELOPE Fortran code structure

PENELOPE is a Monte Carlo code written Fortran, and it consists of a set of linked subroutines. They include:

- Penelope.f
- Rita.f
- Penvared.f
- Material.f (and tables.f)
- Timer.f
- Source.f
- Pengeom.f
- Penmain.f
- Other features.

The files in PENELOPE package are not executable themselves, as they need to be compiled with a Fortran compiler to generate the executable files.
The most common Fortran compiler is gFortran [74]. gFortran is a versatile and free tool, which works on Windows/Mac/Linux operative systems (OS). PENELOPE is distributed with a tutorial for generating the executable files using gFortran and an user manual. PENELOPE is distributed as a package and each subroutine is placed in the PENELOPE folder as shown in figure 5.2. All the Fortran libraries are described in the following sections.

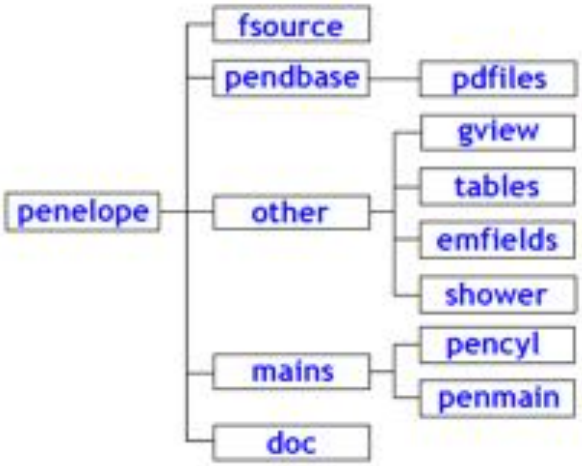

Figure 5.2 Structure of the PENELOPE package. The fsource folder includes the libraries Penelope.f, rita.f, penvared.f, material.f, pengeom.f, timer.f.

5.5.1 Penelope.f

The kernel of the code system is the package penelope.f. This library is fundamental for the Monte Carlo code, as it contains the physics of simulation of the electron-photon transport. Photon histories are created by using the detailed simulation method, that means that all the interaction events are simulated in chronological succession.

The radiation transport is simulated as primary and secondary particles. The primary particles are generated from the source before interacting with the medium. Secondary particles are produced in direct interactions (inelastic collisions, bremsstrahlung emission, positron annihilation, photoelectric absorption, Compton scattering, pair production) and as fluorescent radiation (characteristic X-rays and Auger electrons). They are emitted with initial energy larger than the absorption energy, stored and simulated after the completion of each primary track. For example, in Rayleigh and Compton scattering, the incident photon (primary particle) is absorbed, and the scattered photon is considered as a secondary particle.

The Fortran subroutine Penelope.f is located under the folder “fsource". It consists of about 12500 lines of Fortran source code and contains four blocks of subprograms. The blocks comprise preparatory for calculations and I/O routines,

interaction simulation procedures, numerical routines and transport routines invoked by the main program.

The name of the subroutines identifies the following:

- The kind of particle (E for electrons, P for positrons, G for photons);
- The interaction mechanism (EL for elastic, IN for inelastic, BR for bremsstrahlung, AN for annihilation, PH for photoelectric absorption, RA for Rayleigh, CO for Compton, and PP for pair production);
- The theoretical model used for the description of the interactions, indicated with lowercase;
- The random sampling routines, described with four-letter names.
- If letter names is greater than four, than the subroutine describes auxiliary calculations, such as T for total cross sections and D for DCS, or action (W for writing data file, R for reading, I for initialising).

5.5.2 Rita.f

Rita.f is the random sampling generator of the particles. RITA is the acronym of Rational Inverse Transform with Aliasing algorithm [1]. The sampling from continuous distributions is performed by means of the RITA algorithm.

RITA is performed through the RANECU random generator, written in Fortran by James [55]. In PENELOPE, the random generator is called RAND. RAND produces and delivers a single random number at each call as 32-bit floating point numbers uniformly distributed in the open interval between zero and one. The internal state of the generator is characterised by two integers, ISEED1 and ISEED2. These are the initial values used for determining the sequence of random numbers in the simulation. Each history of random events is entirely determined by the value of the seeds at the beginning of the simulation, and, at the end of a simulation run, the program writes the current number of seeds. The simulation can be resumed and achieve the desired statistics by reading the number of seeds of the latest simulation from the file dump.dat.

In parallel calculations, each processor must produce uncorrelated and independent sequences of random numbers. This is accomplished by feeding the processors with different initial seeds, far enough to avoid overlapping. To achieve this, Badal and Sempau [75] determined the initial seeds for running independent parallel simulation by using a Fortran subroutine. The extended sequence is initiated with the couple (1,1), with separation of 10^{14} calls to avoid overlapping. This special random generator is called RAND0, and it is located at the end of RITA. RAND0 is called in the main program when the number of seeds in the input file (described later in section 5.11) is not the default (1, 1).

5.5.3 Source.f

The program PENMAIN allows the use of mono-energetic sources, monochromatic sources, source spectra as energy-probability distribution. They can also be described as point sources or cone sources, or extended object emitting particles or photons. More arbitrary sources, however, can be described by source.f script. Source.f can be edited by the user to define and simulate the desired primary radiation source.

5.5.4 Timer.f

This subroutine gives the execution time in seconds. The output value of the variable SEC is the time (in seconds) elapsed since the start of the calling program. It also calculates the CPU time and the speed of the simulation and delivers the date and time.

5.5.5 Penvared.f

The subroutine that implements variance reduction techniques in PENELOPE is penvared.f.

Variance reduction optimisation techniques are used to reduce the statistical uncertainty of a quantity without increasing the computer simulation time.

The result is that statistical uncertainty is reduced together with simulation time, and the simulation efficiency overall increases.

In PENELOPE, three methods are developed: interaction forcing**,** splitting and Russian roulette. Interaction forcing is usually applied when the uncertainty is high from an extremely low interaction probability. For example, this can be applied to the simulation of an energy spectrum of bremsstrahlung photons emitted by a target such as tungsten target of an X-ray tube (see chapter 6). Radiative events in this case are much less probable than elastic or inelastic scatter, thus the variance of the simulated photon spectrum is large. In such case, in PENELOPE it is possible to force the specific kind of interaction to occur more frequently than the real process. That is, the mean free path is replaced by a shorter one, so that the number of physical interactions increases. However, the state variable is only recorded when the interaction is real. The weight associated with the kind of interaction is reduced by a factor which is equal to the interaction forcing parameter.

Splitting and Russian roulette are usually applied in conjunction and are used for example for calculation of local dose distribution far from the beam axis.

Similarly to interaction forcing, splitting and Russian roulette are achieved by modifying the weights of the particles. Splitting is a technique which creates identical particles in the same state when the beam is approaching the Region Of Interest (ROI). In the case of splitting, primary particles from the beam are assumed to run with unit weight. Secondary particles, which are generated with interactions within the target materials, have weights equal to the ratio between the assigned unity from the primary particle and the number of multiplied particles.

Russian roulette is instead the reverse process of splitting, as it discardes particles which moves away from the ROI. This technique has a weight

determined by the ratio of the unity assigned to the primary beam and the probability of survival of the secondary particles.

The three variance reduction techniques can be applied together and the user should carefully conceive the input parameters according to the simulated model.

Interaction forcing can effectively reduce the statistical uncertainties. However, this technique is a violation of the energy conservation because the sum of energies deposited along the path differs from the energy lost by the projectile. Therefore, the yields energy deposition spectra are biased. In PENELOPE, interaction forcing introduces forced interactions randomly along the particle trajectory, independently of the geometry, while it keeps the weight of the transported particle unaltered. Thus, the scored quantities are weighted by factors depending on the simulated geometry.

Splitting and Russian roulette can be useful variance reduction techniques to enhance the signal of specific ROIs. However, the user should keep in mind that such techniques fall when the model is too complex, thus the number of secondary particles can be relatively high. Consequently, there is not enough stack to simulate secondary particles and the simulation cannot record all the data and/or the data could not be reliable.

Variance reduction techniques can be recalled on the input file as detailed in section 5.11.4.

5.5.6 Other features

PENELOPE package also contains tools for generating and displaying total cross sections and other interaction data for different materials, the program shower.exe, (available on Windows only) which shows electron/photon showers, and the subroutine to simulate the electro-photon transport in the electromagnetic field. Among the other features, it is also included a simple parallelisation tool PENMAIN-SUM, which allows different summing runs with a different number of seeds.

5.6 PENELOPE preliminary input parameters: material.f, PENGEOM and the input file

PENELOPE main program requires arranging some preliminary input files before running simulations. Information such as materials, geometric models, and beam energy and shapes must be precompiled. PENGEOM is the tool for designing the simulation geometries, material extracts the interaction properties associated to each object, and the input file is a prescription containing all the simulation properties. In the following sections, the programs material, PENGEOM, and the input file will be described.

5.7 Material.f for material input information

PENELOPE reads the information about each material from an input formatted ASCII material file. This file must be generated previously by running the program material.f.

Materials.f includes an extensive database comprising of physical properties, atomic interactions, differential cross sections and total cross sections, for all elements of the periodic table, from hydrogen to einsteinium, covering the energy range from 50 eV to 1 GeV.

The necessary information required to extract the material file from the database are:

- chemical composition, concerning stoichiometric index or weight fraction;
- mass density;
- mean excitation energy;
- energy of the oscillator strength.

The information provided by material data files is fundamental for the description of the input parameters in the input file (see section 5.11).

5.7.1 List of materials and tables.f

PENELOPE is also provided with a set of tabulated materials which can be read and extracted from material program.

The material database includes a set of 280 prepared materials that the program material can read from the pdcompos.pen list. These materials are the elements of the periodic table plus common compounds and mixtures used in the electron-photon transport.

This database can be also recalled by tables.f. Tables.f reads material files and generates tables of interaction data, including cross sections, mean free paths, stopping powers, ranges, etc., as functions of energy.

5.8 PENGEOM for modelling the geometries

PENELOPE is distributed with pengeom.f, a subroutine responsible of the geometrical operations in the simulations. The job of PENGEOM is directing the simulated particles in the material system.

The material system is assumed to be described as a number of homogenous bodies limited by quadric surfaces. The evolution of the particle tracking within the bodies is ruled by the physical simulation routines. The routines describe the particle beam interaction with bodies as if particles were moving into an infinite medium with a given composition stored in memory.

In PENGEOM, the tracking of a particle within a body works as follows: when a particle reaches the body surface, its track is stopped just after penetrating a new material body, and restarted again in the new active medium. This is known as detailed simulation method, and is particularly suitable for tracking of photon histories. Within the Fortran code, the subroutine responsible for the description of the particle tracks is called “jump-and-knock” [76].

In PENGEOM it is possible to describe any materials as homogeneous bodies limited by quadric surfaces. To speed up the geometry operations, the bodies of the materials can be grouped into modules hierarchically. For complex and repeating geometries, it is possible to use the function CLONE, that copies the modules avoiding the manual transcription of the code.

The designed geometry file has the extension .geo and it is later recalled in the input file for running the simulation.

5.8.1 PENGEOM java application

PENGEOM is distributed as a user-friendly Java application named PenGeom.jar [76]. This application includes a text editor for designing the geometries and a 2D and 3D CAD-like geometrical viewer. The CAD viewer describes the different materials and bodies using different colours. An example of the PenGeom.jar editor and 2D-3D viewer is given in figures 5.3 and 5.4, respectively.

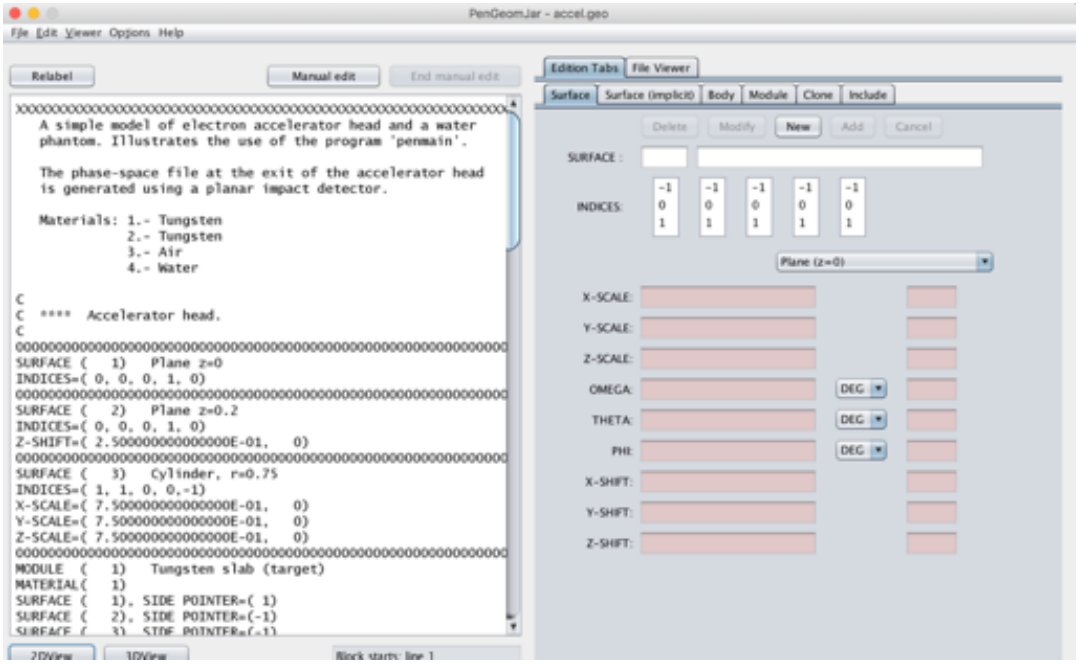

Figure 5.3 PENGEOM.jar Java text editor. In this example, an accelerator head is designed.

The Java application is distributed together with the Fortran libraries in the PENELOPE-2014 [1].

In PenGeom.jar, lengths are in centimetres (cm) and angles in degrees. The position and direction of movement of a particle are referred to the laboratory coordinate system, a right-handed Cartesian reference frame which has the plane $\widehat{zy}$ as default 2D view.

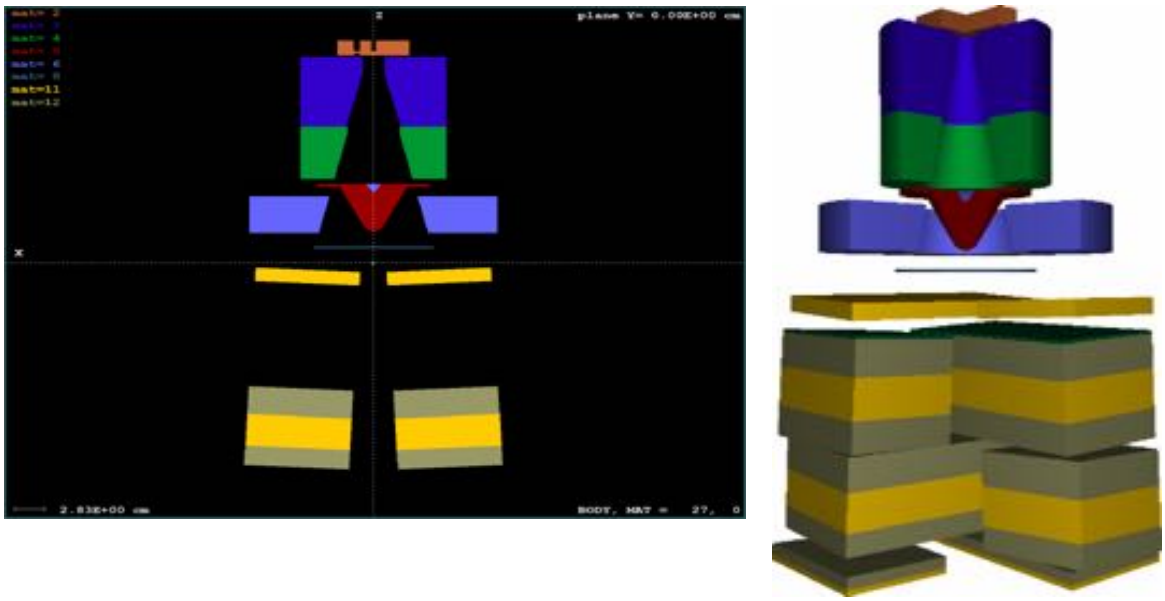

Figure 5.4 Example of 2D (a) and 3D (b) view in PENGEOM of an accelerator head and a water phantom. The different colours represent a different kind of materials in the geometry file.

5.8.2 PENGEOM parameters

In PENGEOM, each quadric surface is described by a set of indexes (I_1, I_2, I_3, I_4, I_5), the scale factors (X-SCALE, Y-SCALE, Z-SCALE), the Euler angles (OMEGA, THETA, PHI) and the displacement vector (X-SHIFT, Y-SHIFT, Z-SHIFT).

A database of reduced quadrics is available for the user to describe the different surfaces in the Java application PenGeom.jar.

If the corresponding reduced form is:

$$I_1 x^2 + I_2 y^2 + I_3 z^2 + I_4 z + I_5 = 0 \qquad 5.39$$

a quadric surface is then obtained by applying the following transformations in this order:

1. A scaling along the directions of the axes, defined by the scaling factors

$$I_1\left(\frac{x}{X-SCALE}\right)^2 + I_2\left(\frac{y}{Y-SCALE}\right)^2 + I_3\left(\frac{z}{Z-SCALE}\right)^2 + I_4\frac{z}{Z-SCALE} + I_5 = 0 \qquad 5.40$$

2. A rotation defined through the Euler angles OMEGA, THETA and PHI
3. A shift, defined by the component of the displacement vector (X-SHIFT, Y-SHIFT, Z-SHIFT).

Table 5.1 shows the reduced quadrics provided in the PENGEOM Java application database. These quadrics are illustrated in figure 5.5, and the rotation in figure 5.6.

Table 5.1 Predefined reduced quadric surfaces in PenGeom.jar

Reduced form	Indexes					Quadric
z-1=0	0	0	0	1	-1	plane
z^2*-1=0*	0	0	1	0	-1	pair of parallel planes
$x^2+y^2+z^2$*-1=0*	1	1	1	0	-1	sphere
x^2+y^2*-1=0*	1	1	0	0	-1	cylinder
x^2-y^2*-1=0*	1	-1	0	0	-1	hyperbolic cylinder
$x^2+y^2-z^2$*=0*	1	1	-1	0	0	cone
$x^2+y^2-z^2$*-1=1*	1	1	-1	0	-1	one-sheet hyperboloid
$x^2+y^2-z^2$*+1=2*	1	1	-1	0	1	two-sheets hyperboloid
x^2+y^2*-z=0*	1	1	0	-1	0	paraboloid
x^2*-z=0*	1	0	0	-1	0	parabolic cylinder
x^2-y^2*-z=0*	1	-1	0	-1	0	hyperbolic paraboloid

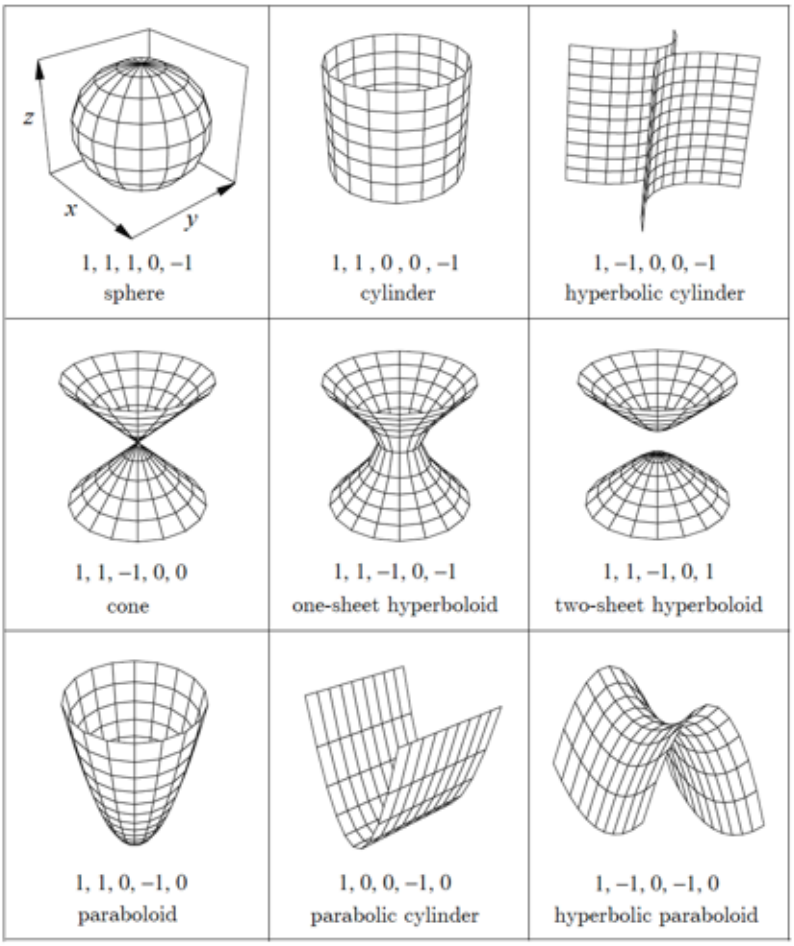

Figure 5.5 Reduced quadrics and their indexes.

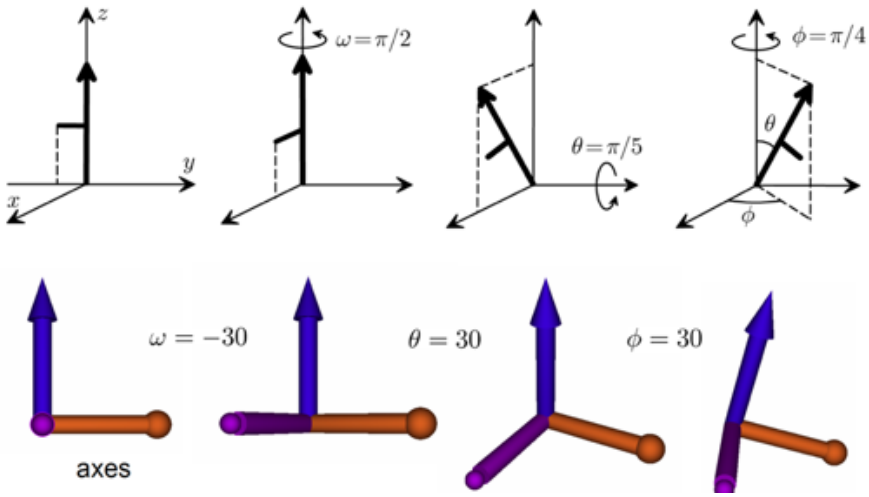

Figure 5.6 Rotation of axes with Euler angles.

The geometry is defined from an input text file, which consists of a sequence of blocks. Each block defines a different element, including surfaces, bodies, and modules. A definition block begins and ends with a line of zeros. The first line in each block must start with a definition string, such as “SURFACE”, “BODY”, “MODULE”, “CLONE”, “INCLUDE”, or “END”. The END string closes the geometry file and reading is discontinued. Each element is assigned with user labels, which are normally consecutive numbers according to their order.

Surfaces can be defined in the reduced form - from the list in PenGeom.jar – or in implicit form. In the implicit form, the indices must be set to zero, and the user will define the custom parameters. Bodies define the objects in the geometry file, each of them surrounded by the declared surfaces.

Each body definition must include the kind of MATERIAL. This must correspond to the materials described in the input file material list section (see section 5.11). MODULE is another way to define objects, with the difference that modules can include other bodies and other modules inside by establishing a hierarchic-tree inclusion. Modules can also be empty (vacuum, for MATERIAL = 0), or filled with air. SURFACEs, BODYs and MODULEs can be scaled (X-SCALE, Y-SCALE, Z-SCALE), rotated (OMEGA, THETA, PHI), and/or shifted (X-SHIFT, Y-SHIFT, Z-SHIFT). PENGEOM is capable of designing up to 5,000 bodies and up to 10,000 surfaces. However, it allows a maximum number 250 bodies in a module.

When the geometry file contains a larger number of elements, the simulation program stops and an error message is printed. The structure of the module hierarchy definition is shown in figure 5.7(a). PENGEOM defines the geometries within a 10^7 unit radius sphere, which represents the overall space (see figure 5.7 (b)).

Modules can be copied by using the function CLONE. Each cloned module can be relocated by rotation and shift. The INCLUDE option allows to include one geometry file within the other. The name of the included file must be written between parenthesis.

When the main simulation program is running, the output file geometry.rep is generated when initialised with the input file. In geometry.rep, all the included structures are defined explicitly, and labelled consecutively.

The use of modules, clones, and included files offers the flexibility for defining and simplify complex geometries. To speed up the simulation, each module should have a small number of daughters (small number of bodies/modules in each node).

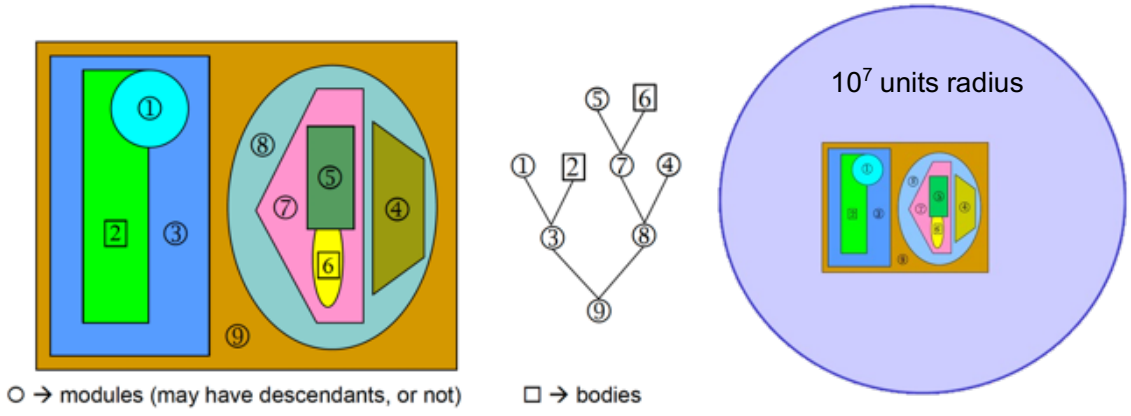

(a) (b)

Figure 5.7 Bodies and modules inclusion hierarchy (a) and PENGEOM space sphere definition (b).

5.9 PENMAIN simulation program

PENELOPE is complemented with a steering main program, which controls the geometry and the evolution of tracks, keeps score of the relevant quantities, and performs the required averages at the end of the simulation [1].

PENELOPE and the main programs are linked together through a file called TRACK_mod. This file is responsible of following the state variables and recording their values in the radiation interaction with the matter. Further details on the state variables will be discussed in section 5.11.6.

To run the simulations, two steering (or main) programs are available in PENELOPE package: pencyl.f and penmain.f. Both guide the evolution of the tracks and keeps score of relevant quantities. Penmain and pencyl are distributed as open-source Fortran libraries and, in principle, the user can customise and adapt them to the specific application.

One of the main programs is pencyl.f. It performs simulations in cylindrical structures, providing more detailed information on the transport process (numbers of interactions of various kinds, path length distributions, position maps of emerging particles, etc.). It may be useful for tuning the simulation parameters [1].

The other steering program is penmain.f. Penmain allows the user to define more detailed input instructions for extraction of information such as energy-probability spectra, particle fluence, energy-deposition spectra, dose distributions.

Compared with pencyl, penmain is more flexible and has the capacity to solve a broader class of practical problems. For this reason, penmain has been chosen for the simulations in this work.

The operational parameters of penmain are defined as an input text file such as *file_name.in*. The input file initialises the main program and contains the job properties of the simulation. In this work, focus will be given to penmain input parameters in section 5.11.

Penmain runs the simulations by assuming primary particles of a given type are emitted from a point or an extended source, either with fixed energy or with a specified energy spectrum. The initial direction of the primary particle is sampled uniformly as a conic or rectangular beam. Penmain also admits user-defined radiation sources. Penmain provides information about the energy and angular distribution of emerging particles, the average energy deposited in each body, etc. To generate more accurate information, the user can define one or more impact and energy-deposition detectors.

Each detector consists of a set of non-void bodies, previously defined in the geometry file. The output spectrum from an impact detector is the energy

distribution of the particles that have entered any of the active bodies between the source and the detector.

The state variables are recorded into a phase-space file. This file can be optionally written to a data file, and it shows the state variables at the entrance of the impact detector. The main program can read the initial state variable from a pre-calculated phase-space file. This option is useful for splitting the simulation of complex problems into several consecutive stages.
Penmain is able to measure the average distribution of the fluence with respect to the energy of the particles detected within the volume of the detector. Impact detectors tally the average distribution of fluence with respect to energy integrated over the volume of the detector and the energy deposited within the volume of the detector. The fluence distribution provides a complete description of the radiation field. The fluence is important as we can obtain various quantities of interest in dosimetry and spectroscopy, such as the absorbed dose (see section 5.11.8). The output spectrum of an energy-deposition detector is the distribution of the absorbed energy per shower in the active bodies. It is also possible to calculate the dose distribution.

The input information used in the simulation are recorded in the file penmain.dat, while the number of simulated showers and the simulation time are written in the penmain-res.dat file.

Penmain produces a set of output data, which are written in the .dat format and can be graphed with an external plotting program such as GNUPLOT. The PENELOPE programmers provided the package with some GNUPLOT routines to visualise the output data. However, for the purpose of this work, scripts for plotting output data were written in MATLAB [77]. They were incorporated in the algorithm PAXI and in PENMAT application (see section 5.14 and 5.15, respectively).

5.10 How to run a simulation with PENMAIN

PENMAIN cannot run the simulation job, unless some preliminary input files are arranged. Firstly, the geometry file/files should be designed/edited. Secondly, the

input file should be set up with the desired simulation parameters. Thirdly, the kind of materials should be extracted from the material database for the steering program to read. These three files are fundamental for the simulation to run. When all the input files are ready, it is possible to execute penmain. Once the simulation is completed, the output data can be visualised. The operational steps for running a simulation by using PENMAIN are shown in figure 5.8. Details on the input files are discussed in the following paragraphs.

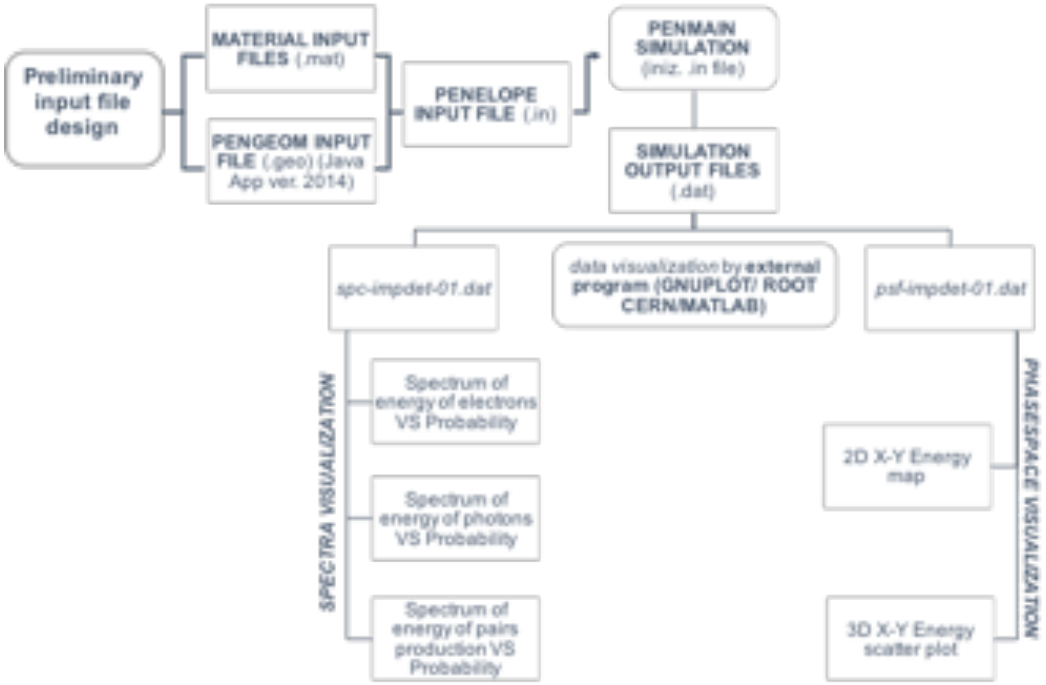

Figure 5.8 Steps for running a simulation in PENELOPE code system.

5.11 The Input file

PENMAIN steering program requires initialisation of input parameters for the simulation to run. These comprises the description of the source, the detector, which is the body designed as active for collecting the state variables and the different spectra, options such as variance reduction techniques, energy-deposited spectra and particle fluence, the number of simulated showers and the

allocated simulation time for each primary interaction. In this section, the simulation parameters will be explored, with particular attention to the source and the detector capabilities.

5.11.1 Source description in the input file

In PENELOPE, the input file must contain the information on the primary beam. Firstly, the kind of particle emitted must be defined with the flag “SKPAR”. SKPAR can be:

- = 1 if the primary emission is of electrons;
- = 2 if the primary emission is of photons;
- = 3 if the primary emission is of positrons.

Secondly, the kind of energy emission must be established. A source in the input file can be mono-energetic, or mono-directional, or both. In all the instances, energy is always in eV. When the source is mono-energetic, the beam is defined by only one energy parameter, which is the initial energy. This can be achieved with “SENERG” functions. For example, if the energy is set SENERG 150e3, then the primary beam initial energy is set to 150 keV. The beam can also be a conic beam or a rectangular beam, options which can be enabled with the functions “SCONE”, and “SRECTA”. The parameters for the conical beam are angles THETA, PHI and ALPHA in degrees. THETA and PHI are the beam axis directions, while ALPHA is the angular aperture (half cone). By default, these parameters are (0, 0, 0), and correspond to a mono-directional beam. Thus, a mono-energetic and mono-directional beam will have a single value of energy plus the conical beam angles (0, 0, 0). If the angular aperture is set equal to 180˚, then the source is emitting isotopically. For a rectangular beam, instead, the SRECTA function will limit the polar and azimuthal angles of a source beam window.

For a source with continuous energy spectrum, the SENERG parameter is replaced with an energy-probability spectrum, whereas each line begins with SPECTR flag and is given with the lower end-point (E_i) of an energy bin of the spectrum and its associated probability (P_i), integrated over the bin. By default, it is possible to input up to 1000 lines in arbitrary order. The upper end of a

spectrum is defined by entering a line with E_i equal to the upper energy end point, and with a negative value of P_i.

After selecting the kind of beam, the source must be placed within the designed geometry. If the source is a virtual point source, only the position of the source needs to be specified. This can be achieved by using the function “SPOSIT”. For an external source, SPOSIT defines the centre of the source volume in cartesian coordinates (x_0, y_0, z_0). If the source is a physical object, it must be described in the geometry file, and it will need to be set as an emitter from the input file. The function which enables the object to emit particles or photons is “SBOX”. The function creates a virtual prism surrounding the emitter, with the source having activity within the volume. The length of the prism is set with (SSX, SSY, SSZ). When the random generator within the volume of the prism finds the emitter, then it generates particles/photons. Note that the active volume of the emitter must be defined in the geometry file, otherwise particles cannot be generated.

The emitter body can be set with the function “SBODY”, and it can be more than just one line. That means it is possible to have more than one source-objects, but they still need to be included within the declared volume of the virtual prism.

5.11.2 Materials for running the simulations

In the input file, the materials to be used in the simulation must be listed in the materials section and material files placed in the simulation folder. Each material file name must be previously generated with MATERIAL program as seen in section 5.7. Each material name must be included in the input file with the flag “MFNAME”, followed by the line “MSIMPA”. This line includes the absorption energies EABS(1:3,M), elastic scattering parameter, C1(M) and C2(M) and cut-off energy losses for inelastic collisions and bremsstrahlung emission, WCC(M) and WCR(M). Default parameters are:

– EABS(1,M)=EABS(3,M)=0.01*EPMAX, EABS(2,M)=0.001*EPMAX
  C1(M)=C2(M)=0.1, WCC(M)=EABS(1,M), WCR(M)=EABS(2,M)

whereas EPMAX is the maximum energy of all particles found in the simulation, and is determined by the source energies. The same materials listed in the input

file must be used in the geometry definition. The input file may contain multiple declarations of the same material, e.g., to specify different sets of simulation parameters in different bodies with the same composition. The main programs in the distribution package allow up to 10 materials. This number can be increased by changing the value of the parameter MAXMAT in the Fortran module PENELOPE_mod, which is at the heading of the penelope.f source file.

5.11.3 Geometry definition

The geometry file is recalled in the input file with the flag “GEOMFN”, which simply reads the file name in the simulation folder. Normally, this is the only line in the geometry section. However, there is the option of changing the maximum step length by defining “DSMAX”, and the local absorption energies “EABS”.

5.11.4 Variance reduction techniques

Variance reduction techniques are optional parameters in the input file, and the dedicated section follows the geometry definition block in the input file. Variance reduction techniques are defined as described in section 5.5.5. In the variance reduction section, interaction forcing is enabled by “IFORCE” function. The parameters include the kind of interaction, the “FORCER” or force factor, which must be greater than one. WLOW, WHIG are the limits of the weight window where interaction forcing is applied. The functions “IBRSPL” and “IXRSPL” activate the bremsstrahlung splitting and the characteristic X-ray emission splitting.

5.11.5 Emerging particles and angular distributions

In the input file, it is possible to enable the collection of the energy and angular distributions of the emerging particles by using the functions “NBE” and “NBANGLE”. NBE allows the collection of the upbound and downbound energy distributions at the edge of the 10^7 ray sphere defining PENELOPE. The upbound spectra are collected in transmission, while the downbound spectra are backscattered. In the definition line, it is necessary to establish the energy range (EMIN, EMAX) where the spectra are tallied, and the number of energy bins within the interval. The collection of the spectra at the edge of PENELOPE sphere

can be useful as a first check for the simulation of the source, especially in backscatter simulations. In this thesis work, even though this function is enabled and the spectra always collected, they are just considered as first assessment, but they were not significant set of data for further analysis.

NBANGLE is the function for collecting the angular distribution. In the input file, the parameters to be defined are the polar and azimuthal angles bins, NBTH and NBPH respectively, which must be ≤ 180˚. The default parameters in this work are NBTH=90, and NBPH=45 for the collection of spectra from the simulated X-ray tube (see chapter 6). As for the NBE, NBANGLE is considered just as preliminary test for the simulations, and the output data are not further analysed.

5.11.6 Impact detector, energy spectra and phase-space file

The definition of the impact detector is fundamental for data collection in the simulations. In PENELOPE input file, impact detectors are defined by the definition “IMPDET”. This line of code must include the energy window with the lower and upper limits of the energy range (EL, EU), and the number of bins NBE of the output energy-spectrum (max 1000). The energy spectrum is collected at the surface of the detector so it is independent of the volume of the detector. The energy spectrum is recorded as spc-impdet-*##.dat*. It is possible to record up to 25 spectra of up to 25 different detectors for each simulation. The data set comprises the detected energy, the total probability coupled with its weight, the probability generated by electron interactions, by photon interaction and pair production, together with their weights respectively. Probability generated by penmain simulation gives is measured in [1/(eV*particle)], while energy of the particles/ photons is in [eV].

In the detector job description code, there are also two flags IPSF and IDCUT. IPSF enables the creation of the phase-space file, which contains the state variables of all the detected particles. If IPSF=0, no psf-file is created, if instead IPSF=1, the phase-space file is created. If the flag IPSF=1, the phase-space file is recorded as psf-impdet-*##*.*dat*.

IDCUT parameter allows tracking of particles that enter the detector. If IDCUT=0, the simulation of a particle is discontinued when it enters the detector, if IDCUT=1, the detector does not stop the particles tracking, that means it does not affect the tracking itself and the detector works as in an experiment. Finally, if IDCUT=2, the detector does not affect the tracking and the particle fluence spectrum with the respect of the energy integrated over the volume of the detector is generated. The calculated fluence has the dimensions of length/energy and is recorded in the file fln-impdet-*##.dat*.

The detector has to be identified as one of the objects in the geometry file. The impact detector will be then “activated” or defined as an “active body”. Active bodies cannot be void because the geometry routines would not stop particles at their limiting surfaces. If an intermediate particle collection step is necessary to detect particles/photons outside the detector geometry, it is possible to fill the void with an arbitrary material of trivial density (i.e. hydrogen, air) to avoid perturbing the transport process.

The active body is identified with the flag IDBODY. It is possible to add up to 25 active bodies in the same input file. However, only one phase-space file at the time can be recorded for the each simulation. The phase-space file and the spectra tallied at the detector are the main sets of data used for further data analysis. In particular, the phase-space file is the fundamental data set for image generation and processing. The features of the phase-space file will be further discussed in section 5.13.

5.11.7 Energy-deposition detectors

Together with the state variables and the energy-probability spectra at the detector, PENMAIN can also record the optional energy-deposition spectrum, which is the energy deposited within the volume of the detector. The energy-deposition detector spectrum is the distribution of absorbed energy (per shower) in the active bodies. The energy-deposition section is separated from the impact detector; however, the definition is similar. For the energy-deposition, we have to define the parameters EL and EU, which are the lower and upper limits of the energy window covered by the detector. NBE is the number of bins in the output

energy spectrum and cannot be greater than 1000. Note that a body cannot be part of more than one energy-deposition detector. In addition, the energy-deposition spectrum may be biased when the interaction forcing is applied, even outside the detector bodies [1].

5.11.8 Absorbed dose distribution

PENMAIN can calculate the absorbed dose distribution inside an user-defined dose box, whose edges are parallel to the axes of the laboratory frame. The dose box is defined by giving the coordinates of its vertexes. The dose is tallied using a uniform orthogonal grid with NDBX, NDBY and NDBZ bins. The bins define the voxels and should be at least 101, and are described along the directions of the respective coordinate axes. These numbers should be odd, to make sure that the central lines that join the centres of opposite faces of the box go through the centres of a row of voxels [1].

5.11.9 Job properties

In the job properties section there are a few options with the regards of number of seeds, dynamically reading/writing partial simulation results file, number of simulated particles, and time allocated for each interaction. The first option is the number of seed to be used for initialising RITA random generator. The flag is RSEED, and the default parameters are (-1, 1). The code is provided with a list of seeds for running “dummy” parallel simulations (see section 5.12). After defining the random seeds, there is the flag for opening a “dump.dmp” file, where the main program stores the partial simulation data. This option allows the user to stop the simulation at any time and to resume it from the last dumping point in a completely consistent way. The regular interval time penmain takes to write simulation results in the output files is defined by the flag DUMPP. This option is useful to check the progress of long simulations. NSIMSH is the number of simulated showers the main program must reach to complete the job described in the input file, while TIME defines the allocated time for each interaction and is expressed in seconds. For complex geometries, TIME should normally be relatively high to guarantee the secondary particles to be produced and stored.

The maximum allocated time is 2e9 sec. Then, all the operations are ended by the line END.

5.12 PENELOPE on High Performance Computer and parallel coding

Thanks to the code flexibility, it is possible to compile and run PENELOPE in any computational environment, including High-Performances Computer (HPC) facilities.

HPC is an ensemble of computing power made up of several “servers”, which can deliver much higher performances than one could get out of a typical desktop computer or workstation in order to solve large problems in science, engineering, or business. Thus, HPC is suitable for getting results from simulations, especially if they require long computational time and high specs resources. Normally, it is possible to access to HPC from a desktop/laptop workstation through tunnelling and by authentication from the command window/terminal. At Cranfield there are two centrally managed HPC systems, known as Crescent and Delta. The Crescent HPC system is for use by students on taught MSC courses. The Delta HPC system is intended for use by Research students and staff. For this work, PENELOPE simulation jobs were running on Delta HPC.

The HPC systems use batch scheduling for running the scheduled jobs through submission scripts.

The submission script simply tells the scheduler how to run the application. It also informs the scheduler how much compute resource the user would need to allocate. The resources include the number of cores/nodes to be used and the computational time to run the job for. Once submitted to the scheduler, the script will give a job ID which is unique to that submission. In the script, the user should also specify the email address. This enables the scheduler to send messages about the progress of the simulations.

Depending on how much resource (CPUs, Memory or Time) the user has asked for, the wait could be from minutes to days.

When the job is completed, the user will be sent an email confirmation. Then the user can back-up the results from the HPC to the local workstation for processing.

It is important to note that the simulation speed relies on the number of CPUs. However, this also depends on the application and the simulation program. In the case of PENELOPE, for example, it is not possible to run parallel simulations as such by default. As seen in section 5.5.2, PENELOPE works on a single core only. That is because the random generator seeds, which is the core of the Monte Carlo code itself, are not automatically changed in the input file. However, the simulation package is provided with a dummy parallel code which includes a list of random seeds which can be used for replacing the default parameters. That means the simulations run for the same problem are independent and have different results. Thus, they can be summed for increasing the statistics (i.e. the number of simulated showers). PENELOPE includes an auxiliary program named penmain-sum to combine the results of independent runs of the same simulation problem allowing to use multiple computing cores simultaneously. Thus, the simulation efficiency increases linearly with the available number of cores. Each independent run produces a dump file with the partial results of the simulation with accumulated statistics. The tool penmain-sum combines all dump files to get the final results of the simulation. Normally, the process of manually generating the simulation files needed for multiple independent runs is tedious and error-prone. M. Hermida-López wrote MATLAB scripts for automating this process. The script is called MUSIMAN [78] and is a software tool to ease the parallelization of simulations run with the Monte Carlo code PENELOPE 2014 that use penmain as steering main program. MUSIMAN can create the files needed for an arbitrary number of independent runs of the same simulation problem. A different pair of seeds for the random number generator is assigned to each run, taken from the list in the rita.f source file included in PENELOPE 2014, which was obtained with the algorithms from the work of Badal and Sempau [75]. Each consecutive pair of seeds in the list is separated from the following pair by 10^{14} positions. In this way, we ensure that each simulation run uses independent sequences of pseudo-random numbers. Then, it is possible to launch simultaneously a number of parallel independent simulation runs, and prepare the dump files to be combined

with penmain-sum to obtain the final results of the simulation. MUSIMAN scripts are included in PENMAT application (see section 5.15). In this thesis work, when required, simulations were prepared for use on HPC multiple cores using MUSIMAN scripts for running parallel simulations and thus decreasing the computational time.

5.13 Phase-Space file as data output for image processing

In simulations it is not possible to generate an image straight forward from the data like an experimental imaging system does. Thus, calculating the image means process the available information recorded by the simulation program. Basically, an image is a colour pixel map with different brightness. The scale for X-rays is grey scale, with the brightest pixel to be white, while the darkest is black. The different grey levels are produced by X-ray attenuation and interactions within the matter. However, an X-ray beam, for example generated from an X-ray tube, travels through the matter with a certain intensity, generated by a combination of current and voltage. That means the X-rays have initial energies before interaction, and final energies after interactions. PENELOPE does not allow to set the beam intensity as an X-ray tube does. In the input file, the information on the beam are always given in energy (eV) (see section 5.11.1). After interaction with the matter, energy can be either the same (elastic scatter), part of it can be lost and the X-rays scattered with a certain direction (Compton scatter) or absorbed and generate characteristic peaks. Yet, information on the energy and kind of interaction is not enough to describe the X-ray state. In PENELOPE, the detector records also the position of each X-ray in (X,Y,Z) coordinates plus the direction cosines.

Energies, positions, direction cosines, and kind of interaction within the matter represent the state variable of each recorded X-ray. An image can be processed by correlating energies and positions recorded at the detector. This correlation, or integration, generates the relative brightness of the image, which is calculated in this thesis work as integrated energy [79]. Integrated energy is essential for this work and thus the state variables are fundamental data for further analysis. Integrated energy will be further discussed in chapter 7.

In PENELOPE, the state variables are recorded on the phase-space file, labelled psf-impdet##.dat, and formatted as a table. In this table, the parameters included are:

- KPAR, which records the kind of particles from the beam. If KPAR=1, it is an electron, if KPAR=2 it is a photon if KPAR=3 it is a positron.
- E, the detected energy in eV.
- X, Y, Z position coordinates in cm.
- U, V W direction cosines, in radians.
- WGHT statistical weight, usually equal to 1.
- ILB parameters, which is a combination of values describing if the interaction is detected from the beam (primary), or after other interactions within the geometry (secondary) (ILB1), the kind of detected particles (ILB2), which can be either electrons (ILB2=1), photons (ILB2=2) or positrons (ILB2=3). ILB3 picks up the kind of interaction, which can either be elastic scatter (ILB3=1), Compton scatter (ILB3=2), photoelectric absorption (ILB3=3), or pair production (ILB3=4). In case of photoelectric absorption, ILB4 is non-zero and identifies the particle transition between shell (a characteristic line for X-ray photons). ILB4 is a sequence number generated as follows: $ILB4 = Z \cdot 10^6 + IS1 \cdot 10^4 + IS2 \cdot 100 + IS3$, whereas Z is the atomic number and IS1, IS2 and IS3 are the labels of the atomic shells involved in the transition. ILB parameters, especially ILB3, is used for exploring fundamental backscatter in chapter 9. Table 5.2 summarises the functions of each ILB parameter.
- NSHI, the number of detected particles for each shower.

In the phase-space file, the number of photons (or particles) detected corresponds to the number of recorded lines. This information can be used to calculate the efficiency of an imaging system in terms of number of detected on the number of simulated particles.

Table 5.2 ILB parameters. They identify the details of the beam interaction with the matter.

ILB			
1=KIND OF PARTICLE	**2=KPAR**	**3=ICOL**	**4=ATOMIC SHELLS**
1=PRIMARY	1=ELECTRONS	1=ELASTIC SCATTER	ATOMIC RELAXATION EVENTS. PARTICLES DO TRANSITION BETWEEN SHELLS
2=SECONDARY	2=PHOTONS	2=INHELASTIC SCATTER	
	3=PAIR PRODUCTION	3=PHOTOELECTIC ABSORPTION	
		4=ELECTRON-POSITRON PAIR PRODUCTION	

5.14 Integrated energy and PAXI algorithm for PENELOPE image processing

PENELOPE distribution package does not include its own data analysis tool. However, the programmers [59] provide with Gnuplot [80] scripts for graphing energy-spectra and scatter plot of the phase-space file.

Scatter plots of the state variables of the phase-space file are limited, as they do not correlate detected energies and relative positions, thus further coding work was necessary for processing the phase-space file. MATrix LABoratory (MATLAB) [77] was found to be the suitable framework for developing the scripts for data processing and analysis for three reasons. Firstly, MATLAB is a popular

an well-established code, many tutorials for learning the code are available on the official website, but also on other e-learning websites, such as edx.org and Lynda.com.

Secondly, it is possible to share scripts among the users. They are available on MATLAB file exchange. This is a precious source, especially for those who are just beginning with coding in MATLAB. The file exchange is free for licenced users.

Thirdly, MATLAB offers the flexibility to include other language codes, such as Python, C/C++, and the user can also develop his own application with MATLAB GUI. MATLAB GUI was used for creating PENMAT application, which will be discussed in the following paragraph (5.15).

MATLAB programming language is quite simple to learn, and its routines, such as the for cycle and if/else statement condition, is similar to the other languages.

MATLAB was used for developing the Phase-space file Algorithm for X-ray Imaging (PAXI) [5] core script for processing the image from the phase-space file.

PAXI consists of a table reading script, it includes the settings for generating the pixel grid corresponding to the number of pixels in the experimental, and the calculation of the integrated energy, which is executed with the parallel function parfor. Then the 2D map figure is created and this map is saved as grey scale image. The PAXI algorithm is also included with cropping script for applying the decoding with coded apertures and calculating the point spread functions. It is also capable of calculating image quality metrics, such as signal-to-noise ratio, contrast-to-noise ratio and spatial resolution in terms of full-width at half-maximum (FWHM) by determining the Region Of Interest (ROI) and background.

PAXI has also the ability to select the kind of detected particles, and the interaction recorded at the detector by selecting the ILB parameters (ILB2 and ILB3 for the specific case) and generates the energy spectra of the selected kind of interaction/interactions. PAXI is included in PENMAT GUI as the data analysis dedicated tool for X-ray imaging.

5.15 PENMAT: PENELOPE GUI on MATLAB

PENMAT is a Graphic User Interface (GUI) created by C. Maire and A. Vella [81] to help prepare, run and analyse PENELOPE- 2014 simulations faster. PENMAT consists of two GUIs. The first creates and edits the input file needed for running PENMAIN. The other interface analyses the data from the simulation.

As the interface was written under MATLAB R2017a, the use of an equal or later version is advised, or it is possible to run the application by installing MATLAB Runtime 2017 [2]. PENMAT requires the simulation executive file penmain and penmain-sum compiled in gFortran and included in the folders 'Penmain' and 'Simulation\Parameters', and 'Simulation' respectively. Also, the geometry file, input phase-space files, input dump files and input spectrum files should be copied in the corresponding folders if needed. In PENMAT it is possible to set all the input parameters such as source beam, materials, impact detector, energy-deposition detector, dose distributions. It is also linked to PENGEOM Java app for reading and editing the geometry file, and it can run parallel simulation by using MUSIMAN scripts [78], which were adapted to PENMAT code structure. When the input file is completed, the user can save it by pressing the 'CREATE INPUT FILE' button, and then run the simulation with 'RUN SIMULATION' command. Once the simulation has ended, the user can launch PENMAT2 GUI. If the simulation has not ended by itself and the user wish to stop, then click on 'STOP THE SIMULATION'. After completion of the simulation, the user can combine the different runs if the option was enabled on the input file. It is also possible to combine the differen phase-space files to one; this was not previously possible with penmain-sum and either with the MUSIMAN scripts. Finally, the user can plot the data from the simulation. PENMAT and PENMAT2 GUIs are shown in figure 5.12.

(a)

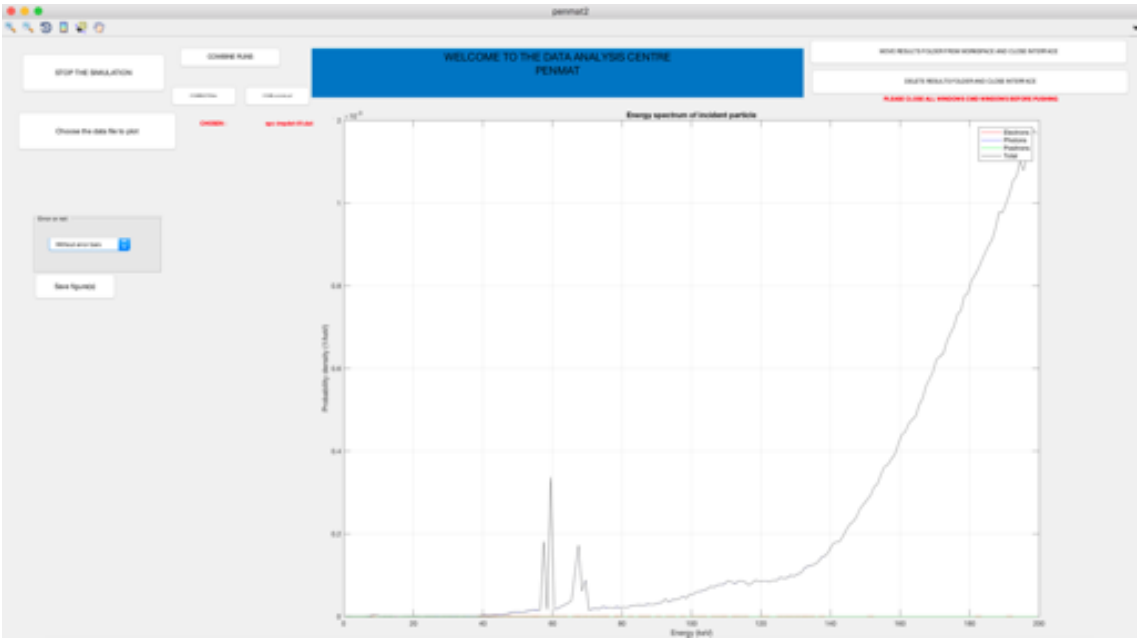

(b)

Figure 5.12 PENMAT (a) and PENMAT2 (b) GUIs. PENMAT can edit the input file and run the simulations (also in parallel), while PENMAT2 is dedicated to the data analysis.

5.16 Chapter summary and critical analysis

PENELOPE is a simulation program for coupled electron-photon transport through homogeneous materials. PENELOPE includes the PENGEOM Java application for designing the geometries and comprises a complete list of material database which is recalled by MATERIAL executive file. PENELOPE is written in

Fortran, hence it is flexible and can be compiled in any computer environment, including High-Performance Computer. PENELOPE has the capability to run detailed simulations, record the state variables at the detector and different energy spectra; however, no data plot is incorporated in the code. Yet, an external program is needed for plotting, and programmers offer some Gnuplot scripts. Nevertheless, if an imaging system is designed, it is not possible to process the state variables for getting an image. For this reason, MATLAB has been introduced, and PAXI algorithm developed. PAXI is a script for X-ray image processing which can be adapted to the detector pixel size for comparisons with experiment. PAXI is also able to calculate image quality metrics such as SNR, CNR, spatial resolution. When CAs are simulated, it also recalls the decoding script [82] for calculation, for example, of point-spread functions. PAXI introduces the selection of the kind of interaction recorded at the detector.

Furthermore, PENMAT [81] MATLAB application was developed, for improving PENELOPE user experience by interfacing with GUI. With PENMAT, editing is now relatively simple, and data analysis after simulation can be straight forwards. However, there is still work to do for the improving the interface before publication to a wider audience. For example, the installation of the application without MATLAB sometime incurs in errors, above all if the user is not well-experienced in IT. Also, the application has been originally developed for Windows only, while a distribution for MacOS is under test. The data analysis tool PENMAT2 would also require some improvements for I/O and figure plots. However, PENMAT2 introduces a feature which was not available before when running parallel simulations, which is the sum of the phase-space files from the different simulations.

6 MODELLING X-RAY SOURCES

6.1 Chapter Outline

This chapter shows one of the greatest potentials of PENELOPE: the ability not only to model real radiation sources, but also virtual sources to explore fundamental X-ray imaging parameters. Firstly, the modelling of X-ray sources is described (section 6.2). Secondly, the model of the VJT thermionic X-ray tube in PENELOPE is explored, and the output spectra collected at the virtual impact detector compared against SpekCalc (section 6.3.1, 6.3.2). Energy spectra were also physically measured with the Amptek X-123 Cadmium tellurite detector (section 6.3.3), and a more realistic model of the experimental setup was realised in PENELOPE (section 6.3.4) with the energy-spectra at different voltages determined by simulating the X-ray tube as input. PENELOPE spectra were validated by comparison against the experiment (section 6.3.5). Finally, a novel flat 0-200keV X-ray wire emitter, designed to avoid the findings being specific to pyroelectric or thermionic sources with different anode targets, or filters for hardening the beam, was designed for appraisal of image quality metrics of X-ray imaging systems (section 6.4).

6.2 Modelling virtual X-ray Sources

In PENELOPE and in any Monte Carlo simulation codes, the definition of the source is fundamental for running a simulation job, as it defines the characteristics of the incident beam as in the experiment. In PENELOPE, there is a set of sources the user can apply to the simulations. The source properties are described in the input file as in section 5.11.1. In this work, the kind of incident beam in input are electrons (SKPAR=1) or photons (SKPAR=2), either mono-directional or mono-energetic, or cone beam, or even energy-spectra distributions. Although mono-energetic and mono-directional point source/pencil beams are often impractical, they are used in simulations for fundamental studies. In this work, mono-energetic and mono-directional beams were applied to electrons and photons. Electrons were used as mono-energetic mono-directional pencil beams for generating X-ray spectra from a model of the internal layers of

an X-ray tube at a range of anode voltages. Mono-energetic and mono-directional pencil photon beams were applied in exploring the fundamental physics of backscatter imaging (chapter 9). X-ray photons generated as energy-probability distributions from the model of the X-ray tube with the properties of point source and cone beam were used for generating X-ray images by simulations (chapter 7). Knowledge of the energy spectra produced by an X-ray tube is valuable, particularly when trying to characterize target materials and structures by analyzing the spectra transmitted, scattered or generated within them. X-ray generator spectra have been extensively investigated [83] [84] [85] [86] [87], and modelled with analytical/deterministic codes [47] and Monte Carlo simulation [86]. The analytical models use deterministic equations for bremsstrahlung productions, combined with numerically pre-calculated electron distributions [87]. Monte Carlo codes are generally more versatile and are capable of tracking particle histories such as their trajectories and the nature of their interactions which is useful in identifying the underpinning origins of features in X-ray images and in spectra used for materials characterisation [88]. In the first part of this chapter, we aim to establish a Monte Carlo modelling process for determining X-ray spectra from a VJ Technologies conical beam X-ray source [6] at the exit window, for versatile use in X-ray imaging systems and X-ray spectroscopy. The X-ray source was simulated in PENELOPE 2014 [1] Monte Carlo simulation code. X-ray spectra were also calculated with SpekCalc [47] deterministic model. By modelling the VJ Technologies X-ray source separately from the other parts of an imaging system, it is possible to increase computational speed and flexibility in Monte Carlo modelling. The same X-ray source data can be reused in a range of different imaging systems that may include coded aperture [89] [90], pinhole [38] [91] [79] or other objects, or exploring some features in X-ray spectroscopy, without the need to simulate the same computational expensive electron interactions in the anode each time. This is achieved by first determining the source spectra separately for each anode voltage, and then storing the state variables and energy distributions for future repeated use. Further, by simulating current source technology (rather than relying on physical experiment) it becomes feasible to test conditions/options that are viable in the near term even

if they are not yet implemented. Examples include modelling the operation of an existing X-ray tube structure at higher voltages than its power supply currently supports, or investigating its capability should the tungsten anode be replaced with a different material. Also, simulation can be used to explore how sources that are not yet physically possible to produce may perform, such as how a small truly monochromatic source may benefit materials characterisation. By identifying what theoretical X-ray energy distributions best reveal image features [79] we can forecast types of source that may be most attractive to develop for the future. For this reason, in the second part of this chapter, the energy-probability was customised with an ideal distribution independent from any kind of thermionic or pyroelectric sources for exploring image quality metrics. The input file in PENELOPE also allows the user to set a specific object in the geometry file as emitter. The following sections will illustrate the range of different source applications for this research work.

6.3 Modelling an X-ray tube in PENELOPE

In this section, the model of an X-ray tube simulated in PENELOPE will be explored. A diagnostic VJ Technologies' thermionic X-ray tube, commonly used imaging systems, was modelled in PENELOPE.

In an X-ray tube, X-rays are generated when the anode electrons hit the target material and are then redirected through different layers towards the exit window. In most of the diagnostic and industrial X-ray tubes tungsten is used as the target material. X-ray tubes were simulated with different Monte Carlo codes [86] [92] [93]. In this section, X-ray generation of VJT X-ray tube will be described by following up the radiation transport of electrons/photons under vacuum modelled in PENELOPE. In previous work, Bote et al. [94] showed PENELOPE capability of efficiently simulating the radiation transport of X-ray tubes. In the current work the X-ray tube inner section was designed in PENELOPE 3D modelling tool PENGEOM [76], and simulations were executed in PENMAIN [68]. The model of the X-ray tube was designed with material and dimensional information provided by the manufacturer [6], and consisted of a tungsten anode and four layers of window material. The model is shown in figure 6.1.

The anode was greater than 1 mm thick tungsten cylinder cut at 35◦ on the right edge (in purple on figure 1), which is 57mm away from four 50mm diameter disks of different materials and thicknesses as seen in table 6.1 (figure 1, material 2 to 5) representing the exit window. PENMAIN generates a mono-energetic mono-directional 1.2mm diameter beam of electrons incident on the target. X-rays are generated at the target and some exit the four layers window.

Table 6.1 Window materials and thicknesses used for the simulations. This information was provided by VJ Technologies [6] manufacturer.

Material	**Thickness (mm)**
Beryllium	0.8
Glass	1.5
Transformer Oil	3.0
Ultem 1000 (exit window)	1.5

Finally, the X-ray and electron spectra are collected at the incident surface of a virtual 1 mm thick CdTe impact detector (material 6 on figure 6.1) in contact with the exit window. The material of this impact detector is irrelevant as it is set to have no interactions with any radiation. Its purpose is to record the spectra for direct use as the X-ray source for subsequent simulations.

6.3.1 Simulation parameters in the input file

The X-rays are produced predominantly by bremsstrahlung and characteristic fluorescence as the electrons penetrate the tungsten target. The X-ray spectrum is continuous and emerges as a 40° full-cone from the Ultem exit window. The virtual CdTe detector was set to have 256 channels, an energy bin width of 0.64

keV and maximum energy equal to the highest voltage of the X-ray tube (160 kV). Spectra were collected for anode voltages at 80 kV, 90 kV, 100 kV, 120 kV, 140 kV, and 160 kV and are shown in figure 4 as PENELOPE-A.

PENELOPE facilitates the use of variance-reduction techniques to increase the efficiency of the simulation of specific low-probability events, such as bremsstrahlung. Variance reduction techniques were enabled in the input file to increase the precision of the spectrum [68] for the finite simulation time available. Variance reduction techniques include interaction forcing, bremsstrahlung splitting and X-ray splitting [95]. Interaction forcing consists of artificially forcing particle and photon interactions along the particle trajectory which is effective when the cross sections are small [96]. Bremsstrahlung splitting enhances the photon production through bremsstrahlung, and X-ray splitting multiplies the number of X-rays with the same energy.

The PENELOPE default maximum values for enhancement via variance reduction techniques are limited by the number of particles the secondary stack can hold and then follow up in a simulation. For this work it was necessary to increase the computational efficiency by raising the capacity of the secondary stack to 10^6, and setting interaction forcing to 1000 and X-ray splitting and bremsstrahlung to 100 at each layer.

With this input configuration it was possible to achieve sufficient statistics with just 10^6 showers for each simulation.

The simulations were performed on many single cores of a High-Performance Computer.

Figure 6.1 The model of the VJT X-ray tube in PENELOPE. The model has been designed with PENGEOM and consists of a tungsten target anode (Mat 1), and four layers of window material in vacuum (beryllium, glass, transformer oil, Ultem 1000, Mat 2-5). A pencil beam of electrons hits the tungsten and then the photons irradiate the layers before being collected by a virtual CdTe detector placed just outside the exit window.

6.3.2 Simulation with SpekCalc

To increase confidence in the output of the PENELOPE simulation, a comparison was made to SpekCalc [47], a computer code for simulating the output of medical X-ray sources. This software facilitates simple modelling of an anode under electron bombardment at different voltages, with filters of different materials and thicknesses, and gives the emergent X-ray energy spectrum produced by electron bombardment at different anode potentials by analytical means. The theoretical approach underlying SpekCalc combines semi-empirical models of X-ray production. It uses pre-calculated survival probabilities for an electron reaching certain depths within the target, and the electron energy distributions at those depths [48]. SpekCalc allows the user to calculate, display and save, in energy bins of user-defined width, X-ray spectra emitted from tungsten anode tubes. The user selects the electron energy in keV, the X-ray take-off angle, and the amount of filtration by layer thicknesses [49]. Filtration can be selected according to thickness and is limited to ten materials: air, beryllium, aluminum, copper, tin, tungsten, tantalum, water, titanium, graphite. The range of voltages

that can be modelled is wide (40–300 kV) making the utility useful in both diagnostic imaging and radiotherapy. Spectra are generated within a few seconds computation time. Although this program is user-friendly, it presents some limitations. These include a limited range of materials, physical interactions, and more importantly it is only possible to model the generation of X-rays rather than to model the transport and interactions of X-rays beyond the generator and its filters as seen in chapter 4. As in SpekCalc the range of filtering layers and target materials was limited compared to PENELOPE, X-ray spectra were calculated using the same information of target material, and take-off angle (tungsten target at 35˚), and spectra were collected at the same distance (1500 mm). The range of filters in SpekCalc included beryllium, which was set to 0.8mm as in PENELOPE simulation, but do not include the other materials, such as the Ultem-1000 exit window. Thus, the other layers in SpekCalc were used to determine spectra equivalent those of PENELOPE. The filters of aluminum and copper were added to adjust the shape of the spectrum for generating an output compatible with PENELOPE. Aluminum was 0.8 mm thick and copper 0.2 mm thick. Spectra generated with SpekCalc at 80-160kV are shown in figure 4 and compared against PENELOPE-A. Relative intensities for comparing energy spectra at different voltages

Spectra from the PENELOPE model of the virtual detector, i.e. the output at the X-ray tube will be identified from now on as PENELOPE-A, and they were compared with SpekCalc for validating the model at 80 kV, 90 kV, 100 kV, 120 kV, 140 kV and 160 kV anode voltages. Figures of the spectra are shown in figure 6.2. Simulated spectra from SpekCalc are in blue, PENELOPE–A are in red. When comparing simulated X-ray spectra, the following aspects should be considered. In PENELOPE, the relative X-ray output is expressed as energy-probability spectra (probability is in units of keV^{-1}), whereas in SpekCalc the output is expressed as energy-counts.

Thus, to compare the various simulations the spectra amplitudes were normalized to their local bremsstrahlung averaged maxima as expressed in equation 6.1 below.

$$I(a.u.) = \frac{Output\ on\ Y\ axis}{\langle Maximum\ Bremsstrahlung(output\ on\ Y\ axis)\rangle} \quad 6.1$$

By introducing the normalization on the data, it is also possible to check if the tungsten characteristic lines from both simulations and experiments are comparable as all the data have the same units.

6.3.3 Measuring the VJ Technologies X-ray source spectra

The second part of this set of work consisted in measuring the X-ray spectra from the physical VJT X-ray tube. The spectra were measured with a shielded Amptek X-123 Cadmium Telluride detector placed directly in front of the source.

The experimental arrangements are shown in figure 6.3. The X-123 CdTe is a compact X-ray and low energy gamma-ray detector with a 0.1 mm thick beryllium window mounted on a Peltier type thermo-electric cooler keeping components at -30°C. The X-123 CdTe includes the detector, preamplifier, digital pulse processor and MCA, and power supply, and it connects via USB to PC [97]. The CdTe detector itself is 1 mm thick and 3x3 mm in area. A highly linear energy calibration was determined with ^{241}Am and ^{238}Pu gamma sources. The Amptek X123 CdTe energy-dispersive detector is often used for measuring low intensity X-ray spectra for materials characterisation purposes. However, with a fan beam X-ray generator for imaging, it is difficult to measure the spectra directly, as the flux is too high. Fernandez et al. [98] measured the X-ray spectra of a source by reconstruction from inverse Compton scatter. This reduces the flux but introduces uncertainty and requires computation of the conversion matrices.

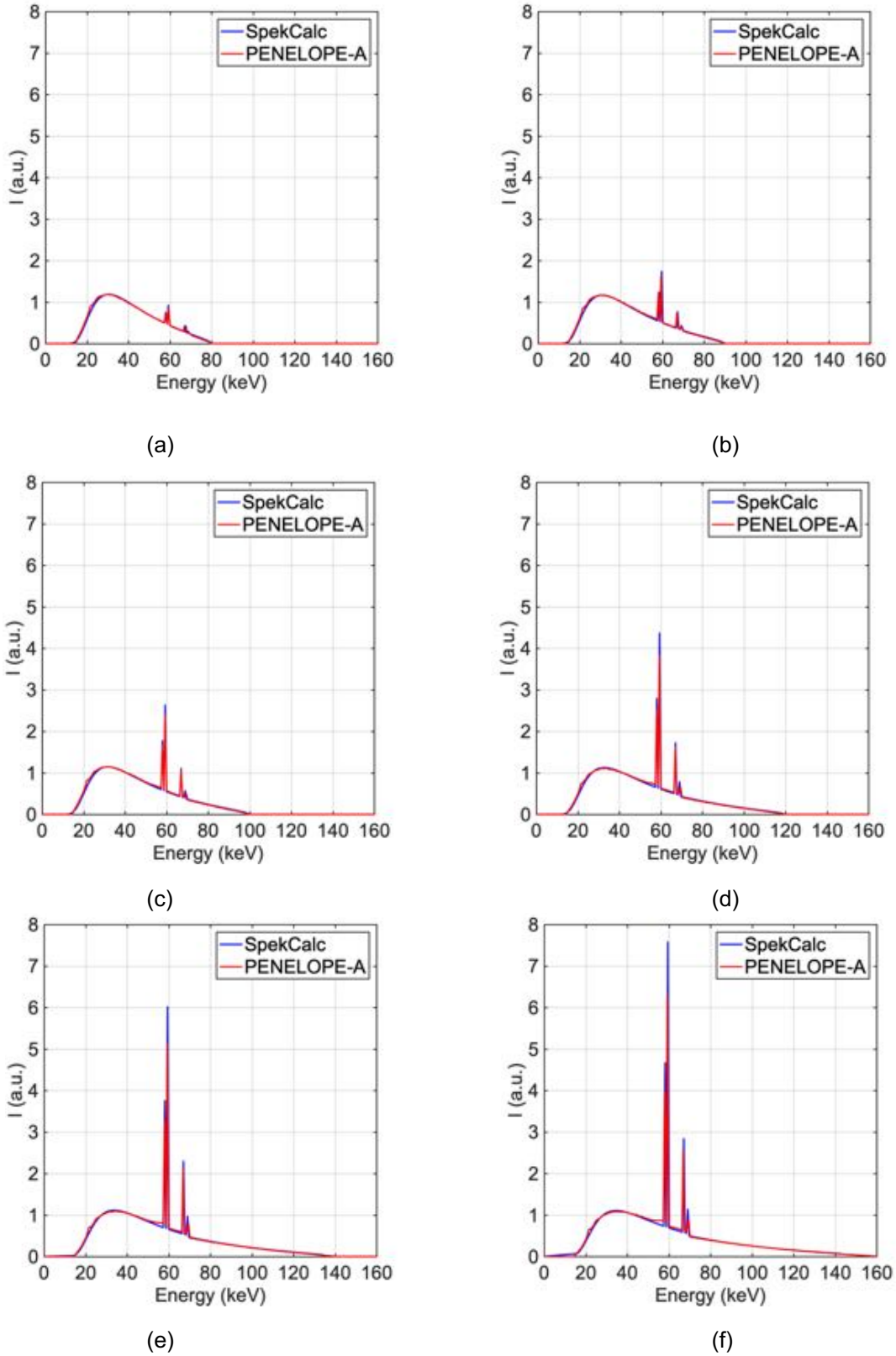

Figure 6.2 X-ray spectra at 80 kV (a), 90 kV (b), 100 kV (c), 120 kV (d), 140 kV (e) and 160 kV (f) simulated in SpekCalc (red) and PENELOPE -A (blue).

It is possible to measure the X-ray spectra directly from the X-ray tube by increasing the distance from source to detector or shielding the detector from most of the direct X-rays with a collimator. The last option was chosen for this work.

In an initial experiment, the detector was covered with a 0.5mm diameter aperture 10 cm thick tungsten collimator and placed 1.5m from the source to decrease the photon flux and so reduce dead time and spectrum artefacts such as pulse pile up and sum peaks. However, these measures were still not enough to enable the spectra to be collected without distortion. On request, the manufacturer (VJ Technologies [6]) reduced the minimum operational current from 2 mA to 0.2 mA by a software patch. It was believed X-rays direct from the source and scattered from the walls could interact directly with the processing electronics at such high fluxes to contribute to system noise so a 4mm thick lead shield with a 10mm aperture (to house the Tungsten collimator) was introduced to further shield against direct X-rays and a combination of lead and concrete bricks was added to cover top, sides and rear. The scheme of the experimental setup can be seen in figure 6.3. This confined the signal to that coming direct from the source. The spectra were then collected using the Amptek software ADMCA, and a correction for escape peaks was applied to the spectra with the XRS-FP software bundle [99].

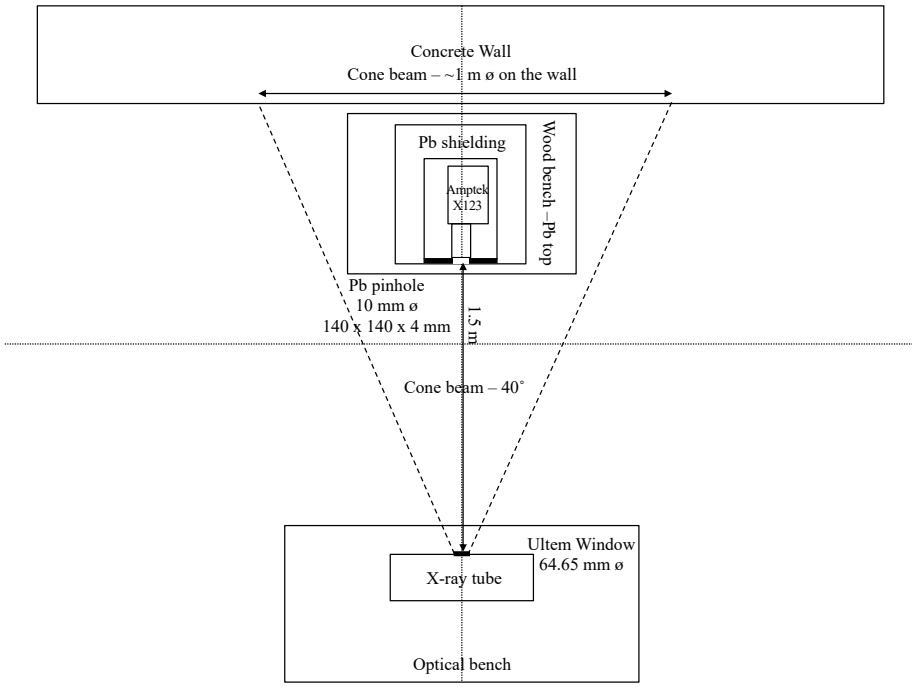

Figure 6.3 Experimental setup for detecting the X-rays emitted by the X-ray tube with the Amptek X123 CdTe detector. The unshielded detector was placed 1.50 m from the source, then it was shielded with lead to minimize scatter from walls.

6.3.4 Identifying artefacts in experimental X-ray spectra

The modelled spectra determined at the source exit window with PENELOPE (section 6.3.1) and SpekCalc (section 6.3.2) were compared to spectra experimentally determined with a shielded Amptek X-123 Cadmium Telluride (CdTe) detector directly placed in front of the VJT source (figure 6.3) [50]. As it is possible to observe from figure 6.3, the experimental spectra were found to be far from the ideal output of PENELOPE and SpekCalc, as they were distorted by scattering (red circle in figure 6.3), charge trapping and hole tailing effects at the low-energy tail of the fluorescence peaks (orange circle, in figure 6.3). At voltages greater than 100kV, a broad peak in the background between 70 keV and 120 keV was observed which increased with anode voltage and was considerably higher when the shielding was not applied [50].

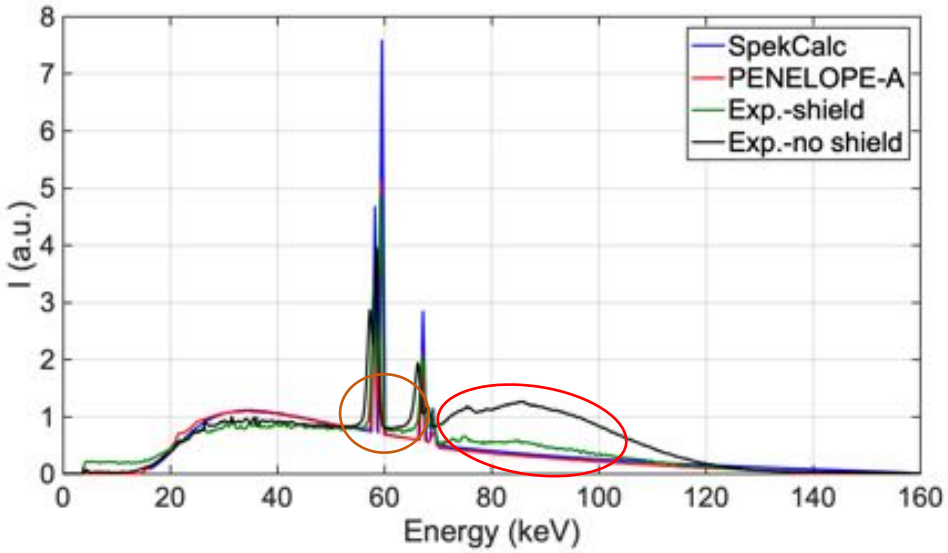

Figure 6.4 Experimental spectra without shielding (in black), with the shielding (in green), both without RTD, and simulated in PENELOPE-A (in red) and SpekCalc (in blue). The scatter artefact is present in the experiment within the region 70-120 keV, more evident without the shielding (red circle). Hole tailing affects the tungsten peak areas without RTD enabled (orange circle).

This effect is unlikely to be attributed to bremsstrahlung alone, since the theory predicts the spectrum should decrease with increasing of energy, rather than increasing in the 70-120 keV region. Previous studies of Gonzales et al. [100] and Cluggish et al. [101] attributed this broad peak to materials from the physical laboratory. By applying the shielding to the detector, it was observed the broad peak was mitigated. Thus, X-ray scatter from the surrounding materials in the laboratory environment and possibly the thick tungsten collimator were identified as the reason for scatter to arise.

Rise Time Discriminator (RTD) could be enabled for minimising the hole-tailing effect at the tail of tungsten fluorescence peaks [102]. Thus, the experiment with the shielded detector was repeated with the RTD ON. Efficiency corrections were also applied to the spectra by using the efficiency package provided by the manufacturer [99].

6.3.5 Modelling Amptek X-123 CdTe in the laboratory environment

Experimental spectra were more accurately simulated by including further details on surrounding structures. The X-ray spectra at the exit window were used as input in a second set of simulations for comparisons with the X-ray spectra of a physical detector in an experimental environment. In the model, the Amptek X-123 CdTe used for physically measure the X-ray spectra, was replicated. The geometrical model included the thick tungsten collimator, the aluminum box where the electrical components of the physical detector are stored, and the lead shielding which was physically applied for avoiding scatter as in the physical experiment in the scheme in figure 6.3 and is shown in figure 6.4. The model comprises a 1000x1000x500 mm concrete wall (in red in fig. 6.4(a)), a 600x600x2 mm lead table top (in blue in fig. 6.4(a)), 150x150x50 mm lead bricks for shielding (in orange in fig. 6.4(a)), and a 100x100x4 mm lead pinhole mask (in purple in fig. 6.4(a)). The modelled Amptek X-123 CdTe detector is located inside the lead wall behind the pinhole mask (fig. 6.4(b)). The model of the detector includes the aluminum box hosting the detector electronics (in dark blue in fig. 6.4(b)(c)), the 15.87x36 mm tungsten collimator 3 mm aperture (in green in fig. 6.4(b)(c)), the 3x3x1 mm CdTe crystal (in purple in fig. 6.4(c)), and the 7x0.1 mm Be disk window (in orange in fig. 6.4(c)).

Replicating the physical experiment was necessary for the validation against simulations, as although the spectra at the impact detector can be correct, they are not accounting for the physical experimental conditions, such as detector solid angle, shielding materials, and collimation, etc. Shielding materials and the collimator could generate secondary scatter, which is counted by the physical detector and deforms the output spectrum. It becomes then fundamental to estimate the correctness of the experimental spectra against the ideal spectra at the exit window of the X-ray tube for identifying arising artefacts.

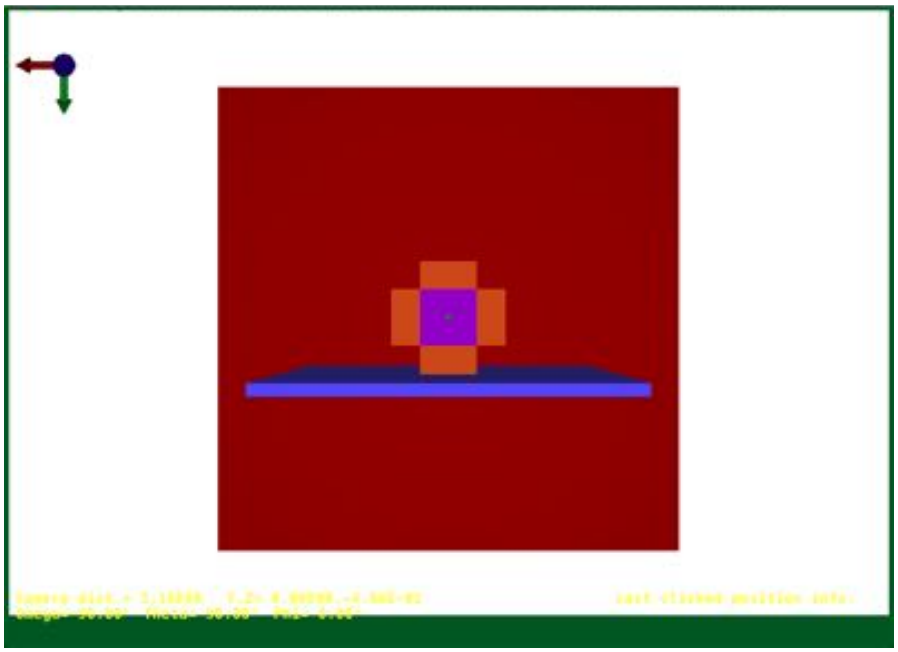

(a)

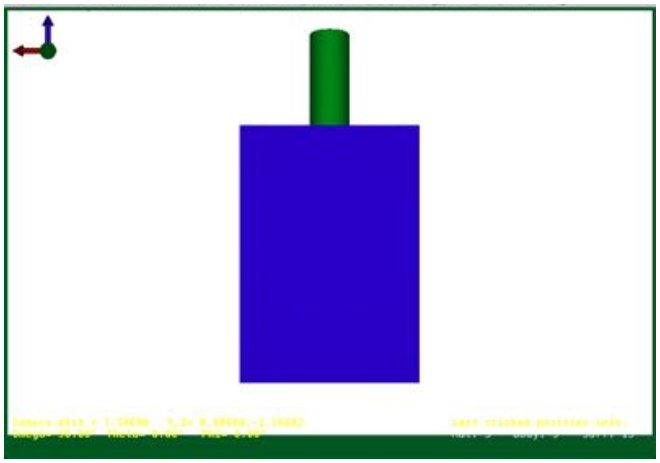

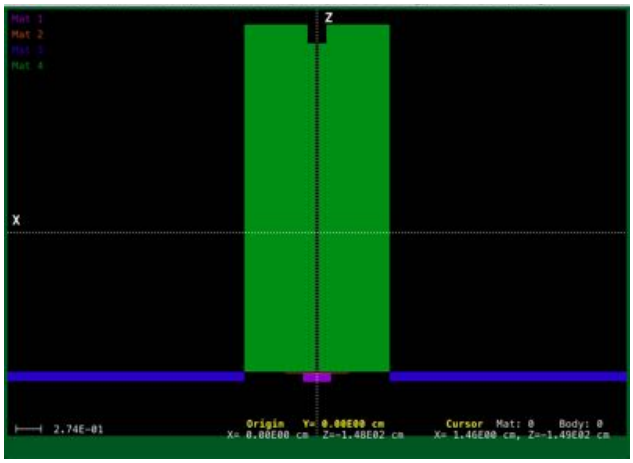

(b) ¶ (c)

Figure 6.5 PENGEOM three-dimensional model of the laboratory environment (a). The concrete wall is in red, the lead table top in blue, the lead shielding is in orange, and the lead pinhole is in purple. Inside, the model of Amptek X-123 CdTe (b) with aluminum box (in dark blue) and tungsten collimator in green. (c) is the section of the inside of the Al box (in dark blue), the CdTe crystal is in purple and the thin beryllium window (in orange) between the CdTe crystal and the tungsten collimator (in green).

For these reasons, it was chosen to simulate the whole experiment by replicating the Amptek X-123 CdTe, plus the components of the laboratory environment. The simulated laboratory room included the wooden bench with lead lining (2 mm thick, 600 x 600 mm width/length), the CdTe detector with the thick tungsten collimator in front, the lead shielding and the lead aperture as described in the previous section. A 100 mm thick 1 m wide wall was also added behind the detector. For this simulation, the energy-probability spectra at 80 kV, 90 kV, 100 kV, 120 kV, 140 kV and 160 kV anode voltages collected at the modelled CdTe detector with the X-ray tube PENELOPE spectra were used as input. For these simulations, the phase-space file collection was enabled to explore if any scatter events occurred within the volume of the CdTe crystal in the detector. No variance reduction techniques were used this time. In general, variance reduction techniques work well for simple simulations, and results are improved and unbiased. For complex models it is hard to predict if a variance reduction technique is appropriate, and there is not a specific method for applying variance reduction techniques to the different kind of models [37]. In complex models, the simulation could lose unbiasedness, or even consistency of estimators, and even when they are preserved, the computational cost might be high. In our specific case, in the attempt of applying variance reduction techniques, the output spectra were distorted compared to what expected, and PENELOPE was recording some non-existent kind of interactions on the phase-space file. Thus, it was required a high number of simulated showers, equal to 10^{10}. PENMAIN was modified to increase the number of bins in the input file up to 2048 to match the same number of channels (2048), bin width (0.16keV), and energy range (328keV) of the real Amptek X-123 CdTe detector. X-ray spectra were collected as previously between 80-160kV and are shown in figure 6.6 as PENELOPE-B and compared with the experiment. As in section 6.3.2, to compare PENELOPE-B simulations and real data all the results were normalized to their local bremsstrahlung averaged maxima as expressed in equation 6.1.

6.3.1 Peak area comparisons between simulations and experiment

The output results from both simulations and experiment visually appear to be in general good agreement, both in the bremsstrahlung area and the $K_{\alpha 1}$ tungsten characteristic peak region. The $K_{\alpha 1}$ tungsten characteristic peak regions were estimated as peak areas for PENELOPE-A, PENELOPE-B, SpekCalc and experiment and results were compared as shown in table 6.2.

Table 6.2 Tungsten characteristic peak areas at the different anode voltages of SpekCalc (SK) simulation and experiment against PENELOPE-A (PEN-A) and PENELOPE-B (PEN-B), and SpekCalc against the experiment (EXP). The peak areas' comparisons are presented as percentage.

	80 kV	90 kV	100 kV	120 kV	140 kV	160 kV
SK/PEN-A	95.3%	96.1%	93.2%	100.0%	85.6%	82.9%
SK/PEN-B	71.8%	75.9%	93.2%	71.9%	69.1%	66.4%
EXP/PEN-A	73.8%	85.5%	96.5%	87.5%	97.0%	94.0%
EXP/PEN-B	90.4%	102.1%	96.5%	112.1%	111.0%	107.2%
SK/EXP	70.5%	82.3%	90.4%	87.5%	84.8%	80.2%
PEN-A/PEN-B	81.6%	83.8%	100.0%	78.0%	87.4%	87.7%

Table 6.2 highlights where simulations and experiments agree and disagree more clearly by comparing spectrum height at the tungsten target $K\alpha_1$-line. Overall, the relative peak area appears in good agreement between PENELOPE-A/experiment, PENELOPE-B/experiment. The best agreement is achieved between PENELOPE-B model and experiment at all the anode voltages, on average $(103.2\% \pm 8.6\%)$. The relative peak area from PENELOPE-B suggests the geometrical model is more accurate than the simpler PENELOPE-A (on

average $89.0\% \pm 8.8\%$) X-ray tube model, as PENELOPE-B model includes the radiation transport within experimental arrangement, and the area under the spectra $K\alpha_1$-lines appears closer to the measured spectra.

Although SpekCalc simulations are in good agreement with experimental data (on average $82.6\% \pm 6.9\%$) and PENELOPE-A (on average $92.2\% \pm 6.6\%$) and PENELOPE-B (on average $74.7\% \pm 9.6\%$), SpekCalc analytical spectra appear closer to the model of the X-ray tube of PENELOPE-A, with a 100% agreement at 120 kV. The difference then increases at higher voltages $(84.2\% \pm 1.2\%)$, probably because of the limited capacity of SpekCalc to incorporate unusual filter materials such as the Ultem-1000 present in the window material of the VJ source. The high-energy tail on the right of the experimental spectra also appears to differ from the more ideal spectra of PENELOPE-A and SpekCalc models. However, when simulating the laboratory environment and introducing more elements of the real Amptek X-123 CdTe, such as the tungsten collimator and the beryllium window, then the high-energy tail of PENELOPE-B agrees with experiment up to 120 kV. At higher voltages, it was observed in the experiment a broad peak arising between 70-120 keV which although small (mainly within the boundaries of the different simulations) is of interest. This broad peak may not be inherent in the VJ-Technologies tube emission, but instead could be some artefact arising from interactions in the room or even some function of the detector. The hypothesis was it was scatter from surrounding materials, including the lead bricks and the thick tungsten collimator. However, neither PENELOPE-A and PENELOPE-B spectra showed such effect. It was suspected the probability of such scatter events was too low for showing on the spectra, but if there were any undertaken scatter events of photons hitting any prior bodies, PENELOPE would have recorded them in the phase-space file.

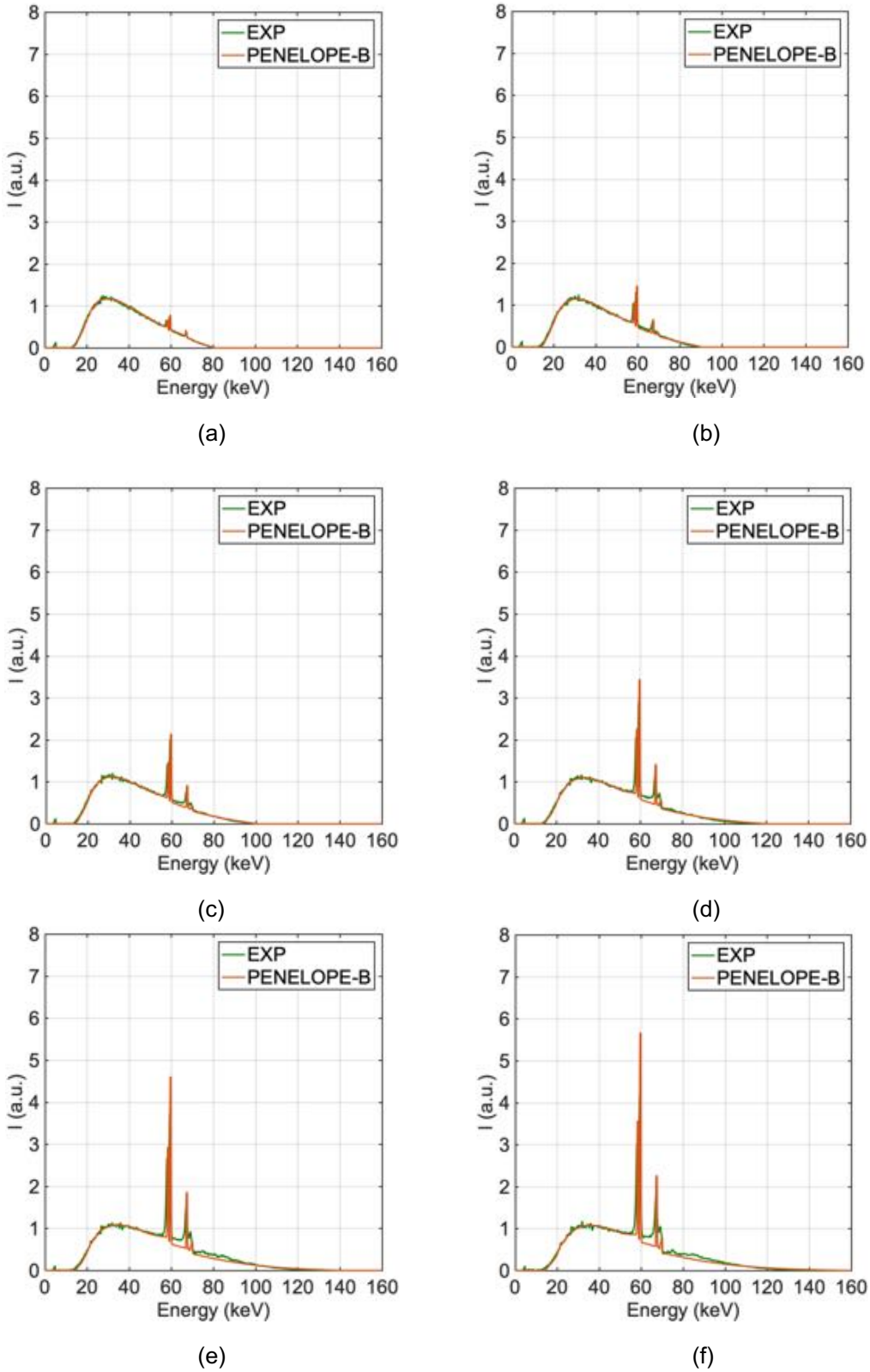

Figure 6.6 X-ray spectra at 80 kV (a), 90 kV (b), 100 kV (c), 120 kV (d), 140 kV (e) and 160 kV (f) simulated in PENELOPE-B (orange) and experiment (green).

The phase-space file is the data file where simulation programs usually record the state variables, such as energy, position x-y-z, Euler angles, kind of detected particles, kind of interactions [95]. The phase-space file was processed in MATLAB as in previous work by Vella et al. [77] with the algorithm PAXI (Phase-space file Algorithm for X-ray Imaging) [5] for generating a spatial distribution of the detected photons [79] by dividing the detector area into an arbitrary virtual grid of 100x100 pixels.

The spatial distribution is generated as brightness over the detector surface, i.e. integrated energy of the photons impacting each pixel in the area. For clarity, the Amptek is not a pixelated detector, this is simply a theoretical investigation to identify the origin of the low bump feature. By selecting the Compton and elastic scatter events, it is possible to isolate the brightness of scattered photons contributing to the spectra between 70-120 keV.

The brightness of the detected scatter photons over the pixel area of the detector at 160 kV anode voltages can be seen in figure 6.7.

PAXI algorithm can also calculate the energy-probability spectrum from the specific interactions. At the highest anode voltage 160 kV the probability of scatter (both elastic and Compton) photon interactions between 70-120 keV is ~10^{-4} lower than the probability of the total spectrum in the same region (see fig. 6.8).

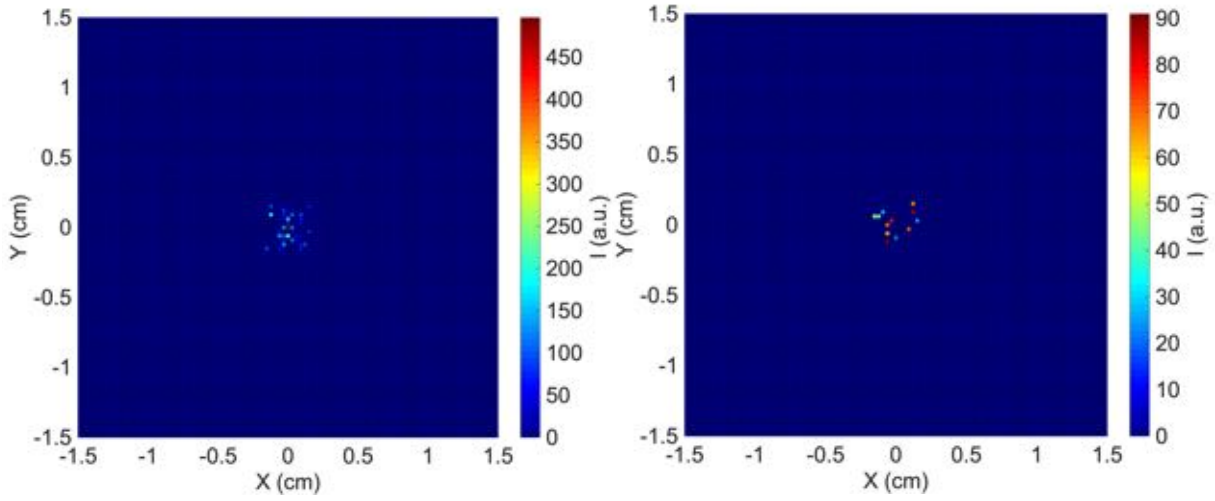

Figure 6.7 Spatial distribution of scatter photons over the pixel area 100x100. The pixel area is generated as virtual pixel grid over the 3 mm x 3 mm surface of the detector. In figures, the brightness at 160 kV for Compton scatter (a), and elastic scatter (b).

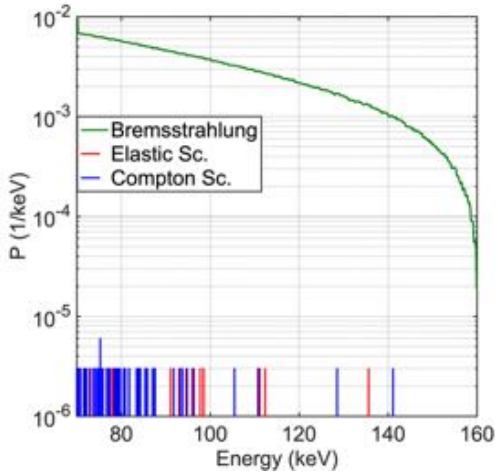

Figure 6.8 Energy-probability spectrum of PENELOPE-B between 70-160 keV. Scatter contribution from simulation is ~10^{-4} less than the total spectrum.

6.4 Extended sources and custom energy-distributions

Simulation permits any mono-energetic, polychromatic, point or extended X-ray source to be modelled whether it is physically feasible yet or not. In this section, a novel energy-distribution wire emitter capable of appreciating and exploring image quality metrics will be described. The novel custom-distribution wire emitter is independent from any kind of known emission, which can not only be useful for theoretically estimating image quality metrics, but also a model for identifying the nature of future sources that might be particularly suitable for imaging or materials characterisation. Although the wire test object was applied for testing pinhole and coded apertures optics, this section will only be focused on the wire. Further details on the X-ray camera and image quality metrics can be found in chapter 7.

6.4.1 Wire source for testing backscatter X-ray detector

The novel test object consists in a wire 0-200 keV flat emitter which was designed in PENGEOM for testing an X-ray imaging pinhole and coded apertures camera. The wire was placed in front of the imaging system as it can be seen in figure 6.8.

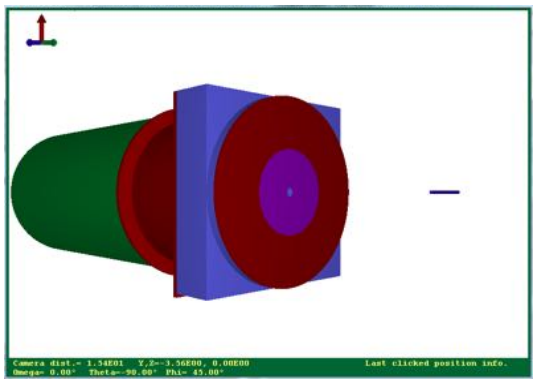

Figure 6.9 Wire 0-200 keV flat X-ray emitter (in blue, on the right) in front of the X-ray pinhole camera (on the left).

The test object was designed for simultaneous appraisal of the image resolution and field of view from different pinhole masks with minimal computation time. The test object was a long thin metal wire placed 16.6cm in front of the pinhole mask to give a magnification of unity. It was set to be narrow (0.3mm) so that broadening reveals resolution deterioration caused by imaging system. The extreme thinness of the object was expected to result in a Gaussian image profile useful to calculate the resolution of the system in terms of its FWHM. It was set to be long (4.6cm) where any reduction in its length in the image reveals the collimation effect of the pinhole reducing the Field of View (FOV) [79]. To allow the emission from the wire as an extended source the function SOURCEBOX in the input file was enabled by surrounding the material with a virtual transparent box. The emission occurred when the random generator found the object inside the virtual box and then it created the X-rays.

Backscatter imaging is usually performed with a source of X-rays near the camera directed at the target area. X-rays scatter from the target area in all directions, including back to the camera. However, to test the characteristics of various pinhole masks it is computationally more efficient to make the test object the source of X-rays rather than to unnecessarily simulate X-rays that miss the ‘wire like’ object, radiation interactions inside the wire and follow the propagation of scattered X-rays that would clearly miss the camera. Emission was restricted to a 20° cone in the forward direction to match the area of the mask and the photons generated had equal probability to be produced everywhere within the source wire. In our case the test object generated photons with a uniform yield across the defined energy range so that the transmission function of the pinhole mask is easily apparent and to avoid the findings being specific to pyroelectric or thermionic sources with different anode targets, or filters for hardening the beam.

The 0-200 keV flat energy-distribution of the wire emitter can be seen in figure 6.9.

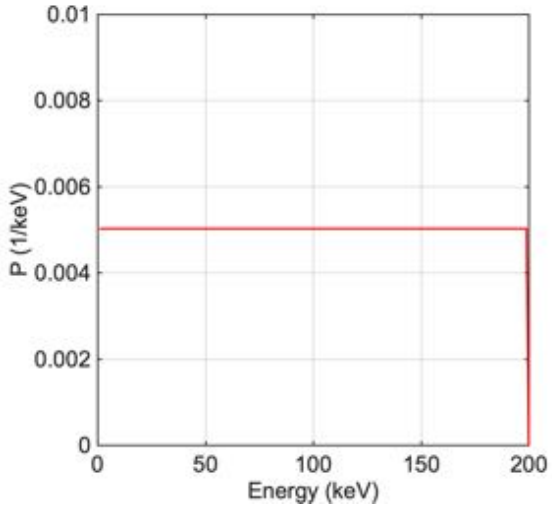

Figure 6.10 Wire 0-200 keV flat X-ray emission.

6.4.1 The thin wire 0-200keV flat X-ray emitter for appraisal of leakage through the masks, image brightness and image quality metrics

This section aims to give an idea of the capabilities of a thin wire 0-200 keV flat X-ray emitter within an imaging system.

Firstly, as the X-ray emission is directed towards the pinhole/CA mask (in purple in figure 6.8), it can reveal if any leakage occurs within the mask material. This is one of the first elements helpful in the decision-making process of materials for physically manufacturing. Such a source is capable of exposing features without being influenced by other characteristic features which could for example arise from diagnostic X-ray tube. The emission was also set to expose the features of the masks within the typical operational energy region, with the features actually belonging only to the mask materials and not to any other targets.

Secondly, by using such a test object, it was possible to quickly and efficiently generating a simulated image through PAXI [5] algorithm by estimating the image brightness as a function of the integrated energy [79].

Finally, when manufacturing a pinhole or CA mask for X-ray optics, the apertures diameter and thicknesses of the materials are fundamental, and such parameters should be optimised before manufacturing to decrease the costs. One way to achieve the optimum configuration is to use the power of simulations. In that sense, the narrow and relatively small shape of the test object was set for exploring possible manufacturing optimisations, but also for finding any limitations in the field of view, i.e. collimation effects, through the simulated image brightness.

Such a versatile source can be applied, in principle, to any X-ray pinhole and coded apertures optics. Results from these simulations can be found in chapter 7.

6.5 Chapter summary and critical analysis

In this chapter, a set of different approaches to simulate an X-ray source were discussed. These included the simple but efficient mono-energetic and mono-directional beam, which can be either applied for exploring the fundamental physics (in our case of backscatter, in chapter 9), and for generating X-ray spectra with the aid of variance reduction technique used for enhancing less-probable events such as bremsstrahlung. The VJT source was modelled for 80 kV, 90 kV, 100 kV, 120 kV, 140 kV and 160 kV anode voltages, and X-rays from the tungsten target were filtered with four different layers, and the output spectra at the exit window calculated. Spectra were computed in SpekCalc deterministic code and were compared against PENELOPE output. It was appreciated PENELOPE Monte Carlo code offers a wider variety of parameters to match exactly the layers as the specified by manufacturer. Spectra were also physically measured with Amptek X-123 CdTe detector, and results were affected by scatter and hole tailing effect. Such effects were more evident at higher voltages and without shielding. Measures were taken to mitigate scatter by shielding the detector with lead, and hole tailing effect by enabling RTD. However, the spectra collected by the physical CdTe detector were not totally matching with the ideal PENELOPE and SpekCalc simulations. The reason for this is because the two physical process considered in simulations and experiment were different. In

PENELOPE (and also SpekCalc) the spectra are collected outside the exit window, while in the experiment, although the detector was placed 1500 mm away from the source to decrease the incoming flux of the tube, it was not enough to prevent scatter events to affect the spectra. Thus, a more comprehensive and realistic model was created in PENGEOM and longer simulations were done to assess the spectra within the laboratory environment. Yet, PENELOPE was unlikely to determine scatter events between 70keV-120keV, as the probability of such events was 10^{-4} lower than the regular X-ray spectra.

Modelling the VJ Technology X-ray generator allowed us to check that our approach using PENELOPE was indeed correct. The output of the generator was calculated for anode voltages up to 160 kV. Comparing the PENELOPE predictions to both experimental spectra measured using a CdTe detector and the output from an established X-ray tube simulation code SpekCalc showed that our approach to modelling was indeed correct and gives us confidence in our other simulation results, and the opportunity to explore different types of X-ray generator. Further, it gives us a fast and versatile capacity to generate a range of source terms for any imaging geometry we need to study in the future.

PENELOPE also offers the flexibility to model real source and real detectors within a laboratory environment, proving to be essential to for recognizing and understanding the origin of artefacts which may arise in realistic experimental situations. The ability to model the correct X-ray spectrum output by the VJT source is a foundation for replicating further experiments as realistically as possible, especially with a view to materials discrimination and X-ray backscatter imaging.

While comparing tungsten characteristic peak areas from PENELOPE-A, PENELOPE-B, SpekCalc and experiment, PENELOPE-A and PENELOPE-B remained within 89% and 103% of experiment, respectively, whilst SpekCalc matched experiment of 83% the experiment on average. It is likely SpekCalc's narrow choice of the beam filtering materials is partially responsible for this disparity given the VJ source uses multiple low Z filter materials in its window construction, however SpekCalc is much quicker and easier to use than

PENELOPE. PENELOPE-A and PENELOPE-B difference in models can be appreciated as equal to ~86%, that is in PENELOPE-B the $K_{\alpha 1}$-line is attenuated of 14% peak area when the experimental environment is replicated in the model.

Finally, PENELOPE capability is not limited to simulating mono-energetic/mono-directional beams and physical sources. With PENELOPE, in principle, it is possible to design electron beams, and X-ray (and also gamma-ray) sources which may not feasible today but can be achievable in the future. In this work, a novel X-ray 0-200keV wire X-ray emitter was designed. The X-ray emission was set to 200keV, which deliberately (for reason of penetration into test objects) lies at the higher energy end of small X-ray generators. Also, the majority of current X-ray generators produce most of their X-rays significantly below their maximum energy. The wire emitter was designed for simultaneous appraisal of image quality metrics, independent material characterisation, and pinhole/CA masks optimisation for X-ray optics and backscatter imaging system, with suggestions for more suitable physical design which could be achieved experimentally.

7 MODELLING BACKSCATTER IMAGING SYSTEM

7.1 Chapter Outline

This chapter presents major contributions for designing and evaluating a backscatter (but not only) X-ray imaging system by replicating the physical imaging plate and process raw data from the simulation output to form an image. Firstly, a pinhole/coded apertures camera was modelled based on a physical camera (section 7.3).

Secondly, a transmission study was delivered with a novel thin wire 0-200 flat X-ray emitter (section 7.4-7.5) to appreciate the range of materials which were good candidates for manufacturing pinhole/CA masks, and the choice was restricted to three materials, tungsten, tungsten epoxy resin and bismuth low-melting alloy (section 7.6). Then, a study of suitable thicknesses and aperture diameters of pinhole masks (modelled in section 7.7) (but applicable to coded apertures) was accomplished, and image quality metrics were calculated (section 7.8- 7.10). This was achieved by using the flat 0-200keV X-ray wire emitter, with the aim to give a measure which was independent from any specific kind of X-ray/gamma ray sources. Image quality metrics determined for pinhole masks included contrast-to-noise ratio, signal-to-noise ratio, spatial resolution and field of view, and its restrictions which may lead to partial coding. A combination of these results was found to aid the manufacture decision-making for achieving the best performances of the imaging system (section 7.11).

This work also included modelling the upgraded imaging system and coded apertures masks (section 7.12). Modelled CA masks were MURA, mosaicked MURA, NTHT mosaicked MURA, Singer Set and NTHT Singer Set. A pilot test was done with the thin wire emitter and some of the CAs (section 7.13). Simulations were conducted with simulated Am-241 gamma-ray source, both as point source and physical source, to measure image quality metrics of the imaging system. Performances of simulated CAs were compared against pinhole masks, and experiment (section 7.14).

Finally, a pilot backscatter simulation with the same physical apparatus in the laboratory was conducted. The test object was the quadrant, an object made up of four cubes of different materials, and results from simulations were compared against experiment (section 7.15).

7.2 Modelling the X-ray imaging system

The first geometrical setup of the X-ray backscatter imaging system comprises a silicon detector enclosed by lead shielding, a brass rotation stage, and a pinhole mask placed in front of the rotation stage (see figure 7.1(a)). The X-ray camera was designed in PENGEOM subtool [76]. The mask is simulated for a set of different materials, thicknesses and aperture sizes. The different materials were tested by simulating the novel thin wire 0-200keV X-ray flat emitter as X-ray source [79], described in chapter 6, sections 6.4 and 6.5.

In a preliminary study of material thickness and properties, each material was examined without the pinhole to characterise the leakage through the mask material. The leakage spectra were generated in PENELOPE as energy-probability distributions. This led to the study of the probability photons can be transmitted through the mask materials and aid the first selection for manufacturing (see section 7.5). Then, the three materials were selected, and simulations were repeated by adding to each of three thicknesses and each of three materials a pinhole aperture of three different diameters. The simulated ‘image’ at the silicon detector was then collected as a phase-space file by the main program PENMAIN and was processed using MATLAB [2] to show the overall detected energy spectrum and explore the image quality metrics.

7.3 X-ray camera model: first setup

The model of the physical imaging system comprises a Gemstar X-ray detector in a lead-lined black aluminium case. The case is fixed to an aluminium mount which is clamped securely to an optical bench. Attached to the front of the camera

case is a 100 mm lead lined aluminium extension tube, which supports a brass rotation stage [79]. The inner face of the rotation stage is lined with a 4 mm lead sheet. The pinhole mask is supported at the very front of the camera in an aluminium plate attached to the stage, and the whole system is tightly sealed, other than the apertures of the pinhole optic. The experimental camera is shown in figure 6.1(a). The model of the camera replicates the relevant features of the experimental setup, and can be seen in figures 6.1(b)(c). It contains the following components:

- The 90 mm pinhole mask (pink) with a thickness of either 0.5, 1, 2, 3, 4, 5, 6, 7, 8, 9 and 10 mm and an aperture diameter of either 1, 2 or 3 mm.
- A 200 mm diameter aluminium support disk (red) 10 mm thick, with a 90 mm diameter inner hole.
- The 200 mm wide brass rotation stage (purple), 47 mm thick, with a 90 mm diameter inner hole;
- The silicon detector (orange) 92.4 × 123.2 mm, sitting 166 mm behind the pinhole.
- Two 166 mm diameter aluminium cylinders (green and red) to support the pinhole and detector.
- The volume surrounding the detector was filled with air to make the simulation more realistic. Air is represented in yellow/gold in the detector section on figure 6.1(c).

7.4 Thin wire 0-200 keV flat X-ray emitter for testing the camera

The physical system itself was set to image X-rays backscattered off objects. However, the imaging system required some preliminary studies before performing backscatter imaging.

The thin wire 0-200 keV flat X-ray emitter explore in chapter 6 was used to perform simulations without and with holes. When no hole was simulated in the disk mask, transmission was extracted from a range of suitable materials.

Once the materials were selected, the wire emitter was used for testing the pinhole masks, generate the images from the phase space file, and calculate imaging performances.

The X-ray source object was placed 16.6cm in front of the pinhole mask to give a magnification of unity. The object was a metal wire with a length of 46mm and 0.3mm thickness. In figure 6.1(b) it is represented as a blue thin cylinder, and it is in front of the pinhole mask in purple. The object was set to be narrow to reveal the resolution of the camera and long to expose any collimation effect and how it affects the Field of View (FOV). The length of the object was chosen to exceed the expected detected length for the range of pinhole geometries investigated, the aim being to expose any collimation effect should it occur.

The extreme thinness of the object was expected to result in a Gaussian image profile useful to calculate the resolution of the system in terms of its FWHM.

Emission was restricted to a 20° cone in the forward direction to match the area of the mask whilst minimising simulation time and the photons generated had equal probability to be produced everywhere within the source wire.

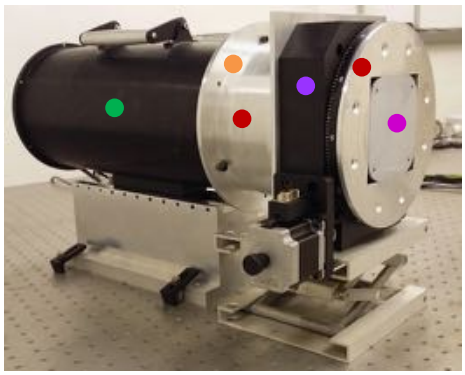

(a)

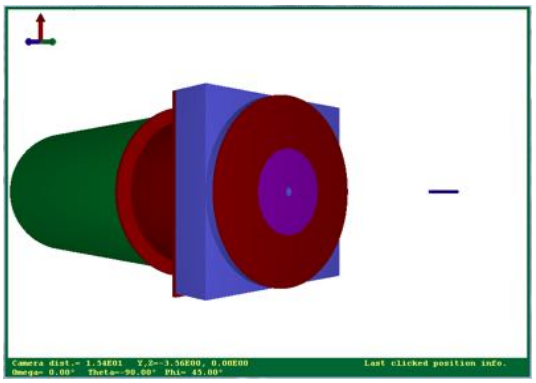

(b)

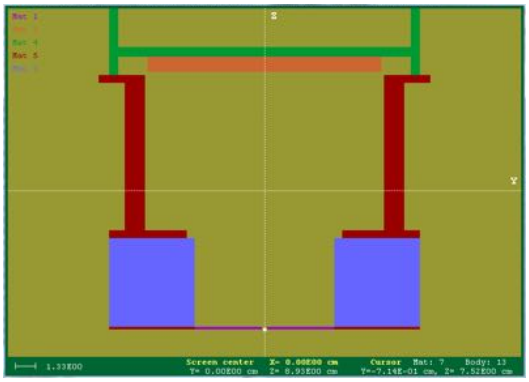

(c)

Figure 7.1 (a) shows the X-Ray camera in the experimental setup, (b) shows the PENGEOM model in 3D. (c) is a cross section showing the position of the detector inside the shielding. The following components can be seen in 1b and 1c with the PENGEOM colour code: pinhole mask (W, W Ep. Or Bi All.), in purple, rotation disk, placed in front in front (Al), in red, rotation stage (brass), in light blue, extension (Al), in red, external cylindrical envelopment (Pb), in green, CCD detector (Si), in orange, wire test object (metal) in dark blue.

7.5 Energy spectra of the incident beam through the mask materials

The simulated results generated by PENMAIN are recorded in the phase-space file captured at the CCD camera (see in orange in figure 7.1(c)). The phase-space file contains diverse useful information including the position, direction and energy of each photon that strikes the model detector. The energy spectra are

deduced from the phase-space file by tallying all the photons falling in each energy bin. The quantity of ‘probability/keV’ refers to the fraction of photons in each keV width energy bin that reach the detector per 0.1 keV bin. The photon energy spectra through/from the thin 0.5 mm thickness masks are shown in figure 7.2.

The spectra show several characteristic features linked to mask material properties. Drops in mask transmission at around 70 and 90 keV are caused by the tungsten and bismuth K absorption edges, and sharp peaks are caused by fluorescence generated within the masks. Although the absorption cross section of materials generally falls with increased photon energy, there are abrupt rises at absorption edges. A fluorescence photon is less energetic than the incident photon that produced it through electron excitation. When they lie closely either side of a strong absorption edge, then the lower energy fluorescent photon can be more penetrating than the higher energy incident photon that generated it. Further, if the application involves characterising the materials of a distant object through a small pinhole, then even signals generated strongly by that object could be obfuscated by weak fluorescence across a wide mask close to the detector, especially if the energy dispersive detector has poor spatial resolution. Photons caused by fluorescence are an important feature, as their existence means the ideal mask property should not just prevent incident photons being transmitted, but also that it should not generate secondary photons either.

For this study, the upper photon energy was set to 200 keV because this is approximately the practical ceiling of many current compact X-ray generators. If these masks were used for imaging photons with significantly higher energy, then there would be a large increase in transmission through the bulk of the mask and image contrast would decrease significantly. Contrast would be further reduced by increased fluorescence from the mask, and there would be a slight degradation in spatial resolution as pinhole edges impacted by photons obliquely would become particularly transparent.

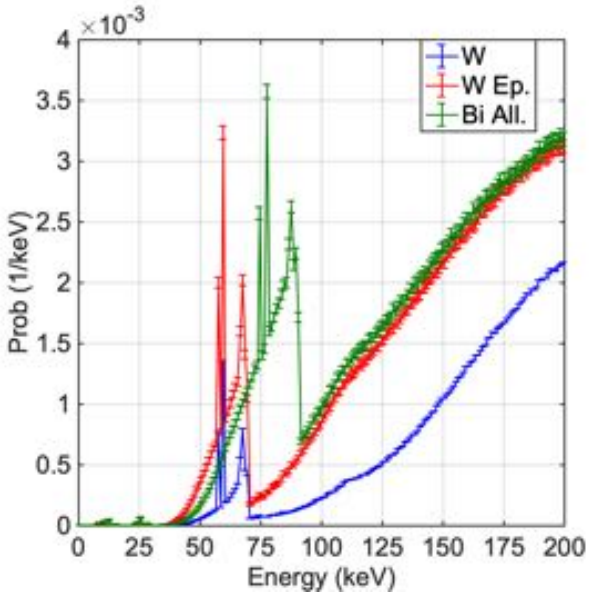

Figure 7.2 The photon energy-probability spectrum for 0.5 mm thickness masks for W, W Epoxy composite and Bi alloy masks without a pinhole [79]. Spectra were tallied at the detector (in orange in figure 1c), behind the pinhole mask (in purple in figure 1b-c) and shielded by a lead-aluminium cylinder (in green in figure 1b-c).

7.6 Preliminary study on mask materials transmission

Photon transmission through the material of the mask reduces the contrast and increases noise in images produced using pinhole or coded aperture optics [103] [104]. This section assesses the capacity of masks to prevent photons from the X-ray emitting wire reaching the detector [79]. The number of photons emitted from the wire was set to 10^7, to achieve acceptable statistics in a relatively short time. Although some of the following figures appear noisy, this is because they show the energy deposited into each pixel to expose our method. The calculations of image characteristics such as spatial resolution and contrast are deduced from many pixels, which makes the statistics acceptable.

Masks of 1-6 mm thickness and materials as indicated in table 7.1 were simulated. The X-rays pass through the mask and are collected at the detector. The position they impact the detector, their energies and their direction are all recorded in a phase-space file (psf-impdet-01.dat), and the energy-probability

spectra in the spectrum at the impact detector file (spc-impdet-01.dat). The transmission function is the energy dependent ratio of the photon intensity at the detector (beyond the mask disc) to the photon intensity incident upon the mask, according to the formula:

$$T_E(\%) = \frac{I_E}{I_{\mathrm{E}_0}} = \frac{Energy \times Probability\ (detector)}{Energy \times Probabilty\ (source)}$$

The transmission function has been plotted in figures 7.3 for selected thicknesses.

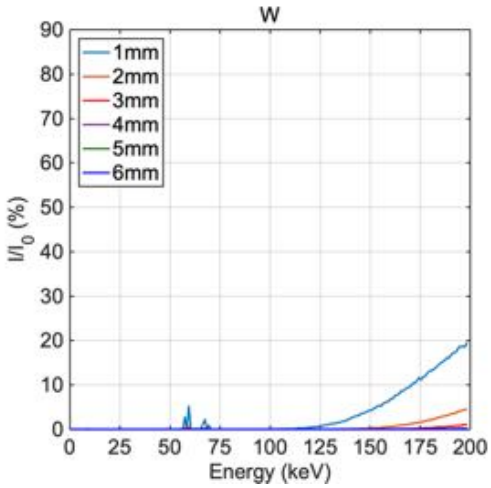
W
1mm
2mm
3mm
4mm
5mm
6mm
I/I0 (%)
Energy (keV)

(a)

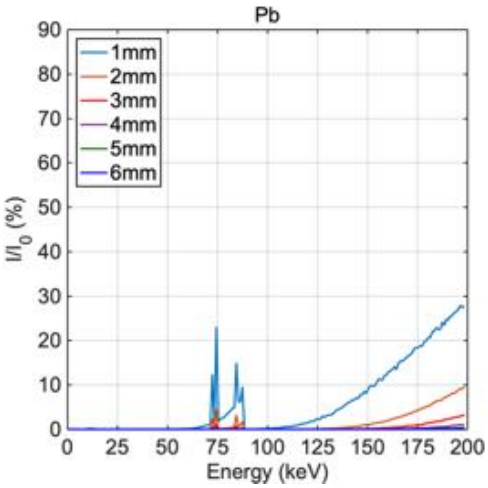
Pb
1mm
2mm
3mm
4mm
5mm
6mm
I/I0 (%)
Energy (keV)

(b)

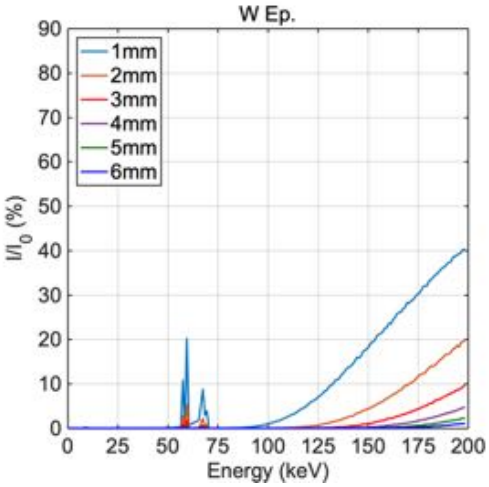
W Ep.
1mm
2mm
3mm
4mm
5mm
6mm
I/I0 (%)
Energy (keV)

(b)

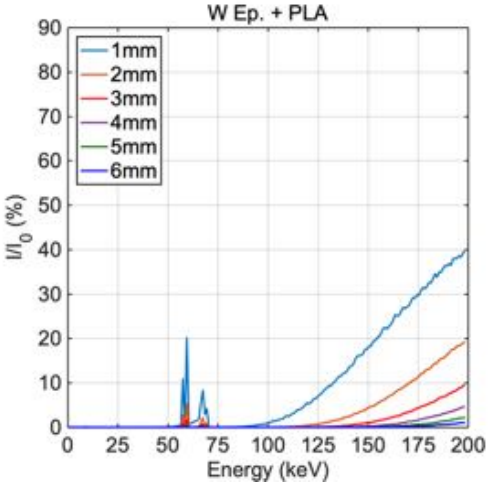
W Ep. + PLA
1mm
2mm
3mm
4mm
5mm
6mm
I/I0 (%)
Energy (keV)

(d)

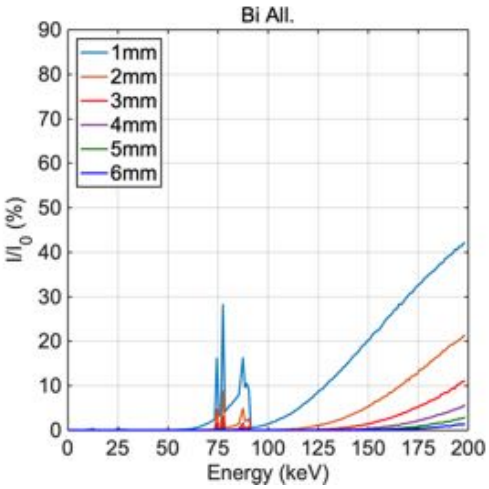
Bi All.
1mm
2mm
3mm
4mm
5mm
6mm
I/I0 (%)
Energy (keV)

(e)

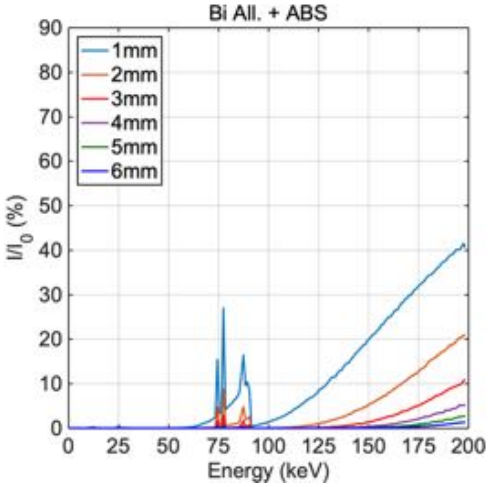
Bi All. + ABS
1mm
2mm
3mm
4mm
5mm
6mm
I/I0 (%)
Energy (keV)

(f)

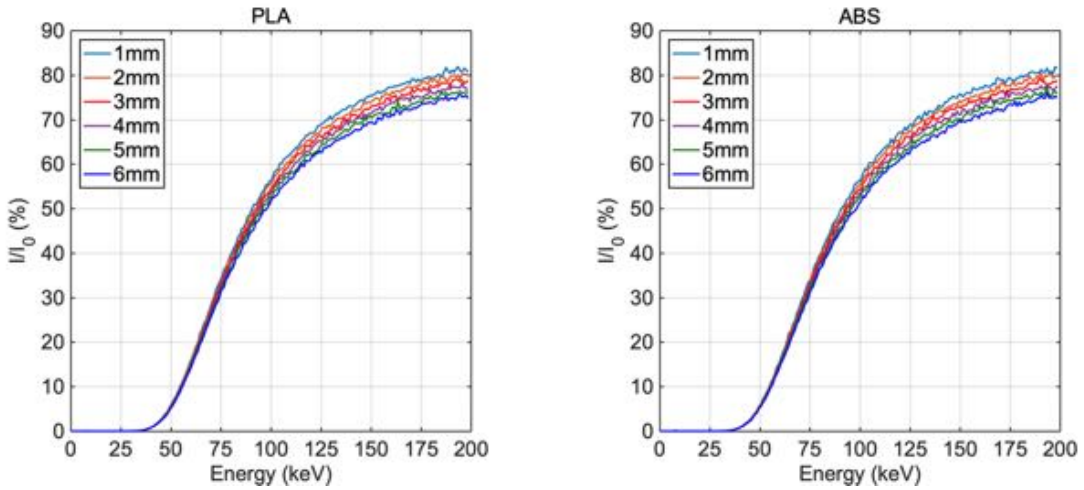

Figure 7.3 Transmission of X-rays through masks of material-thickness (1-6 mm) of (a) solid tungsten, (b) lead, (c) tungsten epoxy resin, (d) tungsten epoxy on a 1 mm layer of PLA, (e) bismuth low-melting alloy, (f) bismuth low-melting alloy on a layer of 1 mm ABS, (g) PLA and (h) ABS.

These fluorescent photons originate from all points on the mask and also travel in a range of directions that cannot be linked to the source in this case, or more importantly an object being imaged. These fluorescent photons thus represent a measure of noise in the system, and their production must be balanced against the ability of a pinhole or coded aperture optics to allow the signal through to be imaged above noise.

The spectra in figure 7.2 show several characteristic features caused by mask materials. These include sharp drops in transmission at around 70 and 90 keV caused by the tungsten and bismuth K absorption edges, and several groups of sharp peaks caused by fluorescence of mask materials outlined below

- At ~58 keV – the tungsten Kα2 (57.54 keV) and Kα1 (59.54 keV) lines

- At ~67 keV – the tungsten Kβ1 (67.53 keV) and the Kβ2 (69.53 keV) lines
- At ~74 keV – the bismuth Kα2 (74.53 keV) and Kα1 (77.53 keV) lines
- At ~87 keV – the bismuth Kβ1 (87.53 keV) and the Kβ2 (89.53 keV) lines
- At ~87 keV – the bismuth Kβ2 (74.8 keV) and Kβ1 (77.1 keV) lines
- At ~72 keV – the lead Kα2 (72.53 keV) and Kα1 (74.53 keV) lines
- At ~72 keV – the lead Kβ2 (84.53 keV) and Kβ1 (87.53 keV) lines

In parallel, another theoretical investigation was conducted to choose the best thicknesses, materials and aperture size for manufacturing the masks based on the NIST XCOM database [105].

The selected range was between 1mm and 6mm. This range was reasonable to find the right thickness to manufacture the masks. For most of the materials, at 1mm the mask is too thin, so that a strong transmission occurs and the characteristic X-rays coming from the masks would affect the final imaged object. No mask was thus manufactured with less than 2mm thickness and 2mm solid tungsten was chosen to be the model for its performance (fig. 7.3(a)). In order to find a material that was cheaper and easier to manufacture, 4mm tungsten epoxy on 1mm PLA (Polylactic Acid) and 4mm bismuth alloy on 1mm ABS (Acrylonitrile butadiene styrene) were simulated. For both combinations, 4mm thickness would have very similar transmission properties to 2mm of solid tungsten, where less than 5% transmission can be seen in figures 7.3 (c)(d) (e)(f). Tungsten, tungsten epoxy and bismuth alloy with and without baking transmission spectra at the suitable thicknesses are summarised and compared in figure 7.4.

Figures 7.4 in orange and violet show 4mm tungsten epoxy mixture and bismuth alloy without any backing both still give transmission less than approximately 5%. However, experimental work has shown the casting of bismuth alloy to be impractical in the presence of other options [42].

Table 7.2 shows the transmission of X-rays detected at 170 keV for practical thicknesses of mask for various mask materials. 170 keV is marginally above the

upper energy of what could be generated on our VJT X-ray source (chapter 6). For the tungsten / epoxy the simulation gives 1.4% transmission whilst the experimentally determined transmission for a mask cast in air was 7%. The difference arises because air bubbles are included in the tungsten powder / epoxy mixture whilst the PENELOPE objects are homogeneous and exclude air [106].

Transmission has been measured for tungsten epoxy at 170 keV and it is equal to 7%. This result is far from the simulated transmission (1.35%). The reason of this different result may be due to the difference between the simulated and the real material: the first is homogeneous; while the second consists of tungsten grains supported in epoxy resin and may include bubbles due to the casting method (in air) [42].

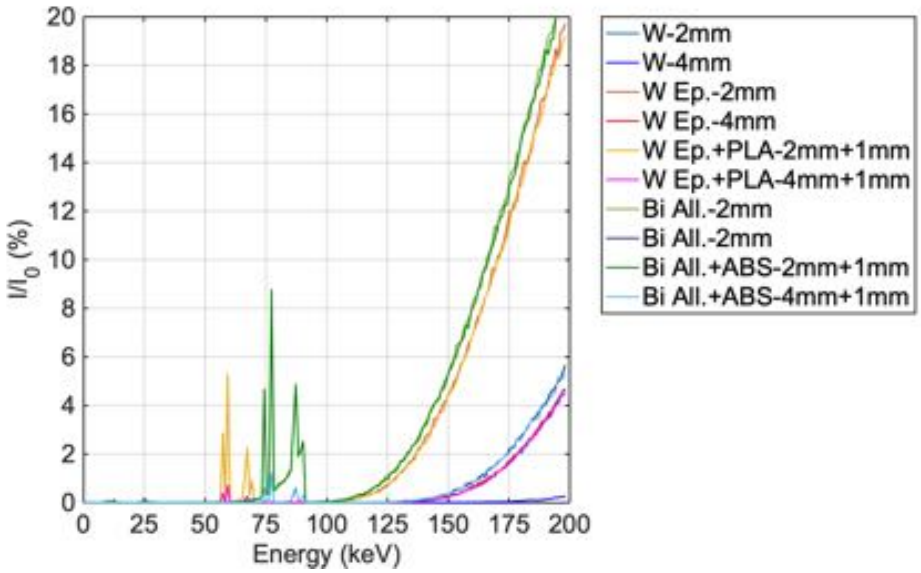

Figure 7.4 Transmission of X-rays through masks of material-thickness combinations suitable for use with small pinholes.

Table 7.1 Chemical composition in %wt and density of range of materials suitable for pinhole/CA masks [42].

Materials	**Composition (%wt)**	**Density (g cm^{-3})**
Tungsten metal	W 100	19.6
Lead metal	Pb 100	11.4
Tungsten-epoxy composite	W 93.5 Epoxy A 5.4 Epoxy B 1.1	9.6
PLA (Polylactic Acid)	C 50 H 5.6 O 44.4	1.24
Bi Alloy	Bi 70.3 Sn 18.2 In 11.5	8.26
ABS (Acrylonitrile butadiene styrene)	C 85 H 8 O 7	1.05

Table 7.2 Transmission of X-rays detected at 170 keV for practical mask thicknesses. The materials and thicknesses identified as suitable for manufacturing are those with * in the table.

MATERIAL	THICKNESS (mm)	TRANSMISSION (%)
W*	2	1.26
W	4	0.03
W Alloy	2	2.43
W Alloy	4	0.08
W Epoxy	4	1.35
W Epoxy + PLA*	4 + 1	1.07
Bi Alloy	4	1.66
Bi Alloy + ABS*	4 + 1	1.52
Pb	2	3.75
Pb	4	0.17

7.7 Modelling pinhole masks

Pinhole masks of different material thicknesses were modelled in PENGEOM and included in a separate geometry file which was included in the detector geometry file. Separating the geometry file from the detector guaranties versatility and flexibility to organise the different pieces of the overall geometries. PENGEOM offers the capability to include different geometry files into a main one, which is declared in the input file and read by the main program PENMAIN during simulations. When simulating the pinhole mask separately from the detector, we are practically ready to interchange the different set of masks (including CAs masks).

The model of the pinhole mask is relatively simple. It consists in a solid disk with a hole in the centre. In this work, the pinhole hole was filled with air or with plastic materials, such as PLA and ABS at convenience.

In PENELOPE, the disk volume is declared with three surfaces, two of them for determining the material thickness and one for the diameter. A separate surface is declared for the hole diameter. In the pilot model of the imaging camera in 7.2.1 for studying the image quality metrics, the central hole was filled with air, while the upgraded camera pinhole masks were made of materials filled with air (pure tungsten mask), PLA (tungsten epoxy mask) or ABS (bismuth low-melting alloy).

The pinhole masks used in the X-ray optics were made of pure tungsten and tungsten-epoxy composite, with the chemical composition in %wt and density as shown on table 7.1. The pinhole masks were 1-2-3 mm aperture diameter and 0.5 to 10 mm thick.

7.8 Adapting the phase-space file to replicate an imaging plate.

The phase space file (PSF) contains the energy and position data of each photon hitting the detector (see chapter 5). This file can be represented as a three-dimensional energy-scatter plot, (e.g. figure 7.5(a)). However, this does not inherently replicate images in the same way as sensors capture images, as sensors measure deposited energy over a time period within digitised spatial regions instead of the precise position [79]. For the phase-space file to be

presented as an image, the raw data needs to be processed in a similar way to how the detector actually works; i.e. by integrating the energies of all photons hitting each particular pixel over some exposure period. The integrated energy I(E) seen is defined as the sum of the energy of the photon data in the phase space file correlated with the positions and areas. In the simulated X-ray optics, the number of pixels was set equal to 1040 x 1392 as the real detector. A MATLAB routine was written to integrate and map. Maps were constructed and show how the integrated energy varies at x-y positions across the surface of the detector (see figure 7.5(b)). The images in figure 7.5 are based on a 4 mm thick tungsten plate with 2 mm pinhole equidistant from the test object and detector to give a magnification equal to 1 [106].

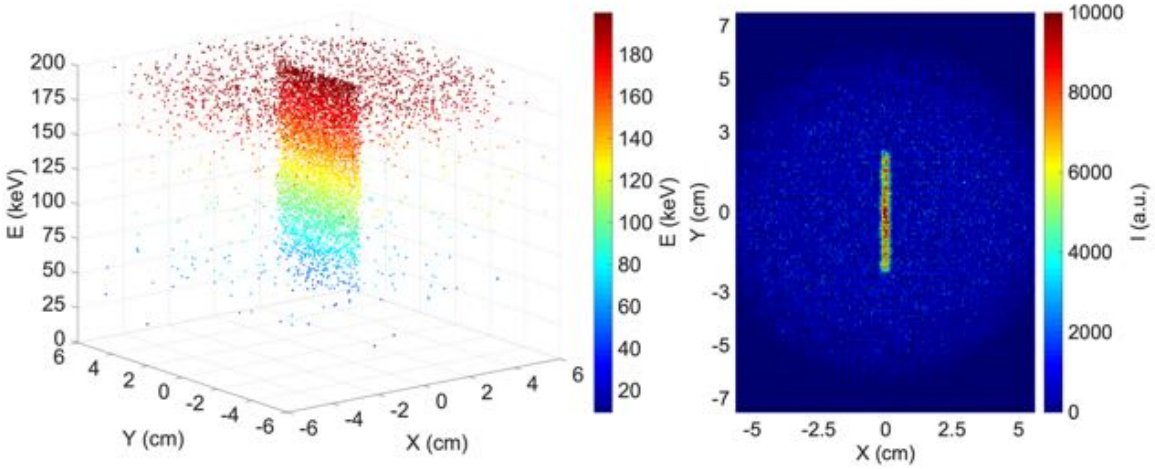

(a) (b)

Figure 7.5 (a) is a scatter plot of the energy of each photon incident on the detector for a 4 mm thickness W mask with a 2 mm diameter aperture (colour scale energy in keV). Fig (b) shows the same integrated energy per pixel presented in 2D to reflect the brightness of an image.

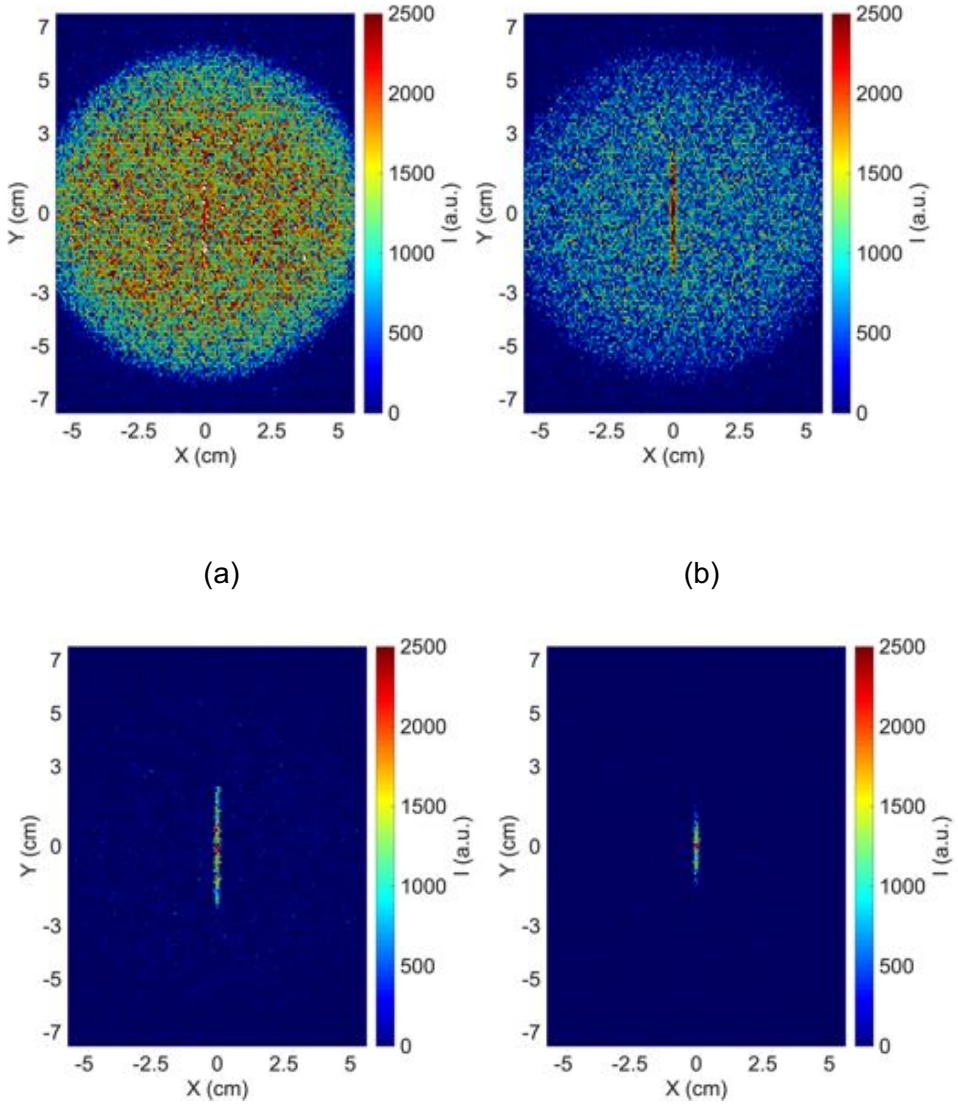

Figure 7.6 Image of 0-200 keV photons through pure tungsten for a 1 mm aperture diameter and (a) 1 mm thickness, (b) 2 mm thickness, (c) 4 mm thickness and (d) 10 mm thickness. At 10 mm thickness, only the central area of the ROI is detected, and the detected wire appears cropped.

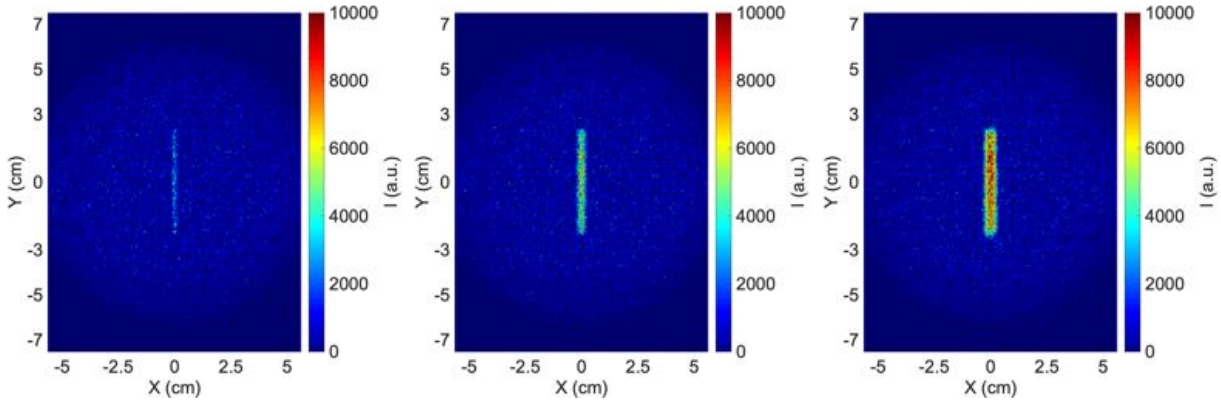

Figure 7.7 (a) Image of 0-200 keV photons through pure tungsten for a 2 mm thickness and (a) 1 mm aperture diameter, (b) 2 mm aperture diameter, (c) 3 mm aperture diameter. Note large apertures (c) admit more photons than small ones (a, b).

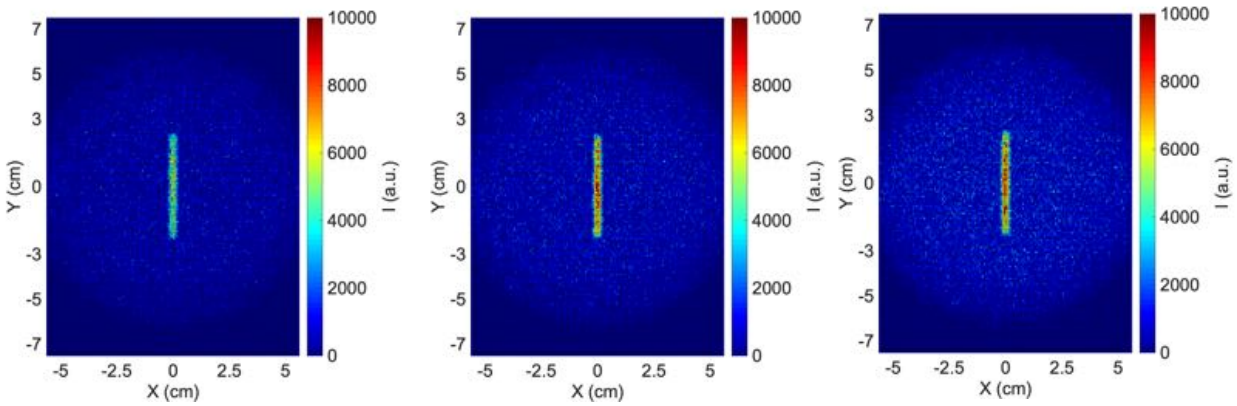

Figure 7.8 Image of 0-200 keV photons through a) pure tungsten for thickness 2 mm, b) W Epoxy for thickness 4 mm, and c) Bi alloy for thickness 4 mm.

7.9 Determining the ROI

The geometry of the simulation was set to give an image size equal to the 46 mm 0.3 mm test object. The object image should ideally fully occupy and be confined to the pixels that correspond to the source dimensions as the magnification is equal to unity. However finite resolution broadens the image beyond these confines. The limits of the Region Of Interest (ROI) were thus set $-23 \leq y \leq 23$ mm and $-2 \leq x \leq 2$ mm for the smallest aperture, but the horizontal x-axis ROI parameters were raised for larger apertures to ensure image broadening was accommodated. These limits were set on MATLAB for extraction of the ROI against the image background. Once ROI is determined, the background noise was estimated as the whole image integrated energy minus the ROI. An example of the applied method is shown in figure 7: a) is the whole image, b) is the identified ROI and c) is the background noise [79].

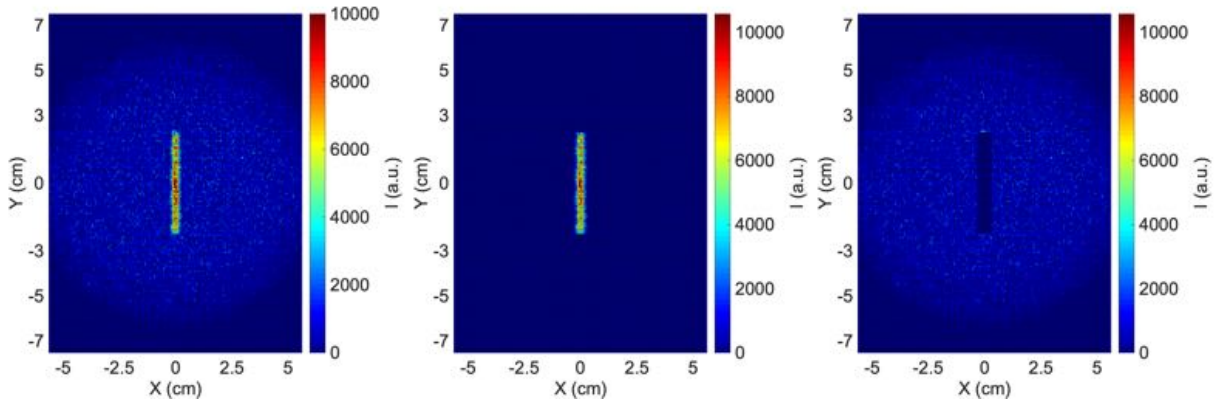

(a) (b) (c)

Figure 7.9 Image obtained from test wire using a 2 mm aperture in 2 mm W epoxy. (a) represents the whole image, (b) just the area closely surrounding where the test object signal should geometrically lie, (c) the background region only.

7.10 Imaging quality metrics

7.10.1 Spatial resolution

Spatial resolution is a metric to quantify the ability of an imaging system to distinguish between two unique objects closely separated in space.

The resolution of an experimental system can usually be defined by a Gaussian profile that is characterised by its full-width at half maximum (FWHM).

$$\mathrm{FWHM} = 2.355 \cdot \sigma \qquad 7.1$$

An example image of the test object can be seen in Fig 7.10(a). Spatial resolution FWHM is determined as the sum of the integrated energy along the x-axis, while the sum of the integrated energy down the y direction columns is used to maximise counting statistics. The column sum as a function of x is shown in Fig 7.10(b), where a Gaussian fit is applied to determine the FWHM. The graphs on figures 7.11 and 7.12 show how the FWHM varies with aperture diameter and mask thickness.

7.10.2 Spatial resolution as function of aperture diameter and thickness

Generally, the resolution improves (i.e. FWHM reduces) with reducing pinhole diameter. Pinhole masks were also simulated at narrower apertures, such as 0.1 mm and 0.5 mm, and wider apertures such as 6 mm and 10 mm. The effect of the resolution as FWHM against the aperture diameter can be seen in figure 7.12. As the FWHM decreases, the resolution increases. However, due to the pixel size limitation, there is a plateau between 0.1 mm and 1 mm aperture diameter for all the three materials.

On the other hand, the resolution reduces slightly with increasing mask thickness for the same aperture diameter. This is because thin masks allow large numbers of X-rays to be transmitted through the aperture edges obliquely which effectively increases the diameter of the aperture, whilst thick masks only allow X-rays that hit the mask aperture perpendicularly to pass (collimation). In figure 7.13, pure

tungsten, tungsten-epoxy and bismuth alloy FWHMs were compared against the thickness. For the thin mask thicknesses tested here the same spatial resolution achieved by tungsten-epoxy and bismuth alloy can be achieved by half the thickness of pure tungsten because of its low transmission.

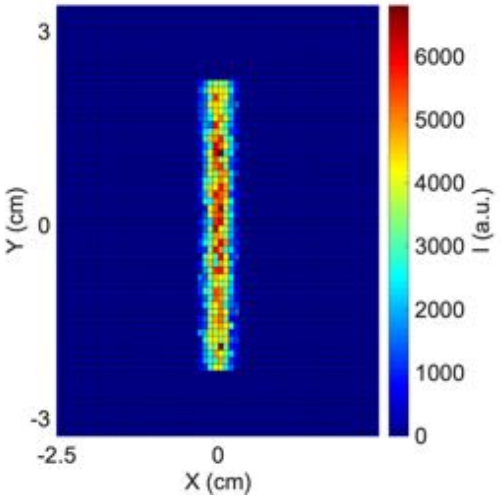

(a)

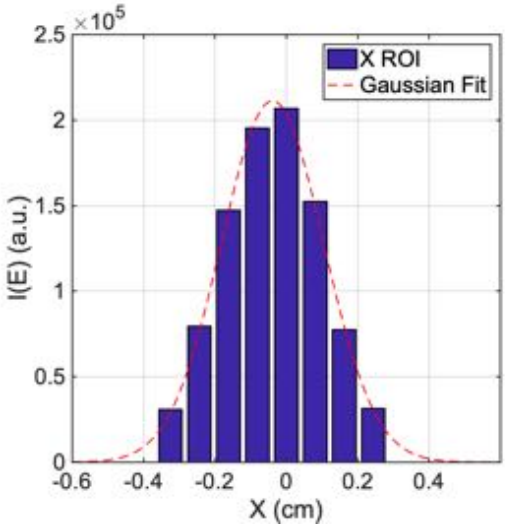

(b)

Figure 7.10 Image of the test object for a 2 mm thick 2 mm aperture tungsten pinhole mask (a) and the summed y-column pixels across the thin x-axis (maximum uncertainty $\pm 0.87 \cdot 10^3$) (b). A Gaussian fit has been plotted on the histogram to calculate the FWHM (red line).

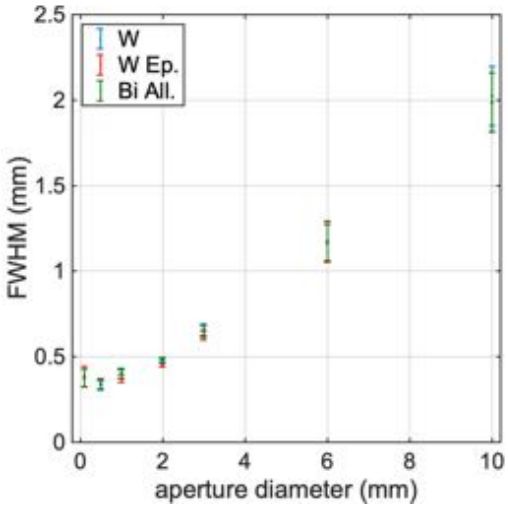

Figure 7.11 The image spatial resolution available for pinhole masks of different apertures and materials and 2 mm thickness pure tungsten and 4 mm thickness tungsten-epoxy resin and bismuth alloy.

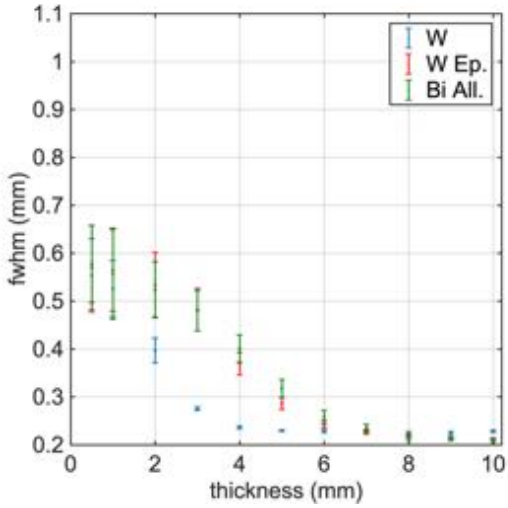

(a)

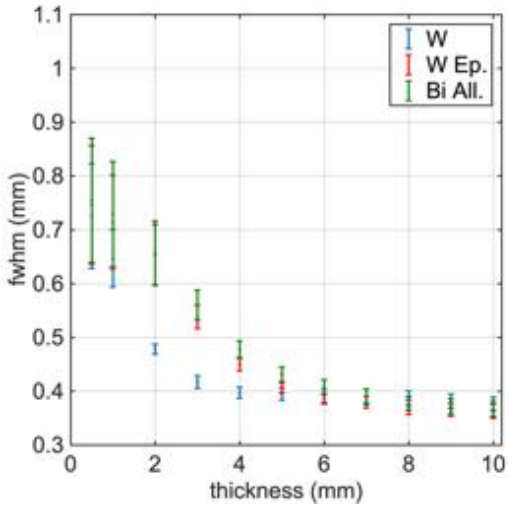

(b)

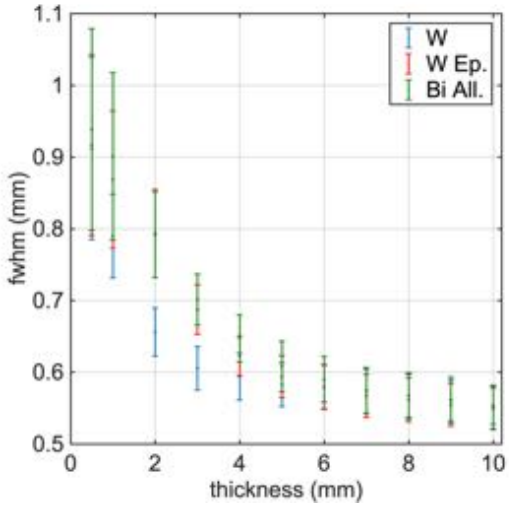

(c)

Figure 7.12 Image spatial resolution available for pinhole masks of 1 mm, 2 mm and 3 mm apertures, 0.5 – 10 mm thicknesses for W, W epoxy, Bi alloy.

7.10.3 Estimating the Field of View and Collimation effects

An ideal pinhole mask would transmit photons through a single locus from across 4π steradians. In practice, as the mask thickness increases the acceptance angle and the field of view decrease. Simple pinhole images would thus appear cropped at their edges. This effect is shown in figure 7.6. Figure 7.13 is the image of the wire at 2 mm (a) and 10 mm (b) thickness at the same aperture diameter (2 mm) and material (pure tungsten). Images taken with coded apertures would exhibit partial coding and produce artefacts, even if the nominal field of view (FOV) were achieved.

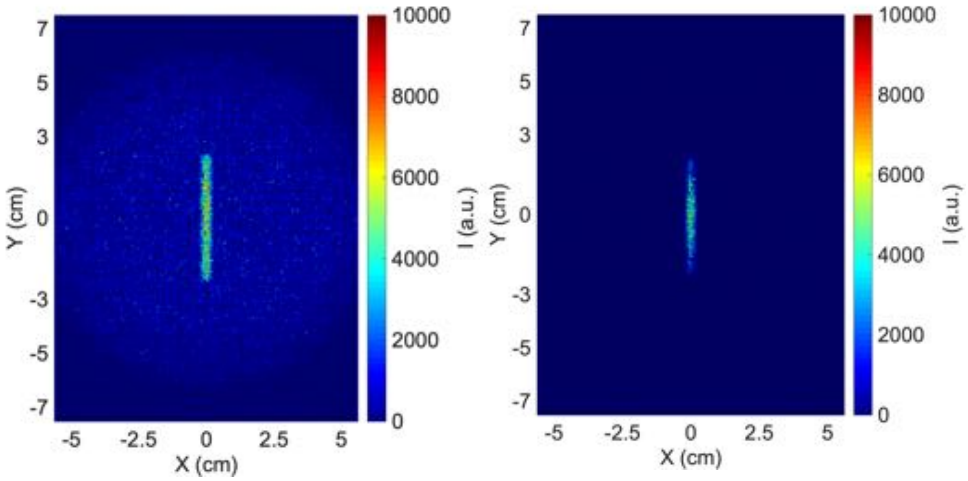

(a) (b)

Figure 7.13 Image of 200 keV photons through pure W for thickness (a) 2 mm and (b) 10 mm. (b) shows how the effect of the collimation occurs when the mask is thick. The wire is not fully resolved, and edges appear cropped.

The wire test object was designed to be long specifically to evaluate the FOV and collimation effect. Figure 7.13(b) shows that the wire's image is not cropped abruptly, instead the signal weakens near the ends. A Gaussian fit along the y-axis of the wire's image was used as a simple reproducible measure of its apparent length. Figure 7.14 shows the collimation effect via the apparent length of the 46 mm test object, as a function of mask material and thickness. Figure

7.15 shows the effect as function of aperture size, but as the image plate is 166 mm from the pinhole then FOV can be expressed in terms of Angle of View (AOV) for general use in other applications. For thin masks with wide apertures the Gaussian fit can extend a little beyond the true length of the wire because of degraded spatial resolution. The collimation effect is observed most strongly for thick pure tungsten masks with narrow apertures. The FOV for small apertures is more sensitive to changes in mask thickness than for large apertures, and similarly the AOV for thick masks is more sensitive to changes in aperture than for thin masks. The data presented is based on a test object centred in the field of view; the consequences could be more extreme for objects which are offset from the centre axis of a pinhole. Only one of the many apertures from a coded aperture can be at the centre so evaluating the consequences of partial coding caused by collimation would not be trivial.

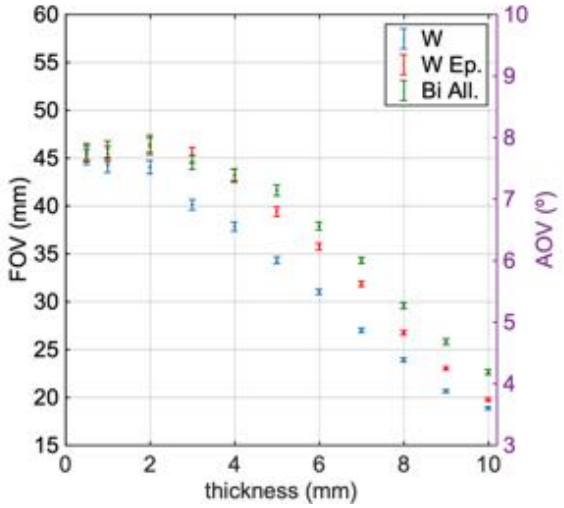

(a)

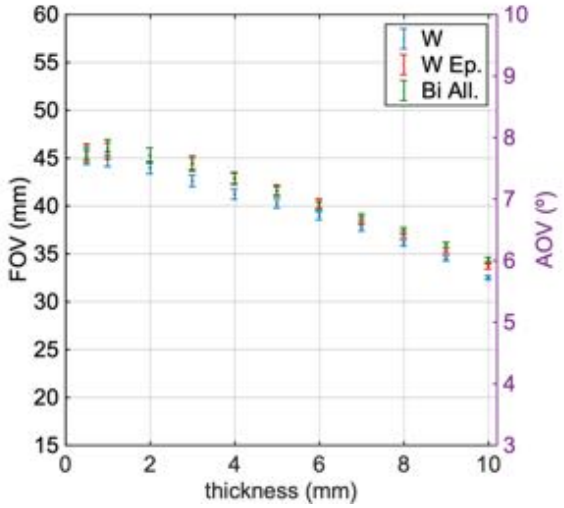

(b)

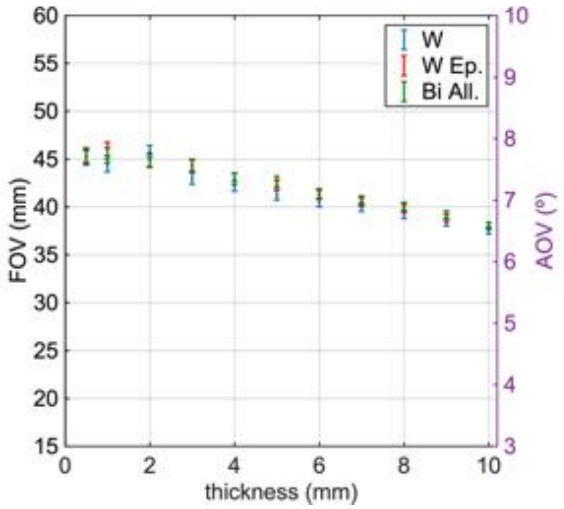

(c)

Figure 7.14 The Field of view in terms of the apparent length (left axis) of a 46 mm test object as a function of pinhole mask thickness at 1 mm (a), 2 mm (b) and 3 mm (c) aperture diameters.

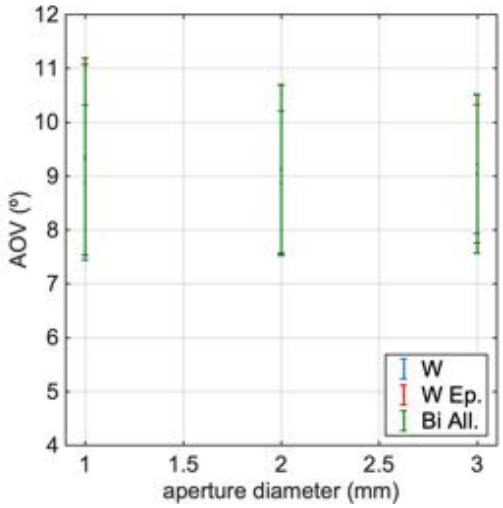
12
11
10
9
8
7
6
5
4
AOV (°)
1
1.5
2
2.5
3
aperture diameter (mm)
W
W Ep.
Bi All.

(a)

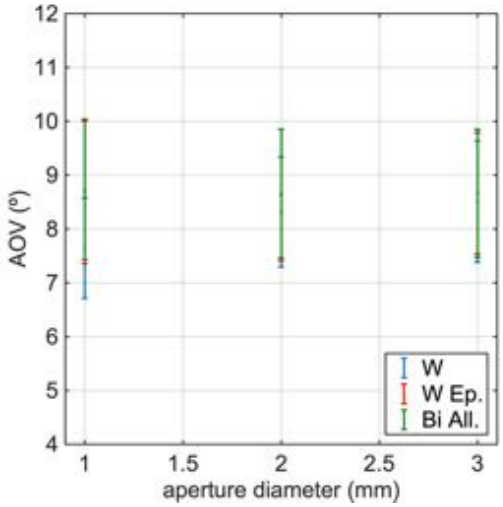
12
11
10
9
8
7
6
5
4
AOV (°)
1
1.5
2
2.5
3
aperture diameter (mm)
W
W Ep.
Bi All.

(b)

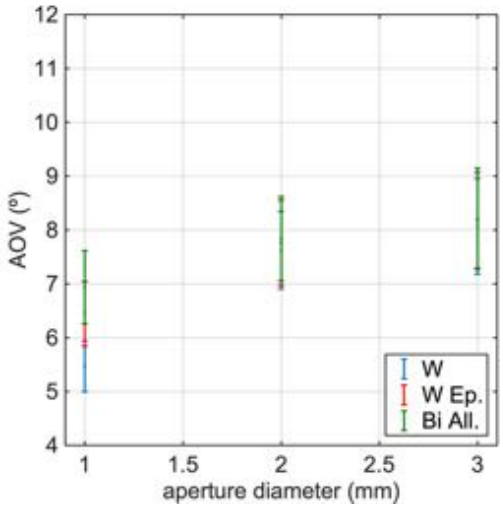

(c)

Figure 7.15 The Field of View in terms of angle as a function of pinhole mask aperture diameter for 2 mm (a), 4 mm (b) and 7 mm (c) thicknesses.

7.10.4 Contrast

Contrast is typically defined as the ratio of the signal difference to the average signal [107]. In imaging, we define the Michelson contrast or modulated contrast as

$$CNR = \frac{f_f - f_b}{f_f + f_b} \leq 1 \qquad 7.2$$

where f_f and f_b represent the total signal and the background, respectively. The Michelson contrast is commonly used in cases where small features are present on a large uniform background and cannot be more than 1. Michelson contrast is acceptable whereas its value is more than 0.1 [108]. In our case, we have applied this definition by considering the parameters f_f as the average of the integrated energy of the ROI (figure 7.9(b)), and f_b as the average of the background (figure 7.9(c)).

For each thickness contrast was calculated at 1, 2 and 3 mm apertures, and plotted in a graph to compare the behaviour of the masks. The following graphs (figure 7.16) show how the contrast varies with mask thickness and aperture.

Generally, at all the apertures, pure tungsten appears the best in terms of contrast, while tungsten epoxy and bismuth alloy have lower contrast performances. However, at the thinnest thicknesses (0.5 and 1mm), all the three materials contrast is below 0.1, which means the ROI integrated energy is not high enough to be distinguished from the background. This occurs also at the narrowest aperture (1 mm) and 2 mm thickness for all the materials. When the thickness increases, pure tungsten contrast arises (0.2), whilst tungsten epoxy and bismuth alloy contrast is below 0.1. Pure tungsten contrast keeps growing up to 6mm thickness at all the apertures, then it becomes constant. However, at the narrowest aperture (1 mm), the maximum value for pure tungsten is 0.7, while at 2 and 3mm apertures it stays around 0.9. Tungsten epoxy and bismuth alloy have similar contrast at all the thicknesses and apertures. Nevertheless, contrast is above 0.1 at 4mm thickness and 2mm aperture. At the most extreme conditions, all the materials have the highest contrast, as the background is quite low or almost zero. Although its highest value, contrast at such a high thickness cannot be considered as a possible working condition, as it could cause side effects, such as partial coding or collimation effect.

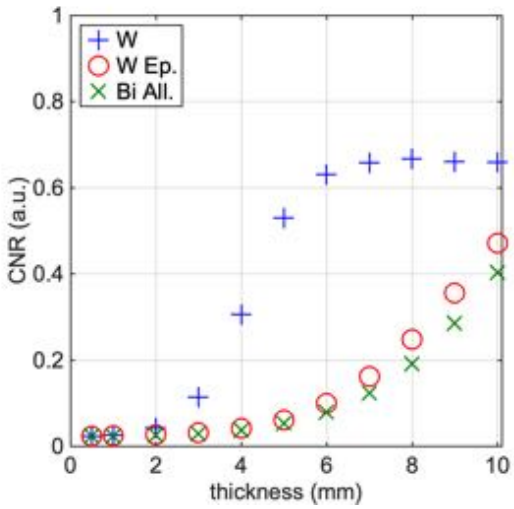

(a)

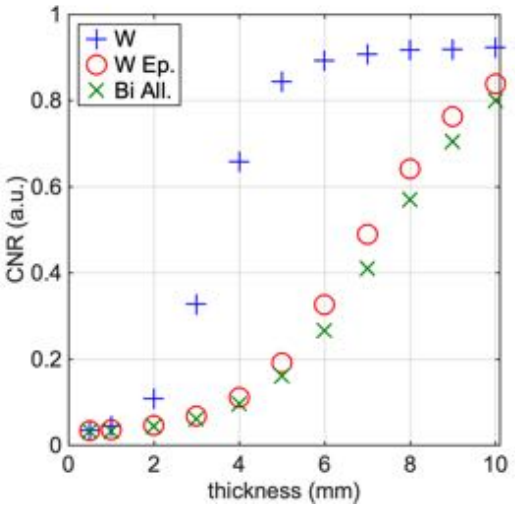

(b)

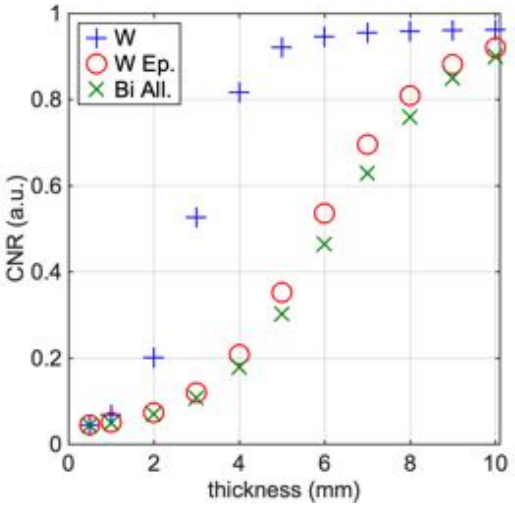

(c)

Figure 7.16 Contrast for a 1 mm (A), 2 mm (B) and 3 mm (C) diameter aperture.

7.10.5 Signal-to-noise ratio

The ability to detect an object and distinguish it from background is called signal to noise ratio (SNR). Generally, the SNR is defined by the Rose Criterion, which states that an object is distinguishable from the background noise if SNR ≥ 5 and it only occurs when the signal is always positive [109]. Practically it is defined as the ratio of the average of the signal to the standard deviation of the noise:

$$SNR = \frac{f_f}{\sigma_b} \geq 5 \qquad 7.3$$

In the case of study, the Rose Criterion was applied as the average of the ROI divided by the standard deviation of the background:

$$SNR = \frac{\langle x_M \rangle}{\sigma_b} \qquad 7.4$$

where $\langle x_M \rangle$ is the average value of the integrated energy in the image pixels obtained as the difference between the whole signal and the background and corresponding to the true location of the source (ROI), while σ_b is the standard deviation of the integrated energy of the background noise.

The graphs in figures 7.17 show the SNR at the simulated thicknesses and apertures. By the Rose criterion, as SNR must be at least equal to 5 for an image to be acceptable, we can see that for pure tungsten this occurs at 2 mm for a 1 mm pinhole diameter, while, according to the data, bismuth alloy starts working well at 4 mm thickness 2 mm aperture.

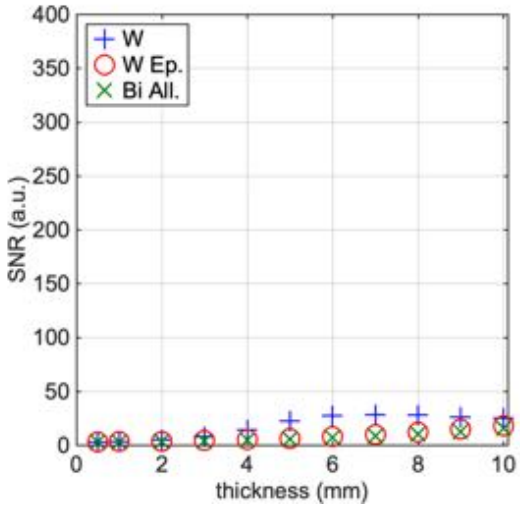

(a)

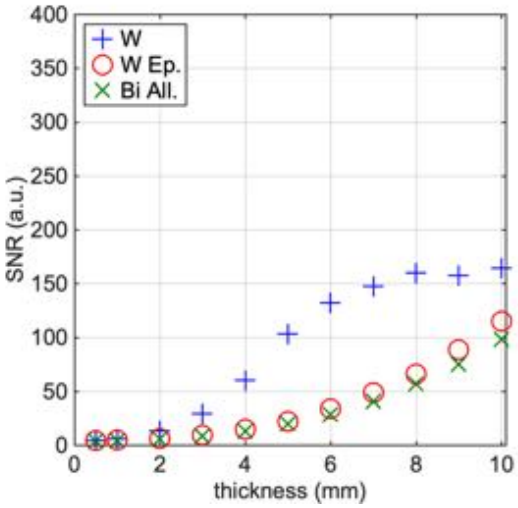

(b)

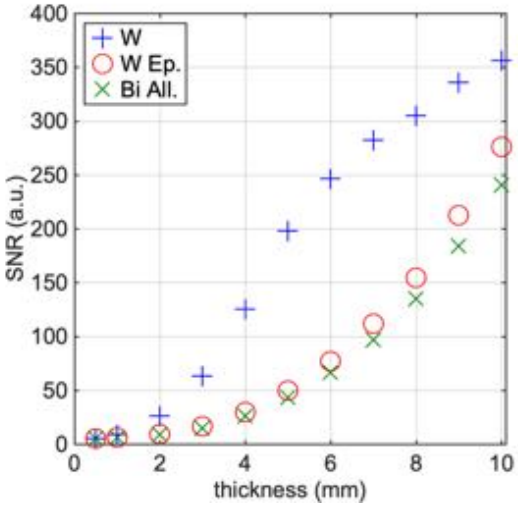

(c)

Figure 7.17 SNR for a 1 mm (A), 2 mm (B) and 3 mm (C) diameter aperture.

7.11 Finding the optimum thickness and aperture diameter of pinhole masks

This section aims to give advice on material thicknesses and aperture diameters suitable for manufacturing according to the previous data of SNR, CNR, spatial resolution, and AOV. We will explore the results of SNR, CNR, spatial resolution and AOV and combine them to find the optimum configuration. The selection criterium consists in defining the optimum configuration as the minimum combination thickness/aperture diameter by using the image quality metrics results.

In figures 7.18 and 7.20 are shown three-dimensional surface plots of contrast-object detail in mm (7.18) and as the more general angle of view (7.20). Signal-to-noise ratio and spatial resolution are correlated in figure 7.22. The three-dimensional plots correlate the different quantities calculated in previous sections with thicknesses, which are represented along y-axis, and aperture diameters, which vary as gradient of the surface.

In figures 7.19, 7.21 and 7.23 are shown the plots of the same data, with the points representing the thicknesses 0.5-10 mm. Boundaries were added as dashed black lines to show which combinations of thicknesses-aperture diameters should be acceptable. These limits are set according to eq. 7.1 for CNR, 7.2 for SNR and for the boundaries of the object size (46 mm) and equivalent angle of view (~8˚).

According to the PENELOPE model, solid tungsten at 2 mm thickness and 2 mm aperture was the best compromise of contrast, spatial resolution, and field of view. In figure 7.18 and 7.20, 2 mm 2 mm aperture diameter tungsten appears the minimum acceptable configuration. At 1 mm thickness and same aperture diameter, tungsten would be still acceptable, but the contrast would be too low, and the object would barely be distinguishable from the background. If the material was thicker, for example >5 mm, then at the same aperture diameter we would see only the central area of the wire, as the field of view would be limited, and the object would be cropped. For this reason, the results from modelling

suggest that mask thicknesses of 5 mm and thicker are not suitable for imaging close large objects with the resolution afforded by small pinholes. The 2 mm aperture 2 mm thickness is also confirmed to have acceptable SNR from figures 7.22-7.23. The equivalent of 2 mm tungsten performances is 4 mm thickness 2 mm aperture diameter of both tungsten-epoxy resin and bismuth low-melting alloy mask as minimum operational configurations. From figure 7.19, we can observe also 3 mm apertures of both masks would be suitable, but that would degrade the spatial resolution as the wire would appear less sharp, even though the SNR is relatively higher than the other two set of aperture diameters (see figure 7.23).

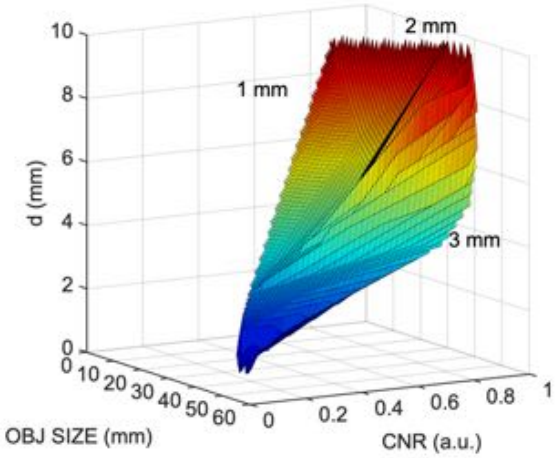

(a)

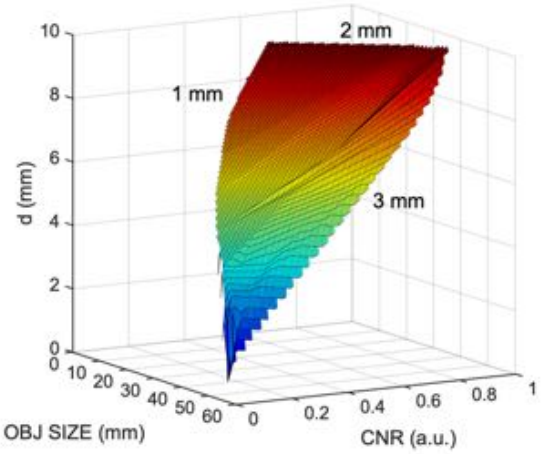

(b)

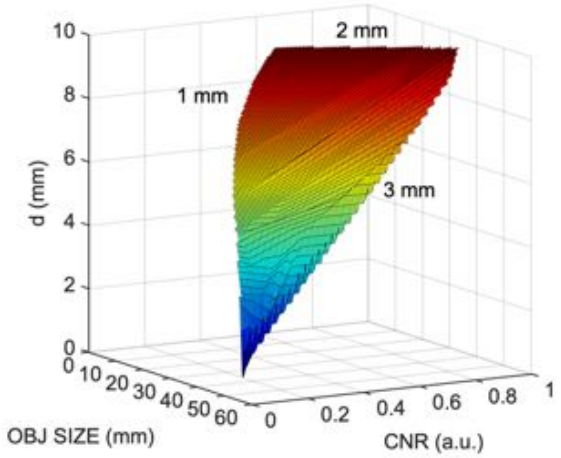

(c)

Figure 7.18 Contrast-object detail 3D surface plot of W (a), W Ep. (b), and Bi all. (c) at 0.5-10 mm thicknesses and 1-2-3 mm aperture diameters.

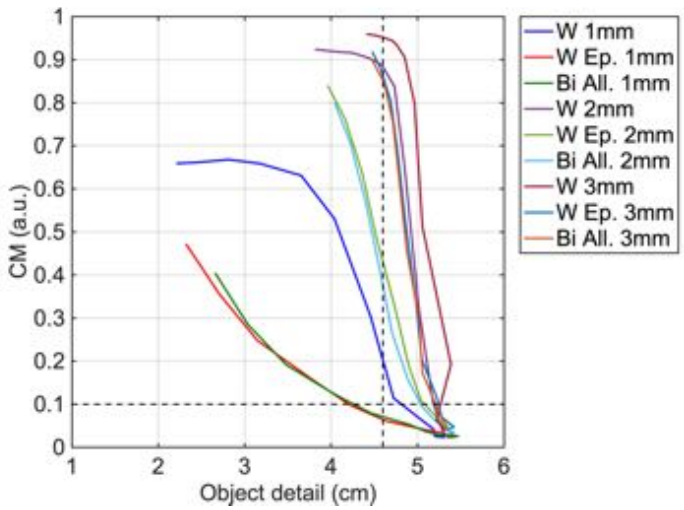

Figure 7.19 Contrast-object detail 2D plot as object size of W, W Ep., and Bi all. at 0.5-10 mm thicknesses and 1-2-3 mm aperture diameters.

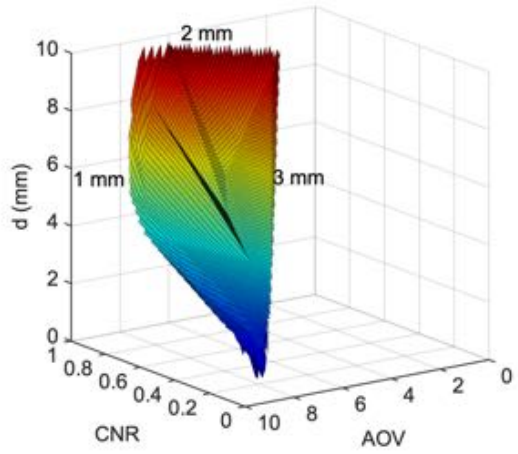
2 mm
1 mm
3 mm
d (mm)
10
8
6
4
2
0
1
0.8
0.6
0.4
0.2
0
CNR
10
8
6
4
2
0
AOV

(a)

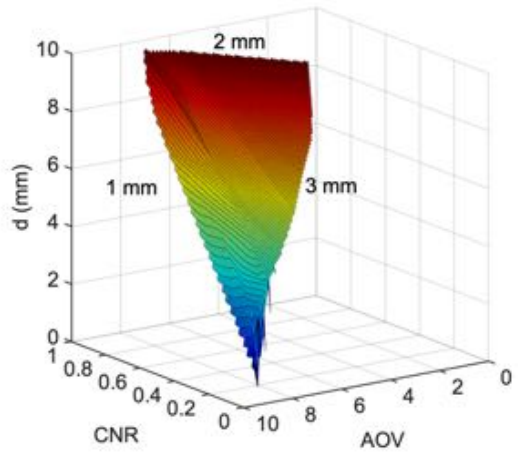
2 mm
1 mm
3 mm
d (mm)
10
8
6
4
2
0
1
0.8
0.6
0.4
0.2
0
CNR
10
8
6
4
2
0
AOV

(b)

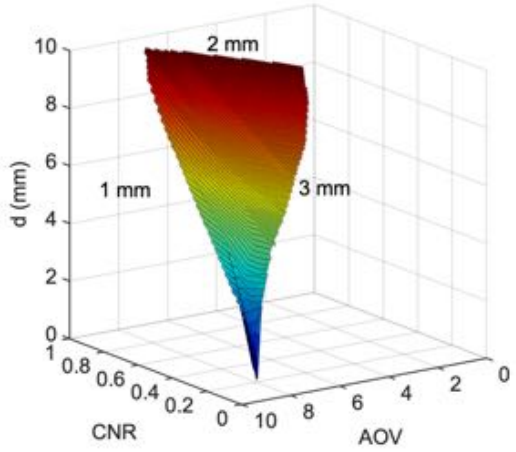

(c)

Figure 7.20 Contrast-angle of view 3D surface plot of W (a), W Ep. (b), and Bi all. (c) at 0.5-10 mm thicknesses and 1-2-3 mm aperture diameters.

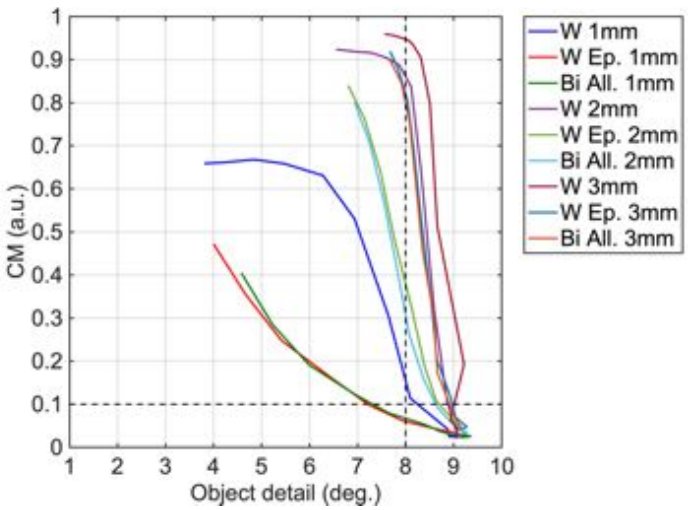

Figure 7.21 Contrast-object detail as angle of view 2D plot of W, W Ep., and Bi all. at 0.5-10 mm thicknesses and 1-2-3 mm aperture diameters.

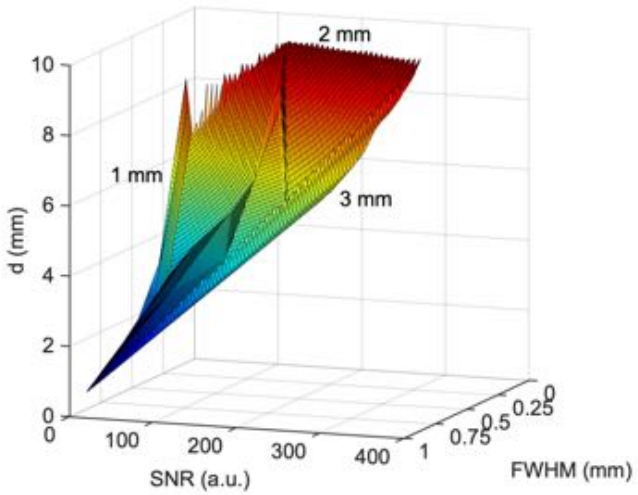

(a)

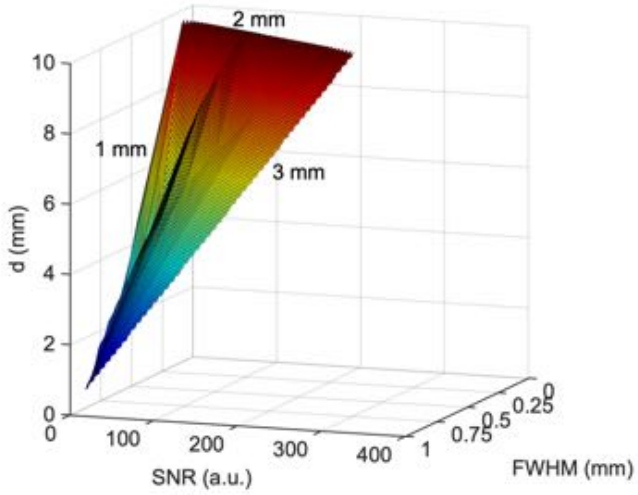

(b)

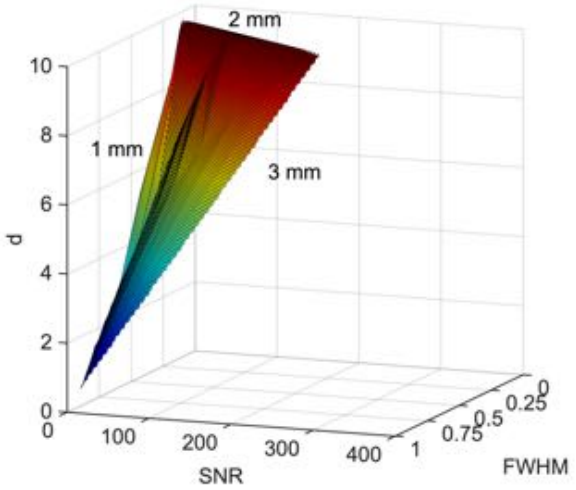

(c)

Figure 7.22 SNR-FWHM 3D surface plot of W (a), W Ep. (b), and Bi all. (c) at 0.5-10 mm thicknesses and 1-2-3 mm aperture diameters.

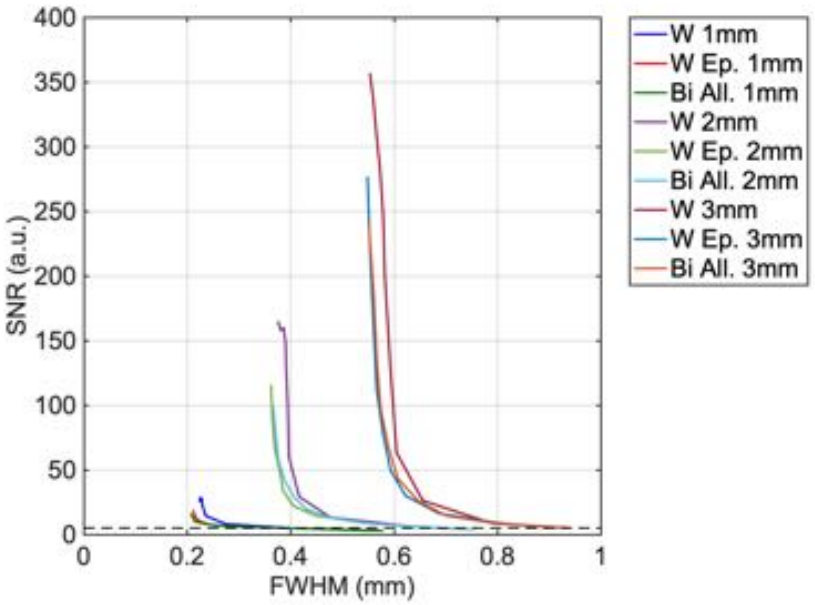

Figure 7.23 FWHM SNR 2D plot of W, W Ep., and Bi all. at 0.5-10 mm thicknesses and 1-2-3 mm aperture diameters.

7.12 X-ray camera model: updated model for pinhole and CA imaging

PENGEOM was used again for modelling the upgraded camera. The new experimental X-ray camera configurations are shown in figure 7.24(a) and sizes of the physical camera are in figure 7.23(b).

The imaging system was upgraded by replacing the aluminium extension and the rotation stage with a lead lined truncated cone, mounted on the front of the lead-lined cylinder. This cone supports the mask mount, and in turn, the mask itself. In PENGEOM, the front mount was replaced by the truncated cone in blue and the mask was simplified with a pinhole disk (figure 7.25), or with coded apertures (figures 7.26). As in 7.2.1, the Gemstar CCD camera is enclosed inside the cylinder. The whole systems were simulated in a space filled with air to make the simulation as close as possible to the real experiment.

The pinhole masks used in the upgraded X-ray optics were made of pure tungsten and tungsten-epoxy composite, with the chemical composition in %wt and density as shown on table 7.1.

The pure tungsten pinhole mask was 2 mm thick while the tungsten-epoxy mask was 4 mm thick. Both circular apertures were 2 mm in diameter. The two pinhole mask geometries are shown in figure 7.25.

(a)

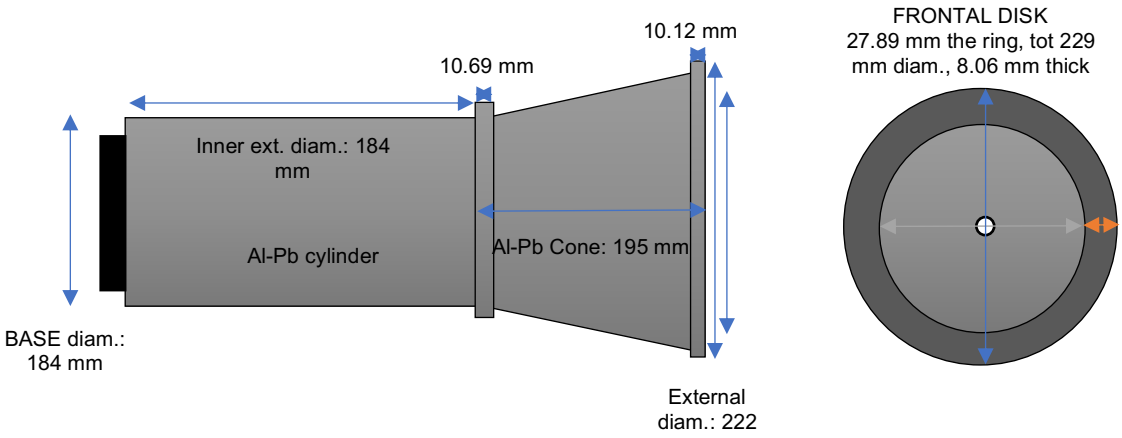

(b)

Figure 7.24 The upgraded (a) X-ray camera system setup. (b) Measurements of the X-ray camera.

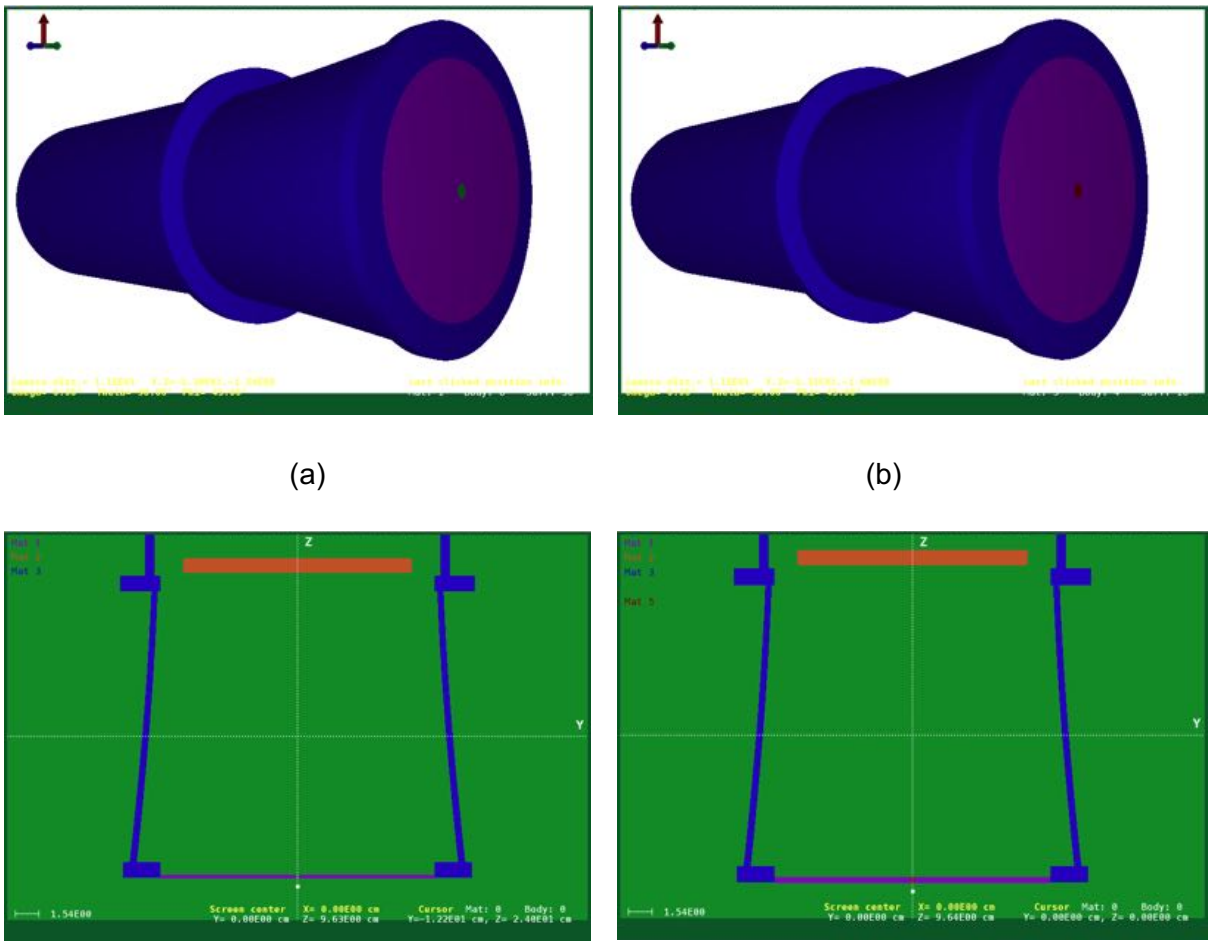

(a) (b)

(c) (d)

Figure 7.25 Three-dimensional representation of the X-ray camera with air filled 2mm thick pure tungsten pinhole mask (a) (top left) and 4mm thick tungsten-epoxy PLA filled aperture (b) (top right). Two-dimensional camera sections for pure tungsten (c) (bottom left) and tungsten-epoxy (d) (bottom right) mask. The CCD camera is in orange, enclosed in lead-lined shielding in blue while pinhole masks in purple. The X-ray detector is coloured orange and placed in a space filled with air (green).

7.12.1 Modelling Coded Aperture MURA and mosaicked MURA masks

The fundamental idea of coded apertures is to increase signal throughput by opening multiple small pinholes. Increasing the diameter of a single pinhole would clearly degrade resolution [103], but the effect on resolution of creating multiple apertures is not so obvious and forms part of this work. With multiple holes the

detector cannot produce an image directly, since each pinhole generates an image of the object at the detector and all projections overlap [89]. However, from the overlapped copies and knowledge of the pinhole locations one can retrieve an image of the object. Coded aperture masks introduce specific arrangements of the pinholes. Each point source is not revealed by a single bright spot, but rather by a pattern of spots. That means the mask is encoding the signal from the source. Due to encoding, the data are not immediately interpretable and need to be decoded.

Modelling coded apertures is not simple; it is necessary to know the exact position of each pinhole in the pattern and recognise whether there are symmetries and/or repetitions, and it requires high precision. Some of the masks used for experimental work were replicated in PENGEOM. An example of the detector model with CA in front is shown in figure 7.26.

The modelled masks configurations and materials are included in table 7.3 and mask models are shown in figure 7.27. The following subsections will illustrate the method for designing the different CA masks.

Table 7.3 CAs modelled in PENGEOM, material and thicknesses.

CA	Material	Thickness
19 x19 MURA	W epoxy + PLA	4 mm + 1 mm
19 x 19 MURA NTHT	Drilled W	2 mm
17 x 21 Singer Set	W epoxy + PLA	4 mm + 1 mm
17 x 21 Singer Set NTHT	Drilled W	2 mm

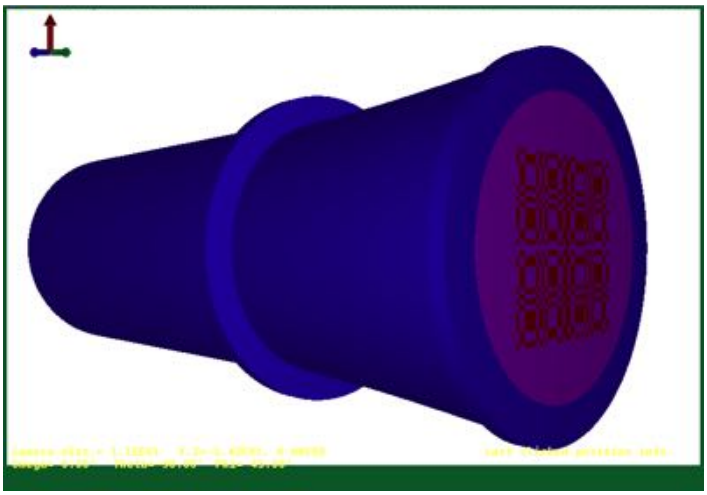

Figure 7.26 X-ray camera with 19x19 mosaicked MURA 2 mm aperture diameter (b) (in front in 3D.

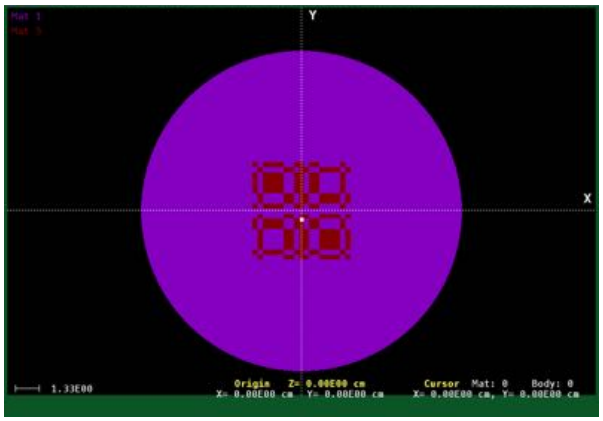

(a)

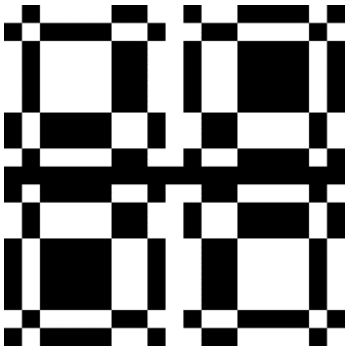

(b)

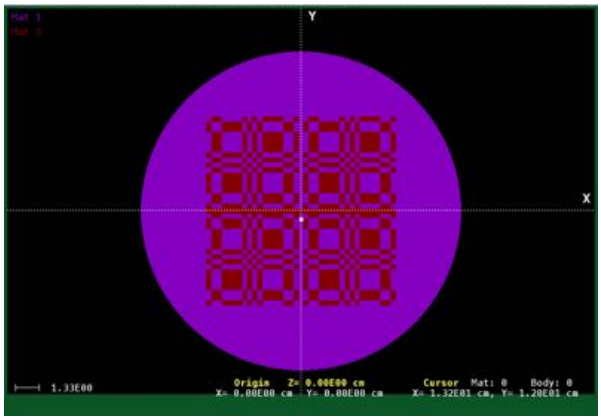

(c)

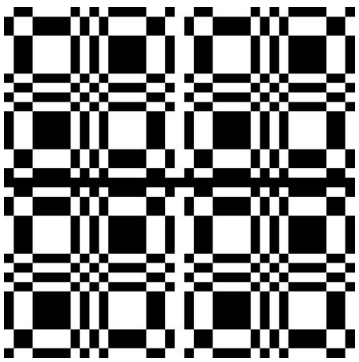

(d)

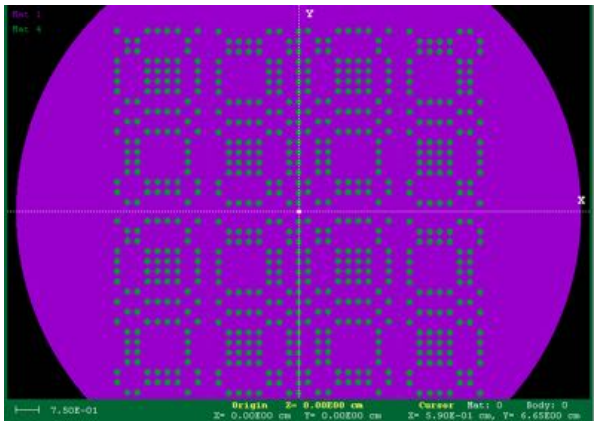

(e)

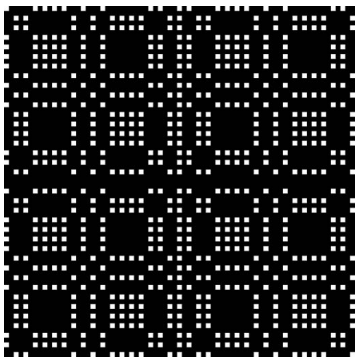

(f)

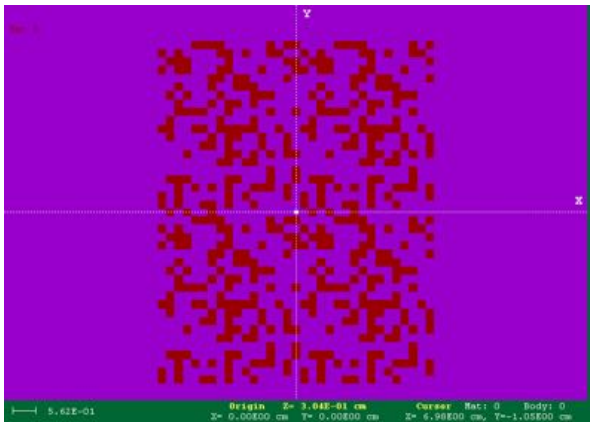

(g)

(h)

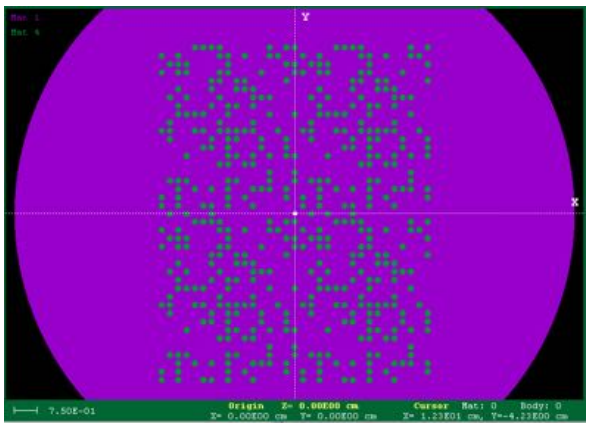

(i)

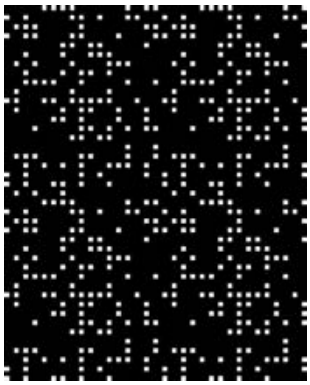

(l)

Figure 7.27 CA masks modelled in PENGEOM (on the left) and theoretical (on the right).

7.12.1.1 MURA CA

A MURA (Modified Uniformly Redundant Array) coded aperture model is a combination of squares and rectangles of different materials. These shapes are repeated and the CLONE function of PENGEOM can be used to replicate them. This was done for a 19 MURA and a mosaicked 19 MURA both of which can be seen in figures 7.28. The materials used for the model are tungsten-epoxy and polylactic acid (PLA). In the PENGEOM model, tungsten-epoxy is represented by pink, PLA is in red. Both MURA and mosaicked MURA masks are placed inside a disk in tungsten-epoxy as seen in figures 19a to 19d to simplify the model. The unit pattern is represented in figure 7.28(a), while the mosaicked 19 MURA is in figure 7.28(c).

In figure 7.28, the green box on the upper left side is created hole by hole (a square is 3mm by 3mm), this square is then cloned and rotated by 180 degrees to create the second green box. The same is done with yellow box and by swapping the two materials. This unit is then cloned four times to obtain the whole mask. This allows to reduce the number of surfaces in the geometry file not reaching the limited number (chapter 5). This is especially true with masks made with cubes as holes as it takes six surfaces to create the body of a square hole (against three surfaces for a cylindrical hole).

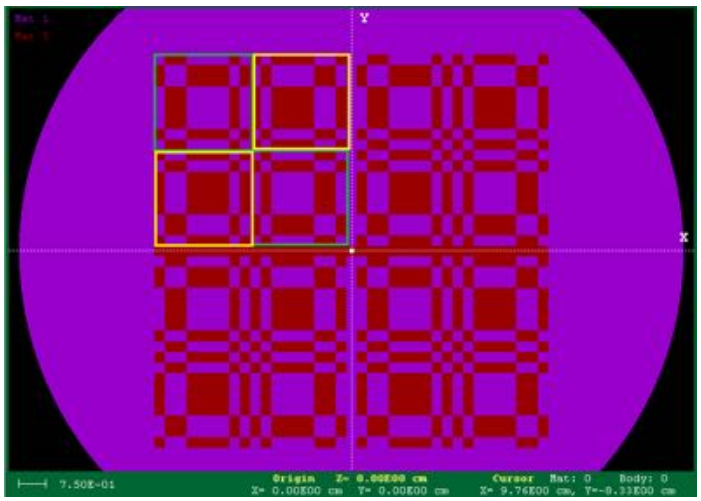

Figure 7.28 CA 19x19 MURA mosaicked mask modelled in PENGEOM. The mask appears having a symmetric unit pattern, which was reproduced in PENGEOM by using the CLONE function.

7.12.1.2 NTHT MURA CA

MURA mask can be also designed by applying the No-Two-Holes-Touching (NTHT) rule pattern: separating each hole by a defined distance. NTHT allows for a self-supporting mask against the other masks, which are unstable and harder to create physically due to the successive holes. This advantage comes at the price of an increased background noise.

Cylindrical holes are created inside a tungsten alloy plate of 2 mm thickness. Each hole is separated by 1.21 mm. It is created with the same technique as the MURA except it is easier since holes are made by cylinders (three surfaces to define) instead of cubes (six surfaces) (fig. 7.28(e)).

7.12.1.3 Singer Set CA

This mask is done by creating holes of 2 mm by 2 mm of air inside a tungsten plate. Singer Set patterns are designed to have the best SNR for a pattern with no symmetry and also to reduce the background noise [110]. This mask does not show any symmetry for easily designing. This implies that it is very difficult to not reach the limited number of surfaces. The only way to reproduce the mask is to detect the largest repeated shapes in order to optimise the number of surfaces. Technically, as soon as a pattern (even as small as two cubical holes) is repeated more than one time, it is worth to define it as a module and clone it (fig. 7.28(g)).

7.12.1.4 NTHT Singer Set CA

The difference with the regular SS mask is that cubical holes are replaced by cylindrical holes (thus easier to create). Each hole is separated by 0.67mm. Also, holes are made of PLA inside a tungsten epoxy resin plate of 2 mm thickness (fig. 7.28(l)).

7.13 Preliminary testing the CA imaging system with a thin wire X-ray emitter

In this section, the 'wire-like' method previously applied to pinhole imaging was employed for testing the X-ray camera. The source is an X-ray emitter that was flat up to 200 keV in the form of a fine wire, and the camera was exposed to 10^6 photons for calculating the line-spread function for each pinhole/CA mask. This preliminary test was applied to 19 MURA, 19 MURA mosaicked, 2 mm thickness 2 mm aperture diameter tungsten pinhole mask, and 4 mm thickness 2 mm aperture diameter tungsten epoxy pinhole mask. The hole was filled with air for the tungsten pinhole mask, and PLA for tungsten epoxy resin mask.

An example of the geometrical setup is shown in figure 7.29. The test object was a long thin metal wire placed 196 mm in front of the simulated mask to give a magnification of unity (in blue, on the right, in fig. 7.29).

The extreme thinness of the object was expected to result in a Gaussian image profile used to calculate the resolution of the system in terms of its Full Width at Half Maximum (FWHM). Previous work manifested in good methods to evaluate image quality metrics with the old X-ray detector and they are here applied to the upgraded system and pinhole/CA masks.

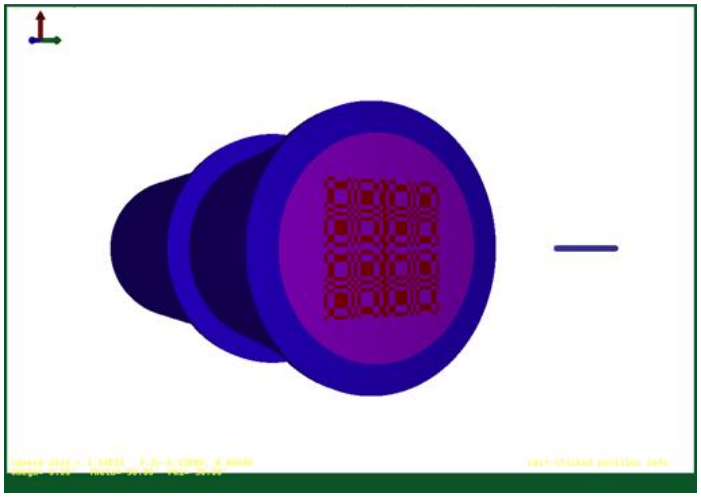

Figure 7.29 Model of the X-ray detector with a thin wire test object that emits X-rays up to 200 keV.

7.13.1 Energy-Spectra at the detector

Photon transmission through the masks reduces the contrast and increases noise in images produced using pinhole or coded aperture optics [103]. This section assesses the noise generated by the four masks. The number of photons emitted from the wire was set at 10^6 to achieve acceptable statistics in a relatively short time (maximum half an hour). The photon energy spectra from the four masks are shown in figure 7.30.

The spectra show tungsten characteristic sharp peaks caused by fluorescence within the masks. The MURA (yellow) and mosaicked MURA (purple) show more photons coming through the masks than the pinholes with the mosaicked MURA understandably letting most photons through. The photons must get through either Tungsten epoxy or PLA to reach the detector, where low energy photons are unlikely transmitted and high energy photons likely transmitted. The spectra for the pinholes demonstrate how 2mm tungsten is superior to 4mm tungsten epoxy at high energies.

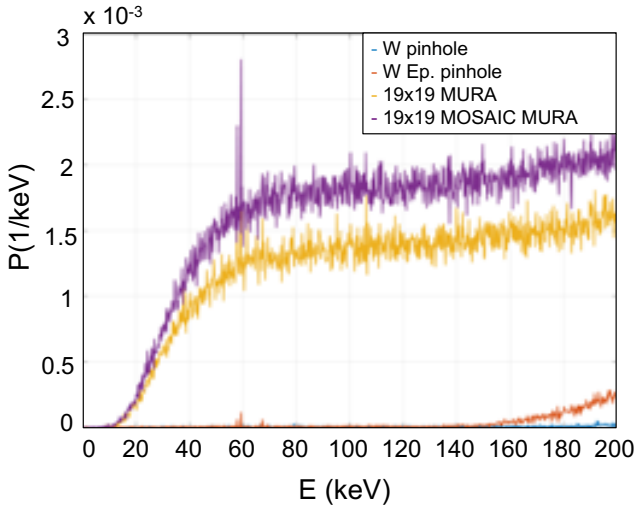

Figure 7.30 X-ray spectra as energy-probability distribution for W and W Ep. Pinhole masks, 19 MURA and mosaicked MURA masks. All the spectra show characteristic lines from tungsten. MURA and mosaicked MURA present higher intensity as more photons are coming through, and the spectrum appears as a combination of PLA and tungsten spectra.

7.13.2 200 keV flat wire source image correlation with MATLAB Encoding

PAXI was combined with the function ENCODE.m [82]. However, for the image to be decoded, it is necessary to crop the image size from 1392x1040 to 1040x1040 to match both sizes of MURA unit patterns. After generating the .tif image, PAXI automatically crops the image down to 1040x1040, and then recalls ENCODE.m for correlating the image. Firstly, ENCODE asks for the path of the CA mask, secondly for the image to be processed and lastly it generates the encoded image. An example of the process is given in figure 7.31. Note that for the pinhole masks, the images were correlated with the pinhole mask itself for generating the image.

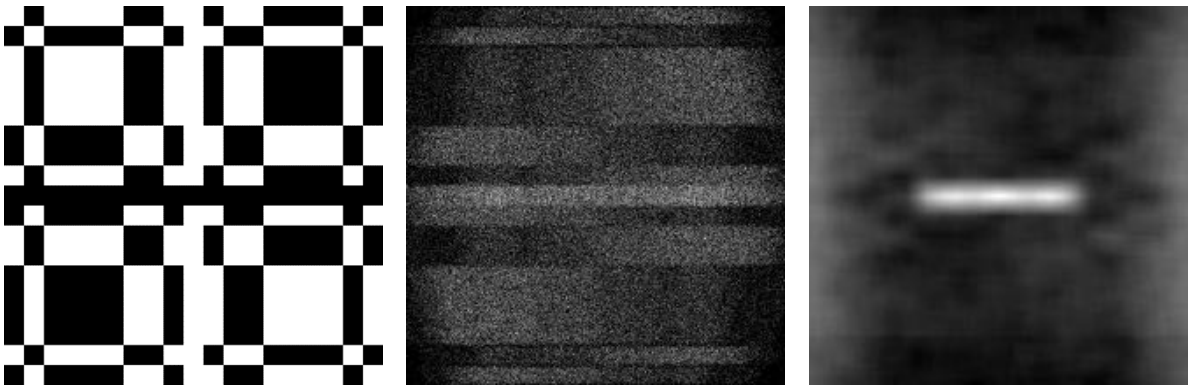

(a) (b) (c)

Figure 7.31 MURA pattern (a) is correlated with the image generated at the detector (b) from a 200 keV flat X-ray wire source emitting 10^6 photons to give the correlated (decoded) image (c).

7.13.3 Exposures from simulating the wire emitter

Exposures were taken with the 200 keV flat X-ray wire source with the four different masks: two from tungsten and tungsten-epoxy pinhole masks and two for CA 19 MURA and mosaicked MURA. The images are shown in figure 7.32. The image from tungsten pinhole mask has almost no background noise, while the exposure on the tungsten-epoxy pinhole mask does. The MURA CA exposure seems blurred but well defined over the edges, while the mosaicked CA exposure presents a blurred tail on both sides of the wire.

7.13.4 Line-spread-function calculation

From the previous exposures, it is possible to generate the 'line-spread function'. After encoding, the PAXI algorithm recalls the saved images and generates surface plots. Line-spread functions are shown in figure 7.33. Determining the line-spread function allows image quality metrics to be calculated with the same method used with the previous configuration. Signal-to-noise and contrast-to-noise ratios and spatial resolution in terms of full-width at half maximum were calculated for the four masks.

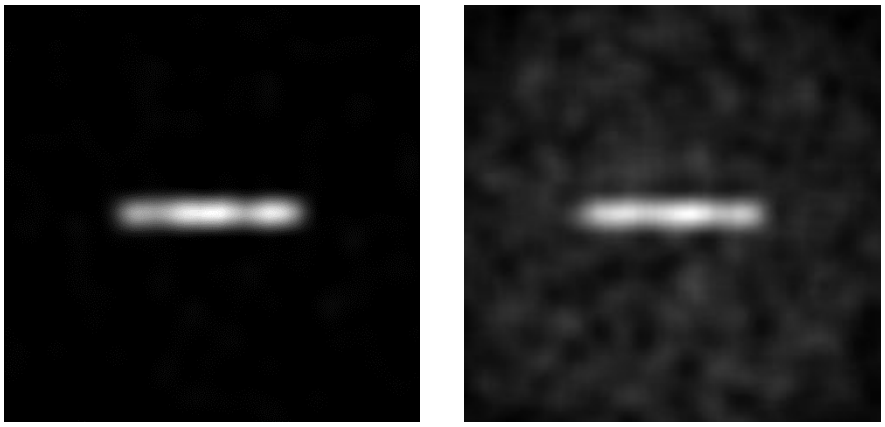

(a) (b)

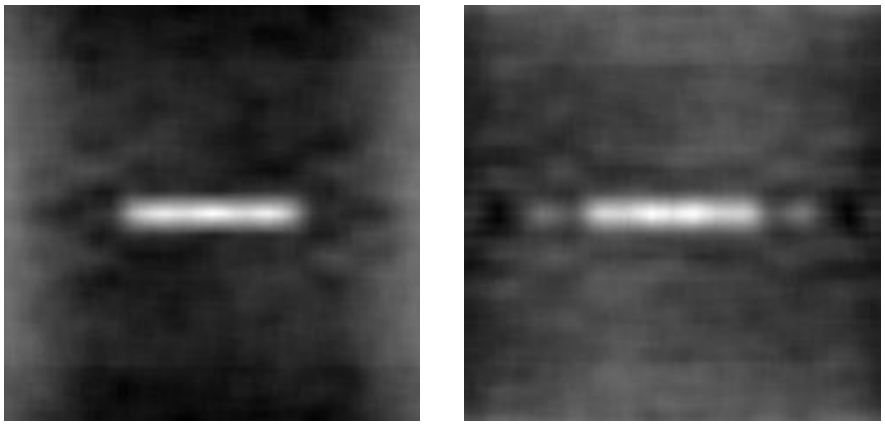

(c) (d)

Figure 7.32 Exposures generated from a 200 keV flat X-ray wire source emitting 10^6 photons detected and recorded at the detector on the psf-file: (a) pinhole mask, (b) W epoxy pinhole, (c) 19 MURA and (d) mosaicked MURA. Pinhole exposures show a well-defined wire, while MURA and mosaicked MURA exposures appear more blurred and mosaicked MURA presents tails on both sides of the wire (artefact).

7.13.5 Signal-to-noise, Contrast-to-noise ratios and Full-Width at half maximum

After determining the line-spread function, the next step is estimating image quality metrics with the thin wire emitter. Signal-to-noise and contrast-to-noise ratios and spatial resolution in terms of full-width at half maximum were calculated. PAXI was customised for the 200 keV flat X-ray wire source for recognising the ROI with a rectangle-shaped crop around the central area on the exposures where the wire was detected. Note the signal from the profile presents a baseline with some noise so for this purpose of establishing spatial resolution the background was subtracted with a median filter from the whole image. SNR and CNR were calculated as discussed for the point source.

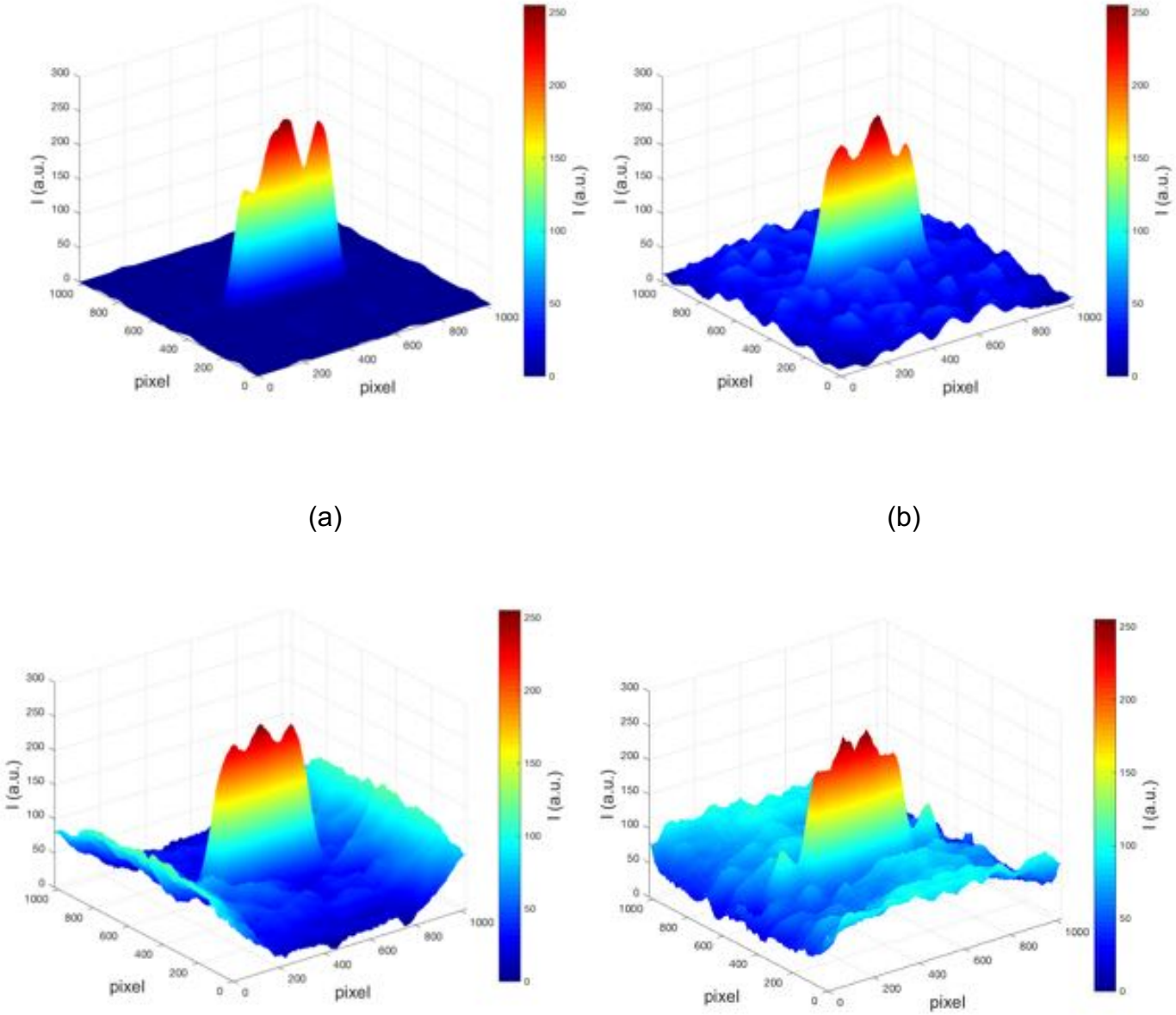

Figure 7.33 Line-spread functions generated from a 200 keV flat X-ray wire source emitting 106 photons detected and recorded at the detector on the psf-file: (a) pinhole mask, (b) W epoxy pinhole, (c) 19 MURA and (d) mosaicked MURA.

The full-width at half maximum (FWHM) was analysed across the line-spread function down the y-axis and a Gaussian profile was calculated. From the standard deviation of the Gaussian curve, the FWHM was calculated using

formula 7.1. An example of the Gaussian profile from the exposure of the 200 keV flat X-ray wire source through a pure tungsten pinhole mask is given in figure 7.34.

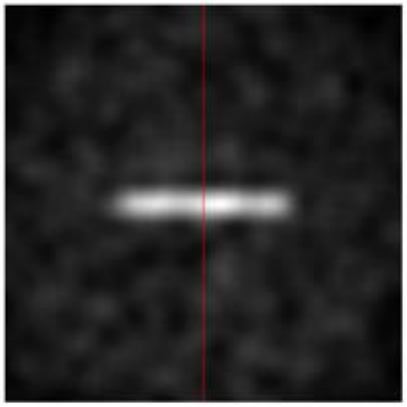

(a)

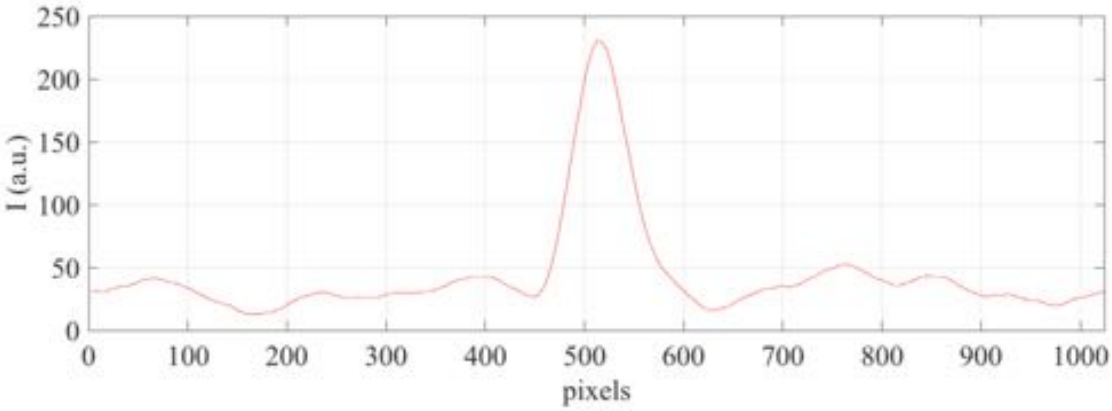

(b)

Figure 7.34 Gaussian profile from the exposure (a) of a 200 keV X-ray flat X-ray wire source for calculating the FWHM (b).

In PENELOPE, it is not possible to control the exposure time, but only the number of simulated showers. NSHI was kept to 10^6 for the all the simulated experiments with the 200 keV flat X-ray wire source. This allows simulation to give consistent comparisons between mask designs, but as the thin wire cannot be constructed

physically, there was no drive to set NSHI to match any experiment. To give an idea of the % of photons passing through the mask materials, the ratio between the number of detected photons and those simulated from the source was calculated and is given on table 7.4

Table 7.4 Fraction of photons at the detector, SNR, CNR and FWHM from the exposure of a 200 keV flat X-ray wire source.

MASK	**MAT.**	**THICK. (mm)**	**AP. DIAM. (mm)**	**N PH.**	**SNR**	**SNR (dB)**	**CNR**	**FWHM (Pixels)**
Pinhole A	W	2	2	0.07%	26.80	17.27	0.96	18.49
Pinhole B	W Ep.	4	2	0.6%	14.72	11.68	0.74	28.48
MURA	W Ep.	4	19x19	23%	6.48	8.11	0.59	26.07
MOSAICKED MURA	W Ep.	4	19x19 (mosaic)	31%	9.13	9.61	0.50	24.40

When the source is a thin wire emitting 200 keV flat X-rays and consider again the performance of the 2 mm thick/2 mm aperture/pure tungsten pinhole as the reference, then the 4 mm tungsten-epoxy pinhole mask has a significantly lower general performance. The SNR, CNR and FWHM are worse by 45%, 23% and 54% respectively. The origins of this may include scatter and fluorescence from the increased inner wall area of the epoxy pinhole and a major feature will be increased leakage through the mask material by photons significantly higher in

energy. Tungsten-epoxy appears still acceptable; however, pure tungsten has the best overall performances.

When exposed to the thin wire source, mosaicked MURA performs generally better than19 MURA: it shows 41% greater SNR, 15% greater CNR, and 6% lower FWHM, thus better resolution.

7.14 Measuring point spread functions of simulated pinhole and CA masks

The Phase-Space file algorithm for X-ray Interaction with the matter (PAXI) was written to accomplish the mapping and integration of the phase-space file. PAXI processes the information from the simulation by correlating the detected energy to the x-y pixel position of each photon hitting the detector. The necessary information is integrated energy, which is calculated by integrating the energies of all photons hitting each particular pixel over some exposure period. Specifically, the integrated energy I(E) is defined as the sum of the energy of the photon data in the phase space file correlated with the positions and areas of the 1040 x 1392 pixels of the real detector. Integrated energy is associated with image brightness and from now on they will be assumed to be equivalent. Hence PENELOPE and PAXI can be used to generate x-y maps of integrated energy across the surface of the detector, i.e. brightness images, for the different masks.

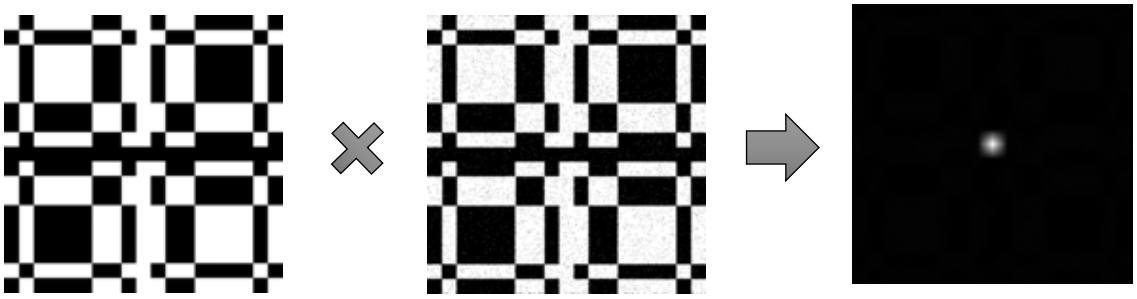

(a) (b) (c)

Figure 7.35 CA 19x19 MURA image correlation for generating the point spread function. (a) is the theoretical 19 MURA mask, (b) is from the phase-space file, (c) is the psf exposure.

7.15 Modelling Am-241 point source

For this section of work, exposures of pinhole and coded apertures masks were taken with two different models of the Am-241.

The two models aim to reflect the characteristics of a physical Am-241 source available for experiment at Cranfield and is described in table 7.5.

Table 7.5 Am-241 physical source gamma emission lines and geometrical parameters.

Am-241 source NS454	
Current Activity of the source	1.06 1E9 Bq = 2.9 mCi
γ-emission (gamma)	60 keV (36%)
	18 keV (18%)
	14 keV (13%)
Half-life	432.7 years
Constant decay	5.07E-11
Dimensions	15 mm external diameter
	5 mm internal diameter (hole)
	8.5 mm thickness
	~0.5 mm thickness cylinder

The Am source is coated inside the top cap ~ 1mm thickness and the cylinder is opened on the bottom and has a hole on the top. A scheme of the source is represented in figure 7.36.

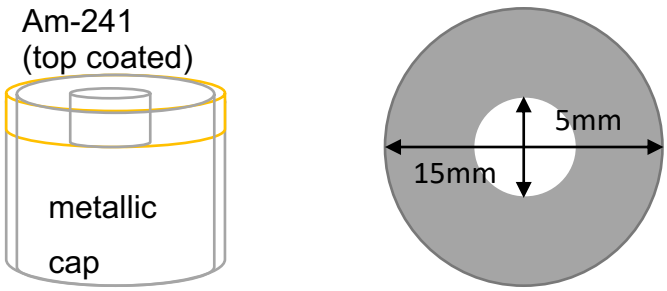

Figure 7.36 Am-241 source scheme.

While matching experiment and simulations, two factors should be considered. The first is simulation can achieve higher counting statistics with lower number of simulated showers by inputting ideal sources; the second is while comparing against experiment, we need to model geometries as close as possible to the physical laboratory environment. Two sets of simulations were performed; one reflecting the nature of simulation by inputting a point source, the other by attributing the emission lines to a geometrical object.

In the first set of simulations, the Am-241 source was represented as point source by inputting the emission lines as in figure 7.36. The source was placed at 1 m from the frontal mask, and the aperture cone (half-cone) was set equal to 3.5 degrees. This first set of simulation was used as preliminary study for calculating the optimum number of simulated showers for achieving a good image data on the phase-space file.

```
TITLE  X-ray detector test with Am241
       .
       >>>>>>>> Source definition.
SKPAR  2        [Primary particles: 1=electron, 2=photon, 3=positron]
SPECTR 14e3    0.13e0        [E bin: lower-end and total probability]
SPECTR 14e3    1.0e-35       [E bin: lower-end and total probability]
SPECTR 18e3    0.18e0        [E bin: lower-end and total probability]
SPECTR 18e3    1.0e-35       [E bin: lower-end and total probability]
SPECTR 60e3    0.36e0        [E bin: lower-end and total probability]
SPECTR 60e3    1.0e-35       [E bin: lower-end and total probability]
SPOSIT 0 0 -100                          [Coordinates of the source]
SCONE  0 0 3.5                         [Conical beam; angles in deg]
       .
```

Figure 7.37 Description of the Am-241 point source in PENELOPE input file.

At this distance, it was calculated the solid angle is equal to:

$$\Omega = 2\pi(1 - \cos\vartheta) = 2\pi(1 - \cos(rad(7^{\circ}))) \cong 5.52 \qquad 7.5$$

From 7.5, we can determine the absolute detector efficiency. In simulations, we assuming the total efficiency is equal to the absolute efficiency:

$$\varepsilon = \frac{\Omega}{4\pi} \cong 0.44 \qquad 7.6$$

At this point, we can calculate the efficiency calibration for the 60 keV gamma line of Am-241:

$$\varepsilon = \frac{N(E)}{A \cdot I_{\gamma}(E)} \qquad 7.7$$

Whereas N(E) is the number of photons emitted, A is the activity of the source, $I_{\gamma}(E)$ is the probability of emission at 60 keV.

But $\varepsilon = 0.44$, hence we can calculate the number of photons N(E):

$$N(E) = \varepsilon \cdot A \cdot I_{\gamma}(E) = 0.44 \cdot 1.06 \cdot 10^{9} \cdot 0.36 = 1.68E8 \qquad 7.8$$

Thus, from eq. 7.8, the number of simulated showers was set to 1.68E8 in the input file.

In the second set of simulations, it was required to model physical Am-241 source to realise simulations comparable with experiment. The model of the physical Am-241 is shown in figure 7.37.

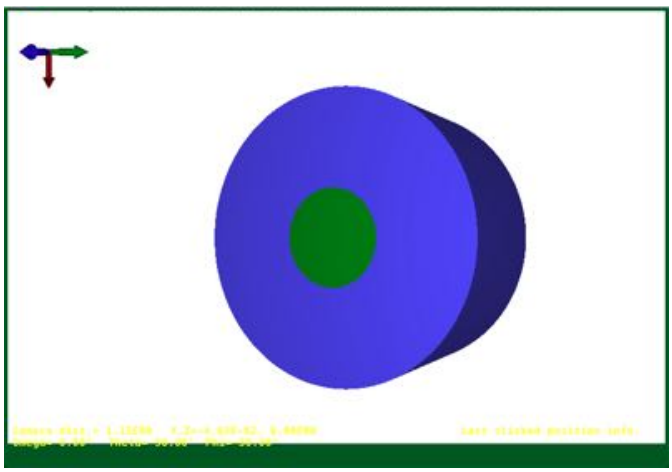

Figure 7.38 Am-241 model in PENGEOM.

The model is simplified as a disk with the same size as the physical one (15 mm), with a hole filled with air of 5 mm diameter.

In this set of simulations, the number of simulated showers was increased up to 1E9, as the source box flag in PENELOPE slowed down the random generation of photons, and the image on the phase-space file decoded with PAXI was not well formed.

The two different configurations were simulated for a 2 mm thickness 2 mm aperture diameter solid tungsten pinhole mask, 4 mm thickness 2 mm aperture diameter tungsten epoxy pinhole mask, with the hole filled with PLA, a 4 mm thick 19 MURA mosaicked made of tungsten-epoxy and PLA, a 2 mm thick 19 MURA mosaicked NTHT made of tungsten, a 4 mm thick 17x34 Singer Set made of tungsten-epoxy, and a 2 mm thick 17x34 Singer Set NTHT made of tungsten. The simulated exposures (on the left column) and point spread functions (on the right column) are shown in figures 7.39 and 7.40 for point source and physical source, respectively. PAXI algorithm recalls the saved images in the left column and generates the surface plots on the right. Determining the point-spread function allows us to calculate image quality metrics, such as signal-to-noise and contrast-to-noise ratios, and spatial resolution in terms of full-width at half maximum, and presenting them as 3D surface plots reveals features, such as side lobes, that will affect the decoded images.

A physical experiment was fulfilled for measuring the exposures of the Am-241 source placed at 1m from the front of the mask for comparing against simulations. The experimental exposures were taken for 500 seconds with a 2 mm thickness 2 mm aperture tungsten pinhole mask, for 300 seconds with a mosaicked MURA, NTHT MURA, Singer Set and NTHT Singer Set masks, with the signal at the detector cropped around the central unit pattern (figure 7.41).

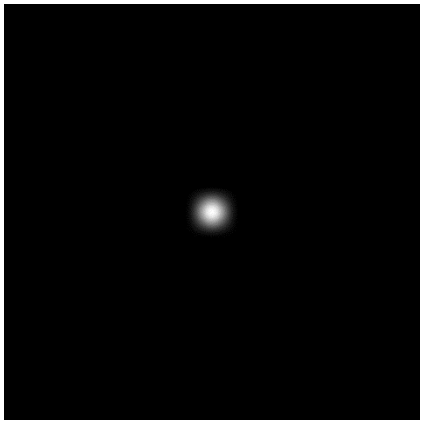

(a)

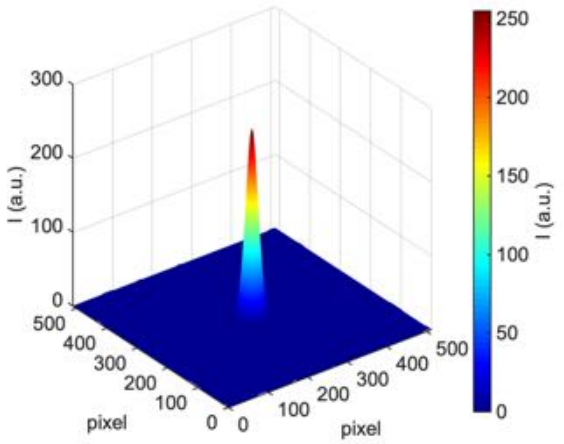

(b)

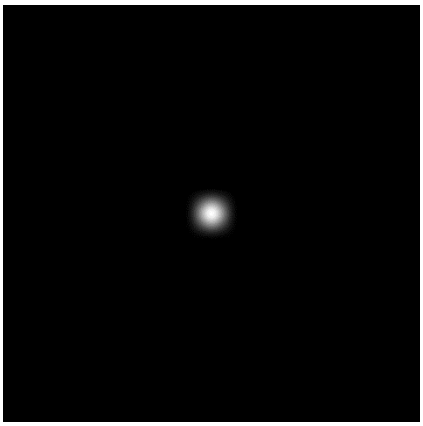

(c)

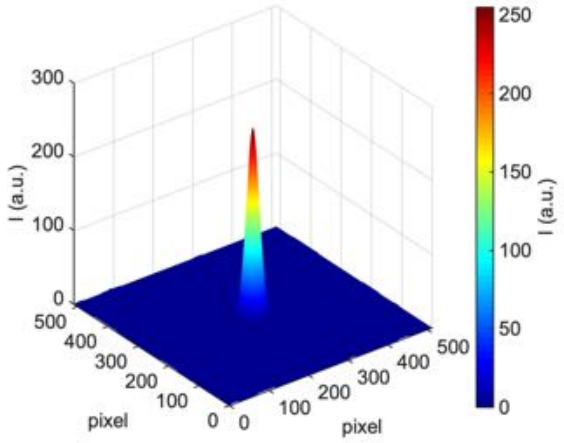

(d)

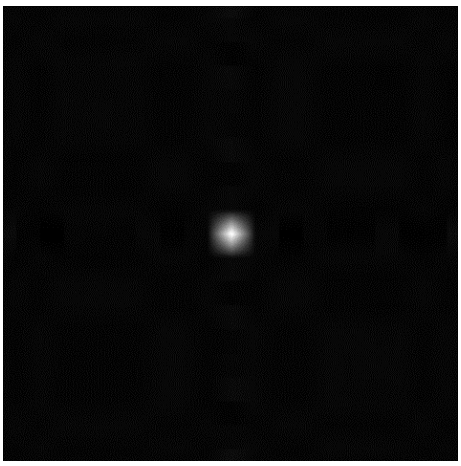

(e)

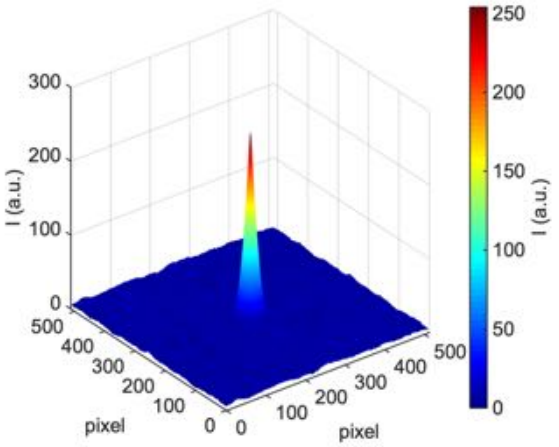
I (a.u.)
300
200
100
0
500
400
300
200
100
0
pixel
0
100
200
300
400
500
pixel
250
200
150
100
50
0
I (a.u.)

(f)

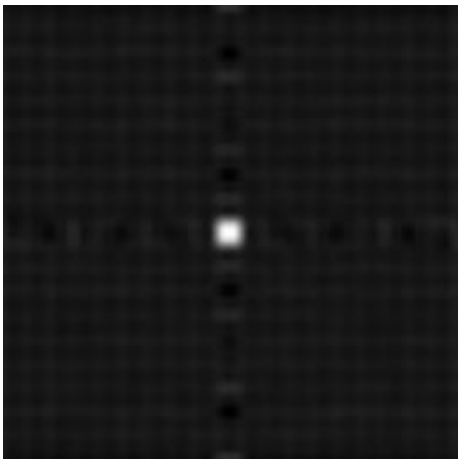

(g)

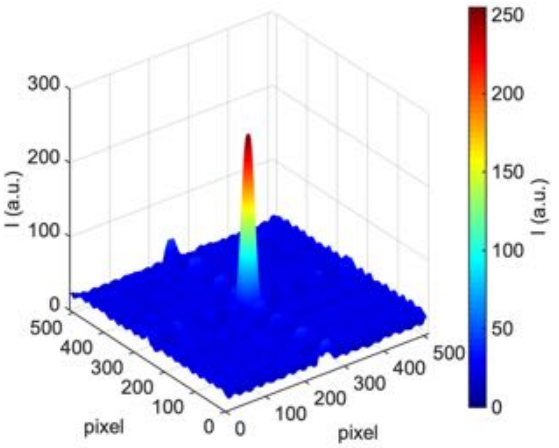
I (a.u.)
300
200
100
0
500
400
300
200
100
0
pixel
0
100
200
300
400
500
pixel
250
200
150
100
50
0
I (a.u.)

(h)

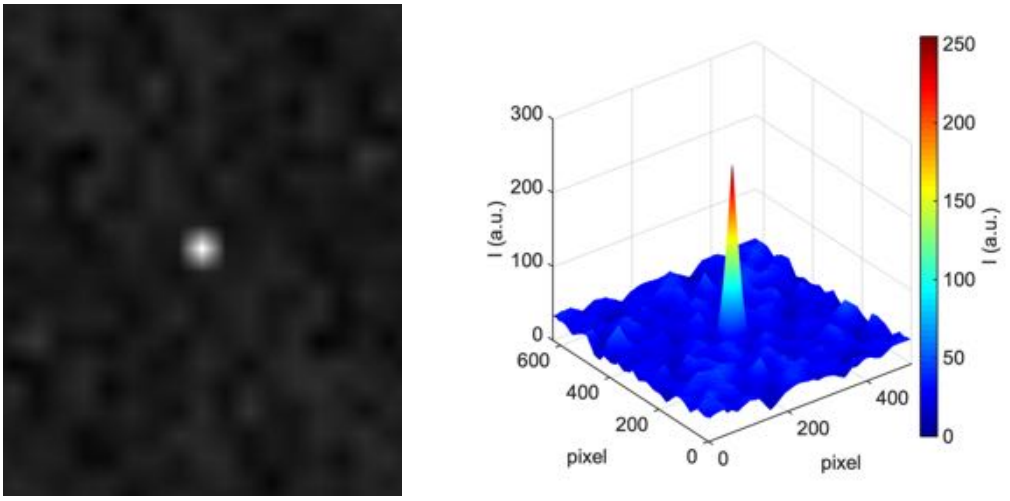

(i) (j)

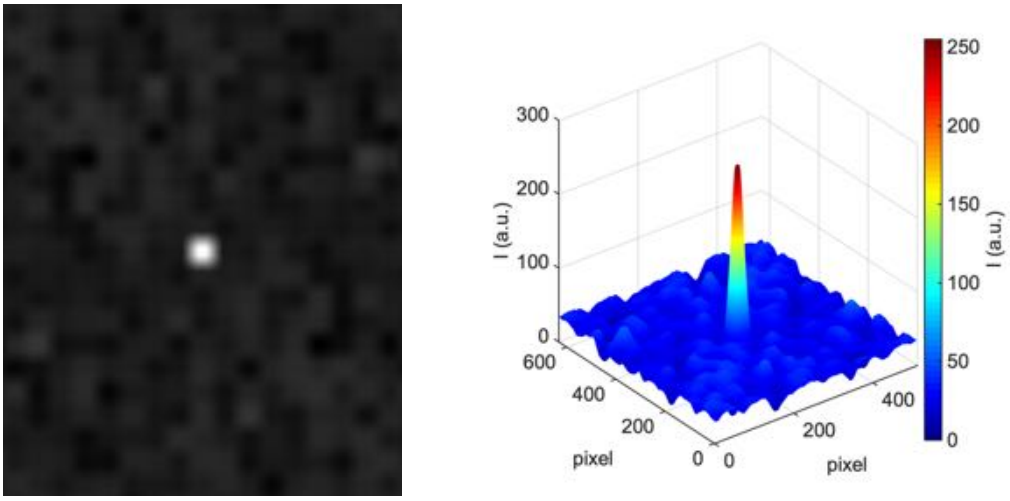

(k) (l)

Figure 7.39 Pinhole and CA masks exposures (on the left) and point spread functions (on the right) of Am-241 point source. (a) (b) are 2 mm thick 2 mm aperture diameter W pinhole, (c) (d) are 4 mm thick 2 mm aperture diam. (filled with PLA) W Epoxy pinhole, (e) (f) are 19 mosaicked MURA, (g) (h) are NTHT 19 mosaicked MURA, (i)(j) are Singer Set and (k)(l) are NTHT Singer Set masks.

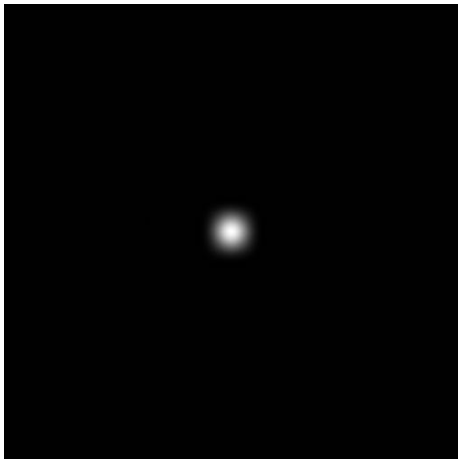

(a)

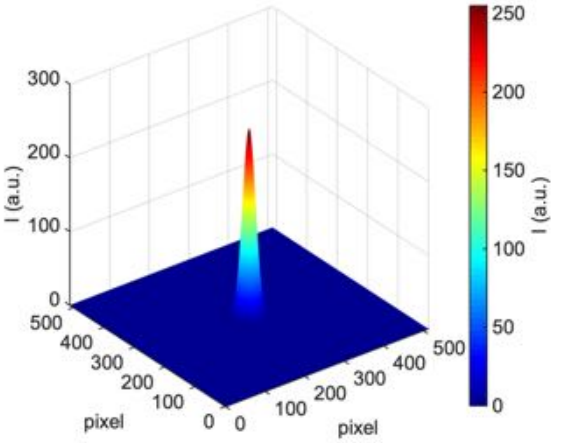
I (a.u.)
300
200
100
0
500
400
300
200
100
0
pixel
0
100
200
300
400
500
pixel
250
200
150
100
50
0
I (a.u.)

(b)

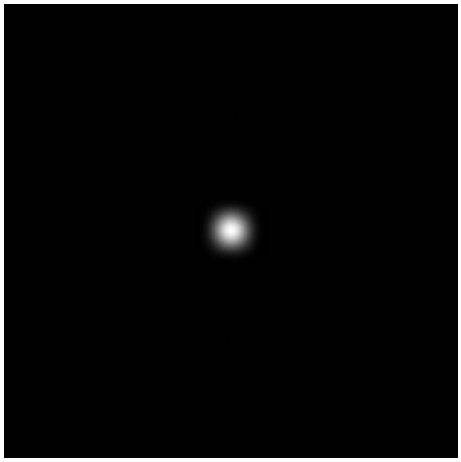

(c)

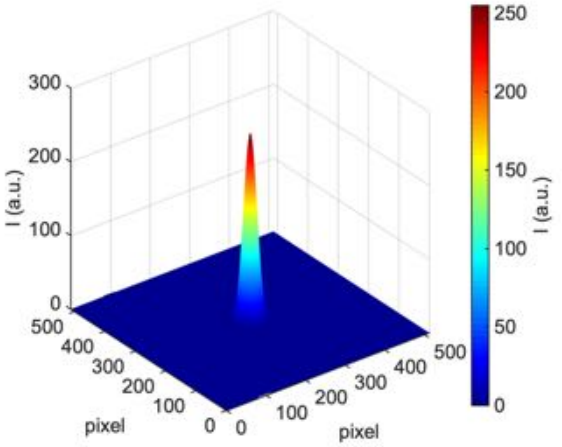
I (a.u.)
300
200
100
0
500
400
300
200
100
0
pixel
0
100
200
300
400
500
pixel
250
200
150
100
50
0
I (a.u.)

(d)

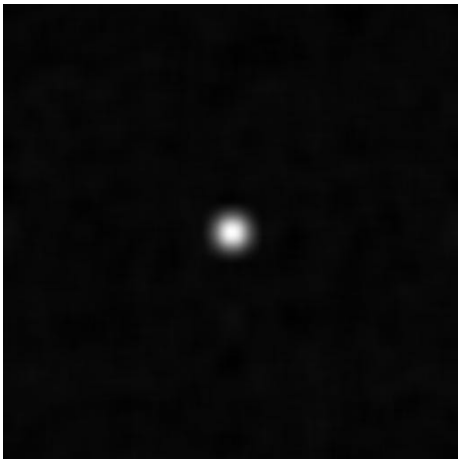

(e)

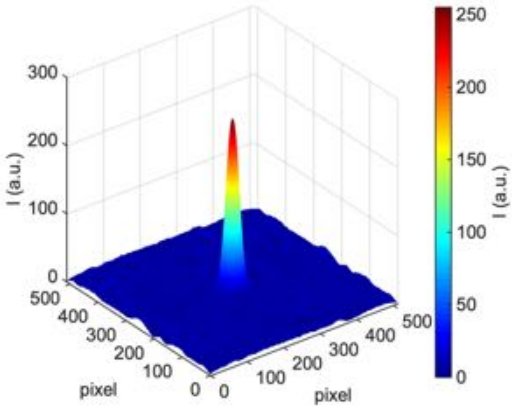
I (a.u.)
300
200
100
0
500
400
300
200
100
0
pixel
0
100
200
300
400
500
pixel
250
200
150
100
50
0
I (a.u.)

(f)

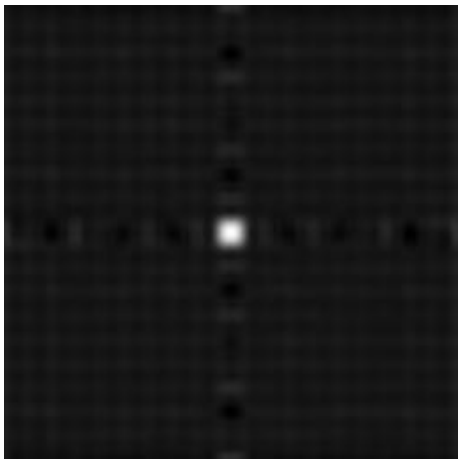

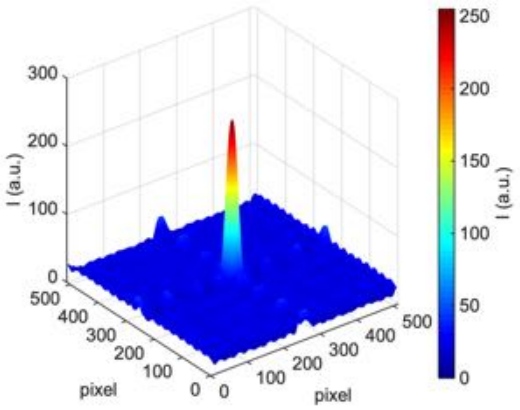

(g) (h)

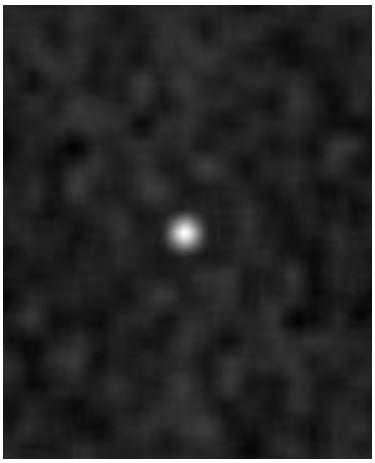

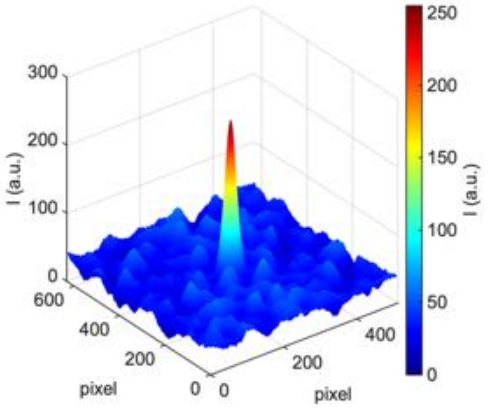

(i) (j)

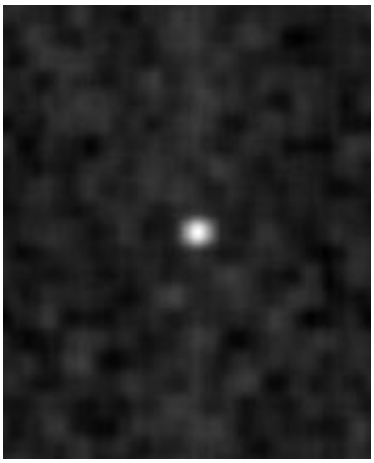

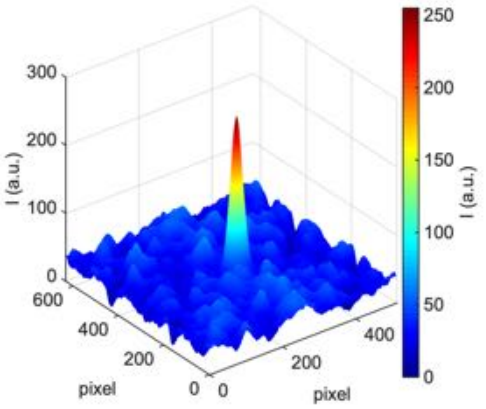

(k) (l)

Figure 7.40 Pinhole and CA masks exposures (on the left) and point spread functions (on the right) of physical Am-241. (a) (b) are 2 mm thick 2 mm aperture diameter W pinhole, (c) (d) are 4 mm thick 2 mm aperture diam. (filled with PLA) W Epoxy pinhole,

(e) (f) are 19 mosaicked MURA, (g) (h) are NTHT 19 mosaicked MURA, (i)(j) are Singer Set and (k)(l) are NTHT Singer Set masks.

(a)

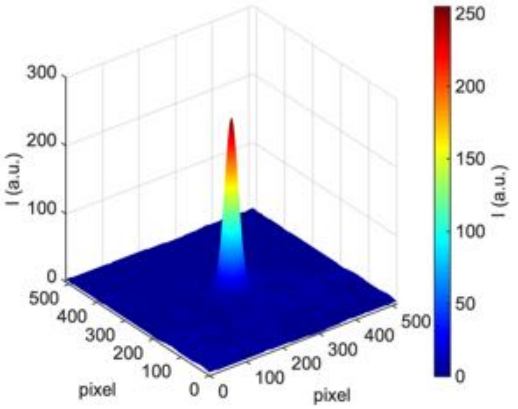

(b)

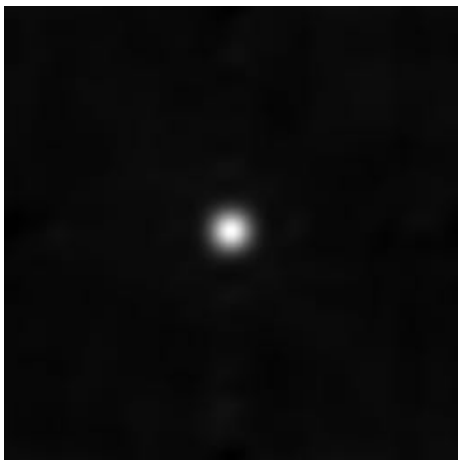

(c)

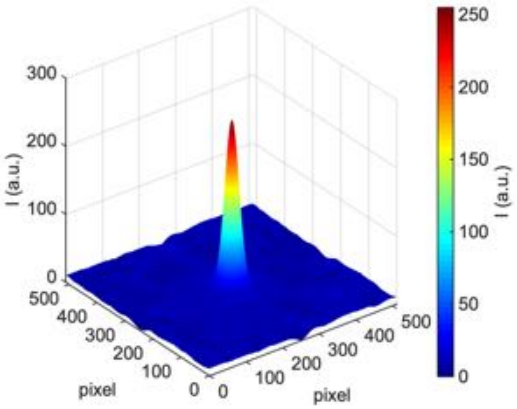

(d)

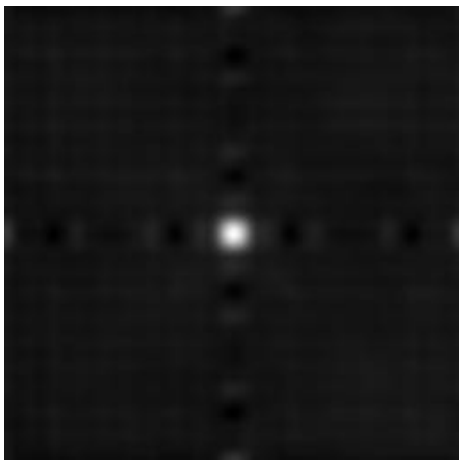

(e)

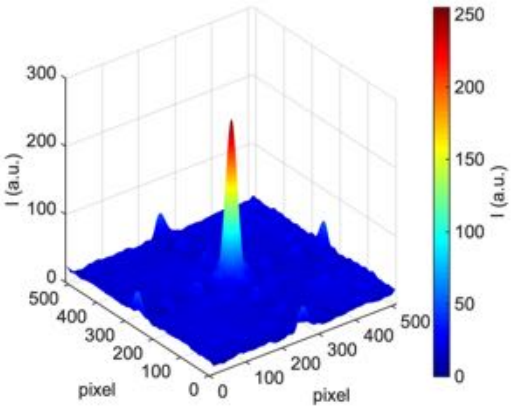

(f)

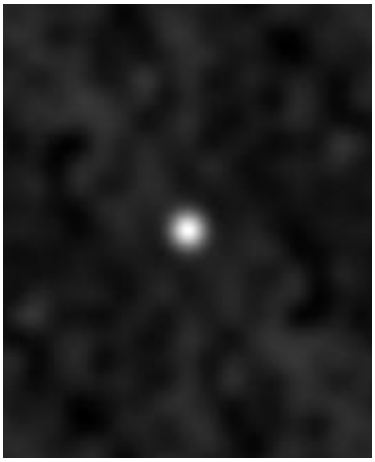

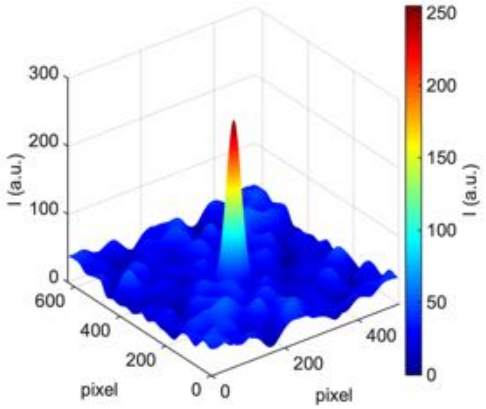

(g) (h)

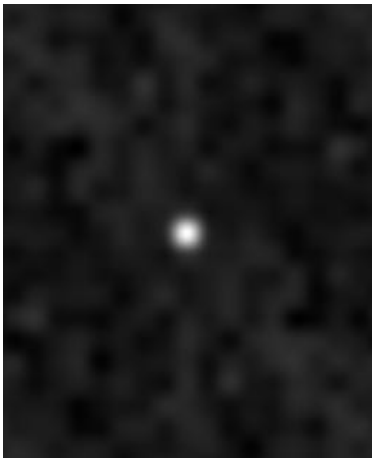

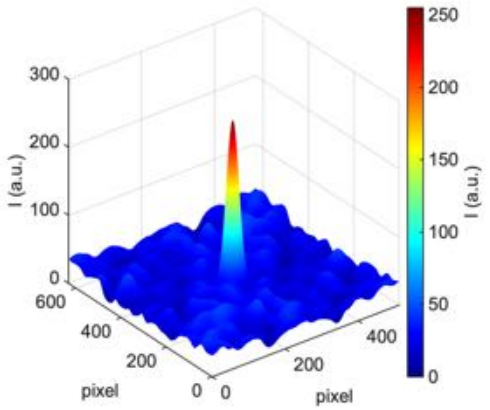

(i) (j)

Figure 7.41 Pinhole and CA masks experimental exposures (on the left) and point spread functions (on the right) of physical Am-241. (a) (b) are 2 mm thick 2 mm aperture diameter W pinhole, (c) (d) are 19 mosaicked MURA, (e) (f) are NTHT 19 mosaicked MURA, (g)(h) are Singer Set and (i)(j) are NTHT Singer Set masks.

7.16 Signal-to-noise, Contrast-to-noise ratios and Full-Width at half maximum

After determining the point-spread function, the next step is estimating image quality metrics. Signal-to-noise and contrast-to-noise ratios and spatial resolution are perhaps the most important metrics. The resolution was calculated in terms of full-width at half maximum. For calculating the image metrics, it is necessary to identify the Region of Interest (ROI). PAXI was customised for the Am-241 point-source to recognise the ROI with a disc-shaped to crop around the central bright area on the exposures. The background image was determined by subtracting the ROI from the whole image.

SNR was calculated, and the Rose Criterion in eq. 7.3 was taken as a measure of sufficiency. The noise is described by the standard deviation of the image brightness of the background over the whole detector outside the ROI. CNR ratio was applied as defined in eq. 7.2, and full-width at half maximum as in eq. 7.1, by estimating the Gaussian profile as shown in figure 7.42. Results from both simulations and experiment are given in table 7.5 and plotted in figure 7.43.

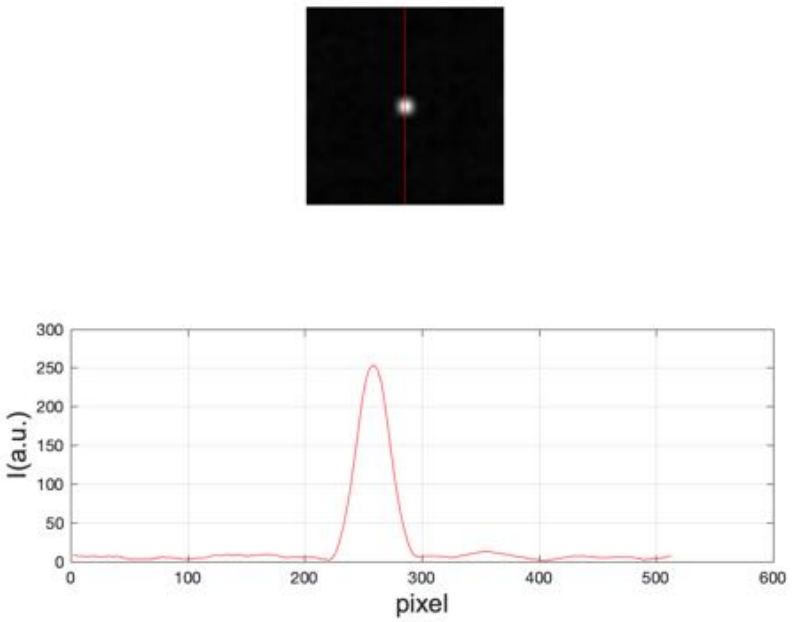

Figure 7.42 Example of profile along y-axis of the central bright area for calculating the FWHM.

Table 7.6 Pinhole and CA masks simulated and measured CNR, SNR, and FWHM.

MASKS	MATERIAL	THICK. (mm)	AP. DIAM. (mm)	SOURCE	CNR (a.u.)	SNR (db)	FWHM (pixels)
Pinhole A	W	2	2	Am-241 point source	0.99	14.65	13.14
Pinhole B	W Ep.	4	2	Am-241 point source	0.99	14.59	13.27
19 MURA (mosaicked)	W Ep.	4	2	Am-241 point source	0.90	15.64	12.43
19 MURA NTHT (mosaicked)	W	2	2	Am-241 point source	0.77	15.11	15.85
17x21 SS (mosaicked)	W Ep.	4	2	Am-241 point source	0.67	12.30	14.03
17x21 SS NTHT (mosaicked)	W	2	2	Am-241 point source	0.68	12.49	12.74
Pinhole A	W	2	2	physical Am-241	0.99	14.53	14.43
Pinhole B	W Ep.	4	2	physical Am-242	0.99	14.34	14.69
19 MURA (mosaicked)	W Ep.	4	2	physical Am-243	0.94	16.45	14.90
19 MURA NTHT (mosaicked)	W	2	2	physical Am-244	0.77	15.01	14.90
17x21 SS (mosaicked)	W Ep.	4	2	physical Am-245	0.65	11.91	14.08
17x21 SS NTHT (mosaicked)	W	2	2	physical Am-246	0.65	11.44	13.04
Pinhole A	W	2	2	Exp	0.96	13.05	14.91
19 MURA (mosaicked)	W Ep.	4	2	Exp	0.91	13.19	15.44
19 MURA NTHT (mosaicked)	W	2	2	Exp	0.79	13.98	12.66
17x21 SS (mosaicked)	W Ep.	4	2	Exp	0.73	11.58	17.01
17x21 SS NTHT (mosaicked)	W	2	2	Exp	0.72	12.15	14.69

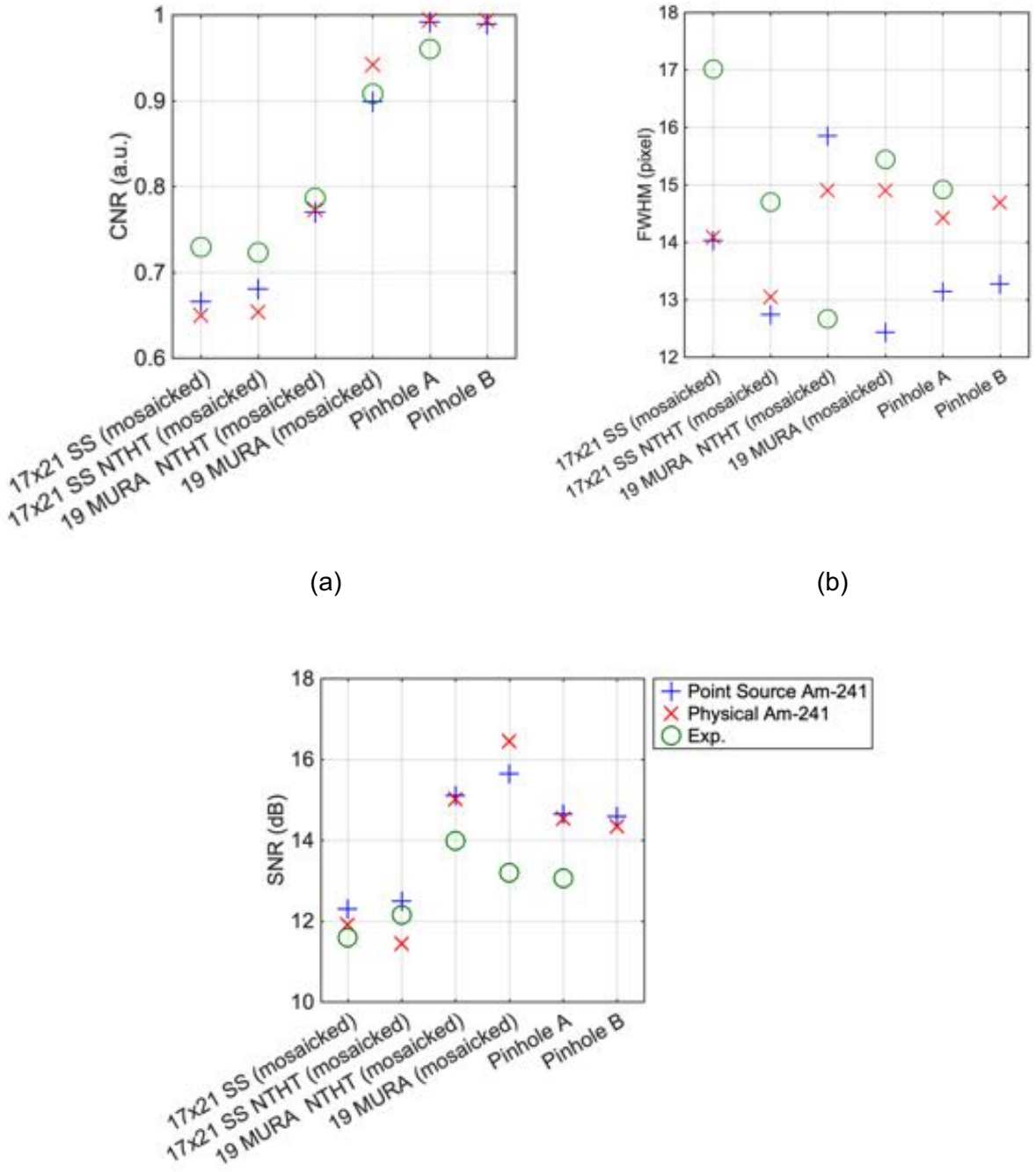

Figure 7.43 CNR (a), SNR (b), and FWHM (c) of the different pinhole and CA masks.

As we can see from table 7.5, the results from both simulations and experiment appear consistent. Taking the favoured 2 mm thickness 2 mm aperture diameter pure tungsten pinhole as a reference, we can observe the performance of

simulated 4 mm thickness 2 mm aperture diameter tungsten-epoxy pinhole mask is nearly equivalent in all the cases. Within reasonable confidence, the tungsten-epoxy pinhole mask has the same spatial resolution, SNR and CNR. Unfortunately, no pinhole masks in tungsten-epoxy resin was available for taking physical exposures.

Mosaicked MURA has a lower resolution when it exposed to a point source, but similar or slightly greater resolution when exposed to the physical source, in simulation and experiment, respectively. When compared against the NTHT MURA, we can observe CNR decreases of ~15% on average in both simulations and experiment as the hole configuration introduces more noise. This is consistent with the SNR, which varies of ~6% between simulated and physical MURA and NTHT MURA masks.

In the ideal case scenario of a simulated Am-241 point source, NTHT MURA exceeds FWHM performances of MURA of 27%, while is the same when Am-241 is simulated geometrical object. With the regards of the experiment, the situation is inverted, as MURA mask is greater than NTHT MURA of 17%. Singer Set and NTHT Singer Set masks are not different in terms of their performances, as the average difference is for CNR ~1.4%, SNR ~3%, and FWHM ~8%. Singer Set has greater contrast and FWHM in the experiment compared with both simulations (~11% and ~21%, respectively), while the difference in SNR is below 5%, while the NTHT Singer Set from simulations appear to have a better agreement with experiment (CNR ~8%, SNR ~4% and FWHM 14%).

7.17 Pilot backscatter simulation of a quadrant test object

In this section, a pilot backscatter imaging simulation is presented. In this pilot experiment, the quadrant test object was exposed to 160 kV spectrum of the VJ Technologies X-ray tube already simulated in chapter 6.

The quadrant is a test object made of four cubes of different materials, 100x100x100 mm each. The materials were copper, PLA, wax and aluminium, and they were placed 1300 mm away from the detector frontal mask. The detector geometries of the upgraded model in previous sections was reused for performing the simulations. Results from simulations were compared against physical exposures. In the physical experiment, the test object was placed in front of a concrete wall and a lead sheet. These laboratory components were added to the geometry to create a more realistic model and explore any scatter effects. The geometrical model can be seen in figure 7.44.

Only two sets of simulations and experiments were performed, one with the tungsten pinhole and one with the 19 MURA mosaicked masks. Simulating a backscatter imaging system is computationally expansive, as it requires a relatively high number of simulated showers for the phase-space file to form an image of a complex scene. For the phase-space file to be populated, it was first observed the minimum number of simulated showers in backscatter geometry was 1E9. If this number was kept to lower values, then the phase-space file did not record any events, and the simulations, when stopped, were not able to resume from the phase-space file as it was empty. For this reason, simulations were strictly running on Cranfield HPC for guaranteeing stability environment and avoiding any data loss. Simulation performances are given in table 7.7.

We can observe the backscatter simulations were running for more ten million seconds, and only 1E5% photons reach the detector when the mask in front is a pinhole. The number of detected photons improves to 1.5E3% when the mask is the 19 MURA. Simulated data from the phase-space file were again converted into an image with PAXI algorithm, which included the decoding function [82] and accommodated for the distance object-mask and mask-detector.

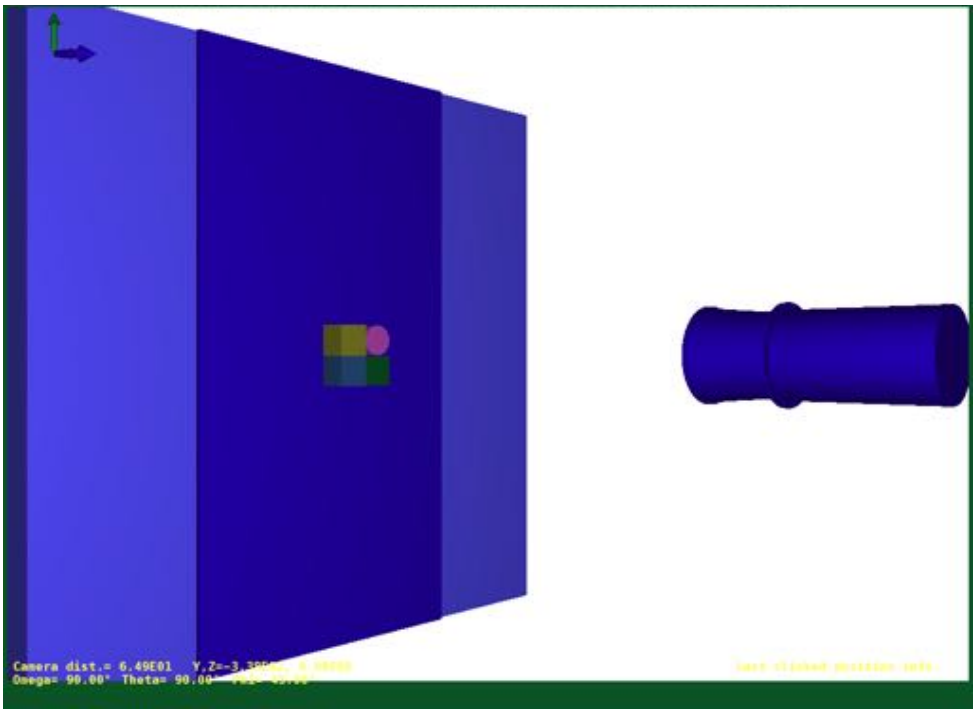

Figure 7.44 Geometrical model of the quadrant exposure setup in front of a 1 m x 1 m x 0.5 m wall and a 0.2 thick lead panel. The detector is placed at 1.30 m and has a 2 mm thickness 2 mm aperture tungsten pinhole mask or a 19 MURA mosaicked mask in front.

Table 7.7 Pinhole and 19 MURA mask backscatter simulation data.

	N DET	NSHI	% N PH	TIME (sec)
PINHOLE A	1759	1.68E+11	0.0000010	1.04E+07
19 MURA	2292830	1.51E+11	0.0015	1.16E+07

Exposures of the pinhole and MURA mask are shown in figure 7.45 (a) and (c) and compared against physical exposures of ~10 seconds in figures 7.45 (b) and (d). Pinhole mask simulated exposure in fig. 7.45(a) appears defined, and we can visibly distinguish the four materials as in fig. 7.45(b). On the top right we can see PLA cylinder, on the bottom left the wax cube, and on the bottom right the aluminium cube. MURA mask simulated image is not as well defined as the pinhole image, yet we can distinguish the wax on the bottom left and PLA on the top right. However, the image appear more blurred than the experimental

exposure, and in particular scatter seems to affect the image quality on the bottom.

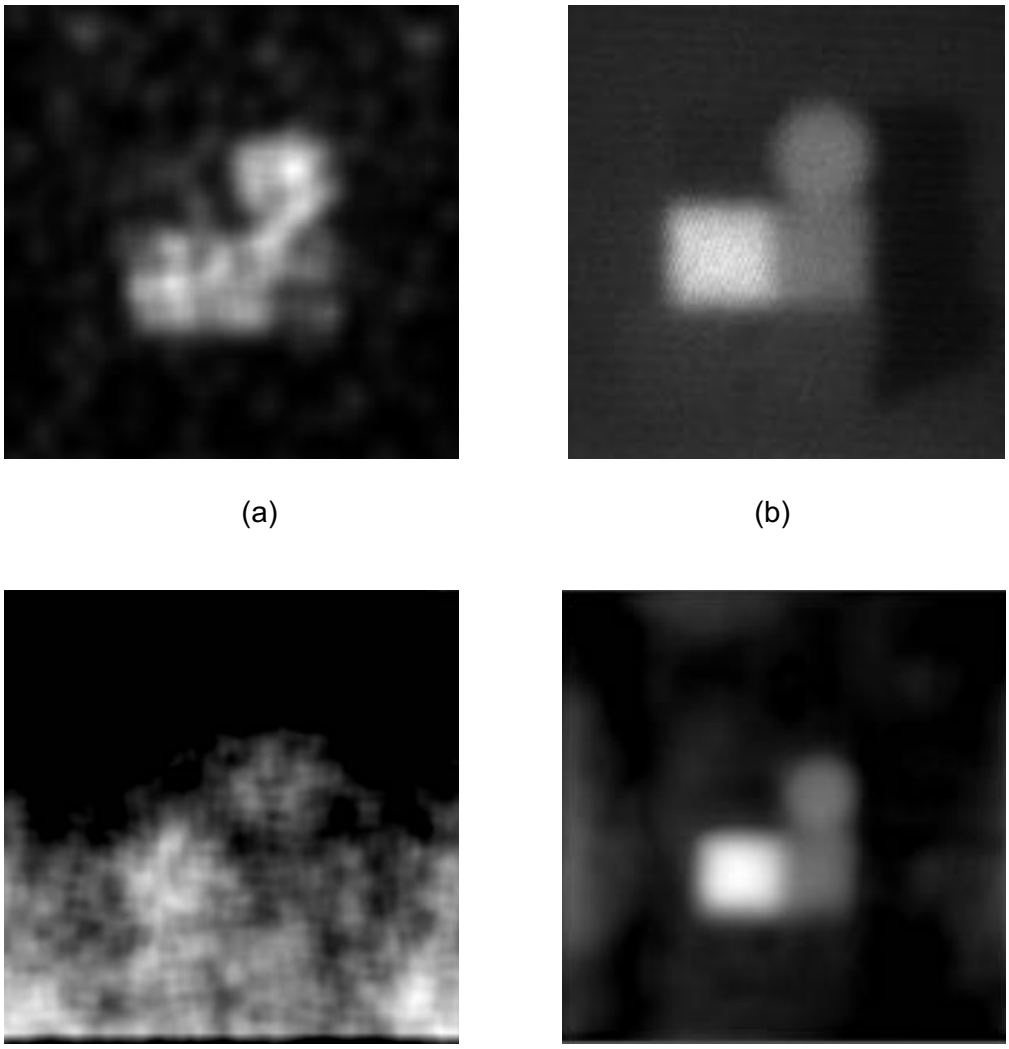

(a) (b)

(c) (d)

Figure 7.45 Pinhole simulated (a) and physical (b) exposures, and 19 MURA mosaicked simulated (c) and physical (d) exposures.

7.18 Chapter summary and critical analysis

PENELOPE has been applied to design, test and optimise pinhole optics. The long thin X-ray emitting test wire was shown to be an efficient means to characterise parameters such as resolution, field of view, contrast and noise. A MATLAB code to convert PENELOPE's output into the spatial 'brightness' across a typical pixelated imaging plate was created. With the test object and sensor modelling established, a detailed systematic exploration of pinhole mask parameters was conducted. This involved varying the pinhole aperture diameter, mask thickness and material. Finally, methods were developed to quantifiably evaluate the image characteristics of contrast, signal to noise ratio, spatial resolution and field of view. This showed that for any aperture size, tungsten/epoxy fails to give a sufficiently high contrast and signal to noise ratio until 4mm of material is used, whereas pure tungsten can achieve this at 2mm thickness. To sufficiently reduce the background and noise for small apertures (1mm), the thickness of pure tungsten must exceed 3mm whereas for larger apertures (≥2mm) the thickness may be 2mm. For W epoxy masks the material must be significantly thicker. No aperture of 3mm and greater diameter had acceptable resolution. For the system examined the best obtainable resolution a 1mm aperture must be used where only pure tungsten gives both sufficiently high contrast and low noise. Pure tungsten is the most versatile material tested and allows small pinholes to be used in thin masks. The best minimum configuration for pure tungsten was found to be 2mm thickness and 2mm aperture.

The geometry model of the camera itself needed to be upgraded to include lead lining to match the new lead lined configuration. The geometries of CAs are of course complex, although functions with PENGEOM can be used to copy, mirror and rotate elements to make modelling them achievable. Then, the algorithm (PAXI) that transforms PENELOPE's phase-space files into images as sensed by a CCD detector was parallelised and had to be adapted to accommodate very large file sizes. Further, the way that SNR and CNR is calculated by averaging signal and background over various regions of interest and excluding other

regions etc. was made more reliable and consistent across the simulated and experimental programs of work.

The sources used to 'test' various X-ray optics by simulation comprised an ideal Am-241 point-source and a thin wire X-ray emitter with a flat profile from 0 to 200 keV. The simulated Am-241 point-source was chosen to determine the point spread function in a direct and simple way, and to enable a reasonably direct comparison with practical experimental work that was performed with a 1 GBq source over a 300s exposure. The thin wire source is more useful to look at spatial resolution and observe artefacts that may arise form partial coding. All the simulations were run on the High-Performances computer for between 10^6 and 10^9 showers.

A significant milestone has been achieved in that the characteristics of CA images obtained by the dual avenues of practical experiment and simulation were found to be comparable, giving confidence in both paths. The comparison is not perfect, because although the Am-241 simulation represented the full photon flux, simulation does not include electronic noise in the detector. Hence, it is possible that the greater noise in the simulation (arising from poorer signal statistics) is compensated for by the absence of electronic noise and the fact that the simulated detector is 100% efficient whereas the real detector is not (it has some energy dependent response which has not been modelled). In terms of spatial resolution, the FWHM figures determined from simulation and physical experimentation are again comparable; however, this was not ideal when simulating a point source, because the real source is 15 mm in diameter. Thus, a second simulation was required, and the geometry of the physical source were added to the point source model. The simulation of the 15 mm Am-241 source geometry was achieved by using a higher flux. The alignment of physical and virtual experimentation (recognizing these sources of uncertainty) is a notable advance. This advance is a good platform for the future use of modelling in design and understanding, and the future use of experimentation to reveal previously unconsidered factors and to evolve physical systems and maybe even consider more factors relevant to higher TRL systems.

Simulation was also applied to various pinholes and CAs and allows a direct comparison between them free of potential experimental errors such as alignment. However, it does not yet accommodate real world factors such as electronic noise and detector energy response. The results tend to show that CAs are generally superior to pinholes in imaging the point source, but when the near field line source was imaged (arguably a more cluttered scene) the 2 mm pinhole was significantly superior in terms of SNR and with marginally better spatial resolution. The comparisons that were made were based on equivalent 'X-ray exposure times' and choices of mask design/material and pinhole diameter dominated by manufacturing characteristics and past experience. There are other ways that comparisons could be made, such as by determining the relative exposure times or pinhole diameters that are needed to give comparable SNR or spatial resolution, which depend on factors such as weight or power that may be more limiting than exposure time in some situations. The basis for comparison and the specification of criteria are not yet fully evolved but are likely to link into the optimisation of SNR and the CCD equation as discussed.

8 MODELLING AND TESTING HEXITEC DETECTOR

8.1 Chapter Outline

This chapter will explore the capabilities of the HEXITEC pixelated detector for backscatter X-ray imaging and material characterisation. HEXITEC is a suitable detector for backscatter imaging as it can capture exposures and spectra at the same time (section 8.2). HEXITEC capabilities will be described in 8.3. In this chapter, the first approach was experimental (section 8.2), and exposures were taken for different objects (sections 8.4). The detector was also modelled in PENELOPE (section 8.6) and was tested with a quadrant test object. Results from both experiment and simulations will be compared in section 8.7, and they will show not only how the approach by simulation can achieve results comparable with HEXITEC experiment, but also information on the kind of interactions which at the moment are only available by simulation (8.8, 8.9).

8.2 HEXITEC for backscatter imaging

The HEXITEC (High energy X-ray imaging technology) detector was used in the backscatter geometry, placed to the side of the existing the VJ-Technology X-ray tube [6]. The detector was appropriately shielded, and a 2mm thickness tungsten pinhole mask was placed in front for imaging the objects. The detector was also modelled and simulated through PENELOPE simulation package [51], and then compared to the experiment.

Most radiographic imaging plates only measure the spatial distribution of the total energy of photons hitting pixels of a detector. The following sections introduce a little more awareness of what can be extracted using a detector that measures the energy of an incident photon as well as its impact position. There are many processes that influence this energy, but this chapter introduces mainly two. The first is characteristic X-rays that are most often used to uniquely determine what type of metal generates photons that arrive at some location in an image, and the second is Compton scattering that usually highlights regions of certain low Z materials. The work in the following sections help introduces a small selection of the ways that an image obtained by pinhole or coded aperture can be

supplemented with material specific information, and early challenges in using an energy dispersive imaging detector such as the HEXITEC to achieve that. These results will lead also to the study of the fundamental physics of backscatter imaging by using a hemispherical detector, which will be discussed in chapter 9.

8.3 HEXITEC as energy-dispersive detector

The HEXITEC is a high-resolution energy dispersive pixelated X-ray imaging detector [35]. HEXITEC was born from a collaborative project with the aim of developing a new range of detectors for high-energy X-ray imaging [111]. The detector has a wide range of applications in medicine, security, tomography and space. It can be used in energy dispersive diffraction imaging, X-ray fluorescence imaging, K-edge enhanced imaging and has the potential to be applied for scientific and industrial inspection, security scans and medical imaging.

The detector consists of a Cadmium Telluride 80 × 80 pixels (= 20 x 20 mm) of 0.25 mm pitch sensor bump-bonded to a large area ASIC and packaged with a Field Programmable Gate Array (FPGA) for a fast data acquisition. The detector has a < 1keV FWHM energy resolution [112], and it provides, at the same time, a high-speed imaging performance. The detector is self-contained and requires only Ethernet connection to a computer and power supply. It includes a GUI to provide the calibration and operate the detector. The application is an open source and can be customised and integrated to the user own system.

The HEXITEC detector can produce images that discriminate photons across a wide energy range from approximately 5keV to 150keV. This gives it the capacity to simultaneously image the distribution of elements across a sample. It can capture spectroscopic information for each imaged pixel as a function of time [113].

8.3.1 Characteristics of the HEXITEC detector

The HEXITEC detector sensor consists of a Cadmium Telluride (CdTe) crystals. These are particularly attractive materials for X-ray imaging pixelated devices

down to 55μm geometry, and they can function with acceptable spectroscopic performance [111].

The HEXITEC detector does not offer the highest available spatial resolution potentially available because of the choice to make it small. However, the energy resolution is 0.8 keV FWHM at 59.5 keV and 1.5 keV FWHM at 141 keV [35] is comparable with the spectroscopic performances of single crystal detectors such as the Amptek X-123 (energy resolution at 122 keV <1.2 keV FWHM) (Amptek Material Analysis Division, 2016), used for measuring the X-ray spectra of the VJ-Technology source in chapter 6.5.1. The 80 × 80 pixels HEXITEC detector has instead been designed to make spectroscopic measurements on each pixel so that the position and energy of each X-ray event is recorded.

In CdTe and CdZnTe, the charge carrier cloud generated by a photon will typically diffuse and expand to a diameter of up to 100 μm when it reaches the pixels [36]. As the charge carrier cloud is a significant fraction of the pixel size (250 μm), a large fraction of single photon events will be shared between neighbouring pixels. If this charge sharing is not identified and corrected, false events and noise will be registered in the image. For this reason, the detector is equipped with a charge sharing discriminator, which is enabled from the software front panel together with the other correction algorithms, that also available offline for further investigation. The detector operates at a maximum frame rate of 10 kHz and can support a maximum global count rate of around 10 Mcps with effective charge sharing discrimination.

The spectroscopic detector was provided with two calibration files, called the ‘gradient’ and the ‘intercept’, for enabling the energy calibration from the Graphic User Interface (GUI). Both files are 80 × 80 tables, each element containing the linear calibration gradient and intercept per pixel for calculating the correspondent energies per channel. The output images were thus energy calibrated such that each pixel has a common energy axis; the calibrations for each pixel were found from their response to known gamma emission lines from the radioactive decay of Am-241 [112]. The supplied calibration, however, presented some faults. Exposures collected without calibrations showed the pixels were fully working,

while when the calibration was enabled, they appeared physically dead. For this reason, the calibration files were checked, and it was spotted some values on both tables were incorrectly given the value of zero. The calibration was amended, and new exposures were taken. More details on the calibration of the HEXITEC detector are shown in section 8.3.4.

8.3.2 How the HEXITEC can be used for material characterisation

The HEXITEC detector is suitable for material characterisation and spatial elemental mapping. This pixelated energy-dispersive X-ray detector which records the energy (colour) and intensity of the photons [114] can support the identification of materials by their characteristic X-rays generated by fluorescence or other mechanisms. There are many potential mechanisms by which materials can be identified based on energy characteristics. The HEXITEC software allows the possibility to select the energy Region of Interest (ROI) where key material signatures are located, and also to restrict the analysis to sets of pixels representing an area of the target of interest. This is a peculiarity for this spectroscopic detector, as it is possible to generate spatial and energy ROI's. In our specific case, we can detect materials such as thin wires, and explore their spectra from the backscatter geometry. Moreover, it is possible to select a group of pixels, sum their yield, and generate the spectrum of the summed yield.

8.3.3 Detector and target layout, shielding and collimation.

The HEXITEC detector was used in backscatter geometry and placed to the side of the existing VJT X-ray source (figure 8.1). The detector was shielded from radiation direct from the source or scattered from walls by lead shielding, and a collimator was used to confine the field of view to the target area. This was done to reduce noise in the system.

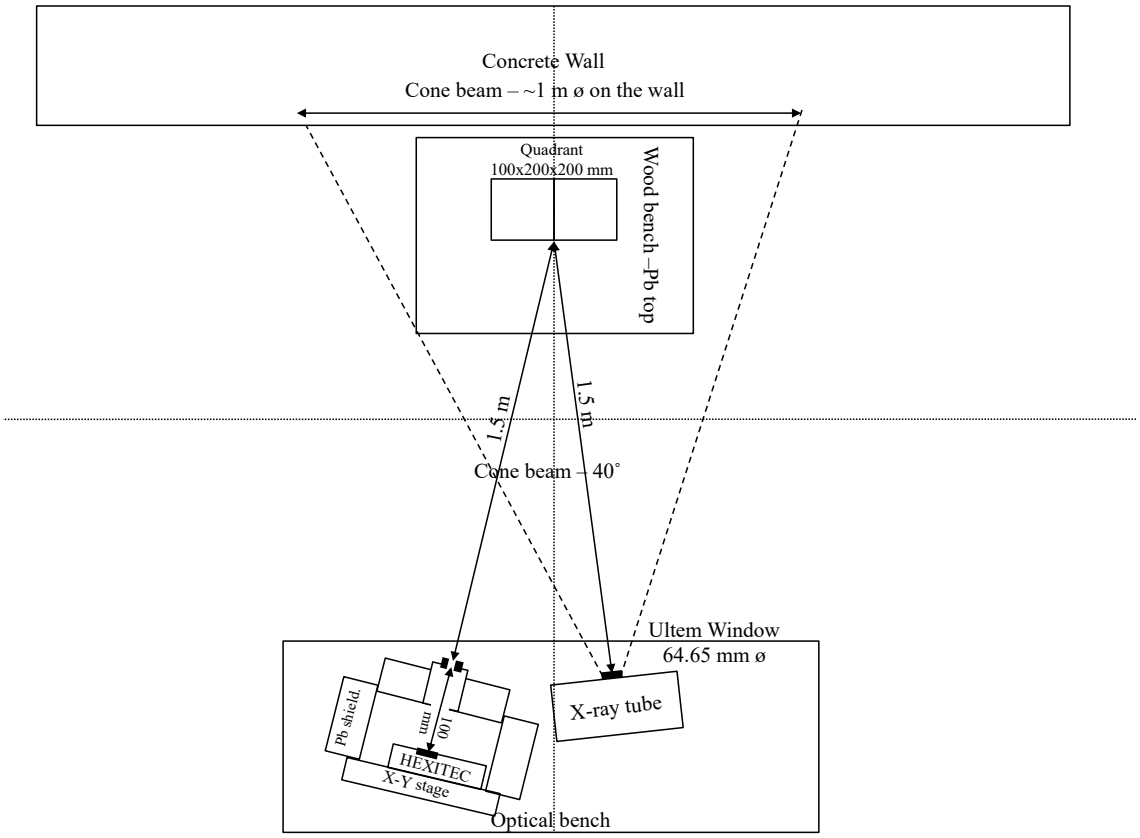

Figure 8.1 HEXITEC detector experimental setup. The detector was shielded with lead bricks and a tungsten pinhole mask placed in front.

The detector was kept near room temperature (~20˚C) and operated under an applied bias voltage of -500 V. The bias was removed and refreshed at each measurement, to avoid the Dew point temperature alert, which occurs when the temperature is below 19˚C.

The detector was held vertically by an X-Y stage that consisted of two arms orthogonally placed one on the other (see figure 8.2). As a result, it is possible to move the detector up-down/left-right using the application Autostep [115]. This software is open source and can be customised. Alongside alignment, another potential application of this stage is the capacity to increase field of view by creating a mosaic of images. However, the mosaic configuration will not be applied in this work, as the field of view was limited by a 3cm diameter lead brick collimator.

The spatial resolution of the detector is good, but its area is small, which can limit field of view at large stand-off distances. A tungsten pinhole mask (figure 8.3) was placed in front of the detector to image the objects, together with lead bricks shielding to avoid the backscatter from the walls. The pinhole mask was 20 x 20 mm, and 2 mm thickness, with 1 mm and 2 apertures. The pinhole was placed at 10 cm from the detector for the whole experiment. A 3 cm diameter aperture in a 10 cm long lead brick collimator was placed in front of the detector to reduce noise caused by X-rays hitting room walls and surrounding materials.

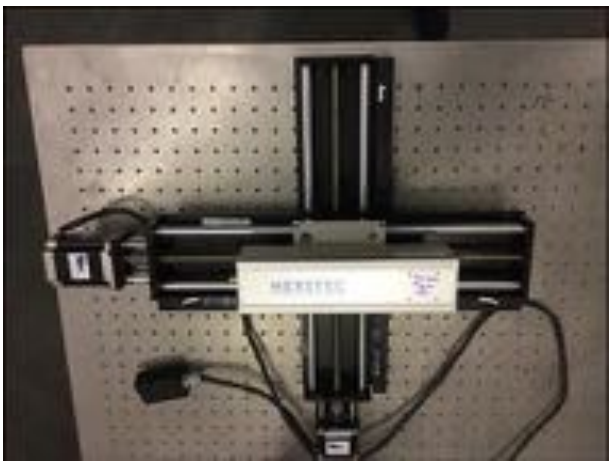

Figure 8.2 HEXITEC detector mounted on the X-Y stage. It is possible to move the HEXITEC up/down and/or left/right by driving the two motors using the Autostep application.

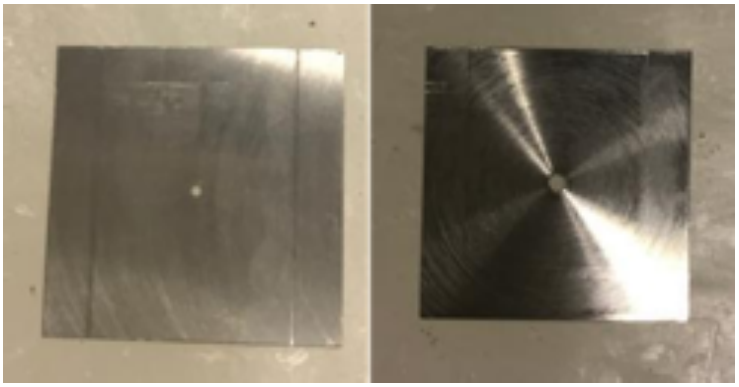

Figure 8.3 Tungsten pinhole mask 20 x 20 x 2 mm with 1 mm aperture (on the left), and 2 mm aperture (on the right).

The sample was placed at 150 cm away from the detector and the source, close to the room wall, which was covered by a lead sheet. The object was centred to the X-ray beam using the cross lasers mounted on the X-ray tube, and the detection system was aligned with the potential target X-ray backscatter by using a laser light from the centre of the target to the pinhole-HEXITEC central axis (figure 8.4).

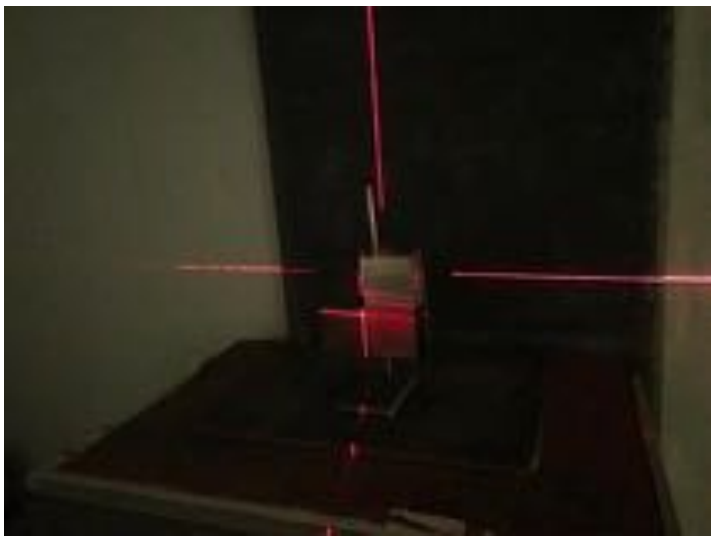

Figure 8.4 Sample alignment to the X-ray source.

As the size of each set of data captured by the HEXITEC can easily reach >5 Gb, the exposure time was kept down to 100 seconds to make the data manageable. Generally, the backscatter image and the total spectrum is collected and stored in a raw data file (.bin), in tables (.htx and .csv). The raw data can also be read offline for further analysis, producing other tables files at convenience. The .htx files can be read by MATLAB (see section 8.4). Test objects to explore materials discrimination and spatial resolution were to include a Quadrant with a tin obscurant, the Pentaliths and` a small computer cooling fan.

8.3.4 Detector energy calibration, noise and dead pixels.

During operation, each photon impact event has its energy and pixel position and the frame in which it occurs recorded. Events are processed and histogrammed in ADU units, i.e. the number of channels. The energy calibration was enabled, and the bin width was kept at 0.5 keV. This value was carefully chosen as it is

about half of the energy resolution for energies up to 59.5 keV, which corresponds to the tungsten Kα_1 energy fluorescence peak of the VJT X-ray source. The total number of bins that were occupied varied according to the voltage of the X-ray tube, the target materials and calibration settings. During the measurement, the charge sharing discrimination function was employed to correct for events where a photon interacts between neighbouring pixels and causes it to deposit fractions of the total energy between neighbouring pixels.

The HEXITEC requires two calibration files called the ‘gradient’ and the ‘intercept’ to be input into the software interface to enable the energy calibration (see figure 8.5). Both files are 80 x 80 tables, each element containing the linear calibration gradient and intercept specific to each pixel for calculating the correspondent energies per channel. The HEXITEC software interface also allows low energy event rejection bespoke to each pixel. The calibration and low energy discriminator can be changed and applied to raw data that has already been collected. The low energy threshold is set via ADU units (channels) where photons are then collected only upwards of a specific energy value. It is possible to calculate the general lower energy cut-off from the calibration files in terms of pixel averages as follows:

$$\langle \mathrm{E} \rangle_{\mathrm{th}} = \langle \mathrm{c} \rangle + \langle \mathrm{m} \rangle \cdot \mathrm{ADU} \qquad 8.1$$

where $\langle c \rangle$ is the average of the intercept table, $\langle m \rangle$ is the average of the gradient, ADU are the channels, and $\langle E \rangle_{th}$ is the correspondent energy threshold.

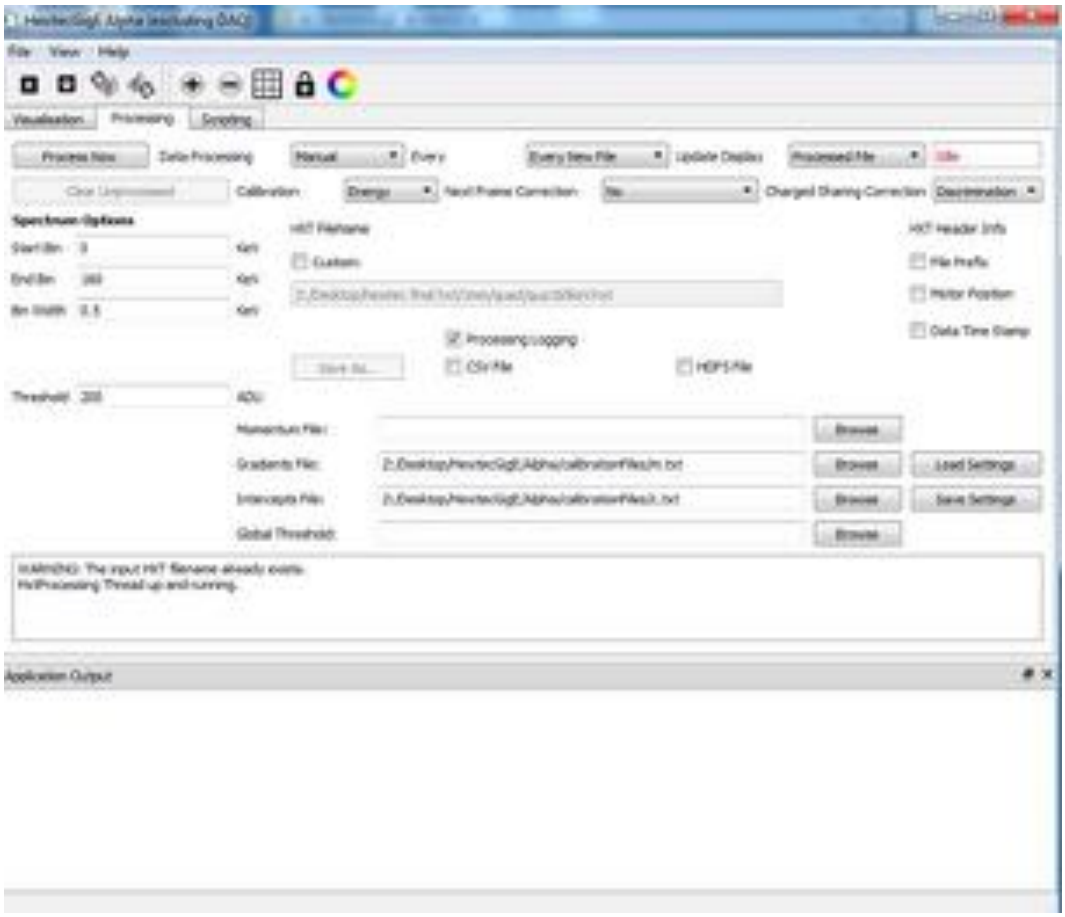

Figure 8.5 HEXITEC software processing panel. It is possible to browse the calibration files from the options ‘Gradients file’ and ‘Intercepts file’.

For the HEXITEC detector used for this work, $\langle c \rangle$ = 1.048 keV and $\langle m \rangle$ = 0.028 keV/ADU. Table 8.1 shows the calculated energy threshold from 10 to 500 ADU for the linear calibration specific to this HEXITEC detector in this work. Note that this lower energy cut off is comparable in energy to the K characteristic X-ray emissions from many light and transition elements.

Whilst taking pilot X-ray backscatter images to set up the detector, some pixels on the array edges were seen to count far more photons than they should (figure 8.6b). This detector noise appears as a broad peak at the lower energy of the spectrum of summed pixels. To avoid this issue, the lower energy threshold for pixels at the right edge of the detector was set to a very high value (10000 ADU), so that these pixels stopped counting photons. The top, bottom, and left edges, were customised with a threshold between 2000 and 3000 ADU, whilst the main

central imaging region was kept at a lower threshold value (150 ADU). This last value was suitable for detecting fluorescence peaks for various materials and corresponds to 5.28 keV energy cut-off according to the average of the individual pixel energy calibration as appears in equation 8.1 and table 8.1. It is important to note that each pixel has its own energy calibration which is the 80x80 files of gradient and intercept that were provided by the supplier of the HEXITEC detector.

Table 8.1 Energy threshold values calculated from the average of the calibration files and the ADU channels.

ADU	Energy (keV)
10	1.365
50	2.485
100	3.886
150	5.286
200	6.687
250	8.0875
300	9.488
350	10.889
400	12.289
450	13.690
500	15.090

Further, it was observed that some pixels were not counting any photons and so appear to be black in any image (figure 8.6a). It was first suspected that these were physically dead pixels. However, when the supplied calibration was removed and a default blanket calibration was applied across all pixels then the same physical experiment showed no ‘dead’ pixels. Exploring the supplied energy calibration files showed that the ‘dead’ pixels corresponded with a pixel specific calibration given as zero on both intercept and gradient tables which

artificially shuts down these detector elements. To quickly mitigate this issue whilst retaining the best of the calibration as was supplied, the calibration for the 'dead elements' was adjusted to be the same as the subsequent pixel. This quick solution was adopted as the false dead pixels were not located in the spatial region of interest ROI but on the image region representing the lead wall in the background. Also, the number of 'dead' pixels requiring adjustment was only 22 out of the 1600 element detector matrix. Further work with the HEXITEC detector would require a new calibration to ensure the right intercept and gradient tables for each pixel. Figure 8.6a shows how the adjusted calibration applies in the previously 'dead' pixels.

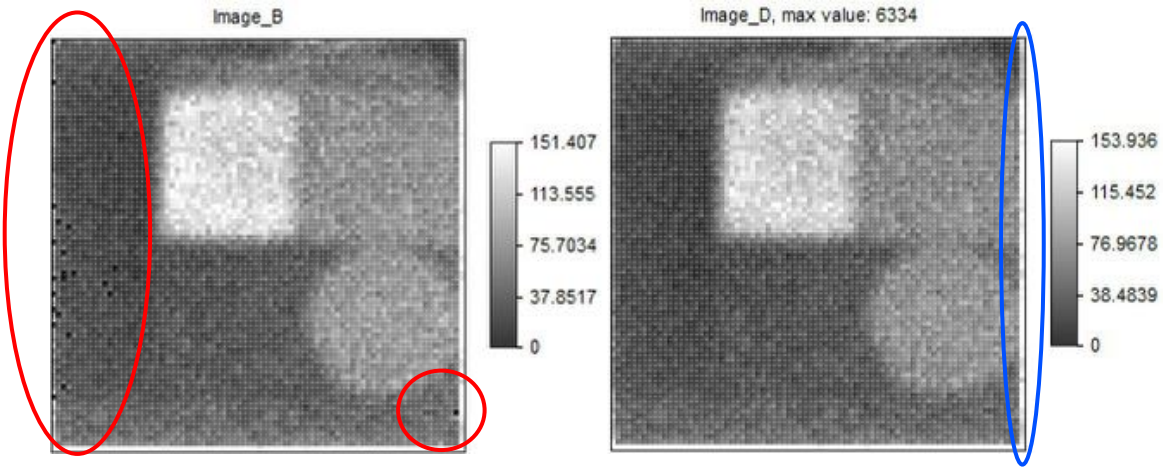

(a) (b)

Figure 8.6 (a) Backscatter images of the quadrant with the false dead pixels (red circles) and the adjusted calibration (b). The edges of the detector are in white as they are overcounting (blue circle).

8.4 Pilot use and optimisation of the HEXITEC detector

Energy dispersive backscatter imaging was piloted with the HEXITEC detector and pinhole optics for a set of test objects exposed to different energy X-rays. These preliminary experiments explore the characteristics of the HEXITEC detector and show how to mitigate some of its shortcomings and reveal

opportunities of how materials characterisation could become part of imaging capability.

8.4.1 Pilot backscatter images for system optimisation.

The test object for this phase of the work was the quadrant (figure 8.7) made up of 4 different materials:

- One 100×100×100 mm copper cube
- One 100×100×100 mm aluminium cube (in this case covered with tin)
- One 100×100×100 mm wax cube
- One 100×100 mm PLA cylinder.

A 99.9% tin sheet of 100×100×2 mm was put in front of the aluminium cube to generate high energy fluorescence energy peaks.

The quadrant plus tin was exposed to X-rays from the VJT tube at 70, 100 and 160 kV anode voltages for 100 seconds. The detector pinhole aperture was 1 mm and the HEXITEC threshold was initially set to 200 ADU (~6.69keV) for all detector pixels. The following figures show the collected image and the spectra at 70 keV (figure 8.8(a), 8.9 green), 100 keV (figure 8.8 (b), 8.9 blue), and 160 keV (figure 8.8(c), 8.9 red). These spectra are the sum of all spectra collected from each pixel of the HEXITEC detector during image capture and so represent backscatter over the whole Field of View.

Compare figure 8.7 to figure 8.8 to see that the action of the pinhole is to invert the image vertically. The pinhole action of mirroring left to right does not manifest in figure 8.8 because the detector pixels are considered left to right by looking at the HEXITEC front face i.e. along the direction the X-rays travel rather than from the detector rear view.

All the spectra show a large peak at low energy which was deduced to be a noise peak. This overlapped the lower energy characteristic X-ray emissions of materials such as copper near 8keV. The only visible fluorescence peaks in all the spectra (figure 8.9) are the tin fluorescence peaks which are $k\alpha_1$ (25.27 keV) and the $K\beta_1$ (28.49 keV).

Figure 8.7 Quadrant test object on an aluminium support and lead sheet on the back. On the top left the copper cube, on the top right the PLA cylinder, on the bottom left the wax cube and, on the bottom, right tin sheet on the aluminium cube.

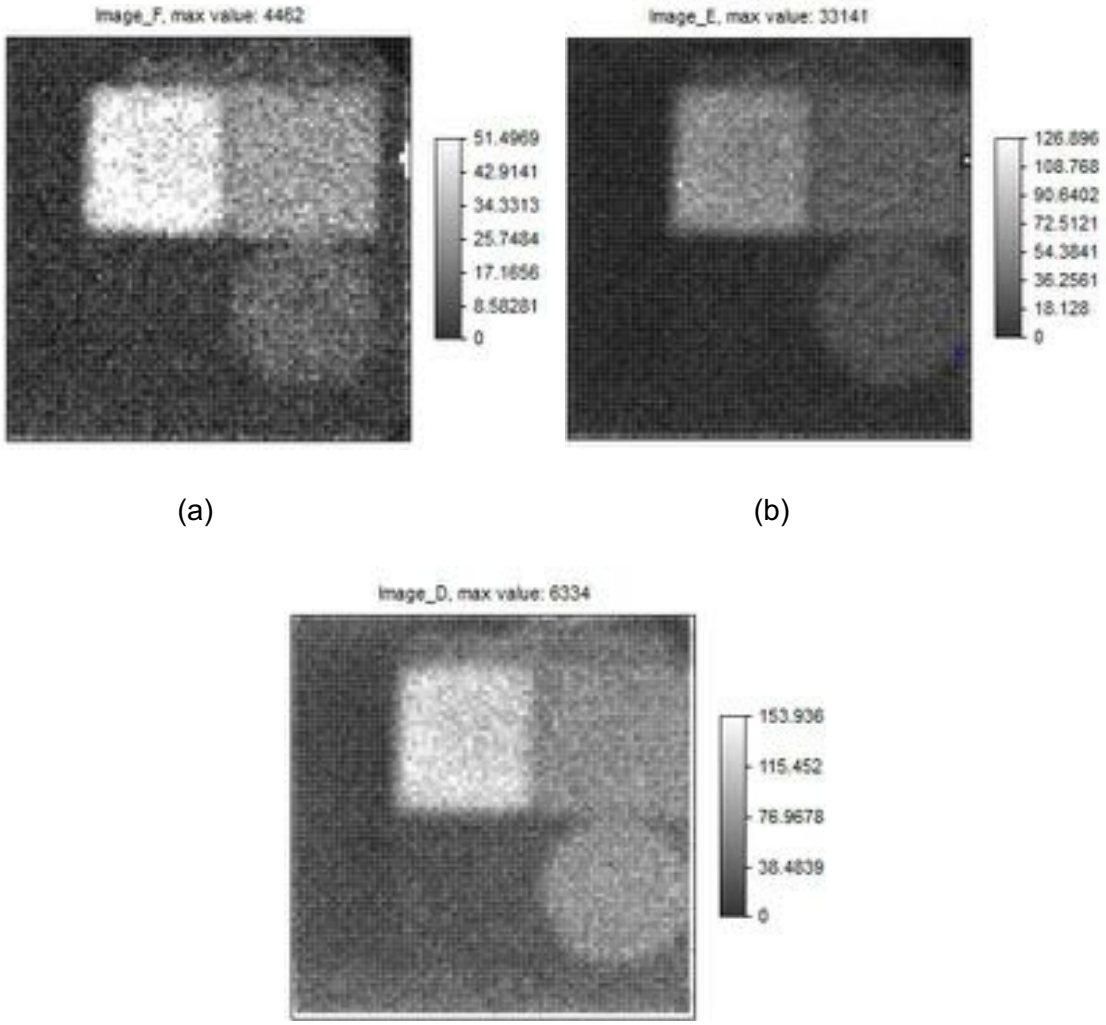

Figure 8.8 Quadrant plus tin 100 s, 1 mm aperture exposure at 70 kV, 100 kV and 160 kV tube anode voltages. Wax appears top left, tin on Al top right, copper bottom left and PLA circle bottom right.

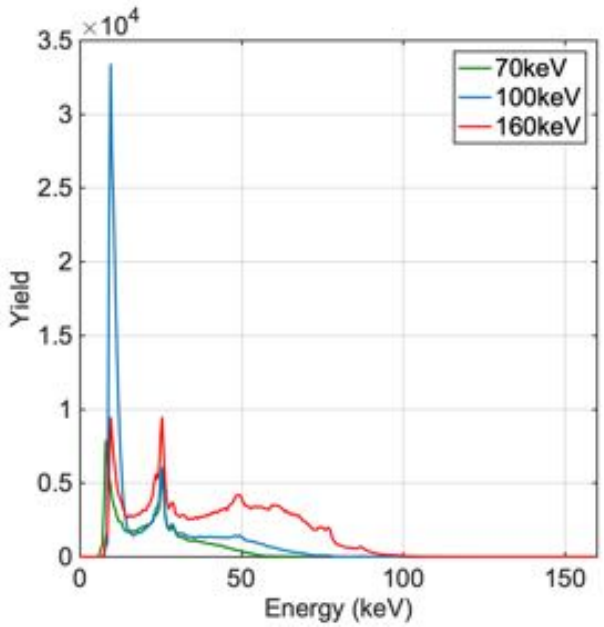

Figure 8.9 Quadrant plus tin 100 s, 1 mm aperture energy spectra at 70 kV, 100 kV and 160 kV tube anode voltage.

8.4.2 Noise mitigation by tailoring the low energy threshold

The noisy signal was found to be caused from the edges of the detector. This area appears more sensitive to either low energy radiation or electrical; noise and was found to be the source of most of the low energy noise peak. To solve this issue, a high threshold was applied on all the edges, while within the main spatial ROI it was lowered to 100 ADU (~4 keV) to become sensitive to the characteristic X-rays of more elements.

As a result, the images have black pixels at the edges, but the energy spectrum is much clearer at lower energies and low energy fluorescence peaks become visible above system noise. The exposures with the threshold applied are shown in figure 8.10, while the spectra are in figure 8.11. The spectra show the following characteristic peaks:

- copper Kα(~8.05 keV)
- lead Lα (~10.55 keV) and the Lβ (~12.61 keV)
- cadmium fluorescence peak Kα (~23.17 keV)

- tin fluorescence peaks Kα (~25.27 keV) and the Kβ (~28.49 keV)
- tellurium fluorescence peak Kα (~27.47 keV)
- tungsten Kα (~58.65 keV) and the Kβ (~67.25 keV)
- lead Kα (~74.97 keV) and the Kβ (~84.94 keV)*.

The cadmium and tellurium characteristic peaks arise from fluorescence in the HEXITEC sensor itself, while the lead fluorescence comes from the lead sheet on the wall behind the sample, and the tungsten peaks from the X-ray source.

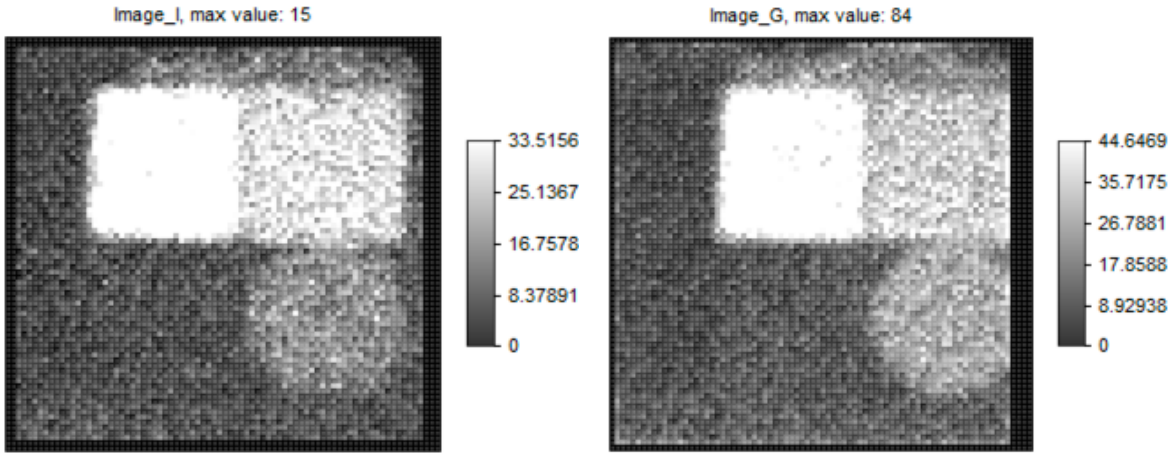

(a) (b)

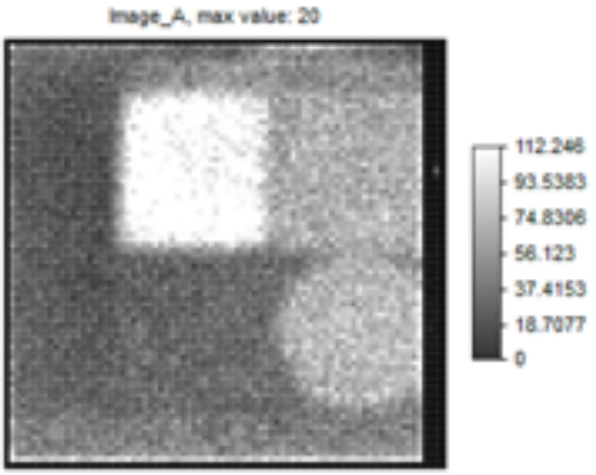

(c)

Figure 8.10 Quadrant plus tin 100 seconds exposure, 1 mm aperture, 70 kV (a), 100 kV (b) and 160 kV (c) tube anode voltage with the tailored threshold applied.

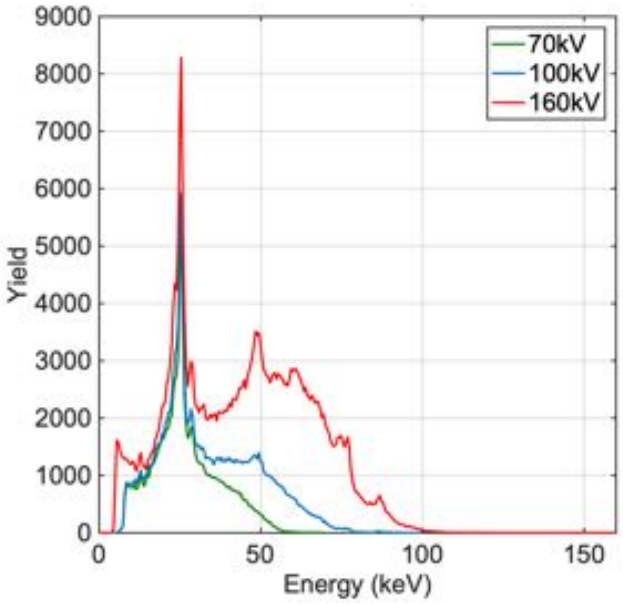

Figure 8.11 Quadrant plus tin, 100 seconds exposure, 1 mm aperture, 70 kV (green), 100 kV (blue) and 160 kV (red) tube anode voltages, with the tailored threshold applied.

8.4.3 Imaging and material characterisation with the HEXITEC detector

The tailored threshold to reduce noise and eliminate ‘dead’ pixels was used for taking exposures of a test object at 1 mm and 2 mm apertures to expose the spatial resolution. The chosen test object for this pilot was a computer vent and the exposures were taken at the highest anode voltage (160 kV). The exposures are shown in figure 8.12, and the spectra in figure 8.13. The exposure in figure 8.12 are taken at 1 mm (a) and 2 mm (b), respectively. At 1 mm, the image appears sharper, with more visible details, while the image at 2 mm is more blurred. Yet, the image at 2 mm reveals difference in grey-scale in terms of the depth of the material.

The characteristic lines from the spectra are the same as in 8.4.2(*), but with difference in yield intensity as more photons pass through the larger aperture mask.

We can again observe cadmium and tellurium characteristic peaks from the detector material, the lead from the sheet on the wall behind the sample, and the tungsten from the X-ray source.

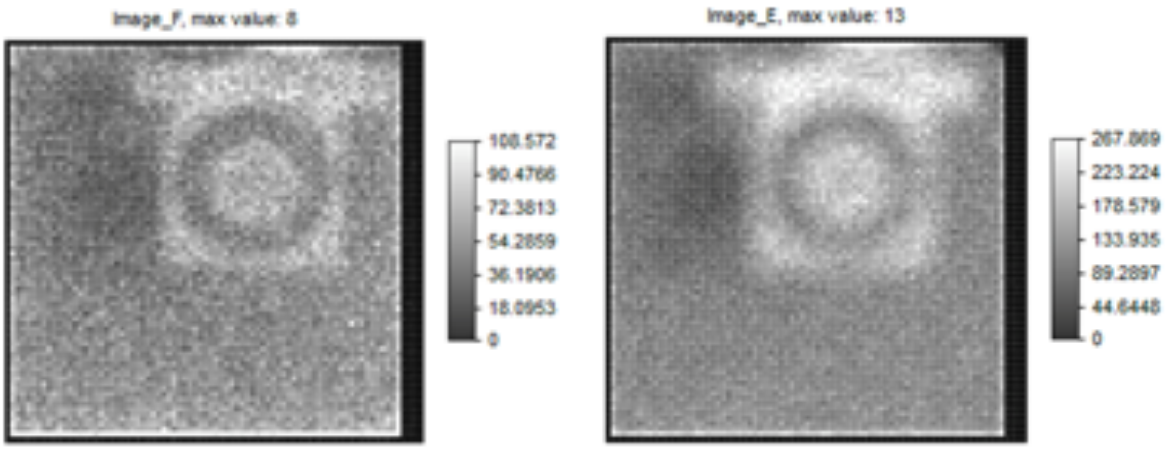

(a) (b)

Figure 8.12 Fan on aluminium support 100 sec at 1 mm (a) and 2 mm (b) aperture exposure at 160 kV and tailored threshold applied.

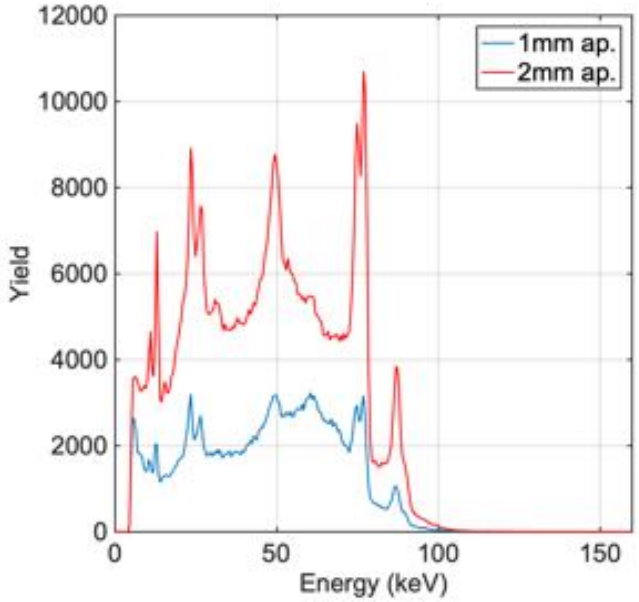

Figure 8.13 Fan on aluminium support 100 second exposure, 1 mm (blue) 2 mm (red) aperture, 160 kV and tailored threshold applied.

8.5 Unpacking HEXITEC energy data using MATLAB scripts

MATLAB [77] is a versatile data analysis tool which gives the possibility to read, modify and elaborate the images from the .htx files produced by the HEXITEC program.

From the GUI (see figure 8.5), the function to export MATLAB slices is not yet enabled as the manufacturer is still developing the code. However, the manufacturer provided three routines for reading the HEXITEC data:

- hxtV3Read.m: this routine returns the data set that is 80×80×number of bins in the spectrum – and the energy bins. This is the array of 80x80 spectra.
- hxtV3Write.m is used to put rows × columns × bins 3D array back into .hxt format
- read80x80Frame.m (Matt Wilson) returns one 80x80 frame.

Further MATLAB functions have been written at Cranfield for this work. These functions process the 80 × 80 pixels' images, the total spectrum and images and spectra of selected spatial regions of interest.

These functions were:

- htxrunning.m which calls the reading routine and create a matrix representing the pixel location of photon impacts with energy.
- htximage.m is the algorithm which creates the false colour images.
- htx1pixelspectrum.m plots the spectrum from a selected pixel.
- htxfullspectrum.m plots the spectrum of the sum yield across all pixels.
- htxROI.m shows the image of the selected ROI and plots the relative energy spectrum.

An example of the image processed in MATLAB is shown in figure 8.14. This example is the image of the quadrant plus tin at 160 kV anode voltage previously shown in fig 8.10(c), now enhanced through MATLAB. However, note the MATLAB program does not invert the image unlike the HEXITEC, the bright square is wax.

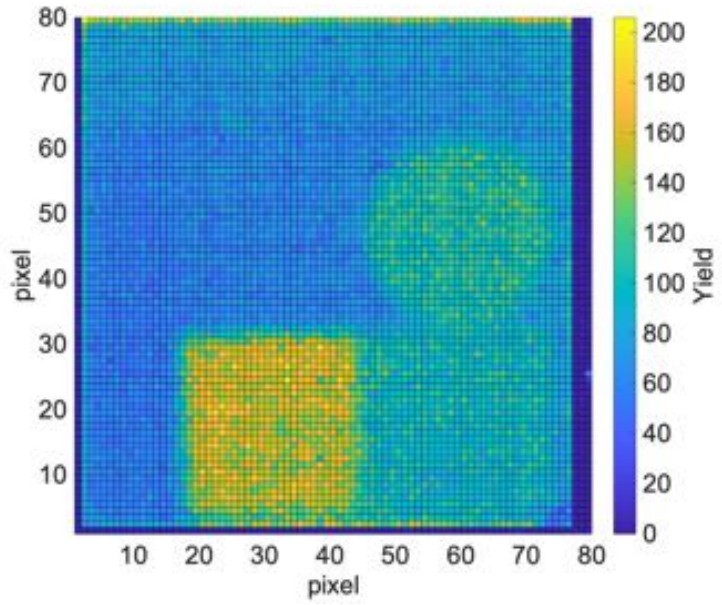

Figure 8.14 Quadrant plus tin 100 seconds exposure at 160 kV and 1 mm pinhole aperture in MATLAB.

The colour scale in figure 8.14 corresponds to the number of photons detected in each energy bin. More details can be found in section. 8.10. The whole spectrum

calculated in MATLAB is shown in figure 8.11, red line. The fluorescence characteristic peaks are tin, copper, tungsten from the X-ray source, and lead from the backing.

8.5.1 Spatial windowing / Region of Interest

Using the script htxROI.m, it is possible to select the patial region of interest, process the relative image and calculate the spectrum. Figure 8.15 shows the four areas of fig 8.14 individually representing the four locations of the four different materials. Figure 8.15 shows the sum of the spectra from all the pixels for each individual windowed area. The lower right spectrum in this figure shows the strong fluorescence of tin near 24 keV, however the other three quadrants also show a contribution from photons at this energy which is five-ten times less. The pinhole optics and good spatial resolution of the HEXITEC suggests the photons from the tin square should not directly hit these sensor elements. It is possible photons generated at the tin are then Compton scattered by wax and PLA given that the energy shift for forward scattering will be small. Other options exist, for instance that the calibration is a little inaccurate and much of the contribution comes from tellurium fluorescence in the detector itself, that is the calibration may be out of a factor of ~8% However, if the signal is scattered tin fluorescence, then there could be an impact on the potential to image certain materials with good spatial resolution in the presence of strongly scattering materials regardless of the imaging system.

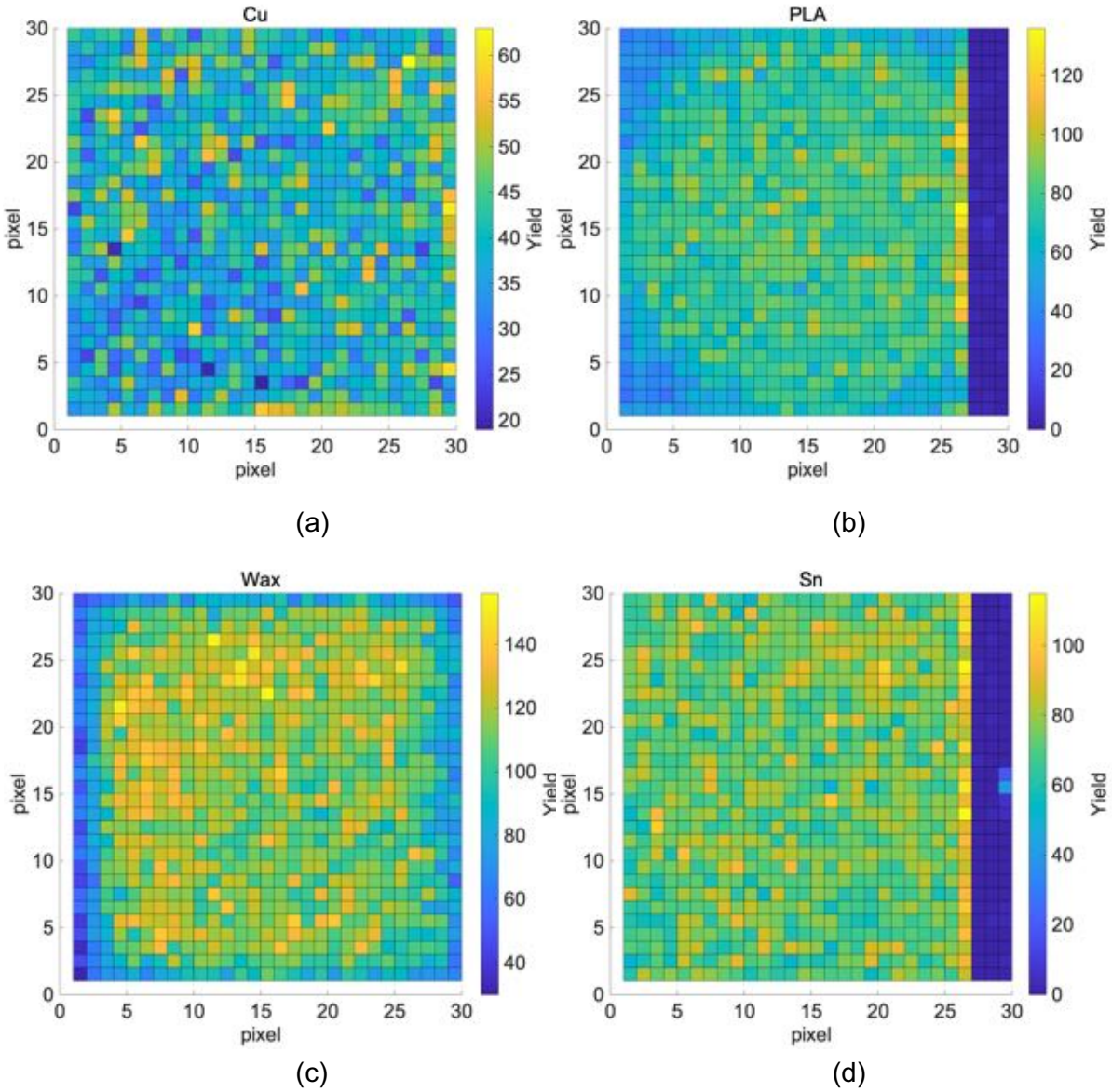

Figure 8.15 MATLAB images of four distinct regions of interest from figure 8.14. MATLAB auto-scales the brightness so each quadrant does not appear exactly the same as in figure 8.14.

Figure 8.16 shows the four spectra from each area added back together to recreate the spectrum form the whole object, the match between figure 8.17 and 8.11, red line shows deconstruction and synthesis is successful. Synthesis of these spectra opens the possibility to simulate the spectrum that would be detected by a single pixel (non-imaging detector) by adding component areas to get a feel for possible combinations of materials present in an object [116].

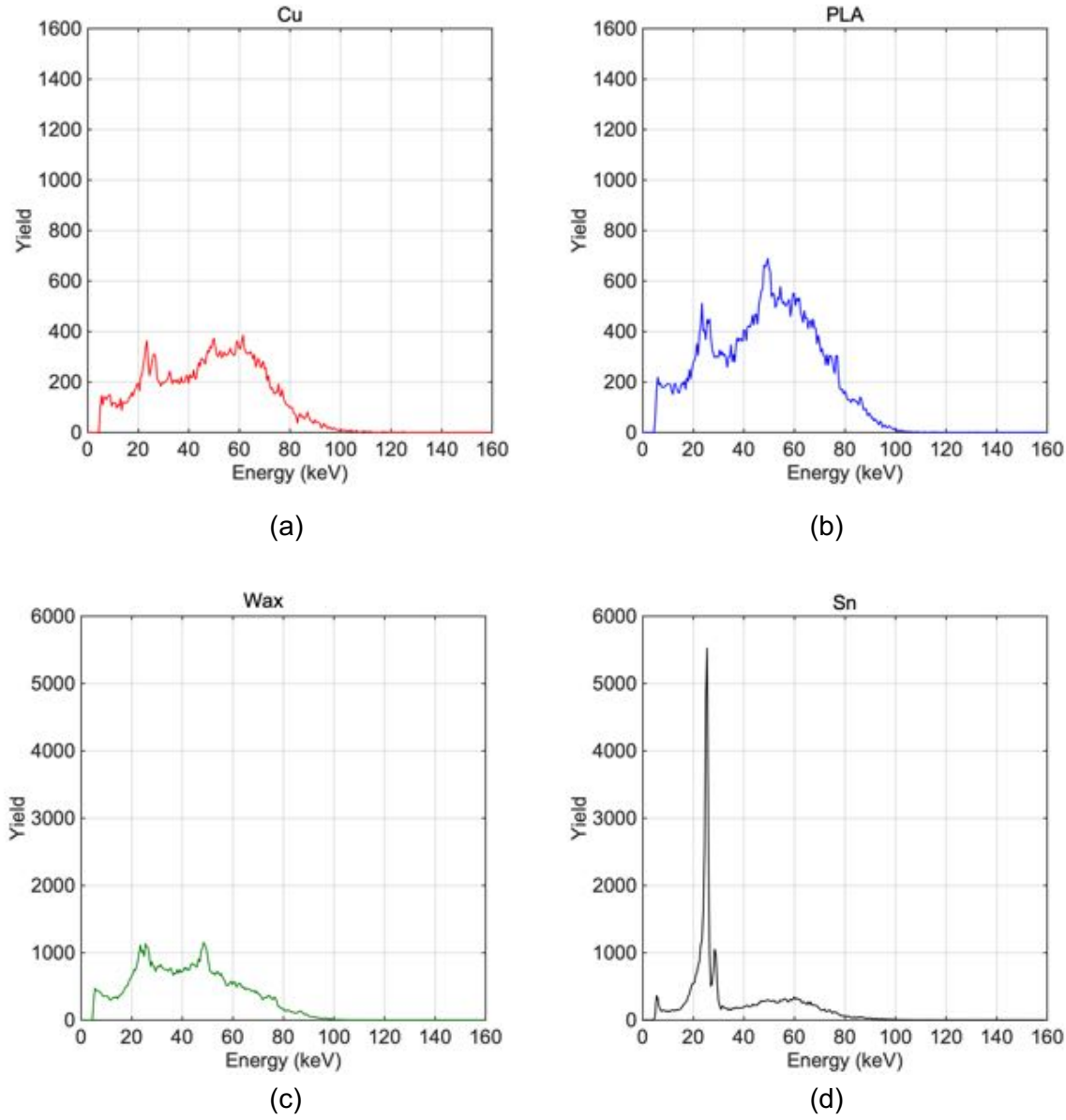

Figure 8.16 MATLAB energy spectra for the four regions of interest identified in figure 40 with different vertical axis scales. Tin's strong fluorescence at 25.27 keV is not enough for it to exceed the summed energy of Compton scattered photons off wax, and so it does not appear brighter in a conventional image. Energy windowing at 24 keV would reveal tin clearly.

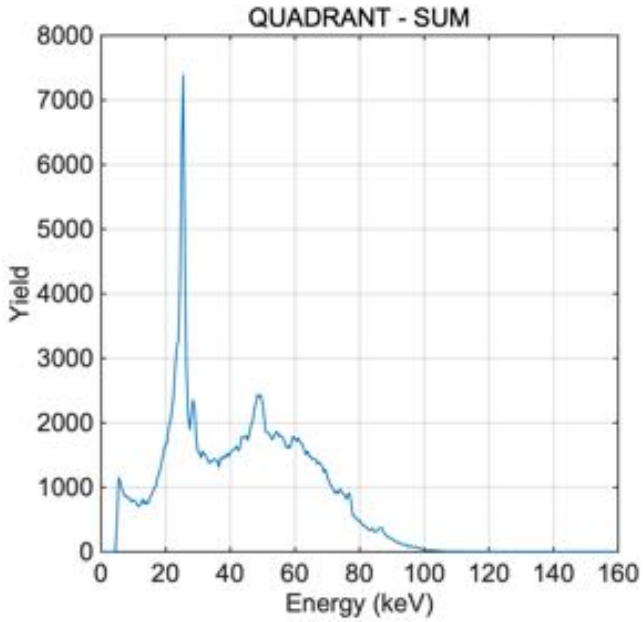

Figure 8.17 The MATLAB spectra from fig 8.16 are summed to create the spectrum visibly identical to the whole spectrum from the whole quadrant shown in figure 8.11, 160 kV, red line. This demonstrates successful deconstruction and synthesis of component spectra.

8.6 Monte Carlo modelling HEXITEC image and spectra with different materials and structures.

The simulation package PENELOPE [37] was used to simulate the HEXITEC detector for comparing the theory to the experiment. In this section, the modelled geometries and the simulation parameters will be described, and the data will be analysed and compared to the real experiment previously discussed.

8.6.1 Construction of the geometry file for the HEXITEC detector and test objects

The model was designed through the sub-tool PENGEOM [76] provided with PENELOPE package, which feeds the main radiation transport program PENMAIN [68].

The model comprises the following (see figure 8.18):

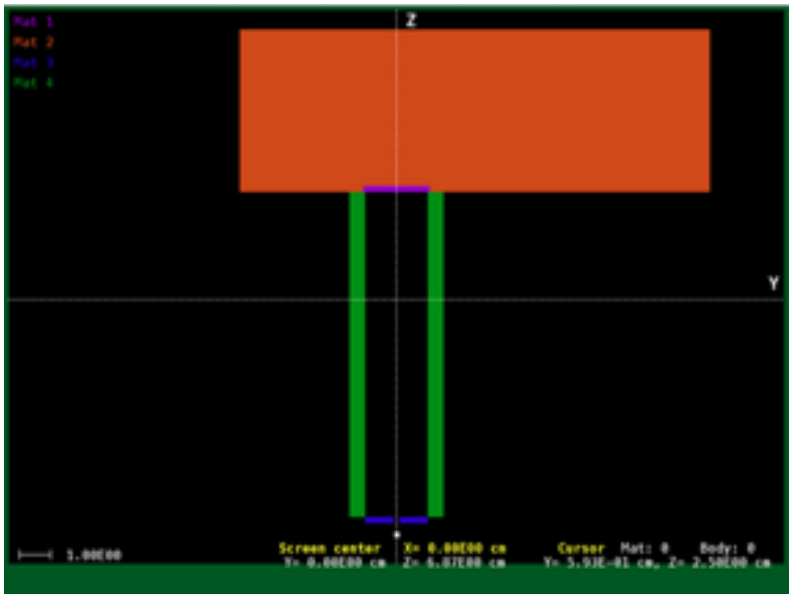

Figure 8.18 The HEXITEC detector modelled in PENELOPE through PENGEOM.

- the HEXITEC detector, made up of two pieces: the aluminium box (orange) and the 20×20×2mm CdTe detector (purple), replicating the same dimensions as the real detector
- the lead collimator (green)
- the tungsten pinhole mask (blue).

The source was placed within the hole of the pinhole mask, with a half cone aperture of 30 degrees. The X-ray energy spectrum calculated for 160 kV tungsten in previous work was used.

Two samples were simulated, the quadrant with the tin sheet, and the tin sheet on wax. The design of the experiment was adapted to the geometry in PENELOPE to speed up the simulation as it will be explained. The backscatter geometry is a low efficiency process for PENELOPE, as it requires it a high number of simulated showers (at least 10^{10}) to produce an image from the samples. First, both the quadrant and the tin on wax were simulated at 100 mm away from the pinhole mask, whilst the real position of the samples was at 1500 mm from the pinhole. At this distance, to generate the full-size image, it was necessary to reduce the size of the sample object to get a magnification equal to

1. The thicknesses of the objects were instead kept at 100 mm. However, the number of simulated showers to achieve the acceptable statistics was still high (> 10^{10}) for generating the images equivalent with the HEXITEC ones. To further decrease the simulation time, the simulations were split into bunches and each simulation run with different number of seeds. Then, the different phase-space files, generated from each simulation, were summed together.

8.6.2 Optimising PENELOPE for high backscatter simulation

The backscatter geometry is a low efficiency process for PENELOPE, as it generally requires a large number of simulated showers (at least 10^{10}) to produce an image from the sample object. In the real setup, the samples were placed far from the pinhole mask with its limited field of view. However, reproducing the real object-pinhole distance would produce a very inefficient simulation, as too few generated photons would reach the detector. Therefore, to enhance the simulation efficiency it helped to move the object closer to the detector (such that the target and detector became equidistant from the pinhole) whilst reducing the size of the object appropriately to preserve the original magnification. The source was also placed closer to preserve the correct angles of the real setup, and the energy spectrum from previous work calculated at 160 keV was used.

Modularisation is a useful concept across this programme of work. Currently only the X-ray source is modularized i.e. the transport of electrons in the tungsten target is not modelled, instead three X-ray output files from previous long-run electron transport simulations at 70 kV, 100 kV and 160 kV are input modules for target exposures. The quadrant and its individual components are studied under various energy exposures whilst the X-ray optics (i.e. pinhole) changes only once and the detector is unchanged.

Even undertaking a level of modularisation and modifying the geometry for speed, the number of simulated showers to achieve the acceptable statistics was still high (10^{10}). Therefore, it was necessary to split the simulations into bunches and run each simulation separately with a new seed number and sum the phase-space files.

8.6.3 Practical aspects of running on the High-Performance Computer

The generic input file was then replicated for the use in the High-Performances Computer (HPC) servers at Cranfield. Simulating the backscatter geometry requires at least 10^{10} simulated showers to produce an image. It is necessary to change the seed number in each bunch so that each bunch is independent from the previous bunch. If the seed number was not changed then the 'random numbers' of the Monte-Carlo simulation would in fact be the same as although they are complex they are not actually random. This would render each bunch dependent not independent and so the statistics of the combined parallel run would be inferior to the long serial run that it is trying to represent.

The generic input file was then replicated for the use in the High- Performances Computer (HPC) servers at Cranfield, and each run was simulated separately.

8.6.4 Running on HPC

The input file was replicated using the MATLAB application PENMAT, which included the Musiman routine (Hermida-Lupez, 2016). Musiman routine comprises three different MATLAB scripts: one creates the number of runs by replacing the number of seeds in the input file and editing the number of simulated showers, the second one recalls PENMAIN within MATLAB framework and runs the simulations with the different number of seeds, and the last one sums the results. The package was included in PENMAT and has the functions to create, run and sum the results from the simulations locally on a MATLAB equipped desktop. In this case, the function used for preparing the files for the HPC was the one which reads and edits the input file and generates the desired number of simulations all with different seed numbers. Our allocation on the Cranfield HPC was 8 cores and so 8 simulations were exported and run simultaneously on the HPC. However, the Musiman routine does not contain functions to add the output phase-space files, so PENMAT capability was extended to combine the phase-space files from different simulation into a summed phase-space file for post

processing. The phase-space file was analysed through the MATLAB PAXI algorithm. PAXI was used to calculate the image brightness as integrated energy and determine the energy spectra.

Typically, to simulate 2.5E10 showers (i.e. 2.5E10 source photons and all their subsequent interactions, products, and paths) on a 2.6 GHz quad-core Intel Core i7, 256 SSD laptop took almost 3 days (~68 hours) without splitting the simulations in more runs. This represents an average simulation speed of 1.03E+05 showers/sec. On the HPC, each core generally runs the simulations 55% slower (~81 hours) than the laptop. To reduce the computational time, the total number of simulated showers was split into 8 smaller runs, each simulating up to 3.125E09 photons. To complete all 8 runs, it took about 10 hours, but it then took a little further time to manually sum the eight phase-space files together.

8.7 Simulating backscatter from the quadrant as detected by the HEXITEC

The quadrant is made up of 4 different materials:

- One 12 × 12 × 100 mm copper cube (green)
- One 12 × 12 × 2 mm tin cube (red)
- One 12 × 12 × 100 mm wax cube (blue)
- One 12 × 100 mm PLA cylinder (cyan).

The frontal area of these samples (approx. 12 × 12 mm^2) is less than that of the real object to preserve the same images as the real object, because the simulated object has been brought closer to the detector to speed up the simulation. The simulated geometries and orientation are shown in figure 8.19. The integrated energy for each pixel element was calculated for this sample and is shown in figure 8.20a, which is compared to the exposure from experiment figure 8.20b. The action of PENELOPE and MATLAB is to create the image as seen from the back of the sensor looking through the sensor towards consistently along the z axis toward the test object. This means the action of the pinhole is to invert the image and mirror it left to right. It can be seen in fig. 8.20(a) that PLA and wax

(top right and bottom left respectively) give the highest detector response, followed by the thin foil of tin, and thick cube of copper (top left), which is the lowest. This reflects how Compton backscatter imaging is capable of detecting well low-Z materials such as plastic and paraffin. The low number of electrons within the atom structure combined with the 10 cm thickness allow more Compton scatter than high Z materials as more photons can escape from the materials and scatter back. On the other hand, although copper scatter cross section is much higher than plastic and paraffin, its thickness and atomic structure cause self-absorption of the scatter photons, hence it is less or almost no visible. This is consistent with the experimental HEXITEC image shown in fig. 8.20(b) for 160 kV X-rays, remembering the experimental image is upside down.

The spectrum for the whole quadrant from simulation is shown in figure 8.21 in red and is compared with experiment (in blue) at 160 kV. The characteristic features in the spectrum are the copper fluorescence peaks $K\alpha_1$ (~8 keV) the tin fluorescence peaks $K\alpha_1$ (~25.04 keV) and the $K\beta_1$ (~28.49 keV). The experimental spectrum does not see the copper fluorescence peak because it was experimentally necessary to have a low energy cut-off to reduce detector noise. The experimental spectrum also shows larger background over the energy range consistent with the ‘bump’ artefact discussed in previous chapters. The difference is that this simulation did not include the general room features such as walls and lead backing.

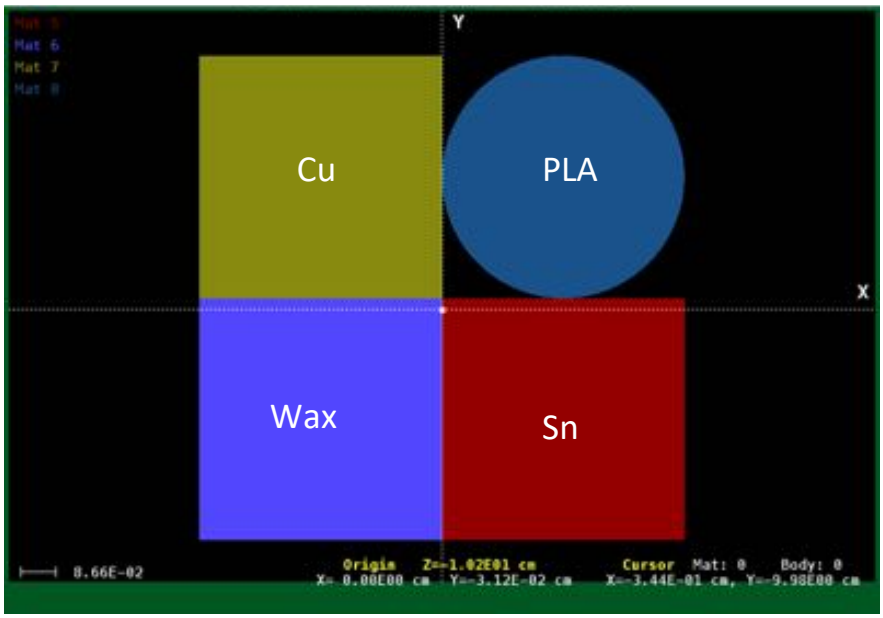

Figure 8.19 Geometry of the quadrant sample. The different colours correspond to the different simulated materials, red for the tin cube, blue for wax, green for copper and blue-teal for the PLA.

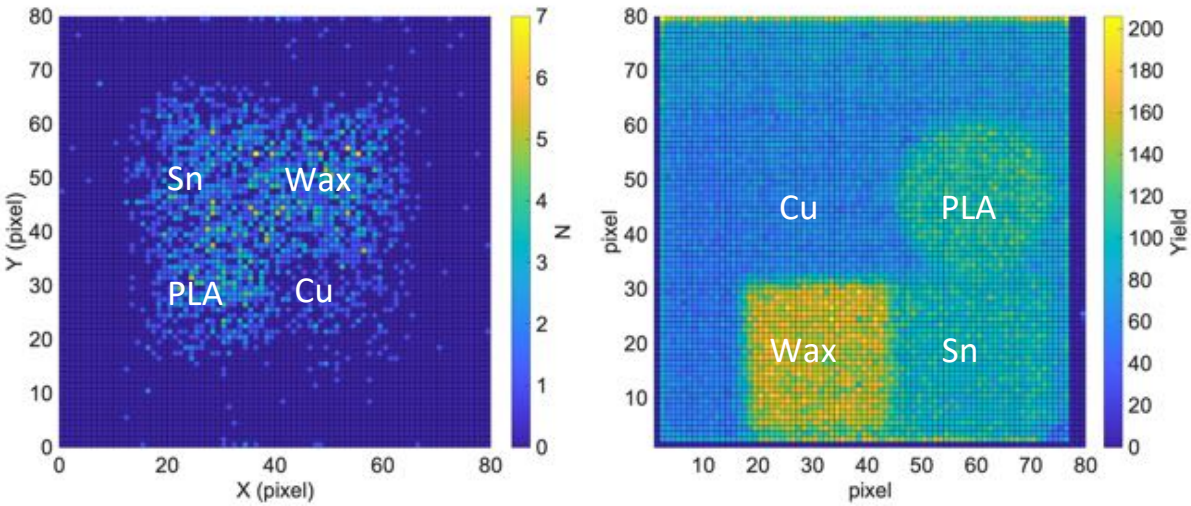

(a) (b)

Figure 8.20 Simulated quadrant plus tin integrated energy for number of simulated showers equal to 2.5E10 (a). (b) is the quadrant from HEXITEC pinhole mask exposure.

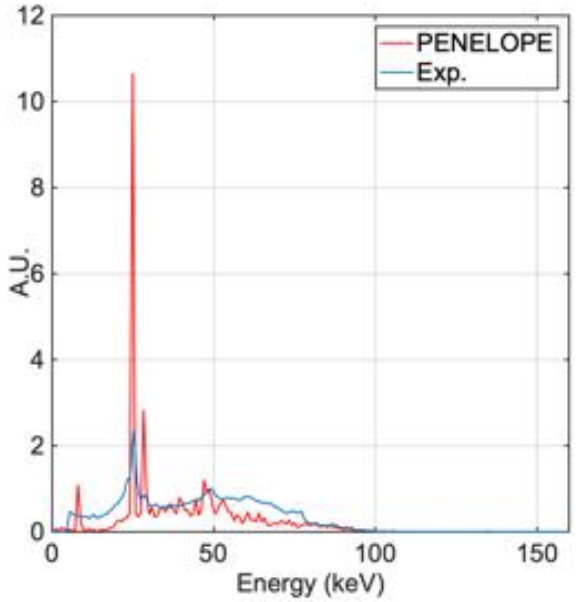

Figure 8.21 Simulated quadrant plus tin spectrum at 180˚ backscatter. The characteristic peaks are: copper at 8.05 keV (K_α), tin at 25.27 keV (K_α) and 28.49 keV (K_β), tungsten at 48.81 keV (Compton), 59.32 (K_α), lead at 74.97 keV (K_α).

8.7.1 Simulating backscatter from the single objects of the quadrant as detected by the HEXITEC

To confirm that the different objects do indeed appear inverted and mirrored in the images (post PENELOPE and PAXI image processing) in the same positions as shown in figure 8.19 the simulations were repeated with 3 of the 4 objects removed. The other reason was to generate spectra from each individual material separately. Figure 8.22a shows the modelled image for just tin, noting that auto-scaling of the false colour deceives that tin would be nearly as bright as wax. Fig 8.23a shows the tin energy spectrum which has similarly strong fluorescence as the experimental figure 8.16(d) lower right. Figure 8.22b shows the modelled image to just wax, and figure 8.23b the energy spectrum form just wax. The wax spectrum shows a strong Compton scattering peak at 48.84 keV. Figures 8.22c and 8.23c shows the round image and spectrum from PLA, it is notable that the spectrum does not show such a strong Compton backscatter as wax as a significant portion of PLA is oxygen rather than carbon. Figures 8.22d and 8.23d

show the image and spectrum from copper, there is little elastic or inelastic scatter and what fluorescence exists is at a low energy, near the bottom of what was possible to easily detect with the HEXITEC in initial experiments.

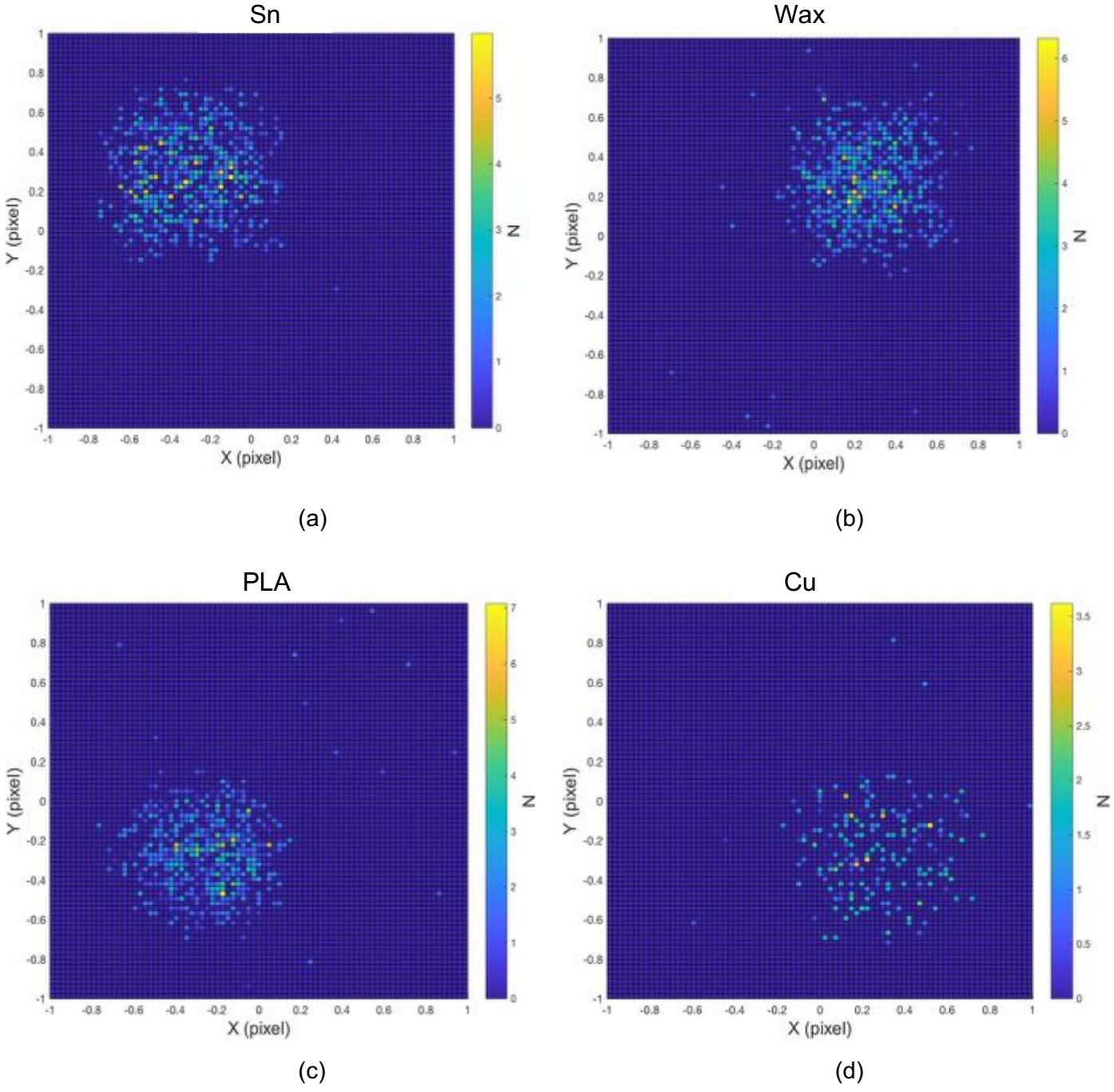

Figure 8.22 MATLAB energy spectra for the four regions of interest identified in figure 40 with different vertical axis scales. Tin's strong fluorescence at 25.27 keV is not enough for it to exceed the summed energy of Compton scattered photons off wax, and so it

does not appear brighter in a conventional image. Energy windowing at 24 keV would reveal tin clearly.

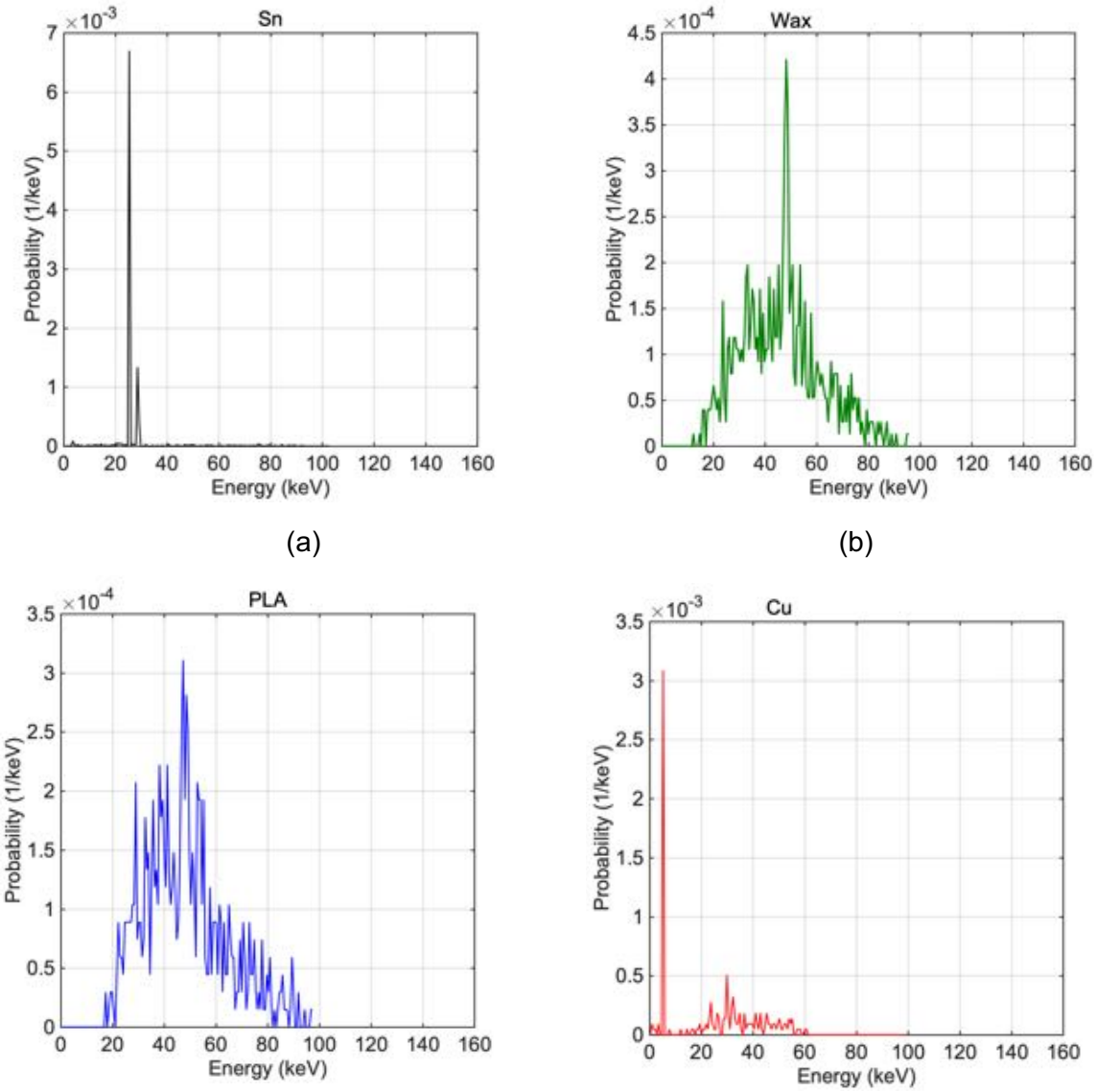

Figure 8.23 MATLAB energy spectra for the four regions of interest identified in figure 40 with different vertical axis scales. Tin's strong fluorescence at 25.27 keV is not enough for it to exceed the summed energy of Compton scattered photons off wax, and so it does not appear brighter in a conventional image. Energy windowing at 24 keV would reveal tin clearly.

8.8 Energy windowing to discriminate materials from a whole quadrant simulated image

The whole quadrant images direct from the HEXITEC in figure 8.10c, or given false colour with MATLAB in fig. 8.20b or the ideal (not in terms of counting statistics) produced by PENELOPE in fig 8.20a are able in themselves to uniquely identify a material. For example, figures 8.10c and 8.20b both show tin and PLA as being very similar in ‘brightness’ at 160 kV exposure. However, the energy dispersive capacity of detectors can be used.

The following figures are based purely on PENELOPE simulations, and are derived from figure 8.20(a) which in itself shows little ability to discriminate materials. Figure 8.24 shows how energy windowing between 7.5 and 9.5 keV exposes copper. Figure 8.25 shows how energy windowing around tin kα energies emphasizes the tin portion of the quadrant. However, photons of this same energy could reach the detector from areas of wax and PLA either from tin fluorescence then scattered by wax/PLA, or from high energy source photons Compton scattered by PLA/wax without any interaction with tin. Both processes may exist, and their effect can be seen over the PLA and wax areas of fig 8.25. PENELOPE has the capacity to isolate the processes that give rise to a detected photon as will be discussed later. Figure 8.26 shows photons detected above 30 keV which is above the kα and Kβ fluorescence of tin. The likely processes given rise to this scatter is just Compton scattering of photons from the source, hence fig 8.26 exposes the lower Z materials with high carbon concentration that have higher inelastic scattering cross sections.

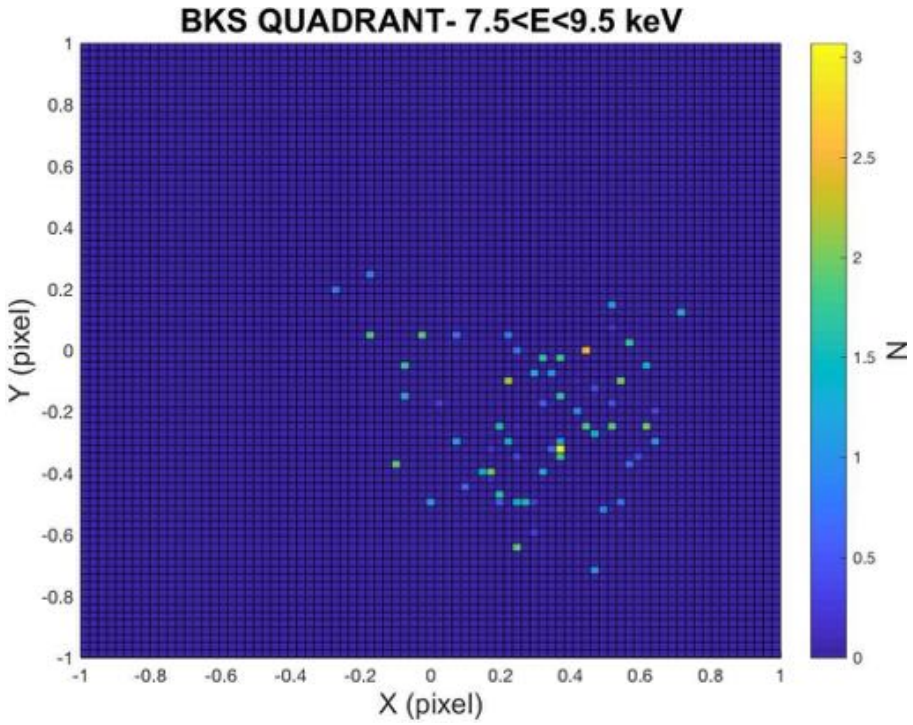

Figure 8.24 Simulated image emphasising the copper in the quadrant.

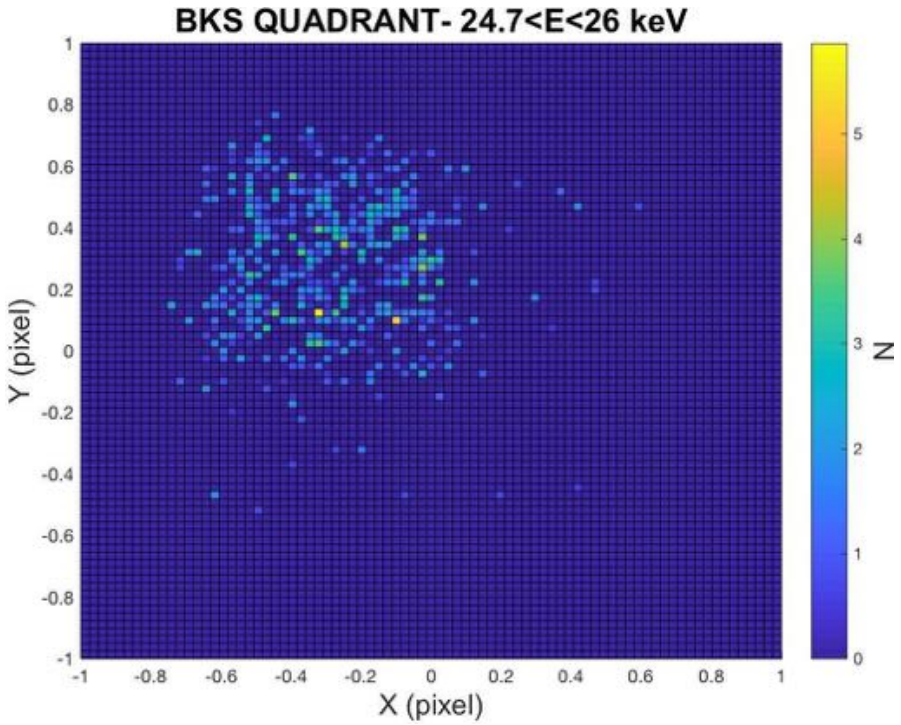

Figure 8.25 Simulated image emphasising the tin in the quadrant.

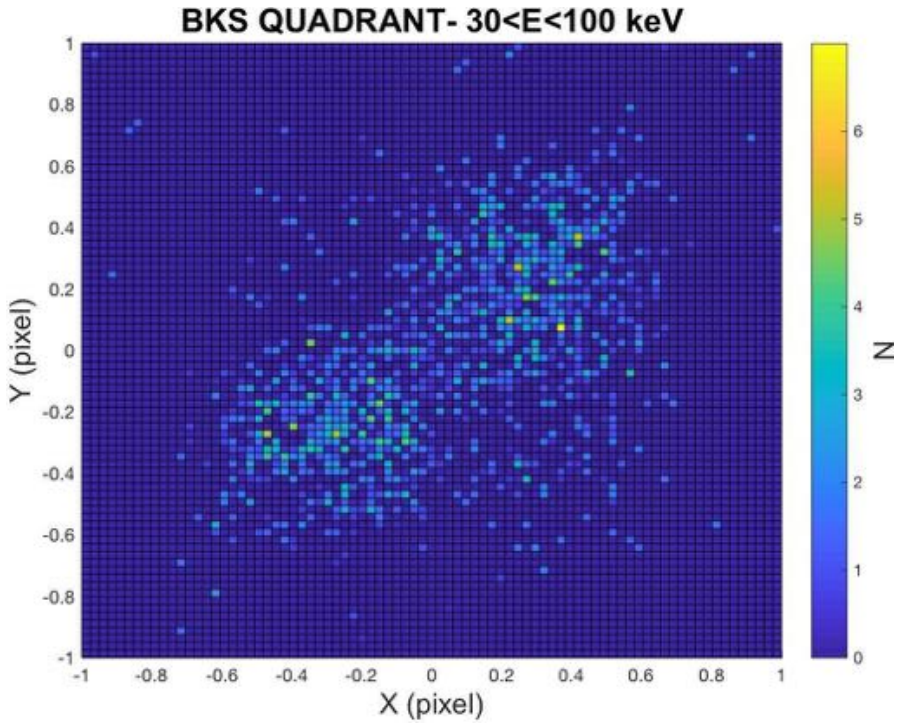

Figure 8.26 Simulated image emphasising materials with large Compton scatter cross sections.

8.9 Determining the origin of image features through particle tracking

Some of the features in the images of the previous section arise form processes that cannot be separated by energy in this experimental arrangement. However, by knowing the nature of the process that gives rise to a feature it may be possible to predict experimental configurations that can separate the features and hence discriminate materials. For example, there are multiple phenomena that can give rise to the signal coming from wax/PLA shown in fig 8.25 whilst energy windowing around the k lines of tin. Fig 8.27 shows PENELOPE particle tracking only the photons generated by fluorescence and isolates the metals in this case. Fig 8.28 shows PENELOPE tracking only photons that have exhibited inelastic (Compton) scatter which is very similar to fig 8.26. The similarity between the figures 8.26 and 8.28 gives confidence that if energy windowing were used to look at this configuration then the signals from wax and PLA are dominated by Compton scatter.

Figure 8.29 shows a PENELOPE simulated image of photons that have been both generated by fluorescence and also then scattered in the test object. The fact that very few photons generated by tin fluorescence have also undergone secondary scattering in other parts of the target before being detected gives confidence that there is no fundamental reason associated with the radiation transport in the test object that would undermine good spatial mapping of tin. Had there been a very high rate of fluorescent photons been scattered throughout the target then it would forecast that it may not fundamentally be possible to attribute their spatial origin by imaging.

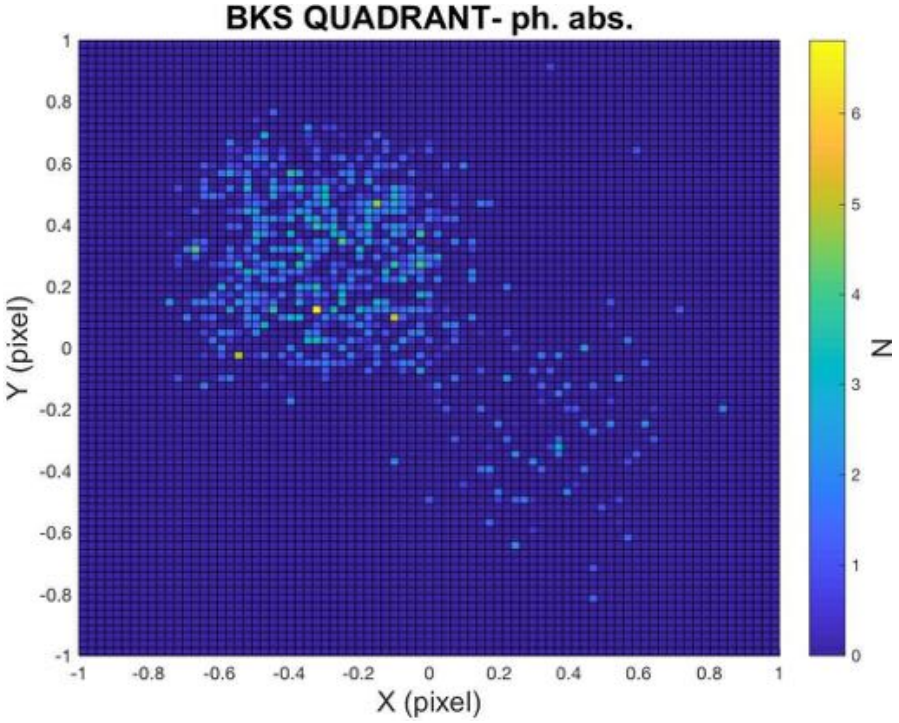

Figure 8.27 PENELOPE simulation revealing only photons generated by fluorescence.

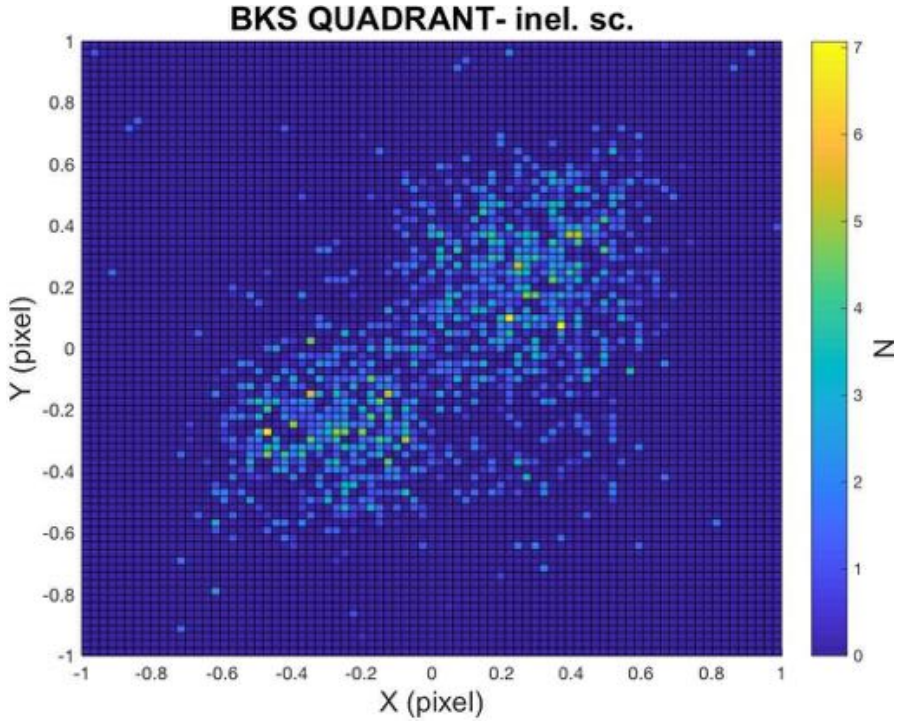

Figure 8.28 PENELOPE simulation revealing only photons undergoing Compton scatter.

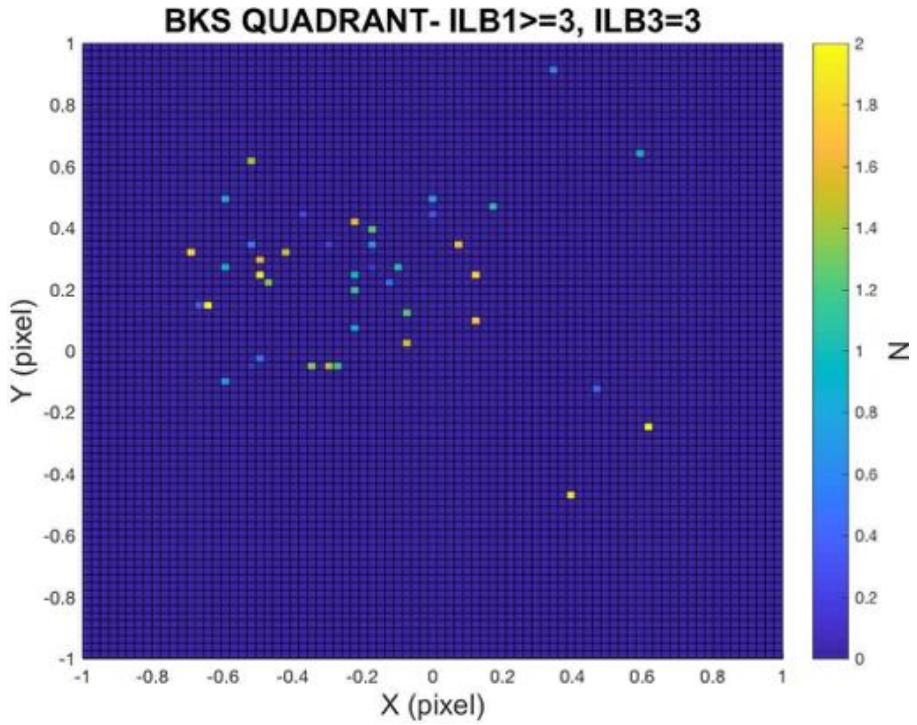

Figure 8.29 PENELOPE simulation revealing photons that have been generated by fluorescence and have also been scattered in the test object.

8.10 Chapter summary and critical analysis

The HEXITEC detector has the capability to generate X-ray images with energy discrimination and so has the potential to characterise the material of structures in the image. This ability to highlight or suppress specific materials or families of materials can be used to indicate features of specific relevance to an operator or suppress irrelevant clutter that could otherwise distract them. The detector is small, light and has low power consumption and its 80×80 array appears to be a fair match to the resolution available with pinholes of an aperture large enough to collect spectra in a reasonable time. However, the software associated with the HEXITEC does require considerable operator knowledge. The calibration file for the HEXITEC that was used should be revisited to account for dead pixels, and would benefit from being re-calibrated in energy if we are to be accurate and confident in the attribution of close spaced characteristic X-ray lines. The energy resolution is believed to be about 1keV and is not as good as some single element CdTe detectors. The low energy noise associated with the detector could make it difficult to look for some elements by their characteristic X-ray lines, but realistically this may need to be considered alongside the depth into a structure that we would wish to analyse, as such low energy X-rays may not be able to escape from deep inside a structure anyway. The detector proved capable of being a simple ‘brightness’ imager for a range of different structures and generated spectra that showed the same major features as we expected from PENELOPE simulation. This work also showed how spatial regions of interest could be isolated in an image to interrogate the material in a specific area of the structure. External MATLAB routines created in this work proved useful in enhancing the raw image output by the HEXITEC.

It is important to note that the HEXITEC does not work in the same way as a conventional CCD camera. A CCD camera looks at the entire energy deposited into each pixel and does not fundamentally discriminate between energy deposition achieved by a single high energy photon that is absorbed, and numerous low energy ones depositing the same overall energy. The HEXITEC identifies the energy of each photon hitting a pixel before allocating it to an energy bin, where the ‘brightness’ of raw HEXITEC images are believed to be

constructed from the numbers of photons hitting each pixel rather than total deposited energy. This means that there is a fundamental difference in modelling the ‘brightness’ of a CCD (requiring integrated energy per pixel) and the HEXITEC (requiring only the number of photons hitting per pixel). This distinction was made in the MATLAB routines used to post process the files generated by PENELOPE. Figures 8.10 a-c show how the raw relative brightness from tin and PLA change with incident photon energy, affording the possibility of highlighting or suppressing certain materials in conventional CCD imaging by changing incident photon energy.

Modelling backscatter from a range of test objects using PENELOPE was challenging in terms of computational time, and the structure was adapted to hasten the simulation; it was brought closer to the detector but shrunk in size. Such adaptions can cause errors, care had to be taken to ensure other aspects such as X- ray scattering angle were not accidentally misrepresented.

The potential to separate and recombine the spectral components from different areas of interest in a HEXITEC image was shown, which demonstrates the potential to identify components and simulate a structure respectively.

PENELOPE was used to replicate images of the quadrant test object and spectra. The simulations showed the key sharp features of characteristic lines and Compton scattering of the tungsten source line, but the general broad background was low, probably due to the lack of room features and lead backing incorporated into the simulation which was focussed on the quadrant.

The images from PENELOPE were sliced in terms of energy windowing to forecast one of the ways how an optimised HEXITEC could attribute different areas of an image to different materials. Further, particle tracking in PENELOPE was used to identify the physical processes that gave rise to photons hitting different areas of the detector. This is important, as it reveals the different physical processes that give rise to photons that hit the detector with identical energies, which it is unlikely that experimentation could ever discriminate. This information helps guide what would need to be changed (such as source energies or angles)

in order to enhance or suppress different processes that may discriminate materials.

9 EXPLORING THE FUNDAMENTAL PHYSICS OF X-RAY BACKSCATTER IMAGING BY SIMULATION WITH A HEMISPHERICAL DETECTOR

9.1 Chapter Outline

This chapter will explore the fundamental physics of X-ray backscatter imaging by simulation with a hemispherical detector. The chapter consists in two parts. In the first half the model of the hemispherical detector will be described, and concepts such as image brightness, relative yield and energy-probability as angular distributions will be defined. The approach validation by extracting the differential cross section from PENELOPE phase-space file with PAXI algorithm and comparison to the NIST database will be explored. The second part of the chapter will be focused on the data analysis. Image brightness as integrated energy and relative yield as function of angular distribution and of sample material will be explored. The materials were simulated at different thicknesses, rotated and with a barrier on top. Each configuration was simulated at 25 keV, 150 keV and 500 keV.

9.2 Exploring the fundamental physics of X-ray backscatter imaging by simulation with a hemispherical detector

Images of concealed objects can be formed using X-rays backscattered from an object and can have operational benefits over conventional transmission radiography. Image quality depends on the intensity and energy of the backscattered X-rays, which in turn depends not only on the material properties of the structure of interest, but also on the incident beam energy, the overlying layers and the camera angle. Although data and analytical expressions exist for various X-ray interaction cross-sections, the situation is not as simple as considering cross sections for attenuation, fluorescence, Compton and elastic scatter, and the mass and atomic densities individually. The final ‘through barrier’ image of complex multi-material structures arises from a complex sequence of

these radiation interactions that is difficult to predict. Consequently, it becomes necessary to explore the system as a whole.

The unique and innovative theoretical hemispherical detector concept was devised to efficiently and rapidly evaluate and understand how the various materials, X-ray interactions and geometric parameters combine to form an image. Such a detector would be difficult to fabricate in reality and would not reveal the level of detail that can be achieved by modelling with an established Monte-Carlo radiation transport code. PENELOPE [37] was used to model the hemispherical detector and then study the fundamental physics underpinning X-ray backscatter imaging. The use of simulation (as opposed to experiment) uniquely allows us to isolate different interactions occurring within the material thickness and attribute them to properties of the image. This allows us to explore which phenomena are dominant for different materials at various scattering angles and incident energies, with the ultimate purpose of predicting the configuration of an X-ray imaging system that would best expose the required features of a test object. These properties may be image brightness or contrast for standard imaging or yield at a particular photon energy for elemental characterisation purposes.

9.3 Rationale and modelling of a hemispherical detector

The detector was designed to be a hemisphere in order to most efficiently capture all backscatter data. It was designed using the PENGEOM [76] sub-tool and is shown in figure 9.1 in 2D (a) and 3D (b). The hemispherical detector is computationally efficient for three reasons. Firstly, there is no tracking of inbound photons that is wasted as with 2π solid angle all backscattered photons are recorded. Secondly, any erroneous preconception of what scattering angles are most useful to study is avoided; the data leads the investigation and emerging trends can be fully investigated at a later date without further simulation. Thirdly, the counting statistics for a given backscattering angle (relative to the incoming beam) will be high (compared to a point detector) as the ‘scattering’ is independent of azimuthal angle for layered materials, and an annulus on the hemispherical detector is easily examined. Finally, this simulated detector is not

subject to the compromises between spatial resolution and energy resolution that exist in real world detectors. In physical studies, most single element energy dispersive detectors have areas of tens of square millimetres, which generally means that even the limited fraction of scattered data they can collect will actually be an average over a significant range of scattering angles. The situation is improved with energy dispersive pixelated detectors such as HEXITEC [35], but they still cannot match the coverage and resolution available by studying this theoretically.

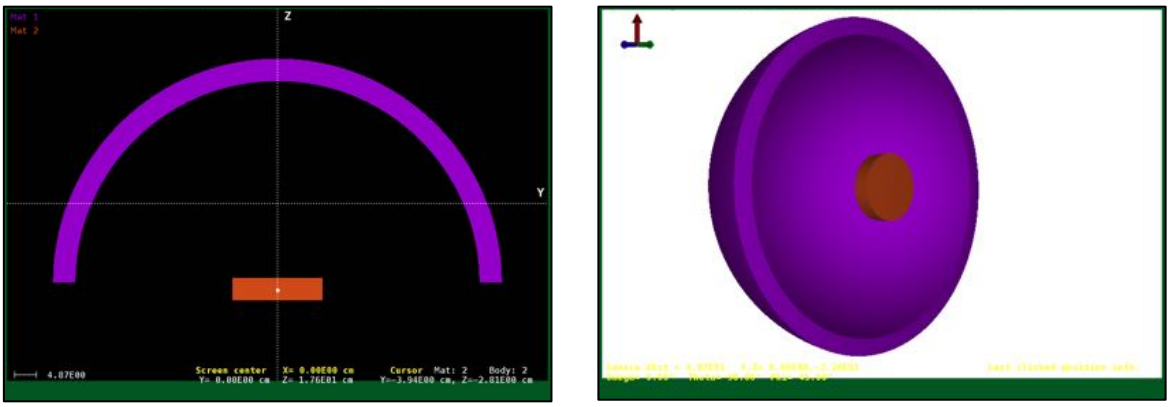

Figure 9.1 Hemispherical detector model in purple and the target material in orange are shown in two dimensions and three dimensions in (a) and (b). Target materials were carbon, copper, manganese dioxide, aluminium, iron and lead simulated with different configurations.

The output of the modelled detector is captured in the phase-space file, which contains information about the history of X-ray interactions in the concealed object and overlying layers. Using PAXI algorithm for data analysis, relevant data at different angles and from different scattering interactions can be extracted from the phase-space data and isolated. Information concerning different scattering mechanisms obtained from the simulation in the phase-space data cannot ordinarily be obtained by detectors used experimentally. The simulations therefore enable additional understanding of fundamental principles.

9.4 Target materials studied with the hemispherical detector

The target materials of carbon, copper, manganese dioxide, lead, aluminium and iron were chosen to span organic and electronic materials. Carbon is found in polymers such as insulation and plastic components, copper is the material for wires, manganese dioxide for batteries, and lead, aluminium and iron for shielding. Carbon and lead are commonly studied materials associated with radiation and so are good candidates for benchmarking the output against cross sections from the NIST XCOM database [105]. In this part of the study, the materials were set to be relatively thin 1 mm (as opposed to thick materials, at least 10 times thicker) to give little X-ray attenuation (especially for carbon) making a benchmark against published scattering data feasible. Further configurations include 45˚ rotated thin materials, 5 cm thick materials (50 times thicker than 1 mm thick material) and finally 5 cm thick material with a 2 mm thick barrier on top. In the final configuration, carbon, copper and manganese dioxide were the target thick materials, while aluminium and iron were the barrier layer.

9.5 The X-ray source

Each material was studied with mono-energetic mono-directional beams incident initially normal to the sample surface. The energies were low (25 keV), intermediate (150 keV) and high (500 keV) to reflect what is possible in small X-ray systems. Although mono-energetic mono-directional beams are not physically practical, this allows a precise and clear preliminary study of the effects of energy and detection angle. Whilst an X-ray thermionic source such as the VJT X-ray tube explored in chapter 6 would be more practical, the X-ray tube would not be capable to uniquely expose features which could be characteristic of the target materials only. A thermionic X-ray source generates spectra as an energy-distribution with its own characteristic features. Those features cannot easily be separated from the signature of the materials, and they may hide information which could be fundamental for material discrimination.

9.6 Hemispherical detector for backscatter X-ray imaging of concealed materials

Data were stored on the phase-space file by PENMAIN, the executive program responsible for running the simulation process. The phase-space file contains all the information about radiation impacting the inner surface of the hemispherical detector, including position, direction, energy and nature, along with some history of the interactions giving rise to that radiation. Data on particular interactions are stored in the ILB parameters (see chapter 5-9). The parameter ILB3 is of particular interest, as it can separate the Compton scatter that is likely to dominate image brightness for low Z materials, from fluorescence that may have utility in elemental characterisation particularly for high Z materials. This information is fundamental for exploring the physics and trends underpinning backscatter imaging.

Although PENELOPE can produce the data, it is necessary to use an external program to analyse them, and MATLAB computational environment was chosen for the purpose (see chapter 5). PAXI [5] algorithm was written in MATLAB to read, process and select the data from the phase-space file. The phase-space file records the spatial distribution of the detected particles as Euler angles, and among them, the azimuthal angle. This information was used to determine the angular distribution as the elevation of each annulus calculated by clustering the azimuthal angle. For this section of work, PAXI algorithm was customised to allow a particular backscattering angle to be manually selected, which can be seen as an annulus in figure 9.2. Each annulus was set to have an angular ‘width’ of 2.5°. The brightness, yield and cross section derived from annuli between 0 and 90° backscattering are presented for different materials and beam conditions in the later sections.

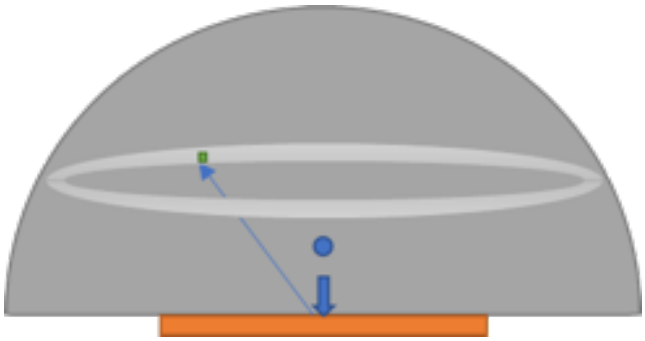

Figure 9.2 Hemispherical detector annulus from the azimuthal angle recorded on the phase-space file. Annuli were calculated from 0 to 90 degrees. Each annulus is 2.5 degrees thick.

9.7 Image 'brightness' as a function of angle

The 'brightness' of an image is not given by the numbers of photons hitting a pixel, nor the energy of a photon hitting a pixel, but instead by the total energy of all photons hitting that pixel within the capture time frame a digital system or film exposure. Hence, to study brightness, the phase-space file was processed by calculating the integrated energy defined as 'the sum of the energy of photons in the phase-space file correlated with the positions and areas of the pixels of the real detector'. In formula:

$$I(E) = \sum_{i,j} E_{i,j} \cdot pixel(x_i, y_j) \qquad 9.1$$

Integrated Energy (I(E)) is useful for describing the brightness and sensitivity in CCD imagers and other non-energy dispersive detectors. Energy dispersive detectors have utility in elemental mapping.

To illustrate (using a broader annulus than in later sections), the IE for inelastic scattering from MnO_2 for 25keV incident X-rays is shown in figure 9.3. The scattering over all angles is shown as top projection (XY) in (a) and side projection (YZ) in fig (c). The backscattering ~20° is shown in figures (b) (d), (where 0° would be scatter back along the incoming beam). The I(E) of Compton scatter can be compared with the I(E) of that calculated when fluorescence occurs over all

angles in figure 9.4. Figure (a) is the top projection and side projection is in fig (c). The fluorescence at ~20° is shown in figures (b)(d).

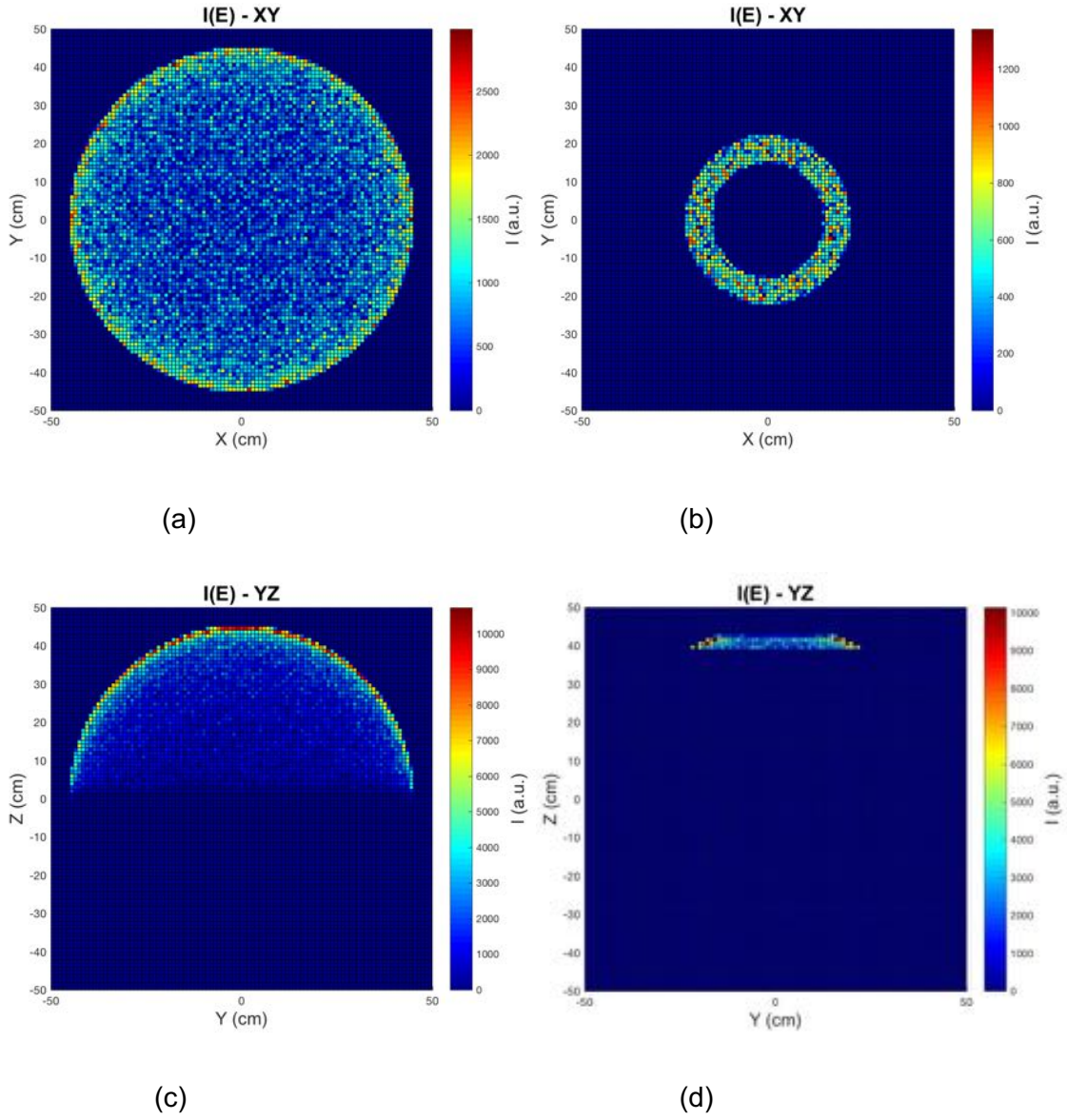

(a) (b)

(c) (d)

Figure 9.3 Detected inelastic scatter relative brightness in terms of I(E) at all angles in XY (a) and I(E) YZ (c) projections for MnO_2 at 25keV. From the psf-file it is possible to select the annulus from the azimuthal angle (b) (d).

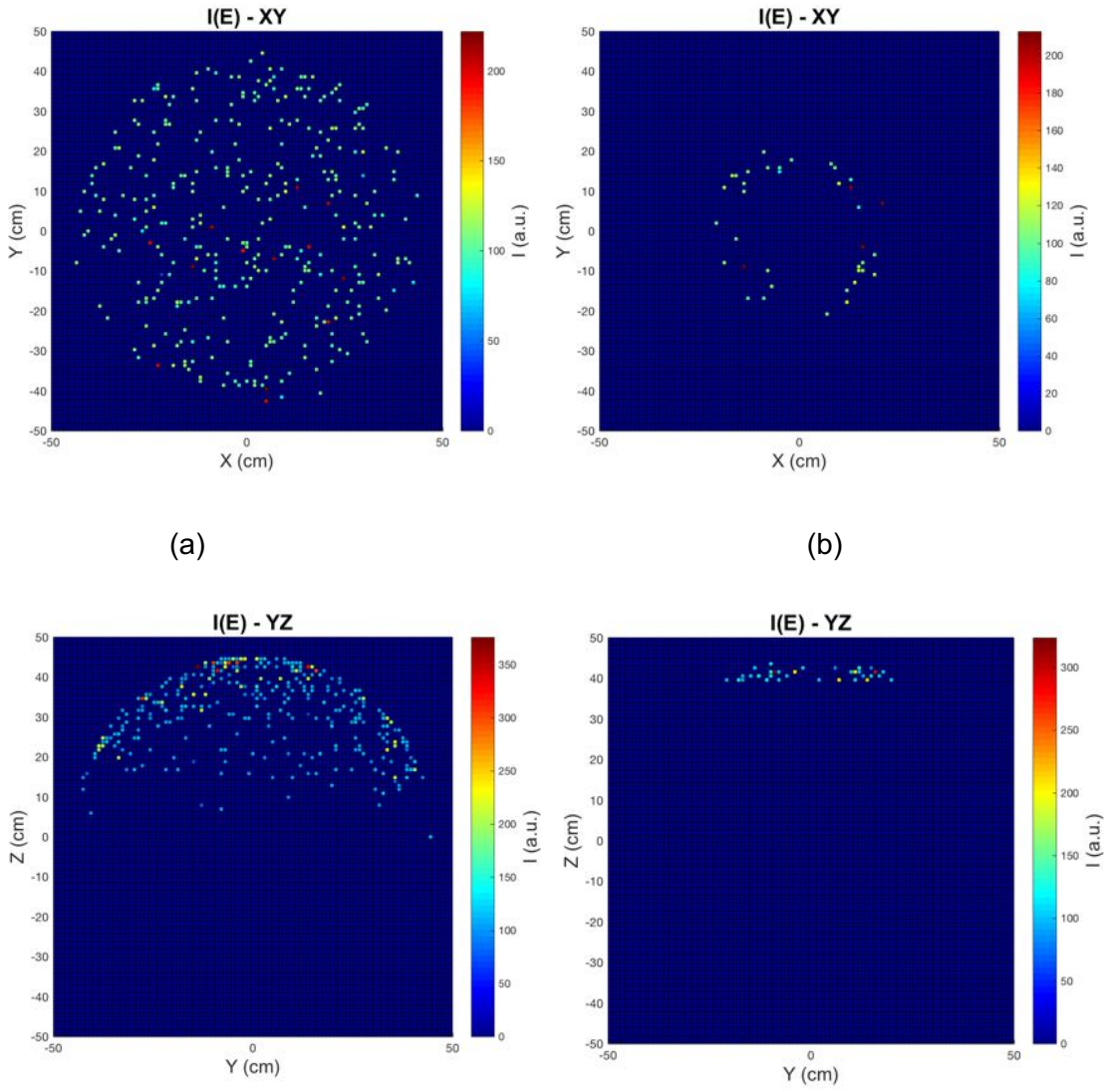

Figure 9.4 Detector detected fluorescence relative brightness in terms of I(E) at all angles in XY (a) and YZ (b) projections for MnO2 at 25keV. From the psf-file it is possible to select the annulus from the azimuthal angle (c) (d).

In this work the image brightness was calculated for a set of different combinations of materials, thicknesses positions and through barriers at three different beam energies (25 keV, 150 keV, and 500 keV) (section 9.14).

9.8 Relative yield as a function of angle

We define relative yield as a quantity that measures the number of detected photons (N) per unit solid angle ($\Delta\Omega$) for a given number of incident photons (N_0). Relative yield is a step towards estimating the detection sensitivity of an element, such as may be achieved with energy dispersive detectors during X-ray fluorescence, facilitating materials discrimination with energy dispersive detectors such as HEXITEC.

From the above definition, we can define relative yield in formula as:

$$Y(\vartheta) = \frac{1}{\Delta\Omega}\frac{N}{N_0} \qquad 9.2$$

Differences in relative yield as function of angle can expose contrast between materials, helping detection against the background.

As for the integrated energy, PAXI algorithm estimates relative yield of Compton scattering, elastic scatter and fluorescence at every 2.5˚ with width 2.5˚ azimuthal angle. Compton scattering yield is likely a less useful imaging metric than fluorescence yield, as there is a range of backscattered photon energies from any one material, which means that even using an energy dispersive detector there is little inherent information with which to uniquely identify a particular material. The different Compton yields from different materials may indicate that multiple materials are present and give a visual indication of shape and structure. However, it is possible that there may be no contrast between completely different materials if their thicknesses compensate for any differences in their Compton scattering efficiency. Although Compton scatter relative yield may have the potential to be used for material identification in cases where fluorescence is unlikely, only fluorescence at this point appears to give the information for uniquely identifying an element. The Compton scatter spectrum may contain some material information, but it will be susceptible to a wide range of influences such as the effect of overlying material. There may be ways to construct images that are influenced by multiple parameters (such as attenuation and different forms of scattering) that can constrain the possibilities of which materials are present, such as occurs in dual energy transmission radiography. The energy

spectrum of different materials at different angles is still worthy of exploration, as, at best there might be unforeseen features with potential, and at worst it is good to understand the likely Compton background at specific energies where we may be looking for characteristic fluorescent X-rays and so would be interested in the signal to noise ratio. In this work the relative yield was calculated for a set of different combinations of materials, thicknesses positions and through barriers at three different beam energies (25 keV, 150 keV, and 500 keV) (section 9.15).

9.9 Cross-section as a function of angle

The differential scattering cross-section is a fundamental atomic property, and so this is 'reverse engineered' from our thin film data with the aim of validating our process against published cross section data.

The differential cross section is calculated for the inelastic backscatter only by dividing the yield by the thickness (t) of the material and density number (n).

$$\frac{d\sigma(\vartheta)}{d\Omega} = \frac{1}{nt} Y(\vartheta) \qquad 9.3$$

where $n = \frac{N_A}{A\rho}$ (N_A is Avogadro's number, A is the atomic mass and ρ is the density of the material).

This process shows how the physical density and the atomic number influence the ultimate brightness and relative yield at a specific energy at the detector, this helps build intuition of what physically makes a material 'bright' in a backscatter image, and hence how images should be interpreted. However, the main purpose of back calculating the Compton differential cross section by simulating simple thin materials at just one incident energy is to compare the PENELOPE output to published data, and so validate the whole simulation process. This may at first appear cyclic, but in order to perform any simulation we are entering a range of parameters such as materials, angles, energies, but also using (and often assuming) various input and output units, approximations, specifying track end points, limiting reactions, etc., and so we are validating how well we are using PENELOPE as well as with the fundamental capacity of PENELOPE. The cross-

section data cannot be extracted directly from the PENELOPE files, and doing so would not validate PENELOPE with how we use it. The intent is to compare the cross sections, determined from the phase-space file to NIST data. NIST is not just theoretical data, it is derived directly from experiment, and so indirectly we are comparing PENELOPE's output to experiments that have been validated by prior publication. If we were to try to repeat those physical experiments, we would probably not have enough confidence that we have sufficiently avoided factors such as scene scatter, and accommodated factors such as the ill-established efficiency of the detector. etc. Earlier in this thesis in chapter 6 the output of an X-ray generator was simulated, and the form of the spectrum was consistent with experimental results obtained by experiment. However, that was achieved by normalising against Bremsstrahlung rather than accurately measuring target exposure, solid angle and detector efficiency. What was suitable to explore the X-ray generator would not be an ideal basis for validation of the work on fundamental data. Compton and elastic scatter data at 1 mm thickness will be shown in the following sections (9.9.1 and 9.9.2, respectively) and the validation against NIST database with xraylib tool.

9.10 Xraylib for calculating the theoretical cross section

Xraylib [9] provides access to some of the most respected databases of physical data in the field of X-rays, such as NIST XCOM [105] and LLNL [4]. Xraylib consists of a core library, written in ANSI C, containing over 40 functions to be used to retrieve data from these databases. This library was linked with MATLAB (see chapter 5). In MATLAB, it is possible to retrieve the functions related to the differential cross section, including the Klein-Nishina (see Appendix C) differential cross section, and Compton differential cross section.

9.11 Benchmarking PENELOPE differential cross section against xraylib database with PAXI

PENELOPE differential cross sections are benchmarked against the well-known databases in MATLAB through xraylib, which was incorporated in PAXI algorithm

for comparisons against the Compton differential cross sections calculated from the phase-space file.

Compton differential cross sections (DCS) are calculated as angular distributions within PAXI from the relative yield as defined in section 9.9.

The angular distributions were determined by spacing the hemispherical detector 2.5˚ by 2.5˚ elevation angle from 0˚ to 90˚. In order to generate the angular distribution with such divisions, Compton DCS formula 9.3 was applied to the psf-file data, and the average was calculated at each annulus.

We assume the elevation spacing of 2.5˚ to be thin enough for clustering a sufficiently homogenous number of interactions. Then, the average of the differential cross section would reflect the behaviour of the overall differential cross sections within every 2.5˚ annuli. As we are estimating the angular distribution of the differential cross section as averages at every 2.5˚ degrees elevation angle, the associated uncertainty is then the standard deviation of the average.

The theory behind the differential cross section states the target material is infinitively thin (see chapter 2). For this reason, the hemispherical detector was simulated with the same materials of the integrated energy and relative yield (carbon, copper, manganese dioxide, lead, aluminium, iron), but with decreased thicknesses where required to match the ideal Compton differential cross section.

Differential cross section is commonly represented as energy distributions, thus the first approach for validation of this work consists in studying the behaviour of PENELOPE calculated Compton DCS as energy distribution, where the set of energies used for simulating the hemispherical detector, i.e. 25 keV, 150 keV and 500 keV monoenergetic and monodirectional beam energies, were extracted at specific angles. The materials chosen for this preliminary check are carbon, copper and manganese dioxide. Target materials such as carbon, copper and manganese dioxide are common materials which can be found behind barriers, and their scatter cross section may be of particular interest for material identification.

Carbon was kept at 1 mm thickness at all the beam energies, copper was 0.01 mm thick at 25 keV and 150 keV, and 1 mm thick at high beam energy 500 keV, manganese dioxide was set to be 0.1 mm at 25 keV and 150 keV, 1 mm at 500 keV. Such plots can be seen in figure 9.5, where (a) is the plot of Compton DCS at 45˚, and (b) are captured at 45˚ and 75˚, respectively. We should note 75˚ is still acceptable as self-absorption at the edge of the target material may occur at wider angles. All the energy-Compton DCS plots are represented with associated standard deviation uncertainties. PENELOPE output is compared against the theoretical Compton DCSs of the three materials at the same angles and are represented with dashed lines in figure 9.5.

At 10˚, 45˚ and 75˚ carbon seems close to the ideal DCS, while this is not the case of copper and manganese dioxide, as the output from PENELOPE and theory are quite close to the theoretical DCS except at higher beam energies (500 keV). In theory, the DCS at higher beam energy should drop, while PENELOPE DCS at 500 keV of copper and manganese dioxide is similar to the DCS at 150 keV. Even though the theoretical DCS should drop as energy increases because X-rays are more penetrating, and the probability of a scatter event should decrease, at 45˚ and especially at 75˚, self-absorption occurs within the target thicknesses and secondary events are eventually added to the scatter events. The secondary events become more visible as we increase the azimuthal angle.

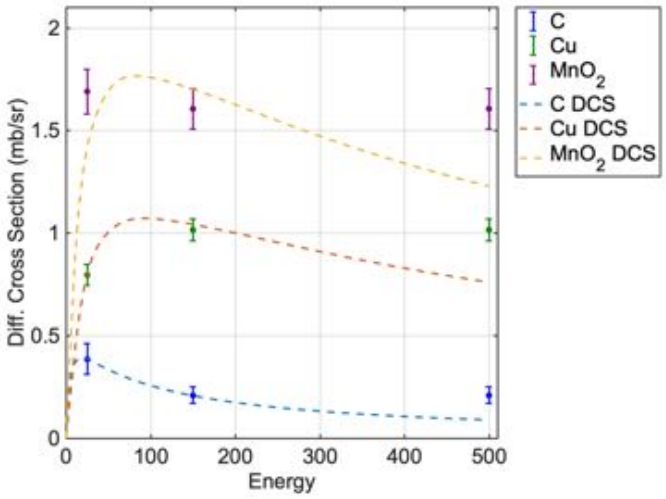
Diff. Cross Section (mb/sr)
Energy
C
Cu
MnO2
C DCS
Cu DCS
MnO2 DCS

(a)

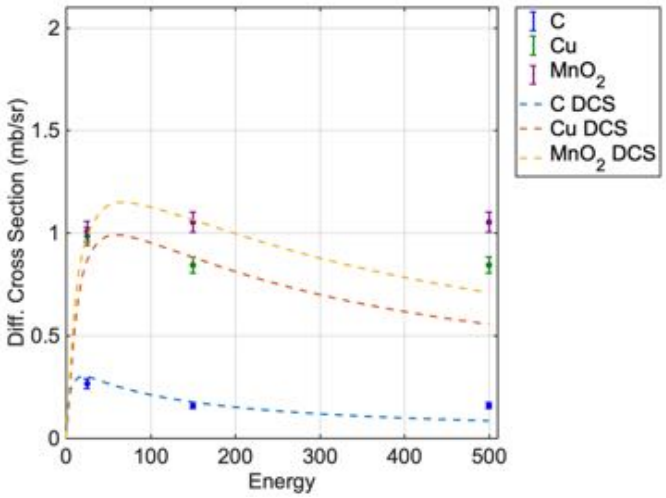
Diff. Cross Section (mb/sr)
Energy
C
Cu
MnO2
C DCS
Cu DCS
MnO2 DCS

(b)

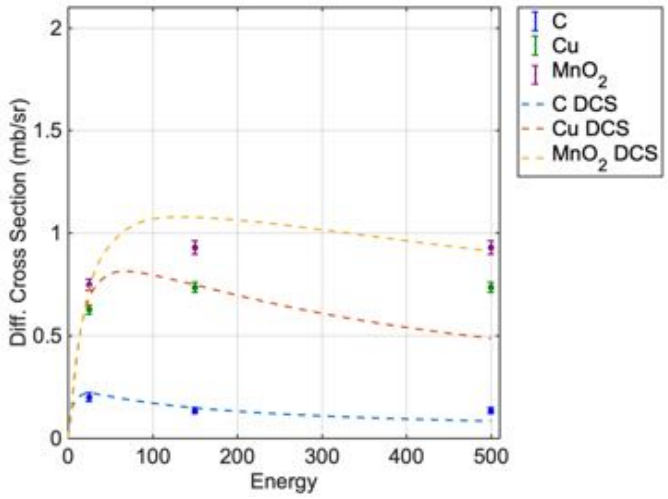

(c)

Figure 9.5 Differential cross section of thin carbon, copper and manganese dioxide at different monoenergetic and monodirectional beam (25, 150 and 500 keV) at 10˚ (a), 45˚ (b) and 75˚ (c). The dashed lines are the theoretical DCS from NIST database [104], while the bars are the DCS from PENELOPE simulations.

9.12 Comparison of PENELOPE Compton differential cross section against NIST data

In this section, the preliminary study in 9.11 will be extended to all the materials, but with the extent to observe the DCSs as angular distributions rather than energy distributions.

PENELOPE output will be validated again with using xraylib in PAXI, and data from well-known databases will be retrieved as angular distributions. PENELOPE DCSs are calculated as averages as explained in section 9.11 and are plotted with their uncertainties at each monoenergetic monodirectional beam energies (25 keV, 150 keV and 500 keV).

The validation includes, in order, the DCSs of carbon, aluminium, iron, copper, manganese dioxide, lead, and are shown in figures 9.6-9.11. In figures 9.6-9.11 (a) the DCS is computed at 25 keV, (b) at 150 keV, and (c) at 500 keV.

The DCS is associated with error bars which are calculated as the standard deviation of the DCS (which is averaged for each annulus). The error bar appears

relatively higher at 0˚ compared with the other elevation angles, that is because the counting statistics at 0˚ is lower than the other angles as the annulus area is smaller.

Overall, PENELOPE DCSs are in good agreement with the theory up to ~40˚ for all the materials. At wider angles of the hemispherical detector, self-absorption of exiting X-rays within the target occurs. There are a few exceptions where the agreement is not fair enough, for example for iron (figure 9.8 (a)), copper (figure 9.9 (a)) and lead (figure 9.11 (a)) at 25 keV. For these materials, at lower beam energies, it is more likely to observe more fluorescence than scatter, and the DCSs are less close to the ideal DCSs. When the beam energy increases, the DCSs of those materials appear more regular (up to ~40˚) as the probability for scatter to occur decreases. Carbon-based materials are not visible with fluorescence yield, thus the only possible signature to identify them is by using Compton scatter. By calculating Compton scatter DCS for comparisons to the theoretical DCS, we assume the material is infinitely thin. In the case of carbon, Compton DCS is lower than the other materials. But in Compton backscatter X-ray imaging, carbon-based materials are the brightest surfaces. For a finite thickness, the relative yield will tell us how many photons out of the total from the beam are exiting the material and/or escaping through a barrier (see section 9.15). For a relatively thick layer, Compton relative yield of carbon will be higher than the other materials, and comparable (or even higher) than fluorescence relative yield. This justifies the image brightness due to Compton scatter of carbon is high, especially at lower energies (see section 9.14.1). This may change when there is a barrier in front. In the following sections (9.14 to 9.16), image brightness, relative yield and energy-probability of a selection of materials will be explored with different thicknesses, positions and through barriers.

C

25 keV

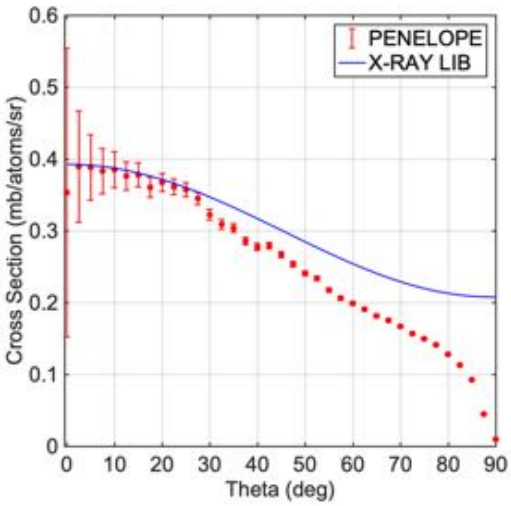

(a)

150 keV

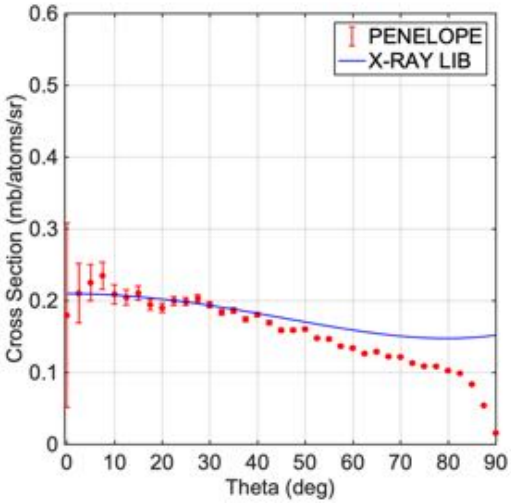

(b)

500 keV

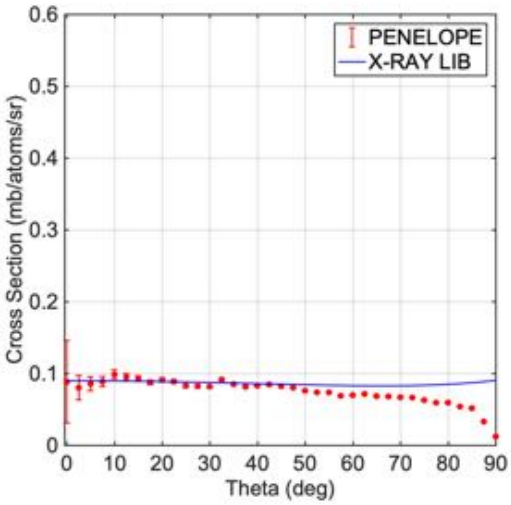

(c)

Figure 9.6 Differential cross section derived from 1 mm thick carbon at 25 keV (a), 150 keV (b) and 500 keV (c). The differential cross section calculated in PENELOPE is plotted in red with error bars, while the Compton scatter differential cross section extracted from NIST database with xraylib tool is plotted in blue.

Al

25 keV

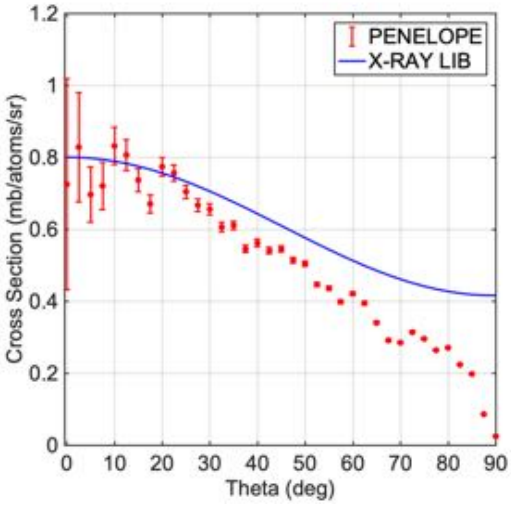

(a)

150 keV

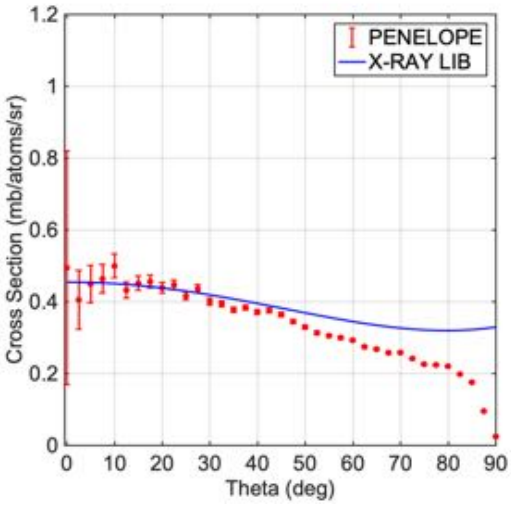

(b)

500 keV

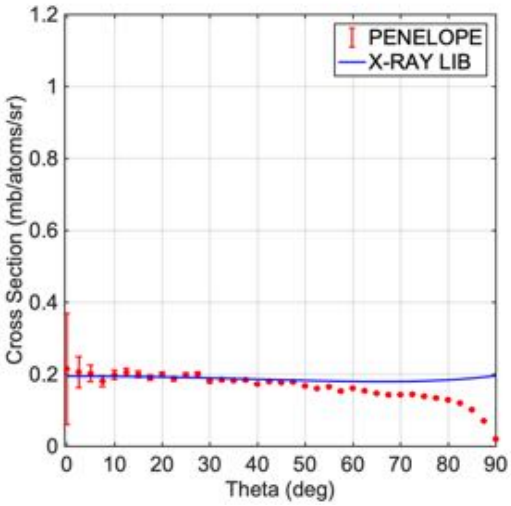

(c)

Figure 9.7 Differential cross section derived from 0.1 mm thick aluminium at 25 keV (a), and 1 mm thick aluminium at 150 keV (b) and 500 keV (c). The differential cross section calculated in PENELOPE is plotted in red with error bars, while the Compton scatter differential cross section extracted from NIST database with xraylib tool is plotted in blue.

Fe

25 keV

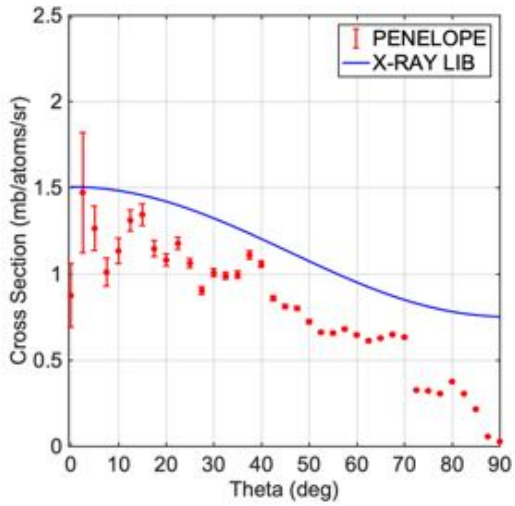

(a)

150 keV

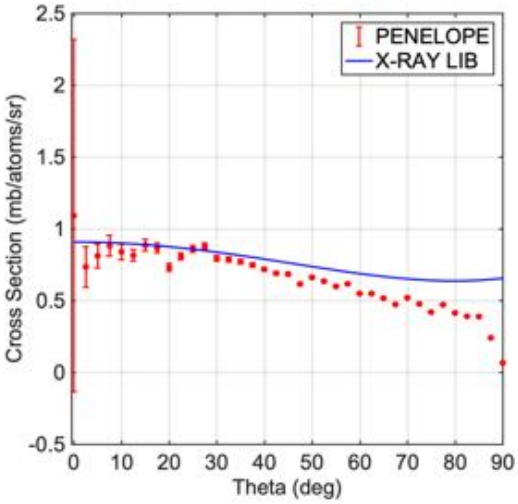

(b)

500 keV

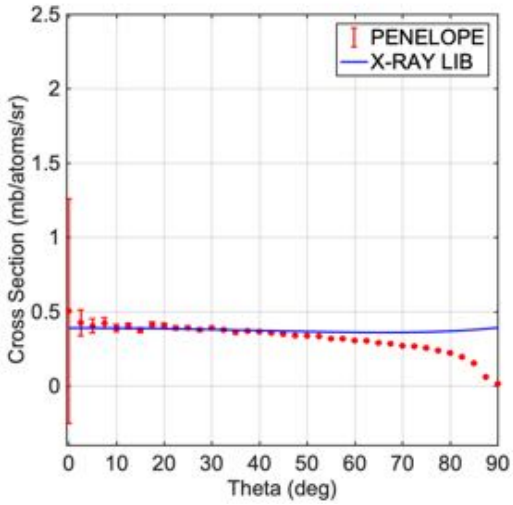

(c)

Figure 9.8 Differential cross section derived from 0.01 mm thick iron at 25 keV (a), 0.1 mm thick iron at 150 keV (b) and 1 mm thick iron 500 keV (c). The differential cross section calculated in PENELOPE is plotted in red with error bars, while the Compton scatter differential cross section extracted from NIST database with xraylib tool is plotted in blue.

Cu

25 keV

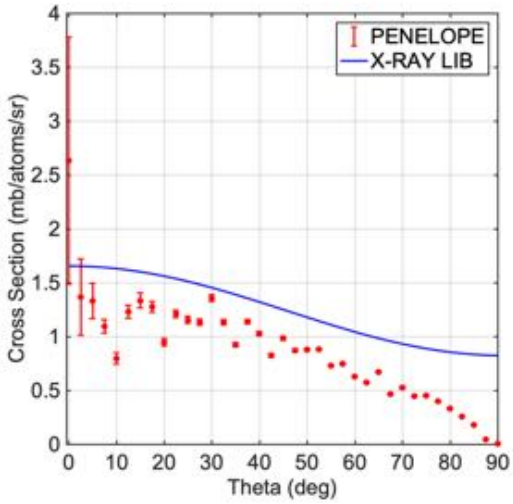

(a)

150 keV

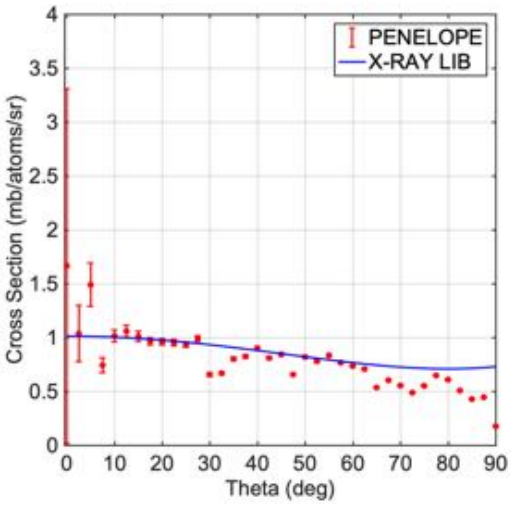

(b)

500 keV

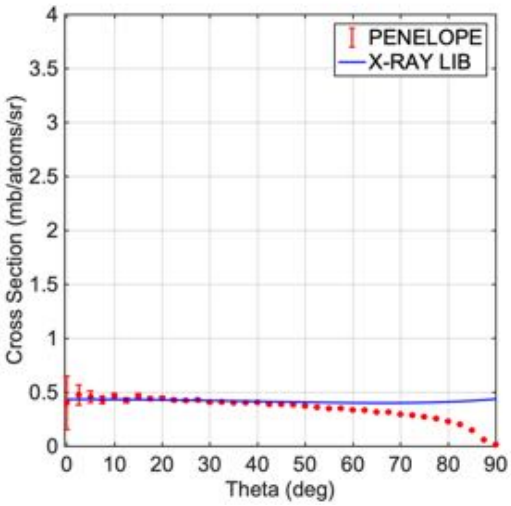

(c)

Figure 9.9 Differential cross section derived from 0.01 mm thick copper at 25 keV (a), 0.01 mm thick copper at 150 keV (b) and 1 mm thick copper 500 keV (c). The differential cross section calculated in PENELOPE is plotted in red with error bars, while the Compton scatter differential cross section extracted from NIST database with xraylib tool is plotted in blue.

MnO_2

25 keV

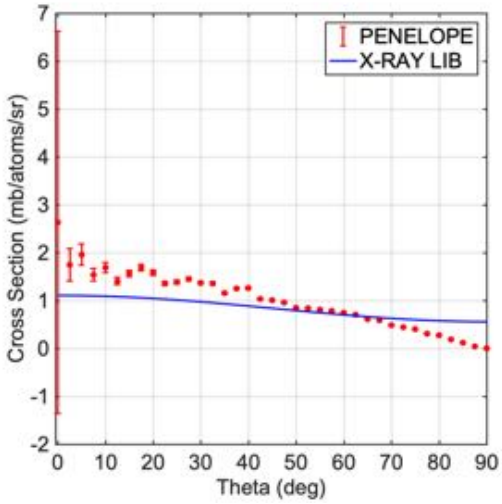

(a)

150 keV

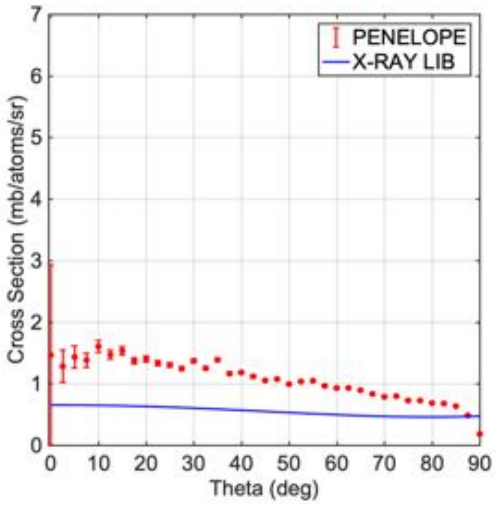

(b)

500 keV

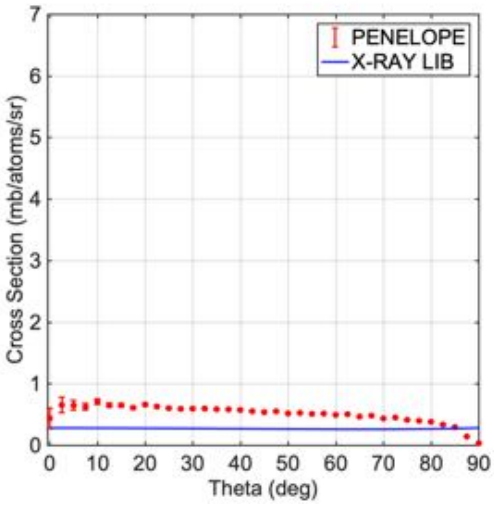

(c)

Figure 9.10 Differential cross section derived from 0.1 mm thick manganese dioxide at 25 keV (a), 0.1 mm thick manganese dioxide at 150 keV (b) and 1 mm thick manganese dioxide 500 keV (c). The differential cross section calculated in PENELOPE is plotted in red with error bars, while the Compton scatter differential cross section extracted from NIST database with xraylib tool is plotted in blue.

Pb

25 keV

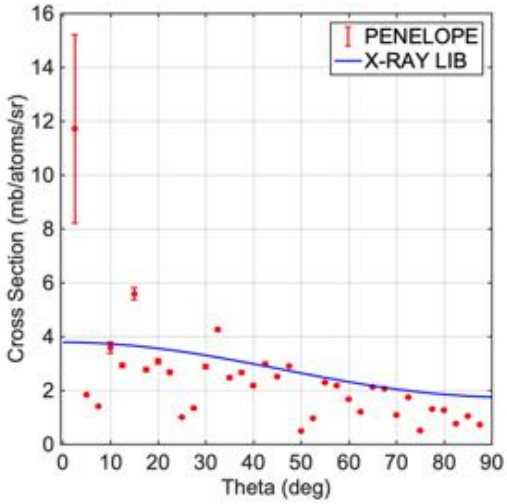

(a)

150 keV

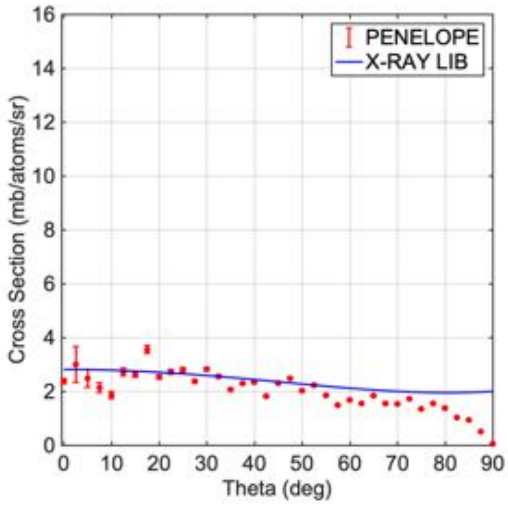

(b)

500 keV

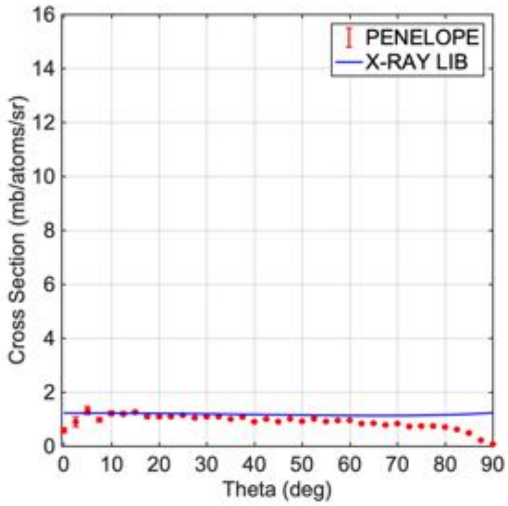

(c)

Figure 9.11 Differential cross section derived from 0.001 mm thick lead at 25 keV (a), 0.01 mm thick lead at 150 keV (b) and 0.1 mm thick lead 500 keV (c). The differential cross section calculated in PENELOPE is plotted in red with error bars, while the Compton scatter differential cross section extracted from NIST database with xraylib tool is plotted in blue.

9.13 Energy-probability as a function of angle

In PENELOPE, the energy-probability spectrum is the spectrum of the incident particles tallied at the entrance of the impact detector. The probability represents the number of counts in the y-axis of an energy spectrum that would be collected by an energy-dispersive detector, such as Amptek-X123 CdTe.

In PENELOPE, the probability is expressed as 1/(eV x particle) (see chapter 5). By default, in PENELOPE the energy spectra at the impact detector are recorded in the file spc-impdet.dat. Within the hemispherical detector model, the default energy spectrum collected as instructed by PENMAIN cannot be plotted as angular distribution, but it gives the overall spectrum at the whole surface of the detector. However, together with the calculation of the integrated energy, PAXI algorithm is capable of generating energy-probability spectra at each angle.

In the case of the hemispherical detector, the spectrum of the overall detector can be limited information, as the position where the specific feature was detected cannot be easily identified. Separating the energy distribution for each angle may extract information aiding the optimisation of the detector practical positioning in order to maximise the signal. For instance, in the perspective of using a pixelated energy-dispersive detector such as the HEXITEC, knowing the best exact position where to detect a specific feature and isolate it from other features, may be fundamental not only for imaging but also for spectroscopy.

In PAXI algorithm, the energy-probability is calculated independently from the integrated energy in a complementary section. Energy-probability distribution is computed from the phase-space file, and PAXI estimates the spectrum as follows:

$$P(E) = dN \frac{1}{\frac{E_{MAX} - E_{MIN}}{nbins}} \qquad 9.4$$

Where dN is the number of particles detected at each 2.5˚ thick annulus, E_{MAX} and E_{MIN} are the maximum and minimum energies, respectively, as defined in the input file in the impact detector section, and nbins is the number of divisions of the histogram. The energy-probability is calculated every 2.5 degrees annulus

between 0 and 90 degrees for all the materials in all the configurations. An example of the energy-probability spectra extracted from PAXI at ~20˚ for the different kind of interactions is shown in figure 9.12. These data can help relate energy, position, and energy-counts as probability.

In PAXI, the angular distribution of the energy-probability is estimated by calculating the maximum of the spectrum at each angle, rather than the average.

The maximum was preferred over the average for generating the angular distributions. In principle, the algorithm should be versatile for any interactions, as in theory we do not know in advance what kind of events we are measuring.

But the power of the hemispherical detector is that it replicates an energy-dispersive detector, thus maximising number of events from a sample is more beneficial than averaging for detecting and discriminating the materials. Fluorescence, for example could be hidden beneath a broad Compton peak, at certain angles, but could be exposed when changing the detector position.

In this work the energy-probability was calculated for a set of different combinations of materials, thicknesses positions and through barriers at three different beam energies (25 keV, 150 keV, and 500 keV) (section 9.16).

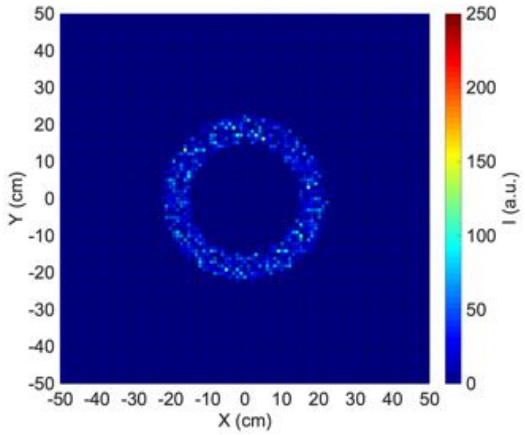

(a)

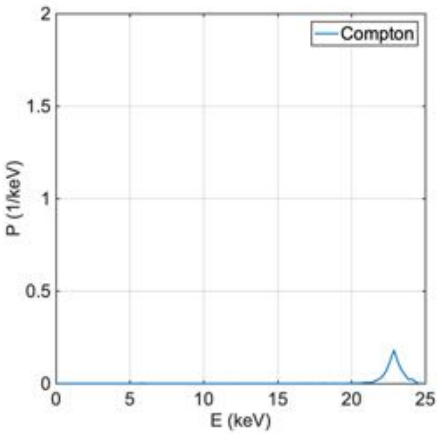

(b)

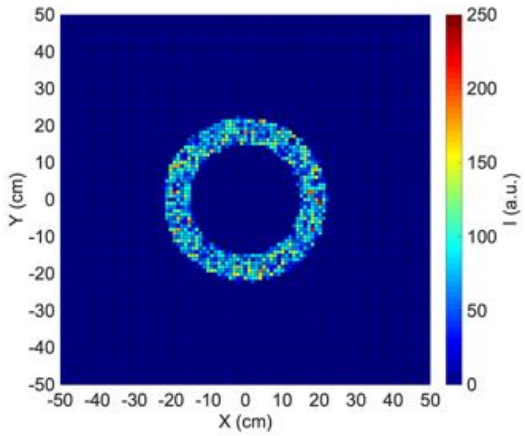

(c)

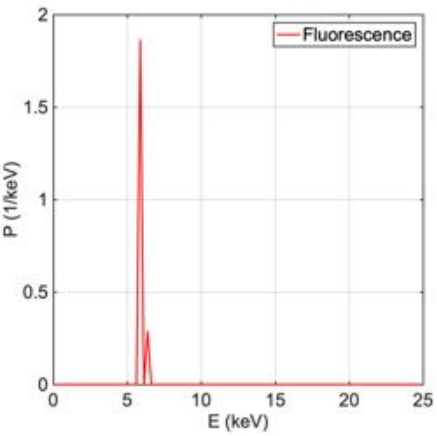

(d)

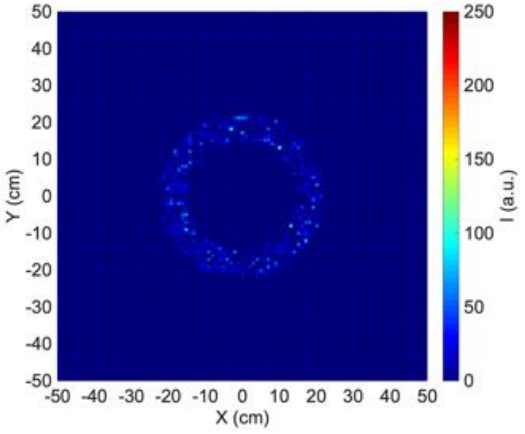

(e)

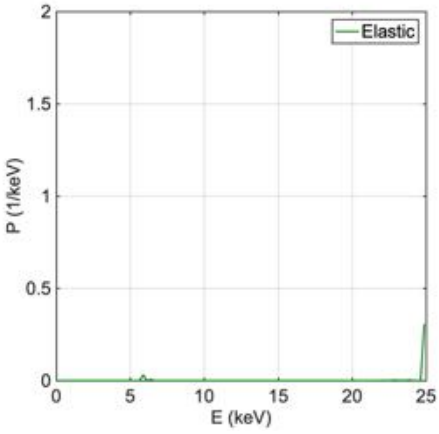

(f)

Figure 9.12 Example of image brightness separated by kind of interactions and relative spectra. They include Compton scatter (a)(b), fluorescence (c)(d) and elastic scatter (e)(f) of 20˚ thick annulus manganese dioxide.

9.14 Interpretation of brightness data

In this section the image brightness as I(E) calculated from PENELOPE phase-space file with PAXI algorithm will be explored. In this section, the image brightness as angular distribution of thin materials (9.14.1), rotated materials (9.14.2), thick materials (9.14.3), and thick materials with barriers (9.14.4) at 25 keV, 150 keV and 500 keV will be explored by separating the data from the psf-file by kind of interactions, i.e. Compton scatter, elastic scatter, and fluorescence, in order to compare the signatures of the materials as image brightness. Image brightness will be compared to identify which material would be brighter when that specific interactions occur. In appendix D, image brightness is plotted material by material.

9.14.1 Interpretation of brightness data for thin materials

The first approach consisted in exploring thin materials for calculating the image brightness. The image brightness was then separated by Compton scatter, elastic scatter and fluorescence events, and they were clustered in 2.5˚ by 2.5˚ annuli 0˚-90˚ azimuthal angle range, with 0˚ equal to total backscatter. In this section of work, carbon, copper, manganese dioxide, lead, aluminium and iron were set to be 1 mm thick, and they were simulated at 25 keV, 150 keV and 500 keV. In the following subsections, the integrated energy of Compton scatter, elastic scatter and fluorescence will be shown.

9.14.1.1 Inelastic (Compton) scattering

Compton scatter brightness angular distributions of carbon, copper, manganese dioxide, lead, aluminium and iron are calculated as angular distributions.

Figure 9.13 shows the value of the Compton scattered pixel brightness (I(E)) calculated every 2.5 degrees between 0 and 90 degrees for all the materials. The graphs for energies of 25keV, 150keV and 500keV are shown on figures (a), (b) and (c), respectively.

We can see carbon is the brightest material at the lowest energy of 25 keV (fig. 9.13(a)), followed by aluminium, which differs from carbon of approximately a factor of eight. We would observe a bright surface of carbon over other materials at this low energy. At a raised energy of 150keV the brightness of iron and copper is twice the other materials. The lowest brightness would be that of lead, which is approximately five times less bright than the other materials. However, if the camera were placed at ~80° to the beam, then figure 9.13 suggests that image contrast could still exist between carbon, copper and MnO_2. At 500 keV the brightness against lead is generally higher but lead brightness may hide that of carbon and aluminium for the same material thickness, unless the detector is placed at 70˚.

Overall, we can observe image brightness appears as a flat angular distribution at low-medium energies, then it increases with angles at high beam energies (500 keV). However, the brightness angular distribution drops for angles > ~75˚ at all beam energies.

When compared against the other kind of interactions, the image brightness originated by Compton scatter is higher, with the exception of the image brightness originated by fluorescence of lead. Lead fluorescence image brightness competes with Compton image brightness of the other materials at low-mid beam energies, as it is around twice Compton image brightness of carbon at 25 keV, and three times greater of copper and iron at 150 keV Compton scatter. At high energies, lead fluorescence is three times lower than copper and iron, but close to carbon image brightness by Compton scatter.

25 keV

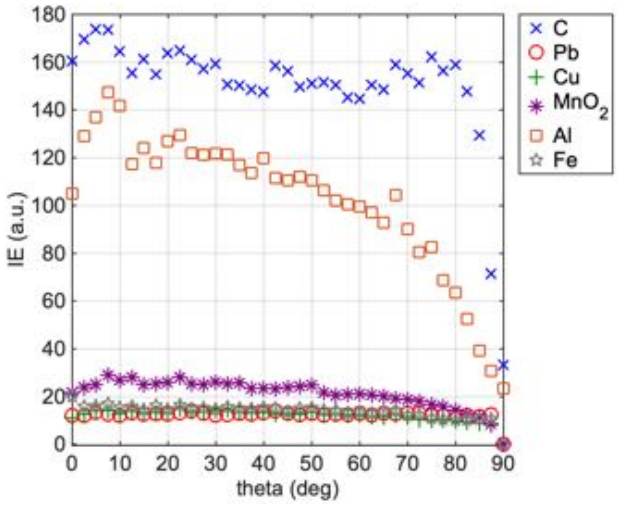

(a)

150 keV

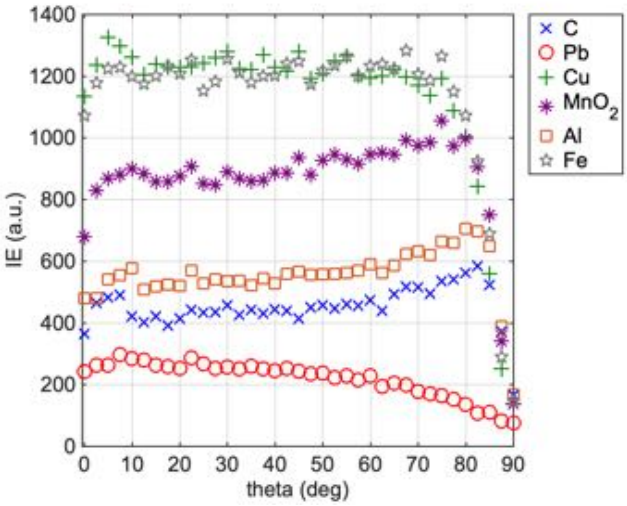

(b)

500 keV

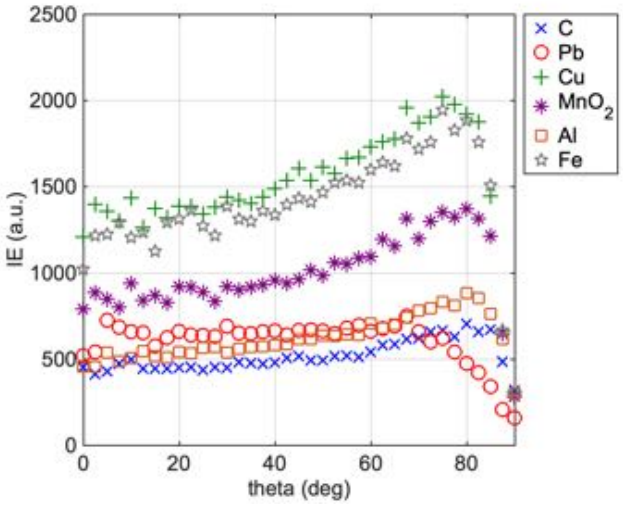

(c)

Figure 9.13 Compton scatter brightness angular distribution at 25 keV (a), 150 keV (b) and 500 keV (c) for carbon, copper, manganese dioxide, lead, aluminium and iron thin films. In (a) the graph I(E) y-scale was zoomed (top right) to a smaller scale.

9.14.1.2 Elastic scatter

Elastic scatter brightness angular distributions of carbon, copper, manganese dioxide, lead, aluminium and iron are calculated as angular distributions. Elastic scatter is recorded at the detector on the phase-space file and in PAXI is identified by selecting ILB3=1.

Figure 9.14 shows the value of the elastic scattered pixel brightness (I(E)) calculated every 2.5 degrees between 0 and 90 degrees for all the materials. The graphs for energies of 25keV, 150keV and 500keV are shown on figures (a), (b) and (c), respectively.

Generally, we can observe events due to elastic is less likely to significantly contribute to the image brightness, since the values calculated in PAXI from the psf-file are the lowest compared against Compton scatter and fluorescence, which have the highest brightness.

By observing figure 9.14, at 25 keV (a) elastic scatter of aluminium would be significantly higher of carbon, unless we placed the detector at wider angles (>70˚), but in that case practical measurements would be difficult as self-absorption would come into place causing the image brightness to drop. At mid-high beam energies (b) (c), if we were to determine the brightness from elastic scatter of layers included lead, then it would be difficult to deconvolute the image brightness of the other surfaces, as lead is higher (150 keV) or equal (500 keV) to the elastic scatter brightness of the other materials.

We can also observe in figures 9.14(b) and (c) carbon and aluminium abruptly drops to zero at certain angles. This does not necessarily mean there is no elastic scatter at those angles, but the counting statistics is not enough for elastic events at that specific annulus. Carbon and aluminium are relatively low Z materials, and they are also described in the geometry as thin films. In PENELOPE the mean free path is a function of the beam energy, material thickness and density (chapter 5). At medium and high energies, the beam then goes through carbon and aluminium without interacting.

25 keV

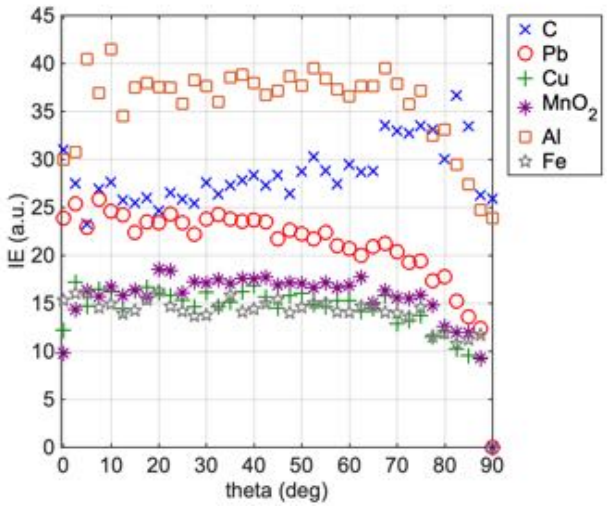

(a)

150 keV

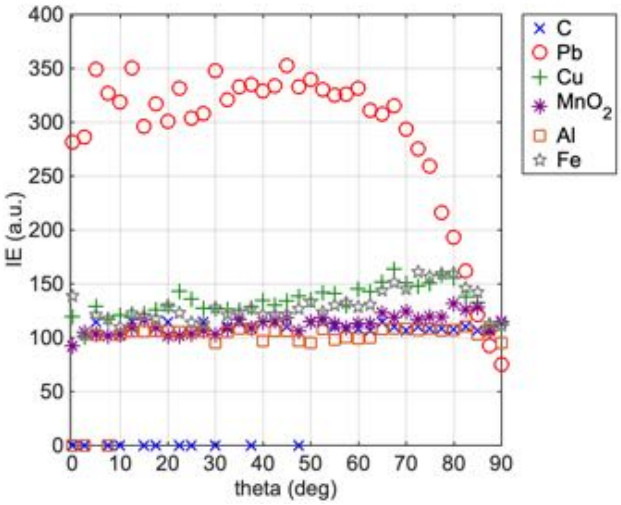

(b)

500 keV

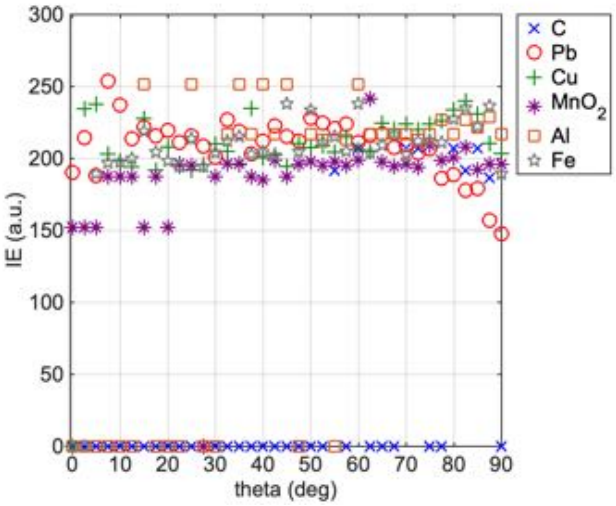

(c)

Figure 9.14 Elastic scatter brightness angular distribution at 25 keV (a), 150 keV (b) and 500 keV (c) for carbon, copper, manganese dioxide, lead, aluminium and iron thin films. In (a) the graph I(E) y-scale was zoomed (top right) to a smaller scale.

9.14.1.3 Fluorescence

Brightness by fluorescence angular distributions of carbon, copper, manganese dioxide, lead, aluminium and iron are calculated as angular distributions.

Figure 9.15 shows the value of the fluorescence pixel brightness (I(E)) calculated every 2.5 degrees between 0 and 90 degrees for all the materials. The graphs for energies of 25keV, 150keV and 500keV are shown on figures (a), (b) and (c).

Lead, overall, is the brightest material if we considered the image brightness by fluorescence.

At the lowest beam energy of 25 keV (fig. 9.15(a)), lead is followed by iron, manganese dioxide, while aluminium fluorescence brightness is the lowest and carbon has no fluorescence contribution. In this case, we would observe a series of bright surfaces hiding carbon-based materials, if we were to consider fluorescence brightness only. At a raised energy of 150 keV and 500 keV the brightness of aluminium is negligible. If there was no lead, then it would be difficult to unfold the image brightness due to fluorescence only at mid-high beam energies, as the brightness of copper, manganese dioxide and iron are competing each other and their signal is quite low, especially if other kind of events such as Compton scatter would occur (Compton would be ten times greater). Nevertheless, copper fluorescence is higher at narrow angles at 150 keV if we considered both fluorescence and Compton scatter.

We can see in figures 9.15 carbon is consistently zero, while aluminium abruptly drops to zero at certain angles and medium-high beam energies. While carbon image brightness due to fluorescence reflects the theory, that is untrue for aluminium. As seen in the previous section for elastic scatter, lack of aluminium do not necessarily mean there is no fluorescence at those angles, but the counting statistics is not enough for elastic events at that specific annulus.

25 keV

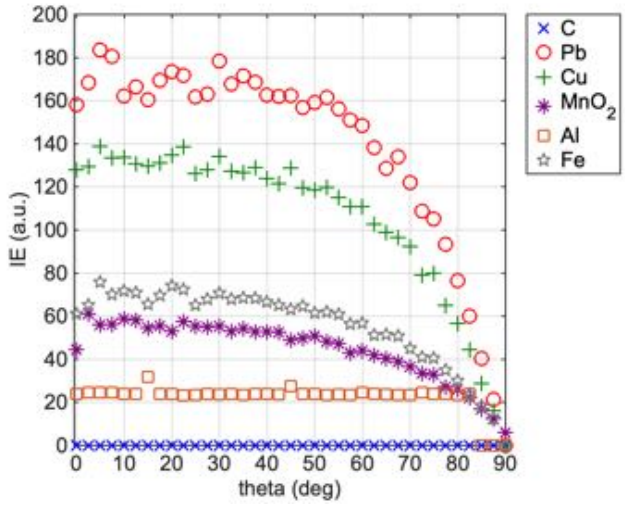

(a)

150 keV

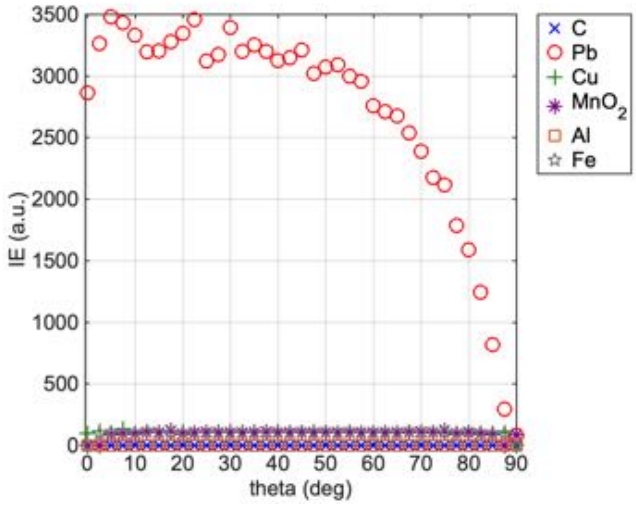

(b)

500 keV

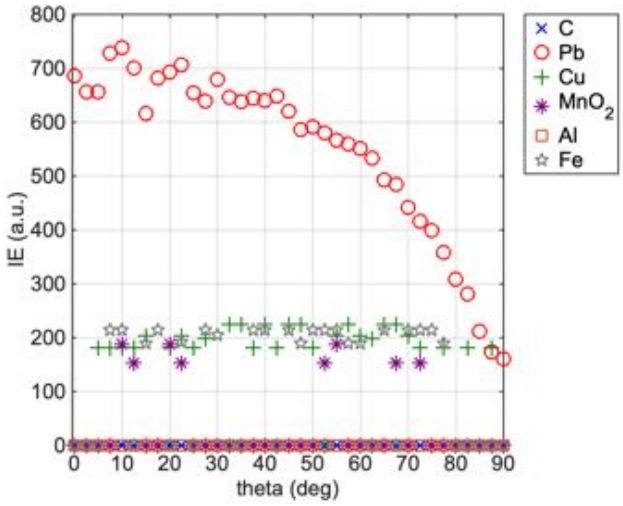

(c)

Figure 9.15 Fluorescence brightness angular distribution at 25 keV (a), 150 keV (b) and 500 keV (c) for carbon, copper, manganese dioxide, lead, aluminium and iron thin films.

9.14.2 Interpretation of brightness data for rotated materials

In this section, thin materials were rotated, and image brightness calculated. The rotation of the materials was necessary to expose the image brightness of wider angles, since with the brightness of thin materials parallel to the detector dropped at angles greater than ~70˚ due to self-absorption within the material thickness.

However, the following graphs of image brightness are not expected to much differ from those of thin films in 9.14.1. This can be a quick self-check to appreciate the correctness of the hemispherical model.

The image brightness was again separated by Compton scatter, elastic scatter and fluorescence events, and they were clustered in 2.5˚ by 2.5˚ annuli 0˚-90˚ angle range, with 0˚ equal to total backscatter. In this section of work, carbon, copper, manganese dioxide, lead layers were set to be 1 mm thick and rotated of 45˚. They were simulated at 25 keV, 150 keV and 500 keV. In the following subsections, the integrated energy of Compton scatter, elastic scatter and fluorescence will be shown.

9.14.2.1 Compton scatter

Compton scatter brightness angular distributions of carbon, copper, manganese dioxide and lead are calculated as angular distributions.

Figure 9.16 shows the (average azimuthal) value of the Compton scattered pixel brightness (I(E)) calculated every 2.5 degrees between 0 and 90 degrees for all the materials. The graphs for energies of 25keV, 150keV and 500keV are shown on figures (a), (b) and (c), respectively.

Overall, we can observe image brightness appears as a flat distribution at all beam energies up to ~ 40˚, then increases with angles, as the material layers are rotated of 45˚. Since with the brightness of thin films parallel to the detector dropped at angles greater than ~70˚ due to self-absorption within the material thickness as seen in section 9.14.1, the rotation of the materials exposed the image brightness of wider angles.

We can see carbon is again the brightest material at the lowest energy of 25 keV (fig. 9.16(a)), followed by the other materials by approximately a factor of four-five. Once again, we would observe a bright surface of carbon over other materials at this low energy. At a raised energy of 150keV (9.16 (b)), the brightness of copper and manganese dioxide is twice the other materials. The lowest brightness would be that of lead, which is approximately five times less bright than the other materials. At 500 keV the brightness against lead is generally higher but lead brightness would hide that of carbon for the same material thickness, even by placing the detector at wider azimuthal angles.

When compared against the other kind of interactions, the image brightness originated by Compton scatter of carbon compete with the image brightness originated by fluorescence of lead at low energies (25 keV). Lead image brightness by fluorescence is overwhelming at mid beam energies (150 keV), as lead image brightness by fluorescence is twice copper and manganese dioxide Compton scatter brightness. At high beam energy (500 keV), the image brightness of Compton is higher than that determined by fluorescence, meaning

copper and manganese dioxide image brightness would still be visible against a lead background. However, lead, in this case, would hide carbon rotated layer.

25 keV

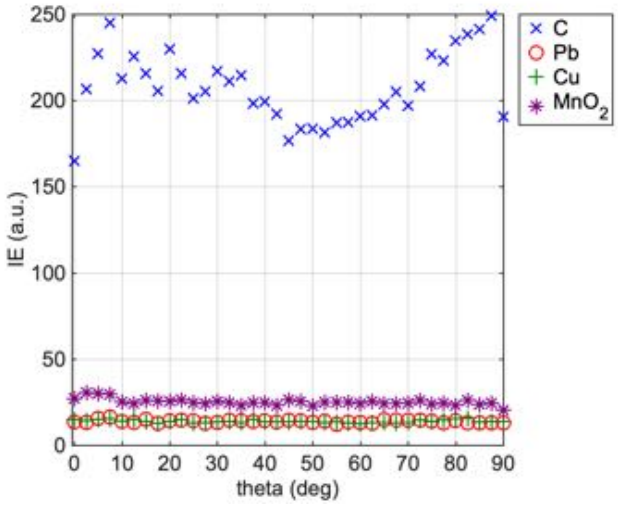

(a)

150 keV

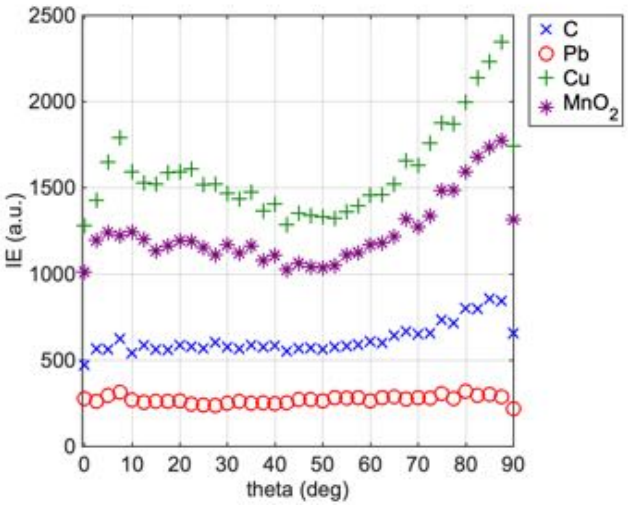

(b)

500 keV

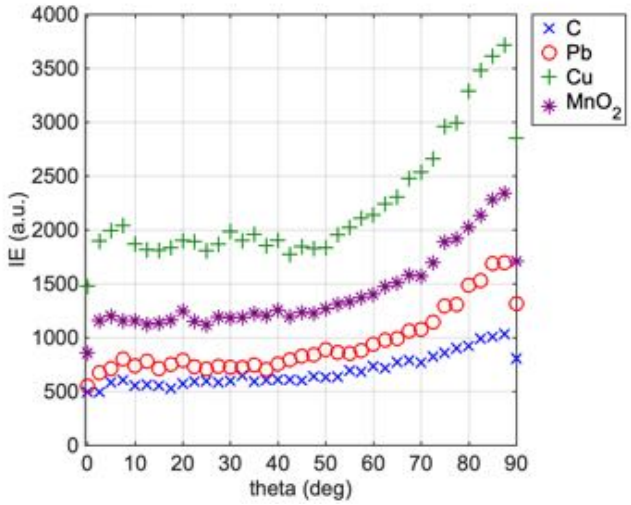

(c)

Figure 9.16 Compton scatter brightness angular distribution at 25 keV (a), 150 keV (b) and 500 keV (c) for carbon, copper, manganese dioxide, lead thin rotated 45˚ film. In (a) the graph I(E) y-scale was zoomed (top right) to a smaller scale.

9.14.2.2 Elastic scattering

Elastic scatter brightness angular distributions of rotated layers of carbon, copper, manganese dioxide and lead are calculated as angular distributions.

Figure 9.17 shows the (average azimuthal) value of the elastic scattered pixel brightness (I(E)) calculated every 2.5 degrees between 0 and 90 degrees for all the materials. The graphs for energies of 25keV, 150keV and 500keV are shown on figures (a), (b) and (c), respectively.

Once again, we can observe that events due to elastic are less likely to significantly contribute to the image brightness at low-mid energies, since the values calculated in PAXI from the psf-file are lower by a factor of ten compared against Compton scatter and fluorescence, which have the highest brightness. By observing figure 9.17, at 25 keV (a) elastic scatter of carbon would be higher than the other rotated materials. At intermediate beam energies (150 keV) (b), lead elastic scatter image brightness would instead prevail. At higher energies

(500 keV) (c), elastic scatter would be half of the highest fluorescence I(E) (lead), and lowest Compton scatter (carbon) I(E).

We can again observe in figures 9.17 (b) and (c) as in figure 9.14, carbon abruptly drops to zero at lower angles in (b) and jumps in (c). This does not necessarily mean there is no elastic scatter at those angles, but the counting statistics is not enough for elastic events at those specific annuli.

25 keV

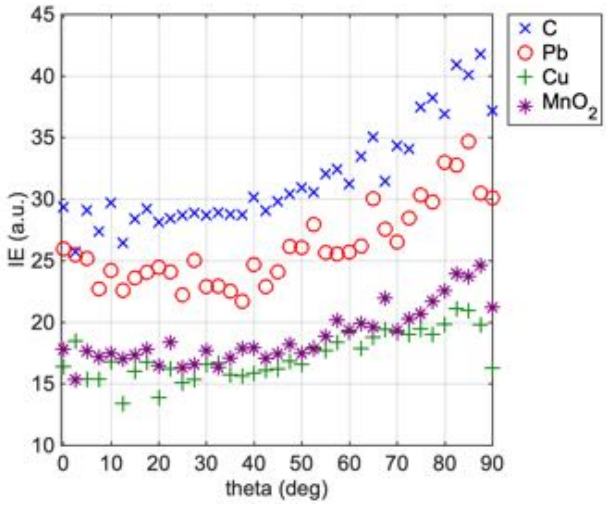

(a)

150 keV

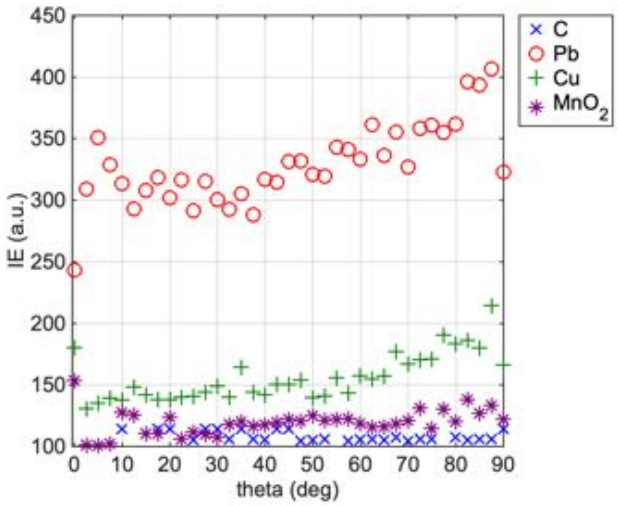

(b)

500 keV

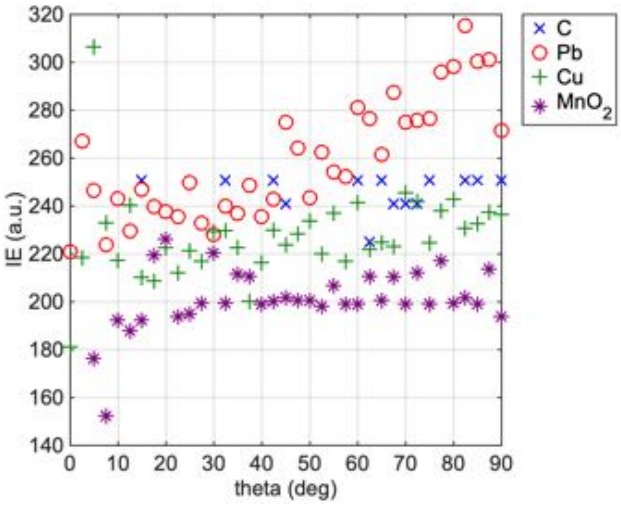

(c)

Figure 9.17 Elastic scatter brightness angular distribution at 25 keV (a), 150 keV (b) and 500 keV (c) for carbon, copper, manganese dioxide, lead thin rotated 45˚ film. In (a) the graph I(E) y-scale was zoomed (top right) to a smaller scale.

9.14.2.3 Fluorescence

Image brightness due by fluorescence events angular distributions of thin rotated carbon, copper, manganese dioxide and lead are calculated as angular distributions.

Figure 9.18 shows the value of the fluorescence pixel brightness (I(E)) calculated every 2.5 degrees between 0 and 90 degrees for all the materials. The graphs for energies of 25keV, 150keV and 500keV are shown on figures (a), (b), (c).

Lead, overall, is the brightest material if we considered the image brightness by fluorescence only.

At the lowest energy of 25 keV of rotated materials (fig. 9.18(a)), lead is followed by copper and manganese dioxide, while carbon has no fluorescence contribution. In this case, we would observe a series of bright rotated surfaces of lead, copper and/or manganese dioxide hiding carbon-based materials, if we

were to consider fluorescence brightness only. At a raised energy of 150 keV and 500 keV the brightness of copper rises but does not reach the I(E) of lead. If there was no lead, then it would be difficult to unfold the image brightness due to fluorescence only of copper and manganese dioxide, as their image brightness are close each other and their signal is quite low, especially if other kind of events such as Compton scatter would occur (Compton would be about ten times greater). Nevertheless, copper fluorescence is again higher at narrow angles at 150 keV and slightly higher at 500 keV, if we considered both fluorescence and Compton scatter.

25 keV

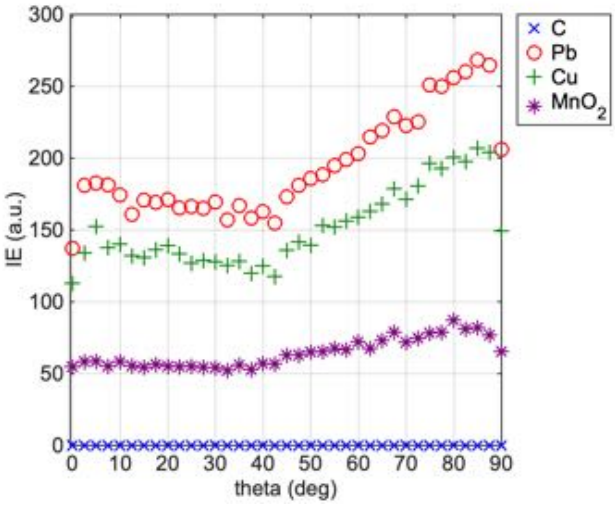

(a)

150 keV

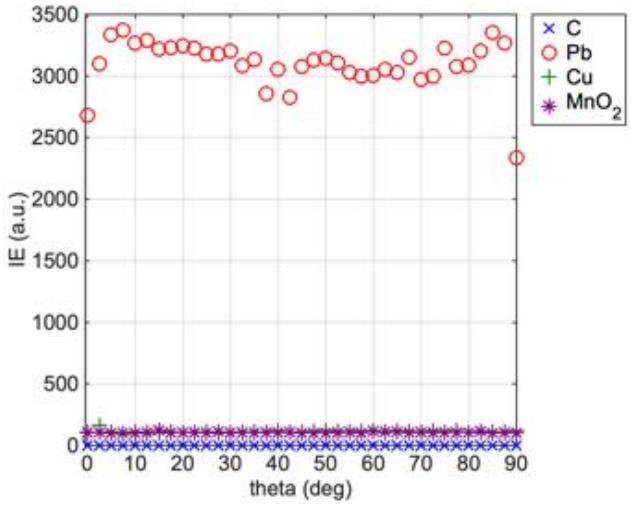

(b)

500 keV

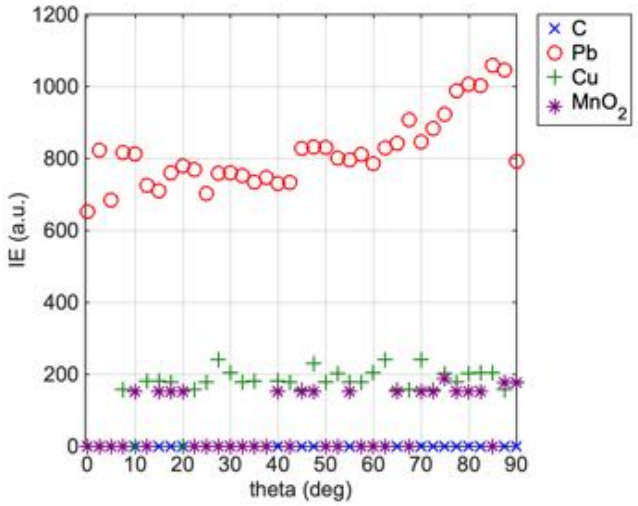

(c)

Figure 9.18 Fluorescence brightness angular distribution at 25 keV (a), 150 keV (b) and 500 keV (c) for carbon, copper, manganese dioxide, lead thin rotated 45˚ film.

9.14.3 Interpretation of brightness data for thick materials

In this section, materials were set to be thick (50 mm) and the beam was perpendicular to the target surface. Image brightness was calculated as in previous sections by separating Compton scatter, elastic scatter and fluorescence events, 2.5˚ by 2.5˚ 0˚-90˚ angular distribution, with 0˚ equal to total backscatter. In this section of work, carbon, copper, manganese dioxide, lead 50 mm thick layers were again simulated at 25 keV, 150 keV and 500 keV. In the following subsections, the integrated energy of Compton scatter, elastic scatter and fluorescence will be shown.

9.14.3.1 Compton scattering

Compton scatter brightness angular distributions of 50 mm thick carbon, copper, manganese dioxide and lead are calculated as angular distributions.

Figure 9.19 shows the value of the Compton scattered pixel brightness (I(E)) calculated every 2.5 degrees between 0 and 90 degrees for all the thick materials. The graphs for energies of 25keV, 150keV and 500keV are shown on figures (a), (b) and (c), respectively.

We can see carbon is the brightest material at the lowest energy of 25 keV (fig. 9.13(a)) of a factor of six against the other materials. We would observe a bright surface of carbon over other materials at this low energy. At a raised energy of 150keV the brightness of manganese dioxide and copper is higher for angles up to ~40˚, then carbon I(E) prevails. We would observe a bright image of carbon if we placed the detector at around 60˚. Compton scatter brightness of lead would be significantly lower compared against the other materials. That means 50 cm lead could be used as background material to enhance the brightness of the others. At 500 keV the brightness of copper is generally higher, but the thick copper layer may hide Compton scatter brightness of carbon and manganese dioxide for the same material thickness, unless the detector is placed at 70˚, where the two materials would be greatly visible.

Once more, we can observe image brightness appears as an almost flat distribution at low energies, then it increases with angles at medium and high beam energies (150 keV and 500 keV, respectively). However, the brightness angular distribution rapidly increased for azimuthal angles greater than ~50˚ at all beam energies, as there are more secondary Compton scatter interactions occurring within the thickness of the materials.

25 keV

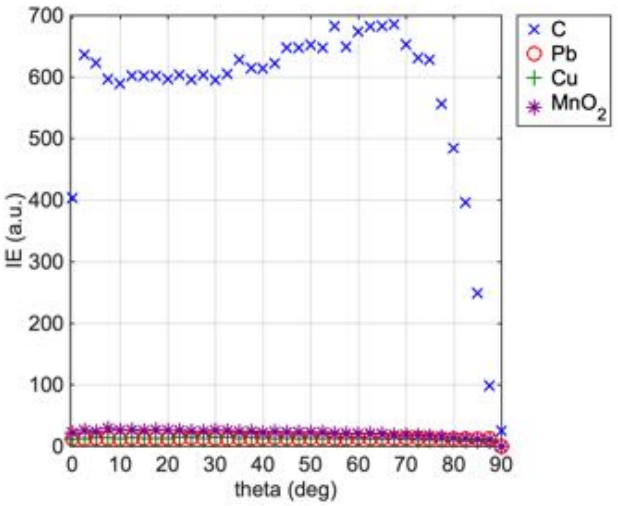

(a)

150 keV

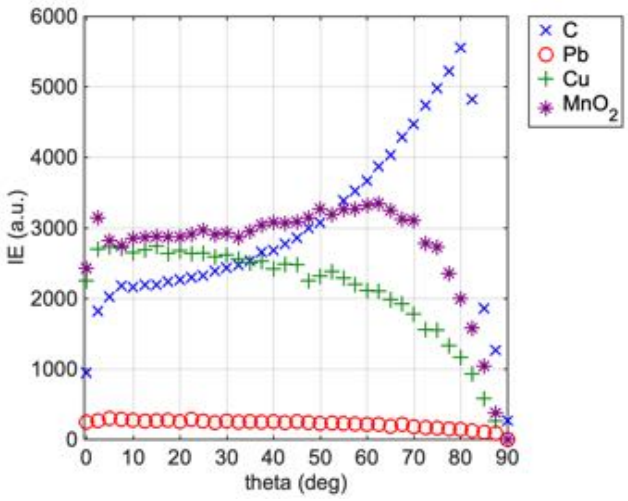

(b)

500 keV

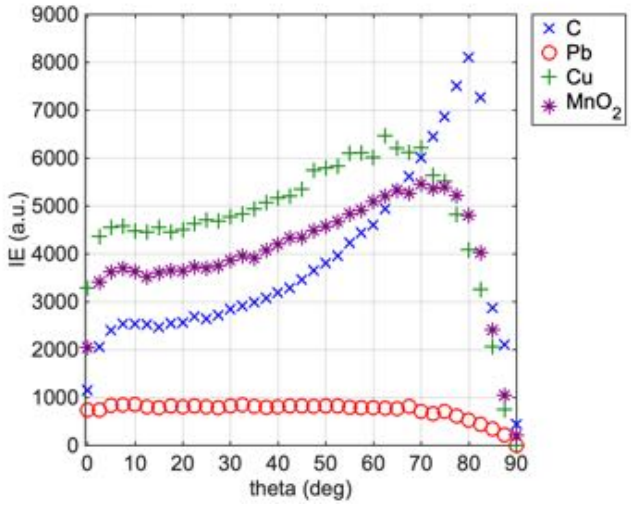

(c)

Figure 9.19 Compton scatter brightness angular distribution at 25 keV (a), 150 keV (b) and 500 keV (c) for carbon, copper, manganese dioxide, lead thick films. In (a) the graph I(E) y-scale was zoomed (top right) to a smaller scale.

9.14.3.2 Elastic scattering

Elastic scatter brightness angular distributions of thick layers of carbon, copper, manganese dioxide and lead are calculated as angular distributions.

Figure 9.20 shows the (average azimuthal) value of the elastic scattered pixel brightness (I(E)) calculated every 2.5 degrees between 0 and 90 degrees for all the materials. The graphs for energies of 25keV, 150keV and 500keV are shown on figures (a), (b) and (c), respectively.

Once again, we can observe events due to elastic is less likely to significantly contribute to the image brightness at low to high energies, since the values calculated in PAXI from the psf-file are lower of more than a factor of ten compared against Compton scatter and fluorescence, which have the highest brightness.

By observing figure 9.20, at all energies we can observe the shape of the angular distributions appear similar to Compton scatter image brightness distributions. At 25 keV (a) elastic scatter of carbon would be higher than the other thick materials. At intermediate beam energies (150 keV) (b), manganese dioxide, copper and lead elastic scatter image brightness would instead prevail up to 70˚.

Carbon rapidly increased at 45˚ and the I(E) becomes higher than the other materials at 70˚. At higher energies (500 keV) (c), elastic scatter highest contribution would be of copper, followed by manganese dioxide. Lead elastic contribution is higher than carbon up to 70˚, then carbon prevails.

25 keV

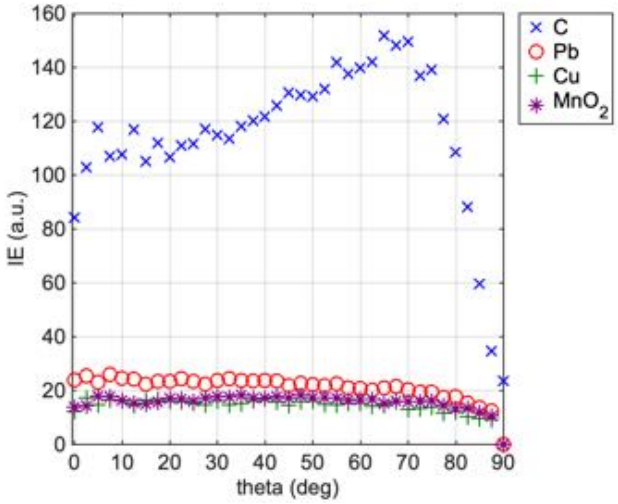

(a)

150 keV

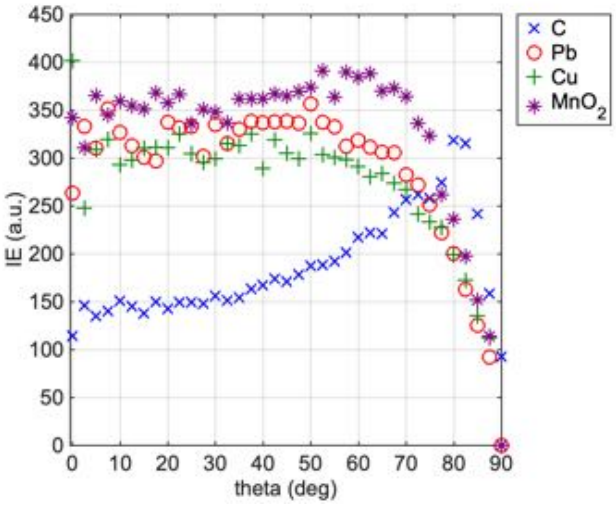

(b)

500 keV

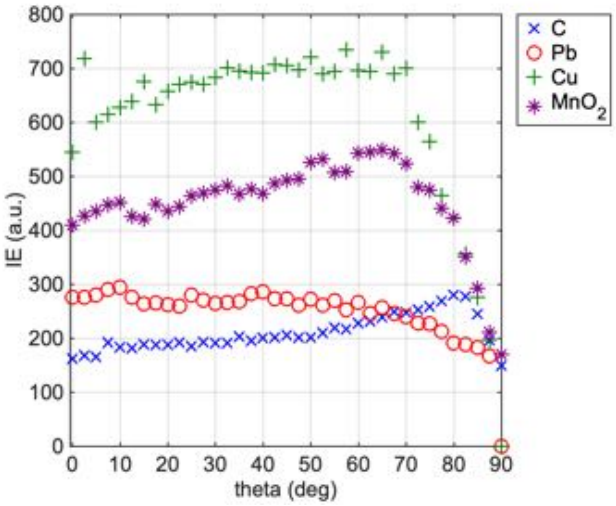

(c)

Figure 9.20 Elastic scatter brightness angular distribution at 25 keV (a), 150 keV (b) and 500 keV (c) for carbon, copper, manganese dioxide, lead thick films. In (a) the graph I(E) y-scale was zoomed (top right) to a smaller scale.

9.14.3.3 Fluorescence

Image brightness due by fluorescence events angular distributions of thick carbon, copper, manganese dioxide and lead are calculated as angular distributions.

Figure 9.21 shows the (average azimuthal) value of the fluorescence pixel brightness (I(E)) calculated every 2.5 degrees between 0 and 90 degrees for all the materials. The graphs for energies of 25keV, 150keV and 500keV are shown on figures (a), (b), and (c), respectively.

Lead, overall, is again brightest material if we considered the image brightness by fluorescence only.

At the lowest energy of 25 keV of thick materials (fig. 9.21(a)), lead is followed by copper and manganese dioxide, while carbon has no fluorescence contribution. In this case, we would observe a series of bright rotated surfaces of lead, copper and/or manganese dioxide hiding carbon-based materials, if we were to consider fluorescence brightness only. At a raised energy of 150 keV and 500 keV the brightness of copper rises but does not reach the I(E) of lead (about 20 times higher). If there was no lead, then it would be difficult to distinguish between the copper and manganese dioxide image brightness, as the I(E)s are close each other Once again, their signal would be quite low, especially if other kind of events such as Compton scatter would occur (Compton would be more than ten times greater). Nevertheless, copper fluorescence is again higher at narrow angles at 150 keV and slightly higher at 500 keV, if we considered both fluorescence and Compton scatter contribution of I(E).

When compared against the other kind of interactions, the image brightness originated by Compton scatter of thick materials prevails even more significantly than thin materials and also for the image brightness by fluorescence of lead. That means a thick carbon-based material would be visible on a lead background of the same thickness as the fluorescence contribution would not be as overwhelming as that of thin materials.

25 keV

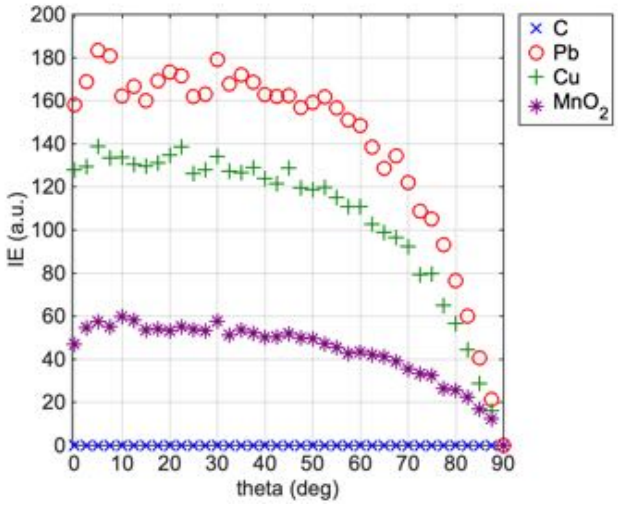

(a)

150 keV

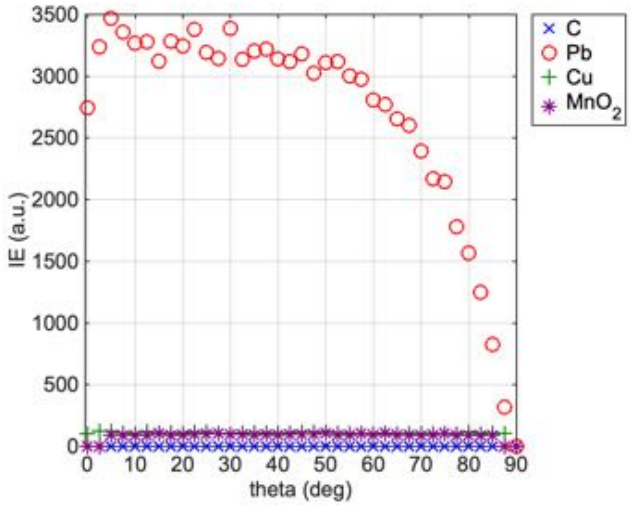

(b)

500 keV

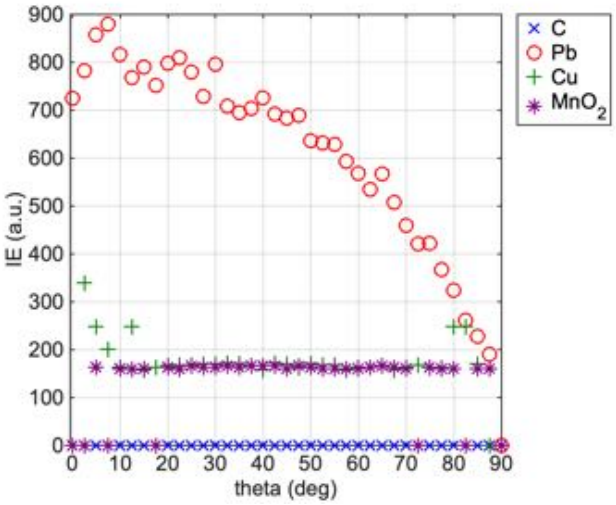

(c)

Figure 9.21 Fluorescence brightness angular distribution at 25 keV (a), 150 keV (b) and 500 keV (c) for carbon, copper, manganese dioxide, lead thick films.

9.14.4 Interpretation of brightness data for thick materials through barriers

Backscatter is often used for imaging materials through barriers. In a situation such as detection through barriers, the following should be considered. If the incident beam energy is too low or the barrier is too thick, then the incoming beam cannot reach the target material. That is the image brightness will only consider the integrated energy of the photons from the barrier. If the energy of the incident beam is enough to reach the target through the target, photons generated at the target can be either absorbed within the target thickness itself or can escape the target but be absorbed by the barrier or escape through the barrier and finally reach the detector. In the hemispherical detector, one way to detect the image brightness from the target only could be considering the integrated energy angular distribution at angles greater than ~60˚, as photons would escape directly from the target. However, this is not usually the case, and the problem of detecting photons from targets through the barrier.

In this section, 50 mm thick carbon, copper and manganese dioxide layers were simulated with 2 mm thick barrier of aluminium and iron, positioned perpendicularly to the incident beam. By putting a barrier on top of the target, we aim to estimate how the image brightness is affected and what the detector actually sees. Image brightness was calculated as in previous sections by separating Compton scatter, elastic scatter and fluorescence events, 2.5˚ by 2.5˚ 0˚-90˚ at 25 keV, 150 keV and 500 keV beam energies. However, when separating the phase-space file by kind of event, it is to be noted that events are recorded at the detector, after the photon has travelled its own path, that is the phase-space file does not record photon tracking. Although it might be a limitation, by exploring the image brightness of aluminium and iron as thin materials, we can give suggestions on how they may affect the image brightness. In the following subsections, the integrated energy of Compton scatter, elastic scatter and fluorescence will be shown.

9.14.4.1 Compton scattering – aluminium barrier

Compton scatter brightness angular distributions of 50 mm thick carbon, copper, manganese dioxide with 2 mm thick aluminium barrier on top are calculated as angular distributions.

Figure 9.22 shows the value of the Compton scattered pixel brightness (I(E)) calculated every 2.5 degrees between 0 and 90 degrees for all the thick materials with aluminium barrier. The graphs for energies of 25keV, 150keV and 500keV are shown on figures (a), (b) and (c), respectively. At 25 keV (fig. 9.22 (a)), we can observe the image brightness at lower energies reflects that of thin film aluminium as seen in section 9.14.1, figure 9.13, except for carbon which has still the highest Compton scatter I(E) but has not the flat shape seen at 1 mm thickness and 50 mm thickness without barrier. That means the beam energy may not be penetrating enough to pass through 2 mm aluminium barrier and generate bright image of manganese dioxide and copper, yet we may still count some image brightness of carbon at low angles close to backscatter.

At a raised energy of 150keV (fig. 9.22 (b)), the image brightness of manganese dioxide, copper and carbon would not be greatly affected by the presence of the aluminium barrier on top of the thick materials. Thus, we can recall the same physical conditions observed in figure 9.19(b). At 500 keV (fig. 9.22 (c)) the brightness of copper drops by a factor of five compared with fig. 9.19 (c), and manganese dioxide image brightness due to Compton scatter would be exposed. No changes for carbon at high beam energies but with an aluminium barrier on top: as seen in figure 9.19 (c), if the detector was placed at 70˚, carbon-based materials would be brighter. We can observe image brightness does not appear as an almost flat distribution anymore, but the brightness angular distribution rapidly increased for azimuthal angles > 50˚-60˚ at all beam energies, as there are more secondary Compton scatter interactions occurring within the thickness of the materials.

When compared against the other kind of interactions, the image brightness originated by Compton scatter of thick materials significantly prevails as the aluminium barrier prevents fluorescence X-rays to reach the detector.

25 keV

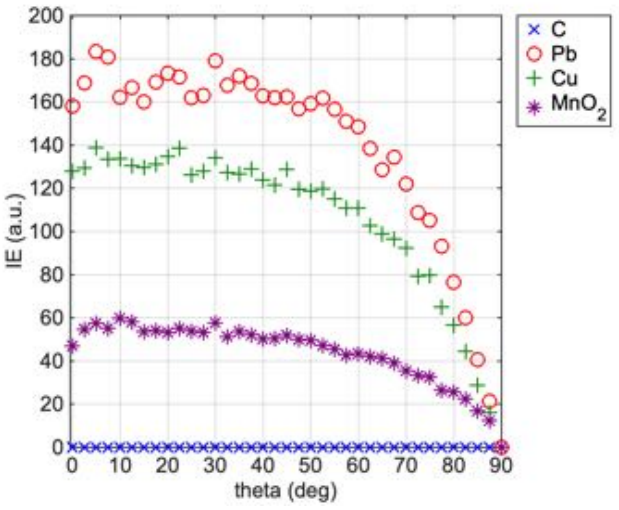

(a)

150 keV

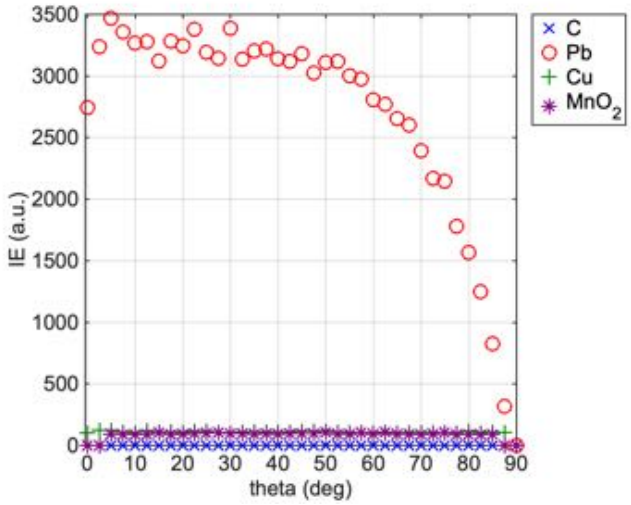

(b)

500 keV

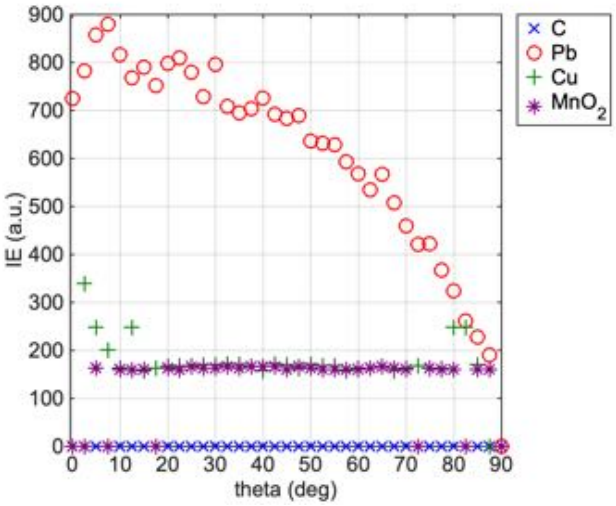

(c)

Figure 9.22 Compton scatter brightness angular distribution at 25 keV (a), 150 keV (b) and 500 keV (c) for carbon, copper, manganese dioxide thick films with aluminium barrier.

9.14.4.2 Compton scattering – iron barrier

Compton scatter brightness angular distributions of 50 mm thick carbon, copper, manganese dioxide with 2 mm thick iron barrier on top are calculated as angular distributions.

Figure 9.23 shows the (average azimuthal) value of the Compton scattered pixel brightness (I(E)) calculated every 2.5 degrees between 0 and 90 degrees for all the thick materials with aluminium barrier. The graphs for energies of 25keV, 150keV and 500keV are shown on figures (a), (b) and (c), respectively.

At 25 keV (fig. 9.23 (a)), we can observe the image brightness at lower energies reflects that of thin iron as seen in figure 9.13(a), and this time also carbon cannot be seen through the iron barrier.

At a raised energy of 150keV (fig. 9.23 (b)), the image brightness of manganese dioxide and copper is not significantly affected by the presence of the iron barrier on top of the thick materials. Carbon integrated energy is attenuated of almost a factor of two at wider angles. At 500 keV (fig. 9.23 (c)) the barrier does not affect the brightness of copper, iron and carbon if we compare the image brightness with fig. 9.19 (c) without barrier.

We can observe image brightness does not appear as an almost flat distribution anymore, but the brightness angular distribution rapidly increased for azimuthal angles > 50˚-60˚ at all beam energies, as there are more secondary Compton scatter interactions occurring within the thickness of the materials.

25 keV

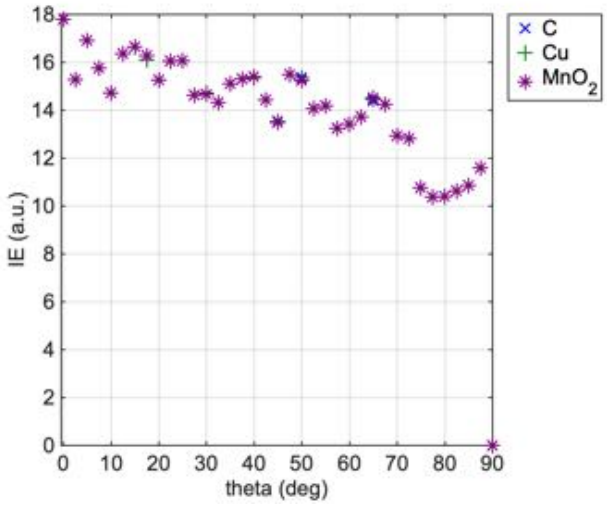

(a)

150 keV

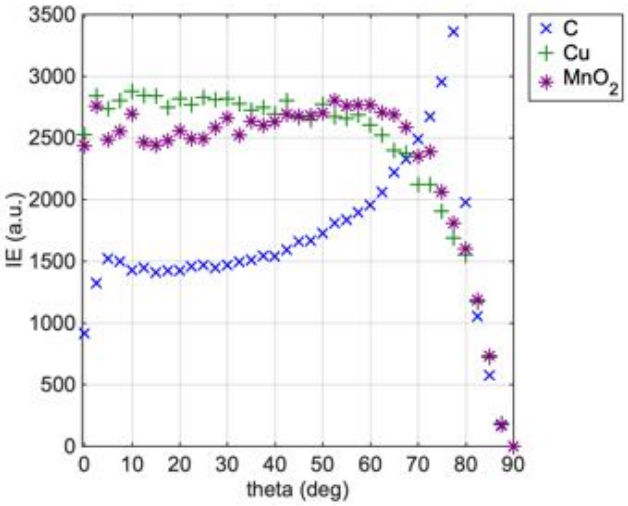

(b)

500 keV

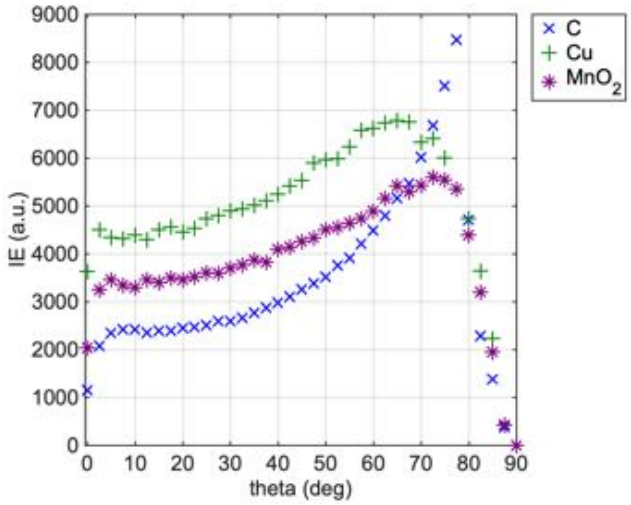

(c)

Figure 9.23 Compton scatter brightness angular distribution at 25 keV (a), 150 keV (b) and 500 keV (c) for carbon, copper, manganese dioxide thick films with iron barrier.

9.14.4.3 Elastic scattering – aluminium barrier

Elastic scatter brightness angular distributions of thick layers of carbon, copper, and manganese dioxide with aluminium barrier are calculated as angular distributions.

Figure 9.24 shows the value of the elastic scattered pixel brightness (I(E)) calculated every 2.5 degrees between 0 and 90 degrees for all the materials. The graphs for energies of 25keV, 150keV and 500keV are shown on figures (a), (b) and (c), respectively.

Generally, events due to elastic are less likely to significantly contribute to the image brightness, since the presence of the barrier generally attenuates the elastic scatter events. However, when introducing the barrier in the geometry, elastic scatter increases as the elastic scatter contribution is not only due to the target material but also by the barrier.

By observing figure 9.24 (a), we can see the shape of the angular distributions appear similar to elastic scatter image brightness distributions of thin aluminium at lower energies (figure 9.14 (a)). At intermediate beam energies (150 keV) (b), manganese dioxide and copper elastic scatter image brightness be the same as if there was no barrier (fig. 9.20(b)). Carbon elastic scatter appears enhanced at angles greater than 45˚ compared to thick carbon without barrier in figure 9.20. The I(E) becomes higher than the other materials at 70˚. At higher energies (500 keV) (fig. 9.24(c)), elastic scatter I(E) of copper is attenuated by a factor of three, while carbon and manganese dioxide are the same as thick materials without barrier in figure 9.20(c).

25 keV

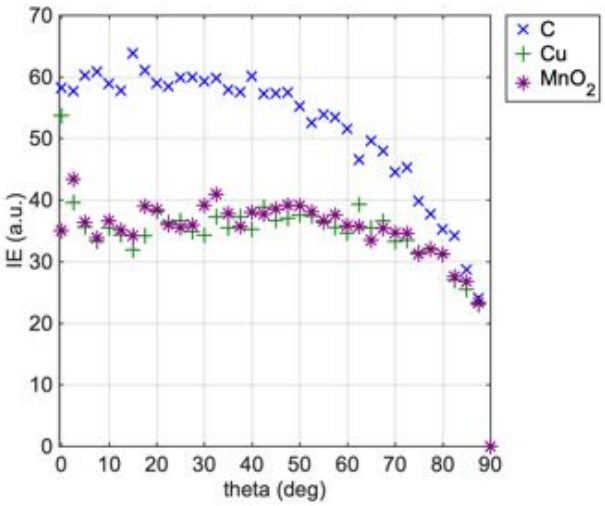

(a)

150 keV

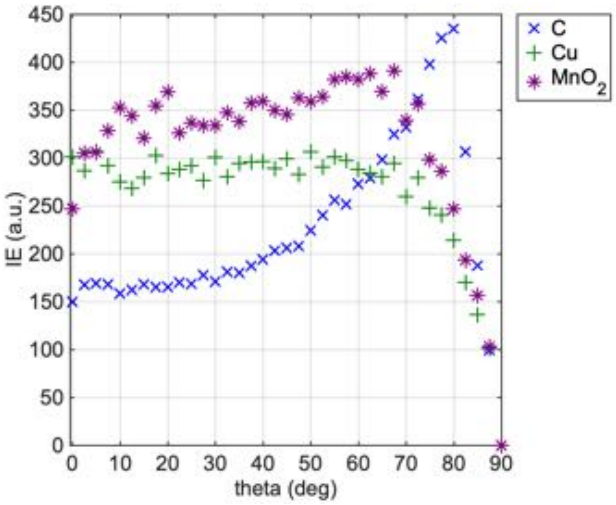

(b)

500 keV

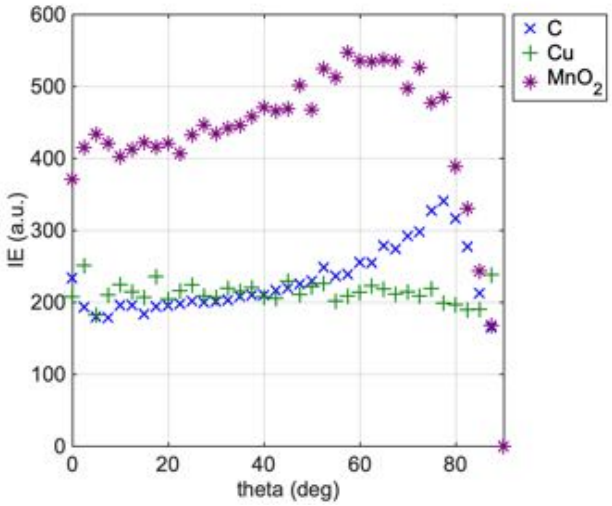

(c)

Figure 9.24 Elastic scatter brightness angular distribution at 25 keV (a), 150 keV (b) and 500 keV (c) for carbon, copper, manganese dioxide thick films with aluminium barrier.

9.14.4.4 Elastic scattering – iron barrier

Elastic scatter brightness angular distributions of thick layers of carbon, copper, and manganese dioxide with iron barrier are calculated as angular distributions.

Figure 9.25 shows the value of the elastic scattered pixel brightness (I(E)) calculated every 2.5 degrees between 0 and 90 degrees for all the materials. The graphs for energies of 25keV, 150keV and 500keV are shown on figures (a), (b) and (c), respectively.

By observing figure 9.25 (a), we can observe the shape of the angular distributions appear similar to elastic scatter image brightness distributions of thin iron at lower energies (figure 9.14 (a)). At intermediate beam energies (150 keV) (fig. 9.25 (b)) and higher beam energies (500 keV) (fig. 9.25 (c)), manganese dioxide, copper and carbon elastic scatter image brightness are the same of the image brightness without barrier (fig. 9.20(b) (c)).

25 keV

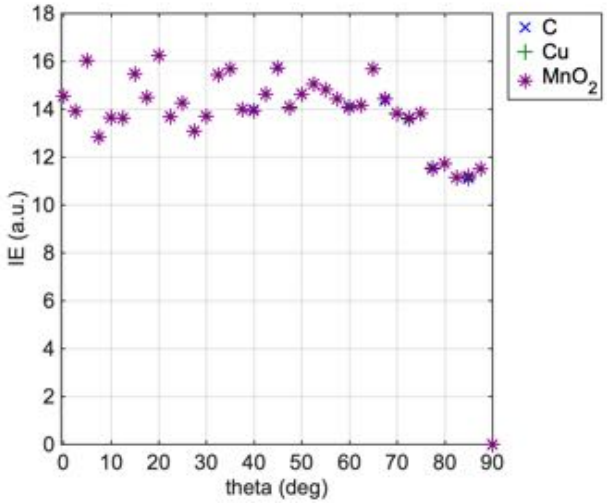

(a)

150 keV

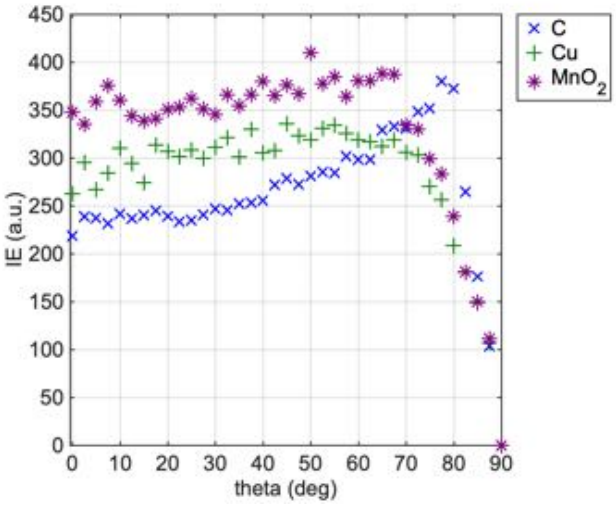

(b)

500 keV

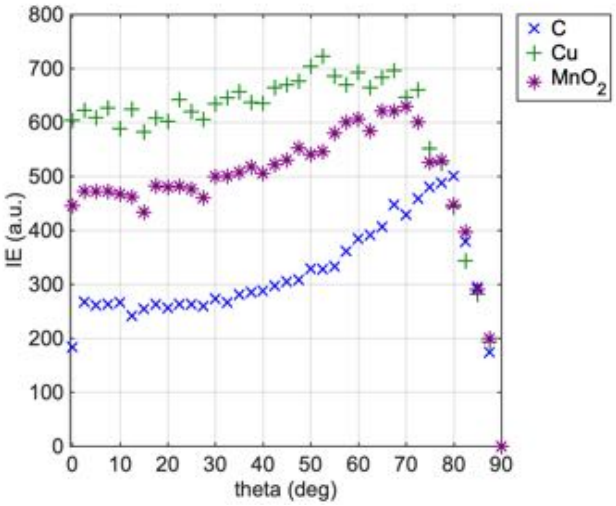

(c)

Figure 9.25 Compton scatter brightness angular distribution at 25 keV (a), 150 keV (b) and 500 keV (c) for carbon, copper, manganese dioxide thick films with iron barrier.

9.14.4.5 Fluorescence – aluminium barrier

Image brightness due by fluorescence events angular distributions of thick carbon, copper and manganese dioxide with aluminium barrier are calculated as angular distributions.

Figure 9.26 shows the value of the fluorescence pixel brightness (I(E)) calculated every 2.5 degrees between 0 and 90 degrees for all the materials. The graphs for energies of 25keV, 150keV and 500keV are shown on figures (a), (b) and (c), respectively.

Overall, aluminium 2 mm barrier appears to screen any fluorescence from the thick materials placed behind at all energies. This means the image brightness signal would be based on Compton scatter and partially on elastic scatter.

25 keV

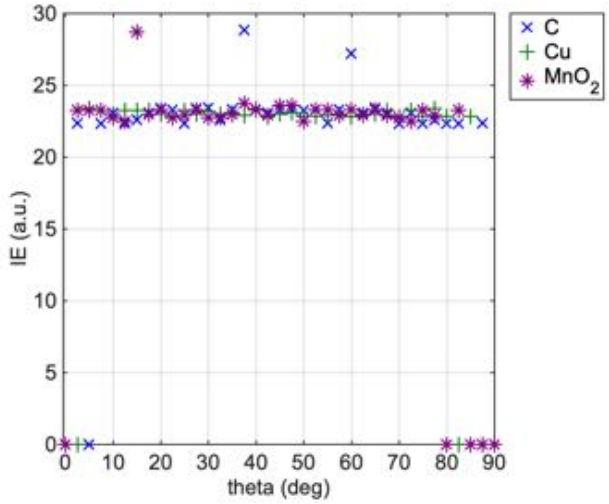

(a)

150 keV

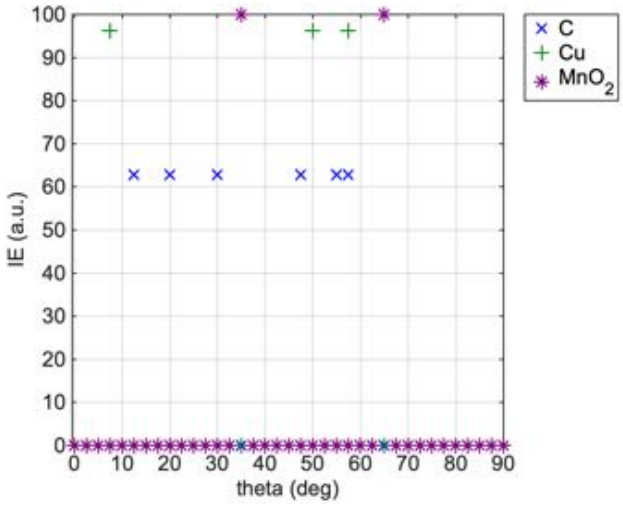

(b)

500 keV

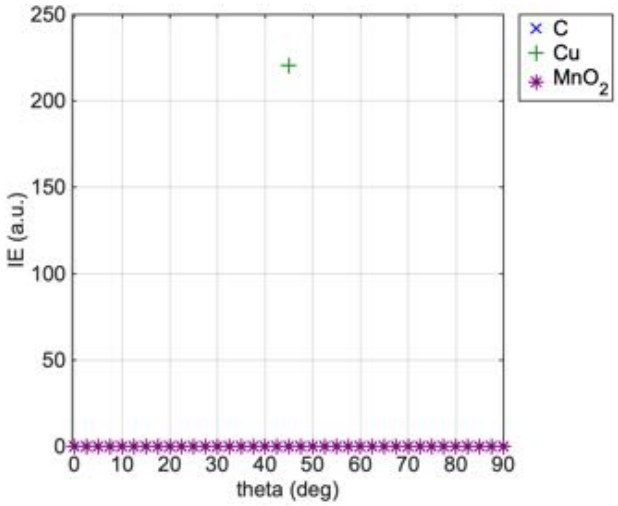

(c)

Figure 9.26 Fluorescence brightness angular distribution at 25 keV (a), 150 keV (b) and 500 keV (c) for carbon, copper, manganese dioxide thick films with aluminium barrier.

s

9.14.4.6 Fluorescence – iron barrier

Image brightness due by fluorescence events angular distributions of thick carbon, copper and manganese dioxide with iron barrier are calculated as angular distributions.

Figure 9.27 shows the (average azimuthal) value of the fluorescence pixel brightness (I(E)) calculated every 2.5 degrees between 0 and 90 degrees for all the materials. The graphs for energies of 25keV, 150keV and 500keV are shown on figures (a), (b) and (c), respectively.

The iron 2 mm barrier appears to screen any fluorescence from the thick copper layer behind at all energies. In figure 9.21 we see only one material angular distribution, which can be linked to the angular distribution of thin iron in figure 9.15(a). At higher energies, we find some fluorescence from carbon, which is not due to carbon itself, but from secondary fluorescence events from the iron barrier. To verify that, we can compare figures 9.21(b) (c) to figure 9.15 (b) (c) at 150 keV and 500 keV, respectively.

25 keV

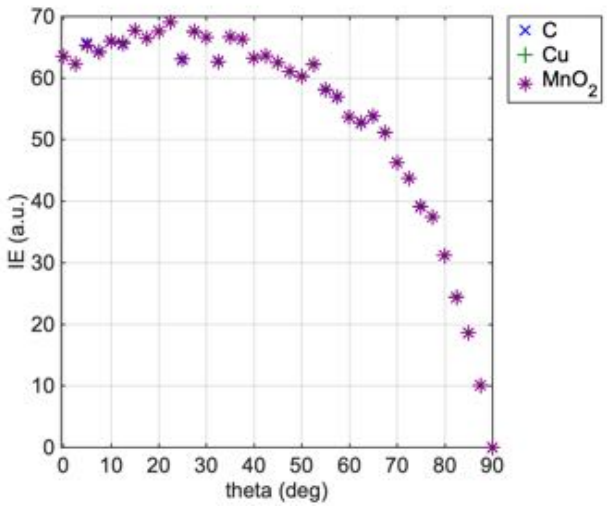

(a)

150 keV

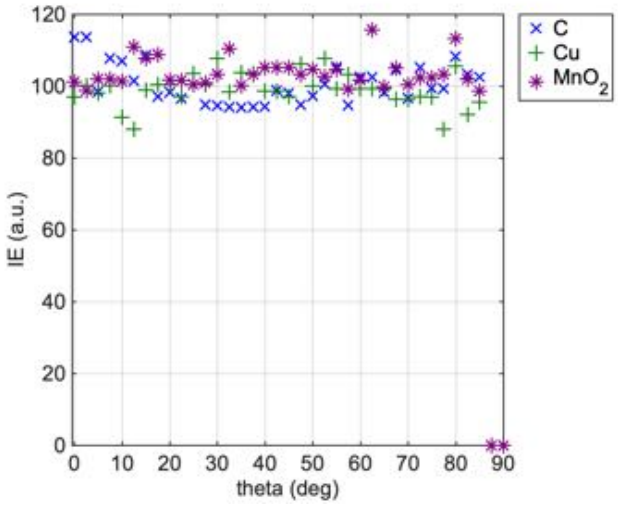

(b)

500 keV

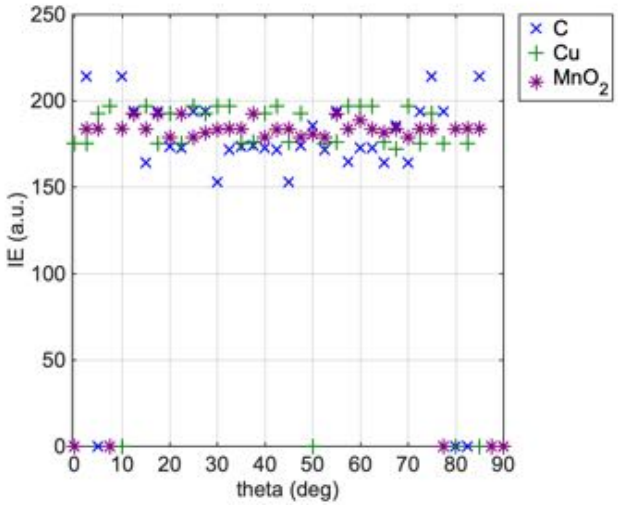

(c)

Figure 9.27 Fluorescence brightness angular distribution at 25 keV (a), 150 keV (b) and 500 keV (c) for carbon, copper, manganese dioxide with iron barrier.

9.15 Interpretation of relative yield data for thick materials

In this section the relative yield calculated from PENELOPE phase-space file with PAXI algorithm will be explored for thick materials and for thick materials with

barrier only. The data were extracted from the phase-space files as the number of detected lines out of the number of simulated showers in the input file. This quantity was averaged per annulus and divided by the annulus solid angle. Then, the calculated relative yield/sr was plotted as angular distribution.

Relative yield was explored similarly to the image brightness, i.e. as angular distribution of thick materials (9.15.1), and thick materials with barriers (9.15.2) at 25 keV, 150 keV and 500 keV, the data of the psf-file from each configuration separated by kind of interactions, i.e. Compton scatter, elastic scatter, and fluorescence, in order to compare the signatures of the materials as relative yield.

The materials were set to be 50 mm thick. A 2 mm aluminium/iron barrier was then added to the configuration. The relative yield was separated by kind of interactions by selecting the right ILB3 parameter, i.e. Compton scatter (ILB3=2), elastic scatter (ILB3=1) and fluorescence (ILB3=3) events, and they were clustered in 2.5˚ by 2.5˚ annuli 0˚-90˚ elevation angle range, with 0˚ equal to total backscatter. Fluorescence relative yield is the most important information to gather from this calculation. Compton scatter events were considered as competing mechanisms when counting the number of photons and could hide fluorescence information for material identification. Elastic scatter relative yield was negligible compared with other events (~ten times lower), so it will not be shown.

9.15.1 Fluorescence

Relative yield was calculated for fluorescence as angular distributions of 50 mm thick carbon, copper, manganese dioxide, and lead.

Figure 9.28 shows the (average azimuthal) value of the relative yield calculated every 2.5 degrees between 0 and 90 degrees (elevation) for all the materials. The graphs for energies of 25keV, 150keV and 500keV are shown on figures (a), (b) and (c) for all the materials.

At low energies in figure 9.28 (a), lead and copper fluorescence relative yield appear overlapped, while lead fluorescence becomes overwhelming at greater energies 9.28 (c), (e). With the regards of the other materials, at 150 keV and 500 keV, the fluoresce relative yield is very low (about ten and hundred times lower) compared with the relative yield of lead.

The fluorescence yield for carbon, copper and manganese dioxide are plotted separately in fig. 9.28 (b)(d) and (f). Carbon has no significant fluorescence, giving confidence to the calculations. Copper fluorescence relative yield is higher at lower, medium and higher energies, followed by manganese dioxide.

25 keV

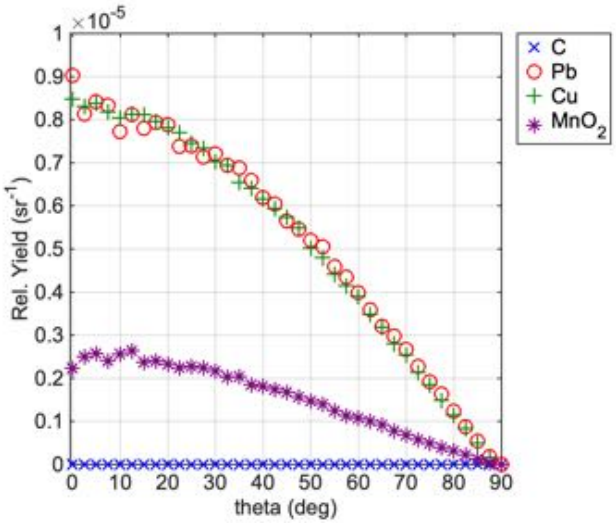

(a)

150 keV

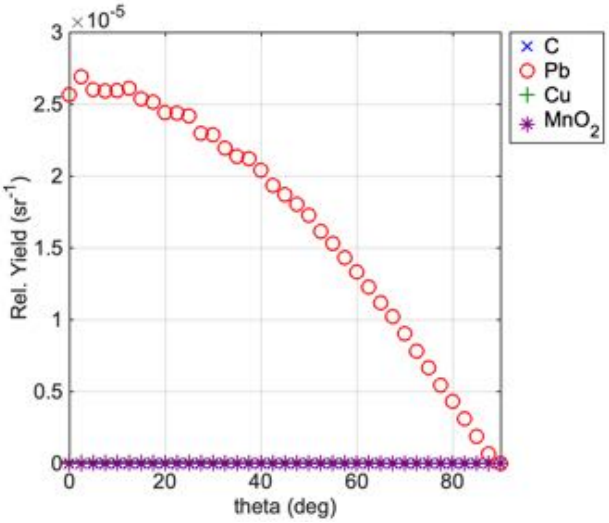

(b)

500 keV

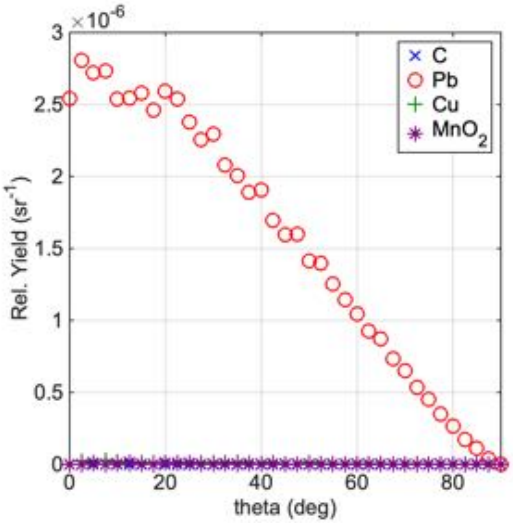

(c)

Figure 9.28 Fluorescence relative yield angular distribution at 25 keV (a), 150 keV (b) and 500 keV (c) for 5 cm thick carbon, copper, manganese dioxide and lead.

9.15.2 Compton scattering

Compton scatter relative yield of 50 mm thick carbon, copper, manganese dioxide and lead are calculated as angular distributions.

Figure 9.29 shows the (average azimuthal) value of the relative yield calculated every 2.5 degrees between 0 and 90 degrees for all the materials. The graphs for energies of 25keV, 150keV and 500keV are shown on figures (a), (b) and (c), respectively.

We see carbon has the highest inelastic scatter yield at all the incident energies. If carbon was the only material to identify, this information can be used for identifying the carbon-based layer. But if we had several layers of different materials, Compton broad peak would count all the Compton events, including not only carbon Compton yield but also the yield from other materials. Thus, in order to identify carbon in pixelated or energy dispersive detector, the separation of carbon Compton yield from the other (mostly unknown) layers would be required. This is not possible at the moment but may be achievable in the future.

With the regards of the other materials, as we can see on the figure 9.29(a), the relative yield at 25keV of the other materials is not significant, while at mid-high energies (fig. 9.29 (b) and (c)) manganese dioxide and copper relative yield arise and lead remains the lowest at the same 50 mm thickness.

If we compare Compton relative yield in figure 9.29 with fluorescence yield in figure 9.28, assuming the energy is as low as 25 keV, and the imaging scene comprises layers of carbon, copper, manganese dioxide and lead of the same thickness (50 mm), it is possible the Compton broad peak generated by the carbon thick layer (and other scatter events, for example from the laboratory environment) hides the characteristic lines of copper and manganese dioxide (and also lead), as the Compton relative yield of carbon is about twice and four times the fluorescence relative yield of copper/lead and manganese dioxide respectively. This situation is recurrent and even worse at medium and higher energies. This is the reason why detecting fluorescence yield from for example copper wires and batteries made of manganese dioxide can be challenging.

25 keV

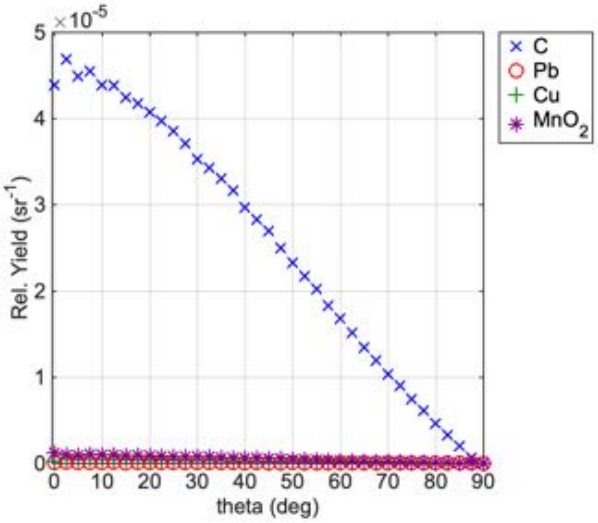

(a)

150 keV

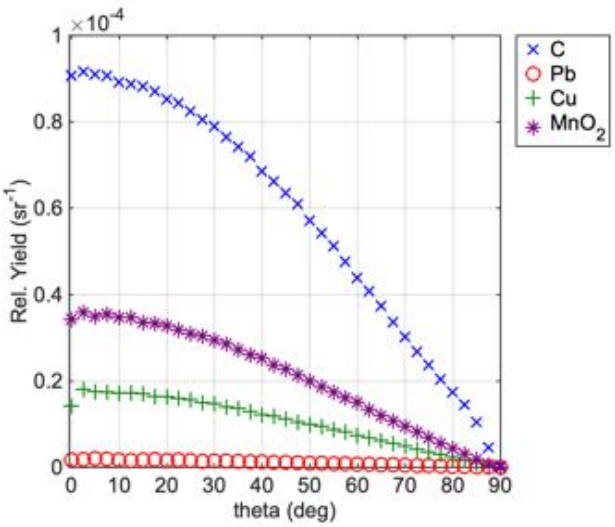

(b)

500 keV

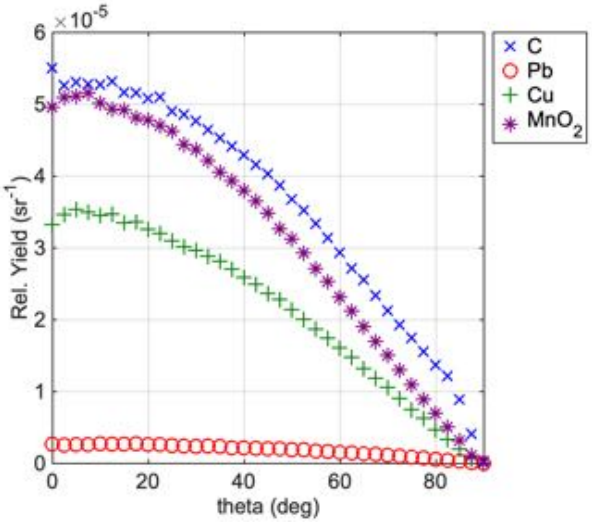

(c)

Figure 9.29 Compton scatter relative yield angular distribution at 25 keV (a), 150 keV (b) and 500 keV (c) for 50 mm thick carbon, copper, manganese dioxide, lead.

9.16 Interpretation of relative yield data for thick materials through barrier

Generally, when adding a barrier or a shielding material, measuring the relative yield due to fluorescence is more challenging. By adding a barrier, we normally introduce a metallic material, i.e. aluminium and iron (or also lead), which contains its own characteristics yield. This may hide the information from the target material behind, not only visually as for the image brightness as seen in section 9.14, but also in terms of number of characteristic photons which can escape from the material and reach the detector after going through the barrier.

In this section, we will explore 50 mm thick materials for calculating the relative yield of carbon, copper, manganese dioxide with a 2 mm barrier of aluminium and iron. The different configurations were again simulated at 25 keV, 150 keV and 500 keV. In the following subsections, the relative yield of fluorescence and Compton scatter (only) of target materials through aluminium and iron barriers will be shown.

9.16.1.1 Fluorescence – aluminium barrier

Relative yield was also calculated for fluorescence as angular distributions of 50 mm thick carbon, copper, manganese dioxide and 2 mm thick aluminium barrier.

Figure 9.41 shows the (average azimuthal) value of the relative yield calculated every 2.5 degrees between 0 and 90 degrees for all the materials. The graphs for energies of 25keV, 150keV and 500keV are shown on figures (a), (b) and (c).

Generally, the relative yield from fluorescence is not significant when placing an aluminium barrier. We find some fluorescence from carbon, but this signal is generated from secondary interactions within the barrier rather than the target itself. At high energy (500 keV), fluorescence is completely screened with a barrier.

25 keV

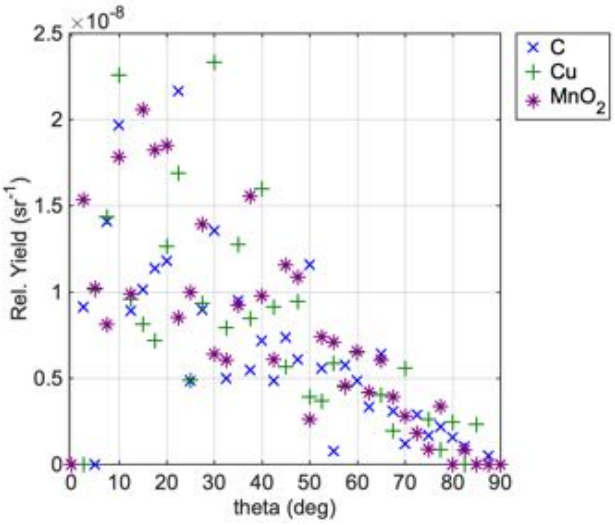

(a)

150 keV

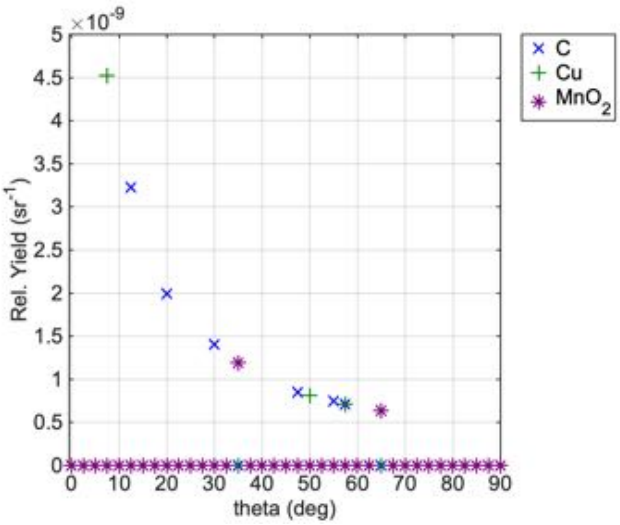

(b)

500 keV

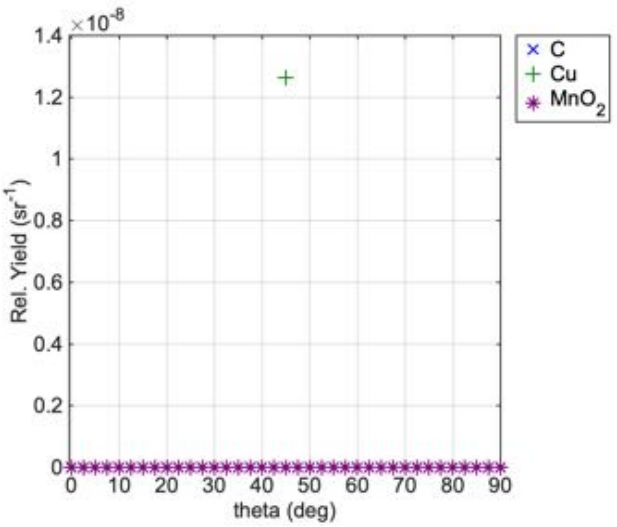

(c)

Figure 9.30 Fluorescence yield angular distribution at 25 keV (a), 150 keV (b) and 500 keV (c) for 5 cm thick carbon, copper, manganese dioxide, lead and 2 mm aluminium barrier on top.

9.16.1.2 Compton scattering – aluminium barrier

Compton scatter relative yield of 50 mm thick carbon, copper and manganese dioxide with 2 mm aluminium barrier are calculated as angular distributions.

Figure 9.37 shows the (average azimuthal) value of the relative yield calculated every 2.5 degrees between 0 and 90 degrees for all the materials. The graphs for energies of 25keV, 150keV and 500keV are shown on figures (a), (b) and (c), respectively.

We see carbon has the highest inelastic scatter yield at all the incident energies. As we can see on the figure 9.37(a), the relative yield at 25keV of the two other materials is the same, that is the value of inelastic relative yield of aluminium, while at mid-high energies (fig. 9.37 (b) and (c)) manganese dioxide and copper relative yield arise. Figure 9.37 can be compared against the previous configuration where there was no barrier on top of the target material (fig. 9.34). Carbon relative yield appears attenuated at 25 keV of a factor of five, while at medium and high energies the beam can penetrate the barrier and Compton scatter is the same as thick materials. At 500 keV inelastic scatter relative yield of carbon is slightly higher than that without aluminium barrier.

25 keV

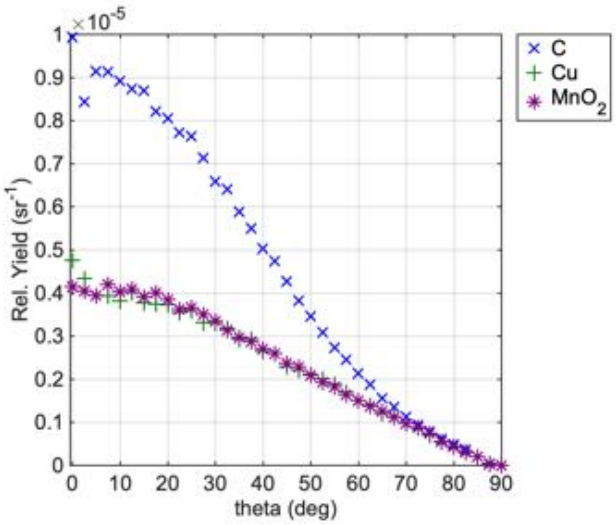

(a)

150 keV

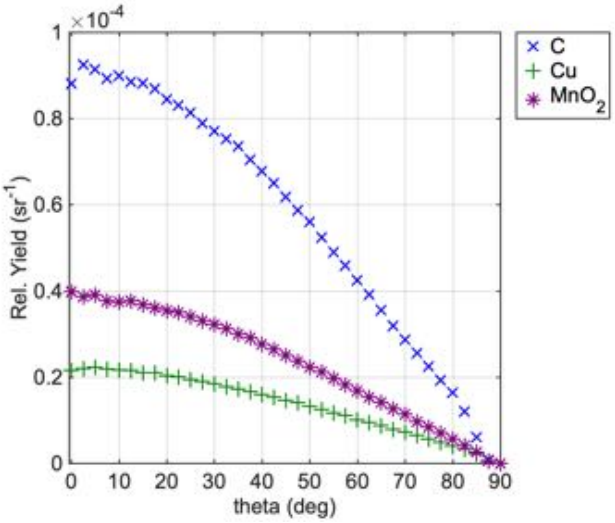

(b)

500 keV

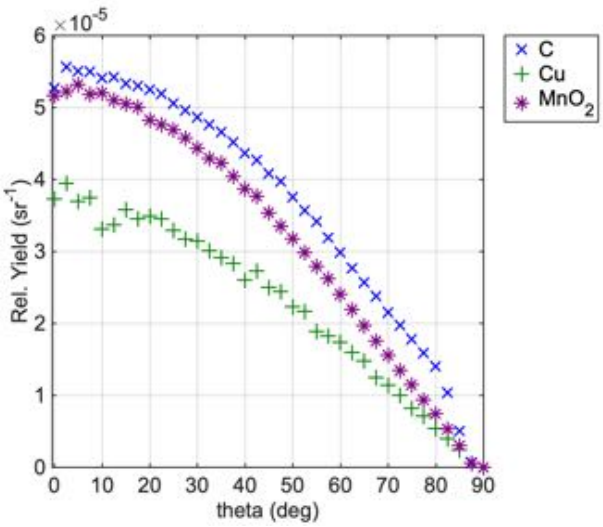

(c)

Figure 9.31 Compton scatter yield angular distribution at 25 keV (a), 150 keV (b) and 500 keV (c) for 5 cm thick carbon, copper, manganese dioxide, lead and 2 mm aluminium barrier on top.

9.16.1.3 Fluorescence – iron barrier

Relative yield calculation was repeated with 2 mm thick iron barrier.

Figure 9.32 shows the (average azimuthal) value of the relative yield calculated every 2.5 degrees between 0 and 90 degrees for all the materials. The graphs for energies of 25keV, 150keV and 500keV are shown on figures (a), (b) and (c).

When placing an iron barrier, the relative yield from fluorescence is the same as thin iron at lower energies (9.32(a)), while it is not significant at medium-high energy (500 keV), and fluorescence is completely screened with a barrier (9.32(b) and (c)).

25 keV

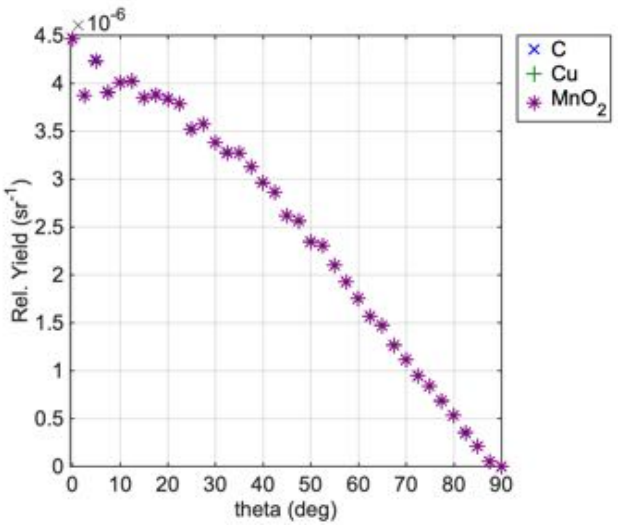

(a)

150 keV

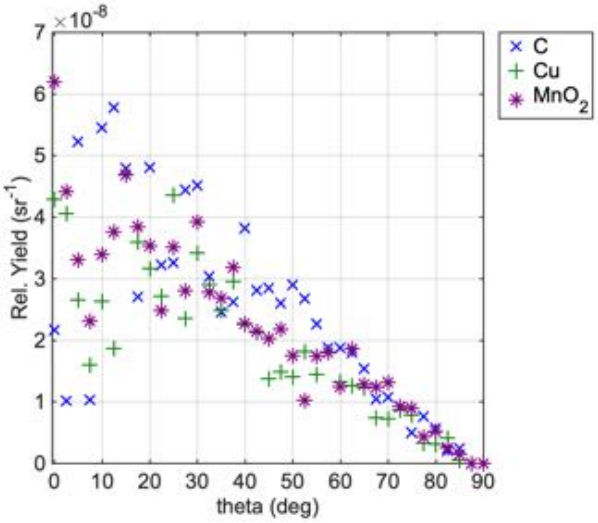

(b)

500 keV

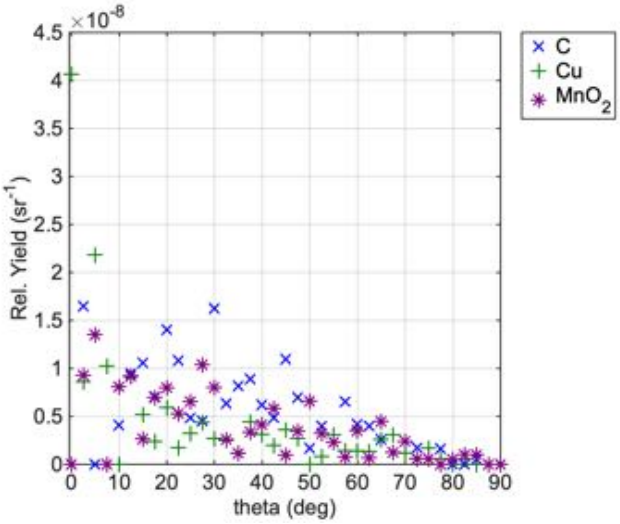

(c)

Figure 9.32 Fluorescence relative yield angular distribution at 25 keV (a), 150 keV (b) and 500 keV (c) for 50 mm thick carbon, copper, manganese dioxide, lead and 2 mm iron barrier on top.

9.16.1.4 Compton scattering – iron barrier

Compton scatter relative yield of thick materials was also calculated with an iron barrier.

Figure 9.38 shows the (average azimuthal) value of the relative yield calculated every 2.5 degrees between 0 and 90 degrees for all the materials. The graphs for energies of 25keV, 150keV and 500keV are shown on figures (a), (b) and (c), respectively.

At low beam energies, there is no scatter relative yield recorded as the beam energy is too low to go through the barrier (fig. 9.38 (a)). Carbon has the highest inelastic scatter yield at medium incident energies (fig. 9.38 (b)), followed by manganese dioxide and copper relative yields. The last two materials relative yields are the same close to the edges of the detector. At high energies (fig. 9.38 (c)), carbon relative yield is attenuated and overlapped with manganese dioxide relative yield until about 40˚. At greater angles, the relative yield angular distribution increases. That is the contrast between carbon and manganese dioxide may be appreciated only for angles greater than 40˚.

25 keV

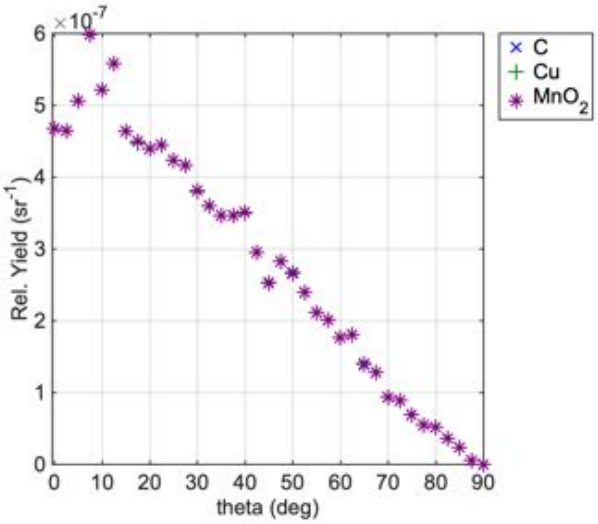

(a)

150 keV

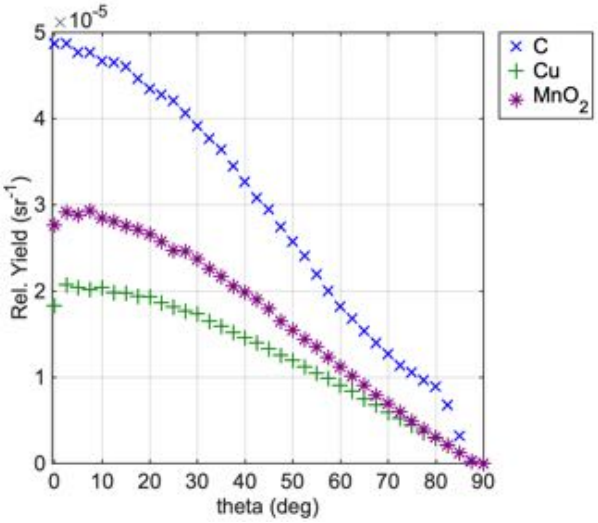

(b)

500 keV

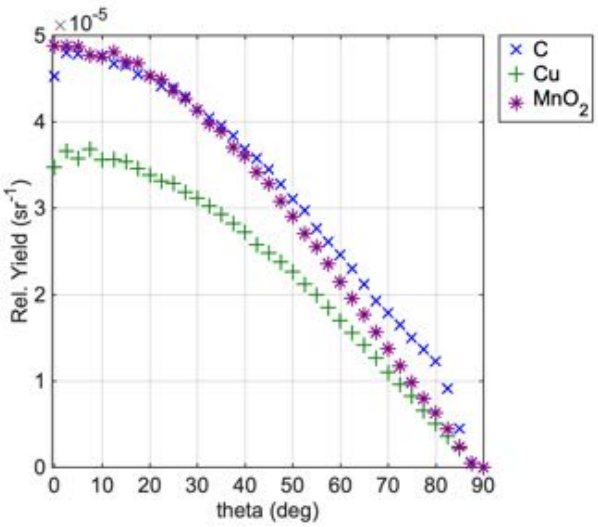

(c)

Figure 9.33 Compton scatter relative yield angular distribution at 25 keV (a), 150 keV (b) and 500 keV (c) for 50 mm thick carbon, copper, manganese dioxide, lead and 2 mm iron barrier on top.

9.17 Interpretation of energy-probability data

In this section the energy-probability calculated from PENELOPE phase-space file with PAXI algorithm will be explored. The data were extracted from the phase-space files as described in section 9.13, where the energy-probability as function of angle was defined.

Energy-probability was explored similarly to the image brightness (section 9.14), i.e. as angular distribution from thin materials (9.16.1), rotated materials (9.16.2), thick materials (9.16.3), and thick materials with barriers (9.16.4) at 25 keV, 150 keV and 500 keV. The data of the psf-file from each configuration was separated by kind of interaction, i.e. Compton scatter, elastic scatter, and fluorescence, in order to compare the signatures of the materials as energy spectra.

In PAXI, the angular distribution of the energy-probability is estimated separately from the image brightness by calculating the maximum of the spectrum at each angle. The power of the hemispherical detector is that of an energy-dispersive detector, thus maximising number of events from a sample is more beneficial than averaging for detecting and discriminating the materials, especially for fluorescence, which could be hidden beneath a broad Compton peak, at certain angles, but could be exposed when changing the detector position.

9.17.1 Interpretation of energy-probability data for thin materials

We will explore thin materials for calculating the energy-probability. The energy-probability was separated by kind of interactions by selecting the right ILB3 parameter, i.e. Compton scatter (ILB3=2), elastic scatter (ILB3=1) and fluorescence (ILB3=3) events, and they were clustered in 2.5˚ by 2.5˚ annuli 0˚-90˚ elevation angle range, with 0˚ equal to total backscatter. In this section of work, carbon, copper, manganese dioxide, lead, aluminium and iron were set to be 1 mm thick, and they were simulated at 25 keV, 150 keV and 500 keV. In the following subsections, the energy-probability of Compton scatter, elastic scatter and fluorescence will be shown.

9.17.1.1 Compton scattering

Compton scatter energy-probability of 1 mm thick carbon, copper, manganese dioxide, lead, aluminium and iron are calculated as angular distributions.

Figure 9.34 shows the value of the energy-probability calculated every 2.5 degrees elevation between 90˚ and 0˚ for all the materials. The graphs for energies of 25keV, 150keV and 500keV are shown on figures (a), (b) and (c), respectively.

We can observe in figure 9.34 the energy-probability at 25 keV is ten times and hundred times higher than 150 keV and 500 keV, respectively.

We can also observe the probability is the lowest at lower angles <20˚, then it increases towards wider angles until it reaches the maximum between 40˚-50˚ and finally drops towards the edges at >60˚, which is likely due to strong attenuation along the long exit path inside the target material. That means a broad Compton peak is likely to be seen at around 45˚, which will be counted in the background of the energy spectrum. This should be taken into account when measuring fluorescence in the energy spectra. Positioning the detector in the elevation angle could lead to missing fluorescence peaks as opposed as 'incorrect' fluorescence peaks, fundamental for material identification, as they would be hidden by the broad Compton background.

We see carbon has the highest inelastic scatter probability when the incident energy is low at 25 keV (fig. 9.34 (a)), followed by aluminium (about twice lower) and manganese dioxide (ten times lower). At 150 keV and 500 keV (fig. 9.34(b) and (c)) Compton scatter probability of the other materials arises and they all have similar values, that is their Compton scatter would contribute to total energy spectrum background. Compton scatter energy-probability of iron at medium-high energies in figures 9.34(b) (c) can explain why image brightness and relative yield due to fluorescence is significantly reduced when iron is the barrier on top of the target materials, such as copper and manganese dioxide as seen in figures 9.27 and 9.32.

25 keV

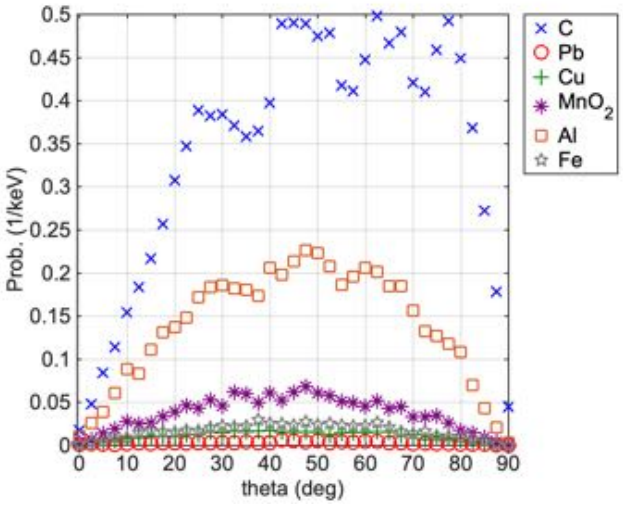

(a)

150 keV

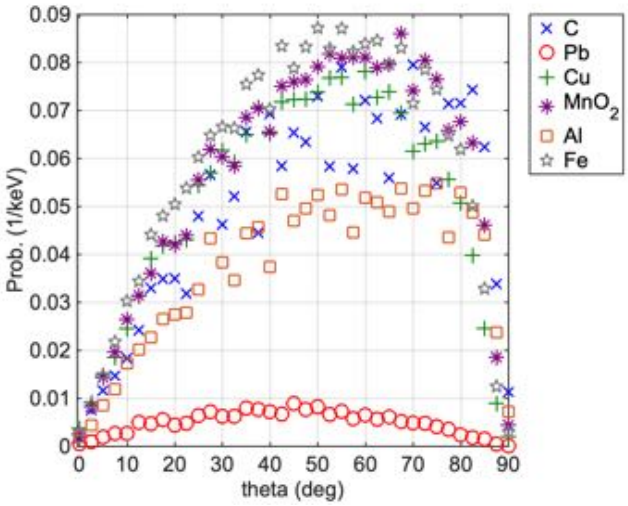

(b)

500 keV

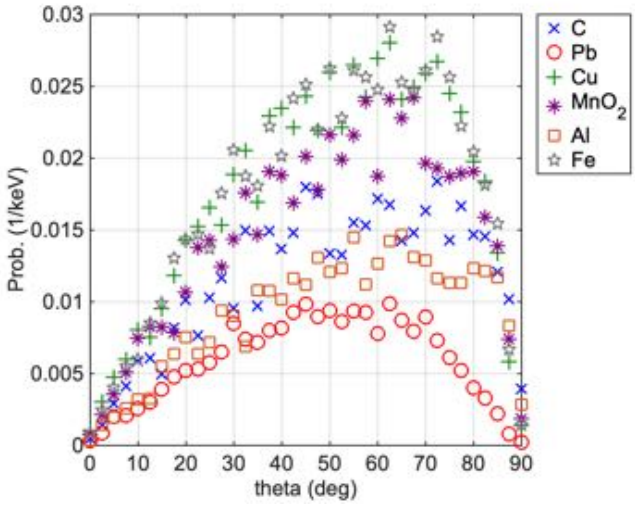

(c)

Figure 9.34 Compton scatter energy-probability angular distribution at 25 keV (a), 150 keV (b) and 500 keV (c) for 1 mm thick carbon, copper, manganese dioxide, lead, aluminium and iron thin films.

9.17.1.2 Elastic scattering

Elastic scatter energy-probability of 1 mm thick carbon, copper, manganese dioxide, lead, aluminium and iron are calculated as angular distributions.

Figure 9.35 shows the value of the energy-probability calculated every 2.5 degrees between 0˚ and 90˚ for all the materials. The graphs for energies of 25keV, 150keV and 500keV are shown on figures (a), (b) and (c), respectively.

Elastic scatter appears four times lower than Compton scatter in figure 9.34, thus the lower probability is unlikely to significantly affect the energy spectra and would not be determinant for shaping the background energy spectrum. Although elastic scatter here does not seem to significantly contribute to the total energy spectrum, elastic scatter could lead to secondary inelastic scatter which then would contribute to the background spectrum. For example, lead has the largest elastic scatter contribution for the total energy spectrum and secondary events may arise and generate artefacts.

25 keV

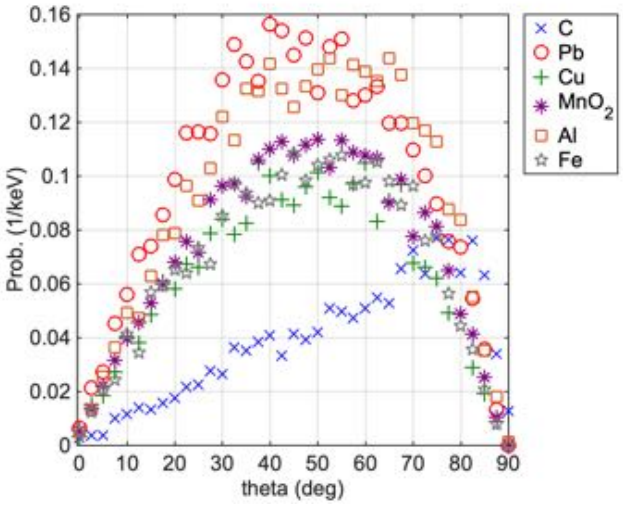

(a)

150 keV

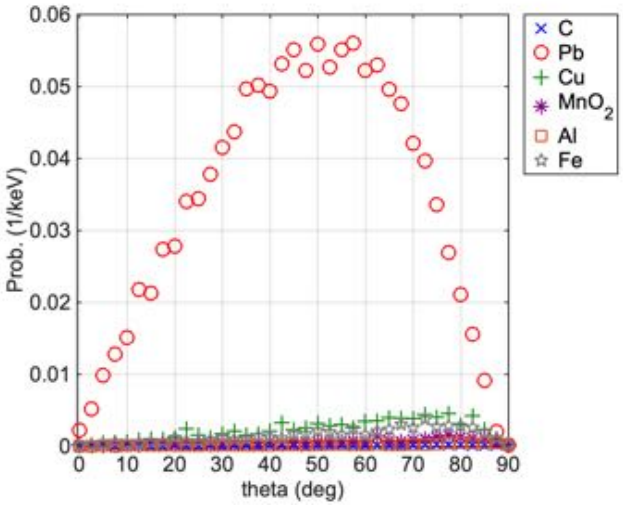

(b)

500 keV

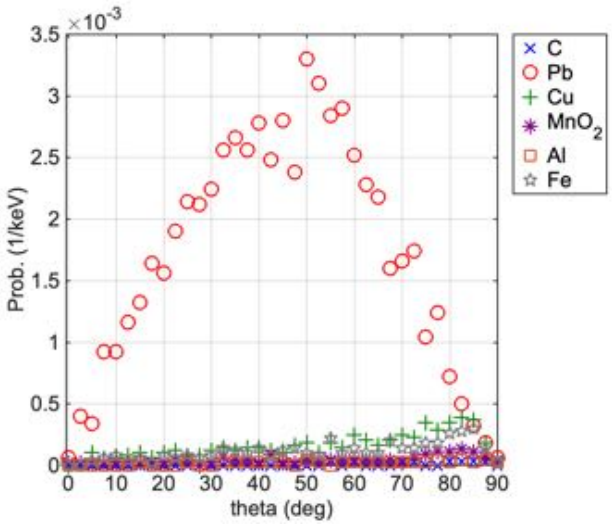

(c)

Figure 9.35 Elastic scatter energy-probability angular distribution at 25 keV (a), 150 keV (b) and 500 keV (c) for 1 mm thick carbon, copper, manganese dioxide, lead, aluminium and iron thin films.

9.17.1.3 Fluorescence

Fluorescence energy-probability of 1 mm thick carbon, copper, manganese dioxide, lead, aluminium and iron are calculated as angular distributions.

Figure 9.36 shows the value of the energy-probability calculated every 2.5 degrees between 0 and 90 degrees for all the materials. The graphs for energies of 25keV, 150keV and 500keV are shown on figures (a), (b) and (c), respectively.

At lower energies (25 keV) (figure 9.36(a)), fluorescence appears four times higher than Compton scatter in figure 9.34(a), that is the copper characteristic lines are more likely to be detected at ~45˚. When the energy arises, fluorescence from all the materials except lead is not significant if compared with Compton energy-probability. Only lead has a significant contribution, but lead is typically a shielding material or a background material used for enhancing image contrast, and its characteristic lines can arise from the spectrum background and hide those from other materials at the same thickness.

25 keV

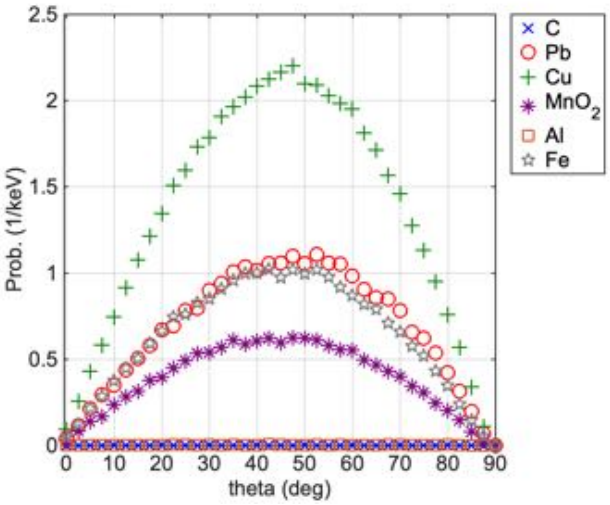

(a)

150 keV

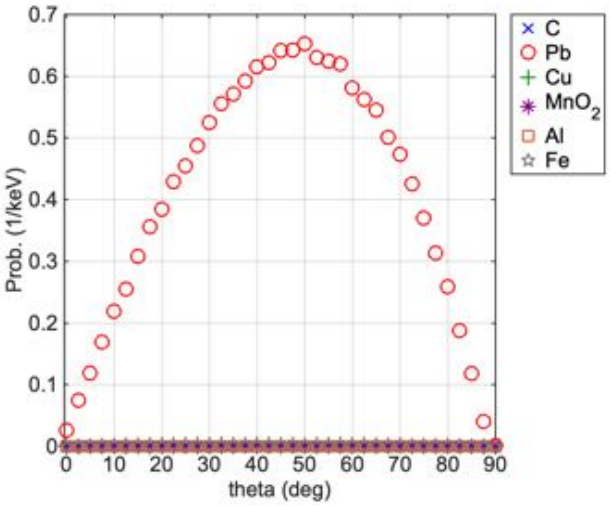

(b)

500 keV

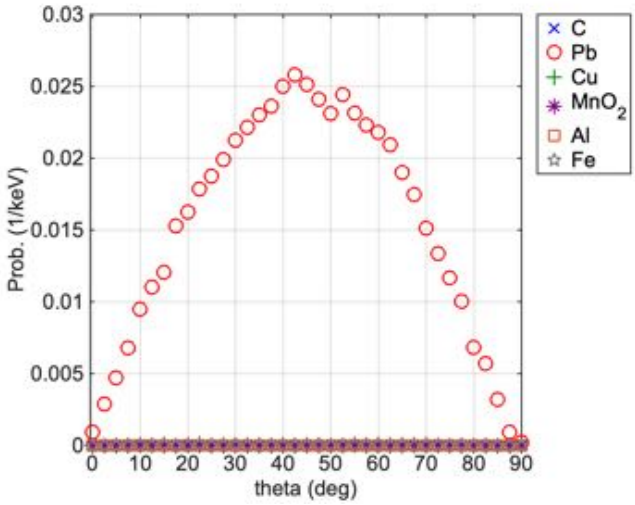

(c)

Figure 9.36 Fluorescence energy-probability angular distribution at 25 keV (a), 150 keV (b) and 500 keV (c) for 1 mm thick carbon, copper, manganese dioxide, lead, aluminium and iron thin films.

9.18 Interpretation of energy-probability data for thin rotated materials

In this section, we will explore thin (1 mm) materials rotated of 45˚ for calculating the energy-probability angular distribution. The energy-probability was again separated by kind of interactions as seen for thin materials in section 9.17, and they were clustered in 2.5˚ by 2.5˚ annuli 0˚-90˚ elevation angle. In this section, only carbon, copper, manganese dioxide, lead were studied at 25 keV, 150 keV and 500 keV. In the following subsections, the energy-probability of Compton scatter, elastic scatter and fluorescence will be shown.

9.18.1.1 Compton scattering

Compton scatter energy-probability of 1 mm thick 45˚ rotated carbon, copper, manganese dioxide, and lead are calculated as angular distributions.

Figure 9.37 shows the value of the energy-probability calculated every 2.5 degrees between 0 and 90 degrees for all the materials. The graphs for energies of 25keV, 150keV and 500keV are shown on figures (a), (b) and (c), respectively.

Compared with figure 9.34 thin non-rotated materials, we can observe the probability in figure 9.37 is consistently increasing towards greater angles at ~60˚, as the target materials are now rotated. That means a broad Compton peak is likely to be seen in the energy spectrum from around 45˚.

We see again carbon has the highest inelastic scatter probability when the incident energy is low at 25 keV (fig. 9.37 (a)), followed by manganese dioxide (about six times lower). At 150 keV and 500 keV (fig. 9.37(b) and (c)) Compton scatter probability of the other materials arises and they all have similar values, that is their Compton scatter would contribute to total energy spectrum background. Compton scatter energy-probability of manganese dioxide is higher at medium energies in figures 9.37(b), while copper has the greatest energy-probability at high beam energies (fig. 9.37 (c)).

25 keV

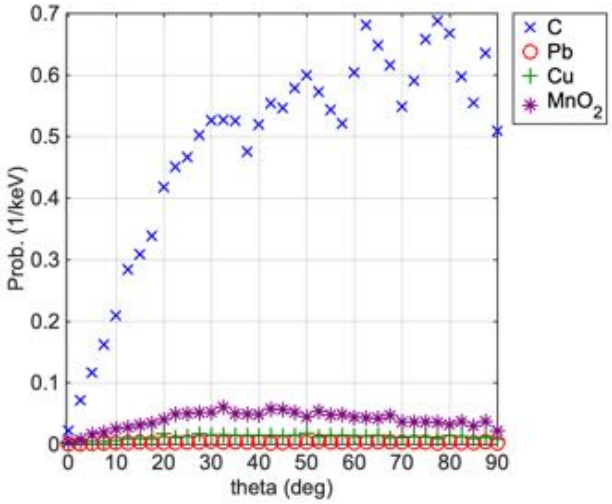

(a)

150 keV

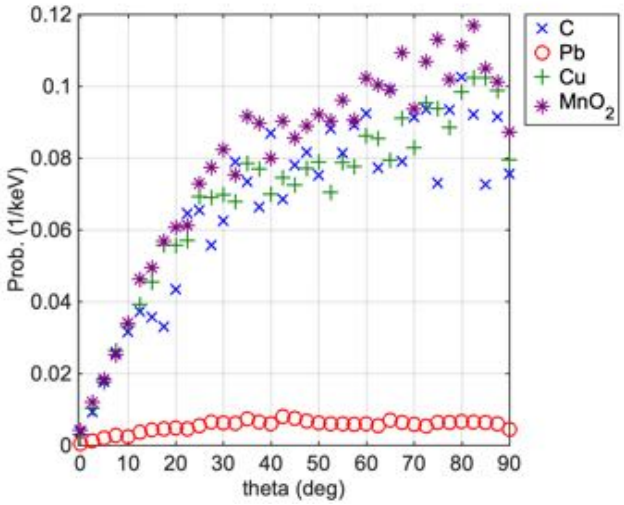

(b)

500 keV

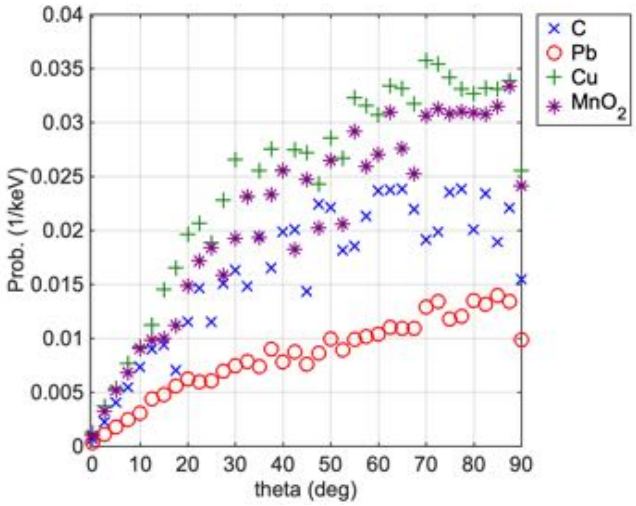

(c)

Figure 9.37 Compton scatter energy-probability angular distribution at 25 keV (a), 150 keV (b) and 500 keV (c) of 1 mm thick rotated carbon, copper, manganese dioxide, lead, aluminium and iron thin rotated 45˚ films.

9.18.1.2 Elastic scattering

Elastic scatter energy-probability of 1 mm thick rotated carbon, copper, manganese dioxide, lead, aluminium and iron are calculated as angular distributions.

Figure 9.38 shows the value of the energy-probability calculated every 2.5 degrees between 0˚ and 90˚ for all the materials. The graphs for energies of 25keV, 150keV and 500keV are shown on figures (a), (b) and (c), respectively.

Elastic scatter appears about four times lower than Compton scatter in figure 9.37, repeating what already seen in figure 9.35 when the target materials were not rotated. Thus, the lower probability is unlikely to significantly affect the energy spectra and would not be determinant for shaping the background energy spectrum but could potentially lead to secondary inelastic scatter which then would contribute to the background spectrum. Lead has the largest elastic scatter contribution at all the energies also when the target was rotated.

25 keV

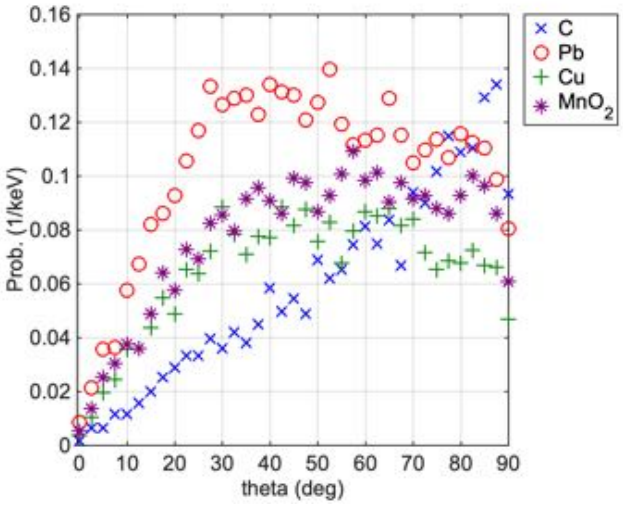

(a)

150 keV

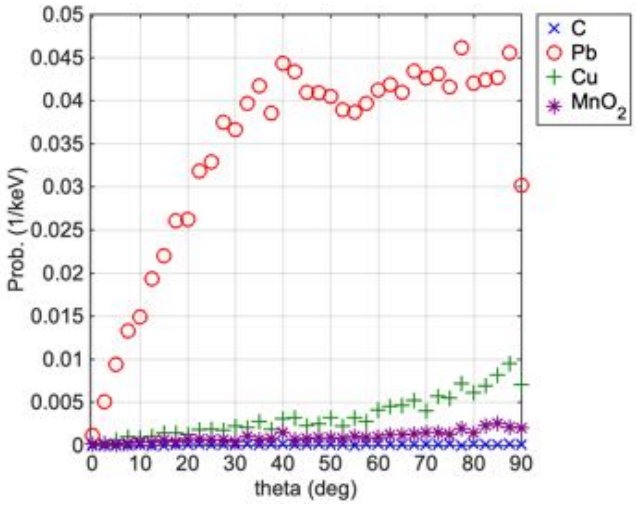

(b)

500 keV

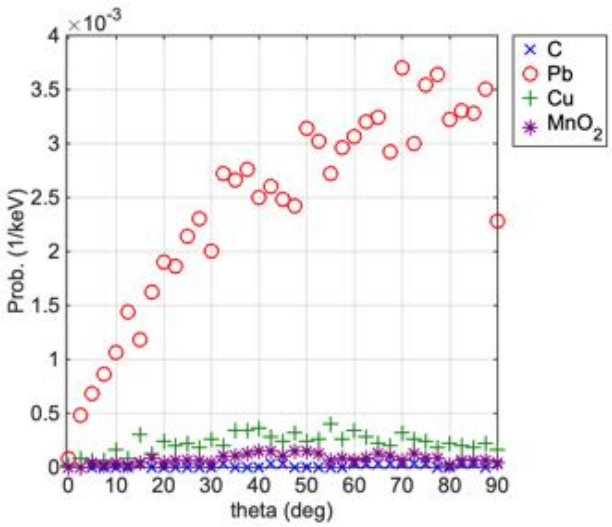

(c)

Figure 9.38 Elastic scatter energy-probability angular distribution at 25 keV (a), 150 keV (b) and 500 keV (c) of 1 mm thick rotated carbon, copper, manganese dioxide, lead, aluminium and iron thin rotated 45˚ films.

9.18.1 Fluorescence

Fluorescence energy-probability of 1 mm thick rotated carbon, copper, manganese dioxide, lead, aluminium and iron are calculated as angular distributions.

Figure 9.39 shows the value of the energy-probability calculated every 2.5 degrees between 0˚ and 90˚ for all the materials. The graphs for energies of 25keV, 150keV and 500keV are shown on figures (a), (b) and (c), respectively.

At lower energies (25 keV) (figure 9.39(a)), fluorescence appears four times higher than Compton scatter in figure 9.37(a), repeating what was found for thin materials in figure 9.36(a). When the energy arises, fluorescence from all the materials except lead is not significant if compared with Compton energy-probability as for thin materials. As only lead has a significant contribution, its characteristic lines can arise from the spectrum background and hide those from other materials at the same thickness as for thin non-rotated materials.

25 keV

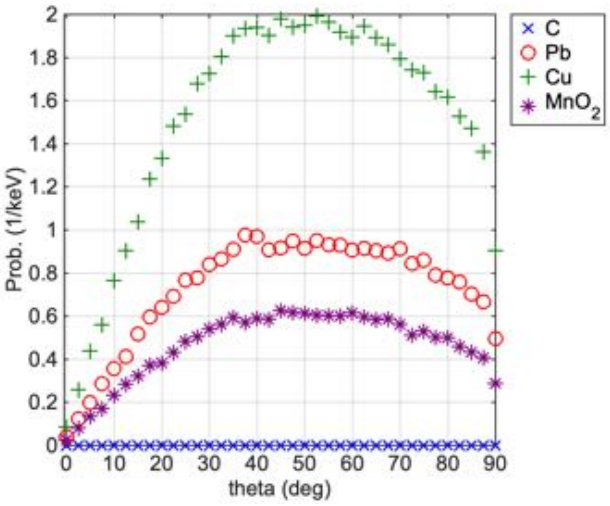

(a)

150 keV

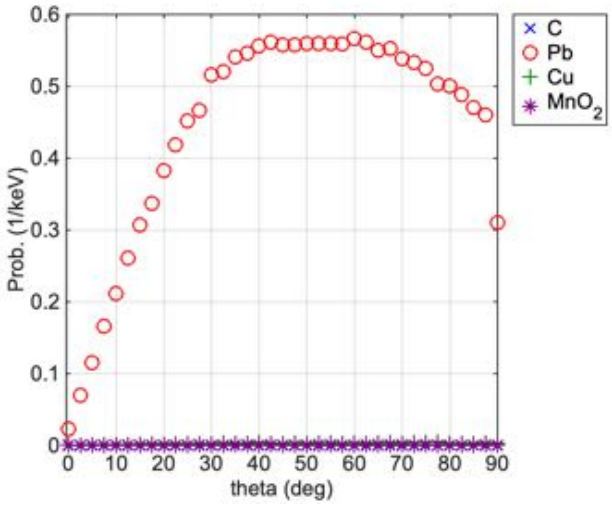

(b)

500 keV

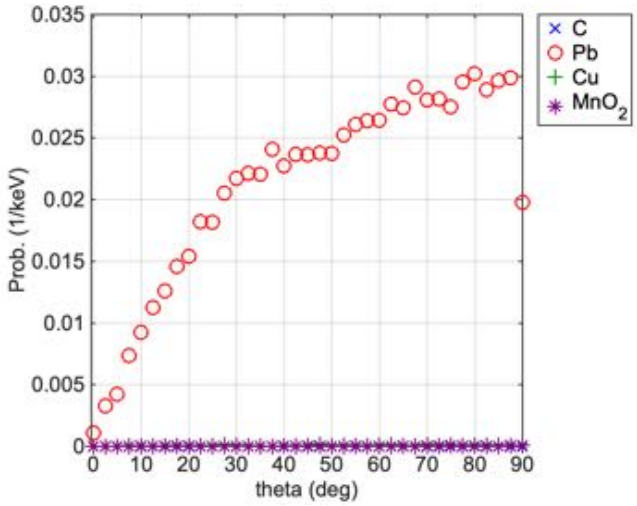

(c)

Figure 9.39 Fluorescence energy-probability angular distribution at 25 keV (a), 150 keV (b) and 500 keV (c) of 1 mm thick rotated carbon, copper, manganese dioxide, lead, aluminium and iron thin rotated 45˚ films.

9.18.2 Interpretation of energy-probability data for thick materials

As for the thin materials, we will explore thick materials for calculating the energy-probability as elevation angular distribution 0˚-90˚separated by kind of interaction. In this section, carbon, copper, manganese dioxide, lead, aluminium and iron were set to be 50 mm thick, and they were simulated at 25 keV, 150 keV and 500 keV. In the following subsections, the energy-probability of Compton scatter, elastic scatter and fluorescence will be shown.

9.18.2.1 Compton scattering

Compton scatter energy-probability of 50 mm thick carbon, copper, manganese dioxide, and lead are calculated as angular distributions.

Figure 9.40 shows the value of the energy-probability calculated every 2.5 degrees between 0˚ and 90˚ for all the materials. The graphs for energies of 25keV, 150keV and 500keV are shown on figures (a), (b) and (c), respectively.

When compared with thin materials in figure 9.34, we see carbon has the highest inelastic scatter probability at all the energies at greater thicknesses. At 25 keV (fig. 9.34 (a)) the energy-probability is higher of a factor of three, at 150 keV and 500 keV (fig. 9.34(b) and (c)) of a factor of two compared with other materials. That is Compton scatter probability is more significant for a thick layer of carbon, and it would produce a broad peak in the energy spectrum which may hide fluorescence peaks of other materials.

25 keV

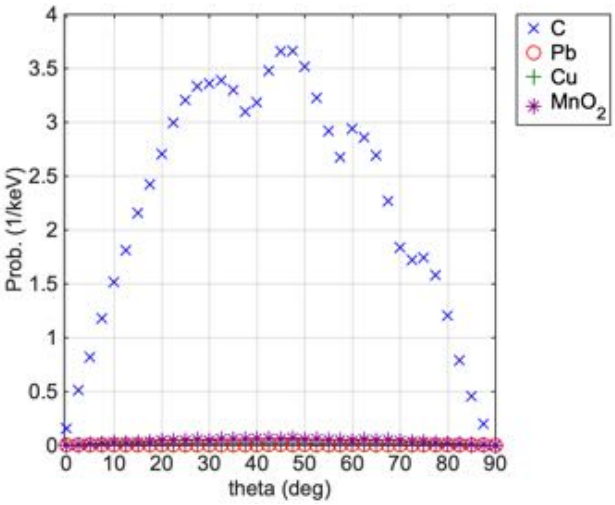

(a)

150 keV

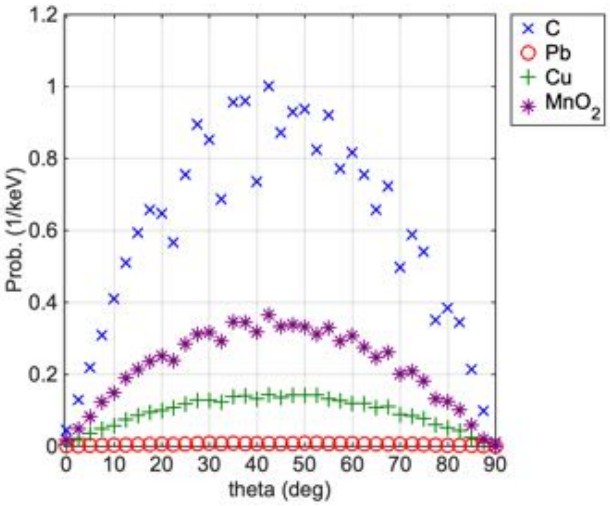

(b)

500 keV

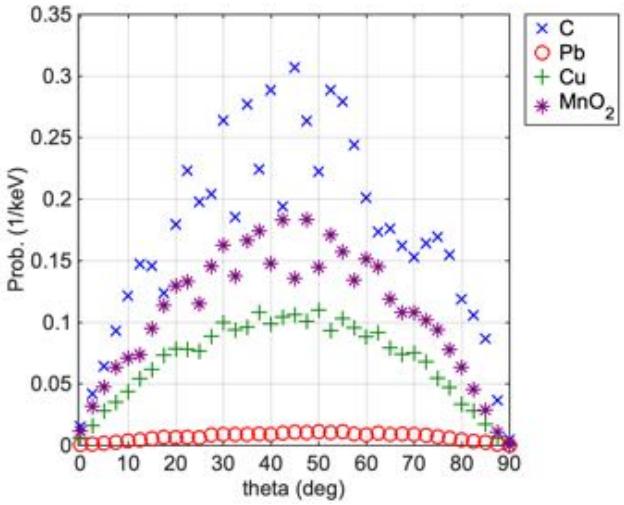

(c)

Figure 9.40 Compton scatter energy-probability angular distribution at 25 keV (a), 150 keV (b) and 500 keV (c) of 50 mm thick carbon, copper, manganese dioxide and lead thick films.

9.18.2.2 Elastic scattering

Elastic scatter energy-probability of 50 mm thick carbon, copper, manganese dioxide, and lead are calculated as angular distributions.

Figure 9.41 shows the value of the energy-probability calculated every 2.5 degrees between 0˚ and 90˚ for all the materials. The graphs for energies of 25keV, 150keV and 500keV are shown on figures (a), (b) and (c), respectively.

Although elastic scatter appears greater for thick materials than thin materials in figure 9.35, the contribution from those events is yet not significant for the overall energy spectrum. At 25 keV (fig. 9.41(a)), carbon has the highest energy-probability angular distribution, followed by lead, manganese dioxide and copper. At medium beam energies (150 keV) (fig. 9.41(b)) lead is confirmed to have the highest elastic scatter angular distribution, while copper is the arises against the other materials at high beam energies (500 keV) (fig. 9.41 (c)).

25 keV

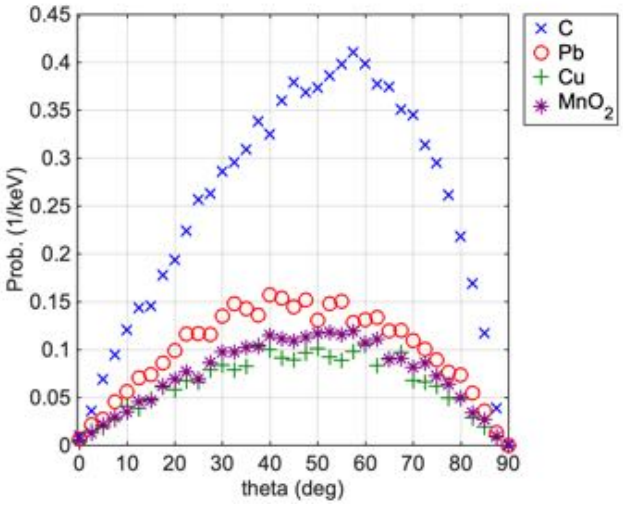

(a)

150 keV

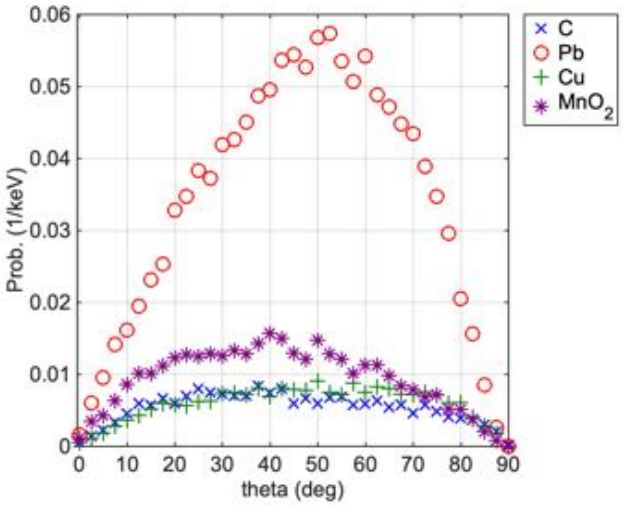

(b)

500 keV

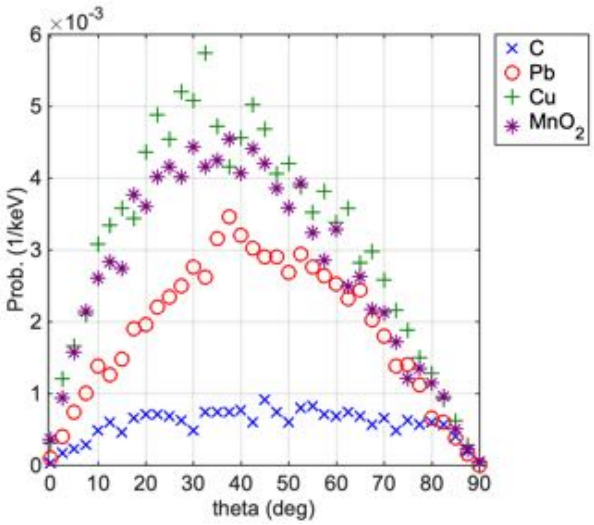

(c)

Figure 9.41 Elastic scatter energy-probability angular distribution at 25 keV (a), 150 keV (b) and 500 keV (c) of 50 mm thick carbon, copper, manganese dioxide, and lead thick films.

9.18.2.3 Fluorescence

Fluorescence energy-probability of 50 mm thick carbon, copper, manganese dioxide, and lead are calculated as angular distributions.

Figure 9.42 shows the value of the energy-probability calculated every 2.5 degrees between 0˚ and 90˚ for all the materials. The graphs for energies of 25keV, 150keV and 500keV are shown on figures (a), (b) and (c), respectively.

At all the energies, fluorescence is lower than Compton scatter in figure 9.40, that is carbon-based materials Compton scatter broad peak would hide any fluorescence of other materials' layers. At medium-high energy lead fluorescence is more significant than other materials, but not comparable with Compton scatter energy-probability in figures 9.42(b)(c).

25 keV

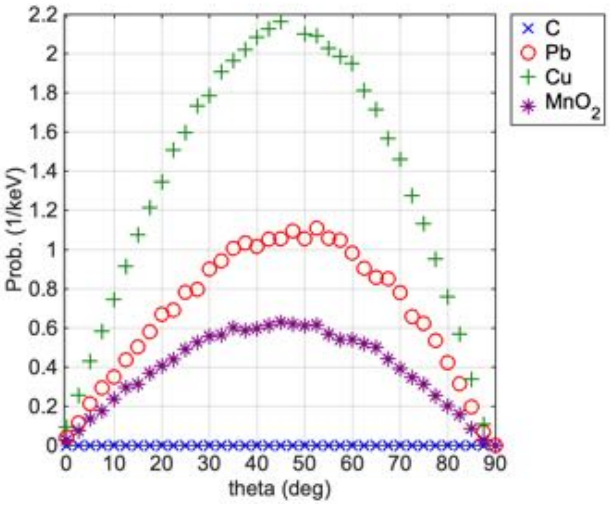

(a)

150 keV

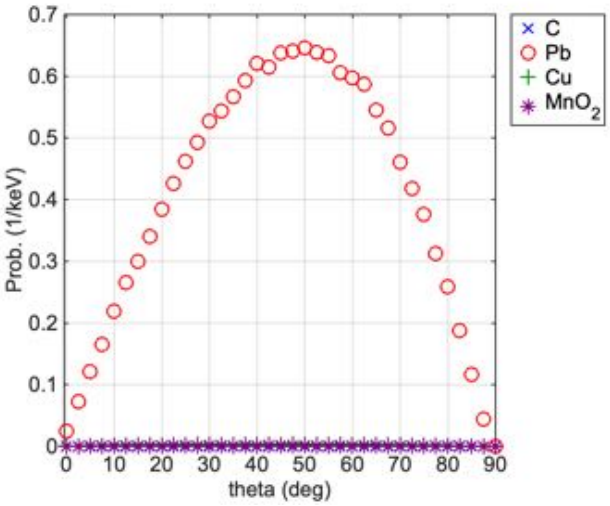

(b)

500 keV

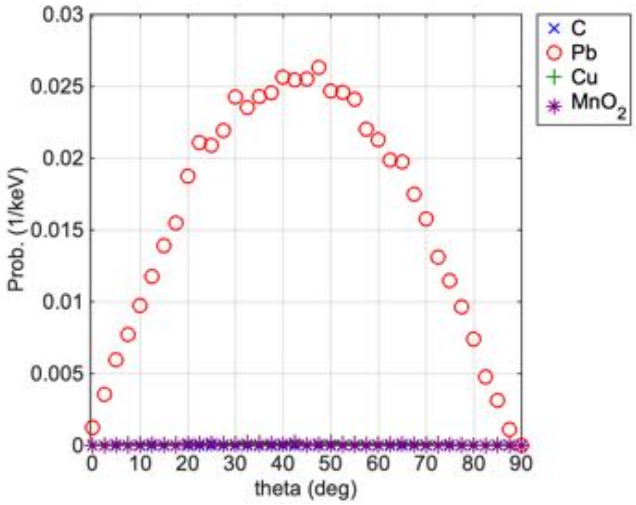

(c)

Figure 9.42 Fluorescence energy-probability angular distribution at 25 keV (a), 150 keV (b) and 500 keV (c) of 50 mm thick carbon, copper, manganese dioxide, and lead thick films.

9.19 Interpretation of energy-probability data for thick materials with barrier

In this section, we will explore thick materials with an aluminium or iron thin barrier for calculating the energy-probability. In this section of work, carbon, copper, and manganese dioxide were set to be 50 mm thick, while the thin aluminium or iron barrier was set to be 2 mm thick. The configurations were simulated at 25 keV, 150 keV and 500 keV. In the following subsections, the energy-probability of Compton scatter, elastic scatter and fluorescence will be shown.

9.19.1.1 Compton scattering – aluminium barrier

Compton scatter energy-probabilities of 50 mm thick carbon, copper, manganese dioxide, and 2 mm thick aluminium barrier on top are calculated as angular distributions.

Figure 9.52 shows the value of the energy-probability calculated every 2.5 degrees between 0 and 90 degrees for all the materials. The graphs for energies of 25keV, 150keV and 500keV are shown on figures (a), (b) and (c), respectively.

When compared with thick materials in figure 9.42, we see carbon has still the highest inelastic scatter probability at all the energies at greater thicknesses, but the aluminium barrier attenuates the energy-probability of a factor of around five. That is Compton scatter probability is still the most significant for a thick layer of carbon, even with an aluminium barrier on top, and would produce a more significant contribution to the broad Compton background in the energy spectrum.

25 keV

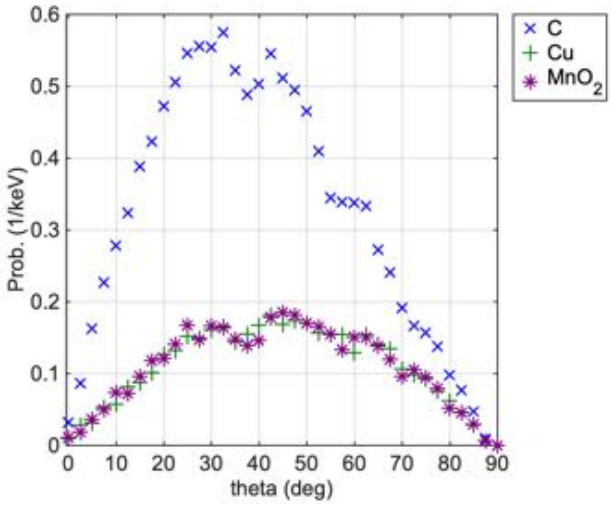

(a)

150 keV

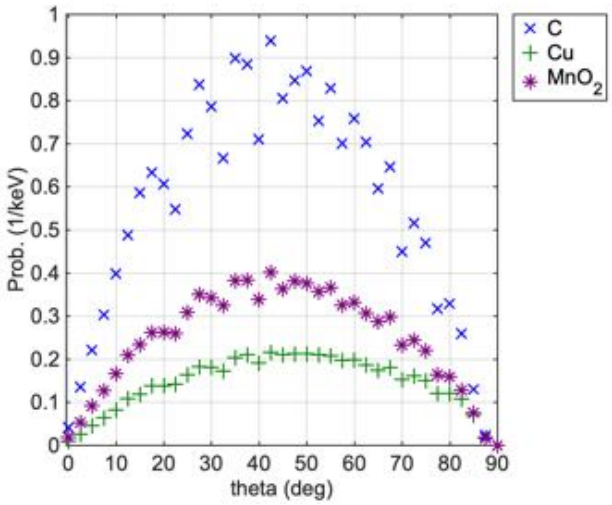

(b)

500 keV

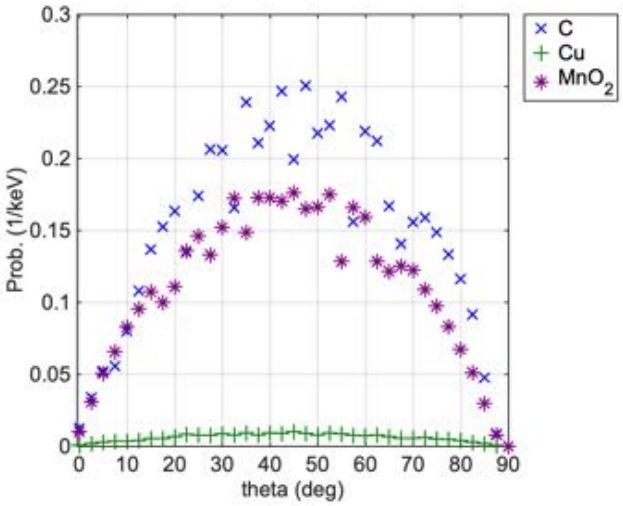

(c)

Figure 9.43 Compton scatter energy-probability angular distribution at 25 keV (a), 150 keV (b) and 500 keV (c) of 50 mm thick carbon, copper, manganese dioxide and 2 mm barrier of aluminium on top.

9.19.1.2 Compton scattering – iron barrier

Compton scatter energy-probabilities of 50 mm thick carbon, copper, manganese dioxide, and 2 mm thick iron barrier on top are calculated as angular distributions.

Figure 9.44 shows the (average azimuthal) value of the energy-probability calculated every 2.5 degrees between 0 and 90 degrees for all the materials. The graphs for energies of 25keV, 150keV and 500keV are shown on figures (a), (b) and (c), respectively.

When compared with thick materials in figure 9.40, we generally see Compton scatter is generally attenuated of a factor of almost six. Carbon has still the highest inelastic scatter probability at medium and high energies (fig 9.44 (b)(c)). for greater thicknesses, but the iron barrier prevents any energy-probability to be counted at low beam energies (fig 9.44(a)).

25 keV

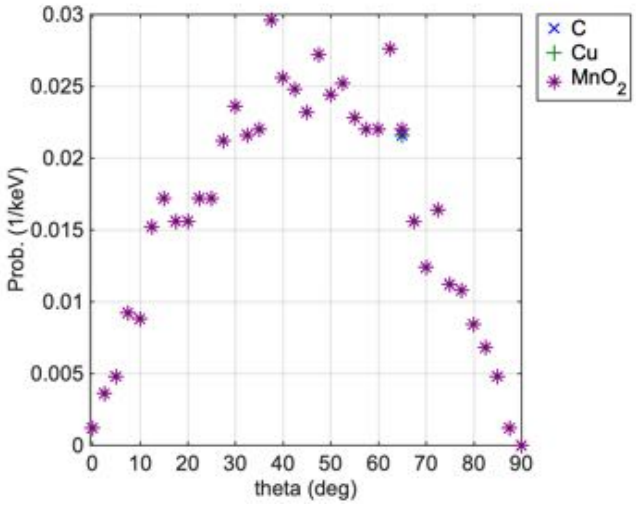

(a)

150 keV

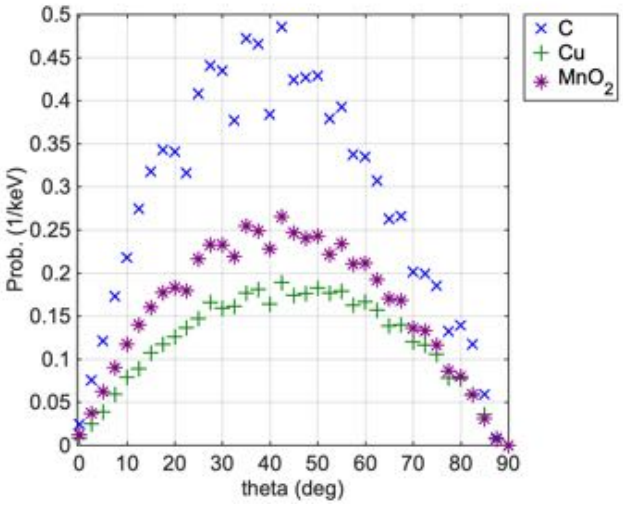

(b)

500 keV

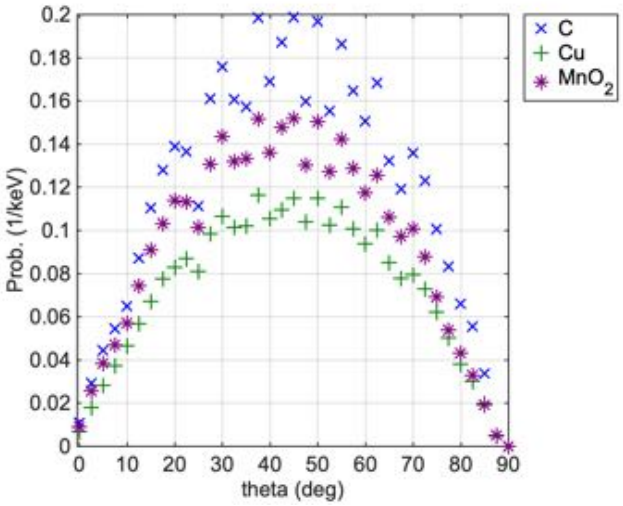

(c)

Figure 9.44 Compton scatter energy-probability angular distribution at 25 keV (a), 150 keV (b) and 500 keV (c) of 5 cm thick carbon, copper, manganese dioxide and 2 mm barrier of iron on top.

9.19.1.3 Elastic scattering – aluminium barrier

Elastic scatter energy-probabilities of 50 mm thick carbon, copper, manganese dioxide, and aluminium 2 mm thick barrier are calculated as angular distributions.

Figure 9.45 shows the (average azimuthal) value of the energy-probability calculated every 2.5 degrees between 0 and 90 degrees for all the materials. The graphs for energies of 25keV, 150keV and 500keV are shown on figures (a), (b) and (c), respectively.

Elastic scatter contribution is also attenuated when placing a barrier on top when compared with the elastic scatter without barrier in figure 9.41. With and without barrier, carbon has the highest elastic energy-probability angular distribution at low energies, while manganese dioxide elastic contribution arises at medium-high energies (fig. 9.45(b)(c)). That is the effect of the aluminium barrier may generate secondary events from manganese dioxide, especially at high beam energies.

25 keV

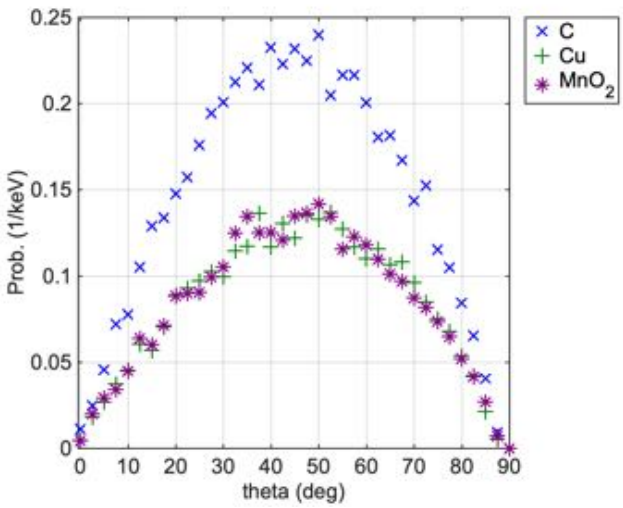

(a)

150 keV

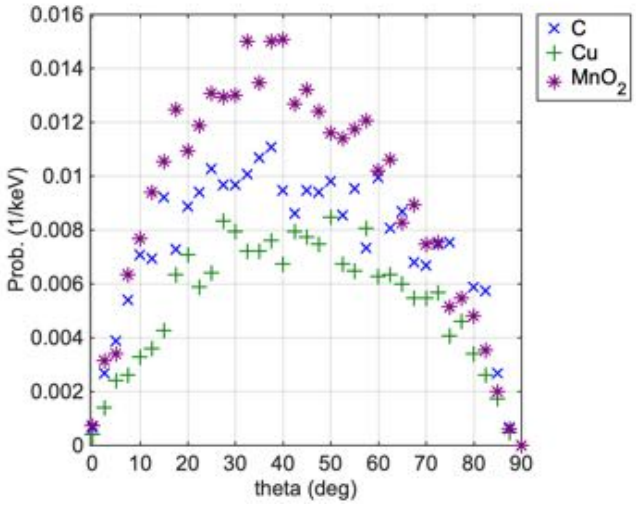

(b)

500 keV

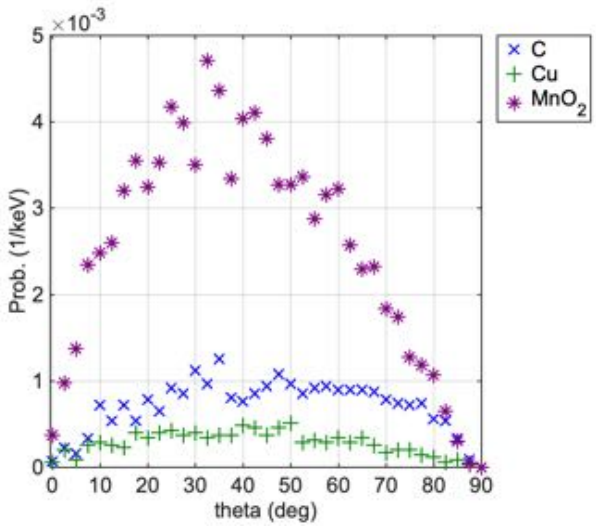

(c)

Figure 9.45 Elastic scatter energy-probability angular distribution at 25 keV (a), 150 keV (b) and 500 keV (c) of 50 mm thick carbon, copper, manganese dioxide and 2 mm barrier of aluminium on top.

9.19.1.4 Elastic scattering – iron barrier

Elastic scatter energy-probabilities of 50 mm thick carbon, copper, manganese dioxide, and iron 2 mm thick barrier are calculated as angular distributions.

Figure 9.46 shows the value of the energy-probability calculated every 2.5 degrees between 0 and 90 degrees for all the materials. The graphs for energies of 25keV, 150keV and 500keV are shown on figures (a), (b) and (c), respectively.

Elastic scatter contribution is also attenuated when placing an iron barrier on top when compared with the elastic scatter without barrier in figure 9.41, especially at low energies (fig. 9.46(a)). With barrier, the highest elastic scatter contribution would have been that of manganese dioxide, while with iron barrier carbon has the highest elastic energy-probability angular distribution (fig. 9.46 (b)). At high energies, manganese dioxide elastic contribution arises at (fig. 9.46(c)). That is the effect of the iron barrier generally reduces elastic scatter.

25 keV

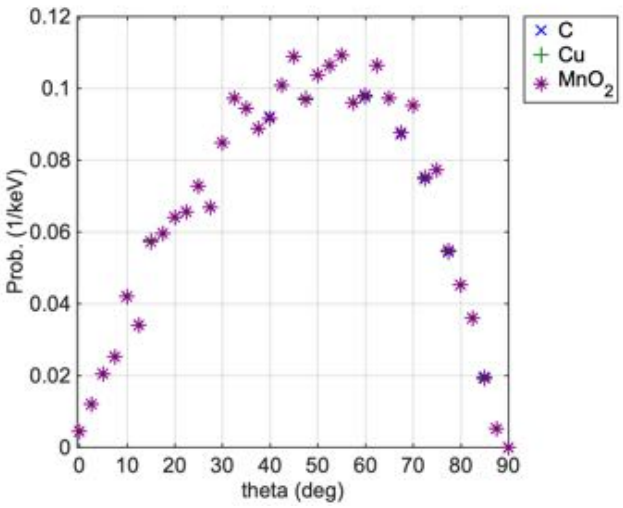

(a)

150 keV

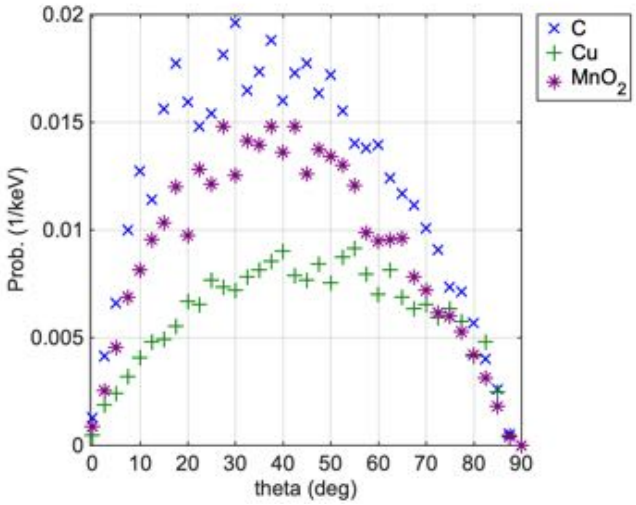

(b)

500 keV

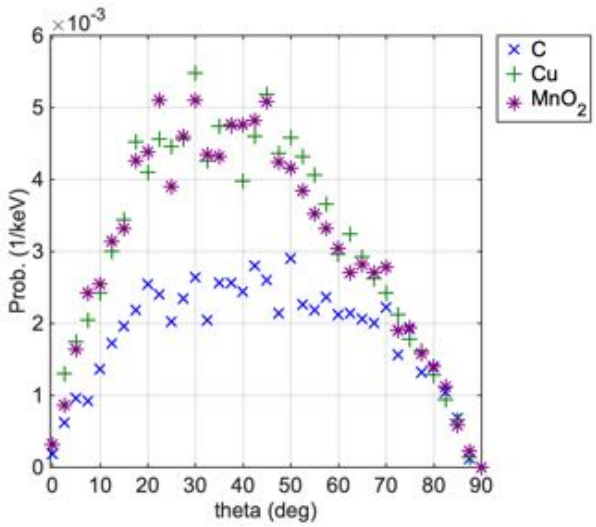

(c)

Figure 9.46 Elastic scatter energy-probability angular distribution at 25 keV (a), 150 keV (b) and 500 keV (c) of 50 mm thick carbon, copper, manganese dioxide and 2 mm barrier of, iron on top.

9.19.1.5 Fluorescence – aluminium barrier

Fluorescence energy-probability of 50 mm thick rotated carbon, copper, manganese dioxide, and aluminium 2 mm thick barrier are calculated as angular distributions.

Figure 9.47 shows the value of the energy-probability calculated every 2.5 degrees between 0˚ and 90˚ for all the materials. The graphs for energies of 25keV, 150keV and 500keV are shown on figures (a), (b) and (c), respectively.

At all the energies, fluorescence is consistently and significantly reduced compared with thick materials without barrier in figure 9.42.

25 keV

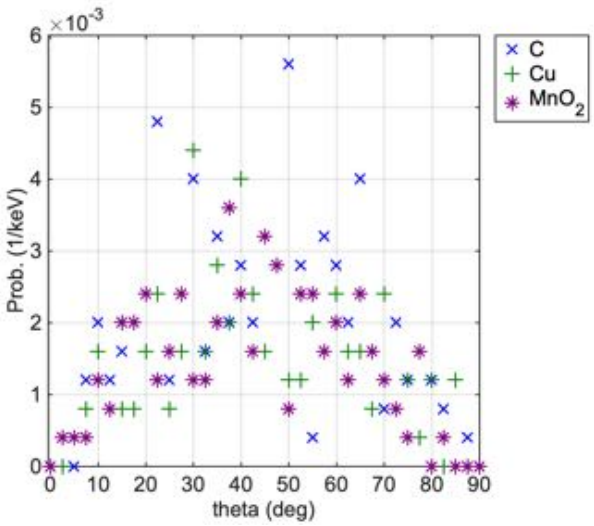

(a)

150 keV

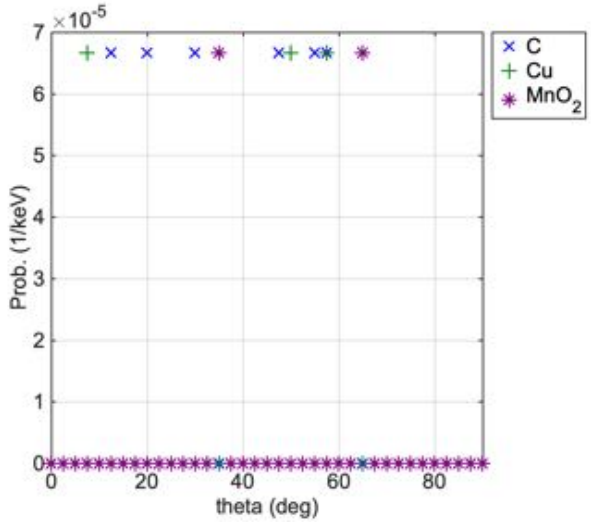

(b)

500 keV

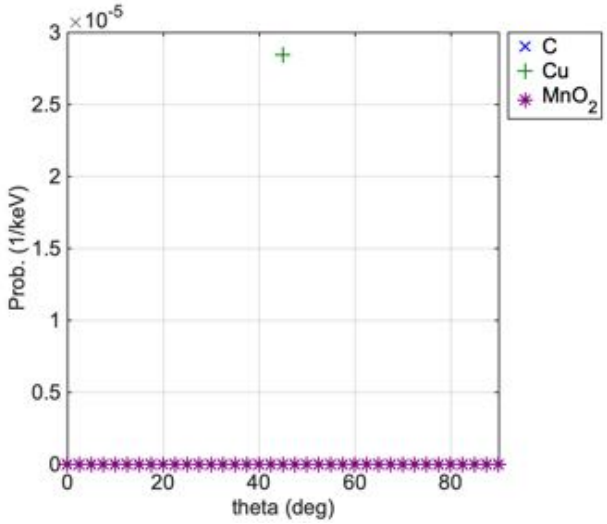

(c)

Figure 9.47 Fluorescence energy-probability angular distribution at 25 keV (a), 150 keV (b) and 500 keV (c) of 50 mm thick carbon, copper, manganese dioxide and 2 mm barrier of aluminium on top.

9.19.1.6 Fluorescence – iron barrier

Fluorescence energy-probability of 50 mm thick rotated carbon, copper, manganese dioxide, and iron 2 mm thick barrier are calculated as angular distributions.

Figure 9.57 shows the value of the energy-probability calculated every 2.5 degrees between 0 and 90 degrees for all the materials. The graphs for energies of 25keV, 150keV and 500keV are shown on figures (a), (b) and (c), respectively.

At all the energies, fluorescence is consistently and significantly reduced compared with thick materials without barrier in figure 9.50, and the detection of fluorescence characteristic lines worsen if we were placing an iron barrier when we compare the energy-probabilities of the two barriers in figure 9.57 (iron) and 9.56 (aluminium barrier).

25 keV

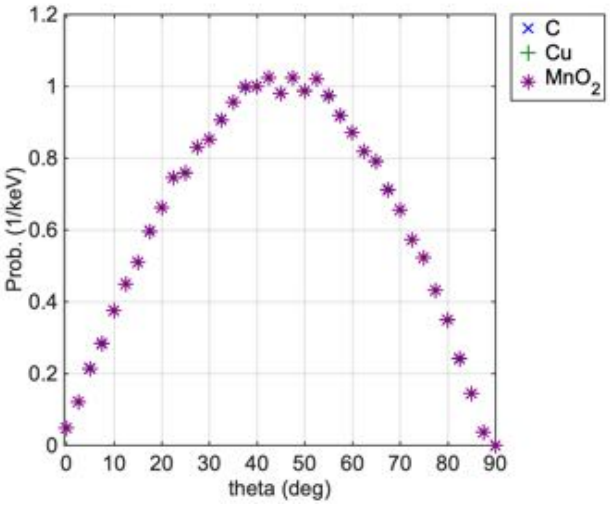

(a)

150 keV

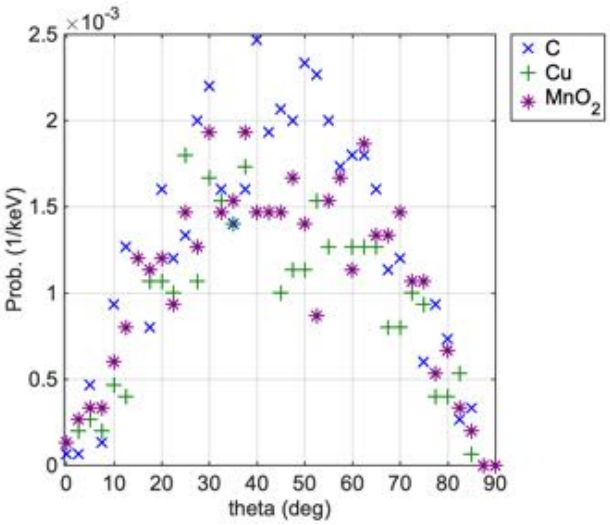

(b)

500 keV

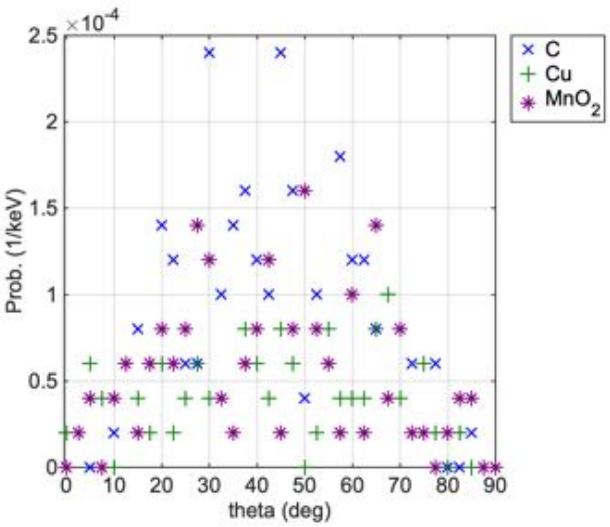

(c)

Figure 9.48 Fluorescence energy-probability angular distribution at 25 keV (a), 150 keV (b) and 500 keV (c) of 50 mm thick carbon, copper, manganese dioxide and 2 mm barrier of, iron on top.

9.20 Chapter summary and critical analysis

The hemispherical detector was modelled, and the presented results highlight the strong potential of this technique in forecasting the X-ray field that a backscatter can be adapted to most efficiently image and energy analyse. With its encompassing design, this detector model efficiently uncovers the fundamental scattering information needed to select the right conditions for good brightness and contrast and suggestion on the detector positioning in X-ray backscatter imaging. This model 'unpacks' and isolates the various fundamental scattering processes for different materials and geometries which gives a deeper understanding of what underpins image characteristics. Such data and principles can be used to guide the selection of experimental conditions, such as incident X-ray energy and relative camera angle to achieve good X-ray backscatter imaging of structures involving carbon, copper, manganese dioxide, lead, aluminium and iron. While computer modelling gives us unique opportunities to understand the physics behind imaging and provides information on techniques and concepts that would be otherwise impractical to explore experimentally, it is often difficult to verify its results.

The hemispherical detector simulation process was developed to help rapidly forecast the source X-ray energy and camera location that is most suitable for achieving the right brightness, contrast or energy information to reveal structures or elements of interest. In order to explore the range of possible camera angle simultaneously a hemispherical detector was modelled to simultaneously explore all backscattering angles. By modelling X-rays incident on thin, thin rotated, thick and thick through barrier materials and using the power of simulation to combine the processes of attenuation, elastic, inelastic and fluorescence and atomic and physical density the final effect of the competition between various processes can be witnessed at the detector. Also, the process allows us to 'unpack' and isolate the various fundamental scattering processes giving rise to the effect at detector which gives a deeper understanding of what underpins image characteristics. Such data and principles can be used to guide the selection of experimental conditions, such as incident X-ray energy and relative camera angle to achieve good X-ray backscatter imaging of structures. PENELOPE data output was

validated with well-known databases with xraylib tool, which was included in PAXI algorithm to retrieve the theoretical differential cross section for applying the validation against the simulated data. The preliminary data is consistent with our theoretical understanding that low energies lead to increased Compton scatter particularly directly back toward source, and fluorescence increases at high energies. It also highlights that changing energy can expose different materials by relative changes in their ‘brightness’ and contrast.

10 DISCUSSION, CONCLUSIONS AND FUTURE WORK

10.1 Chapter Outline

Compton Backscatter Imaging principles is a one-side imaging technique based on Compton scatter, as described by Klein-Nishina [16].

Compton scatter imaging requires three basic elements: an X-ray source, typically a diagnostic X-ray tube (as described in chapter 6), a target sample, and an imaging camera coupled with an X-ray collimator/mask. The mask can either be a pinhole or Coded Aperture as illustrated in chapter 7.

As discussed in chapter 3, Compton backscatter imaging finds one of the main applications in detecting concealed objects through barriers (i.e. from one side of the target only). This is a huge advantage over X-ray transmission for which it is impossible to access both sides of the target.

In this chapter, a critical discussion of the key findings will be presented, and conclusions of this work are drawn, in addition to recommendations for future work. In this chapter, each component of this work which contributed to knowledge is a dedicated section. Discussion, conclusions and future work are individually explored section by section. Section 10.2 will be dedicated to adapting PENELOPE as computational instrument for exploring backscatter imaging, in section 10.3 the development of PAXI algorithm and the conversion of the phase-space file into an image will be presented. Section 10.4 will be focused on X-ray and gamma ray sources models, sections 10.5 and 10.6 will exploit pinhole X-ray imaging optics and image quality metrics, sections 10.7 and 10.8 coded aperture masks and image quality metrics (compared to pinhole masks). Section 10.9 will explore the modelling of detectors, followed by the HEXITEC detector in section 10.10, and finally the hemispherical detector in 10.11.

10.2 Adapting PENELOPE as a computational instrument for exploring backscatter imaging

10.2.1 Discussion

For this work, PENELOPE Monte Carlo code was chosen as the base module for simulating X-ray optics and exploring the fundamental physics of backscatter imaging. Various factors influenced this decision. First of all, the scattering model reliability was the key factor for putting PENELOPE on the top of the list.

This work is based on simulation of the electron-photon transport through matter for exploring backscatter X-ray imaging system, and, in this sense, PENELOPE performances were overall the best. PENELOPE is a dedicated tool for electron-photon transport; it is flexible and versatile. PENELOPE scatter model is widely known and included within the NIST database, and it also used for modelling electron-photon transport in other codes such as GEANT4. This is an example of the capability of PENELOPE to be incorporated in any other simulation and/or data analysis codes. A practical example is given with PENMAT application, developed during this work for running PENELOPE simulations within a user-friendly framework. Another example is the algorithm PAXI [5], which processes the state variables recorded in the phase-space file for recreating an image, as physical detectors do. PENELOPE phase-space file and energy-spectra are the fundamental data file which were used for this research, and PAXI algorithm was written for replicating an image plate from the state variables recoded within the phase-space file.

PENELOPE proved to be a valid instrument for modelling X-ray and gamma-ray sources, and physical detectors. This validity was confirmed with physical experiments. This laid solid foundation for studying the fundamental physics of backscatter imaging by modelling and simulation.

PENELOPE can be run in any computational environment and is provided with the user-friendly geometry application PENGEOM. With PENELOPE we can potentially create any kind of X-ray and gamma-ray sources, either virtual or physical. The thin wire 0-200 keV flat X-ray emitter is an example of a versatile

source/test object for estimating the image quality metrics as in chapter 7. The geometry and spectrum of this test piece was designed specifically for this work and characterises fundamental system image characteristics efficiently.

Although generally the models performed correctly most of the time, there were some failures. For example, the model of the X-ray tube within the laboratory environment in chapter 6 showed the scatter contribution from the materials surrounding the CdTe detector (including the thick tungsten collimator) was underestimated in the region 70-120keV compared to the experiment.

10.2.1 Conclusions regarding the use of PENELOPE

PENELOPE is a complete and generally reliable instrument for simulating electron-photon transport. It is written in Fortran, and has the kind of flexibility an expert user may appreciate, as it is completely open-source, and can run in any computational environment. However, the 2014 distribution is not distributed as straight-forward parallel code as other Monte Carlo simulation codes, but with a sub-tool for manual parallelisation. In this work, MUSIMAN MATLAB algorithm, which creates the simulations from the same physical situation but with different number of seeds, was incorporated in PENMAT for a better user experience.

PENELOPE was found to replicate experimental results well when determining the optimum combination of material/thickness/aperture diameter for pinhole masks, and image quality metrics were calculated (chapter 7). The X-ray tube model proved to be reliable and in line with the spectra generated with SpekCalc.

PAXI algorithm, written for generating images from PENELOPE phase-space file, succefully replicated the image plate and generated the point spread functions from Am-241 exposures.

It was also observed PENELOPE simulations in backscatter geometry may be computationally expensive (>~10^9 to populate the phase-space file). For this reason, a manual parallelisation was applied by using different seeds for initialising the random number generator. However, if we were exploring different

conditions at the same time, this may not be efficient, as the number of slots (on the HPC available per user is limited.

10.2.1 Future work regarding the use of PENELOPE

In future work, PENELOPE simulations would benefit from running automatically in parallel, especially on HPC as several nodes/cores can run the simulation process and reach the number of desired simulation showers in less computational time. This is translated as a more abundantly and quickly populated phase-space file and consequently a better image.

With regards to simulation artefacts, it would be advisable to look at completeness of the physical models. It would also be useful to recognise the origin of VR techniques failures and try to improve them by identifying and probably by constraining their use to within acceptable parameters. This would contribute to a more efficient and less computationally expensive backscatter simulation.

10.3 Development of PAXI: converting the phase-space file into an image

10.3.1 Discussion

The Phase-space Algorithm for X-ray Imaging (PAXI) was developed to enable processing the data from PENELOPE simulations into an image.

PAXI code was written to essentially replicate an imaging plate by converting PENELOPE's phase-space file into the spatial 'brightness' across a typical pixelated imaging plate. PAXI computes the image brightness in terms of integrated energy as defined in chapter 5 (used in 7, 8 and 9), i.e. as the sum of the photon energies per pixel. PAXI is a script for X-ray image processing which can be adapted to the detector pixel size for comparisons with experiment.

PAXI allows image processing of the phase-space file; it was tailored for appraisal of image quality metrics, and determination of point spread functions, and was also incorporated with the decoding function for coded apertures imaging [82].

PAXI introduces also the selection of the kind of interaction recorded at the detector. Selecting ILBs is an interesting feature, as it is unique of simulations only. Nowadays, it is still not possible to discriminate between the kind of interaction in an experiment, but simulation may help developing an apparatus with such characteristics in the future.

PAXI can also generate the energy-probability spectra over the whole detector and/or specific angles, it was customised to calculate quantities such as relative yield and differential cross sections, which were also compared to the data from NIST database for validation purposes through xraylib, also incorporated within the code.

10.3.1 Conclusions regarding PAXI

PENELOPE Monte Carlo simulation code is not provided with a sufficient interface or post processing algorithm to fully exploit its potential.

PAXI was equipped with the ILB kind of interaction detected selection for studying the fundamental physics of backscatter as in chapter 9.

PAXI succefully calculated energy-probability spectra over the whole detector and/or specific angles, it has the capability to estimate relative yield and differential cross sections and compare the differential cross section to the well-known databases via xraylib.

PAXI was essential used in chapter 6, 7, 8 and 9 for generating X-ray images from pinhole and coded apertures masks. PAXI core image processing is relatively fast as it works in parallel (depending on the number of lines on the phase-space file).

The development of PAXI facilitated image quality metrics and decoding functions are fundamental for future development in backscatter imaging.

The work in chapter 9 of exploring the different kind of interactions is a key feature that may help future development and detector design for material characterisation.

10.3.1 Future work regarding PAXI

PAXI algorithm works in parallel within MATLAB environment. However, in future it would be an advantage to export this instrument into a more general application.

Large data phase-space file may represent a downside as the importing process may be relatively long. The algorithm would benefit from a more optimised file import.

10.4 X-ray/gamma-ray sources

10.4.1 Discussion

The first component of the X-ray backscatter imaging system explored was the X-ray source. In chapter 6, different approaches to simulate an X-ray source were discussed. These included the simple but efficient mono-energetic and mono-directional beam, the generation of X-ray spectra by simulating the physical VJT source, and the novel 0-200 keV flat X-ray wire emitter.

The mono-energetic and mono-directional X-ray beam was applied for exploring the fundamental physics of backscatter imaging in chapter 9. As such beams are very difficult to produce physically, simulation is the only practical method. Isolating a specific beam energy and direction is essential to attribute the cause of an observed effect.

The VJT X-ray source was modelled for different anode voltages up to 160 kV and the output spectra at the exit window calculated. The spectra of the modelled X-ray tube were used in chapter 7 for backscatter X-ray imaging in the input file. In chapter 6, the X-ray spectra were compared to SpekCalc spectra. PENELOPE Monte Carlo code offers a wider variety of parameters to match exactly the layers specified by manufacturer, compared to SpekCalc. Modelling the VJ Technology

X-ray generator and a good match with experiment allowed to check that the approach using PENELOPE was indeed correct.

Spectra were also physically measured with an Amptek X-123 CdTe detector to give PENELOPE model more confidence. However, the results from experiment were affected by scatter and hole tailing effect artefacts. Such effects were more evident at anode voltages higher than 100kV, and without shielding. Measures were taken to mitigate scatter by shielding the detector with lead, while hole tailing effect was decreased by enabling RTD.

An Am-241 gamma-ray source was simulated for exploring the point spread functions of pinhole and coded aperture masks. Although the point source is not real, this initial simulation allowed us to appreciate the correctness of the simulation parameters, such as gamma emission of the source, position of the source, number of simulated showers, etc. Then, the physical (non-point) source was modelled with confidence.

10.4.1 Conclusions regarding X-ray/gamma-ray sources

Simulation of the physical X-ray tube was successful when the PENELOPE model of the X-ray tube was compared to SpekCalc, and both spectra, considered at the exit window of the X-ray tube, were in good agreement (>90% up to 120 kV, >85% up to 160 kV). The model of the laboratory environment was found to be accurate for the tungsten K-alpha peak.

Comparing the PENELOPE predictions to both experimental spectra measured using a CdTe detector and the output from an established X-ray tube simulation code SpekCalc showed that the approach to modelling was indeed correct and gives us confidence in our other simulation results, and the opportunity to explore different types of X-ray generator.

An Am-241 source was simulated for generating the point spread functions of pinhole and coded aperture masks and calculating image quality metrics of pinhole/CA masks. Simulated exposures were compared with physical experiment, and results gave us the confidence that PENELOPE is capable of simulating X-ray optics properly.

10.4.1 Future work regarding X-ray/gamma-ray sources

The X-ray emission of the thin wire X-ray emitter was set to 0-200keV, which deliberately lies at the higher energy end of small X-ray generators. New avenues could include applying the novel thin wire X-ray emitter monoenergetically or within greater energy range (for example 0-500 keV).

10.5 Pinhole imaging

10.5.1 Discussion

In chapter 7, PENELOPE has been applied to design, test and optimise pinhole optics. The 0-200 keV flat X-ray thin wire virtual emitter was used to characterise image quality parameters such as spatial resolution, field of view, contrast and signa-to-noise ratio. PAXI MATLAB code was created and then used to convert PENELOPE's output into the spatial 'brightness' across a typical pixelated imaging plate was created. With the test object and sensor modelling established, a detailed systematic exploration of pinhole mask parameters was conducted. This involved varying the pinhole aperture diameter, mask thickness and material.

A preliminary study was conducted for selecting suitable materials for manufacturing the masks, including solid tungsten, tungsten epoxy resin, bismuth low-melting alloy and lead. Three materials were designated for a further study of pinhole optics thicknesses and aperture diameters for applications in coded aperture masks, solid tungsten, tungsten epoxy and bismuth low-melting alloy. Tungsten epoxy resin and bismuth alloy were studied with and without the addition of a PLA and ABS thin layer respectively. PLA and ABS are plastic materials used for 3D printing and self-supporting coded apertures masks. PENELOPE recorded the spectra at the impact detector and the transmission function was calculated for determining if any leakage/scatter could occur within the mask thicknesses, especially when the plastic materials were added for manufacturing CA masks.

A pinhole was added to selected mask materials, and the aperture diameter was varied. Suggestions were given for finding the optimum material/thickness/aperture diameter combinations, by estimating the image quality metrics.

Exploring pinhole imaging was useful for appreciating imaging conditions which may be reflected in the more complex multi-hole CA masks. A simple pinhole may reveal information such as leakage, collimation of the field of view, which could affect CA imaging as well. Although this is a simpler step, it is also fundamental for a better understanding of backscatter imaging. The work on the selection of optimum combination of materials/thickness/aperture diameter based on the image quality metrics can be useful in the development of future systems.

10.5.2 Conclusions regarding pinhole imaging

Pure tungsten at 2 mm thickness and 2 mm aperture was found to have the best overall performances in terms of image quality metrics, and it was taken as reference for finding the optimum combination for the other two materials, tungsten epoxy resin and bismuth alloy. Tungsten epoxy and also bismuth alloy were found to match pure tungsten at 4 mm thickness 2 mm aperture diameter. Then, for manufacturing reasons, bismuth alloy was discarded [110].

The results led to select solid tungsten, tungsten epoxy plus PLA and bismuth alloy plus ABS for manufacturing, as PLA and ABS were not significantly affecting the overall mask performances.

10.5.3 Future work regarding pinhole imaging

Future work could include demonstrating how limited FOV propagates through to partial coding in CA’s (which was the reason we started this as we could foresee its potential). Further work could also include chamfered edge pinholes.

10.6 Image quality metrics of pinhole masks

10.6.1 Discussion

Methods were developed to quantifiably evaluate the image characteristics of contrast, signal-to-noise ratio, spatial resolution and field of view. These methods were firstly applied to pinhole images for exploring and finding the best combination of materials/thickness/aperture diameters with application to CAs.

Image quality metrics of contrast, signal-to-noise ratio, and spatial resolution have multiple and different definitions in literature. For example, contrast can be defined as Weber's contrast [117] and Michelson's contrast [108]. Weber's contrast is limited as it can be applied for small features on a large uniform background, while Michelson's contrast (also known as contrast-to-noise ratio) is commonly used repeating patterns. Spatial resolution can be defined as line pairs and full-width at half maximum. Thus, before quantifying the image quality metrics, a preliminary study was undertaken to appreciate the different definitions. Then, the definitions were implemented in PAXI and applied to estimate the image quality metrics of pinhole optics.

For the implementation of image quality metrics, it was fundamental to define the region of interest and background of the simulated image. The thin wire 0-200 keV X-ray emitter was placed at a specific distance from the pinhole mask to give the magnification of the unity. The boundaries of the region of interest were then the size of the imaged object. PAXI enabled the automatic selection of the region of interest and background by setting the wire object size, and image quality metrics were calculated.

10.6.2 Conclusions regarding image quality metrics of pinhole masks

Image quality metrics are well established methods for measuring the performances of an imaging system.

Michelson's contrast was chosen as the best measure for CNR for pinhole imaging and coded aperture imaging as it is defined within the boundaries $0.1 \leq CNR \leq 1$, and it helped guiding the selection of the best mask material.

Full-width at half maximum was selected against line-pairs as more versatile to measure spatial resolution of the imaged objects.

Measures of CNR, SNR, FWHM and AOV were given in two different situations, both with the exposure of a thin wire 0-200 keV X-ray emitter and a small, almost point gamma-ray source. This gives the confidence the method can be applied in future to any pinhole/CA mask imaging system.

This study showed that for any aperture size, tungsten/epoxy fails to give a sufficiently high contrast and signal to noise ratio until 4mm of material is used, whereas pure tungsten can achieve this at 2mm thickness. To sufficiently reduce the background and noise for small apertures (1mm), the thickness of pure tungsten must exceed 3mm whereas for larger apertures (≥2mm) the thickness may be 2mm. For W epoxy masks the material must be significantly thicker. No aperture of 3mm and greater diameter had acceptable resolution. For the system examined the best obtainable resolution a 1mm aperture must be used where only pure tungsten gives both sufficiently high contrast and low noise. Pure tungsten is the most versatile material tested and allows small pinholes to be used in thin masks. The best minimum configuration for pure tungsten was found to be 2mm thickness and 2mm aperture.

10.6.3 Future work regarding image quality metrics of pinhole masks

In future it could be useful working with industry to uniquely establish image quality metrics definitions and imaging objects standards specifically for characterising backscatter imaging systems.

10.7 Coded aperture imaging

10.7.1 Discussion

The theoretical template pattern of coded aperture can be represented as binary images characterised by zeros (empty space) and ones (spaces filled with materials).

In PENELOPE, it was not possible to create the geometrical model directly from the binary image template, as PENGEOM required a different definition of the mask pattern based on complex descriptions of surfaces and modules as described in chapter 5. The design of CA masks was achieved efficiently by observing and utilising the symmetries of the patterns, as seen in chapter 7. The geometries of CAs are of course complex, although functions with PENGEOM can be used to copy, mirror and rotate elements to make modelling them achievable. The following CA masks were designed: 19 MURA, 19 MURA NTHT, 17x34 Singer Set and 17x34 Singer Set NTHT. The masks were exposed to the simulated Am-241 source (as point source and physical source) and point spread functions were calculated. The simulated exposures and point spread functions were compared to pinhole masks and to experiment.

The comparison between simulation and experiment is not perfect, because although the Am-241 simulation represented the full photon flux, simulation does not include electronic noise in the detector. Hence, it is possible that the greater noise in the simulation (arising from poorer signal statistics) is compensated for by the absence of electronic noise and the fact that the simulated detector is 100% efficient whereas the real detector is not (it has some energy dependent response which has not been modelled).

10.7.2 Conclusions regarding coded aperture imaging

A significant milestone has been achieved in that the characteristics of CA images obtained by the dual avenues of practical experiment and simulations were found to be comparable, giving confidence in both paths especially when comparing the physical Am-241 simulated exposures to experiment.

This advance is a good platform for the future use of modelling in design and understanding, and the future use of experimentation to reveal previously unconsidered factors and to evolve physical systems and maybe even consider more factors relevant to higher TRL systems.

10.7.1 Future work regarding coded aperture imaging

Future work in modelling CAs should include exploring other CA masks and testing them not only with Am-241 source for measuring the point-spread functions, but also with other kind of sources such as the thin wire emitter. The additional CAs should also be simulated within a backscatter geometry and backscatter radiation transport optimised for achieving the simulated exposures in shorter computational time and validate the simulated results via experiment.

10.8 Image quality metrics of CAs vs pinholes

10.8.1 Discussion

Image quality metrics such as SNR, CNR and spatial resolution as FWHM were calculated for CAs included in the upgraded camera. The algorithm PAXI that transforms PENELOPE's phase-space files into images as sensed by a CCD detector was applied for generating the simulated exposures. The simulated exposures were further processed in PAXI to decode the image and generate the point spread functions.

Simulation was also applied to various pinholes and CAs and allows a direct comparison between them free of potential experimental errors such as alignment. However, it does not yet accommodate real world factors such as electronic noise and detector energy response.

10.8.1 Conclusions regarding image quality metrics of CAs vs pinholes

The results tend to show that CAs are generally superior to pinholes in imaging the Am-241 source, but when the near field line source was imaged (arguably a more cluttered scene) the 2 mm pinhole was significantly superior in terms of SNR and with marginally better spatial resolution.

10.8.1 Future work regarding image quality metrics of CAs vs pinholes

Point spread functions were extracted from simulated exposures and compared with experiment. Future work should be done to extend this study to other CA masks and compare with experiment.

10.9 Modelling detectors in PENGEOM

10.9.1 Discussion

PENELOPE can be used to simulate detectors. All the detectors were designed in PENGEOM [76] geometry Java application.

With PENELOPE, it is possible to create virtual detector as seen in chapter 6 for collecting the X-ray spectra, or replicating physical detectors, such as the Amptek-X123, both X-ray backscatter imaging cameras used for CA imaging in chapter 7, and HEXITEC in chapter 8, or for capturing 2π data for generating angular distribution for studying the fundamental physics of backscatter as the hemispherical detector in chapter 9.

10.9.1 Conclusions regarding modelling detectors

The ability of PENELOPE to replicate real detectors in PENGEOM is a valuable resource for testing any future X-ray detectors we might use. Physical detectors allowed us to compare results to experiment and give PENELOPE models more confidence.

The use of virtual detectors succefully enabled a two-steps ‘source’ process for computational speed. The development of novel detectors (i.e. hemispherical detector) allows efficient exploration of energy/source/type of interactions that physical ones cannot.

10.9.1 Future work regarding modelling detectors

Virtual detectors, such as the hemispherical detector, are the key for exploring conditions which may be useful in the future. The work of the hemispherical detector should be extended from 2π to 4π to support forward emission.

Extending this study may give the fundamental information for material characterisation and future development.

10.10 Energy-dispersive backscatter X-ray Imaging with the HEXITEC detector

10.10.1 Discussion

The HEXITEC detector has the capability to generate X-ray images with energy discrimination and so has increased potential to characterise the material of structures in the image. This ability to highlight or suppress specific materials or families of materials can be used to indicate features of specific relevance to an operator or suppress irrelevant clutter that could otherwise distract them. The detector is small, light and has low power consumption and its 80×80 array appears to be a fair match to the resolution available with pinholes of an aperture large enough to collect spectra in a reasonable time. The energy resolution is believed to be about 1keV and is not as good as some single element CdTe detectors.

Initial experiment showed the calibration files that came with the detector contained errors, as some fully functioning pixels were attributed the value zero, i.e. working as dead pixels, which disabled any collection of data from those specific pixels. Pixels at the edges of the detector were overcounting and contributing to the low energy background noise. The low energy noise associated with the detector could make it difficult to look for some elements by their characteristic X-ray lines, but realistically this may need to be considered alongside the depth into a structure that we would wish to analyse, as such low energy X-rays may not be able to escape from deep inside a structure anyway. The provided calibration files were revised to account for dead pixels.

HEXITEC exposures of a physical test object, a quadrant of four different 100 mm thick materials, were captured and backscatter simulations in PENELOPE executed and compared to experiment. MATLAB routines were created for enhancing the raw image output by the HEXITEC. The potential to separate and

recombine the spectral components from different areas of interest in a HEXITEC image was shown, which demonstrates the potential to identify components and simulate a structure respectively.

10.10.1 Conclusions regarding the HEXITEC detector

The HEXITEC detector proved capable of being a simple ‘brightness’ imager for a range of different structures and generated spectra that showed the same major features as we expected from PENELOPE simulation. HEXITEC detector has showed to be the most suitable detector for comparisons with PENELOPE simulations, as it allows to isolate the spatial regions of interest in an image as we would do with PAXI algorithm. However, PAXI algorithm permits not only the spatial isolation of ROIs, but also the separation of the kind of interactions. A first approach of separation by kind of interactions applied to the simulated HEXITEC detector is shown in chapter 8, section 8.9.

The images from PENELOPE were sliced in terms of energy windowing to forecast one of the ways how an optimised HEXITEC could attribute different areas of an image to different materials by reason of characteristic X-ray energy. Further, particle tracking in PENELOPE was used to identify the physical processes that gave rise to photons hitting different areas of the detector. This revealed the different fundamental physical processes that give rise to photons that hit the detector with identical energies, which it is unlikely that experimentation could ever discriminate. This information helps guide what would need to be changed (such as source energies or angles) in order to enhance or suppress different processes that may discriminate materials.

The HEXITEC detector uniquely captures images which can be spatially separated within specific regions of interest and can be used as energy-dispersive detector as it generates the energy-spectra of the ROIs. For these reasons, it was considered to be a suitable candidate to compare with imaging and energy-dispersive PENELOPE output processed with PAXI.

10.10.1 Future work regarding the HEXITEC detector

In future work, HEXITEC detector is recommended for further validating results from PENELOPE simulations and exploit energy dispersive capability.

However, the detector would benefit from being re-calibrated in energy if we are to be accurate and confident in the attribution of close spaced characteristic X-ray lines.

10.11 Fundamentals of backscatter imaging with the hemispherical detector

10.11.1 Discussion regarding the hemispherical detector

The hemispherical detector simulation process was conceived and modelled to help rapidly forecast the source X-ray energy and camera location that could be most suitable for achieving the right brightness, contrast or energy information to reveal structures or elements of interest.

In order to explore the range of possible camera angles simultaneously a hemispherical detector was modelled to simultaneously explore all backscattering angles. By modelling X-rays incident on thin, thin rotated, thick and thick through barrier materials and using the power of simulation to combine the processes of attenuation, elastic, inelastic and fluorescence and atomic and physical density the final effect of the competition between various processes can be witnessed at the detector.

Also, the process allows us to ‘unpack’ and isolate the various fundamental scattering processes giving rise to the effect at detector which gives a deeper understanding of what underpins image characteristics. Such data and principles can be used to guide the selection of experimental conditions, such as incident X-ray energy and relative camera angle to achieve good X-ray backscatter imaging of structures involving carbon, copper, manganese dioxide, lead, aluminium and iron. While computer modelling gives us unique opportunities to understand the physics behind imaging and provides information on techniques

and concepts that would be otherwise impractical to explore experimentally, it is often difficult to verify its results.

Integrated energy, which is a measure of the image brightness, was calculated for all the materials and different thickness combinations. Integrated energy is useful for describing the brightness and sensitivity in CCD imagers and other non-energy dispersive detectors. Energy dispersive detectors have utility in elemental mapping.

Energy-probability was also calculated for each elevation and plotted as angular distribution (0˚-90˚). The energy-probability was separated for each angle to extract information aiding the optimisation of the detector practical positioning in order to maximise the signal. For instance, when using a pixelated energy-dispersive detector such as the HEXITEC, knowing the best position where to detect a specific feature and isolate it from other features may be fundamental not only for imaging but also for spectroscopy.

10.11.1 Conclusions regarding the hemispherical detector

The results presented in chapter 9 highlight the strong potential of this technique to forecast the X-ray field that exists and so how a backscatter system can be adapted to most efficiently image and energy analyse. With its spatially encompassing design, this detector model efficiently uncovers the fundamental scattering information needed to select the right conditions for good brightness and contrast and guides the best detector positioning in X-ray backscatter imaging.

PENELOPE data output was validated with well-known databases with xraylib tool, which was included in PAXI algorithm.

The data from PENELOPE is consistent with our theoretical understanding that low energies lead to increased Compton scatter particularly directly back toward source, and fluorescence increases at high energies. It also highlights that

changing energy can expose different materials by relative changes in their ‘brightness’ and contrast.

Generally, when compared to the other kind of interactions, the image brightness originated by Compton scatter is higher than fluorescence and elastic scatter for thin, thin rotated and thick materials. But image brightness originated by fluorescence of lead can be overwhelming and may mask the brightness of other materials.

Carbon brightness is mainly originated by Compton scatter, and is the brightest material when thick (and also thin, and thin rotated) at low energies. At medium and high energies and thick, carbon would be only visible against copper and manganese dioxide at angles greater of ~60˚, while is not as bright as the other materials when thin (copper and manganese dioxide Compton scatter is higher than carbon at 150 keV and 500 keV).

The practical positioning of an energy-dispersive detector was also explored by correlating the energy-probability to the angular distribution in terms of elevation.

At low energies and angles, we would see a Compton broad peak generated from thin or thick carbon-based materials. At low energies, this may represent a problem if we would like to detect the fluorescence lines generated by a copper wire or a manganese-dioxide battery. If the carbon film was thick and the wire was thin, and energy was ~25 keV, it would be difficult to detect copper characteristic lines unless we maximised the signal as much as possible by placing the detector at ~45˚. At medium and higher energies, carbon Compton scatter and lead fluorescence would overwhelm the detector and hide the fluorescence lines from the other materials.

10.11.2 Future work regarding the hemispherical detector

The hemispherical detector work can be extended from 2π to 4π to explore also forward emission. Extending this study may give the fundamental information for material characterisation and future development.

Further work should also be done with target object behind barriers, in estimating the photons escaping from the target through the barrier against those from the barrier itself.

10.12 Overall conclusions

In this work, X-ray backscatter imaging systems were successfully simulated in PENELOPE. Although PENELOPE proved to be a valuable resource, it is not user-friendly, it does not automatically support parallel cores, and it is not provided with image processing tools.

PENMAT was developed for enhancing the user experience and enabling parallel calculations. PENMAT core is PAXI, a fast, versatile and comprehensive imaging algorithm for processing data from simulations. PAXI successfully reproduces imaging plates, incorporates the calculation of imaging quality metrics for appraisal of SNR, CNR, spatial resolution, and FOV. PAXI can determine the simulated exposures by processing the data on the phase-space file, it calculates point-spread functions, and defines the ROIs against the background of the image.

PENELOPE upgraded tool was used to model a real thermionic source and virtual sources. The model of the thermionic source was favourably validated by comparison with experiment. Virtual sources are suitable for exploring fundamental principles of backscatter. Virtual sources included mono-directional and mono-energetic sources for isolating energy dependant scattering cross sections, flat spectrum sources for objectively characterising transmission through mask materials, and thin ‘wire shape’ sources for simultaneously characterising the spatial resolution and field of view of X-ray optics.

With this efficient process and parallel computing, various combinations of pinhole and Coded Aperture optics could be efficiently tested and compared. To enable systematic comparisons, the image quality metrics of signal-to noise ratio, contrast-to-noise ratio, spatial resolution, field of view etc. are identified and procedures developed to extract them from images.

It was found that pure tungsten masks were superior to other alloys studied and that a 2 mm thickness 2 mm aperture diameter pinhole gave the most generally suitable resolution/signal compromise. The results were consistent with physical experiment. Coded aperture pattern of MURA, NTHT MURA, Singer Set and NTHT Singer Set were replicated, and tested with an Am-241 (almost) point source, point spread functions extracted from PENELOPE output, and results were compared to experiment.

The HEXITEC energy dispersive image plate was used to collect experimental images from a multi material quadrant test object. The image was reproduced accurately using PAXI. Further, modelling with PAXI allowed isolating the physical interaction processes giving rise to image characteristics.

A unique and innovative 2π detector was modelled, extending the concept of isolation by kind of interaction. Image characteristics from the HEXITEC detector study. Simulations were performed at different mono-energetic and mono-directional energy beams with the aim of studying the fundamental physics of backscatter imaging. PAXI was applied to perform theoretical comparisons to the well-known databases for self-checking the simulation models of differential cross sections. PAXI efficiently extracted angular distributions of image brightness, relative yield and energy-probability from the 2π detector to determine characteristic features of carbon, copper, manganese dioxide, lead at different thicknesses, positions and with/without barriers. Further, the relative contributions from Compton, elastic and fluorescent processes to image brightness and spectral features were isolated and compared with angle. This study cannot be achieved by experiment, and guides how modelling can inform the best detector positioning and beam energies where the backscatter X-rays contain the right information to characterise materials and structures.

This work comprised significant use of simulation and also a strong supporting element of physical experimentation. The development of modelling techniques and their exploitation can give information that physical experiment cannot, while experimentation has been shown to validate the use of simulation and identify some limitations.

REFERENCES

[1] F. Salvat, “PENELOPE-2014: A code system for Monte Carlo simulation of electron and photon transport,” OECD/NEA Data Bank, Issy-les-Moulineaux, France, 2015.

[2] MathWorks, “MATLAB runtime,” 2017. [Online]. Available: https://uk.mathworks.com/products/compiler/mcr.html.

[3] NIST, “National Institute of Standards and Technology,” 17 December 2018. [Online]. Available: hhttps://www.nist.gov. [Accessed 2018].

[4] LLNL, “Lawrence Livermore National Laboratory,” 2018. [Online]. Available: https://www.llnl.gov.

[5] A. Vella, *PAXI: Phase-space file Algorithm for X-ray Imaging,* Shrivenham, 2018.

[6] VJ Technologies, “VJ Technologies,” 2018. [Online]. Available: https://www.vjt.com.

[7] M. Berger, J. Hubbell, S. Seltzer, J. Chang, J. Coursey, R. Sukumar, D. Zucker and K. Olsen, XCOM: Photon Cross Sections Database, 1998.

[8] A.Brunetti, M. d. Rio, B. Golosio, A.Simionovici and A.Somogyi, “A library for X-ray–matter interaction cross sections for X-ray fluorescence applications,” *Spectrochimica Acta Part B: Atomic Spectroscopy,* vol. 59, no. 10-11, pp. 1725-1731, 2004.

[9] T. Schoonjans, A. Brunetti, B. Golosio, M. S. d. Rio, V. A. Solé, C. Ferrero and L. Vincze, “The xraylib library for X-ray–matter interactions. Recent developments,” *Spectrochimica Acta Part B: Atomic Spectroscopy ,* vol. 66, no. 11-12, pp. 776-784 , 2011.

[10] B. Cullity, Element of X-ray diffraction, 2014 ed., Pearson, Ed., 2014.

[11] W. Leo, Techniques for nuclear and particle physics experiments - A how-to approach, Second ed., Springer-Verlag, 1993.

[12] M. J. Cooper, P. E. Minjnarends, N. Shiotani and A. Bansil, X-ray Compton Scattering, Oxford: Oxford University Press, 2004.

[13] J. H. Hubbell and S. M. Seltzer, “X-Ray Mass Attenuation Coefficients - Tables of X-Ray Mass Attenuation Coefficients and Mass Energy-Absorption Coefficients from 1 keV to 20 MeV for Elements Z = 1 to 92 and 48 Additional Substances of Dosimetric Interest,” NIST, 1989. [Online]. Available: http://www.nist.gov/pml/x-ray-mass-attenuation-coefficients.

[14] A. H. Compton, “A Quantum Theory of the Scattering of X-rays by Light Elements,” *Physical Review Letter,* vol. 21, no. 5, pp. 483-502, 1923.

[15] J. T. Bushberg, The essential Physics of Medical Imaging, Philadelphia: Lippincott Williams & Wilkins, 2012.

[16] O. Klein and Y. Nishina, “Über die Streuung von Strahlung durch freie Elektronen nach der neuen relativistischen Quantendynamik von Dirac,” *Zeitschrift für Physik,* vol. 52, no. 11-12, pp. 853-868, 1929.

[17] J. H. Hubbell, “Photon Cross Sections, Attenuation Coefficients, and Energy Absorption Coefficients From 10 keV to 100 GeV,” *NSRDS - NBS,* vol. 29, 1969.

[18] G. Harding and E. Harding, “Compton scatter imaging: A tool for historical exploration,” *Applied Radiation and Isotopes,* vol. 68, p. 993–1005, 2010.

[19] C. Hastings, Approximations for Digital Computers, Princeton Legacy Library ed., Princeton University Press, 1955.

[20] J. W. Motz and G. Missoni, “Compton Scattering by K -Shell Electrons,” *Phys. Rev. ,* vol. 124, no. 1458, 1961.

[21] J. Varma and M. A. Eswaran, “Inelastic Scattering of Gamma Rays by Bound Electrons,” *Phys. Rev. ,* vol. 127, no. 1197, 1962.

[22] J. H. Hubbell, W. J. Veigele, E. A. Briggs, R. T. Brown, D. T. Cromer and R. J. Howerton, “Atomic form factors, incoherent scattering functions, and photon scattering cross sections,” *Journal of Physical and Chemical Reference Data ,* vol. 4, p. 471, 2009.

[23] Thomas and Fermi, Quantentheorie und Chemie, Rend. Accad. Naz. Lincei, 1927.

[24] D. T. Cromer and J. B. Mann, “Compton Scattering Factors for Spherically Symmetric Free Atoms,” *The Journal of Chemical Physics, Volume 47, Issue 6, p.1892-1893,* vol. 47, no. 6, pp. 1892-1893, 1967.

[25] L. M. Brown and R. P. Feynman, “Radiative Corrections to Compton Scattering,” *Phys. Rev.,* vol. 85, no. 231, 1952.

[26] H. E. J. Martz, C. M. Logan, D. J. Schneberk and P. J. Shull, X-ray Imaging - Fundamentals, Industrial Techniques, and Applications, Boca Raton, FL: CRC Press, 2017.

[27] H. Moseley, “The high-frequency spectra of the elements,” *Philosophical Magazine.,* vol. 6, no. 26, p. 1024–1034., 1913.

[28] C. D. Anderson, “The Positive Electron,” *Phys. Rev. ,* vol. 43, no. 491, 1933.

[29] P. Dirac, “The quantum theory of the electron,” *Proceedings of the Royal Society A,* 1928.

[30] M. Marshall, Aspects of explosives detection, Boston: Elseviewer, 2009.

[31] W. Neumann and S. Zahorodny, “Status and future aspects of X-ray backscatter imaging,” in *Review of Progress in Quantitative Nondestructive Evaluation.* , T. D.O. and C. D.E., Eds., Boston, MA, Springer, 1998, pp. 379-385.

[32] G. Harding, “On the sensitivity and application possibilities of a novel Compton scatter imaging system,” *IEEE Transactions on Nuclear Science,* Vols. NS-29, no. 3, 1982.

[33] G. Harding, H. Strecker and R. Tischler, “X-ray imaging with Compton-scatter radiation,” *Philips Tech. Rev.,* vol. 41, no. 2, pp. 46-59, 1983.

[34] G. Harding, “Inelastic photon scattering: effects and applications in biomedical science and industry,” *Radiat. Phys. Chem.,* vol. 50, no. 1, pp. 91-111, 1997.

[35] P. Seller, S. Bell, C. Cernik, C. Christodoulou, C. Egan, J. Gaskin, S. Jacques, S. Pani, B. Ramsey, C. Reid, P. Sellin, J. Scuffham, R. Speller, M. Wilson and M. Veale, “Pixellated Cd(Zn)Te high-energy X-ray instrument,” 2011.

[36] J. Scuffham, M. Wilson, P. Seller, M. Veale, P. Sellin, S. Jacques and R. Cernik, “A CdTe detector for hyperspectral SPECT imaging,” 2012.

[37] F. Salvat, “PENELOPE 2014,” 2014. [Online]. Available: oecd-nea.org/tools/abstract/detail/nea-1525.

[38] S. D. Metzler, J. E. Bowsher, M. F. Smith and R. J. Jaszczak, “Analytic Determination of Pinhole Collimator Sensitivity With Penetration,” *IEEE Transaction on Medical Imaging,* vol. 20, no. 8, pp. 730-741, 2001.

[39] T. E. Peterson and a. S. Shokouhi, “Advances in Preclinical SPECT Instrumentation,” *J Nucl Med.,* vol. 53, no. 6, p. 841–844, 2012.

[40] R. C. Lanza, R. Accorsi and F. Gasparini, “Coded aperture imaging”. United States of America Patent US006737652B2, 2004.

[41] M. J. Cieslak, K. A. Gamage and R. Glover, “Coded-aperture imaging systems: Past, present and future development e A review,” *Radiation Measurements,* vol. 92, no. 92, pp. 59-71, 2016.

[42] A. A. M. Muñoz, A. Vella, M. J. F. Healy, D. W. Lane, I. Jupp and D. Lockley, “3D-printed coded apertures for x-ray backscatter radiography,” in *Proc. SPIE 10393, Radiation Detectors in Medicine, Industry, and National Security XVIII, 103930F* , San Diego, California, 2017.

[43] L. Gulyás and G. Kampis, “Models, Representations and Comparisons in Computer Simulations,” *Procedia Computer Science,* vol. Volume 66, p. Pages 5–12, 2015.

[44] J. Vallverdú, “What are Simulations? An Epistemological Approach,” *Procedia Technology ,* vol. 13, p. 6 – 15, 2014.

[45] M. Pereira, M. Maceira, G. Oliveira and L. Pinto, “Combining analytical models and Monte-Carlo techniques in probabilistic power system analysis,” *IEEE Transactions on Power Systems,* vol. 7, no. 1, pp. 265 - 272, 1992.

[46] Safety and Reliability Society, “Part D - Supporting Theory - Monte-Carlo Simulation,” in *Applied R&M Manual for Defence Systems*, http://www.sars.org.uk, 2018.

[47] G. Poludniowski, G. Landry, F. DeBlois, P. Evans and F. Verhaegen, “SpekCalc: a program to calculate photon spectra from tungsten anode X-ray tubes,” *Physics in Medicine and Biology,* vol. 54, pp. 433-438, 2009.

[48] G. G. Poludniowski, “Calculation of x-ray spectra emerging from an x-ray tube. Part I. Electron penetration characteristics in x-ray targets,” *Medical Physics,* vol. 34, no. 6, 2007.

[49] G. G. Poludniowski, “Calculation of x-ray spectra emerging from an x-ray tube. Part II. X-ray production and filtration in x-ray targets,” *Medical Physics,* vol. 34, no. 6, pp. 2175-2186, 2007.

[50] A. Vella, A. M. Munoz, M. J. F. Healy, L. D. W., D. Lockley and J. Zhou, “A fast and reliable approach to simulating the output from an Xray tube used for developing security backscatter imaging,” San Diego, CA, 2017.

[51] F. Salvat, The PENELOPE code system. Specific features and recent improvements, 2014.

[52] CERN; INFN, “GEANT4,” 2018. [Online]. Available: https://geant4.web.cern.ch.

[53] M. Fippel, “Basics of Monte Carlo Simulations,” in *Monte Carlo Techniques in Radiation Therapy*, J. Seco and F. Verhaegen, Eds., CRC Press, 2013.

[54] W. R. Nelson, H. Hirayama and D. W. 0. Rogers, The ESG4 Code System, Stanford University, Stanford, California 94305: Stanford Linear Accelerator Center, 1985.

[55] F.James, “A review of pseudorandom number generators,” *Computer Physics Communications ,* vol. 60, no. 3, pp. 329-344 , 1990.

[56] A. Ferrari, P. Sala, A. Fassò and J. Ranft, “FLUKA,” 2018. [Online]. Available: http://www.fluka.org/fluka.php.

[57] LANL, “MCNP,” 2018. [Online]. Available: laws.lanl.gov/vhosts/mcnp.lanl.gov/index.shtml. [Accessed 2018].

[58] National Research Council Canada, “EGSnrc,” 2018. [Online]. Available: nrc-cnrc.gc.ca/eng/solutions/advisory/egsnrc_index.html.

[59] J. Baró, J. Sempau, J. Fernández-Varea and F. Salvat, “PENELOPE: An algorithm for Monte Carlo simulation of the penetration and energy loss of

electrons and positrons in matter," *Nuclear Instruments and Methods in Physics Research B,* vol. 100, no. 1, pp. 31-46, 1995.

[60] S. Agostinelli, J. Allison, K. Amako, J. Apostolakis, H. Araujo, P. Arcel, M. Asai, D. Axen, S. Banerjee, G. Barrand, F. Behner, L. Bellagamba, J. Boudreau, L. Broglia, A. Brunengo, H. Burkhardt, S. Chauvie, J. Chumah and D. Zschiesche, "Geant4—a simulation toolkit," *Nuclear Instruments and Methods in Physics Research Section A: Accelerators, Spectrometers, Detectors and Associated Equipment,* vol. 506, no. 3, pp. 250-303, 2003.

[61] H. Yoriyaz, M. Moralles, P. d. T. D. Siqueira, C. d. C. Guimarã, F. B. Cintra and A. d. Santos, "Physical models, cross sections, and numerical approximations used in MCNP and GEANT4 Monte Carlo codes for photon and electron absorbed fraction calculation," *Med. Phys. 36,* vol. 36, no. 11, 2009.

[62] G. Battistoni, T. Boehlen, F. Cerutti, P. W. Chin, L. S. Esposito, A. Fassò, A. Ferrari, A. Lechner, A. Empl, A. Mairani, A. Mereghetti, P. G. Ortega, J. Ranft, S. Roesler, P. R. Sala, V. Vlachoudis and G. Smirnov, "Overview of the FLUKA code," *Annals of Nuclear Energy ,* vol. 82, pp. 10-18, 2015.

[63] A. Y. Lee, A. Jablonski and F. Salvat, "NIST Standard Reference Database (SRD) 64 NIST Electron Elastic-Scattering Cross-Section Database," 2002. [Online]. Available: https://srdata.nist.gov/srd64/.

[64] V. N. Ivanchenko, O. Kadri, M. Maire and L. Urban, "Geant4 models for simulation of multiple scattering," 2010.

[65] J. Sempau, A. Sánchez-Reyes, F. Salvat, H. O. b. Tahar, S. B. Jiang and J. M. F.́ndez-Varea, "Monte Carlo simulation of electron beams from an accelerator head using PENELOPE," *Physics in medicine and biology,* vol. 46, p. 1163–1186, 2001.

[66] J. P. Archambault and E. Mainegra-Hing, "Comparison between EGSnrc, Geant4, MCNP5 and Penelope for mono-energetic electron beams," *Physics in Medicine & Biology,* vol. 60, p. 4951–4962, 2015.

[67] J. Almansa, F. Salvat-Pujol, G. Diaz-Londona, A. Carnicer, A. M. Lallena and F. Salvat, "PENGEOM – A general purpose geometry package for Monte Carlo simulation of radiation transport in complex material structures," *Computer Physics Communications (in press),* 2015.

[68] F. Salvat and J. M. Fernaddez-Varea, “Overview of physical interaction models for photon and electron transport used in Monte Carlo codes,” vol. 46, pp. S122-S138, 2009.

[69] OECD Nuclear Energy Agency, “NEA Data Bank,” 2018. [Online]. Available: https://www.oecd-nea.org/databank/. [Accessed June 2018].

[70] D. E. Cullen, J. H. Hubbell and L. Kissel, “EPDL97: the Evaluated Photon Data Library, '97 Version,” *UCRL-50400,* vol. 6, 1997.

[71] D. Brusa, G. Stutz, J. Riveros, J. Fernández-Varea and F. Salvata, “Fast sampling algorithm for the simulation of photon Compton scattering,” vol. Volume 379, no. 1, pp. 167-175, 1996.

[72] W.R.Nelson, H.Hirayama and D.W.O.Rogers, “The EGS4 code system,” SLAC Report-265, 1985.

[73] J. von Neumann, “Various Techniques Used in Connection With Random Digits,” *J. Res. Nat. Bur. Stand. Appl. Math.,* vol. Series 3, pp. 36-38, 1951.

[74] GNU, “gfortran — the GNU Fortran compiler, part of GCC,” 2008. [Online]. Available: https://gcc.gnu.org/fortran/. [Accessed 2018].

[75] A. Badal and J. Sempau, “A package of Linux scripts for the parallelization of Monte Carlo simulations,” *Computer Physics Communications ,* vol. 175 , p. 440–450 , 2006.

[76] J. Almansa, F. Salvat-Pujol, G. Díaz-Londoña, A. Carnicer, A. M. Lallena and F. Salvat, “PENGEOM – A general purpose geometry package for Monte Carlo simulation of radiation transport in complex material structures,” *Computer Physics Communications ,* vol. 199, pp. 102-113, 2016.

[77] MathWorks Inc., “MATLAB and Statistics Toolbox Release 2018a,” Natick, 2018.

[78] M. Hermida-López, “ Improvements to the dosimetry of 106Ru/106Rh ophthalmic plaques: Monte Carlo simulations and radiochromic film measurements,” Universität Duisburg-Essen, Essen, 2016.

[79] A. Vella, A. Munoz, M. J. F. Healy, D. W. Lane and D. Lockley, “An artificial X-ray wire test emitter and calculations on the resolution and field of view

of X-ray pinhole optics by simulation," *Nuclear Instruments and Methods in Physics Research A,* 2018.

[80] T. Williams and C. Kelley, "Gnuplot," 2018. [Online]. Available: http://www.gnuplot.info.

[81] C. Maire and A. Vella, *PENMAT: PENELOPE 2014 MATLAB GUI,* Shrivenham, 2017.

[82] A. A. M. Munoz, *ENCODER,* Shrivenham, 2018.

[83] H. Ebel, "X-ray tube spectra," *X-ray Spectrometry ,* vol. 28, pp. 255-266, 1999.

[84] A. L. Finkelshtein and T. O. Pavlova, "Calculation of X-ray Tube Spectral Distributions," *X-ray Spectrometry,* vol. 28, pp. 27-32, 1999.

[85] N. Sasaki, K. Okada and J. Kawai, "X-ray tube spectral measurement method for quantitative analysis of X-ray fluorescence analysis," *X-ray Spectrometry,* vol. 39, pp. 328-331, 2010.

[86] X. Llovet, L. Sorbier, C. S. Campos, E. Acosta and F. Salvat, "Monte Carlo simulation of X-ray spectra generted by kilo-electron-volt electrons," *Journal of Applied Physics,* vol. 93, no. 7, 2002.

[87] G. Hernández and F. Fernández, "A model of tungsten anode x-ray spectra," *Medical Physics,* vol. 43, no. 8, 2016.

[88] J. Harry E. Martz, C. M. Logan, D. J. Schneberk and P. J. Shull, X-Ray Imaging - Fundamentals, Industrial Techniques, and Applications, CRC Press, 2017.

[89] E. E. Fenimore, "Coded aperture imaging: predicted performance of uniformly redundant arrays," *Applied Optics,* vol. 17, no. 22, p. 3563, 1978.

[90] R. Accorsi, F. Gasparini and R. C. Lanza, "A Coded Aperture for High-Resolution Nuclear Medicine Planar Imaging With a Conventional Anger Camera: Experimental Results," *IEEE Transactions on Nuclear Science,* vol. 48, no. 6, 2001.

[91] R. Accorsi and S. D. Metzler, "Analytic Determination of the Resolution-Equivalent Effective Diameter of a Pinhole Collimator," *IEEE Transactions on Medical Imaging,* vol. 23, no. 6, 2004.

[92] F. Pozuelo, S. Gallardo, A. Querol, G. Verdú and J. Rodenas, “X-ray simulation with the Monte Carlo code PENELOPE. Application to Quality Control,” in *34th Annual International Conference of IEEE EMBS*, San Diego, California, USA, 2012.

[93] C. B. G.-R. J. A. Deresch, “A general spectrum model for X-ray generators,” *NDT&E International,* vol. 79 , p. 92–97, 2016.

[94] D. Bote, X. Llovet and F. Salvat, “Monte Carlo simulation of characteristic X-ray emission from thick samples bombarded by kiloelectronvolt electrons,” *Journal of Physics D: Applied Physics,* vol. 41, 2008.

[95] F. Salvat, “The PENELOPE code system. Specific features and recent improvements,” *Annals of Nuclear Energy,* vol. 82, pp. 98-109, 2015.

[96] G. Díaz-Londoño, S. García-Pareja, F. Salvat and A. M. Lallena, “Monte Carlo calculation of specific absorbed fractions: variance reduction techniques,” *Physics in Medicine & Biology,* vol. 60, no. 7, 2015.

[97] Amptek Material Analysis Division, “Amptek.com,” 2016. [Online]. Available: http://amptek.com/products/x-123-cdte-complete-x-ray-gamma-ray-spectrometer-with-cdte-detector/.

[98] J. E. Fernandez, V. Scot, J. Bare, F. Tondeur, S. Gallardo, J. Ródenas and P. L. Rossi, “Reconstruction of the X-ray tube spectrum from a scattering measurement,” *Applied Radiation and Isotopes,* vol. 2012 , p. 1238–1242, 2012.

[99] Amptek, “XR-100T-CdTe Cadmium Telluride Detector Efficiency Application Note,” Amptek, 2018. [Online]. Available: http://amptek.com/xr-100t-cdte-cadmium-telluride-detector-efficiency-application-note/.

[100] A. L. Gonzales, A. Tomal and P. Costa, “Evaluation of characteristic-to-total spectrum ratio: Comparison between experimental and a semi-empirical model,” *Applied Radiation and Isotopes,* vol. 100, pp. 27-31, 2015.

[101] B. P. Cluggish, I. N. B. L. Zhao, J. Kim, R. C. Vondrasek, R. Pardo and R. H. Scott, “Measurements of X-ray spectra on ECR-II,” in *Proceedings of ECRIS08*, Chicago, IL, USA, 2008.

[102] B. Redus, “Efficiency and Attenuation in CdTe Detectors,” Amptek Inc, 2010.

[103] R. Accorsi, F. Gasparini and R. C. Lanza, “A Coded Aperture for High-Resolution Nuclear Medicine Planar Imaging With a Conventional Anger Camera: Experimental Results,” *IEEE TRANSACTIONS ON NUCLEAR SCIENCE,* vol. VOL. 48, no. NO. 6, p. 2411, 2001.

[104] NIST, “XCOM: Photon Cross Sections Database,” 17 December 2017. [Online]. Available: http://www.nist.gov/pml/data/xcom/index.cfm. [Accessed 01 April 2016].

[105] NIST, “XCOM: Photon Cross Sections Database,” 16 April 2016. [Online]. Available: http://www.nist.gov/pml/data/xcom/index.cfm.

[106] A. Vella, A. A. M. Munoz, M. J. F. Healy, D. W. Lane and D. Lockley, “Use of simulation to optimize the pinhole diameter and mask thickness for an x-ray backscatter imaging system,” San Diego, 2017.

[107] D. R. Dance, S. Christofides, A. D. A. Maidment, I. D. McLean and K. H. Ng, D. R. Dance et al., “Diagnostic Radiology Physics – A handbook for teachers and students, Vienna: IAEA International Agency Energy Agency, 2014.

[108] A. Michelson, Studies in Optics, Chicago: U. of Chicago Press, 1927.

[109] H. Rose, *Adv. Electron.,* vol. 1, p. 131, 1948.

[110] A. M. A. Munoz, A. Vella, M. Healy, W. D. Lane, I. Jupp and D. Lockley, “Rapid prototyping-coded masks for x-ray backscatter imaging,” *Optical Engineering,* vol. 57 , no. 8, 2018.

[111] L. Jones, P. Seller, M. Wilson and A. Hardie, “HEXITEC ASIC—a pixellated readout chip for CZT detectors,” *Nuclear Instruments and Methods in Physics Research Section A: Accelerators, Spectrometers, Detectors and Associated Equipment,* pp. 34-37, June 2009.

[112] M. Wilson, L. Dummot, D. Duarte, F. Green, S. Pani, A. Schneider, J. Scuffham, P. Seller and M. Veale, “A 10 cm x 10 cm CdTe Spectroscopic Imaging Detector based on the HEXITEC ASIC,” 2015.

[113] M. Wilson, T. Connolley, I. Dolbnya, P. Grant, E. Liotti, A. Lui, A. Malandain, K. Sawhney, P. Seller and M. Veale, “Energy Dispersive Detector for White Beam Synchrotron X-ray Fluorescence Imaging,” 2016.

[114] C. Egan, M. Wilson, M. Veale, P. Seller, S. Jacques and R. Cernik, “Material specific X-ray imaging using an energy-dispersive pixel detector,” *Nuclear Instruments and Methods in Physics Research B,* pp. 25-28, 2014.

[115] PC Control Ltd., StepperBee, Stepper motor control from a PC’s USB port, PC Control Ltd., 2009.

[116] M. J. F. Healy, “Energy calibration by silicon resonance: Completing system calibration with one reference material,” *Nuclear Instruments and Methods in Physics Research Section B: Beam Interactions with Materials and Atoms,* vol. 249, no. 1-2, pp. 918-920, 2009.

[117] G. Fechner, Elemente der Psychophysik, New York: Holt, Rinehart, and Winston, 1860/1966.

[118] M. Yücel, E. Emirhan, A. Emirhan, C. Emirhan and E. Barlas Yücel, “Comparison of simulated and measured spectra from an X-ray tube for the energies between 20 and 35 keV,” *Nuclear Instruments and Methods in Physics Research A,* vol. 799, pp. 50-53, 2015.

[119] K. Wells and D. Bradley, “A review of X-ray explosives detection techniques for checked baggage,” *Applied Radiation and Isotopes ,* vol. 70, p. 1729–1746, 2012.

[120] K. Wells, A review of X-ray explosives detection techniques for checked baggage, Applied Radiation and Isotopes ed., vol. 70, IOP, Ed., 2012.

[121] F. Verhaegen, A. E. Nahum, S. V. d. Putte and Y. Namito, “Monte Carlo modelling of radiotherapy kV X-ray units,” *Phys. Med. Biol.,* vol. 44, p. 1767–1789, 1999.

[122] A. Tomal, J. C. Santos, P. R. Costa, A. H. Lopez Gonzales and M. E. Poletti, “Monte Carlo simulation of the response functions of CdTe detectors to be applied in x-ray spectroscopy,” *Applied Radiation and Isotopes,* no. 100, pp. 32-37, 2015.

[123] S. T. Thornton, Modern Physics for Scientists and Engineers, London: Thomson Learning, 2006.

[124] M. Siegbahn, “Relations between the K and L Series of the High-Frequency Spectra,” *Nature ,* vol. 96, no. 676, 1916.

[125] F. Salvat, “Overview of physical interaction models for photon and electron transport used in Monte Carlo codes,” *Metrologia,* vol. 46, no. 2, 2009.

[126] T. L. Saaty, “Decision-making with the AHP: Why is the principal eigenvector necessary,” *European Journal of Operational Research,* vol. 145, pp. 85-91, 2003.

[127] K. Rossmann, “Point spread-function, line spread-function, and modulation transfer function. Tools for the study of imaging systems,” *Radiology,* pp. 257-272, 1969.

[128] G. McKinney, J. Durkee, J. Hendricks, M. James, D. Pelowitz and L. Waters, “Review of Monte Carlo All-Particle Transport Codes and Overview of Recent MCNPX Features,” Cape Town, South Africa, 2006.

[129] G. Matscheko and G. A. Carlsson, “Compton spectroscopy in the diagnostic X-ray energy range: I. Spectrometer design,” *Physics in Medicine & Biology,* vol. 34, no. 2, p. 185, 1989.

[130] A. Lopez, R. Bacelar, I. Pires, T. G. Santos, J. P. Sousa and L. Quintino, “Non-destructive testing application of radiography and ultrasound for wire and arc additive manufacturing,” *Additive Manufacturing,* vol. 21, pp. 298-306, 2018.

[131] R. J. Jaszczakt, J. Li, H. Wang, M. R. Zalutsky and R. E. Coleman, “Pinhole collimation for ultra-high-resolution, small- field-of-view SPECT,” *Phys. Med. Biol. ,* vol. 39, pp. 4-37, 1994.

[132] IEEE, “American National Standard for measuring the image performance of X-ray and gamma-ray systems for security screening of humans,” IEEE, NY, 2010.

[133] M. Hermida-Lupez, “Musiman”. 2016.

[134] R. L. Harrison, “Introduction To Monte Carlo Simulation,” 2010.

[135] M. Gieles, H. W. A. M. De Jong and F. J. Beekman, “Monte Carlo simulations of pinhole imaging accelerated by kernel-based forced detection,” *Phys. Med. Biol. ,* vol. 47, p. 1853–1867, 2002.

[136] J. Fulop, “Introduction to Decision Making Methods,” *Laboratory of Operations Research and Decision Systems,* 2005.

[137] C. Fiorini, R. Accorsi and G. Lucignani, “Single Pinhole and Coded Aperture Collimation Systems for High-Resolution Gamma-Ray Imaging in Nuclear Medicine: a Comparative Study,” *IEEE Nuclear Science Symposium Conference Record,* Vols. J03-43, 2005.

[138] A. Einstein, “On a Heuristic Point of View about the Creatidn and Conversion of Light,” *Ann. Physik ,* vol. 17, p. 132, 1905.

[139] D. R. Dance, S. Christofides, A. D. A. Maidment, I. D. McLean and K. H. Ng, Diagnostic Radiology Physics – A handbook for teachers and students, Vienna: IAEA International Agency Energy Agency, 2014.

[140] K. Chen, Architectures and algorithms for x-ray diffraction imaging, vol. 9020, SPIE, 2014.

[141] C. Chantler, “Theoretical Form Factor, Attenuation, and Scattering Tabulation for Z=1 - 92 from E=1 - 10 eV to E=0.4 - 1.0 MeV,” *Journal of Physical and Chemical Reference Data,* vol. 24, pp. 71-643, 1995.

[142] E. D. Castro, R. Pani, R. Pellegrini and C. Bacci, “The use of Cadmium telluride detectors for the qualitative analysis of diagnostic X-ray spectr,” *Phys. Med. Biol.,* vol. 29, no. 9, pp. 1117-1131, 1984.

[143] Autodesk Inc., “AutoCAD 2015,” San Rafael, 2015.

[144] I. Amptek, Materials Analysis Division, Bedford: Amptek.com, 2017.

[145] Crossroad Scientific, “XRS-FP,” 2016. [Online]. Available: http://crossroadsscientific.com/xrs-fp.html.

[146] Sparkling Logic, “SMARTS Decision Manager,” 2017. [Online]. Available: https://www.sparklinglogic.com/smarts-decision-manager/.

[147] The MathWorks Inc., “MATLAB and Statistics Toolbox Release 2017a,” Natick, 2017.

APPENDICES

Appendix A PUBLISHED PAPERS

Following, the list of conference papers and peer-reviewed published papers.

A.1 Conference Papers

- Vella A, Munoz AAM, Healy MJF, Lane DW, Lockley D & Zhou J (2017) A fast and reliable approach to simulating the output from an x-ray tube used for developing security backscatter imaging. In: Advances in Computational Methods for X-Ray Optics IV, San Diego, CA, 9-10 August 2017.
- Vella A, Munoz AAM, Healy MJF, Lane DW & Lockley D (2017) The use of simulation to optimize the pinhole diameter and mask thickness for an x-ray backscatter imaging system. In: Advances in Computational Methods for X-Ray Optics IV, San Diego, CA, 9-10 August 2017.
- Munoz AAM, Vella A, Healy MJF, Lane DW, Jupp I & Lockley D (2017) 3D-printed coded apertures for x-ray backscatter radiography. In: Radiation Detectors in Medicine, Industry, and National Security XVIII, San Diego, CA, 6-10 August 2017.
- Munoz AAM, Vella A, Healy MJF, Lane DW, Jupp I & Lockley D (2017) X-ray backscatter radiography with lower open fraction coded masks. In: Radiation Detectors in Medicine, Industry, and National Security XVIII, San Diego, CA, 6-10 August 2017.

A.2 Published Papers

- Vella A, Munoz AAM, Healy MJF, Lane DW & Lockley D (2018) An artificial X-ray wire test emitter and calculations on the resolution and field of view of X-ray pinhole optics by simulation, Nuclear Instruments and Methods in Physics Research Section A: Accelerators, Spectrometers, Detectors and Associated Equipment, 905 119-128.

- Munoz AAM, Vella A, Healy MJF, Lane DW, Jupp I & Lockley D (2018) Rapid prototyping-coded masks for x-ray backscatter imaging, Optical Engineering, 57 (8) Article No. 085104.
- Munoz AAM, Vella A, Healy MJF, Lane DW, Jupp I & Lockley D (2018) Low open fraction coded masks for x-ray backscatter imaging, Optical Engineering, 57 (9) Article No. 093108.

Appendix B NIST Element and Mixtures Cross Sections

B.1 Carbon

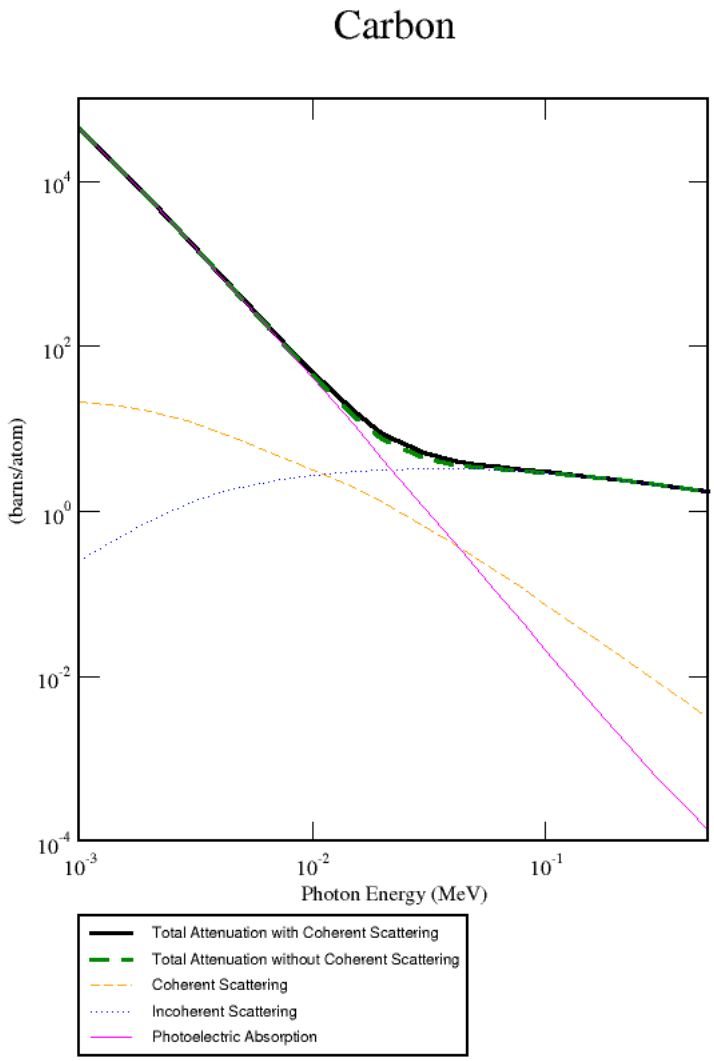

Figure B. 1 Carbon cross section calculated by NIST XCOM up to 500 keV. Total cross section is the sum of photoelectric absorption, Thomson – elastic scattering, Compton scattering, and electron-positron pair production (higher energies). Cross sections are in barns/atom.

B.2 Aluminium

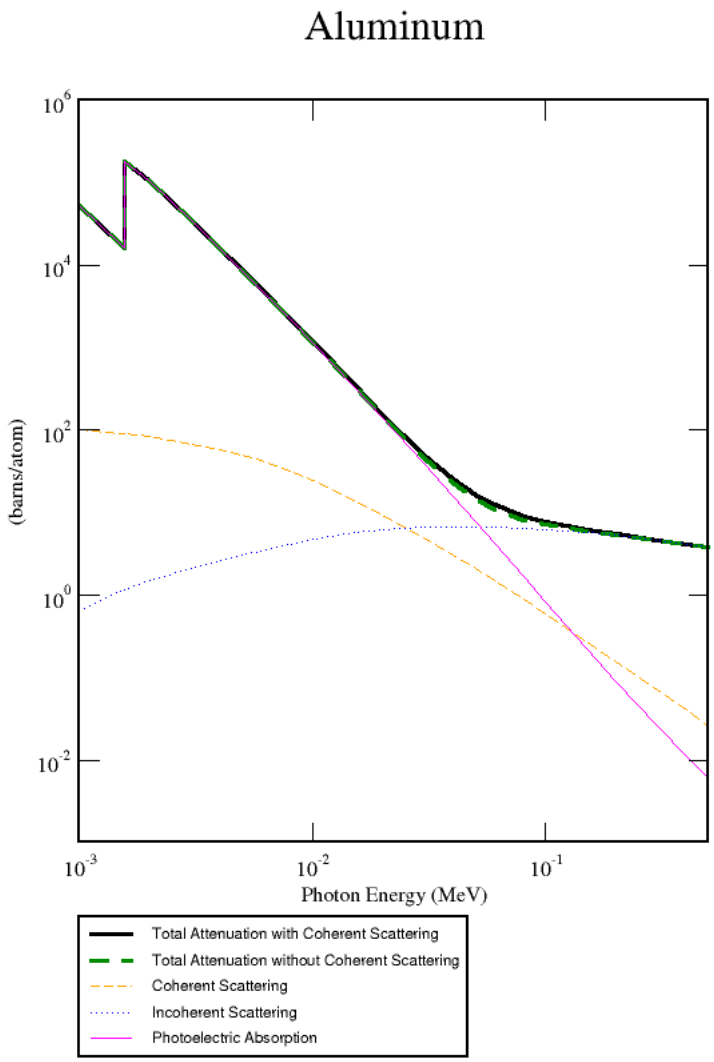

Figure B. 2 Aluminium cross section calculated by NIST XCOM up to 500 keV. Total cross section is the sum of photoelectric absorption, Thomson – elastic scattering, Compton scattering, and electron-positron pair production (higher energies). Cross sections are in barns/atom.

B.3 Copper

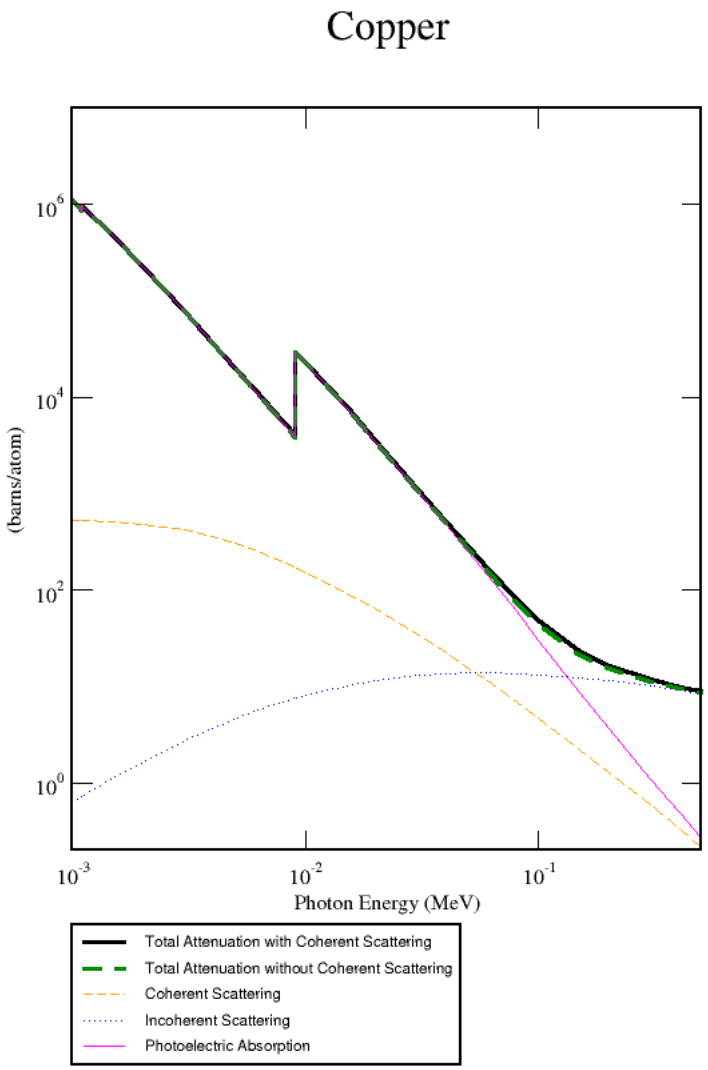

Figure B. 3 Copper cross section calculated by NIST XCOM up to 500 keV. Total cross section is the sum of photoelectric absorption, Thomson – elastic scattering, Compton scattering, and electron-positron pair production (higher energies). Cross sections are in barns/atom.

B.4 Iron

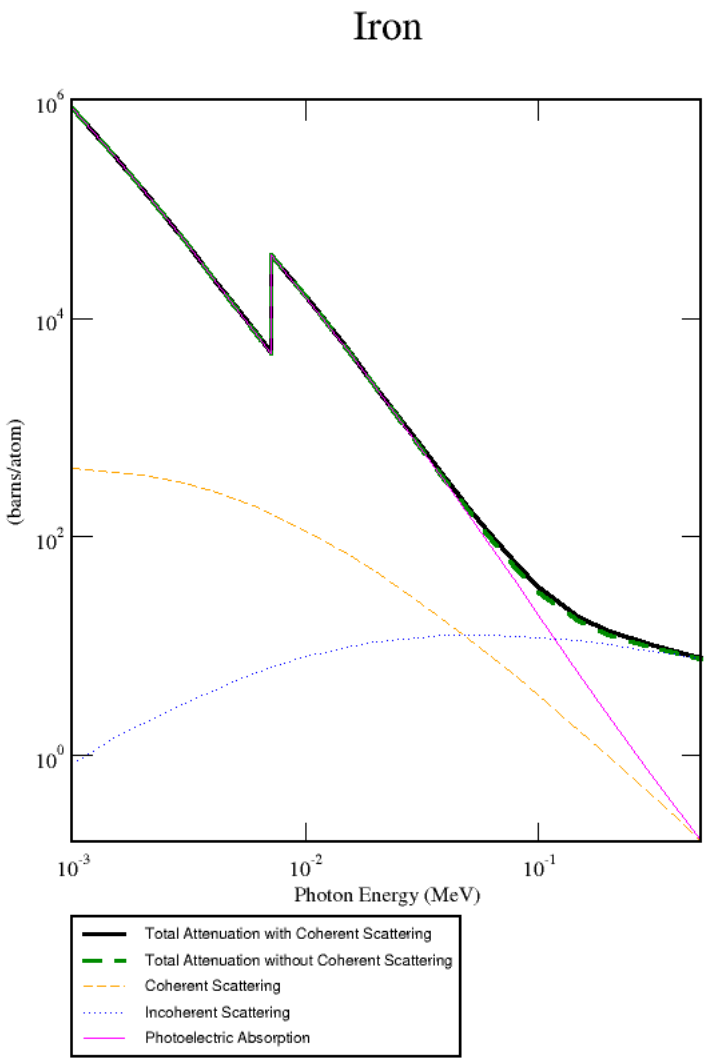

Figure B. 4 Iron cross section calculated by NIST XCOM up to 500 keV. Total cross section is the sum of photoelectric absorption, Thomson – elastic scattering, Compton scattering, and electron-positron pair production (higher energies). Cross sections are in barns/atom.

B.5 Tungsten

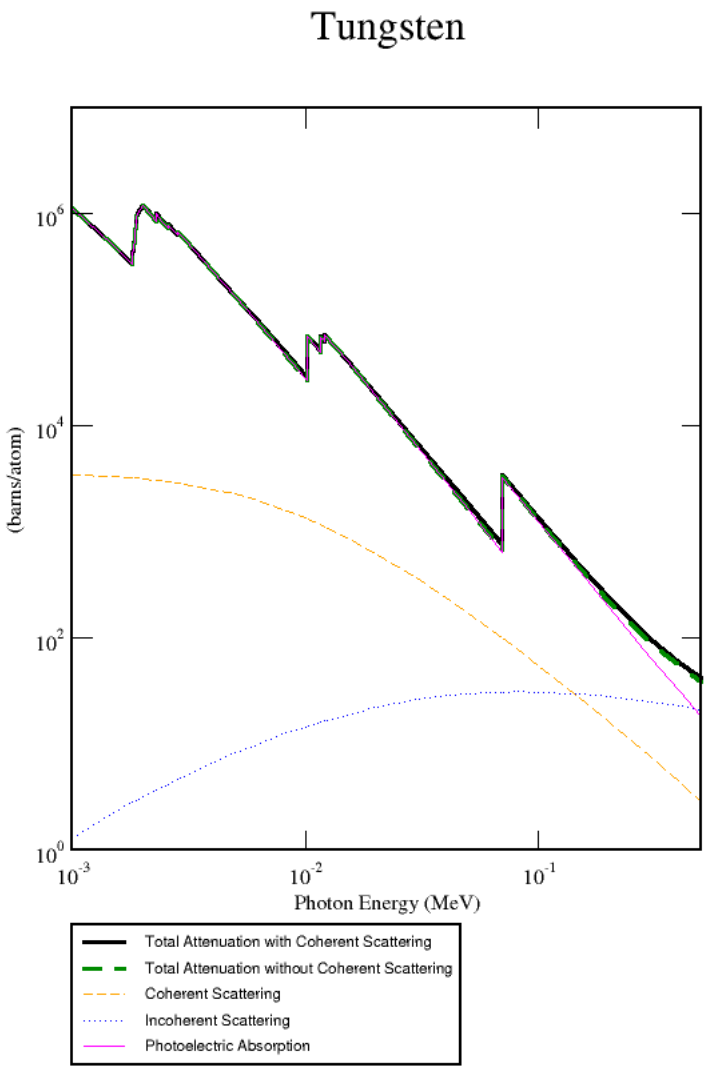

Figure B. 5 Tungsten cross section calculated by NIST XCOM up to 500 keV. Total cross section is the sum of photoelectric absorption, Thomson – elastic scattering, Compton scattering, and electron-positron pair production (higher energies). Cross sections are in barns/atom.

B.6 Lead

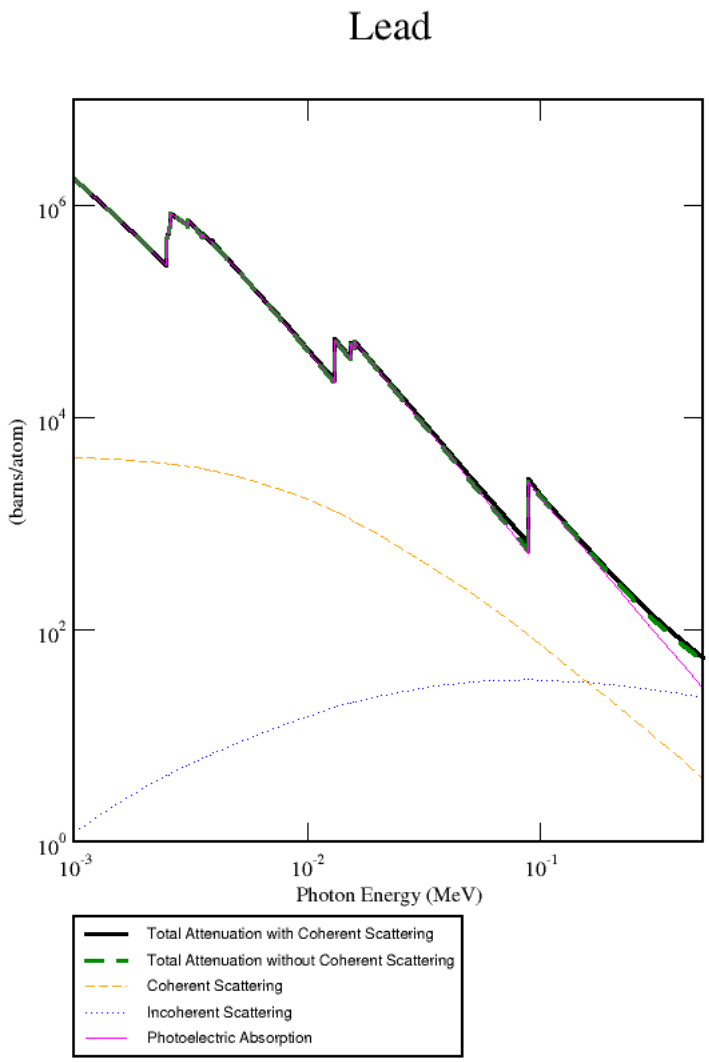

Figure B. 6 Lead cross section calculated by NIST XCOM up to 500 keV. Total cross section is the sum of photoelectric absorption, Thomson – elastic scattering, Compton scattering, and electron-positron pair production (higher energies). Cross sections are in barns/atom.

B.7 Tungsten Epoxy

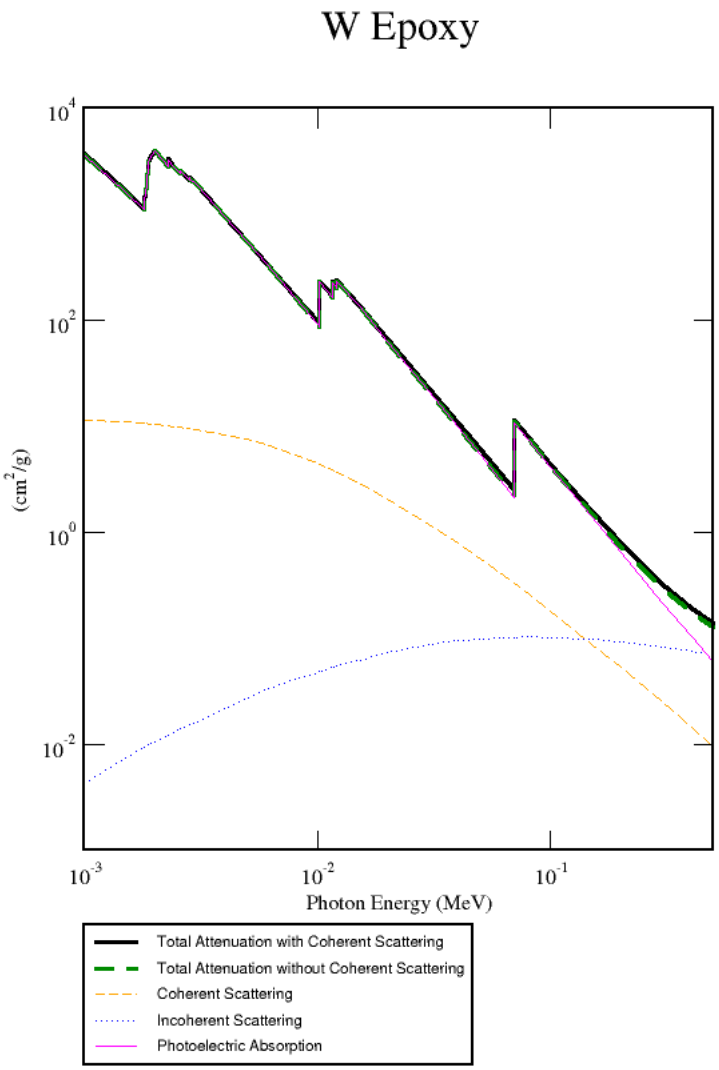

Figure B. 7 Tungsten-epoxy cross section calculated by NIST XCOM up to 500 keV. Total cross section is the sum of photoelectric absorption, Thomson – elastic scattering, Compton scattering, and electron-positron pair production (higher energies). Cross sections are in cm^2/g.

B.8 Bismuth low-melting alloy

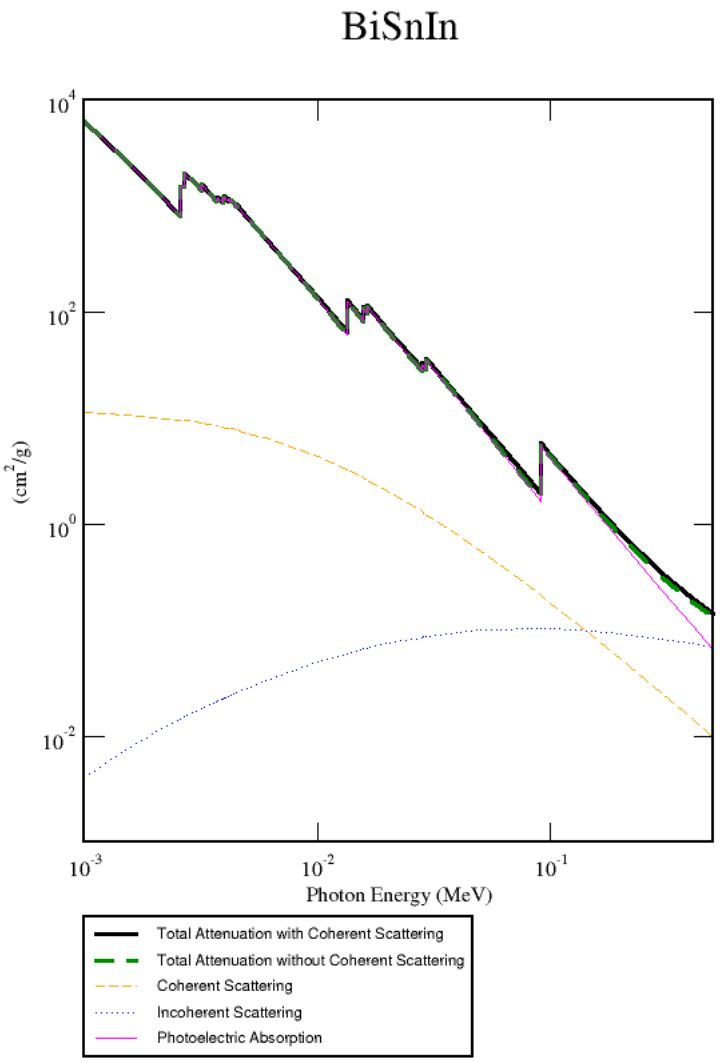

Figure B. 8 Bismuth-alloy cross section calculated by NIST XCOM up to 500 keV. Total cross section is the sum of photoelectric absorption, Thomson – elastic scattering, Compton scattering, and electron-positron pair production (higher energies). Cross sections are in cm^2/g.

B.9 PLA

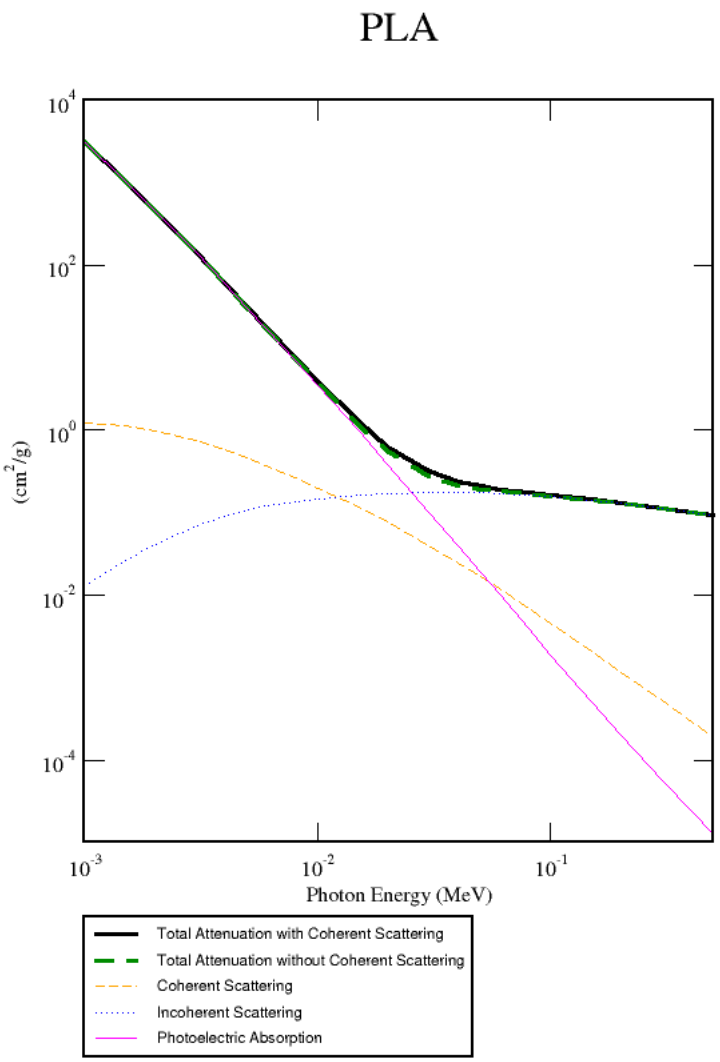

Figure B. 9 PLA cross section calculated by NIST XCOM up to 500 keV. Total cross section is the sum of photoelectric absorption, Thomson – elastic scattering, Compton scattering, and electron-positron pair production (higher energies). Cross sections are in cm^2/g.

B.10 ABS

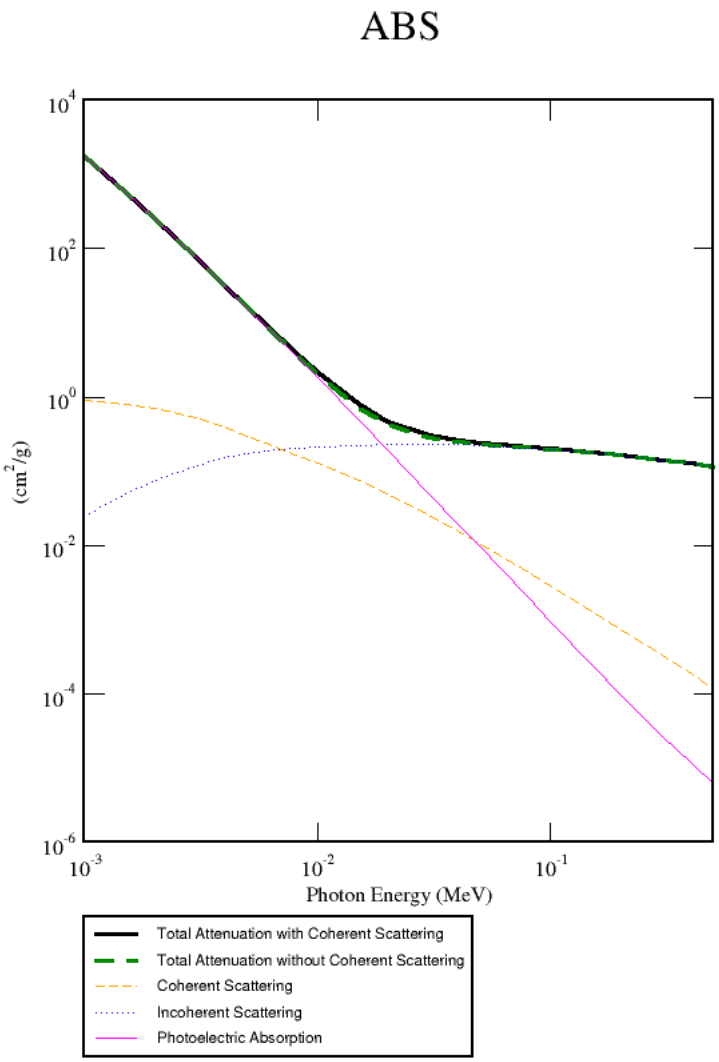

Figure B. 10 ABS cross section calculated by NIST XCOM up to 500 keV. Total cross section is the sum of photoelectric absorption, Thomson – elastic scattering, Compton scattering, and electron-positron pair production (higher energies). Cross sections are in cm^2/g.

Appendix C Xraylib Klein-Nishina DCS

C.1 Carbon

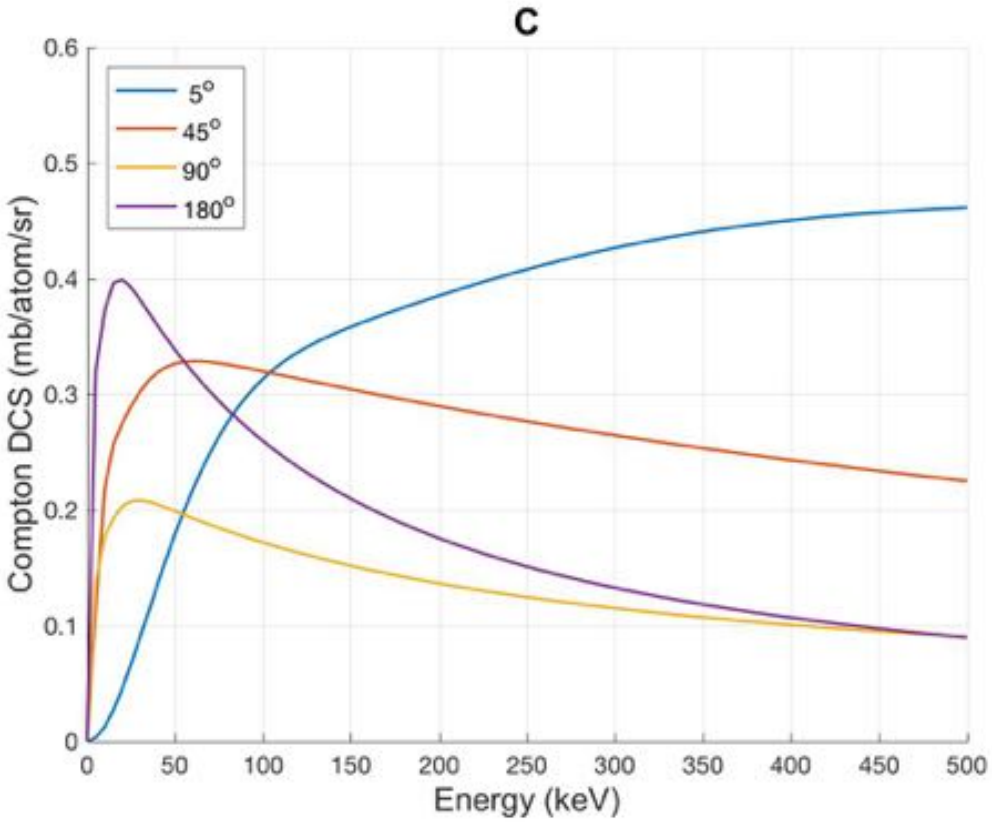

Figure C. 1 Carbon K-N differential cross section calculated by xraylib in MATLAB up to 500 keV at 5˚, 45˚, 90˚ and 180˚.

C.2 Aluminium

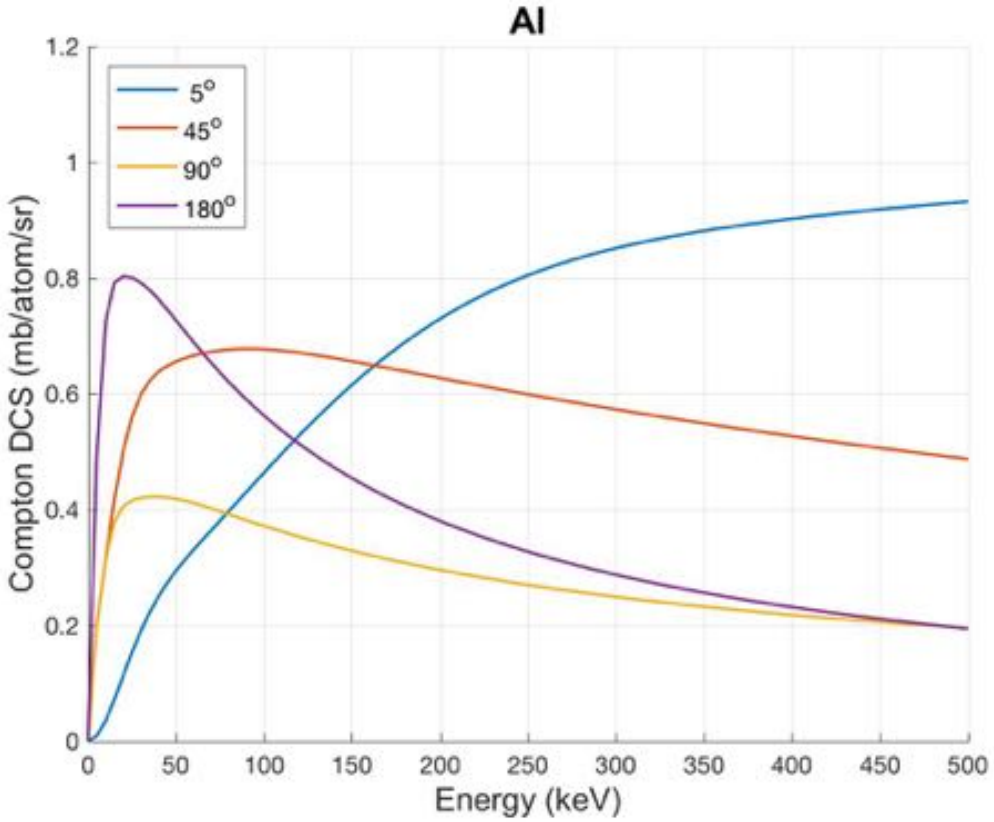

Figure C. 2 Aluminium K-N differential cross section calculated by xraylib in MATLAB up to 500 keV at 5˚, 45˚, 90˚ and 180˚.

C.3 Copper

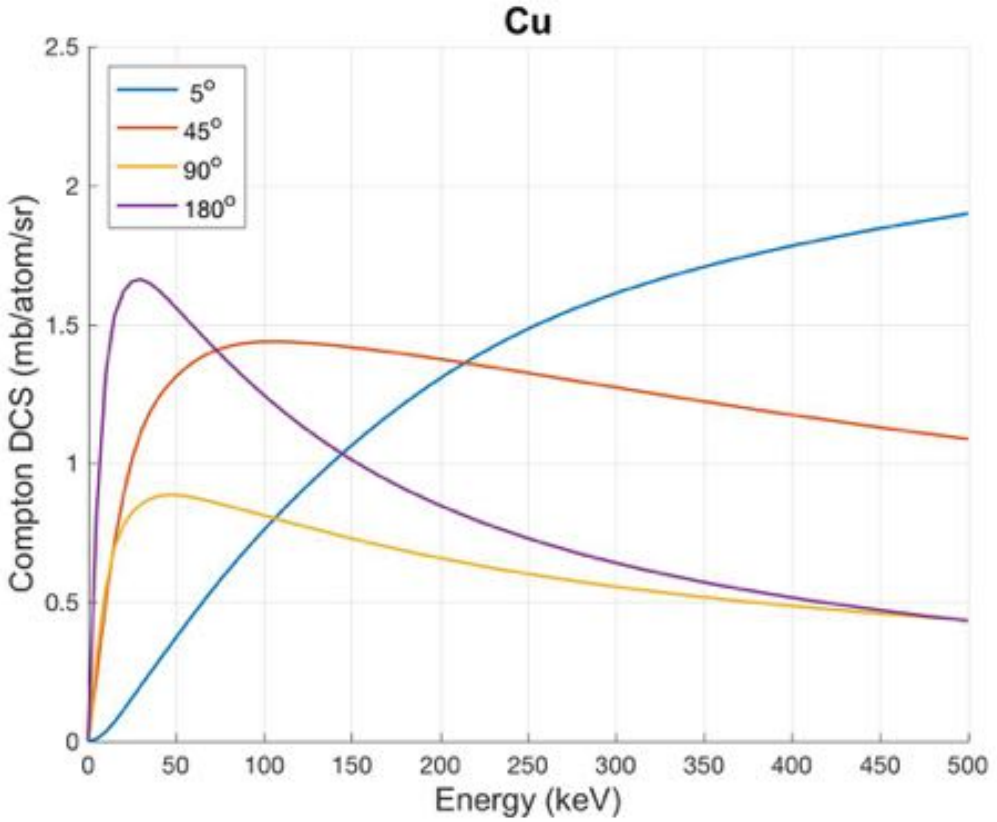

Figure C. 3 Copper K-N differential cross section calculated by xraylib in MATLAB up to 500 keV at 5˚, 45˚, 90˚ and 180˚.

C.4 Iron

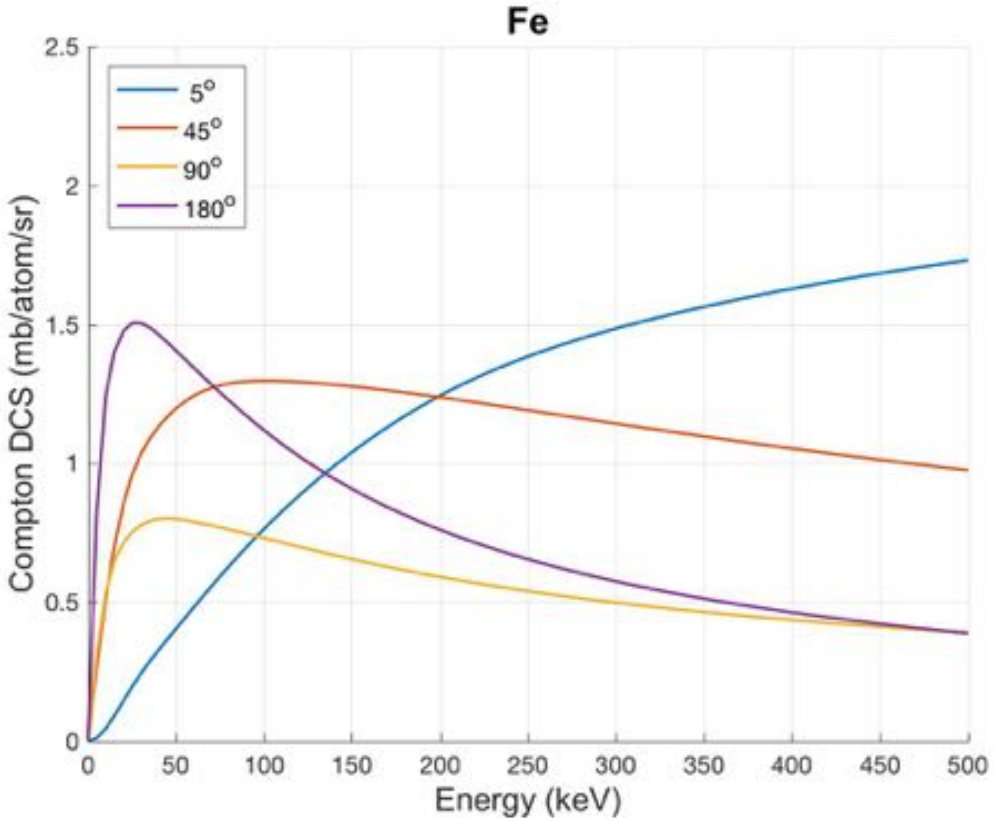

Figure C. 4 Iron K-N differential cross section calculated by xraylib in MATLAB up to 500 keV at 5˚, 45˚, 90˚ and 180˚.

C.5 Manganese Dioxide

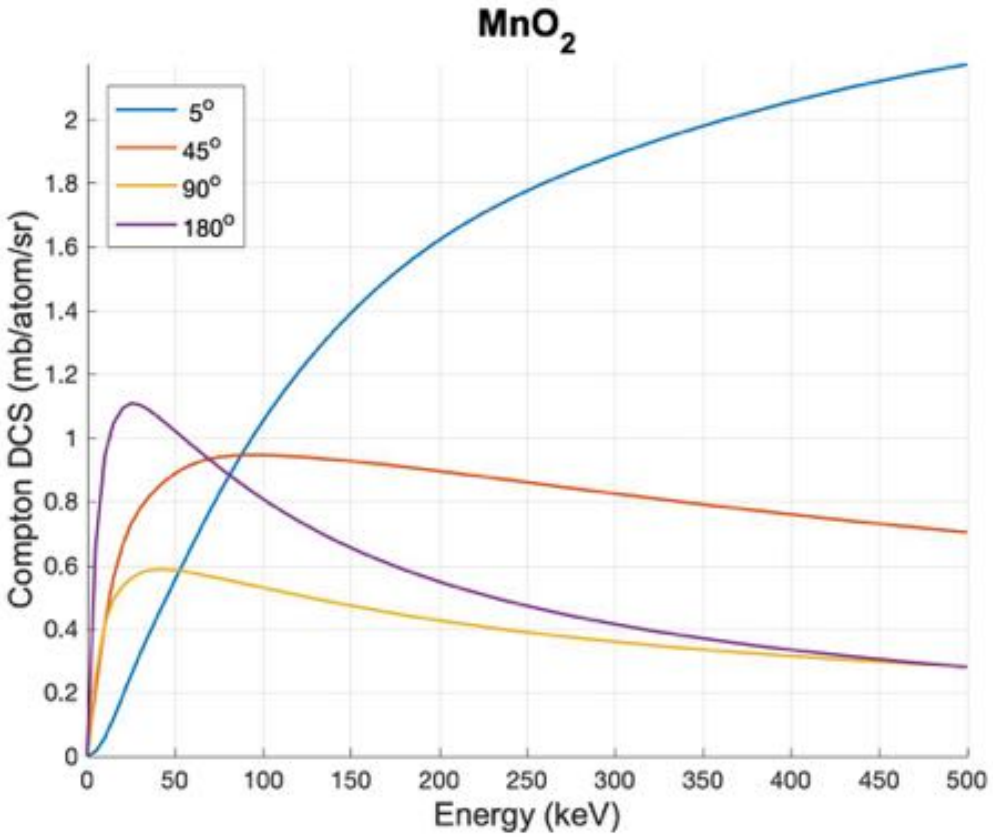

Figure C. 5 Manganese dioxide K-N differential cross section calculated by xraylib in MATLAB up to 500 keV at 5˚, 45˚, 90˚ and 180˚.

C.6 Lead

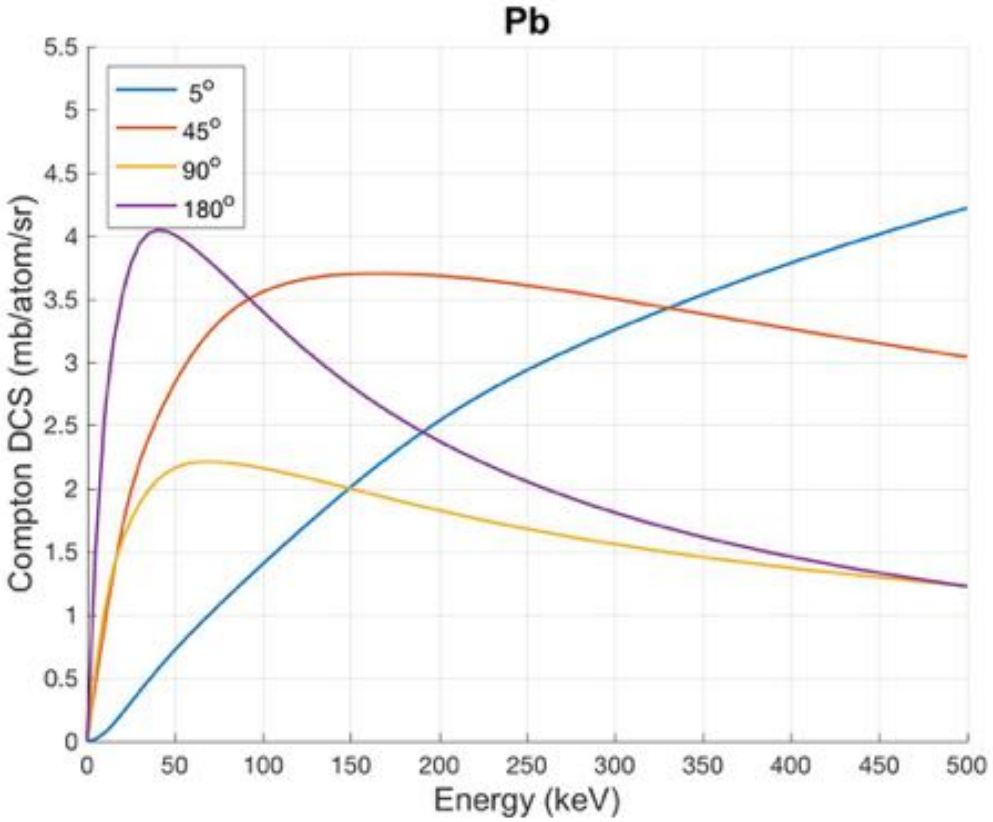

Figure C. 6 Lead K-N differential cross section calculated by xraylib in MATLAB up to 500 keV at 5˚, 45˚, 90˚ and 180˚.

Appendix D Image brightness – materials kind of interactions

D.1 Carbon-1 mm thick

C

25 keV 150 keV 500 keV

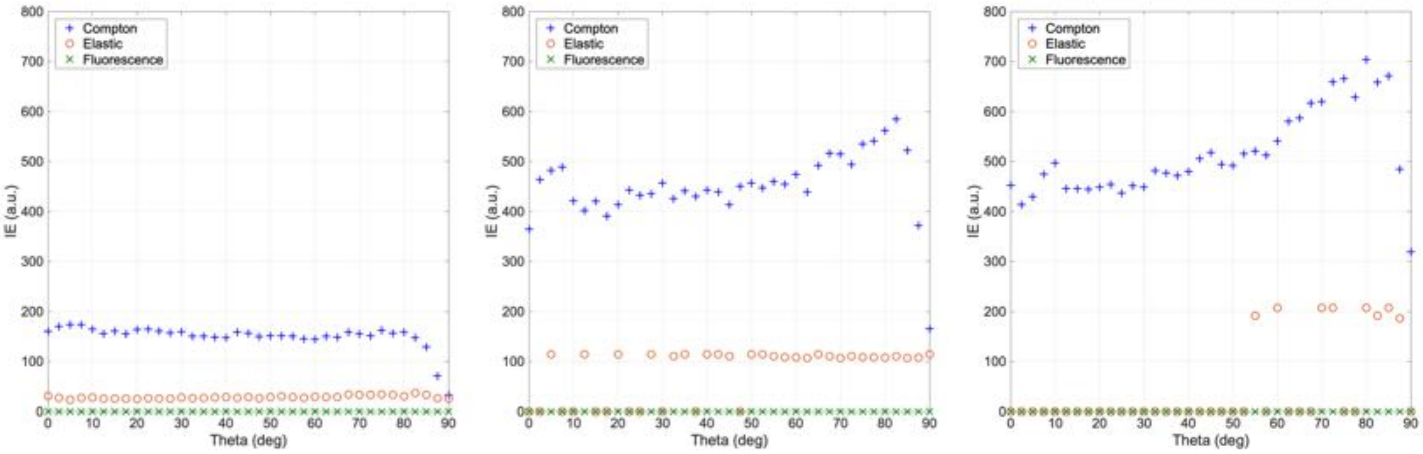

(a) (b) (c)

Figure D. 1 Image brightness as integrated energy of 1 mm thick carbon at 25 keV (a), 150 keV (b) and 500 keV (c). Image brightness is plotted for Compton scatter (blue crosses), elastic scatter (red circles), and fluorescence (green asterisks).

D.2 Carbon-1 mm thick (45˚) rotated

C

25 keV 150 keV 500 keV

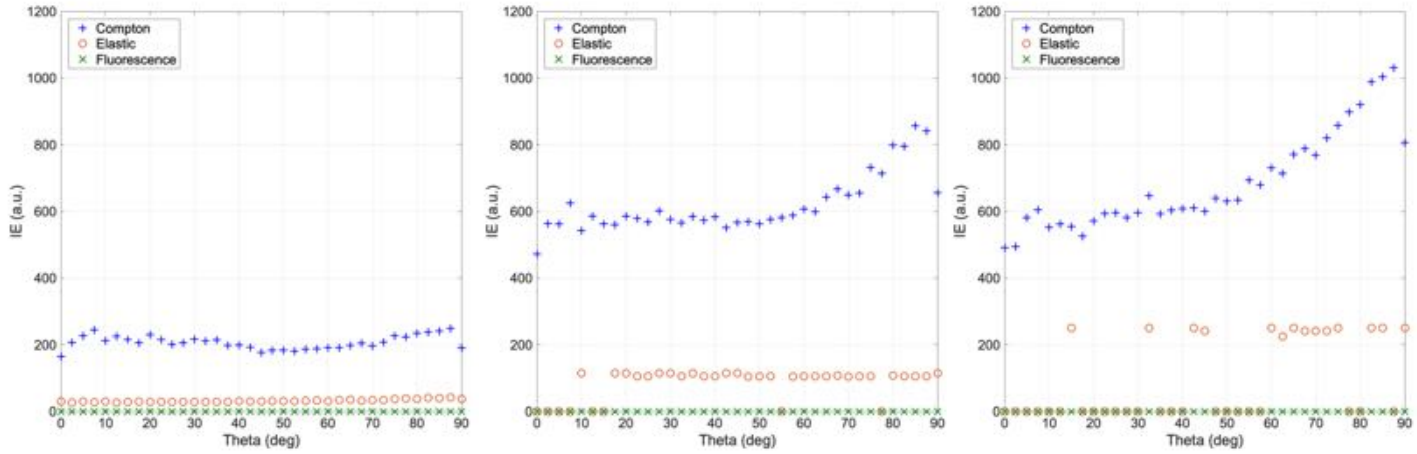

(a) (b) (c)

Figure D. 2 Image brightness as integrated energy of 1 mm thick 45˚ rotated carbon at 25 keV (a), 150 keV (b) and 500 keV (c). Image brightness is plotted for Compton scatter (blue crosses), elastic scatter (red circles), and fluorescence (green asterisks).

D.3 Carbon-50 mm thick

C

25 keV 150 keV 500 keV

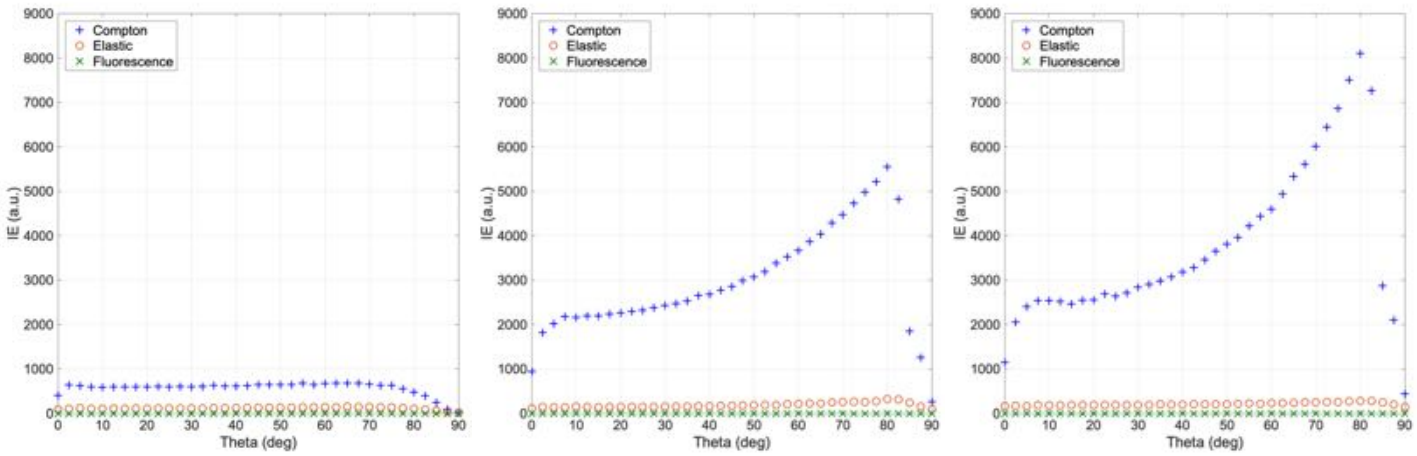

(a) (b) (c)

Figure D. 3 Image brightness as integrated energy of 5 cm thick carbon at 25 keV (a), 150 keV (b) and 500 keV (c). Image brightness is plotted for Compton scatter (blue crosses), elastic scatter (red circles), and fluorescence (green asterisks).

D.4 Carbon-50 mm thick rotated with Al, Fe barriers

C-Al

25 keV 150 keV 500 keV

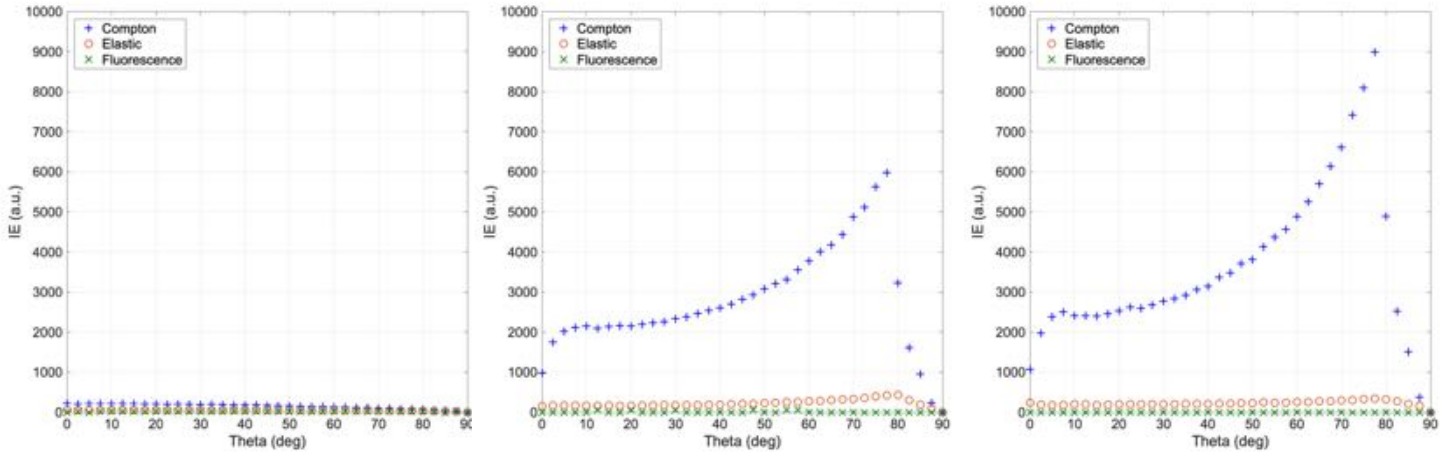

(a) (b) (c)

Figure D. 4 Image brightness as integrated energy of 5 cm thick carbon and 2 mm thick aluminium barrier on top at 25 keV (a), 150 keV (b) and 500 keV (c). Image brightness is plotted for Compton scatter (blue crosses), elastic scatter (red circles), and fluorescence (green asterisks).

C-Fe

25 keV 150 keV 500 keV

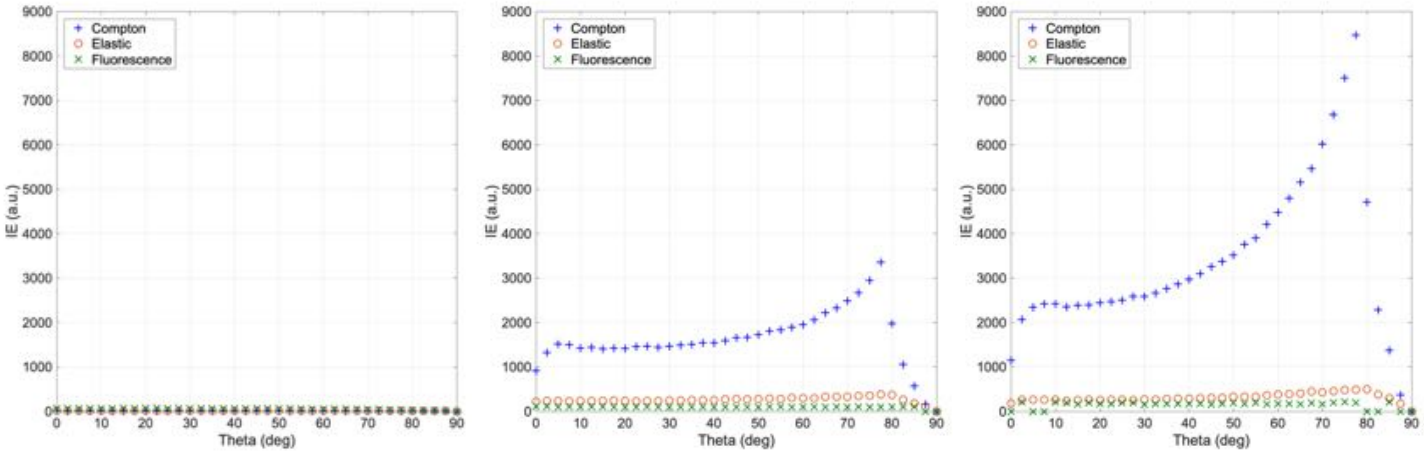

(a) (b) (c)

Figure D. 5 Image brightness as integrated energy of 5 cm thick carbon and 2 mm thick iron barrier on top at 25 keV (a), 150 keV (b) and 500 keV (c). Image brightness is plotted for Compton scatter (blue crosses), elastic scatter (red circles), and fluorescence (green asterisks).

D.5 Aluminium-1 mm thick

Al

25 keV 150 keV 500 keV

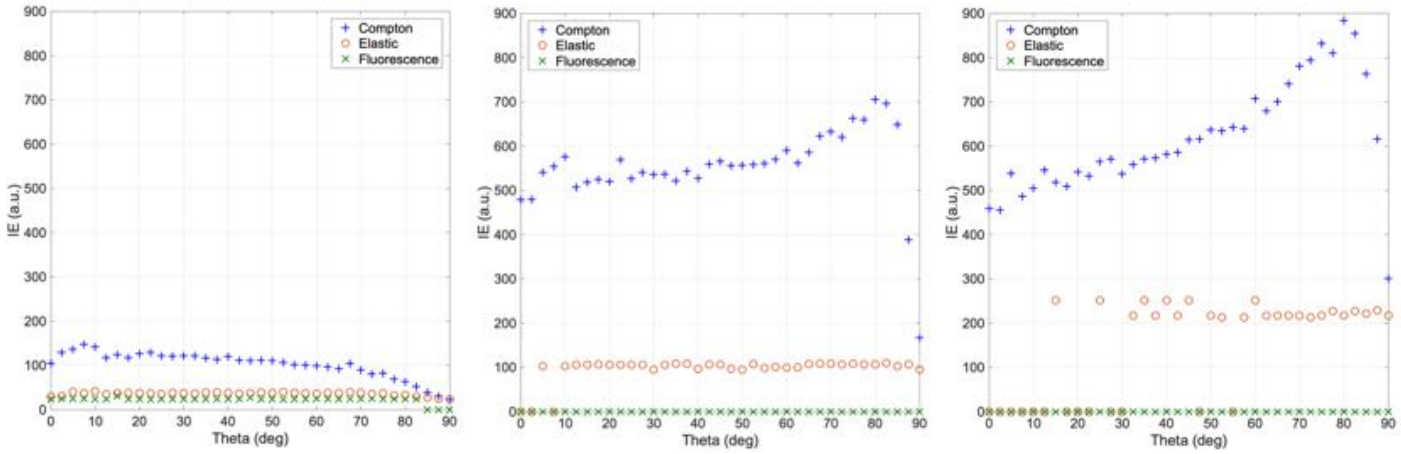

(a) (b) (c)

Figure D. 6 Image brightness as integrated energy of 1 mm thick aluminium at 25 keV (a), 150 keV (b) and 500 keV (c). Image brightness is plotted for Compton scatter (blue crosses), elastic scatter (red circles), and fluorescence (green asterisks).

D.6 Iron-1 mm thick

Fe

25 keV 150 keV 500 keV

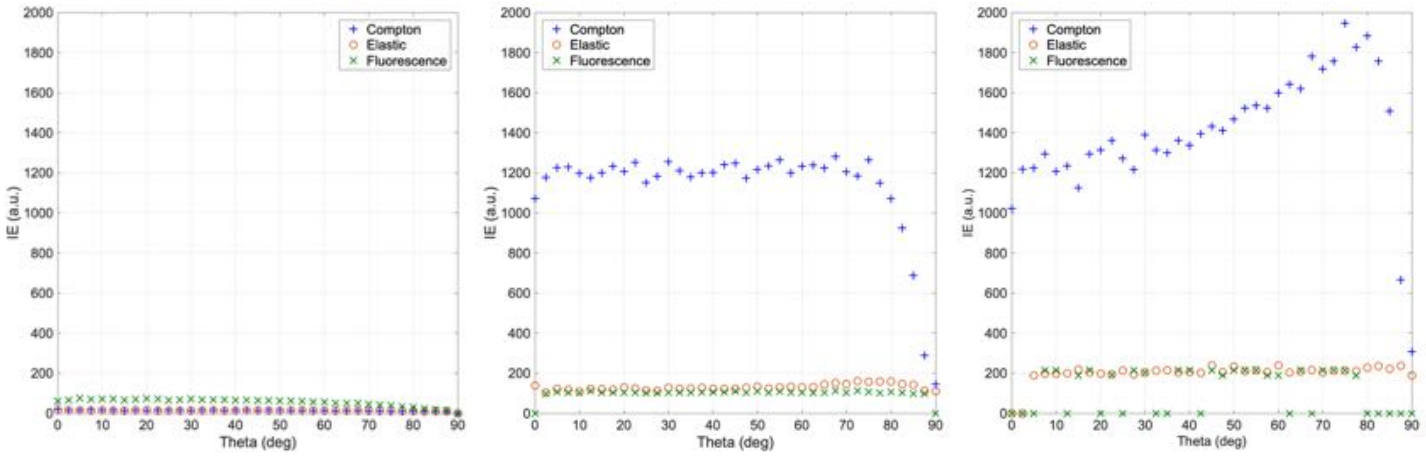

(a) (b) (c)

Figure D. 7 Image brightness as integrated energy of 1 mm thick iron at 25 keV (a), 150 keV (b) and 500 keV (c). Image brightness is plotted for Compton scatter (blue crosses), elastic scatter (red circles), and fluorescence (green asterisks).

D.7 Copper-1 mm thick

Cu

25 keV 150 keV 500 keV

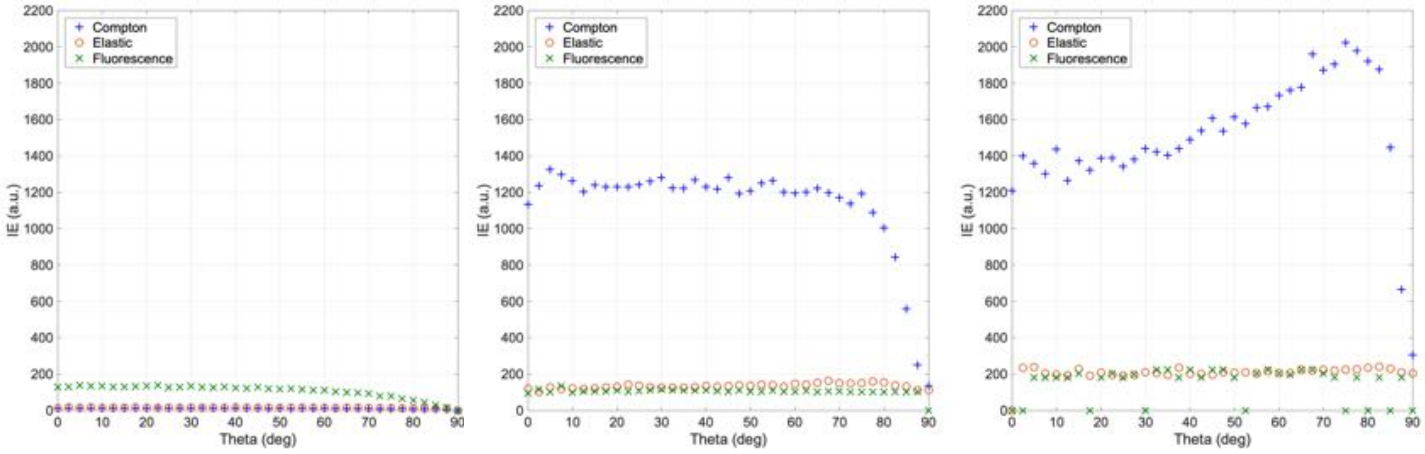

(a) (b) (c)

Figure D. 8 Image brightness as integrated energy of 1 mm thick copper at 25 keV (a), 150 keV (b) and 500 keV (c). Image brightness is plotted for Compton scatter (blue crosses), elastic scatter (red circles), and fluorescence (green asterisks).

D.8 Copper -1 mm thick (45˚) rotated

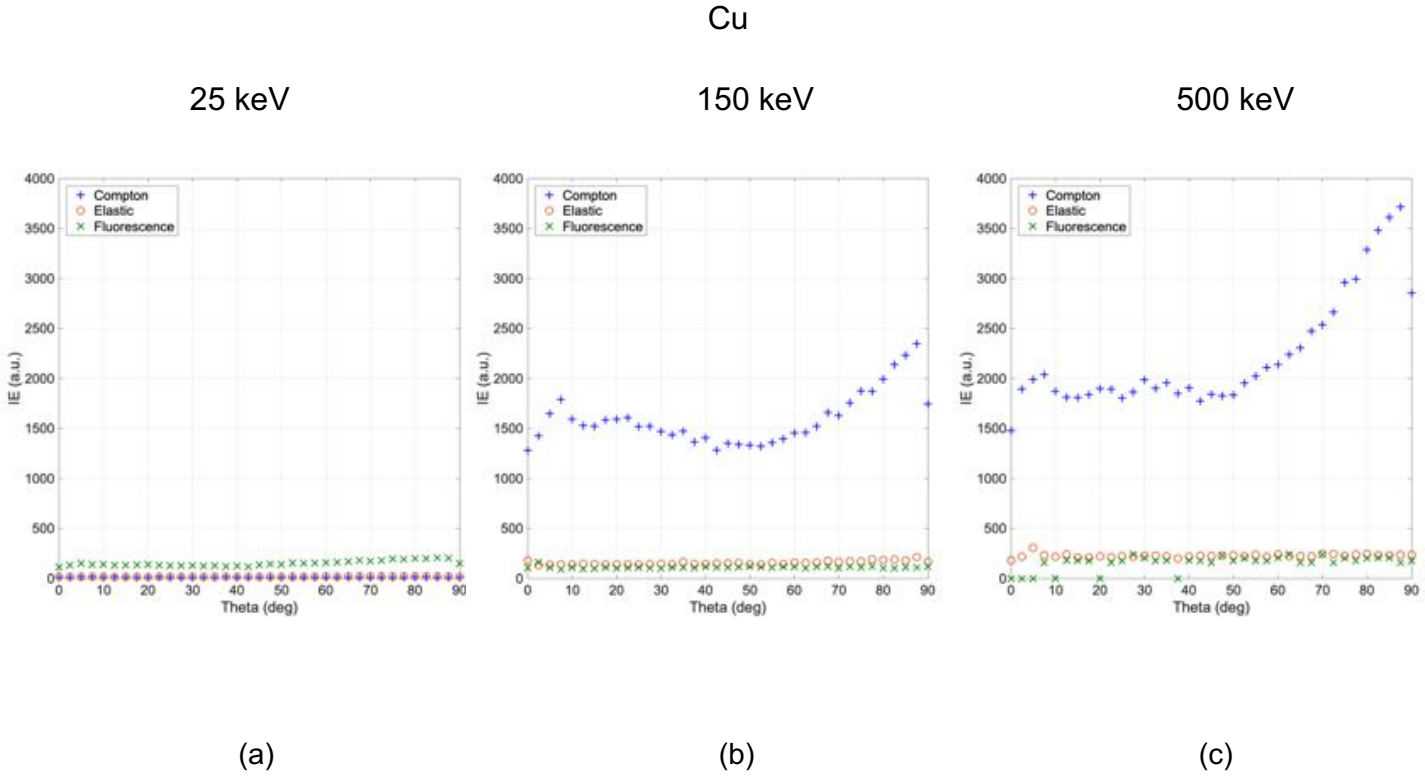

Figure D. 9 Image brightness as integrated energy of 1 mm thick 45˚ rotated copper at 25 keV (a), 150 keV (b) and 500 keV (c). Image brightness is plotted for Compton scatter (blue crosses), elastic scatter (red circles), and fluorescence (green asterisks).

D.9 Copper -50 mm thick

Cu

25 keV 150 keV 500 keV

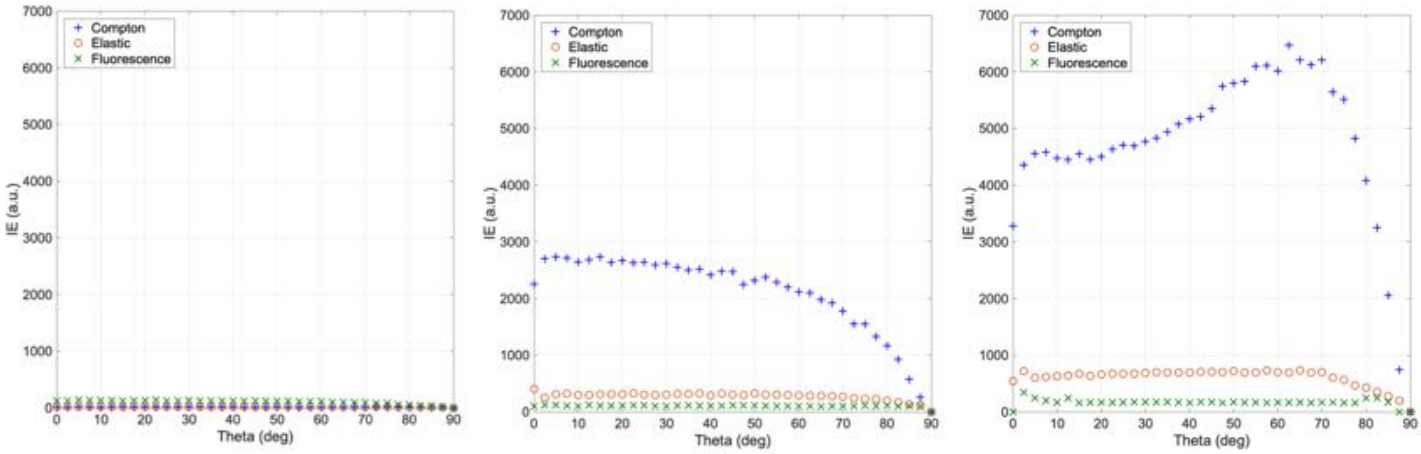

(a) (b) (c)

Figure D. 10 Image brightness as integrated energy of 5 cm thick copper at 25 keV (a), 150 keV (b) and 500 keV (c). Image brightness is plotted for Compton scatter (blue crosses), elastic scatter (red circles), and fluorescence (green asterisks).

D.10 Copper -50 mm thick and 2 mm barrier

Al-Cu

25 keV 150 keV 500 keV

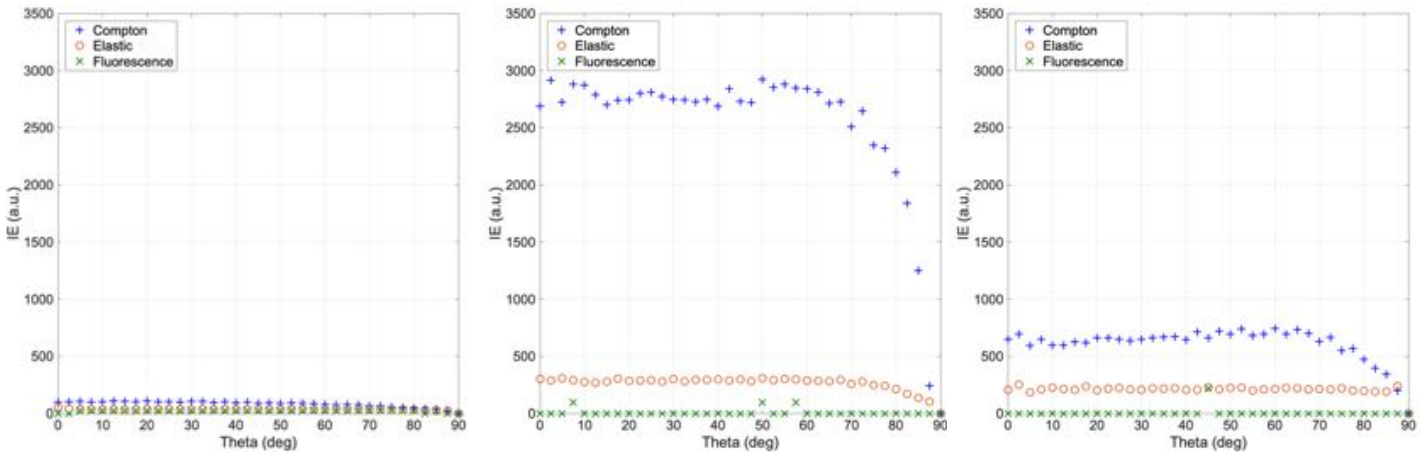

(a) (b) (c)

Figure D. 11 Image brightness as integrated energy of 5 cm thick copper and 2 mm thick aluminium barrier on top at 25 keV (a), 150 keV (b) and 500 keV (c). Image brightness is plotted for Compton scatter (blue crosses), elastic scatter (red circles), and fluorescence (green asterisks).

Fe-Cu

25 keV 150 keV 500 keV

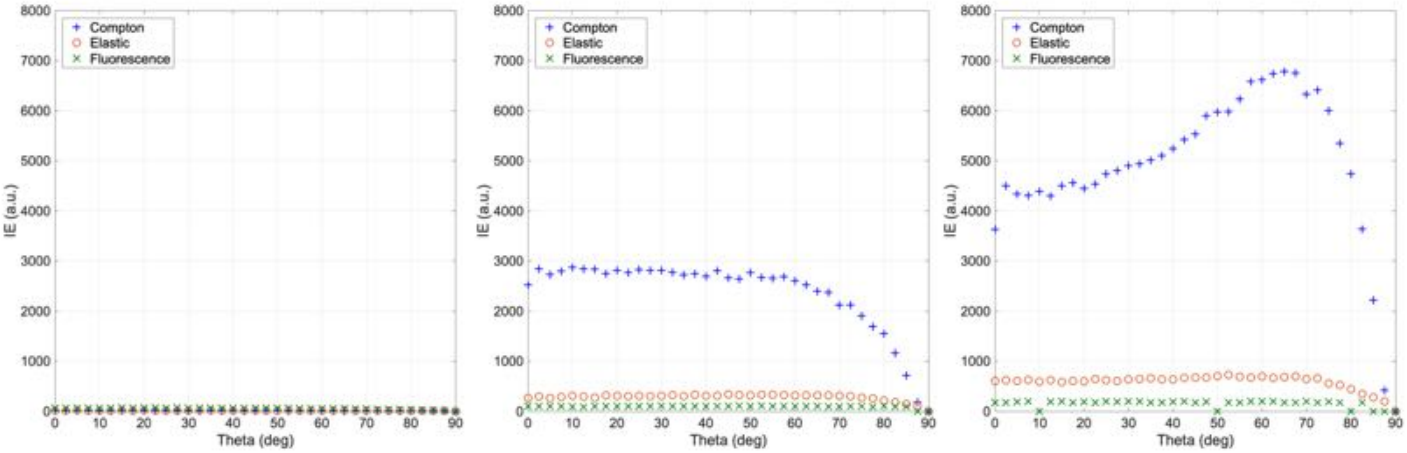

(a) (b) (c)

Figure D. 12 Image brightness as integrated energy of 5 cm thick copper and 2 mm thick iron barrier on top at 25 keV (a), 150 keV (b) and 500 keV (c). Image brightness is plotted for Compton scatter (blue crosses), elastic scatter (red circles), and fluorescence (green asterisks).

D.11 Manganese dioxide -1 mm thick

MnO2

25 keV 150 keV 500 keV

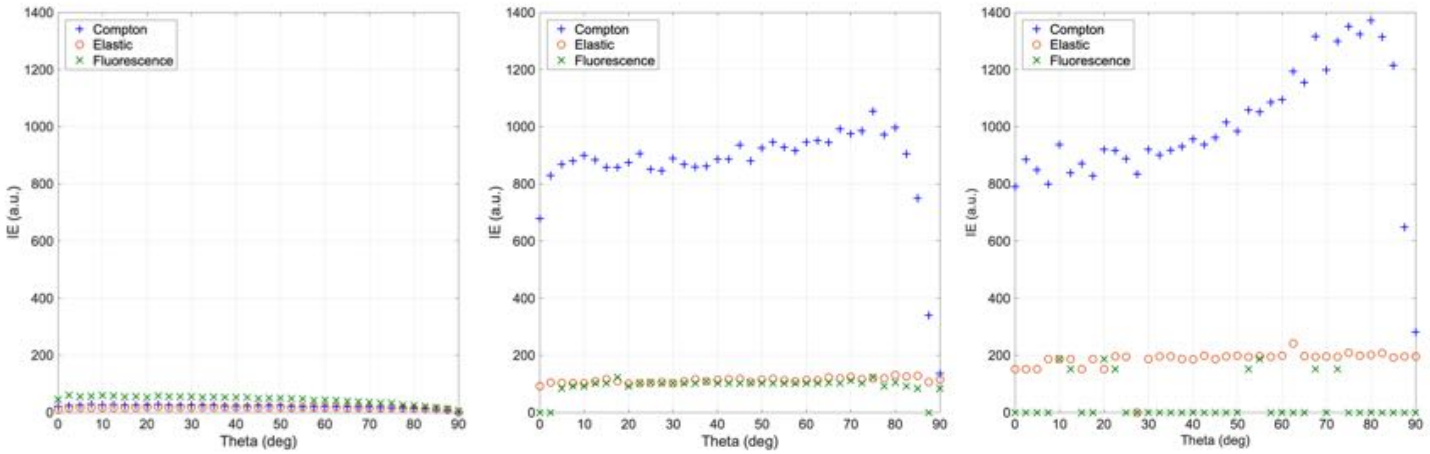

(a) (b) (c)

Figure D. 13 Image brightness as integrated energy of 1 mm thick manganese dioxide at 25 keV (a), 150 keV (b) and 500 keV (c). Image brightness is plotted for Compton scatter (blue crosses), elastic scatter (red circles), and fluorescence (green asterisks).

D.12 Manganese dioxide -1 mm thick (45˚) rotated

MnO2

25 keV 150 keV 500 keV

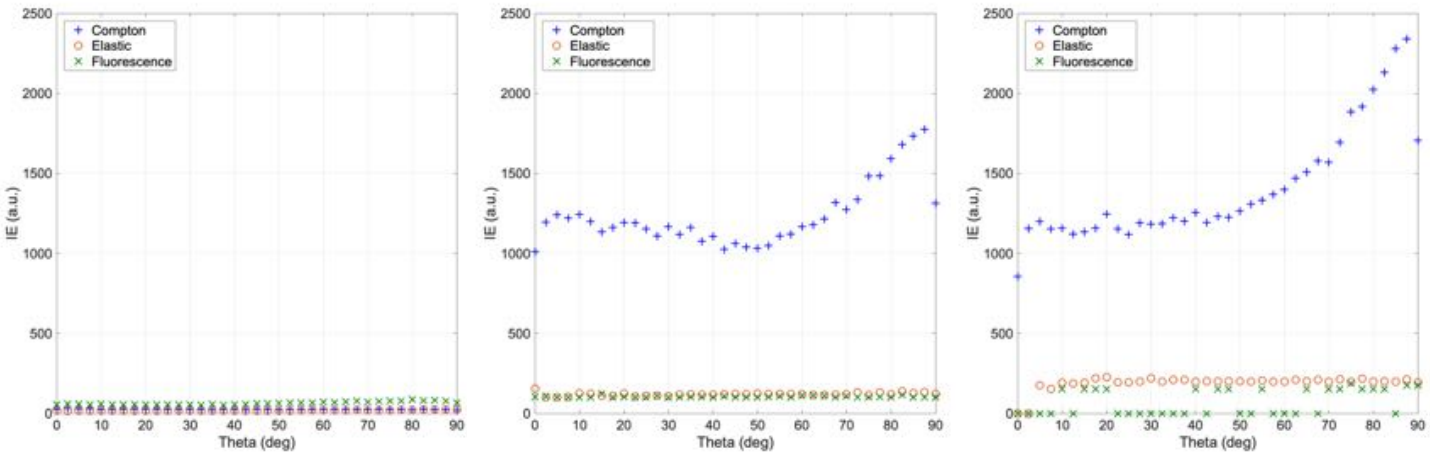

(a) (b) (c)

Figure D. 14 Image brightness as integrated energy of 1 mm thick 45˚ rotated manganese dioxide at 25 keV (a), 150 keV (b) and 500 keV (c). Image brightness is plotted for Compton scatter (blue crosses), elastic scatter (red circles), and fluorescence (green asterisks).

D.13 Manganese dioxide -50 mm thick

MnO2

25 keV 150 keV 500 keV

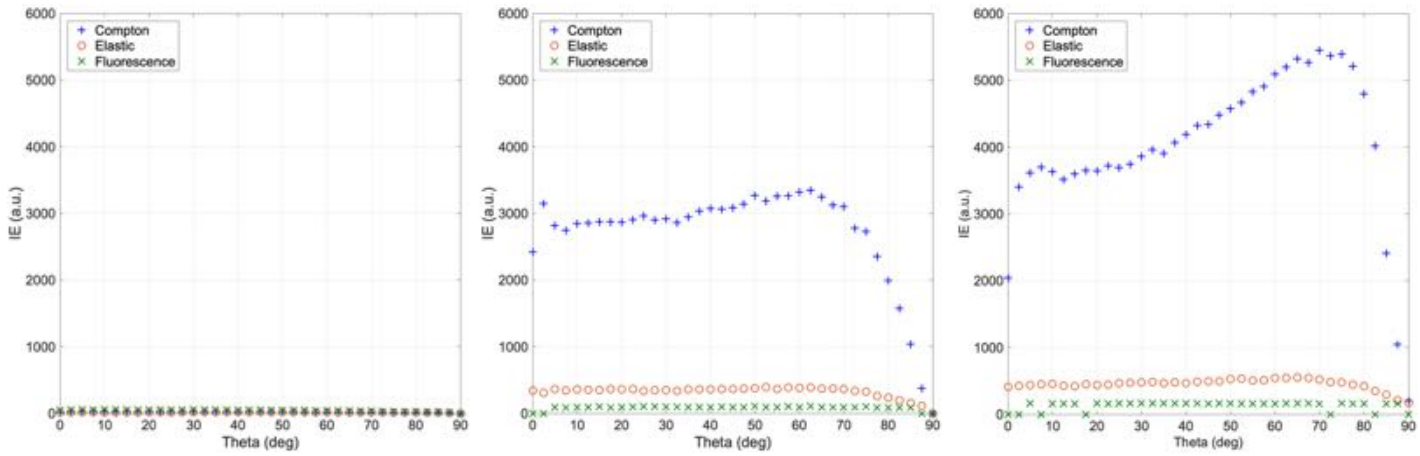

(a) (b) (c)

Figure D. 15 Image brightness as integrated energy of 5 cm thick manganese dioxide at 25 keV (a), 150 keV (b) and 500 keV (c). Image brightness is plotted for Compton scatter (blue crosses), elastic scatter (red circles), and fluorescence (green asterisks).

D.14 Manganese dioxide -50 mm thick and 2 mm barrier

Al-MnO2

25 keV 150 keV 500 keV

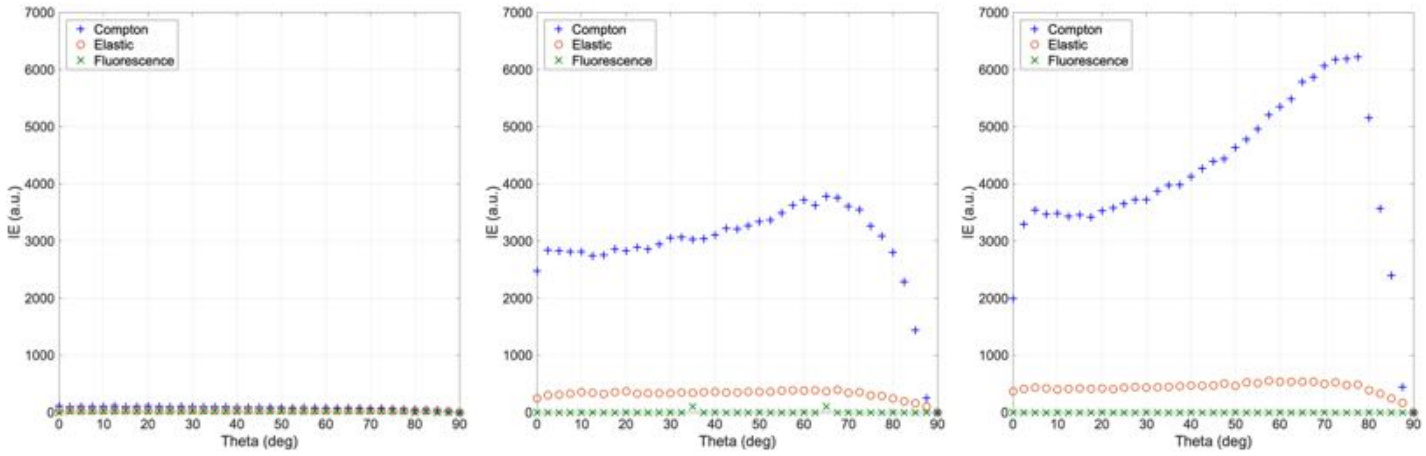

(a) (b) (c)

Figure D. 16 Image brightness as integrated energy of 5 cm thick manganese dioxide and 2 mm thick aluminium barrier on top at 25 keV (a), 150 keV (b) and 500 keV (c). Image brightness is plotted for Compton scatter (blue crosses), elastic scatter (red circles), and fluorescence (green asterisks).

Fe-MnO2

25 keV 150 keV 500 keV

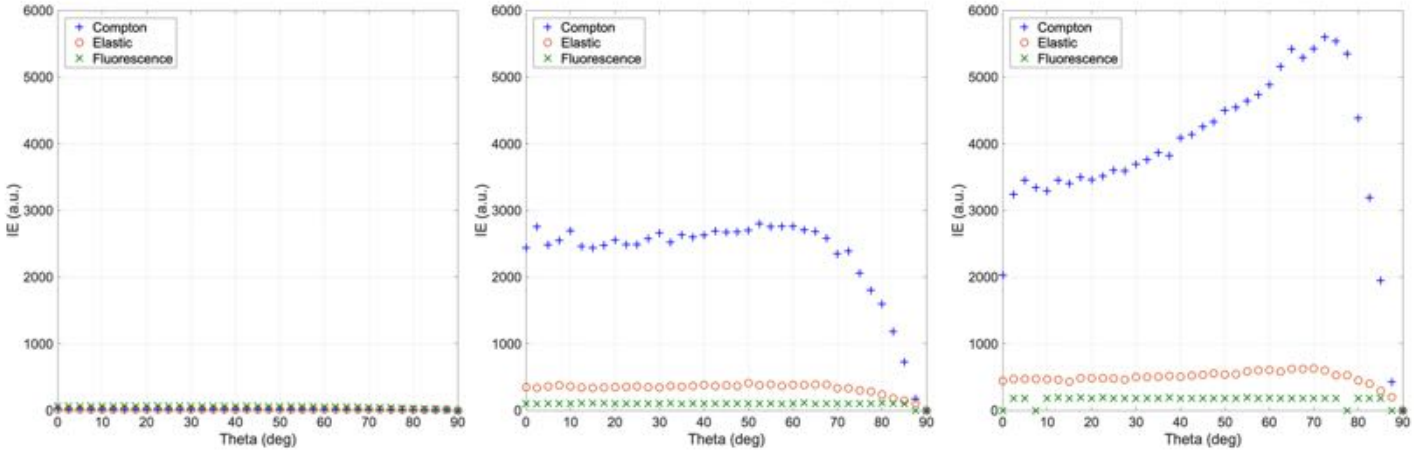

(a) (b) (c)

Figure D. 17 Image brightness as integrated energy of 5 cm thick manganese dioxide and 2 mm thick iron barrier on top at 25 keV (a), 150 keV (b) and 500 keV (c). Image brightness is plotted for Compton scatter (blue crosses), elastic scatter (red circles), and fluorescence (green asterisks).

D.15 Lead -1 mm thick rotated

Pb

25 keV 150 keV 500 keV

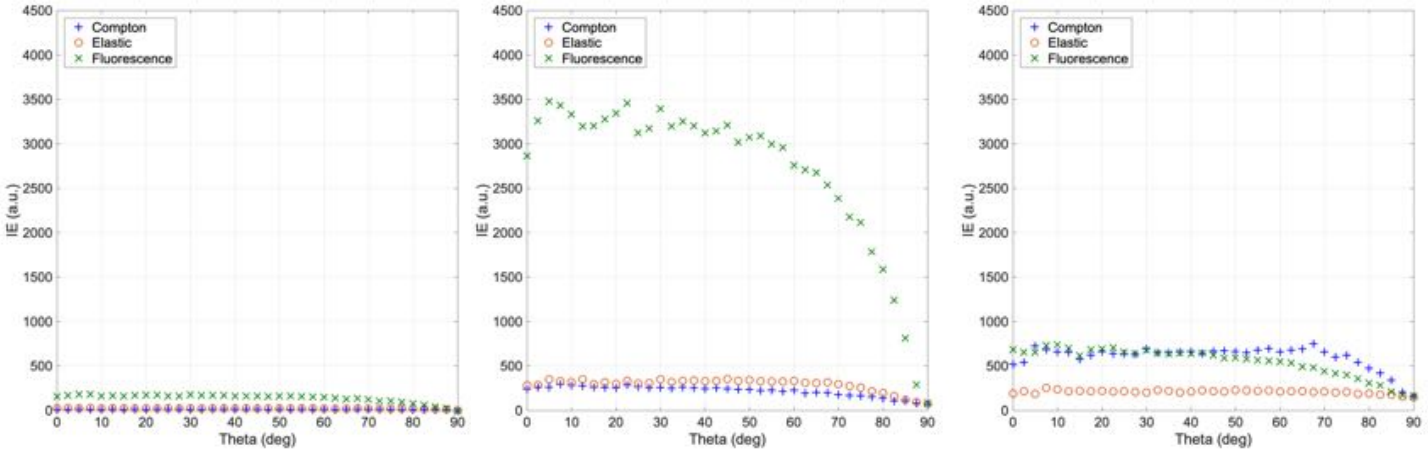

(a) (b) (c)

Figure D. 18 Image brightness as integrated energy of 1 mm thick lead at 25 keV (a), 150 keV (b) and 500 keV (c). Image brightness is plotted for Compton scatter (blue crosses), elastic scatter (red circles), and fluorescence (green asterisks).

D.16 Lead -1 mm thick (45˚) rotated

Pb

25 keV 150 keV 500 keV

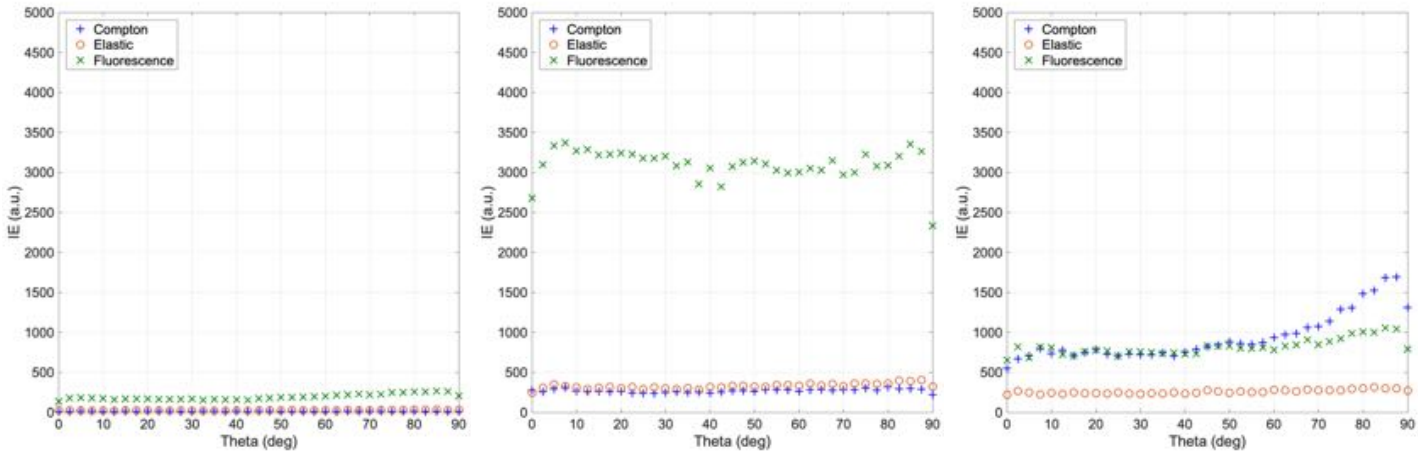

(a) (b) (c)

Figure D. 19 Image brightness as integrated energy of 1 mm thick 45˚ rotated lead at 25 keV (a), 150 keV (b) and 500 keV (c). Image brightness is plotted for Compton scatter (blue crosses), elastic scatter (red circles), and fluorescence (green asterisks).

D.17 Lead – 50 mm thick

Pb

25 keV 150 keV 500 keV

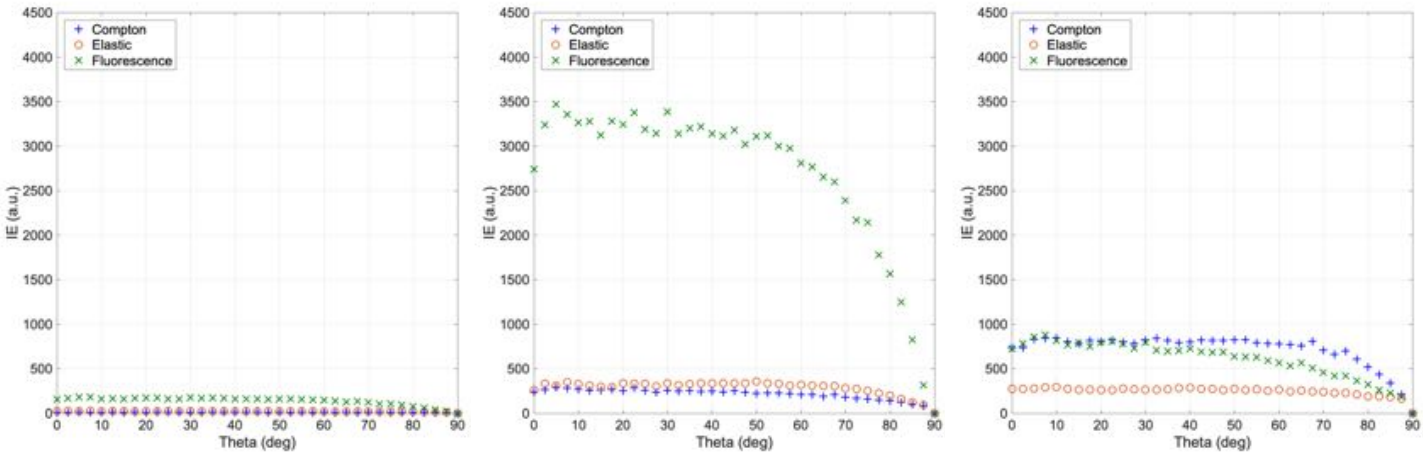

(a) (b) (c)

Figure D. 20 Image brightness as integrated energy of 5 cm thick lead at 25 keV (a), 150 keV (b) and 500 keV (c). Image brightness is plotted for Compton scatter (blue crosses), elastic scatter (red circles), and fluorescence (green asterisks).